NUMERICAL SIMULATION OF SPRAY PROCESSES IN DIESEL ENGINES

by

Demetrios Clerides
Dipl. Mech. Eng.

Thesis submitted for the degree of
Doctor of Philosophy of the University of London
and for
the Diploma of Imperial College

Mechanical Engineering Department
Imperial College of Science, Technology and Medicine
London SW7

May 1997

To those who run
to catch up with the sun

Abstract

This study deals with the mathematical modelling and numerical simulation of Diesel sprays. Particular emphasis is given to the improvement, extension and validation of an existing methodology which is of the Eulerian/Lagrangian kind.

The gas phase Favre-averaged transport equations governing the conservation of mass, species, momentum and energy, expressed in the Eulerian continuum framework, are deduced from the corresponding equations describing the flow field of a system with an arbitrary number of phases. Emphasis is given to the coupling between the phases accounting for the presence of the liquid phase to the maximum extent possible. The closure of the gas phase modelling is achieved via the k-ε turbulence model.

The spray is modelled by the Lagrangian approach in which it is represented by parcels containing a number of identical droplets. The behaviour of each parcel is described by a set of differential equations for the conservation of mass, momentum and energy. Representation of multicomponent fuels is also allowed by developing an efficient, in terms of computational requirements, profile method for solving the one-dimensional conduction and diffusion equations within the droplet. Additional modelling simulates other spray physical processes including cavitation, atomisation, breakup, collision among droplets and impingement on the wall.

The numerical solution of the continuum phase is achieved by an existing finite volume method applied to body-fitted unstructured meshes with moving boundaries, composed of hexahedral control volumes. The discretised gas equations are solved by the LONG-PISO predictor-corrector procedure which also incorporates the spray equations. Local restructuring of this procedure is introduced to handle high-load cases.

The overall method is assessed by reference to experimental data on single droplets, sprays under atmospheric and high pressure and temperature conditions and a DI Diesel engine at several operating conditions. Sensitivity studies on spatial and temporal resolution as well as model parameters are performed. The methodology is successful in extreme applications with high loads, large time steps and fine meshes in which it used to fail. Also, the physical processes are reasonably well predicted compared with the measured data.

Acknowledgements

I would like to express my sincere gratitude to my supervisor, Prof. A. D. Gosman, for his expert guidance and constructive criticism as well as for being a constant source of inspiration, throughout the duration of this study. His thorough reading of the present thesis and his valuable suggestions are highly appreciated.

I wish to thank all the past and present members of the 'SPEED' group, with whom I shared the responsibility and pleasure of developing an advanced scientific tool for industrial use. My special thanks are due to Mr. P. Theodossopoulos and Dr. D. Leskovšek who guided me during the first stages of my research and were always willing to support me in and out of the office. Dr. D. Leskovšek has also kindly allowed me to reproduce from his Ph.D. thesis the discretised equations in LaTeX format which I modified for the requirements of the present thesis.

During my research, I have greatly benefited from numerous discussions held with Mr. H. G. Weller.

My thanks are also due to Mrs. N. Scott-Knight for the arrangement of many administrative matters.

I am indebted to all my friends with whom I shared my good and bad times throughout the duration of this study. Their moral support during times of difficulty is deeply appreciated.

Finally, I take the opportunity to acknowledge the financial support provided by the European Council for Automotive Research and Development (EUCAR), i.e. Fiat, Peugeot SA, Renault, Rover, Volkswagen and Volvo, joined by the Swedish National Board for Industrial and Technical Development (NUTEK) and the Austrian Research Promotion Fund (FFF), within the framework of the JOULE II Programme (Subprogramme: Energy Conservation and Utilisation), funded by the European Commission. I am also grateful for additional funds made available by the A. G. Leventis Foundation. Partial funding provided by the European Gas Turbines Ltd. and the Commission of the European Community (CEC) is also acknowledged.

Contents

List of tables

List of Figures

Nomenclature

Latin characters

$\mathcal{A}$	matrix coefficient
$\mathbf{A}$	matrix coefficient
a	coefficient
B	coefficient; transfer number
Bi	Biot number
$\mathbf{b}$	source term of vector equation
b	source term of scalar equation
$\mathcal{C}$	convective flux
$\mathbf{C}$	work of external surface forces vector
C	coefficient; contraction area ratio
Co	Courant number
c	coefficient; specific heat capacity
$\mathcal{D}$	diffusion flux coefficient; mass diffusivity
$\mathbf{D}$	rate-of-strain tensor
D	diameter
$\mathbf{d}$	diffusion flux vector
d	derivative
$\mathcal{E}$	squared diameter normalised by the initial diameter
E	constant; efficiency of (collision etc.); specific total energy
$\mathbf{e}$	unit vector
e	specific internal energy
$\mathcal{F}$	correction factor
F	cumulative distribution function; factor; force; total flux; wall function
f	cell face; local direction in cell
G	turbulence generation rate
$\mathbf{g}$	gravity acceleration vector
h	heat transfer coefficient
$\mathcal{I}$	imaginary part of the roots of the characteristic equation
$\mathbf{I}$	unit tensor
$\mathbf{j}$	diffusion flux vector
j	imaginary unit
K	coefficient

k	thermal conductivity coefficient; turbulence kinetic energy
L	large number; latent heat of vapourisation; length; length scale
Le	Lewis number
M	molecular weight; number of droplets
m	mass
$\mathcal{N}$	discretised nabla (∇) operator
N	number of (cells, components, droplets etc.)
Nu	Nusselt number
$\mathbf{n}$	normal vector
Oh	Ohnesorge number
P	probability; viscous sublayer resistance factor
Pe	Peclet number
Pr	Prandtl number
p	probability density function; thermodynamic pressure
$\mathcal{Q}$	dimensionless heat
Q	heat; volumetric flow
$\mathbf{q}$	heat flux vector
q	heat flux
$\mathcal{R}$	ratio of evaporation rates; real part of the roots of the characteristic equation
$\mathbf{R}$	rotation matrix
R	gas constant; radius; residual
Re	Reynolds number
$\mathbf{r}$	position vector; random unit vector
r	normalised residual
$\mathcal{S}$	surface vector
$\mathbf{S}$	source term of vector equation
S	boundary of control volume; source term of scalar equation
Sc	Schmidt number
Sh	Sherwood number
St	Strouhal number
$\mathbf{T}$	shear stress tensor
T	absolute temperature; period
$\mathbf{t}$	unit vector
t	time
U	average injection velocity
$\mathbf{u}$	velocity vector
u	velocity
V	volume
We	Weber number
w	weighting factor
$\mathbf{x}$	position vector
Y	number; species mass fraction
y	distance
Z	compressibility factor

Greek characters

α	angle; coefficient; thermal diffusivity
β	coefficient
Γ	diffusivity coefficient
γ	ratio of specific heats, c_p/c_v
Δt	time step
δ	Dirac function; thickness
δt	subcycling time step
$\delta\tau$	dimensionless time step
ε	thickness; turbulence dissipation rate
ζ	dimensionless radius
η	coefficient
Θ	dimensionless temperature
ϑ	void fraction
θ	angle
κ	von Kármán's constant; wavenumber
λ	eigenvalue; friction factor; interpolation factor; small number
μ	dynamic viscosity
ν	collision frequency; kinematic viscosity
π	Ludolf's number
ρ	density
$\boldsymbol{\sigma}$	stress tensor
σ	Prandtl/Schmidt number; standard deviation; surface tension coefficient
$\boldsymbol{\tau}$	shear stress vector
τ	dimensionless time; relaxation time; shear stress; time scale
Φ	dimensionless turbulence energy spectrum; equivalence fuel/air mass ratio
ϕ	general fluid field property
χ	correction factor; mole fraction
ω	dimensionless radius; exponential growth rate

Subscripts

0	initial
A	atomisation
a	average
b	boiling; boundary; breakup
$boun$	bouncing
c	cell; convergence; critical; engine cycle; liquid core; residence

cav	cavitation
ch	chamber
$coal$	coalescence
$crit$	critical
cyl	bulk cylinder value
d	discharge; drag; droplet; liquid
e	eddy; related to specific internal energy
$eddy$	eddy
eff	effective
f	cell face; film; local direction; value at the cell face
i	running index
inj	injection conditions
int	interaction
j	running index
k	related to turbulence kinetic energy
l	lift; liquid; running index
$Leid$	Leidenfrost
M	mass
m	mean; molecular; related to mass
$mean$	mean
mix	mixture
N	neighbouring cell
NN	neighbouring cell of a neighbouring cell
n	normalisation
osc	oscillation
$\mathcal{P}$	implicit part of source term
P	cell; point
p	constant pressure; parcel; related to profile method
r	random; relative
rms	root mean square
ref	reference
S	Saffman
s	secondary; surface
spl	splashing
st	stable
T	heat; related to temperature
t	turbulent
tr	transit
$\mathcal{U}$	explicit part of source term
$\mathbf{u}$	related to momentum
u	underrelaxation
v	constant volume; fuel vapour; valve
W	wall
w	wall; wave
Y	related to species

ε	related to turbulence dissipation rate
σ	surface tension
ϕ	related to general fluid field property

Superscripts

b	boundary
c	cross-diffusion (non-orthogonal) contribution
d	related to liquid
e	related to specific internal energy
i	value at the i^{th} subcycling time step
j	algebraic corrector step
k	corrector step; related to turbulence kinetic energy
n	(orthogonal) diffusion contribution; new
o	old-time value
P	related to cell P
S	related to SFCD
T	transposition
$\mathbf{u}$	related to momentum
Y	related to species
ε	related to turbulence dissipation rate
ϕ	related to general fluid field property
$'$	fluctuation about Reynolds mean value; relative
$''$	fluctuation about density-weighted (Favre) mean value
$(\prime)$	intermediate value
$+$	correction; dimensionless
$*$	friction

Symbols

∂	partial derivative
∇	nabla operator
$\cdot$	scalar product
$:$	double dot tensor product
$\hat{\psi}$	instantaneous value
$\overline{\psi}$	average; normalised; Reynolds mean value
$\widetilde{\psi}$	density-weighted (Favre) mean value
$\dot{\psi}$	rate of change

Abbreviations

ABDC	after bottom dead centre

ATDC	after top dead centre
BBDC	before bottom dead centre
BDC	bottom dead centre
BiCG	bi-conjugate gradient
BTDC	before top dead centre
CA	crank angle
CARS	coherent anti-Stokes Raman spectroscopy
CCD	charge coupled devices
CD	central differencing
CEM	cumulative evaporated mass
CFD	computational fluid dynamics
CG	conjugate gradient
CI	compression-ignition
DDM	discrete droplet method
DI	direct-injection
EOI	end of injection
EVC	exhaust valve closing
EVO	exhaust valve opening
FDM	finite difference method
FEM	finite element method
FVM	finite volume method
HWA	hot wire anemometry
IC	internal combustion
IDI	indirect-injection
IVC	intake valve closing
IVO	intake valve opening
LDA	laser Doppler anemometry
LDV	laser Doppler velocimetry
LHS	left-hand side
LIF	laser-induced fluorescence
LUD	linear upwind differencing
MDM	multidimensional model
PDA	phase Doppler anemometry
PDE	partial differential equation
PDF	probability density function
RHS	right-hand side
RMS	root mean square
rpm	revolution per minute
SFCD	self-filtered central differencing
SI	spark-ignition
SMD	Sauter mean diameter
SOI	start of injection
TDC	top dead centre
UD	upwind differencing
VCO	valve-covered orifice

Chapter 1

Introduction

1.1 Background

The first working Internal Combustion (IC) engine dates back to the late 19^{th} century. In 1876, N. Otto presented his prototype four-stroke spark-ignition (SI) engine. While a number of engineers were trying to improve the characteristics (efficiency, power etc.) of the SI engine of Otto, R. Diesel outlined in his patent, in 1892, a new concept of initiating combustion by injecting a liquid fuel into air heated solely by compression. The compression-ignition (CI) engine gave double the efficiency of other internal combustion engines. In the 20^{th} century, internal combustion engines have played the dominant role in transportation (land, sea, air) mainly, because competition among manufacturers has resulted in improvements in respect of efficiency as well as cost, rendering the internal combustion engine affordable by 'ordinary' people. Rapid development was performed during World War II, when the involved countries realised the necessity to invent new technologies and materials, giving them the advantage of increased power.

Although the IC engines are serving mankind and have become an important and useful tool not only in transportation but also in power plants, they create some negative effects as well. The most important effect is air pollution, which became apparent in the 1940's in Los Angeles. It was demonstrated by Haagen-Smit

[116]* that the smog problem resulted from reactions between oxides of nitrogen and hydrocarbon compounds in the presence of sunlight. The automobile is a major contributor to hydrocarbon and oxides of nitrogen emissions as well as carbon monoxides in urban areas [131]. Diesel engines are also a significant source of small soot or smoke particles. Consequently, emission standards for automobiles were introduced in the early 1960's, first in California and then nationwide in the United States as well as in Europe and Japan. Another negative effect of IC engines is noise pollution and relevant legislation to reduce noise emissions was introduced in the early 1970's. Due to the stringent legislation on both air and noise pollution as well as the pressure from 'green' movements, manufacturers faced the problem of building engines which fulfill these requirements.

The oil crisis in the 1970's, when the price of crude petroleum rose rapidly made manufacturers see the development of high-fuel-exploitation engines as the only way to survive. The oil crisis emphasised the importance of both engine efficiency and ability to work with fuels of different ignition qualities. This requirement is in favour of Diesel engines and their utilisation in passenger cars was envisaged.

The increasing stringency of the legislation regarding emission standards [16] provided the motivation to build engines with lower and lower emissions. The fact that in 1996, sixteen passenger cars emit as much as one passenger car in 1970 [259] is promising. However, the requirement for a better quality of life is endless and the target in the near future is the further reduction of the emissions† and increased fuel exploitation. These demands have inspired the present study, which deals with the simulation of sprays in Diesel engines.

The key role of the spray behaviour in mixing and combustion processes in Diesel engines is obvious and for their further improvement, a detailed analysis of the spray processes is required. However, it became clear that the analysis provided

*The numbers in parentheses indicate the references at the end of the thesis.

†It is worth mentioning that in 2003, 10 % of Californian vehicle sales are expected to be zero emissions vehicle [16].

by the old design tools, mainly consisting of empirical correlations based on measurements, sometimes combined with zero-dimensional analysis, was not sufficient. Consequently, new approaches, both experimental and computational, have been and are being developed. In this study, a three-dimensional analysis is used in order to provide detailed insight into the in-cylinder phenomena offering a useful tool for engine design.

In the following section, a general description of the CI engine is presented and some experimental and computational methods for the investigation of the main physical processes are discussed. A particular emphasis on spray modelling is given in Section 1.3, where modelling approaches are reviewed. The author's contribution is presented in Section 1.4 and finally, the thesis is outlined in Section 1.5.

1.2 Compression-ignition IC engines

Both CI and SI engines can be classified into four-stroke and two-stroke cycles. The former comprises an *induction stroke* which starts with the piston at top dead centre (TDC) and ends at bottom dead centre (BDC). During this stroke, fresh air is sucked into the cylinder, from the inlet valve orifice which opens shortly before the start of the stroke and closes after it ends (Heywood [131]). A *compression stroke* follows during which the piston moves towards TDC and compresses the air. Near TDC the fuel is injected and evaporates because of the high pressure and temperature of the surrounding air as well as the vigorous kinetic energy of the in-cylinder air created by the appropriate design of the bowl-in-piston shape (see Fig. 1.1). The mixture ignites and initiates combustion, which increases the pressure and pushes the piston downwards towards the BDC. During this *expansion stroke* the work done on the piston is about five times as much as the piston had to do during compression (Heywood [131]). As the piston approaches BDC the exhaust valve opens to initiate the exhaust process. The *exhaust stroke* follows which ends at TDC. During this, the burned gas exits the cylinder until the exhaust valve closes just after TDC. Meanwhile, the inlet valve opens as the piston approaches the TDC and the cycle is

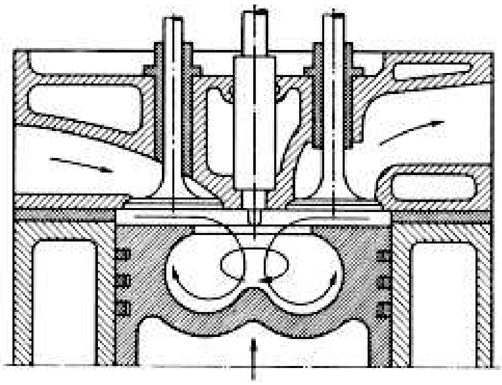

Figure 1.1: In-cylinder charge motion, taken from Kowalewicz [170].

repeated. The four-stroke cycle requires two crankshaft revolutions for each power stroke. A higher power output is obtained from the two-stroke cycle in which one power output corresponds to one revolution of the crankshaft.

CI engines can be subdivided into direct-injection (DI) and indirect-injection (IDI) types. In the former case, the fuel is injected directly into the cylinder (see Fig. 1.2) whereas in the latter, the fuel is injected into a prechamber connected to the cylinder via a nozzle (see Fig. 1.3). The DI concept was originally applicable

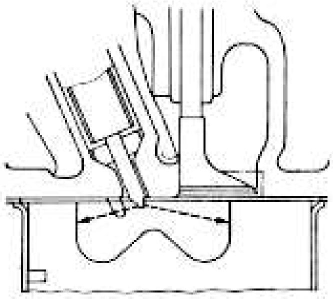

Figure 1.2: Direct-injection Diesel engine, taken from Kowalewicz [170].

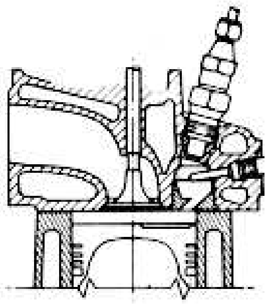

Figure 1.3: Indirect-injection Diesel engine with swirl prechamber, taken from Heywood [131].

to large engines, where the fuel momentum and energy are sufficient to provide adequate fuel distribution and mixing. In automobiles, where the engines are small and high speed is desired, the IDI concept was preferred, in which a vigorous charge motion is generated in the prechamber during compression, because air is forced from the main chamber into the auxiliary chamber (Heywood [131]). However, in recent years, small high-speed DI automobile engines have become attractive, especially for urban driving, owing to their lower fuel consumption compared to their IDI counterparts. In these engines, fast fuel-air mixing rates are achieved via air swirl. The latter is generated by the inlet port which is suitably designed and is then increased as it is forced into the piston bowl, due to angular momentum conservation. As will be seen in Chapter 6, such an engine is used for validation in the present study.

Many and complex physical phenomena are involved in the Diesel engine as listed below [47]:

- Turbulent air motion, shaped and controlled via the design of the inlet port(s) and combustion chamber.

- Fuel sprays, whose characteristics begin to be determined by the flow within the injector nozzle itself and the subsequent atomisation process.

- Fuel evaporation and vapour-air mixing, which are controlled both by the spray dynamics and the pre-injection air motion.

- Compression ignition, whose timing and location are determined by the chemical kinetics of the fuel, together with the prevailing concentration and temperature fields.

- Combustion, of an inhomogeneous fuel-air mixture with large variations in equivalence ratio and burning concentrated in very thin reaction zones called 'flamelets'.

- Emissions reactions within the flamelet zones and bulk gases leading to the net production of NO_x and particulates and involving additional complex chemistry.

Hereafter, a brief review on experimental and numerical methods for investigating the processes in IC engines will be presented.

1.2.1 Experimental methods

Experimental methods for flow measurements can be classified as local, global and visualisation. The last one provides qualitative results, usually in the form of photographs of the flow (with or without seeding particles); and the global methods give only overall information on the flow, for example, pressure trace in IC engines. By contrast, local methods provide details of the flow, for example velocity, temperature, pressure and concentration for multicomponent flows, at individual locations and therefore, they are of particular interest to this study. Indeed, such details are of vital importance in assessment the modelling of individual physical processes.

In the 1950's hot wire anemometry (HWA) was firstly used to measure instantaneous velocities and despite its problems (regarding the calibration and the restricted application due to limitations on the wire diameter) is still used (Hinze [133]). However, nowadays, the most widely-applied method for measuring mean and fluctuating velocities is the laser Doppler anemometry (LDA)* (see Arcoumanis and Whitelaw [22]). Laser-based techniques are accurate and non-intrusive. However, optical access is necessary and modifications or reconstructions of the apparatus, in which the considered flow takes place, are often required. For engine measurements, a transparent piston and/or liner are utilised.

Species concentrations and temperature are measured with Rayleigh scattering, Raman scattering, laser-induced fluorescence (LIF), or coherent anti-Stokes Raman spectroscopy (CARS) techniques (Taylor [284], Maly [193]).

Droplet velocities in sprays are also measured by LDA. Phase Doppler anemometry (PDA), which is an extension of LDA, allows simultaneous measurement of droplet size and velocity for a known fuel refractive index. However, in high shearing regions, as is the case in Diesel sprays, the droplets are non-spherical and they are measured by PDA as droplets with diameter of the order of the large axis of the ellipses and bias the mean diameters towards larger values (Alexander *et al.* [8]). Also, in dense spray regions, they fail because these are not sufficiently transparent

*Laser Doppler anemometry is also called laser Doppler velocimetry (LDV).

to the laser beams. Nevertheless, these techniques are regarded as the most accurate and they are widely used.

Further informations on experimental methods applied to IC engines can be found in Arcoumanis and Whitelaw [22], Taylor [284] and Maly [193].

1.2.2 Computational methods

Computational methods for Diesel engine simulation are based on mathematical description, so-called *modelling*, of the physical processes that take place. A number of assumptions are necessary in order to reduce the complexity of the mathematical description. Two main categories can be distinguished, namely the *phenomenological* and the *multidimensional* (MDM) [105] models. The phenomenological comprise the zero-dimensional and one-dimensional models. The former ignore spatial variations and estimate only temporal engine variations based on thermodynamic cycle simulation. The one-dimensional models take also into account spatial variations on the direction of piston motion, however, ignoring the other two based on assumptions. In contrast, the MDMs take into account variations on all the spatial directions and therefore, are much more complex. However, they provide detailed analysis of the temporal and spatial flow distribution and in this sense, the mathematical model approximates the real processes to the acceptable level of accuracy.

MDMs consist of sets of coupled partial differential equations (PDEs). The solution of this set can sometimes be obtained analytically but under a number of simplifying assumptions and only in special cases. In general, the PDEs must be solved by numerical methods, which discretise the solution domain into a finite number of subdomains and approximate the PDEs by a system of algebraic equations linking the variables in these subdomains. Various approaches of this kind have been developed notably, the finite difference method (FDM) [267], the finite element method (FEM) [64] and the finite volume method (FVM) [228]. The last one is particularly suitable for fluid dynamics problems because it guarantees conservation of mass, momentum and energy in any subdomain. The SIMPLE [228] and the

PISO [145, 146] solution strategies for solving the system of the transport equations are the most commonly employed.

Multidimensional calculations in IC engines were performed for the first time in 1973 by Watkins [300] who simulated the laminar flow in an idealised axisymmetric engine without valves. Three years later, Diwakar *et al.* [82] predicted the two-dimensional inviscid flow and temperature field in an engine with intake and exhaust ports. In 1977, Watkins [301] extended his work to three-dimensional calculation of turbulent engine flow, in the absence of combustion. Two years later, the first combustion calculations in engines were reported by Butler *et al.* [56]. Since then, a number of numerical studies of engine flows have been performed* such as, for example Gosman and Johns [109], Gosman [104], Takenaka *et al.* [281], Adamson *et al.* [2], Gonzalez *et al.* [102] and Theodorakakos and Bergeles [287] among others. In recent years, progress in computer technology, in conjunction with accumulated experience on both numerical methods and physical processes in IC engines has enabled the development of many computer codes capable with spray, autoignition and combustion calculations, for example, STAR-CD [69], FLUENT [98], SPEED [70, 110–112] and KIVA-3 [11] which is an improved version of KIVA-II [12] and its predecessors, KIVA [13] and CONCHAS [56] among others.

All these codes comprise various models which simulate the physical processes in an IC engine (see, for example, [33, 46, 102, 103, 152, 167, 183, 197, 230, 274, 277, 282, 302]), however, adequate agreement with experimental results is not always obtained. The main source of uncertainty in the flow field prediction is the turbulence model which is represented by a two-equation model based on the hypothesis of isotropy†. Furthermore, the spatial and temporal resolutions are not sufficient because they would increase the demand for computational resources beyond the acceptable for practical engineering problems. On the other hand, some physical processes, for example of spray, are not well understood yet and consequently, their modelling is not satisfactory. Further uncertainties are introduced by the necessary

*See Ahmadi-Befrui [5], Gosman [105] and Heywood [131] for review of early works.

†Recently, second-order closure has also been applied for a better representation (see Lebrère and Dillies [183]).

(in order to reduce the problem complexity and render the numerical model affordable in respect of computational resources) simplifying assumptions on which the modelling is based. Additional error sources consist of the numerical method and the solution algorithm. Finally, it is emphasised that experimental errors and uncertainties introduce additional weakness in the modelling of the physical processes.

At present, computational fluid dynamics (CFD) is not a totally reliable tool for engine evaluation and design. It nonetheless offers some advantages over experimental methods although in most cases experiments are still required to provide inputs to calculations. The main advantage of CFD is the ability to provide temporal and spatial informations of the flow, temperature and concentration fields in complex geometries in a reasonably short time and at relatively low cost. In addition, CFD offers the ability to isolate particular physical processes or parameters relevant to the application of interest.

Better CFD simulation of the physical processes in Diesel engines is required and it is the objective of the author to contribute in this effort. The particular target of this thesis is mainly, the improvement and extension of the spray modelling and secondly, the assessment of various submodels by reference of experimental data.

1.3 Spray modelling review

Two main approaches to the treatment of the phases in multiphase flow modelling can be distinguished. The first is the *locally-homogeneous* formulation, which treats multiphase flow as a single-phase flow with varying density due to variation of the phase concentrations. This treatment implies local kinematic and thermodynamic equilibrium, which requires infinite interphase transfer rates. The locally-homogeneous treatment was introduced by Thring and Newby [290] and was employed by Newman and Brzustowski [209] Khalil and Whitelaw [163], Shearer and Faeth [263], Shearer *et al.* [264] and Mao *et al.* [194] among others. According to Faeth [91], the locally-homogeneous treatment is limited to sprays with very small droplets, for which the interphase transport rates are very high and subsequently, local kinematic and thermodynamic equilibrium is almost assured. In contrast, when this approach is applied to practical sprays, such as those in Diesel engines, significant discrepancies with measurements are obtained (Faeth [94]).

The second category is the *separated-flow* analysis, which treats each phase separately, as its name implies and takes into account finite transfer rates between the phases. For the specific system of a gas and a liquid, which is of particular interest in this study, the liquid phase can be treated as *discrete* or *continuum*. The latter framework may be further subdivided into two ways of treating the liquid phase. In the one, it is treated as a second continuum phase, co-existing and interpenetrating with the gas phase (see Harlow and Amsden [120], Bracco [50]). In the second, the liquid phase is described by a multidimensional distribution function for which, a transport equation is solved. Williams [309] and Travis *et al.* [292] defined a general spray distribution function of eight dimensions, comprising the droplet size*, the three spatial coordinates, the three velocity components and the time. More recently, Amsden *et al.* [13] extended this function taking into account the droplet temperature and the fluctuating gas velocity. The disadvantage of this description is that it requires large computer storage space and computational time due to the large dimension of the distribution function (Haselman and Westbrook [122]).

The most widely used formulation for the simulation of liquid sprays in Diesel engines is the discrete method, often called *discrete droplet method* (DDM). This was firstly used in 1954 by El Wakil *et al.* [85] in the aerospace industry and its potential in Diesel engines was recognised by Borman and Johnson [48] in 1962. In the 1970's Crowe [72] and Crowe *et al.* [74] introduced modelling of the coupling between the two phases, which was later extended by Dukowicz [83] and O'Rourke [223]. Since then, the DDM has been comprehensively used for spray and particles simulation in engines, furnaces etc. (see e.g. Gosman *et al.* [108], Clerides *et al.* [65]). In DDM, the spray is represented by a finite number of computational

*The droplet size could be replaced by its mass because a unique relationship between these two properties was assumed. Note that the droplet temperature was not included and therefore, its density was constant (see Travis *et al.* [292]).

samples called *parcels*. Each parcel represents a number of droplets sharing the same properties (diameter, location, velocity, temperature etc.). The properties of the parcel are governed by ordinary differential conservation equations expressed in Lagrangian formulation. Empirical correlations are employed to estimate the inter-phase transfer rates of mass, momentum and energy between the droplets and the gas phase. Consequently, they influence the accuracy of the complete spray model. Also, submodels describing other physical processes, like deformation and breakup of the droplets and collisions between droplets, are incorporated in this method. Further modelling is required to describe additional physical processes taking place in Diesel sprays, such as cavitation in the injector nozzles, atomisation of the liquid jet and impingement of droplets on the walls and formation of liquid film there. All these processes are modelled individually and the submodels are assembled to describe the whole spray process. In the past two decades, substantial progress has been achieved in the modelling of the physical phenomena of spray. Detailed review of each phenomenon will be given in the introductory part of its description in Chapter 3 which presents the spray simulation.

The pros and cons of the continuum and discrete formulations are the subject of continual discussion among researchers and comparisons between the two approaches are reviewed and discussed by many authors (see e.g. Crowe [73], Gosman and Ioannides [107], Beshay *et al.* [39], Sirignano [266], Mostafa and Mongia [201]). A summary of their conclusions will now be described. Both formulations require very fine spatial discretisation in the injector vicinity to resolve steep gradients of the spray properties. However, in the continuum approach, this is necessary to avoid numerical diffusion of the liquid phase* as well. The latter results in unrealistic fuel vapour and gas temperature distributions, which in combustion cases, may lead to wrong ignition location with consequences on the predictions of all other fields. Also, in the continuum formulation, the spray equations must be solved in the whole

*Obviously, the numerical diffusion of the gas phase is the same for the two formulations because the same treatment is used for this phase. However, in Diesel sprays, the liquid velocity is much higher than that of the gas, in this region and consequently, the numerical diffusion of the liquid phase is dominant.

solution domain even though spray may only occupy a small fraction of this domain. In addition, this approach either assumes that the droplets are of the same size or requires a number of liquid phase equations (one for each size range) to be solved. By contrast in the discrete formulation, each droplet may have its own individual size without any effect on the computational time and storage space. Therefore, DDM not only requires lower computational resources but also is more accurate for Diesel spray calculations and consequently, it is adopted in this study.

1.4 Present contribution

This study is concerned with the simulation of Diesel sprays excluding the ignition and combustion processes. The present work is a continuation of research at Imperial College which commenced a decade ago with the target of developing a comprehensive computational tool suitable to evaluate and design IC engines.

The objective of this work is the improvement, extension and validation of an existing spray simulation methodology assembled at Imperial College and especially by Dr. C. Kralj on whose work [171] the present research is based. The specific contributions of the present study are as follows:

- **Improvement**: Improvements in computer speed and memory allow engine calculations to be made on finer meshes than hitherto. However, in these cases, at some computational cells near the injector, the void fraction, representing the volume fraction occupied by the gas, becomes small and conventional DDM methodology usually fails. The following improvements have been developed in order that the methodology is capable of operating in such extreme cases:

    1. Rederivation of the conservation equations for mass, momentum and energy in a multiphase system, with particular reference to conditions of high liquid volume fraction. This work reveals the requirement for additional terms to represent pressure work by the liquid on the gas, for both computational and physical reasons.

2. Restructuring of the overall solution algorithm to allow calculations at low void fraction and high load to improve stability and accuracy.

- **Extension**: The basic methodology has been extended in several important respects:

  1. The single-component droplet treatment has been replaced by a new, efficient multicomponent droplet analysis methodology, involving one-dimensional profile solution of the heat conduction and species diffusion equations.
  2. New spray submodels have been implemented in the code in an effort of a better description of key processes. In particular:
     (a) Implementation of the droplet breakup model of Hsiang and Faeth [138]. This model provides a single correlation for all types of breakup.
     (b) Implementation of the Patterson model [230] for the droplet drag coefficient. This model assumes that the droplet surface oscillates due to aerodynamic forces and the droplet shape changes from spherical to ellipsoidal influencing the drag coefficient.
     (c) Implementation of the modified MPI atomisation model developed at Max-Planck Institut [219]. This model considers cavitation in the nozzle and aerodynamic forces on the liquid jet as well as collisions at the tip of the core to be responsible for atomisation.
     (d) Implementation of the effective conductivity and diffusivity model of Abramzon and Sirignano [1] in the droplet evaporation submodel. This model accounts for faster mixing inside the droplet due to internal circulation, induced by the surrounding gas flow field.

- **Validation**: The improved and extended spray methodology is extensively tested in order to assess its suitability for spray simulation in Diesel engines. The validation studies include:

  1. single droplets,

2. free sprays (under atmospheric conditions),
3. sprays injected into a quiescent pressure chamber,
4. real Diesel engine cases.

In addition, sensitivity studies of the effects of mesh density, time step and parcel introduction rate are performed.

1.5 Thesis outline

In the next chapter, the mathematical modelling of the gas phase is presented. The derivation starts from the instantaneous transport equations of an arbitrary multiphase system in differential form. The equations are then applied to the gas phase of two-phase gas/liquid flow system. The transport equations are ensemble-averaged and the additional turbulent transport terms are represented by the k-ε turbulence model. Finally, the boundary and initial conditions are presented to complete the mathematical description of the continuum phase.

Chapter 3 presents the Lagrangian DDM dispersed phase modelling. The droplet mass, momentum and energy conservation equations are described and the coupling source terms arising from the interactions between the droplets and the gas are derived. Spray submodels describing cavitation in the nozzle, jet atomisation, droplet breakup, collisions between droplets and spray/wall interactions, including review of each process, are also presented. Finally, the initial conditions and other parameters required for spray calculations are discussed.

The integration and discretisation of the governing equations are presented in Chapter 4. The finite volume method is employed for the discretisation of the gas transport equations on general unstructured meshes, with a collocated variable arrangement. The spray equations are integrated and discretised in the first-order Euler implicit fashion. The discretised boundary conditions are also presented.

In Chapter 5, the solution procedure for solving the discretised equations is described. Their temporal decoupling and sequential solution follow the LONG-PISO algorithm, while their linearisation and solution are due to the conjugate gradient method. Convergence criteria are also discussed.

Chapter 6 is devoted to the validation studies comparing the predictions against experimental results for single droplets, free sprays and sprays injected in a pressure chamber and a DI engine. Comparisons of the performance of individual submodels are also presented. Particularly, two atomisation models, three breakup models, three types of liquid conductivity, three sets of Nusselt and Sherwood correlations and two drag coefficients are compared. The effects of grid density, time step and parcel introduction rate on the computational results are also examined.

Finally, the findings and conclusions are summarised in Chapter 7. Also, suggestions for future research are proposed.

Chapter 2

Gas phase modelling

2.1 Introduction

The aim of this chapter is to provide a mathematical description of the in-cylinder gas flow in Diesel engines. The equations are presented in differential form in an Eulerian frame where the characteristic fluid properties are considered as continuous functions in space and time in an absolute frame of reference. The presence of liquid phase in the form of droplets affects the gas phase in two ways:

1. The liquid displaces the gas occupying a fraction of the total volume.

2. Exchange of mass, momentum and energy takes place between the two phases.

Before the presentation of the gas equations, the general case is considered in Section 2.2 where the basic equations of a multiphase system are presented. Then, the gas conservation equations are extracted in Section 2.3.

The solution of the instantaneous gas equations requires for turbulent flows the full range of length and time scales to be resolved. Since prohibitive computer storage and time is necessary to achieve this, the instantaneous equations are ensemble-averaged, in Section 2.4. The additional unknown terms introduced by the averaging technique are then represented by the k-ε turbulence model so that closure is regained.

Finally, the mathematical model is completed by the imposition of the boundary and initial conditions in Section 2.5.

2.2 Basic Equations of Multiphase Systems

In this section, the general conservation equations describing the flow of a multiphase system comprising an arbitrary number of N components are considered.

2.2.1 Mass conservation equation

The mass conservation equation for each component i reads (Nigmatulin [211]):

$$\frac{\partial \rho_i}{\partial t} + \nabla \cdot (\rho_i \mathbf{u}_i) = \sum_{\substack{j=1 \\ j \neq i}}^{N} \dot{m}_{ji} \ , \tag{2.1}$$

where ρ_i is the *macroscopic* or *apparent* or *reduced* density of the i^{th} component and $\mathbf{u}_i$ stands for its velocity. Here, $\dot{m}_{ji}$ is the rate of mass transfer from the j^{th} component to the i^{th} component, when transition $(j \to i)$ takes place, per unit volume.

The macroscopic density of the i^{th} component is defined as:

$$\rho_i = \frac{m_i}{V_i} \frac{V_i}{V} = \rho_{m,i} \vartheta_i \ , \tag{2.2}$$

where $\rho_{m,i}$ is the microscopic density* of the i^{th} component and m_i stands for its mass. Also, V_i and V are the volume occupied by this particular component and the mixture, respectively. Finally, ϑ_i is the fraction of the volume occupied by the i^{th} component, called the *void fraction*. By definition,

$$\sum_{i=1}^{N} \vartheta_i = 1 \ . \tag{2.3}$$

*In the literature, this is also referred to as *effective* or *true* density.

2.2.2 Momentum conservation equation

In a multiphase system, the momentum conservation equation for the i^{th} component is given by (Nigmatulin [211]):

$$\frac{\partial \rho_i \mathbf{u}_i}{\partial t} + \nabla \cdot (\rho_i \mathbf{u}_i \mathbf{u}_i) = \nabla \cdot \boldsymbol{\sigma}_i + \rho_i \mathbf{g} + \sum_{\substack{j=1 \\ j \neq i}}^{N} \mathbf{P}_{ji} \ . \tag{2.4}$$

The first and the second terms on the right-hand side (RHS) stand for the rate of momentum gain due to external surface and body forces acting upon the i^{th} component, characterised by the stress tensor $\boldsymbol{\sigma}_i$ and the gravity acceleration vector $\mathbf{g}$, respectively. The stress tensor $\boldsymbol{\sigma}_i$ is defined by:

$$\boldsymbol{\sigma}_i = -\vartheta_i p \mathbf{I} + \mathbf{T}_{m,i} \ , \tag{2.5}$$

where p stands for the thermodynamic pressure, which is the same for all the components, $\mathbf{I}$ is the unit tensor and $\mathbf{T}_{m,i}$ is the shear stress tensor of the i^{th} component. Finally, $\mathbf{P}_{ji}$, in Eq. (2.4), represents the intensity of momentum exchange between i^{th} and j^{th} components which may be divided into two components:

$$\mathbf{P}_{ji} = \mathbf{R}_{ji} + \dot{m}_{ji} \mathbf{u}_{ji} \ . \tag{2.6}$$

In the above, $\mathbf{R}_{ji}$ is the interphase force (per unit volume of mixture) produced by friction, pressure, cohesion between particles, etc.. The second term on the RHS represents the momentum transferred from j^{th} to i^{th} component when transition ($j \rightarrow i$) takes place. Furthermore, the total component interaction with the i^{th} component can be resolved into the part due to enlargement of the component stream tube, which is equal to $p\nabla\vartheta_i$ and the part $\mathbf{F}_{ji}$ assumed to depend on the degree of the velocity non-equilibrium between j^{th} and i^{th} components (i.e. the drag), thus,

$$\sum_{\substack{j=1 \\ j \neq i}}^{N} \mathbf{R}_{ji} = p \nabla \vartheta_i + \sum_{\substack{j=1 \\ j \neq i}}^{N} \mathbf{F}_{ji} \ . \tag{2.7}$$

Taking into consideration Eqs. (2.5), (2.6), (2.7) and rearranging Eq. (2.4), the momentum conservation equation becomes:

$$\frac{\partial \rho_i \mathbf{u}_i}{\partial t} + \nabla\cdot(\rho_i \mathbf{u}_i \mathbf{u}_i) = -\vartheta_i \nabla p + \nabla\cdot\mathbf{T}_{m,i} + \rho_i \mathbf{g} + \sum_{\substack{j=1\\ j\neq i}}^{N} \mathbf{F}_{ji} + \sum_{\substack{j=1\\ j\neq i}}^{N} \dot{m}_{ji}\mathbf{u}_{ji} \, . \tag{2.8}$$

Harlow and Amsden [120] expressed the pressure gradient term as above (i.e. ϑ_i lies outside the pressure gradient) based on the reasoning that if ϑ_i was within the gradient operator*, then the equations could not represent static equilibrium for an inhomogeneous distribution in the absence of gravity. However, this explanation is not sufficient because even if gravity is considered, equilibrium cannot be reached in the case in which the densities of the components are equal†, when ϑ_i lies inside the pressure gradient.

2.2.3 Energy conservation equation

Having obtained the mass and momentum conservation equations, the energy equation is needed to fully describe the flow of a multiphase system. To this end, the conservation equation of either the specific internal energy, e_i, or the specific total (stagnation) energy, E_i, of the i^{th} component is required. The latter is obtained by adding the specific kinetic energy, $\frac{1}{2}u_i^2$, to the internal energy whose definition is as follows:

$$e_i = c_{v,i}(T_i - T_{ref}) \, . \tag{2.9}$$

Here, T_i stands for the absolute temperature of the i^{th} component while T_{ref} is a reference temperature. Also, $c_{v,i}$ is the specific heat at constant volume and it depends on the temperature.

Following Nigmatulin [211], the conservation equation of the specific total energy is given by:

$$\frac{\partial \rho_i E_i}{\partial t} + \nabla\cdot(\rho_i \mathbf{u}_i E_i) = \nabla\cdot\mathbf{C}_i + \rho_i \mathbf{g}\cdot\mathbf{u}_i - \nabla\cdot\mathbf{q}_i + \sum_{\substack{j=1\\ j\neq i}}^{N} \dot{E}_{ji} \, . \tag{2.10}$$

*Some authors have proposed ϑ_i to lie within the gradient operator (see Lahey [175]).

†Note that in this case, the gravity does not result in pressure difference which would eventually lead to equilibrium.

The first term on the RHS stands for the work of external surface forces acting upon the i^{th} component, characterised by the vector $\mathbf{C}_i = \boldsymbol{\sigma}_i \mathbf{u}_i$ and the second term, for work due to body forces. The third term represents the heat influx and the fourth term, the intensity of energy exchange between i^{th} and j^{th} components.

Multiplying the momentum equation, Eq. (2.8), by $\mathbf{u}_i$, the specific kinetic energy equation is obtained:

$$\frac{\partial \rho_i \frac{u_i^2}{2}}{\partial t} + \nabla\cdot\left(\rho_i \mathbf{u}_i \frac{u_i^2}{2}\right) = -\mathbf{u}_i\vartheta_i \nabla p + \mathbf{u}_i\nabla\cdot\mathbf{T}_{m,i} + \rho_i \mathbf{g}\cdot\mathbf{u}_i + \sum_{\substack{j=1\\ j\neq i}}^{N} \mathbf{F}_{ji}\cdot\mathbf{u}_i + \sum_{\substack{j=1\\ j\neq i}}^{N} \dot{m}_{ji}\mathbf{u}_{ji}\cdot\mathbf{u}_i \ . \quad (2.11)$$

By subtracting the above from the specific total energy equation, Eq. (2.10), the conservation equation for the specific internal energy is obtained:

$$\frac{\partial \rho_i e_i}{\partial t} + \nabla\cdot(\rho_i \mathbf{u}_i e_i) = \mathbf{T}_{m,i} : \nabla \mathbf{u}_i - \nabla\cdot\mathbf{q}_i - p\nabla\cdot(\vartheta_i \mathbf{u}_i) + \sum_{\substack{j=1\\ j\neq i}}^{N} \dot{e}_{ji} \ . \quad (2.12)$$

Here, the first term on the RHS represents the shear work, the second the heat influx and the third term, the pressure work. Finally, the last term on the RHS represents the intensity of specific internal energy exchange between i^{th} and j^{th} components and is given by:

$$\dot{e}_{ji} = \dot{E}_{ji} - (\mathbf{F}_{ji}\cdot\mathbf{u}_i + \dot{m}_{ji}\mathbf{u}_{ji}\cdot\mathbf{u}_i) \ . \quad (2.13)$$

2.3 Gas phase equations

The foregoing general conservation equations of multiphase flow can obviously be applied to gas/liquid systems. Here, only the gas equations are extracted since, the liquid phase (droplets) equations are expressed in a Lagrangian frame as mentioned in Section 1.3. Hence, the subscript 'i' which indicates the i^{th} component of the system is omitted.

2.3.1 Mass conservation equation

From Eq. (2.1) the mass conservation equation of the gas phase reads:

$$\frac{\partial \rho}{\partial t} + \nabla \cdot (\rho \mathbf{u}) = S_m^d \ , \tag{2.14}$$

where S_m^d is the fuel contribution and expresses the rate of supply or removal of vapour mass by evaporation or condensation per unit volume.

2.3.2 Fuel vapour mass fraction conservation equation

Since phase change takes place, the gas composition changes and the mass conservation equation for each component must be defined as well. Following Soo [270], the fuel vapour mass fraction, $Y_{v,i} = \rho_{v,i}/\rho$, conservation equation of component i with density $\rho_{v,i}$, reads:

$$\frac{\partial \rho Y_{v,i}}{\partial t} + \nabla \cdot (\rho \mathbf{u} Y_{v,i}) = \nabla \cdot \mathbf{j} + S_{Y_{v,i}}^d \ , \tag{2.15}$$

where $S_{Y_{v,i}}^d$ is the evaporation rate per unit volume of the fuel component i. By definition, for a multicomponent fuel consisting of N components, it follows that

$$\sum_{i=1}^{N} S_{Y_{v,i}}^d = S_m^d \ . \tag{2.16}$$

Also, $\mathbf{j}$ is the species diffusion flux which, according to Fick's law, reads:

$$\mathbf{j} = \rho \Gamma_{Y_{v,i}} \nabla Y_{v,i} \ . \tag{2.17}$$

Here, $\Gamma_{Y_{v,i}}$ is the diffusion coefficient defined as:

$$\Gamma_{Y_{v,i}} = \frac{\nu_m}{\sigma_{Y_{v,i}}} \ , \tag{2.18}$$

where $\sigma_{Y_{v,i}}$ is the Schmidt number and ν_m is the molecular kinematic viscosity.

2.3.3 Momentum conservation equation

From Eq. (2.8) the momentum conservation equation of the gas phase is given by:

$$\frac{\partial \rho \mathbf{u}}{\partial t} + \nabla \cdot (\rho \mathbf{u}\mathbf{u}) = -\vartheta \nabla p + \nabla \cdot \mathbf{T}_m + \mathbf{S}_{\mathbf{u}}^d \ , \tag{2.19}$$

where $\mathbf{S}_{\mathbf{u}}^{d}$ stands for the rate of momentum exchange between the two phases per unit volume. In the above, the term expressing the body forces has been omitted, since the effect of gravity is negligible compared to inertial and viscous forces, in cases of relatively high speed gas flows (White [303]) like those in engines.

The gas is assumed to be a Newtonian fluid, thus, the molecular shear stress tensor $\mathbf{T}_m$, is given by (Bird *et al.* [41]):

$$\mathbf{T}_m = \rho \left(2\nu_m \mathbf{D} - \frac{2}{3} \nu_m \nabla \cdot \mathbf{u} \mathbf{I} \right) , \tag{2.20}$$

where $\mathbf{D}$ is the rate-of-strain (deformation) tensor, given by:

$$\mathbf{D} = \frac{1}{2} \left[\nabla \mathbf{u} + (\nabla \mathbf{u})^{\mathrm{T}} \right] . \tag{2.21}$$

Here, the superscript 'T' denotes transposition.

2.3.4 Energy conservation equation

The specific internal energy conservation equation of the gas phase can be derived from Eq. (2.12). Thus,

$$\frac{\partial \rho e}{\partial t} + \nabla \cdot (\rho \mathbf{u} e) = -\nabla \cdot \mathbf{q} - p \nabla \cdot (\vartheta \mathbf{u}) + S_e^d , \tag{2.22}$$

where S_e^d represents the energy exchange between gas and liquid. Also, in the above equation, the $\mathbf{T}_m : \nabla \mathbf{u}$ term, representing the molecular shear work, has been neglected due to its small contribution to the overall internal energy balance (Begleris [35]).

In the particular system of gas and liquid considered here, the heat transferred by radiation is neglected, on the basis that on the one hand the droplets are very small and on the other, according to Berlad [36] and Faeth [90] gaseous spectral radiation bands and liquid fuels absorption bands are generally not coincident. Thus, in Eq. (2.22), $\mathbf{q}$ represents the heat influx only by conduction which according to the Fourier's law, is given by:

$$\mathbf{q} = -k \nabla T , \tag{2.23}$$

where k is the thermal conductivity coefficient calculated from:

$$k = \frac{\rho \nu_m c_p}{\sigma_e} \ . \tag{2.24}$$

Here, c_p is the specific heat at constant pressure and σ_e is the Prandtl number. From the definition of the internal energy, given by Eq. (2.9), the Fourier's law reads:

$$\mathbf{q} = -\frac{\rho \nu_m \gamma}{\sigma_e} \nabla e \ , \tag{2.25}$$

where $\gamma = c_p/c_v$ is the specific heat ratio. It is noted that in the above expression, the gradient of c_v, which now is a function of both the gas temperature and composition, i.e. $c_v = c_v(Y_{v,i}, T)$, has been neglected on the ground that it is small compared to $c_v \nabla e/e$. Similarly to the diffusion coefficient of fuel vapour mass fraction, Eq. (2.18), a diffusion coefficient of the internal energy can be defined as:

$$\Gamma_e = \frac{\nu_m \gamma}{\sigma_e} \ . \tag{2.26}$$

By substituting Eq. (2.26) in Eq. (2.25), the Fourier's law reads:

$$\mathbf{q} = -\rho \Gamma_e \nabla e \ . \tag{2.27}$$

Despite the fact that the source term S_e^d in Eq. (2.22) is supposed to represent the effect of the liquid on the gas phase, it fails to completely do so, since it includes only the energy exchange by convection. An additional term must be added to Eq. (2.22) representing the energy due to the interface. This energy expresses the work done from the one phase to the other and therefore, its magnitude is equal for the two phases but its sign is different. If the liquid energy equation is expressed in Eulerian framework, a pressure work term, similar to the corresponding counterpart in Eq. (2.22), will appear. Since the liquid is incompressible, this work is actually exerted on the interface, i.e. it performs like a piston. This work of the interface, on the one hand, cancels out the pressure work term of the liquid phase, preserving its incompressibility and on the other is added to the gas energy equation expressing the pressure work done by the liquid which plays the role of a piston. Thus, the final specific internal energy of the gas phase reads:

$$\frac{\partial \rho e}{\partial t} + \nabla \cdot (\rho \mathbf{u} e) = -\nabla \cdot \mathbf{q} - p \nabla \cdot [\vartheta \mathbf{u} + (1-\vartheta)\, \mathbf{u}_l] + S_e^d \ , \tag{2.28}$$

where the term $-p\nabla\cdot[(1-\vartheta)\,\mathbf{u}_l]$ expresses the pressure work that would appear in the liquid energy equation if it was written in Eulerian formulation. Here, $\mathbf{u}_l$ is the liquid velocity whose value is not available since this phase is expressed in Lagrangian approach. However, this problem can be overcome if a liquid continuity equation similar to that for the gas, Eq. (2.14), is written as follows:

$$\frac{\partial\,(1-\vartheta)\,\rho_l}{\partial t} + \nabla\cdot[(1-\vartheta)\,\rho_l\mathbf{u}_l] = -S_m^d\ , \tag{2.29}$$

where ρ_l is the liquid density. Here, the term $(1-\vartheta)$ stands for the void fraction of the liquid and the term on the RHS represents the rate of mass removal from the liquid due to evaporation per unit volume. Since the liquid is incompressible, the following expressions can be invoked:

$$\frac{\partial\rho_l}{\partial t} = 0\ , \tag{2.30a}$$

$$\nabla\rho_l = 0\ . \tag{2.30b}$$

After substituting the above simplifications in Eq. (2.29), the contribution of the liquid in the pressure work term can be written as:

$$\nabla\cdot(1-\vartheta)\,\mathbf{u}_l = \frac{\partial\vartheta}{\partial t} - \frac{S_m^d}{\rho_l}\ . \tag{2.31}$$

This term is crucial in dense sprays with high droplet velocities, where the gas void fraction is small and presents large time-gradients and hence, the pressure work due to the liquid plays the dominant role. The effect of this term is demonstrated in the following simple examples.

It is assumed that a bounded volume V of arbitrary shape with stationary and adiabatic boundaries contains pure air at state (1) of pressure p_1, temperature T_1 and volume $V_1 = V$. Then, it is assumed that a liquid of volume V_l is introduced in this cell and the new state of the air is referred to as (2) with pressure p_2 and temperature T_2. Also, the volume occupied by the air is now $V_2 = V_1 - V_l$. If the liquid is assumed to have low volatility and temperature the same as that of the air, the evaporation process can be neglected while the heat transfer between the gas and liquid is zero. Thus, by integrating the gas continuity equation over the volume

V and taking into account that the boundary velocity is zero, the following equation is obtained:

$$\frac{\partial \rho}{\partial t} = 0 \; . \tag{2.32}$$

Also, Eq. (2.28), when integrated over the volume V, gives:

$$\frac{\partial \rho e}{\partial t} = -p \frac{\partial \vartheta}{\partial t} \; . \tag{2.33}$$

The combination of these two equations results in:

$$\frac{\partial e}{\partial t} = -\frac{p}{\rho} \frac{\partial \vartheta}{\partial t} \; . \tag{2.34}$$

This equation expresses the increase of the gas energy due to the pressure work, when it is displaced by the liquid. By contrast, when Eq. (2.28) is replaced by Eq. (2.22), constant internal energy is obtained. By introducing the caloric equation, Eq. (2.9) and the state equation for ideal gas, expressed later by Eq. (2.37), the above equation, when integrated from state (1) to state (2), becomes into:

$$\frac{\vartheta_2}{\vartheta_1} = \left(\frac{T_2}{T_1} \right)^{-1/(\gamma-1)} \; , \tag{2.35}$$

where c_p and c_v were assumed not to vary with the temperature. This equation is exactly the same as the equation that describes the isentropic change of a volume* from state (1) to state (2) (see Anderson [14]).

By giving numbers to the above quantities, relevant for Diesel engines (see Chapter 6), the net effect of the pressure work term due to the liquid can be worked out. Thus, for $T_1 = 800\,K$ and $\vartheta_1 = 1$, the new temperature, T_2, when liquid of volume $V_l = 0.1 V_1$ is introduced, becomes† $T_2 = 830.05\,K$. When an extreme case is examined for which it is assumed that the volume of the liquid is $V_l = 0.9 V_1$, the air temperature becomes $T_2 = 1790.98\,K$. It is emphasised that if the pressure work due to the liquid is not included, i.e. Eq. (2.22) instead of Eq. (2.28) is used, the air temperature does not change and hence, the error is larger than 100 %.

It is noted that when the air temperature increases, heat transfer from the air to the liquid will also take place. Although in these examples it is neglected for

*Note that the ratio of void fractions ϑ_2/ϑ_1 is equal to the ratio of volumes V_2/V_1.

†Note that for air at $800\,K$, $\gamma = 1.35$ [241].

the sake of simplicity, it is taken into account in Eq. (2.28) via the source term S_e^d. It is also mentioned that the liquid volume in Diesel engines represents only a negligible fraction of the cylinder and therefore, the absence of the liquid pressure work term does not introduce big errors. However, as will be explained in Chapter 4, the methodology divides the cylinder into a large number of small subvolumes in which the liquid volume fraction cannot be neglected. Of course, again the effect of the liquid pressure work term is not so dramatic as is demonstrated here, because the liquid displaces gas to the neighbouring cells. However, in dense spray regions which is one of the scopes of the present thesis as will be shown in Chapter 6, the void fraction may be even smaller than 10 % and the inclusion of the liquid pressure work term is of vital importance.

2.3.5 The general instantaneous transport equation

The conservation equations, Eqs. (2.14), (2.15), (2.19) and (2.28), can be expressed in a common form as:

$$\frac{\partial \rho \phi}{\partial t} + \nabla \cdot (\rho \mathbf{u} \phi) = \nabla \cdot \rho \Gamma_\phi \nabla \phi + S_\phi + S_\phi^d \, , \tag{2.36}$$

where ϕ is the dependent variable (1, $Y_{v,i}$, $\mathbf{u}$, e), Γ_ϕ is the molecular (kinematic) diffusion coefficient of ϕ, S_ϕ represents the source terms related to the gas and S_ϕ^d the source terms expressing the interphase exchange.

2.3.6 Equation of state

The working fluid is assumed to obey the ideal gas law, expressed by:

$$p = \rho_m R T \, , \tag{2.37}$$

where R is the gas constant. This depends on the composition of the gas and is defined as:

$$R = c_p - c_v \, . \tag{2.38}$$

Here, it should be noted that in high-pressure environments, as is the case in Diesel engines, the ideality of the fluid is not strictly valid. Usually, the non-ideality of a gas is described by the compressibility factor, Z, which is inserted into Eq. (2.37). This factor deviates from the unity by increasing the pressure, however, when the temperature increases, this factor increases and is close to unity (see Reid *et al.* [241]). Since in Diesel engines, not only the pressure but also the temperature is high, the gas can be assumed to obey the ideal gas law. Obviously, this is just a simplification, adopted in this study following the author's predecessors (see Begleris [35], Theodoropoulos [288], Kralj [171] and Leskovšek [186]). For higher accuracy, a real gas state equation (see Reid *et al.* [241]) should be considered.

2.4 Ensemble averaging

The solution of the foregoing instantaneous transport equations fully describes the flow field in internal and external flows. However, high spatial and temporal resolution is necessary, especially in highly-turbulent flows such those in engines due to the small time and length scales (Gosman [105]). Thus, a statistical averaging procedure is applied in order to bypass this requirement.

According to Hinze [133], there are three averaging methods, whose application depends on the characteristics of the turbulent flow:

1. Time averaging for a stationary turbulence;
2. Space averaging for a homogeneous turbulence;
3. Ensemble averaging for a series of identical experiments.

For unsteady and quasi-periodic flows like those in engines, the only feasible method is ensemble averaging. The averaging can be either unweighted (or Reynolds) [52] or weighted. Favre [96] suggested the density-weighted averaging technique, which is useful for applications to compressible and combusting flows because it introduces only one new term while the remaining terms of the averaged transport equations look like the corresponding counterparts of the instantaneous ones. This feature also allows a clearer interpretation of the individual terms than in the case with Reynolds averaging in which many new terms appear, complicating the transport equations. Hence, the Favre averaging approach is adopted in the present study.

The instantaneous value of a variable $\phi(\mathbf{x},\, t)$ at a location $\mathbf{x}$ and time t can be decomposed into two components, as follows:

For Reynolds averaging:

$$\phi(\mathbf{x},\, t) = \overline{\phi}(\mathbf{x},\, t) + \phi'(\mathbf{x},\, t) \ ; \tag{2.39}$$

For Favre averaging:

$$\phi(\mathbf{x},\, t) = \widetilde{\phi}(\mathbf{x},\, t) + \phi''(\mathbf{x},\, t) \ . \tag{2.40}$$

Here, $\phi'(\mathbf{x},\, t)$ and $\phi''(\mathbf{x},\, t)$ represent the fluctuations about the Reynolds $\overline{\phi}(\mathbf{x},\, t)$ and Favre $\widetilde{\phi}(\mathbf{x},\, t)$ mean values, respectively. The latter are defined as:

$$\overline{\phi}(\mathbf{x},\, t) = \lim_{N\to\infty} \frac{1}{N} \sum_{i=1}^{N} \phi\left(\mathbf{x},\, t + iT_c\right) \ , \tag{2.41}$$

$$\widetilde{\phi}(\mathbf{x},\, t) = \frac{1}{\overline{\rho}_m(\mathbf{x},\, t)} \lim_{N\to\infty} \frac{1}{N} \sum_{i=1}^{N} \rho_m\left(\mathbf{x},\, t + iT_c\right) \phi\left(\mathbf{x},\, t + iT_c\right) \ , \tag{2.42}$$

where $\overline{\rho}_m(\mathbf{x},\, t)$ is the Reynolds-mean density and T_c is the period (equivalent to the engine cycle in an engine case) of N identically repeated realisations. Considering Eq. (2.41), Eq. (2.42) can recast into:

$$\widetilde{\phi}(\mathbf{x},\, t) = \frac{1}{\overline{\rho}_m(\mathbf{x},\, t)} \overline{\rho_m(\mathbf{x},\, t)\phi(\mathbf{x},\, t)} \ . \tag{2.43}$$

Although the above equation can be directly applied to the equations of single-phase flows (for example see Begleris [35]), in multiphase flows, the situation becomes complicated because not only the microscopic density but also the void fraction fluctuate about their mean values. The void fraction can be treated as any other variable and its Favre-average can be given by Eq. (2.43). However, the transport equation will become very complicated because many new terms comprising the fluctuation and the mean value of the void fraction will appear. Instead of this, the Favre-average is redefined using the macroscopic density as a weighting factor.

Hence,

$$\widetilde{\phi}(\mathbf{x},\,t) = \frac{1}{\overline{\rho}(\mathbf{x},\,t)}\overline{\rho(\mathbf{x},\,t)\phi(\mathbf{x},\,t)}\;, \tag{2.44}$$

where the Reynolds-mean macroscopic density is calculated by:

$$\overline{\rho}(\mathbf{x},\,t) = \overline{\rho_m(\mathbf{x},\,t)\vartheta(\mathbf{x},\,t)}\;. \tag{2.45}$$

Using the definitions of the Reynolds and Favre averaging and omitting the symbols $\mathbf{x}$ and t, the following relations between weighted and unweighted average quantities can be derived (see Appendix A.1):

$$\overline{\rho}\overline{\phi''} = -\overline{\rho'\phi'}\;, \tag{2.46a}$$

$$\overline{\rho}\overline{\phi''} = -\overline{\rho'\phi''}\;, \tag{2.46b}$$

$$\overline{\rho\phi''} = 0\;, \tag{2.46c}$$

$$\overline{\rho'\phi''} = \overline{\rho'\phi'}\;. \tag{2.46d}$$

Applying the ensemble averaging technique to the transport equations, new correlations appear involving the void fraction fluctuations, e.g. the term $\overline{\vartheta'\nabla p'}$ in the momentum conservation equation (see Ikonomou [143]). Further modelling is required to express these correlations in terms of known quantities. In the absence of any general approach to the modelling of these terms and following the practice of Tabrizi [280], Kralj [171] and Ikonomou [143], they will be omitted. The same practice is adopted for the fluctuations of the spray source terms, $S_\phi^{d'}$.

2.4.1 Favre-averaged transport equation

The application of the density-weighted ensemble averaging to the general transport equation, Eq. (2.36), results in:

$$\frac{\partial\overline{\rho}\widetilde{\phi}}{\partial t} + \nabla\cdot\left(\overline{\rho}\widetilde{\mathbf{u}}\widetilde{\phi}\right) = \nabla\cdot\left(\overline{\rho}\overline{\Gamma}_\phi\nabla\widetilde{\phi}\right) - \nabla\cdot\left(\overline{\rho\mathbf{u}''\phi''}\right) + \overline{S}_\phi + \overline{S}_\phi^d\;. \tag{2.47}$$

In the above equation, the fluctuations of Γ_ϕ have been neglected since in turbulent flows the viscous terms are negligible (see Hinze [133], Tennekes and Lumley [286]).

As expected, the averaging of non-linear terms produces additional unknown correlations. Here, the term $\overline{\rho \mathbf{u}'' \phi''}$ represents the turbulent diffusion flux of ϕ and its modelling will now be discussed for vector and scalar properties.

Vector transport equation

The only one transport equation of a vector variable is the momentum conservation equation in which ϕ stands for the velocity field, $\mathbf{u}$. The term $\overline{\rho}\overline{\Gamma}_{\mathbf{u}}\nabla\tilde{\mathbf{u}}$ represents the molecular stress tensor defined by Eq. (2.5), whose divergence reads:

$$\nabla\cdot\left(\overline{\rho}\overline{\Gamma}_{\mathbf{u}}\nabla\tilde{\mathbf{u}}\right) = -\overline{\vartheta}\nabla\overline{p} - \overline{p}\nabla\overline{\vartheta} + \nabla\cdot\widetilde{\mathbf{T}}_m \ , \tag{2.48}$$

where the averaged shear tensor, $\widetilde{\mathbf{T}}_m$, (see Eq. (2.20)) is defined as:

$$\widetilde{\mathbf{T}}_m = \overline{\rho}\left(2\overline{\nu}_m\widetilde{\mathbf{D}} - \frac{2}{3}\overline{\nu}_m\nabla\cdot\tilde{\mathbf{u}}\mathbf{I}\right) \tag{2.49}$$

and the averaged rate-of-strain tensor, $\widetilde{\mathbf{D}}$, (see Eq. (2.21)) as:

$$\widetilde{\mathbf{D}} = \frac{1}{2}\left[\nabla\tilde{\mathbf{u}} + (\nabla\tilde{\mathbf{u}})^{\mathrm{T}}\right] \ . \tag{2.50}$$

In the above averaged terms, the fluctuations of ν_m have been neglected for the same reason as the fluctuations of the diffusion coefficient were neglected.

The turbulent diffusion term $\overline{\rho \mathbf{u}'' \mathbf{u}''}$ is called Reynolds stress tensor. Assuming an analogy between molecular and turbulent motion (the Boussinesq turbulent viscosity hypothesis [49]), the Reynolds stress tensor, which includes both the normal and shear components, is modelled as:

$$\widetilde{\mathbf{T}}_t = \overline{\rho}\left(2\nu_t\widetilde{\mathbf{D}} - \frac{2}{3}\nu_t\nabla\cdot\tilde{\mathbf{u}}\mathbf{I}\right) - \frac{2}{3}\overline{\rho}\tilde{k}\mathbf{I} \ , \tag{2.51}$$

where ν_t, whose definition will be given later in §2.4.3 by Eq. (2.64b), is the turbulent or eddy kinematic viscosity. This depends on the local state of turbulence, whereas the molecular viscosity is a fluid property. Also, in Eq. (2.51), k represents the turbulence kinetic energy, defined as:

$$\tilde{k} = \frac{1}{2}\widetilde{\mathbf{u}''\cdot\mathbf{u}''} \ . \tag{2.52}$$

Defining the effective kinematic viscosity by:

$$\overline{\nu}_{eff} = \overline{\nu}_m + \nu_t \ , \tag{2.53}$$

the sum of the molecular shear stress and the Reynolds stress reads:

$$\widetilde{\mathbf{T}}_m + \widetilde{\mathbf{T}}_t = \overline{\rho}\left[\overline{\nu}_{eff}\left(2\widetilde{\mathbf{D}} - \frac{2}{3}\nabla\cdot\tilde{\mathbf{u}}\mathbf{I}\right) - \frac{2}{3}\widetilde{k}\mathbf{I}\right] \ . \tag{2.54}$$

Scalar transport equation

By recalling the Boussinesq hypothesis [49], the turbulent diffusion for a scalar property is modelled in analogy with the molecular diffusion. Thus,

$$-\overline{\rho\mathbf{u}''\phi''} = \overline{\rho}\Gamma_{\phi,t}\nabla\widetilde{\phi} \ , \tag{2.55}$$

where $\Gamma_{\phi,t}$ is the turbulent or eddy (kinematic) diffusion coefficient.

An effective diffusion coefficient, which combines the molecular and the turbulent one, can be defined as:

$$\overline{\Gamma}_{\phi,eff} = \overline{\Gamma}_\phi + \Gamma_{\phi,t} \ ; \tag{2.56}$$

and the general averaged transport equation for a scalar variable ϕ (1, $Y_{v,i}$, e) becomes:

$$\frac{\partial\overline{\rho}\widetilde{\phi}}{\partial t} + \nabla\cdot\left(\overline{\rho}\tilde{\mathbf{u}}\widetilde{\phi}\right) = \nabla\cdot\left(\overline{\rho}\overline{\Gamma}_{\phi,eff}\nabla\widetilde{\phi}\right) + \overline{S}_\phi + \overline{S}^d_\phi \ . \tag{2.57}$$

The effective diffusion coefficient is usually expressed in terms of the effective viscosity and the Prandtl/Schmidt number (considered constant), determined from experiments:

$$\overline{\Gamma}_{\phi,eff} = \frac{\overline{\nu}_{eff}}{\sigma_\phi} \ . \tag{2.58}$$

Table 2.1 gives the values of Prandtl/Schmidt numbers for all the scalar variables including the turbulence parameters, k and ε, which will be discussed in §2.4.3.

2.4.2 Favre-averaged constitutive relations

For the sake of simplicity, on the one hand and because no modelling exists, at least to the knowledge of the author, on the other, the fluctuation of the gas constant

Table 2.1: Prandtl/Schmidt numbers for scalar variables, taken from Begleris [35] and Leskovšek [186].

ϕ	$Y_{v,i}$	e	k	ε
σ_ϕ	1.0	0.8	1.0	1.2

R, due to fluctuations of the gas composition, is assumed to be small and can be neglected (see Kralj [171]). Also, by taking into account that the terms involving the void fraction fluctuations, $\overline{p'\vartheta'}$ and $\overline{\rho'_m\vartheta'}$, are neglected on the same ground as the term $\overline{\vartheta'\nabla p'}$ was neglected in the momentum conservation equation, the state equation, when density-weighted averaging is applied, reads:

$$\overline{p} = \frac{\overline{\rho}\,\overline{R}\widetilde{T}}{\overline{\vartheta}} \approx \overline{\rho}_m \overline{R}\widetilde{T} \; . \tag{2.59}$$

Assuming that the correlation $\overline{\rho c_v'' T''}$ is small and can be neglected, the Favre-averaging of the caloric equation yields:

$$\widetilde{e} = \widetilde{c}_v \left(\widetilde{T} - T_{ref} \right) \; , \tag{2.60}$$

where

$$\widetilde{c}_v = c_v \left(\widetilde{Y}_{v,i}, \widetilde{T} \right) \; . \tag{2.61}$$

The Fick's law of diffusion and Fourier's law of heat conduction, when averaged, read:

$$\overline{\mathbf{j}} = \overline{\rho}\overline{\Gamma}_{Y_{v,i}} \nabla \widetilde{Y}_{v,i} \; , \tag{2.62}$$

$$\overline{\mathbf{q}} = -\overline{\rho}\overline{\Gamma}_e \nabla \widetilde{e} \; . \tag{2.63}$$

Finally, the ensemble-averaged Newton's law of viscosity was described in §2.4.1 (see Eqs. (2.49) and (2.50)) and will not be repeated here.

2.4.3 Turbulence model

As evidenced above, the averaging procedure yields additional terms in the transport equations, involving correlations of the fluctuating components. The modelling of these terms is referred to as *turbulence closure.* Among various degrees of complexity (see Wilcox [308]), only the two-equation and second-order closure models are complete. Despite the higher accuracy that the latter provide, only recently have been employed in engine applications (see e.g. Lebrère and Dillies [183]*) because great computer resources are necessary since they consist of by a number of equations†. By contrast, the two-equation models are widely used in engine applications for they offer the best compromise between accuracy and computer resources. One of these models, namely the k-ε, which according to Ahmadi-Befrui [5] provides the best option for practical engine calculations, is adopted in the present study.

The earliest works based on this model were those of Chou [63], Davidov [78] and Harlow and Nakayama [121]. However, the main work is that by Jones and Launder [154], in 1972 and their model is so well known that it is usually referred to as the *Standard k-ε model.* Two years later, Launder and Sharma [178] presented the model closure coefficients. Since then, a number of different versions of the model have been proposed by researchers changing the model coefficients. The k-ε model was used in early works concerning predictions of in-cylinder flows by Watkins [301], Syed and Bracco [279], Moler and Mansour [200], El Tahry [84], Ahmadi-Befrui [5] among others, while nowadays is widely employed also for studies including spray and combustion phenomena in IC engines (see e.g. Patterson *et al.* [230], Kong *et al.* [167], Strauss *et al.* [277], Stephenson *et al.* [274], McLandress *et al.* [197], Ricart and Reitz [253], Leskovšek [186]).

The version of k-ε model employed in this study is that presented by Ahmadi-Befrui [5], which takes into account compressibility effects reported by El Tahry [84], extended to two-phase flow by Kralj [171].

The model is based on the Boussinesq turbulent viscosity hypothesis, according to which, the turbulent stresses and turbulent scalar fluxes can be expressed by

---

*It is mentioned that the work of Lebrère and Dillies [183] excludes spray and combustion which have not yet, at least to the knowledge of the author, been considered using second-order turbulence closure.

†For instance, for a three-dimensional flow, they introduce seven equations, one for the turbulence scale and six for the components of the Reynolds stress tensor (Wilcox [308]).

Eqs. (2.51) and (2.55), respectively. In these equations, the turbulent diffusivity, $\Gamma_{\phi,t}$ and the eddy kinematic viscosity, ν_t, are defined by:

$$\Gamma_{\phi,t} = \frac{\nu_t}{\sigma_{\phi,t}} , \tag{2.64a}$$

$$\nu_t = C_\mu \frac{\widetilde{k}^2}{\widetilde{\varepsilon}} , \tag{2.64b}$$

where $\sigma_{\phi,t}$ is the turbulent Prandtl/Schmidt number, determined from experiments and assumed constant*. Also, C_μ is a coefficient of the model given in Table 2.2, k is the turbulence kinetic energy defined by Eq. (2.52) and ε its dissipation rate defined by:

$$\widetilde{\varepsilon} = \frac{1}{\rho} \overline{\mathbf{T}'_m : \nabla \mathbf{u}''} . \tag{2.65}$$

It should be mentioned here that an additional complexity in turbulence closure in Diesel engines is introduced by the dispersed phase. In particular, the droplets affect the turbulence due to their inertia which prevents them from following the continuum phase motion. Also, the relative velocity between the droplets and the gas induces shear stresses with impact on the turbulence structure. A number of experiments have been performed to study the turbulence modulation and was found that the dispersed phase may reduce or enhance the turbulence intensity depending on the relative velocity between the two phases as well as the relative size between droplets (or particles) and a characteristic turbulent length scale (see Faeth [92]). The modelling of turbulence modulation is usually based on the linearised Lagrangian equation of motion of a spherical particle in a turbulent flow (see e.g. Elghobashi and Abou-Arab [86], Elghobashi *et al.* [87], Mostafa and Mongia [202]). Reitz and Diwakar [246] investigated the effect of turbulence modulation in dense sprays and they found that it increases the gas velocity in the near-injector region while the Sauter mean diameter is rather insensitive. Kralj [171] performed Diesel spray calculations and he obtained enhanced penetration when turbulence modulation was included. However, in respect of validation, the exclusion of turbulence modulation was beneficial. Nevertheless, for the sake of completeness, the turbulence

*Its values for k and ε adopted in this study were given in Table 2.1.

modulation is included in this study. This is based on the work of Kralj [171]* who derived the Reynolds-stresses equation and then, by contraction, he obtained the k equation. Consequently, the source term in this equation is based on the source terms of mass and momentum. The modelling of the source term in ε equation follows that of Mostafa and Mongia [202] and Reitz and Diwakar [246].

Turbulence kinetic energy equation

The full derivation of the turbulence kinetic energy conservation equation is extensively covered by Kralj [171] and only its final form is given here:

$$\frac{\partial \overline{\rho}\widetilde{k}}{\partial t} + \nabla \cdot \left(\overline{\rho}\widetilde{\mathbf{u}}\widetilde{k} \right) = \nabla \cdot \overline{\rho}\Gamma_{k,t}\nabla\widetilde{k} + G - \overline{\rho}\widetilde{\varepsilon} + \overline{S}_k^d \, , \tag{2.66}$$

where $\Gamma_{k,t}$ is the diffusivity of the turbulence energy. The first term on the RHS stands for the turbulence diffusion and the second term represents the generation rate of turbulence kinetic energy. The latter is defined as:

$$G = \widetilde{\mathbf{T}}_t : \nabla \widetilde{\mathbf{u}} \, . \tag{2.67}$$

The third term on the RHS of Eq. (2.66) expresses the viscous dissipation. Finally, the fourth term stands for the spray contribution to the turbulence kinetic energy.

According to Kralj [171], the spray contribution to the turbulence kinetic energy is expressed by:

$$\overline{S}_k^d = \overline{\mathbf{u}'' \cdot \mathbf{S}_{\mathbf{u}}^d} - \overline{\mathbf{u}'' \cdot \mathbf{u} S_m^d} + \frac{1}{2}\overline{\mathbf{u}'' \cdot \mathbf{u}'' S_m^d} \, . \tag{2.68}$$

In the above equation, the first term on the RHS represents the rate of work exchanged between turbulent eddies and droplets due to the drag forces. The second and the third terms express the effects of the mass transfer (evaporation) on the turbulence kinetic energy.

*An extensive literature survey concerning the spray contribution to turbulence can be found in Kralj [171].

Turbulence dissipation rate equation

The transport equation for the turbulence dissipation rate reads (Kralj [171]):

$$\frac{\partial \overline{\rho}\widetilde{\varepsilon}}{\partial t} + \nabla \cdot (\overline{\rho}\widetilde{\mathbf{u}}\widetilde{\varepsilon}) = \nabla \cdot \overline{\rho}\Gamma_{\varepsilon,t}\nabla\widetilde{\varepsilon} + C_{\varepsilon 1} G \frac{\widetilde{\varepsilon}}{\widetilde{k}} - C_{\varepsilon 2}\overline{\rho}\frac{\widetilde{\varepsilon}^2}{\widetilde{k}} + C_{\varepsilon 3}\overline{\rho}\widetilde{\varepsilon}\nabla \cdot \widetilde{\mathbf{u}} + \overline{S}^d_{\varepsilon} \ , \tag{2.69}$$

where $\Gamma_{\varepsilon,t}$ is the diffusivity of ε and $C_{\varepsilon 1}$, $C_{\varepsilon 2}$ and $C_{\varepsilon 3}$ are coefficients of the model given in Table 2.2. The first term on the RHS stands for the diffusion and the second expresses the generation by mean shear and the self-stretching action of turbulence. The viscous destruction is represented by the third term, whereas, the fourth term stands for additional generation/destruction due to compressibility. Finally, the last term expresses the contribution from the spray/turbulence interaction.

According to Mostafa and Mongia [202], the spray source term $\overline{S}^d_{\varepsilon}$ is expressed by:

$$\overline{S}^d_{\varepsilon} = C_{\varepsilon 4}\frac{\widetilde{\varepsilon}}{\widetilde{k}}\overline{S}^d_k \ , \tag{2.70}$$

where $C_{\varepsilon 4}$ is a coefficient chosen by the authors to match the experimental results obtained by Shuen *et al.* [265]. Its value is given in Table 2.2.

Table 2.2: The k-ε model coefficients.

σ_k	σ_ε	C_μ	$C_{\varepsilon 1}$	$C_{\varepsilon 2}$	$C_{\varepsilon 3}$	$C_{\varepsilon 4}$
1.0	1.2	0.09	1.44	1.92	−0.373	1.0

2.4.4 Summary of governing equations

All the governing ensemble-averaged equations of the gas phase are summarised as follows:

Mass conservation equation

$$\frac{\partial \overline{\rho}}{\partial t} + \nabla \cdot (\overline{\rho}\widetilde{\mathbf{u}}) = \overline{S}^d_m \ . \tag{2.71}$$

Fuel vapour mass fraction conservation equation

$$\frac{\partial \overline{\rho} \widetilde{Y}_{v,i}}{\partial t} + \nabla \cdot \left(\overline{\rho} \widetilde{\mathbf{u}} \widetilde{Y}_{v,i} \right) = \nabla \cdot \left(\overline{\rho} \overline{\Gamma}_{Y_{v,i},eff} \nabla \widetilde{Y}_{v,i} \right) + \overline{S}^{d}_{Y_{v,i}} \ . \tag{2.72}$$

Momentum conservation equation

$$\frac{\partial \overline{\rho} \widetilde{\mathbf{u}}}{\partial t} + \nabla \cdot \left(\overline{\rho} \widetilde{\mathbf{u}} \widetilde{\mathbf{u}} \right) = -\overline{\vartheta} \nabla \overline{p} + \nabla \cdot \left\{ \overline{\rho} \left[\overline{\nu}_{eff} \left(2 \widetilde{\mathbf{D}} - \frac{2}{3} \nabla \cdot \widetilde{\mathbf{u}} \mathbf{I} \right) - \frac{2}{3} \widetilde{k} \mathbf{I} \right] \right\} + \overline{\mathbf{S}}^{d}_{\mathbf{u}} \ . \tag{2.73}$$

Energy conservation equation

$$\frac{\partial \overline{\rho} \widetilde{e}}{\partial t} + \nabla \cdot \left(\overline{\rho} \widetilde{\mathbf{u}} \widetilde{e} \right) = \nabla \cdot \left(\overline{\rho} \overline{\Gamma}_{e,eff} \nabla \widetilde{e} \right) - \overline{p} \nabla \cdot \left[\overline{\vartheta} \overline{\mathbf{u}} + \left(1 - \overline{\vartheta} \right) \overline{\mathbf{u}}_{l} \right] + \overline{S}^{d}_{e} \ . \tag{2.74}$$

Following Tabrizi [280], in the above equation, all the terms involving the void fraction fluctuations and those involving the liquid velocity fluctuations, generated from the averaging of the pressure work term, have been omitted. Also, the term $\overline{p} \overline{\vartheta} \, \overline{\nabla \cdot \mathbf{u}'}$ was neglected because according to Ahmadi-Befrui [5] the modelling of this term does not significantly influence the flow predictions. In addition, the term $\overline{\vartheta} \, \overline{p' \nabla \cdot \mathbf{u}'}$ which has been associated with noise generation (Bilger [40]) is considered to be negligible at least in low-Mach-number flows (Jones [153], Ahmadi-Befrui [5]).

Turbulence kinetic energy equation

$$\frac{\partial \overline{\rho} \widetilde{k}}{\partial t} + \nabla \cdot \left(\overline{\rho} \widetilde{\mathbf{u}} \widetilde{k} \right) = \nabla \cdot \overline{\rho} \Gamma_{k,t} \nabla \widetilde{k} + G - \overline{\rho} \widetilde{\varepsilon} + \overline{S}^{d}_{k} \ . \tag{2.75}$$

Turbulence dissipation rate equation

$$\frac{\partial \overline{\rho} \widetilde{\varepsilon}}{\partial t} + \nabla \cdot \left(\overline{\rho} \widetilde{\mathbf{u}} \widetilde{\varepsilon} \right) = \nabla \cdot \overline{\rho} \Gamma_{\varepsilon,t} \nabla \widetilde{\varepsilon} + C_{\varepsilon 1} G \frac{\widetilde{\varepsilon}}{\widetilde{k}} - C_{\varepsilon 2} \overline{\rho} \frac{\widetilde{\varepsilon}^{2}}{\widetilde{k}} + C_{\varepsilon 3} \overline{\rho} \widetilde{\varepsilon} \nabla \cdot \widetilde{\mathbf{u}} + \overline{S}^{d}_{\varepsilon} \ . \tag{2.76}$$

General transport equation

$$\frac{\partial \overline{\rho} \widetilde{\phi}}{\partial t} + \nabla \cdot \left(\overline{\rho} \widetilde{\mathbf{u}} \widetilde{\phi} \right) = \nabla \cdot \left(\overline{\rho} \overline{\Gamma}_{\phi,eff} \nabla \widetilde{\phi} \right) + \overline{S}_{\phi} + \overline{S}^{d}_{\phi} \ . \tag{2.77}$$

For the sake of simplicity, from now on, the symbols '$\overline{\psi}$' and '$\widetilde{\psi}$' indicating the Reynolds-ensemble-average and Favre-ensemble-average values of ψ, respectively, are omitted.

2.5 Boundary and initial conditions

The complete description of the gas phase mathematical model requires specification of the boundary and initial conditions for all the variables. Four types of boundary conditions can be distinguished, as follows:

1. Solid walls;
2. Inflow and outflow surfaces;
3. Symmetry planes;
4. Cyclic (periodic) boundaries.

Each of the above will be individually examined next.

2.5.1 Wall boundaries

The near-wall region presents some characteristics which distinguish the flow there from those of other regions. These are listed below:

- The no-slip condition leads to steep non-linear gradients of the flow variables and low turbulence Reynolds numbers (Tennekes and Lumley [286]).
- The laminar viscosity cannot be neglected compared to the turbulent viscosity, since the Reynolds number is low. Thus, laminar effects influence the production, dissipation and transport of the turbulence energy (Tennekes and Lumley [286]).
- The size of the eddies must diminish as the wall is approached, causing the turbulence to be anisotropic (Reynolds [251]).

The employment of a 'low-Reynolds-number' k-ε model can allow to some extent for all the abovementioned effects (Jones and Launder [155]). However, the calculation of the steep gradients requires very fine mesh* which renders the approach very expensive in terms of computer storage and time. Alternatively, the *wall function method*, suggested by Launder and Spalding [180], bypasses the above problems by employing submodels of the boundary layers (referred to as *wall functions*) which link this region to the conditions at the outer edge of the boundary layer. The wall functions are strictly valid for the steady, one-dimensional turbulent Couette flow. However, their simplicity and computer economy they offer, make them being widely used in practical calculations. Particularly, in engine applications, they have been employed by Ahmadi-Befrui [5], Begleris [35], Tabrizi [280], Kralj [171], Ikonomou [143] and Leskovšek [186] among many other researchers. A couple of modifications on the original model of Launder and Spalding [180] have been made by Reitz [244] who took into account compressibility effects and also calculated the temperature in the near-wall region based on the one-dimensional unsteady energy equation. Reitz [244] compared his modified model to the original one and concluded improved predictions referred to the experimental results of Alkidas [9] for a spark-ignition engine. These modifications have been employed since then in Diesel engines as well (see e.g. Kong *et al.* [166], Patterson *et al.* [230], Kong *et al.* [167], Ricart and Reitz [253]), however, following the author's predecessors, they are excluded in this study and the original model of Launder and Spalding [180] is adopted.

Basis of the wall functions

The following assumptions are used for the derivation of the wall functions:

- The flow is steady and one-dimensional. Hence, the Newton's law of viscosity is expressed by:

$$\tau_W = \rho \nu_{\mathit{eff}} \frac{\partial u'_P}{\partial y} \,, \tag{2.78}$$

  where τ_W is the magnitude of the wall shear stress and y is the normal distance of a point P from the wall W, as illustrated in Fig. 2.1. Also, u'_P is the

*Gosman [104] noted that the number of cells needed to resolve the boundary layer would be comparable to the number required for the bulk flow.

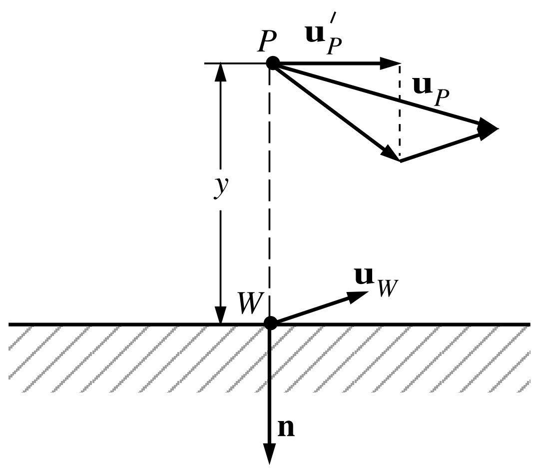

Figure 2.1: Wall boundary.

magnitude of the resultant tangential velocity of the fluid at the point P relative to the wall, i.e.

$$u'_P = |\mathbf{u}'_P| \; , \tag{2.79a}$$

where

$$\mathbf{u}'_P = \mathbf{u}_P - \mathbf{u}_W - [(\mathbf{u}_P - \mathbf{u}_W)\cdot\mathbf{n}]\,\mathbf{n} \; . \tag{2.79b}$$

In the above, $\mathbf{n}$ is the normal to the wall unit vector and $\mathbf{u}_P$ and $\mathbf{u}_W$ are the gas and wall velocity, respectively, as shown in Fig. 2.1.

- The three layers of a turbulent boundary layer, namely viscous layer, buffer zone and inertial layer, are degenerated to two layers at the expense of the buffer zone.

- The shear stress and the heat flux in the boundary layer are constant along a normal to the wall.

- The production and dissipation of the turbulence kinetic energy in the inertial sublayer are in equilibrium, i.e. $G = \rho\varepsilon$. Considering Eqs. (2.67) and (2.78), the generation rate of the turbulence kinetic energy is given by:

$$G = \rho\nu_t \left(\frac{\partial u'_P}{\partial y}\right)^2 = \tau_W \frac{\partial u'_P}{\partial y} \; . \tag{2.80}$$

- The turbulence length scale in the inertial layer is proportional to the distance from the wall. Hence,

$$\nu_t = \kappa u^* y \ , \tag{2.81}$$

where κ is the von Kármán's constant given in Table 2.3 and u^* is the friction velocity given by:

$$u^* = \sqrt{\frac{\tau_W}{\rho}} \ . \tag{2.82}$$

The wall functions are expressed in terms of dimensionless distance, y^+, velocity, u^+ and temperature, T^+, defined respectively, by:

$$y^+ = \frac{y u^*}{\nu_m} = \frac{y}{\nu_m}\sqrt{\frac{\tau_W}{\rho}} \ , \tag{2.83a}$$

$$u^+ = \frac{u'_P}{u^*} \ , \tag{2.83b}$$

$$T^+ = \frac{\rho u^* c_v \left(T_W - T_P\right)}{q_W} \ , \tag{2.83c}$$

where T_W and T_P stand for the gas temperature at the points W and P, respectively, (see Fig. 2.1) and q_W represents the magnitude of the heat flux to the wall.

Velocity and temperature profiles

The dimensionless velocity and temperature profiles in the two sublayers are given by:

Viscous sublayer:

$$y^+ \leq y_c^+ \Rightarrow \begin{cases} u^+ = y^+ \ , \\ \\ T^+ = \sigma_e u^+ \ ; \end{cases} \tag{2.84a}$$

Inertial sublayer:

$$y^+ > y_c^+ \Rightarrow \begin{cases} u^+ = \frac{1}{\kappa} \ln\left(E y^+\right) \ , \\ \\ T^+ = \sigma_{e,t}\left[u^+ + P\left(\dfrac{\sigma_e}{\sigma_{e,t}}\right)\right] \ , \end{cases} \tag{2.84b}$$

where y_c^+ is the critical value of y^+, representing the interface of the two sublayers and E is an experimentally determined constant, which depends on the wall roughness. The values of both y_c^+ and E are given in Table 2.3. The function $P\left(\frac{\sigma_e}{\sigma_{e,t}}\right)$, called the '$P$-function', is the viscous sublayer resistance factor expressing the contribution of the viscous sublayer to the total resistance. Following Jayatilleke [148], for smooth walls, it reads:

$$P\left(\frac{\sigma_e}{\sigma_{e,t}}\right) = 9\left(\frac{\sigma_e}{\sigma_{e,t}} - 1\right)\left(\frac{\sigma_e}{\sigma_{e,t}}\right)^{-1/4} , \tag{2.85}$$

where σ_e and $\sigma_{e,t}$ are the laminar and turbulent Prandtl numbers, respectively, given in Table 2.3.

Table 2.3: Coefficients of the wall functions.

y_c^+	κ	E	σ_e	$\sigma_{e,t}$
11.63	0.4187	9.793	0.7	0.9

Wall shear stress and heat flux

The wall shear stress and the wall heat flux* can be expressed in terms of the velocity and temperature at the point P as follows:

$$\boldsymbol{\tau}_W = F_w^{\mathbf{u}}\mathbf{u}'_P , \tag{2.86}$$

$$\mathbf{q}_W = \mathbf{n}F_w^e c_v\left(T_W - T_P\right) = \mathbf{n}F_w^e\left(e_W - e_P\right) . \tag{2.87}$$

Here, the functions $F_w^{\mathbf{u}}$ and F_w^e are determined by:

Viscous sublayer:

$$y^+ \leq y_c^+ \Rightarrow \begin{cases} F_w^{\mathbf{u}} = -\dfrac{\rho\nu_m}{y} , \\ \\ F_w^e = -\dfrac{\rho\nu_m}{\sigma_e y} ; \end{cases} \tag{2.88a}$$

Inertial sublayer:

*The wall shear stress has a direction parallel to the wall, whereas, the direction of the wall heat flux is normal to the wall.

$$y^+ > y_c^+ \Rightarrow \begin{cases} F_w^{\mathbf{u}} = -\dfrac{\rho\nu_m}{y}\dfrac{y^+}{\dfrac{1}{\kappa}\ln\left(Ey^+\right)} \; , \\ \\ F_w^e = -\dfrac{\rho\nu_m}{\sigma_{e,t}y}\dfrac{y^+}{\dfrac{1}{\kappa}\ln\left(Ey^+\right) + P\left(\dfrac{\sigma_e}{\sigma_{e,t}}\right)} \; . \end{cases} \tag{2.88b}$$

It should be noted that in order to avoid $y^+ \to 0$ when $\tau_W \to 0$ (see Eq. (2.83a)) in the above expressions, y^+ is derived as follows. Combining Eqs. (2.78) and (2.80) and considering also the assumed equilibrium, the following relation is obtained:

$$\tau_W^2 = \rho^2 \nu_t \varepsilon \; . \tag{2.89}$$

Substitution of Eq. (2.64b) into the above expression yields:

$$\tau_W = C_\mu^{1/2} \rho k \; . \tag{2.90}$$

Finally, this equation is substituted into Eq. (2.83a) to produce the following expression for y^+:

$$y^+ = \frac{C_\mu^{1/4} k^{1/2} y}{\nu_m} \; . \tag{2.91}$$

Turbulence energy and its dissipation

If the viscous sublayer is neglected, the equation for ε, which replaces its transport equation, Eq. (2.76), is obtained by combining Eqs. (2.64b), (2.81), (2.82) and (2.90):

$$\varepsilon = \frac{C_\mu^{3/4} k^{3/2}}{\kappa y} \; . \tag{2.92}$$

In the k equation, Eq. (2.75), the local equilibrium between turbulence production and dissipation is accomplished by setting a zero-diffusion condition at the wall and modifying the source terms. These will clearly be shown in §4.6.1.

2.5.2 Inflow and outflow surfaces

In an IC engine, the gas flow to and from the cylinder is controlled by the inlet and outlet valves. The inlet conditions of the gas (pressure, temperature, velocity and turbulence parameters) need to be specified in order to predict the flow field in the cylinder. These quantities can be defined in any cross-sectional area of the flow. They should ideally be defined somewhere in the induction system where the gas field is uniform. However, this requires the computations to be performed not only in the cylinder but also in intake system, which poses additional computing overheads. Thus, the intake surface chosen in the present study is the *valve curtain* which is defined by the circumferential area of the fictitious cylinder created by the valve head and its projection on the cylinder head as illustrated in Fig. 2.2.

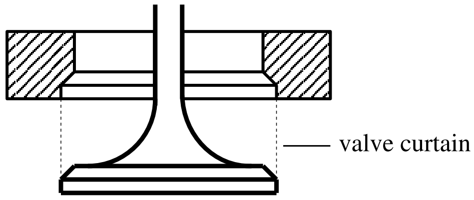

Figure 2.2: Sketch of a valve curtain.

In order to completely specify the intake flow, the following data are required:

- gas velocity (three components) at the valve curtain as a function of time,
- gas pressure, temperature and turbulence parameters (k and ε) at the valve curtain.

These data are usually determined by the experiment as will be demonstrated later in Chapter 6.

2.5.3 Symmetry planes

Some engine geometries are symmetric with respect to a plane, allowing the computational domain to be reduced by half. At symmetry planes the normal velocity component and the normal gradients of all other variables are zero.

2.5.4 Cyclic boundaries

There are circumstances in which the solution domain has pair of geometrically identical boundaries at which the flow repeats itself. Similar to the symmetry plane case, the computational domain can be reduced by applying the cyclic boundary conditions to the two identical boundaries and solving the flow field only in the sector determined by them.

The magnitude of fluxes and the scalar quantities at the corresponding locations of cyclic boundaries are equal; and vector quantities are rotated to have the same relative orientation to the boundary. Thus, the fluxes and the vectors at the point P_2 in Fig. 2.3 can be expressed in terms of the corresponding values of the point P_1 as follows:

$$\begin{aligned} (\rho\phi)_{P_2} &= (\rho\phi)_{P_1} \ , \quad \text{for } \phi = Y_{v,i},\, e,\, k,\, \varepsilon \ , \\ \mathbf{u}_2 &= \mathbf{R}^{\alpha}\cdot\mathbf{u}_1 \ , \\ d\mathcal{S}_2 &= -\mathbf{R}^{\alpha}\cdot d\mathcal{S}_1 \ , \end{aligned} \tag{2.93}$$

where $\mathbf{R}^{\alpha}$ is a rotation matrix which rotates vectors through the angle α. The above

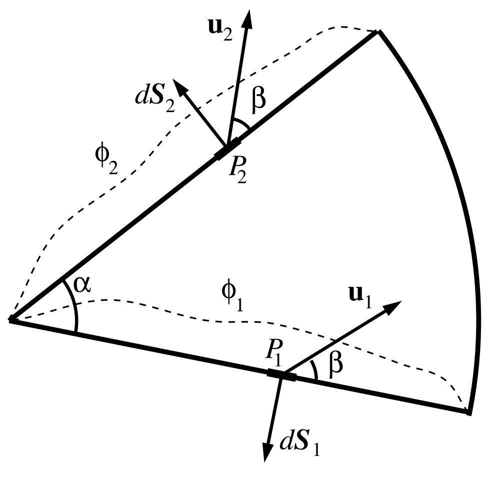

Figure 2.3: Cyclic boundaries.

relations ensure that the sum of the convective and diffusive fluxes of a general scalar property ϕ through two corresponding elementary surfaces $d\mathcal{S}_1$ and $d\mathcal{S}_2$ on the cyclic boundary pair, are respectively equal to zero:

$$d\mathcal{S}_1\cdot(\rho\mathbf{u}\phi)_{P_1} + d\mathcal{S}_2\cdot(\rho\mathbf{u}\phi)_{P_2} = 0 \; , \tag{2.94a}$$

$$d\mathcal{S}_1\cdot(\Gamma_\phi\nabla\phi)_{P_1} + d\mathcal{S}_2\cdot(\Gamma_\phi\nabla\phi)_{P_2} = 0 \; . \tag{2.94b}$$

2.5.5 Initial conditions

In unsteady problems, the initial conditions for all the time-dependent variables in the solution domain are necessary due to the parabolic nature of the governing equations with respect to time. Particularly, in engines the flow is repetitive (periodic) from cycle to cycle and consequently, the initial conditions are of minor importance. However, this implies several cycle calculations which is expensive in terms of computer resources and is therefore, not used in practical engine calculations. Hence, an estimation of the initial conditions becomes necessary. This could be based on one or more of the following, while it is emphasised that it is semantic the initial conditions to be thermodynamically consistent (Begleris [35]):

- physical reasoning,
- previous experience,
- experimental data,
- information obtained by a zero-dimensional model.

The calculations can commence at any crank angle provided that the distributions of velocity, pressure, temperature and turbulence parameters are known. For want of a better practice, it is common the calculations to start before the inlet valve(s) opens since during induction, the in-cylinder flow is mainly controlled by the intake flow and subsequently, the initial conditions are of less importance.

2.6 Closure

In this chapter, the basic equations of a multiphase system have been provided. By applying these equations to the gas phase in Section 2.3 and including a set of constitutive relations (state equation of ideal gas, Newton's law of viscosity, Fourier's law of conductivity and Fick's law of diffusivity) the complete mathematical description of the gas phase has been obtained.

The instantaneous gas equations have been averaged in Section 2.4 by the density-weighted (Favre) ensemble averaging technique where the macroscopic density was used instead of the microscopic density. The additional unknown terms have been modelled by the k-ε turbulence model.

The description of the gas equation has been completed by imposing the boundary and initial conditions in Section 2.5. Wall functions have been employed for wall boundary conditions. Other boundary conditions that have been discussed are inflow and outflow surfaces, symmetry planes and cyclic boundaries.

In the next chapter, the mathematical model of the discrete phase (droplets) and the expressions of the coupling source terms that appear in the gas phase equations, representing the exchange of mass, momentum and energy between the two phases, will be presented.

Chapter 3

Dispersed phase modelling

3.1 Introduction

The modelling of the gas phase has been presented in the previous chapter. The aim of this chapter is the mathematical description of the spray along with the source terms allowing for the coupling between the two phases.

As soon as the liquid jet issues from the injector and enters the engine cylinder it atomises into droplets which might further break up. The droplets decelerate and deform due to the drag force exerted by the surrounding gas and evaporate due to the high ambient temperature and pressure. During their life time, the droplets might also collide with other droplets and/or might hit the engine wall. All these processes are modelled based on theoretical and experimental studies, as will be presented in this chapter.

Following Crowe [72], Gosman and Johns [109] and Dukowicz [83], in this study, the discrete droplet model is employed, according to which the spray is represented by a number of *computational parcels*, each of which represents a large number of droplets of identical size, velocity and temperature. The ordinary differential equations governing the mass, momentum and energy conservation of each parcel are solved for a representative member of the parcel to compute the mass, the motion and the temperature changes. The effects on the gas phase are calculated via source terms in the gas conservation equations expressing the local exchange rates of mass, momentum and energy with the droplets.

The following general assumptions are made:

1. The droplets are spherical (except from the modelling of drag which allows for droplet deformation).

2. The interphase transport of mass, momentum and energy are quasi-steady, i.e. their rates are equal to the steady-state rates for the same boundary conditions.

3. The transfer coefficients of mass, momentum and energy between a droplet and the surrounding gas are independent of the proximity of neighbouring droplets and can be represented by empirical correlations.

It should be noted that these assumptions idealise the real Diesel spray process significantly. However, they are introduced to simplify the mathematical modelling and enable affordable numerical treatments. Other assumptions adopted in relation to particular aspects are given in the presentation of each submodel which also comprises a relevant literature review.

A nozzle flow model allowing for the cavitation phenomenon is described in Section 3.2. Cavitation results in a contraction of the nozzle exit area and consequently, in an increase of the injection velocity.

Two atomisation models are described in Section 3.3. The Huh model, presented in §3.3.2, is based on the assumption that turbulence developed in the nozzle hole induces perturbations on the jet surface resulting in disintegration. On the other hand, the MPI atomisation model, described in §3.3.3, is based on cavitation phenomena taking place in the nozzle. It also accounts for droplet collisions at the tip of the liquid core.

A stochastic treatment is used to model the effect of turbulence on the droplet trajectory as is described in Section 3.4. The droplet velocity is calculated by applying the Newton's second law, as is explained in Section 3.5, in which the drag force is modelled by a correlation of the drag coefficient taking into account distortions of the droplet shape.

The exchange of mass and energy between the droplet and the surrounding gas is presented in Section 3.6. Three different kinds of the thermal conductivity are examined, namely infinite, finite and 'effective'. For the finite and effective cases, the energy equation is solved both 'analytically' and by a novel profile method. The latter method is also applied to the diffusion equation for multicomponent fuels.

Three breakup models are presented in Section 3.7, namely the Reitz-Diwakar, Pilch-Erdman and Hsiang-Faeth. All the models distinguish various types of breakup, however, their main difference is the practice for the calculation of the droplet stable diameter.

The droplet/droplet collision model of O'Rourke is presented in Section 3.8. The model distinguishes three types of collisions, namely separation, permanent coalescence and bouncing.

The spray/wall interaction model of MPI is described in Section 3.9. The model allows for a multiple droplet impact and distinguishes three types of droplet impingement, namely splashing, fragmentation and sticking.

Finally, the initial conditions of the spray and the closure of this chapter are given in Sections 3.10 and 3.11, respectively.

3.2 Nozzle flow

3.2.1 Introduction

The structure of the flow in the nozzle plays a dominant role on Diesel spray formation since it imposes the initial conditions at the nozzle exit. Many researchers have investigated the effect of the injector shape on spray formation (see Hamady *et al.*

[119], Yamamoto and Niimura [311], Potz *et al.* [234], Zhang and Shi [315], Renner and Maly [250]).

Su *et al.* [278] compared the spray structure for two different types of nozzle hole entrances, namely sharp-edged and round-edged. They observed that for the same injection rate, the sharp-edged nozzle needed a higher injection pressure to overcome the higher friction loss, but produced longer spray penetration, larger spray angle and smaller droplet sizes. These positive effects of sharp-edged nozzles were also reported by Karasawa *et al.* [157].

Di Giorgio *et al.* [81] performed a comparison between the sprays from each hole of a 5-hole VCO (valve-covered orifice) nozzle for DI Diesel engines. Different values of droplet size distribution were observed and the authors claimed that this was due to the different hole inclination with respect to the injector axis. The effect of the hole inclination was studied numerically by Bruni *et al.* [55] who solved the 3-D flow equations in a VCO injector with five holes and noted different flow rates between the holes attributed to different losses related to the asymmetry of the nozzle geometry.

However, the spray structure is affected not only by the losses in the hole but also by vapour cavity formation. A conceptual picture of cavitation is given by Chaves *et al.* [59] as follows. Upstream of the nozzle hole, the flow area is large, the flow velocity relatively low and the corresponding static pressure is high. The fuel is accelerated in the inlet region of the hole because of the area contraction. The fluid cannot follow the curvature of the sharp inlet corner because of inertia and therefore, the flow separates at this point. A separated flow region is formed at the nozzle entrance with a contracted core flow. The ratio of the area occupied by the core flow at its smallest cross-section to the geometric area of the nozzle hole is called the *contraction coefficient*. Further downstream the flow reattaches and then occupies the whole hole area again. Thereafter, the flow velocity decreases and the pressure recovers almost to the value present at the nozzle exit. Chaves *et al.* [59] reported that even when the ambient pressure at the exit of the nozzle is as high as encountered in Diesel engines, the local pressure within the nozzle can be low enough to initiate cavitation if the flow velocity is high enough. According to Chaves *et al.* [59], with increasing injection pressure the cavitation zone reaches the nozzle exit (supercavitation). The discharge coefficient and the spray angle then level off at a value that is almost independent of any further increase of injection pressure.

The effect of cavitation on the spray has been reported by many investigators (see Soteriou *et al.* [271, 272], Kegl [161]). Ikonomou [143] attempted to predict the spray penetration of a free spray measured by Arcoumanis *et al.* [19] and he observed that the measured spray tip velocity was roughly 25 % higher than the computed one, which was attributed to the cavitation in the nozzle. In the present study cavitation effects are taken into account, using a cavitation model, developed at Max-Planck Institut (MPI) by Obermeier and Chaves [59, 214, 217]. The main task of this model is to predict the injection velocity. In the next section, a summary of the model will be presented. A detailed description can be found in [221].

3.2.2 MPI cavitation model

In their experiments the developers used a transparent injector and they observed a cavitation region was created at the entrance of the nozzle (section i in Fig. 3.1) and propagated downstream. It could reach the nozzle exit or collapse inside the nozzle, depending on the supply pressure and the flow rate. The cavitation resulted

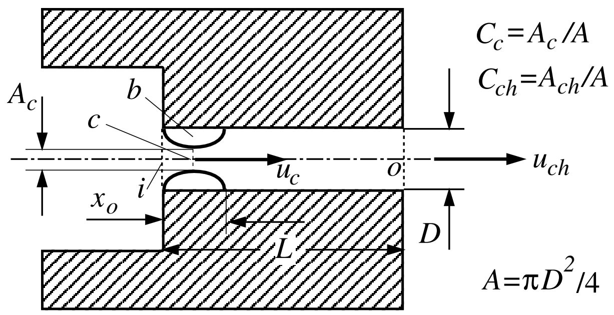

Figure 3.1: Nozzle geometry.

in the reduction of the available cross-sectional area and consequently, increase in the liquid exit velocity.

The MPI model assumes quasi-steady axisymmetric flow and the formation of two characteristic regions. The first region, which is called separation/cavitation *bubble* (denoted by b in Fig. 3.1), takes place at the nozzle entrance. The other region comprises the remaining nozzle, i.e. downstream of this bubble, where a turbulent boundary layer and cavitation region develop. The following assumptions are made:

- The length of the bubble, x_o, is taken to be equal to the nozzle diameter, D.
- The cross-section of the flow between the middle of the bubble, c and the end of the bubble, x_o, (see Fig. 3.2) is constant and there are no frictional losses.
- A turbulent boundary layer starts at the end of the bubble and the velocity profile inside the layer obeys the '1/7 power law'. The velocity profile outside the layer is assumed to be of 'plug' form (see Fig. 3.2).
- The cavitation region is approximated by a quasi-cylindrical cavity of variable cross-section, starting from x_o with a thickness determined from the mass conservation equation.
- The pressure inside the cavity is equal to the saturation fuel vapour pressure.
- The difference between the pressure inside the nozzle and the chamber pressure results in a pressure jump at the nozzle exit. The authors of the model call this a *Carnot shock*. The exit velocity and exit area contraction ratio are determined from mass and momentum balances across the pressure jump.

The critical pressure, $p_{ch,crit}$, below which cavitation occurs is obtained from one-dimensional mass and momentum conservation equations between the minimum cross-section in the region of the bubble, A_c and the exit cross-section, A_{ch}. It is given by:

$$p_{ch,crit} = \rho_{d,inj} \left\{ C_c u_c^2 - \left[C_{ch} + \frac{1}{2}\lambda \left(\frac{L}{D} - \frac{1}{2} \right) \right] u_{\mathit{eff}}^2 \right\} , \tag{3.1}$$

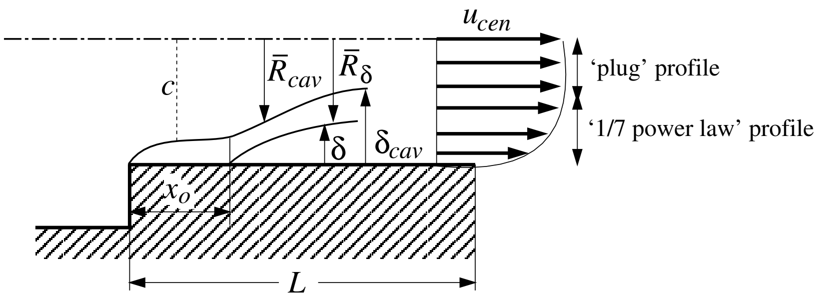

Figure 3.2: Boundary layer and cavitation region in the nozzle.

where $\rho_{d,inj}$ is the liquid density evaluated at the injection temperature, $T_{d,inj}$. Also, L is the nozzle length and C_c and C_{ch} are the contraction area ratios in the entrance and the exit, respectively, i.e.

$$C_c = \frac{A_c}{A} , \tag{3.2a}$$

$$C_{ch} = \frac{A_{ch}}{A} . \tag{3.2b}$$

In the above, A is the nozzle cross-sectional area given by:

$$A = \frac{\pi D^2}{4} . \tag{3.3}$$

For the evaluation of the critical pressure, the exit contraction ratio in Eq. (3.1) is set to 1, which represents its threshold value, while the entrance contraction ratio is an input to the model*. Also, u_{eff} is the effective liquid velocity calculated from the specified volumetric flow rate, $\dot{Q}$,

$$u_{eff} = \frac{\dot{Q}}{A} \tag{3.4}$$

and u_c is the liquid velocity at the cross-section A_c,

$$u_c = \frac{\dot{Q}}{A_c} = \frac{u_{eff}}{C_c} . \tag{3.5}$$

Finally, in Eq. (3.1), λ denotes the friction factor given by:

$$\frac{1}{\sqrt{\lambda}} = -2 \log \left(\frac{2.51}{Re_n \sqrt{\lambda}} + \frac{k_r}{3.71 D} \right) , \tag{3.6}$$

*According to experiments, the value of C_c lies in the range $0.6 - 0.8$ (Obermeier [217]).

where k_r is the nozzle wall roughness and Re_n is the nozzle Reynolds number, defined as:

$$Re_n = \frac{\rho_{d,inj} u_{eff} D}{\mu_{d,inj}} , \tag{3.7}$$

where $\mu_{d,inj}$ is the liquid dynamic viscosity evaluated at the injection conditions.

Three flow regimes are distinguished, as illustrated in the flow chart in Fig. 3.3, depending on the chamber pressure, p_{ch} and the length of the cavitation region:

1. Non-cavitating flow, $p_{ch} > p_{ch,crit}$,
   $\Rightarrow \quad C_{ch} = 1$;

2. Cavitating flow, $p_{ch} \leq p_{ch,crit}$,
   cavitation region collapses inside the nozzle,
   $\Rightarrow \quad C_{ch} = 1$;

3. Supercavitating flow, $p_{ch} \leq p_{ch,crit}$,
   cavitation region reaches the nozzle exit,
   $\Rightarrow \quad C_{ch} < 1$.

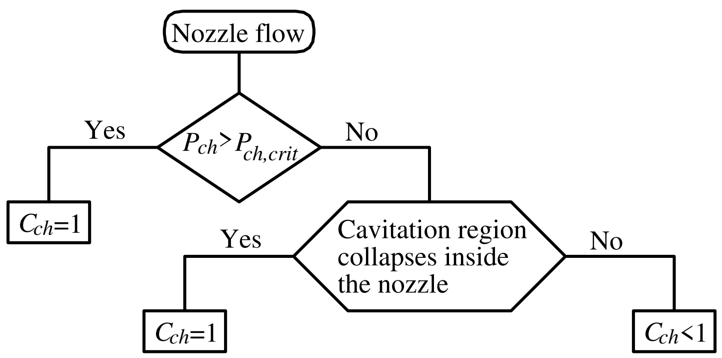

Figure 3.3: Flow chart of cavitation in the nozzle.

If cavitation occurs, the development of the boundary layer and cavitation region along the nozzle wall, as well as the velocity u_{cen} (see Fig. 3.2) are calculated from the following ordinary differential equations:

For $\overline{R}_\delta > \overline{R}_{cav}$:

$$\frac{d\overline{R}_\delta}{d\overline{x}} = -c_f \frac{1}{\dfrac{7}{90} + \dfrac{7}{60}\overline{R}_\delta} \,, \tag{3.8a}$$

$$\overline{R}_{cav} = \sqrt{\frac{49}{60} + \frac{7}{60}\overline{R}_\delta + \frac{1}{15}\overline{R}_\delta^2 - C_c} \,, \tag{3.8b}$$

$$u_{cen} = u_c \,; \tag{3.8c}$$

For $\overline{R}_\delta = \overline{R}_{cav}$:

$$\frac{d\overline{R}_\delta}{d\overline{x}} = -c_f \frac{\dfrac{49}{240} + \dfrac{7}{240}\overline{R}_\delta - \dfrac{7}{30}\overline{R}_\delta^2}{\dfrac{49}{180}\overline{R}_\delta + \dfrac{49}{360}\overline{R}_\delta^2 - \dfrac{49}{120}\overline{R}_\delta^3} \,, \tag{3.8d}$$

$$u_{cen} = \frac{u_c C_c}{\dfrac{49}{60} + \dfrac{7}{60}\overline{R}_\delta - \dfrac{14}{15}\overline{R}_\delta^2} \,. \tag{3.8e}$$

Here, $\overline{R}_\delta$ and $\overline{R}_{cav}$ are the distances of the boundary and cavitation regions from the nozzle axis (see Fig. 3.2), respectively, normalised by the nozzle radius. The coordinate along the nozzle axis, $\overline{x}$, is also normalised by the radius. Also, the quantity c_f is the skin friction coefficient defined by:

$$c_f = \frac{1}{4}\left(\frac{u_{eff}}{u_{cen}}\right)^2 \lambda \,, \tag{3.9}$$

where for fully developed turbulent flow ($\overline{R}_\delta = 0$), λ is calculated from Eq. (3.6) and for $\overline{R}_\delta > 0$, it is calculated from:

$$\frac{1}{\sqrt{\lambda}} = -2\log\left(\frac{2.51}{Re_n\sqrt{\lambda}} + \frac{k_r}{7.42\delta}\right) \,. \tag{3.10}$$

Here, the Reynolds number, Re_n, is defined by:

$$Re_n = \frac{1.633\rho_{d,inj} u_{cen}\delta}{\mu_{d,inj}} \,. \tag{3.11}$$

In the above expression, δ is the boundary layer thickness, given by:

$$\delta = \frac{D}{2}\left(1 - \overline{R}_\delta\right) \,. \tag{3.12}$$

The integration of the above differential equations requires a boundary condition. At $x_o = D$ it is taken that $\delta = 0$ and the thickness of the cavitation region, δ_{cav}, is calculated from the continuity equation, assuming a uniform velocity profile.

The exit contraction ratio is calculated from the mass and momentum conservation equations at the nozzle exit:

$$C_{ch} = \frac{u_c^2 C_c^2}{u_{cen}^2(L)\left[\frac{49}{72} + \frac{7}{36}\overline{R}_\delta(L) + \frac{1}{8}\overline{R}_\delta^2(L) - \overline{R}_{cav}^2(L)\right] - \frac{p_{ch}}{\rho_{d,inj}}} \, . \tag{3.13}$$

Finally, the actual velocity at the nozzle exit is obtained from:

$$u_{ch} = \frac{\dot{Q}}{C_{ch} A} \, . \tag{3.14}$$

If $C_{ch} \geq 1$, the cavitation region collapses inside the nozzle and the actual exit velocity is equal to the effective velocity ($u_{ch} = u_{eff}$), since the available for the liquid cross-sectional area at the exit is the nozzle geometrical cross-sectional area.

3.3 Atomisation

3.3.1 Introduction

As soon as the liquid exits from the nozzle it forms a jet which disintegrates. The atomisation of the jet is desirable, since it helps in mixing and evaporation, which enable the combustion. Various types of injectors are commercially used, depending on application, to improve the atomisation process. A description of the principles of operation of a wide number of atomisers is given by Lefebvre [185].

Based on the injection velocity, Reitz [242] and Faeth [93] distinguished four different jet disintegration regimes shown schematically in Fig. 3.4:

1. **Rayleigh jet breakup regime**: This regime is named after Rayleigh [239] who investigated the jet breakup for low injection velocities. He found that the surface tension forces induce unstable jet surface perturbations whose wavelengths are greater than the jet perimeter (the smaller wavelengths are damped). The amplitude of these unstable perturbations grows, resulting in jet breakup many nozzle diameters downstream from the nozzle exit. The average size of the droplets produced is nearly twice the nozzle diameter.

2. **First wind-induced breakup regime**: In this regime, the jet breakup is induced by the still-dominant surface tension forces, accompanied and augmented by the effects of aerodynamic forces due to the relative motion between the jet and the surrounding air. This produces a twisting motion of the liquid and unstable wave growth at the jet surface. The perturbations, with a smaller wavelength than in the Rayleigh regime, become unstable and the droplets produced have diameters comparable to the jet diameter.

3. **Second wind-induced breakup regime**: As the injection velocity increases, the importance of the aerodynamic forces, opposed by the surface tension forces, becomes higher, leading to surface perturbations with even smaller wavelengths than in the previous regime to be the most unstable. This results, at some jet diameters downstream of the nozzle, in detachment of parts of the jet surface, producing droplets with average diameter much smaller than the jet diameter.

4. **Atomisation regime**: At higher injection velocities, the jet breakup is believed to start very close to or immediately at the nozzle exit, although the evidence is not conclusive. The average diameter of the droplets formed is much smaller than the jet diameter.

Although for the first three of the abovementioned breakup regimes, most researchers agree on the effect of the jet velocity on the breakup length (see Haenlein [118]), for the fourth regime, which is of particular interest in engine applications, conflicting theories have been proposed ascribing the jet breakup to aerodynamic effects, cavitation, liquid turbulence in the nozzle, rearrangement of the jet velocity profile at the nozzle exit and liquid supply pressure oscillations*. None of all these theories alone can explain the atomisation process, since the theory based on aerodynamic effects produces the same atomisation for all nozzle geometries, the theory based on cavitation implies that for non-cavitating flows atomisation does not occur, the theory based on liquid turbulence produces a turbulent jet to be the most

*A comprehensive review on all these theories can be found in Ikonomou [143].

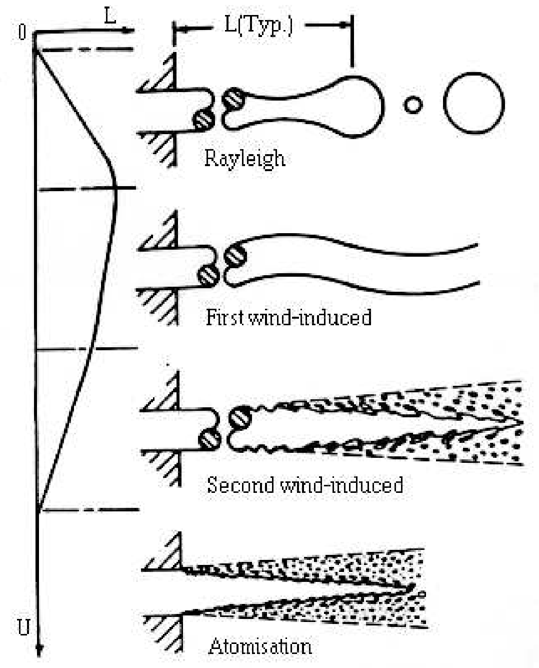

Figure 3.4: Liquid jet disintegration regimes, adapted from Faeth [93].

unstable, the theory based on rearrangement of the jet velocity profile at the nozzle exit yields a Poiseuille flow (high viscosity jet) to be the most unstable and finally, the theory based on liquid supply pressure oscillations implies that for a constant injection pressure, atomisation does not occur.

The most successful theoretical models, to date, are based on the unstable wave growth mechanism, called Kelvin-Helmholtz instability theory (see Kralj [171]). It assumes that initial perturbations on the jet surface result in unstable wave growth due to pressure variations provoked by aerodynamic forces. The detachment of these waves creates droplets.

In the present study, two atomisation models for round-hole Diesel injectors are employed, namely the Huh model developed by Huh and Gosman [141] and the MPI model developed at Max-Planck Institut (MPI) by Obermeier and Chaves [219, 222]. The former assumes that the development of turbulence in the nozzle causes initial perturbations on the jet surface whose growth and detachment from the jet surface occur by the action of aerodynamic forces. The MPI model takes into account cavitation in the nozzle and produces droplets by stripping off the jet surface due to aerodynamic forces and by allowing collisions between large lumps of liquid which result in further breakup. The following sections describe these models in detail.

3.3.2 Huh model

The Huh atomisation model is based on two phenomena. Initial perturbations on the jet surface are induced, when it leaves the nozzle, by the turbulence developed in the nozzle hole. The perturbations grow due to aerodynamic forces until they detach from the jet surface forming droplets. These droplets are called secondary droplets*.

Nozzle turbulence and its decay

The pressure drop, Δp, in the nozzle hole between the inlet, 'i', and outlet, 'o', sections (see Fig. 3.5) is obtained by applying the Bernoulli equation:

$$\Delta p = \frac{\rho_{d,inj} U^2}{2} \left[\frac{1}{c_d^2} - K_c - \left(1 - s^2\right) \right] \ . \tag{3.15}$$

In the above, K_c and c_d represent the form loss coefficient at the contraction corner (section 'i') and the discharge coefficient, respectively and $s = \pi D^2/4A$ is the outlet to inlet area ratio. Also, U is the average injection velocity estimated by integrating the volumetric flow rate $\dot{Q}$ from the time at the start of injection, SOI, to the time at the end of injection, EOI:

$$U = \frac{\displaystyle\int_{\mathrm{SOI}}^{\mathrm{EOI}} \dot{Q}(t) dt}{\displaystyle\int_{\mathrm{SOI}}^{\mathrm{EOI}} \frac{\pi D^2}{4} dt} \ . \tag{3.16}$$

The pressure drop is caused by the friction on the nozzle wall and for fully-developed flow, the force balance for the liquid in the nozzle reads:

$$\pi D L \tau_W = \frac{\pi D^2}{4} \Delta p \ , \tag{3.17}$$

*More details of the model are given by Kralj [171] who implemented the model in SPEED code.

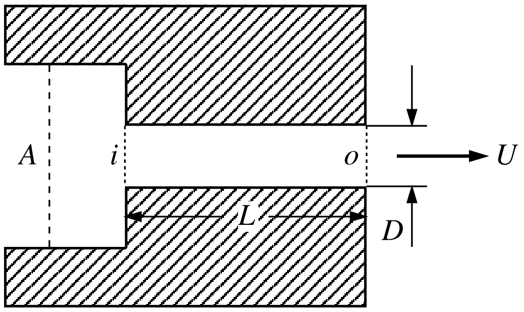

Figure 3.5: Nozzle geometry.

where τ_W is the average tangential stress at the nozzle wall. Substitution of Eq. (3.15) into Eq. (3.17) yields:

$$\tau_W = \frac{\rho_{d,inj} U^2}{8\frac{L}{D}} \left[\frac{1}{c_d^2} - K_c - \left(1 - s^2\right) \right] . \tag{3.18}$$

One-dimensional force and energy balances in the nozzle between inlet and outlet cross-sections are combined with Eq. (3.18) to give an estimation of the average turbulence kinetic energy, k_a and its dissipation rate, ε_a, at the nozzle exit:

$$k_a = \frac{U^2}{8\dfrac{L}{D}} \left[\frac{1}{c_d^2} - K_c - \left(1 - s^2\right) \right] , \tag{3.19a}$$

$$\varepsilon_a = \frac{K_\varepsilon U^3}{2L} \left[\frac{1}{c_d^2} - K_c - \left(1 - s^2\right) \right] . \tag{3.19b}$$

Gosman *et al.* [106] compared the one-dimensional model with multidimensional flow field calculations and tuned the coefficient K_ε to 0.27. The turbulence length and time scales at the nozzle exit, L_t^o and τ_t^o, are respectively expressed by:

$$L_t^o = C_\mu^{3/4} \frac{k_a^{3/2}}{\varepsilon_a} , \tag{3.20a}$$

$$\tau_t^o = C_\mu^{3/4} \frac{k_a}{\varepsilon_a} , \tag{3.20b}$$

where C_μ is a coefficient of the k-ε turbulence model given in §2.4.3.

Once the liquid leaves the nozzle, the internal turbulence of the liquid jet decays with time, since internal generation due to shear stresses gradually ceases. The k-ε model is applied to each parent drop assuming homogeneous isotropic turbulence.

The resulting turbulence length and time scales are given by:

$$L_t(t) = L_t^o \left(1 + C_{a1} \frac{t}{\tau_t^o}\right)^{C_{a2}} \ , \tag{3.21a}$$

$$\tau_t(t) = \tau_t^o \left(1 + C_{a1} \frac{t}{\tau_t^o}\right) \ , \tag{3.21b}$$

where C_{a1} and C_{a2} are empirical coefficients given in Table 3.1.

Table 3.1: The coefficients of the Huh atomisation model.

C_μ	K_c	K_ε	C	C_{a1}	C_{a2}	C_1	C_2	C_3	C_4	C_5
0.09	0.45	0.27	1.0	0.92	0.4565	2.0	0.5	1.0	3.0	0.1

Surface wave growth

The interaction between the liquid jet and the surrounding gas results in the increase of the amplitudes of the initial perturbations on the jet surface, until they become detached as droplets. The amplification is described by the dispersion equation of Taylor [285], which relates the growth rate of amplitude of a surface wave to its wavelength:

$$\left(\omega + 2\nu_d \kappa^2\right)^2 + \frac{\sigma_d \kappa^3}{\rho_d} - 4\nu_d^2 \kappa^3 \sqrt{\kappa^2 + \frac{\omega}{\nu_d}} + \omega + jU\kappa^2 \frac{\rho_m}{\rho_d} = 0 \ . \tag{3.22}$$

Here, ν_d, σ_d and ρ_d are the liquid kinematic viscosity, surface tension coefficient and density, respectively. Also, κ is the wavenumber, $\kappa = 2\pi/L_w$, where L_w is the wavelength of perturbation. Finally, j denotes the imaginary unit and the real part of ω represents the exponential growth rate whose inverse is the wave growth time, τ_w.

Atomisation scales

The estimation of the atomisation scales is based on two hypotheses:

1. The dominant length scale of atomisation, L_A, is proportional to the turbulent length scale, L_t:

$$L_A = C_1 L_t \ , \tag{3.23}$$

where C_1 is an empirical coefficient set to 2 on the assumption that the atomisation scale, L_A, is equal to the eddy diameter which is twice the turbulent length scale, L_t. The corresponding wavelength of perturbations, L_w, is given by:

$$L_w = \frac{L_A}{C_2} \ . \tag{3.24}$$

Here, C_2 is another empirical coefficient set to 0.5, based on the conceptual picture that the half of the jet surface wave will be detached to form a secondary droplet.

2. The time scale of atomisation, τ_A, is expressed by a linear combination of the turbulent time scale, τ_t and the wave growth time scale, τ_w:

$$\tau_A = C_3 \tau_t + C_4 \tau_w \ , \tag{3.25}$$

where the coefficients C_3 and C_4 have been tuned to 1.0 and 3.0, respectively, to match experimental data. The above form of the atomisation time scale guarantees that atomisation does not occur in vacuum ($\tau_w \to \infty$), or when the jet flow is laminar ($\tau_t \to \infty$).

Spray angle

Once the atomisation scales have been determined, the spray semi-cone angle is obtained from:

$$\tan\frac{\theta}{2} = \frac{L_A/\tau_A}{U} \ . \tag{3.26}$$

Droplet size and velocity

It is assumed that the jet consists of large droplets, called parent droplets, with initial diameter, D_d, equal to the nozzle hole diameter, D. Subsequently, they break up with a rate determined by:

$$\frac{dD_d}{dt} = -2\frac{L_A}{\tau_A}\frac{1}{C_5} , \tag{3.27}$$

where C_5 is an arbitrary constant which is determined to fit experimental data such as the breakup length or tip penetration (Ikonomou [143]). Huh and Gosman [141] used $C_5 = 1$ while Kralj [171] and Ikonomou [143] adopted $C_5 = 0.1$. In this study, both values of this parameter will be used to examine its effect on spray structure and development. A parent droplet undergoes atomisation until $L_A \geq D_d/2$. Then, it becomes into secondary droplet and might further break up according to the breakup model described later in Section 3.7.

The probability density function (PDF) of the sizes of the secondary droplets is based on the assumption of isotropic turbulence in the liquid phase and the following four hypotheses:

1. The number of droplets of size x is inversely proportional to the atomisation time scale, τ_A.

2. The number of droplets of size x is proportional to the jet-to-droplet surface area ratio, D_d^2/x^2.

3. The number of droplets of size x is proportional to the dimensionless turbulence energy spectrum, $\Phi(x)$, given, according to Hinze [133], by:

$$\Phi(x) = \frac{[\kappa(x)/\kappa_e]^2}{\left\{1 + [\kappa(x)/\kappa_e]^2\right\}^{11/6}} . \tag{3.28}$$

   Here, the wavenumber $\kappa(x)$ is the inverse of x and κ_e is the inverse of the length scale L_e, given by:

$$L_e = \frac{L_t}{0.75} . \tag{3.29}$$

4. The number of droplets of size in the range $(x, x + dx)$ is proportional to the unit size interval, dx/x.

The PDF is defined as the volume fraction of the droplets of size x per interval dx, per total volume of secondary droplets, V_s:

$$p(x) = \frac{1}{V_s}\frac{dV_s}{dx} \; ; \tag{3.30}$$

and it is evaluated from:

$$p(x) = C\frac{\Phi(x)}{\tau_A(x)} \; , \tag{3.31}$$

where C is a normalisation constant whose value is given in Table 3.1. The cumulative distribution function, $F(x)$, is calculated by integrating the PDF from the minimum droplet size, x_{min}, to the size x:

$$F(x) = \int_{x_{min}}^{x} p(x)dx \; . \tag{3.32}$$

The minimum droplet size is obtained from the Kelvin-Helmholtz instability theory as:

$$x_{min} = 2\pi\frac{(\rho_d + \rho_m)\,\sigma_d}{\rho_d\rho_m U^2} \; . \tag{3.33}$$

The size, x_s and the number, N_s, of the secondary droplets are calculated from the distribution function $F(Y_r)$ where Y_r is a random number in the range [0, 1] and the mass balance of the liquid, respectively:

$$x_s = F^{-1}(Y_r) \; , \tag{3.34}$$

$$N_s = \frac{(D_d)^3 - (D_d^n)^3}{x_s^3} \; , \tag{3.35}$$

where D_d^n is the diameter of the parent droplet after breakup.

The velocity of the parent droplets does not change during breakup and the secondary droplets are assumed to inherit this velocity.

According to Faeth [93], the atomisation process ceases as soon as one of the following criteria is satisfied:

$$We < 40 \; , \tag{3.36a}$$

$$Oh > 2 \; , \tag{3.36b}$$

where We and Oh are the Weber and Ohnesorge number, respectively. The former represents the ratio of inertial to surface tension forces, while the latter represents the ratio of viscous to surface tension forces. Their mathematical expressions are respectively given by:

$$We = \frac{\rho_{m,a}|\mathbf{u}_{inj}|^2 D}{\sigma_{d,inj}} , \tag{3.37}$$

$$Oh = \frac{\mu_{d,inj}}{\sqrt{\rho_{d,inj} D \sigma_{d,inj}}} . \tag{3.38}$$

Here, $\rho_{m,a}$ is the average molecular density of the surrounding gas and $\mathbf{u}_{inj}$ is the injection velocity. Also, the subscript 'inj' indicates that the liquid properties are evaluated at the injection conditions.

3.3.3 MPI model

This atomisation model is described by Obermeier [219] and is based on the previous version of the model* given by Obermeier [220, 222] (see also [60]).

The model allows for cavitation in the nozzle in conjunction with the nozzle model described in §3.2.2. As soon as the liquid leaves the nozzle exit, it is assumed to form a jet which breaks up into large droplets (primary droplets) forming the liquid core. Secondary droplets are produced by stripping off the liquid core due to aerodynamic forces and by allowing collisions between the primary droplets due to their different velocities.

The highly-perturbed liquid surface experiences a high shear-rate caused by cavitation [222] (see Fig. 3.6). When the Saffman lifting force overcomes the adhesive surface tension force, a secondary droplet is formed. The balance between these two forces determines the size of the secondary droplet.

The main assumptions of the model are as follows [222]:

- The diameter of the primary droplets is equal to the diameter of the liquid core.

*Details of the previous version of the model can also be found in Kralj [171] who implemented the model in SPEED code.

- The diameter of the tip of the liquid core is equal to the diameter of the secondary droplet formed there.
- The ejection angle of the secondary droplets randomly varies between 0 and the maximum spray semi-cone angle, α_{max}.
- The diameter of the secondary droplet, formed after collision between primary droplets, is one tenth of that of the primary.

Jet stripping

The liquid core is represented by a chain of primary droplets which leave the nozzle with velocity u_{ch} obtained from the nozzle model and diameter equal to the nozzle diameter, D. Immediately after the start of injection, the length of the liquid core is time-dependent and grows from zero to the experimentally-observed* steady value:

$$L_c = 4D\sqrt{\frac{\rho_d}{\rho_m}} \, . \tag{3.39}$$

The diameter of the liquid core, which is assumed to have the shape of a truncated cone (see Fig. 3.6), at the position x is given by:

$$D_c = D - (D - D_{tip})\,\frac{x}{L_c} \, , \tag{3.40}$$

where D_{tip} is the diameter at the tip of the core.

The diameter of the secondary droplet, D_s, is determined from the equilibrium between a disruptive lift force, F_l, provoked by the gas due to a velocity gradient in the near-core region and an opposing surface tension force, F_σ. The lift force is calculated according to Mei [199], who extended the theory of Saffman [255, 256] by accounting for results obtained by numerical simulation by Dandy and Dwyer [76]:

$$F_l = \begin{cases} \left[(1 - 0.3314\sqrt{a})\, e^{-Re/10} + 0.3314\sqrt{a}\right] F_S \, , & \text{for } Re \leq 40 \, , \\ \left[0.0524\sqrt{aRe}\right] F_S \, , & \text{for } Re > 40 \, , \end{cases} \tag{3.41}$$

*In the original MPI model [222], the coefficient in the expression of the length of the liquid core was set to 7 as suggested by Cheroudi *et al.* [61], however, in the current modified version, this coefficient is set to 4.

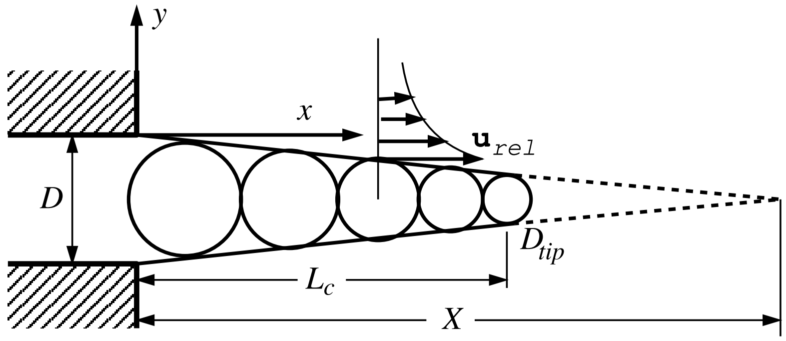

Figure 3.6: Liquid core.

where a is the expression:

$$a = \frac{\frac{du}{dy}D}{2u_{rel}} \ . \tag{3.42}$$

The surface tension force is expressed by:

$$F_\sigma = \pi \sigma_d D_s \ . \tag{3.43}$$

In Eq. (3.41), Re is the Reynolds number given by:

$$Re = \frac{\rho_m u_{rel} D_s}{\mu_m} \ , \tag{3.44}$$

where μ_m is the molecular dynamic viscosity of the surrounding gas. Also, F_S is the Saffman force determined by:

$$F_S = 1.62 \rho_m u_{rel} D_s^2 \sqrt{\nu_m \frac{du}{dy}} \ . \tag{3.45}$$

The relative velocity, u_{rel} and the radial gradient, du/dy at the liquid jet surface are respectively estimated by:

$$u_{rel} = \frac{u_{ch}}{2}\left(1 - 0.75\frac{x}{X}\right) \ , \tag{3.46a}$$

$$\frac{du}{dy} = \frac{2u_{rel}}{1.2D - D_c} \ , \tag{3.46b}$$

where X is the length of the fictitious cone (see Fig. 3.6) calculated from:

$$X = \frac{D}{D - D_{tip}} L_c \ . \tag{3.47}$$

The ejection angle is randomly chosen within the range $[0, \alpha_{max}]$ where α_{max} is the spray semi-cone angle and depends on the distance from the nozzle exit:

$$\alpha_{max} = \alpha_{exp} \left(2 - \frac{x}{L_c} \right) . \tag{3.48}$$

Here, α_{exp} is the experimentally-observed spray angle and it is one of the inputs to the model.

Droplet/droplet collision

It is considered that the leading droplet experiences higher drag force than the trailing one which resides in the wake. Thus, the trailing droplet catches up with the leading droplet resulting in collision at the core tip. If collision takes place, the leading parcel disintegrates into two equal secondary parcels with diameter, D_s, determined by:

$$D_s = \frac{D_{d,1}}{10} , \tag{3.49}$$

where $D_{d,1}$ denotes the diameter of the leading primary parcel. The velocities of the two secondary parcels, $\mathbf{u}_{d,s,1}$ and $\mathbf{u}_{d,s,2}$, are evaluated from overall mass and momentum conservation:

$$\mathbf{u}_{d,s,1} = \mathbf{u}_{d,s} + |\mathbf{u}_{d,1} - \mathbf{u}_{d,2}|\mathbf{r} , \tag{3.50a}$$

$$\mathbf{u}_{d,s,2} = \mathbf{u}_{d,s} - |\mathbf{u}_{d,1} - \mathbf{u}_{d,2}|\mathbf{r} . \tag{3.50b}$$

Here, $\mathbf{r}$ is a randomly chosen unit vector in the plane perpendicular to the injection direction (see Fig. 3.7), $\mathbf{u}_{d,1}$ and $\mathbf{u}_{d,2}$ are the velocities of the leading and the trailing

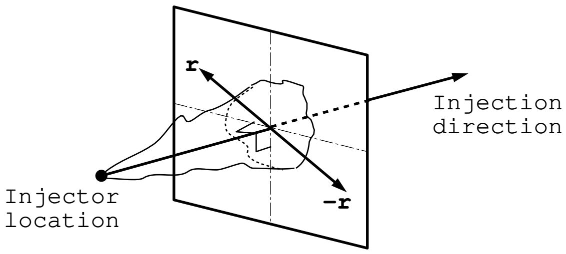

Figure 3.7: Random radial directions of droplets after collision.

primary parcels and $\mathbf{u}_{d,s}$ is given by:

$$\mathbf{u}_{d,s} = \frac{\mathbf{u}_{d,1} m_{d,1} + \mathbf{u}_{d,2} m_{d,2}}{m_{d,1} + m_{d,2}} , \tag{3.51}$$

where $m_{d,1}$ and $m_{d,2}$ are the masses of the leading and the trailing primary parcels, respectively.

Finally, all the properties of the trailing parcel involved in the collision are conserved except its velocity which changes to:

$$\mathbf{u}^n_{d,2} = \mathbf{u}_{d,s} . \tag{3.52}$$

Atomisation ceases according to the criteria of Faeth [93], given by Eq. (3.36). Also, a particular primary droplet no longer participates in atomisation (and switches to secondary droplet), as soon as it exits the liquid core.

3.4 Droplet trajectory

The droplet trajectory is calculated using a stochastic approach, in which the gas instantaneous properties around the droplet are provided by a turbulence model using random sampling. Following Gosman and Ioannides [107], the turbulence is assumed to be isotropic; and the gas fluctuating velocity components obey a Gaussian probability density distribution with zero mean value and standard deviation $\sigma_{u''} = \sqrt{2k/3}$. Thus, the j^{th} component of the fluctuating velocity, u''_j, is randomly selected from a distribution function according to:

$$u''_j = \sigma_{u''} \operatorname{sign}(2Y_{r,j} - 1) \operatorname{erf}^{-1}(|2Y_{r,j} - 1|) , \tag{3.53}$$

where $Y_{r,j}$ is a random number in the range [0, 1] and erf is the error function. Therefore, the instantaneous gas velocity, $\hat{\mathbf{u}}$, is expressed by:

$$\hat{\mathbf{u}} = \mathbf{u} + \mathbf{u}'' . \tag{3.54}$$

The relevant characteristic times are the eddy life time, τ_{eddy} and the transit time, τ_{tr}, required by the droplet to cross the eddy. These are respectively given by:

$$\tau_{eddy} = \frac{L_e}{|\mathbf{u}''|} , \tag{3.55a}$$

$$\tau_{tr} = \frac{L_e}{|\hat{\mathbf{u}} - \mathbf{u}_d|} , \tag{3.55b}$$

where $\mathbf{u}_d$ is the droplet velocity and L_e is the characteristic eddy size, assumed to be the dissipation length scale, given by:

$$L_e = C_\mu^{1/2} \frac{k^{3/2}}{\varepsilon} . \tag{3.56}$$

The fluctuating velocity acts on the droplet during an interaction time, τ_{int}, which is defined as the minimum between the abovementioned characteristic times. Thus,

$$\tau_{int} = \min\left(\tau_{eddy}, \tau_{tr}\right) . \tag{3.57}$$

The droplet trajectory is calculated from:

$$\frac{d\mathbf{x}_d}{dt} = \mathbf{u}_d , \tag{3.58}$$

where $\mathbf{x}_d$ is the droplet position vector. The above equation can also be expressed in terms of computational parcel, p, since the droplets in this parcel have the same location ($\mathbf{x}_p \equiv \mathbf{x}_d$) and velocity ($\mathbf{u}_p \equiv \mathbf{u}_d$). Thus,

$$\frac{d\mathbf{x}_p}{dt} = \mathbf{u}_p . \tag{3.59}$$

The droplet velocity is obtained from the momentum conservation equation described in the following section.

3.5 Momentum conservation equation

The droplet velocity is obtained from the momentum conservation equation neglecting gravitational, virtual mass, Basset, Magnus and Saffman forces and allowing only for drag forces. The gravitational forces are several orders of magnitude smaller than the drag forces (see Kralj [171]) and according to Faeth [91] and Aggarwal and Peng

[4] the virtual mass forces, the Basset forces and the Saffman lift forces are negligible compared to the drag forces. Finally, the Magnus forces are neglected on the ground that droplet rotational motion (spin) is not clearly evident (Kralj [171]).

Applying the Newton's second law, the following equation is obtained:

$$m_d \frac{d\mathbf{u}_d}{dt} = \frac{1}{2}\rho C_d A_d |\hat{\mathbf{u}} - \mathbf{u}_d| \left(\hat{\mathbf{u}} - \mathbf{u}_d\right) \ , \tag{3.60}$$

where m_d, C_d and A_d are the droplet mass, the drag coefficient and the cross-sectional area of the droplet perpendicular to the relative velocity, $\hat{\mathbf{u}} - \mathbf{u}_d$, respectively.

Defining the momentum relaxation time by:

$$\tau_{\mathbf{u}} = \frac{2m_d}{\rho C_d A_d |\hat{\mathbf{u}} - \mathbf{u}_d|} \ , \tag{3.61}$$

the momentum conservation equation, Eq. (3.60), can be recast into:

$$\frac{d\mathbf{u}_d}{dt} = \frac{\hat{\mathbf{u}} - \mathbf{u}_d}{\tau_{\mathbf{u}}} \ ; \tag{3.62}$$

and in terms of computational parcel is expressed by:

$$\frac{d\mathbf{u}_p}{dt} = \frac{\hat{\mathbf{u}} - \mathbf{u}_p}{\tau_{\mathbf{u}}} \ . \tag{3.63}$$

The momentum relaxation time indicates the mutual interaction strength between the droplet and the surrounding gas. Large droplets have large relaxation time which practically implies that the droplet motion is undisturbed. On the other hand, small droplets have small relaxation time and consequently, they almost follow the gas motion.

3.5.1 Drag coefficient

The complexity of the environment in a Diesel engine makes the determination of the droplet drag coefficient difficult. Evidently, the gas turbulence, the high evaporation rate of the droplet due to the high surrounding-gas temperature as well as its deformation due to the pressure affect the droplet drag coefficient (see Renksizbulut and Yuen [249], Hsiang and Faeth [138] and Aggarwal and Peng [4]).

Moreover, the proximity of neighbouring droplets reduces the drag coefficient when the droplet is in the wake of leading droplets since it experiences lower drag force (see White [304]). The effects of turbulence and neighbouring droplets proximity are usually ignored in spray models due to the lack of understanding of their mechanisms and lack of comprehensive experimental data (Kralj [171]).

Yuen and Chen [313] concluded that the droplet evaporation affects the drag coefficient in two ways. First, the temperature and concentration gradients between the droplet surface and the ambient gas cause substantial reduction in the viscosity of the gas, which decreases the friction drag. On the other hand, evaporation affects the boundary layer surrounding the droplet so that the pressure drag increases. They experimentally showed that for low evaporation rates ($B_T = c_{p,d}(T - T_{d,s})/L(T_{d,s}) <$ < 3, where $c_{p,d}$ is the liquid fuel specific heat capacity, T and $T_{d,s}$ denote the surrounding gas and droplet surface temperature, respectively and $L(T_{d,s})$ is the latent heat of vapourisation), the drag coefficient may be approximated by the *standard drag curve**, provided that the gas dynamic viscosity, μ_m, is evaluated at a film temperature and concentration obtained by using the so-called '1/3 rule', described later by Eq. (3.68).

Following Yuen and Chen [313], Renksizbulut and Yuen [248] also observed that the mass transfer reduces the friction drag significantly but at the same time increases the pressure drag by an almost equal amount. The net effect is that the standard drag curve for solid spheres can also be used for evaporating droplets. They proposed the following correlation for the drag coefficient of a droplet evaporating in air:

$$C_d = \frac{24}{Re} \frac{1 + 0.2 Re^{0.63}}{(1 + B_T)^{0.2}} \ , \tag{3.64}$$

for $10 < Re < 300$, where the arithmetic mean is used to evaluate the thermophysical properties except for the density in Re where the free-stream density is used. The factor $(1 + B_T)^{0.2}$ accounts for the reduction in drag due to the blowing effect. A larger influence of the blowing effect was observed by Chiang *et al.* [62] who proposed

*The standard drag curve describes the drag coefficient of a smooth solid sphere, moving in steady-state conditions, as a function of the Reynolds number (Wallis [297]).

the correlation:

$$C_d = \frac{24}{Re} \frac{1 + 0.325 Re^{0.474}}{(1 + B_T)^{0.32}} , \tag{3.65}$$

for $0.4 \leq B_T \leq 13$ and $30 \leq Re \leq 200$.

The upper limit of the Reynolds number of the above correlations is well below the maximum Reynolds number in Diesel sprays, which is usually greater than 1000 and therefore, renders them inapplicable*. Therefore, the drag coefficient for an evaporating spherical droplet used in this study is obtained from the correlation of Yuen and Chen [313]:

$$C_d = \begin{cases} \dfrac{24}{Re_f}\left(1 + \dfrac{1}{6} Re_f^{2/3}\right) , & \text{for } Re_f \leq 1000 , \\ 0.44 , & \text{for } Re_f > 1000 , \end{cases} \tag{3.66}$$

where Re_f is the Reynolds number given by:

$$Re_f = \frac{\rho_m |\hat{\mathbf{u}} - \mathbf{u}_d| D_d}{\mu_f} . \tag{3.67}$$

The gas dynamic viscosity, μ_f, is evaluated at the film temperature, T_f and fuel vapour mass fraction, Y_f, which are obtained applying the '1/3 rule':

$$T_f = T_{d,s} + \frac{1}{3}(T - T_{d,s}) , \tag{3.68a}$$

$$Y_f = Y_{v,s} + \frac{1}{3}(Y_v - Y_{v,s}) , \tag{3.68b}$$

where Y_v and $Y_{v,s}$ denote the fuel vapour mass fraction in the surrounding gas and at the droplet surface, respectively.

However, an additional correction due to droplet deformation will be presented in the following subsection.

Distorted droplet

The aerodynamic forces due to the relative velocity between the gas and the droplet may result in dynamic changes to the droplet shape, from spherical to elliptical (Fig. 3.8). The drag coefficient of a distorted droplet is higher than that of a

*Wide and comprehensive literature reviews can be found in the works of Clift and Grauvin [67], Clift *et al.* [66], Tabrizi [280], Aggarwal and Peng [4] and Kralj [171].

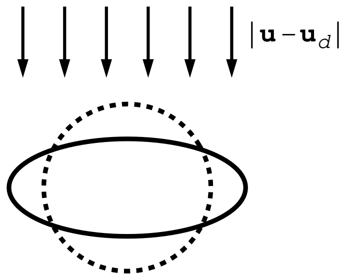

Figure 3.8: Droplet distortion.

spherical droplet, a fact which Patterson *et al.* [230] claimed can influence droplet trajectories. They calculated the distortion of the droplet by solving the spring-mass analogy equation from the Taylor analogy breakup (TAB) model of O'Rourke and Amsden [224]:

$$\ddot{x} + \frac{20\mu_d}{\rho_d D_d^2}\dot{x} + \frac{64\sigma_d}{\rho_d D_d^3}x = \frac{2}{3}\frac{\rho_m}{\rho_d}\frac{(\hat{\mathbf{u}} - \mathbf{u}_d)^2}{D_d} \ , \tag{3.69}$$

where x is the displacement of the surface from its equilibrium position and μ_d is the droplet dynamic viscosity. The coefficients of the TAB model have been derived by matching to the fundamental oscillation frequency and considering that breakup occurs for Weber numbers (see Eq. (3.170)) above the critical value, $We_c = 12$.

A dimensionless distortion parameter y, defined as $y = 4x/D_d$, is introduced and Eq. (3.69) becomes:

$$\ddot{y} + \frac{20\mu_d}{\rho_d D_d^2}\dot{y} + \frac{64\sigma_d}{\rho_d D_d^3}y = \frac{8}{3}\frac{\rho_m}{\rho_d}\frac{(\hat{\mathbf{u}} - \mathbf{u}_d)^2}{D_d^2} \ . \tag{3.70}$$

Because it is considered that the droplet reaches its maximum distortion when the surface displacement is 1/2 of the droplet radius, the distortion parameter y takes values within the range [0, 1]. The minimum value implies that the surface displacement is zero which means that the droplet is spherical, whereas the maximum value implies that the droplet becomes elliptical, with major axis equal to three times the undistorted droplet radius. Since Eq. (3.70) is second order in respect of time, two initial conditions are required to close the problem. These are given by:

$$y(0) = 0 \ , \tag{3.71a}$$

$$\dot{y}(0) = 0 \ . \tag{3.71b}$$

Thus, the droplet is assumed to be initially spherical with zero shape rate-of-change.

Patterson *et al.* [230] related the drag coefficient of the distorted droplet with that of the spherical one, via the following simple expression:

$$C_{d,dist} = C_d \left(1 + 2.632y\right) \ . \tag{3.72}$$

Liu *et al.* [190] investigated the effect of the drag coefficient on spray penetration. They found that even the C_d was multiplied by a factor of 16, the penetration was insensitive to this change. Their explanation was that the higher drag coefficient lowers the relative velocity, which results in larger droplets (according to the breakup model) with higher momentum.

In this study, drag coefficient correlations for both spherical and distorted droplets are used to assess the influence of different drag coefficients on the overall spray behaviour.

3.5.2 Momentum contribution to the gas phase

The exchange of momentum between the droplet and the gas generates an additional source term, $\mathbf{S}^d_{\mathbf{u}}$, in the momentum conservation equation of gas, Eq. (2.73). All the momentum that the droplet looses is absorbed by the gas. The total momentum exchange rate from all parcels at location $\mathbf{x}$ is given by (Kralj [171]):

$$\mathbf{S}^d_{\mathbf{u}}(\mathbf{x}) = -\lim_{\substack{\Delta t \to 0 \\ \delta V \to 0}} \frac{1}{\Delta t \delta V} \int_{\delta V} \left[\sum_{p=1}^{N_p} \int_t^{t+\Delta t} \delta\left(\mathbf{x} - \mathbf{x}_p\right) \frac{d}{dt}\left(m_p \mathbf{u}_p\right) dt \right] dV \ , \tag{3.73}$$

where $m_p = N_d m_d$ is the mass of the computational parcel containing N_d droplets with mass m_d. Also, δ denotes the Dirac function and the summation is performed over all N_p parcels.

3.6 Evaporation and condensation

3.6.1 Introduction

The temperature and concentration differentials between the liquid droplet surface and the surrounding gas in the combustion chamber result in interphase heat and mass transfer, respectively. The processes of evaporation and condensation are in general very complex; and additional complexities are introduced by the Diesel conditions. A brief description of the physical phenomena involved follows. Emphasis will be given on evaporation, while condensation may be regarded as the inverse phenomenon. The latter occurs sometimes in Diesel engines, for example in the near-wall regions due to the relatively low wall temperature.

An amount of heat is supplied by the hot gas to the droplet surface by forced-convection transfer. The rate of heat transfer increases not only with the temperature differential but also with the relative velocity. On the other hand, energy is extracted from the droplet due to mass transfer. This is called *latent heat* and is associated with increasing the kinetic energy of molecules for the liquid-to-vapour phase change (Lock [191]). An additional effect of mass transfer is that it creates a film of vapour around the droplet which reduces the heat-transfer rate, due to the lower temperature gradient between the droplet surface and the surrounding gas. This effect of mass transfer is known in the literature as the *blowing effect* or *Stefan flow* and it is important in Diesel sprays due to the high evaporation rates.

Since the heat transfer in Diesel spray cases is high because of the large temperature differentials, the net effect of the above processes is to increase the droplet temperature until it reaches the wet bulb temperature*, T_{wb}. It is important to note that since in Diesel engines, the temperature of the surrounding gas is high, leading to high transfer rates, T_{wb} is usually well above the critical temperature. The latter introduces its own complexities since as it is approached, the liquid becomes less

*The wet bulb temperature is the temperature at which all the heat transferred to the liquid is used for evaporation. Therefore, the remaining liquid is not heated further and its temperature remains at the wet bulb temperature.

dense and the vapour more dense. The two phases are indistinguishable resulting in a single phase which may be considered as either a liquid or a vapour (Jones and Hawkins [151]). Beyond the critical state, a liquid-vapour transformation is not possible (Wark [298]). Thus, in modelling, when a droplet reaches the critical temperature, it is assumed to be immediately converted into vapour. In cases of mixtures, the *pseudocritical* state is considered which is based on the critical state and mole fraction of each component [34] (see Eq. (3.166)).

The high relative velocity between the gas and the droplet also introduces additional effects on heat and mass transfers. One is that it induces circulation within the droplet, which reduces the internal temperature and concentration gradients. This lowers the surface temperature, increasing the heat transfer from the gas. The other effect is to provoke oscillation of the droplet surface shape (a phenomenon referred to earlier in §3.5.1). This effect was studied by Daidžić *et al.* [75] who found that the oscillations cause higher evaporation rates by a number of mechanisms, such as increase of the surface area, periodic micro-convection and boundary layer destruction and local saturation pressure changes due to local curvature effects.

Other physical processes that may affect evaporation are the rotational motion of the droplet and the turbulent motion of the surrounding gas. The former effect was theoretically investigated by Lozinski and Matalon [192] who considered a single liquid fuel droplet, spinning at a constant angular velocity about its own axis. They concluded that the induced secondary flow from the droplet equator towards its poles enhances the evaporation rate. The effect of turbulence was recently studied by Gökalp *et al.* [101] and Birouk *et al.* [43, 44] who used various hydrocarbon fuels in their experiments. They observed that the turbulence enhances the evaporation rate. However, its effect is most visible on low-volatility fuels: high-volatility fuels are almost insensitive to the turbulent environment. According to Gökalp *et al.* [101], the beneficial effect of turbulence near the droplet surface is to remove the fuel vapour, thereby increasing the fuel vapour concentration gradient. Consequently, turbulence may be more effective in the case of slowly-evaporating droplets.

Obviously detailed modelling of all these processes is almost impossible, since on the one hand prohibitive computer resources are required and on the other, some of these processes are not yet well understood. However, simpler and tractable models can be obtained under some reasonable assumptions and simplifications, neglecting those of the abovementioned processes which are of less importance. Thus, in this study, the rotational motion of the droplet is neglected due to the lack of clear evidence that it exists. The effect of turbulence is also neglected, since the experiments of Gökalp *et al.* [101] and Birouk *et al.* [43, 44] were carried out with relatively large droplets of $1.5\,mm$ diameter and under normal ambient temperature. These result in low evaporation rates and large droplet lifetimes compared to those in Diesel engines where the droplet diameter is less than $100\,\mu m$ and it is exposed to temperatures higher than $800\,K$.

Other assumptions adopted in this study are that the droplet is spherical and the conditions on its surface are uniform. In addition, it is assumed that the gas boundary layer is quasi-steady and the gas obeys the ideal gas law. The latter does not depart significantly from reality since according to Hohmann *et al.* [137], accounting for the non-ideality only slightly changes the spray behaviour (penetration, Sauter mean diameter and evaporation rate) under Diesel engine conditions, despite the fact that enhanced evaporation is obtained for a single droplet. The authors claimed that this is because of the wide droplet size distribution and high evaporation rates in the Diesel spray. The same authors proposed also that a real gas state equation should be considered for pressures higher than $50\,bar$. As will be seen in Chapter 6, in none of the cases examined in this study is the pressure higher than this level.

An additional assumption adopted here is that radiation is neglected (see associated discussion in §2.3.4). Also, following other researchers (see e.g. Renksizbulut and Bussmann [247], Jia and Gogos [149], Varnavas and Assanis [294]), Soret and Dufour effects are also neglected. Finally, it is mentioned that the blowing effect can be included in the evaluation of the heat and mass transfer coefficients, as will be explained later, while the effect of the internal circulation can be considered by using suitably-augmented (effective) conductivity and diffusivity. Further assumptions related to the modelling will be mentioned within its description.

The remaining of this section is organised as follows. The droplet energy equation, considered first, is solved for both uniform and varying internal temperature. In the latter case, this equation is solved both analytically* and using a simple profile method. Enhanced conductivity due to internal circulation is also included. Then, the droplet mass equation is considered and is solved for both single-component and multicomponent fuels. The latter requires solution of the diffusion equation which is also done using the profile method.

3.6.2 Energy conservation equation

Following the internal energy conservation equation of gas, Eq. (2.74), a similar equation for the droplet field can be derived as follows [41]:

$$\frac{\partial \rho_d e_d}{\partial t} + \nabla\cdot(\rho_d \mathbf{u}_d e_d) = \nabla\cdot(k_d \nabla T_d) - p_d \nabla\cdot\mathbf{u}_d + \dot{q} + \Phi \ . \tag{3.74}$$

Here, e_d, T_d, ρ_d and p_d are the internal energy, temperature, density and pressure within the droplet field, respectively. Also, k_d it the liquid thermal conductivity while, here it is noted that $\mathbf{u}_d$ denotes the velocity of an element within the droplet and *not* the droplet velocity defined in the previous section. Finally, the terms $\dot{q}$ and Φ represent the energy generation and dissipation, respectively. The latter expresses the rate at which the viscous forces produce irreversible work on fluid particles within the droplet per unit volume.

In the particular case of Diesel sprays, the energy generation term is zero. Also, for the reasons explained earlier, it is assumed that there is no fluid motion† within the droplet, i.e. $\mathbf{u}_d = 0$. This implies that the dissipation term, which is a function of

*From now on, for consistency it will be called *semi-analytical* since it is obtained under some approximations.

†The internal circulation is taken into account via an augmented diffusion coefficient, as will be explained later.

the fluid velocity (see Kakaç and Yener [156]), is also zero. In addition, following all the other researchers dealing with this problem (see e.g. Delplanque and Sirignano [79], Kneer *et al.* [165], Jia and Gogos [149], Ayoub and Reitz [27], Hohmann *et al.* [137], Al Omari [7]), the time-variations of the liquid density and the specific heat capacity are assumed to be negligible despite the fact that they are functions of temperature and temperature changes cause density and specific heat capacity variations as well.

Since the droplet is assumed to be spherical with uniform conditions on its surface, as mentioned earlier, Eq. (3.74) can be expressed in terms of the $(r,\, \theta,\, \varphi)$ spherical coordinate system as follows:

$$\frac{1}{r^2}\frac{\partial}{\partial r}\left[k_d r^2 \frac{\partial T_d(r,\, t)}{\partial r}\right] = \rho_d c_{p,d} \frac{\partial T_d(r,\, t)}{\partial t} \,, \tag{3.75}$$

where $c_{p,d}$ denotes the specific heat capacity of the droplet. Also, in the above, e_d has been replaced by $c_{p,d} T_d$. This equation is first order in time and second order in space. One initial and two boundary conditions are therefore, necessary to set a closed problem. The former is given by the trivial assumption that the initial droplet temperature is uniform and equal to $T_{d,0}$:

$$T_d(r,\, 0) = T_{d,0} \,. \tag{3.76a}$$

The boundary conditions are expressed by:

$$\frac{\partial T_d(0,\, t)}{\partial r} = 0 \,, \tag{3.76b}$$

$$4\pi R_d^2 k_d \frac{\partial T_d(R_d,\, t)}{\partial r} = \dot{Q}_{gas} + \dot{Q}_{evap} \,, \tag{3.76c}$$

where R_d is the instantaneous droplet radius. Here, $\dot{Q}_{gas}$ and $\dot{Q}_{evap}$ represent the rate of heat transfer from the gas by convection and the rate of heat extracted by evaporation*, respectively. The boundary condition at the droplet centre, Eq. (3.76b), expresses the spherical symmetry there, while Eq. (3.76c) expresses the energy balance on the droplet surface. Thus, the net heat supplied to the droplet is transferred by conduction towards its interior.

---

*Note that $\dot{Q}_{evap}$ is negative since it is proportional to the rate of change of the droplet mass, as will be seen later. This rate is negative for evaporation as is the case here, while in cases of condensation, it is positive.

The rate of heat extracted for evaporation is given by:

$$\dot{Q}_{evap} = \frac{dm_d}{dt} L(T_{d,s}) \ , \tag{3.77}$$

where $dm_d/dt = \dot{m}_d$ is the rate of evaporation and $L(T_{d,s})$ is the latent heat of vapourisation, evaluated at the droplet surface temperature, $T_{d,s}$. In Eq. (3.77), the fuel vapour at the droplet surface is assumed to be at the droplet surface temperature.

The rate of heat transfer between the gas and the droplet, $\dot{Q}_{gas}$, is expressed by:

$$\dot{Q}_{gas} = 4\pi R_d^2 h \left(T - T_{d,s}\right) \ , \tag{3.78}$$

where h is the heat-transfer coefficient evaluated from:

$$h = \frac{Nu k_f}{D_d} \ . \tag{3.79}$$

Here, Nu is the Nusselt number and k_f is the thermal conductivity of the gas, evaluated at the so-called *film* temperature, T_f.

The evaluation of Nusselt number and the definition of the film temperature at which various properties of the ambient gas are evaluated have been the subject of research of many scientists. Various correlations for Nu have been proposed in the literature, but unfortunately, no single one is uniquely accepted, since these correlations strongly depend on the experimental conditions. A review of the literature on this subject follows.

Heat-transfer correlations

Ranz and Marshall [237, 238] investigated the factors influencing the rate of evaporation of pure liquid droplets. Their study was restricted to Reynolds numbers up to 200 and air temperatures up to 493 K. They derived the following Nu correlation for an evaporating droplet:

$$Nu = 2 + 0.6 Re^{1/2} Pr^{1/3} \ , \tag{3.80}$$

where Re and Pr are the Reynolds and Prandtl numbers, respectively, given by:

$$Re = \frac{\rho_m |\hat{\mathbf{u}} - \mathbf{u}_d| D_d}{\mu_f} \,, \tag{3.81}$$

$$Pr = \frac{\mu_f c_{p,f}}{k_f} \,. \tag{3.82}$$

The properties of the mixture in the above expressions are evaluated at the arithmetic mean of the gas temperature and the droplet surface temperature, i.e.

$$T_f = \frac{T + T_{d,s}}{2} \,. \tag{3.83}$$

A similar Nu correlation is proposed by Rowe *et al.* [254] who performed heat-transfer experiments with a single droplet for Re in the range [60, 1800]. They recommended:

$$Nu = 2 + 0.69 Re^{1/2} Pr^{1/3} \,. \tag{3.84}$$

The experimental results of Beard and Pruppacher [32] and Pruppacher and Rasmussen [236] for spherical water droplets suspended by an air flow at their terminal velocity in a vertical wind tunnel with turbulence levels below 0.3 %, are correlated by:

$$Nu = 1.56 + 0.616 Re^{1/2} Pr^{1/3} \,, \tag{3.85}$$

for $2.5 < Re < 3320$.

As mentioned in the introductory part of this section, mass transfer reduces the convective heat-transfer coefficient. However, this effect is neglected in all the above Nu correlations. In 1954, El Wakil *et al.* [85] were the first to consider the blowing effect. To this end, they employed the correlation of Ranz and Marshall [237, 238], given by Eq. (3.80), corrected by a multiplying factor, $\mathcal{F}$, defined as:

$$\mathcal{F} = \frac{z}{e^z - 1} \,, \tag{3.86a}$$

where z is the following function of the mass-transfer rate:

$$z = -\frac{c_{p,v} \dot{m}_d}{\pi D_d k_f Nu} \,. \tag{3.86b}$$

In the above, $c_{p,v}$ is the specific heat of fuel vapour at constant pressure. Later, other correlations were proposed which include a parameter which expresses the blowing effect, as follows.

Yuen and Chen [314] simulated heat-transfer to droplets of water and methanol by injecting the liquid into a heated porous sphere. They found that the heat-transfer rate for $200 < Re < 2000$, is reduced from the solid sphere value by a factor of $(1 + B_T)$ due to evaporation, where B_T is called the *heat-transfer number* and is given by:

$$B_T = \frac{c_{p,v}\,(T - T_{d,s})}{L(T_{d,s})} \,. \tag{3.87}$$

They applied this correction to the Ranz and Marshall [237, 238] correlation given by Eq. (3.80). Thus,

$$Nu = \frac{2 + 0.6 Re^{1/2} Pr^{1/3}}{1 + B_T} \,. \tag{3.88}$$

Here, the film temperature is calculated using the '1/3 rule' explained in §3.5.1.

Renksizbulut and Yuen [248] proposed the following Nu correlation based on their experimental results for droplets of water, methanol and heptane:

$$Nu = \frac{2 + 0.57 Re^{1/2} Pr^{1/3}}{(1 + B_T)^{0.7}} \,, \tag{3.89}$$

for $25 \leq Re \leq 2000$. In this correlation, the coefficient 0.57 has an uncertainty of ± 0.032. The film temperature is the arithmetic mean ($T_f = (T + T_{d,s})/2$) while the viscosity is evaluated applying the '1/3 rule'.

More recently, Abramzon and Sirignano [1] suggested the following correction factor:

$$\mathcal{F}_T = (1 + B'_T)^{0.7} \, \frac{\ln(1 + B'_T)}{B'_T} \,. \tag{3.90}$$

However, they defined a heat-transfer number, B'_T, based not only on the latent heat, but also on the heat given to the droplet, $\dot{Q}_d$, as follows:

$$B'_T = \frac{c_{p,v}\,(T - T_{d,s})}{L(T_{d,s}) + \dot{Q}_d/\dot{m}_d} \,. \tag{3.91}$$

They recommended that correction factor be applied to Nusselt correlations for non-evaporating droplets, Nu_0, as follows:

$$Nu = 2 + \frac{Nu_0 - 2}{\mathcal{F}_T} \,. \tag{3.92}$$

The same authors proposed two Nusselt correlations for non-evaporating droplets. The first is the Frossling correlation,

$$Nu_0 = 2 + 0.552 Re^{1/2} Pr^{1/3} \,, \tag{3.93}$$

while the second one is that of Clift *et al.* [66],

$$Nu_0 = \begin{cases} 1 + (1 + RePr)^{1/3} \,, & \text{for } Re \leq 1 \,, \\ 1 + (1 + RePr)^{1/3} \, Re^{0.077} \,, & \text{for } 1 < Re < 400 \,. \end{cases} \tag{3.94}$$

It is interesting to compare all these correlations under Diesel engine conditions. In such conditions the value of Prandtl number is mainly within the range [0.55, 0.75] while Reynolds may go up to 10000. The heat-transfer number may vary from 0 to 1000 or even higher*, however, typical values for most of the droplet lifetime are within the range [0.5, 50]. For the sake of the comparison, $\mathcal{F}$ should be related to B_T. After substitution of Eqs. (3.77), (3.78), (3.79) and (3.87) into Eq. (3.86b), z can be expressed by:

$$z = -B_T \frac{\dot{Q}_{evap}}{\dot{Q}_{gas}} \,. \tag{3.95}$$

Typical values of z are within the range $[0,\, B_T]$. The smallest value corresponds to a non-evaporating droplet, while the largest is obtained when the droplet reaches the wet bulb temperature ($\dot{Q}_{evap} = \dot{Q}_{gas}$). These values of z lead $\mathcal{F}$ to vary from $B_T/(e^{B_T} - 1)$ to 1.

The comparisons are shown in Figs. 3.9–3.12 in which the correlations are designated according to Table 3.2. In these figures, Nu is plotted as a function of Re for all the combinations of the extreme values of Pr and B_T. The value of $\mathcal{F}$ used in the correlation of Ranz and Marshall corrected by El Wakil *et al.* (Nu4) is $B_T/(e^{B_T} - 1)$ while the maximum value of $\mathcal{F}$, i.e. $\mathcal{F} = 1$, corresponds to the pure correlation of Ranz and Marshall (Nu1).

As can be seen in all these figures, the correlation of Pruppacher *et al.* (Nu3) is very close to that of Ranz and Marshall (Nu1) with a maximum difference less than 2 %. Consistently greater Nu values are given by the correlation of Rowe *et al.* (Nu2)

*As the droplet temperature approaches the critical point, the latent heat falls to zero.

Table 3.2: Nusselt correlations.

Designation	Correlation
Nu1	Ranz-Marshall, Eq. (3.80)
Nu2	Rowe *et al.*, Eq. (3.84)
Nu3	Pruppacher *et al.*, Eq. (3.85)
Nu4	El Wakil *et al.*/Ranz-Marshall, Eqs. (3.86), (3.80)
Nu5	Yuen-Chen, Eq. (3.88)
Nu6	Renksizbulut-Yuen, Eq. (3.89)
Nu7	Abramzon-Sirignano/Frossling, Eqs. (3.92), (3.93)
Nu8	Abramzon-Sirignano/Clift *et al.*, Eqs. (3.92), (3.94)

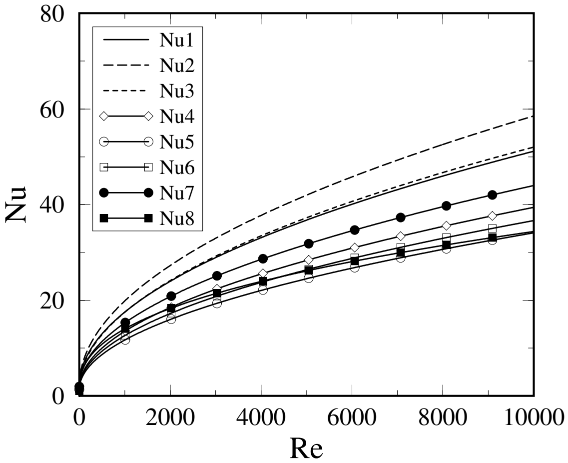

Figure 3.9: Comparison of various Nu correlations for $Pr = 0.55$, $B_T = 0.5$.

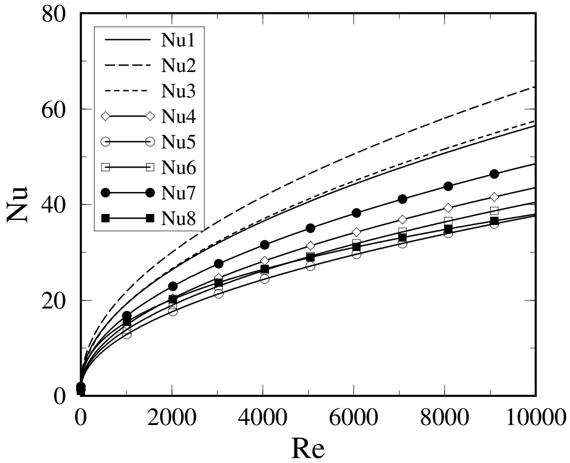

Figure 3.10: Comparison of various Nu correlations for $Pr = 0.75$, $B_T = 0.5$.

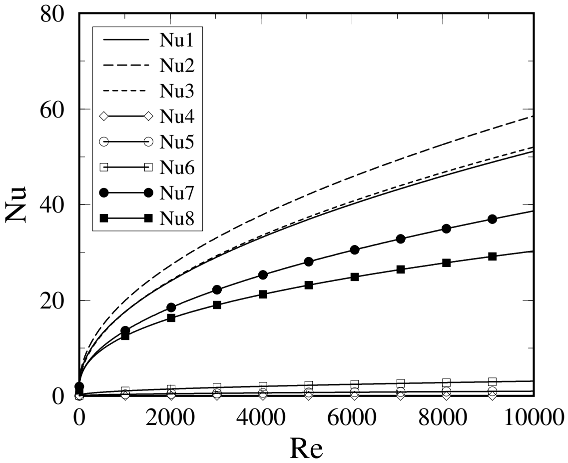

Figure 3.11: Comparison of various Nu correlations for $Pr = 0.55$, $B_T = 50$.

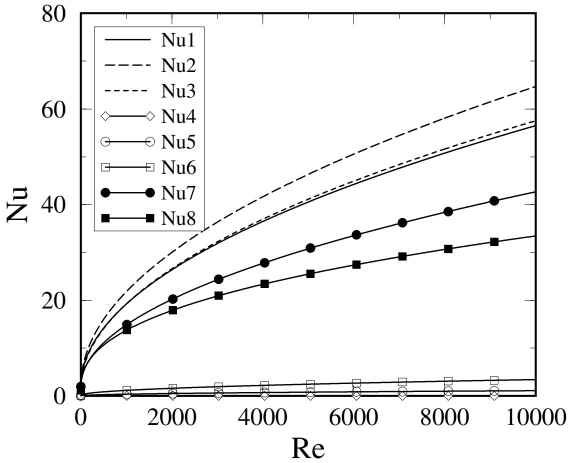

Figure 3.12: Comparison of various Nu correlations for $Pr = 0.75$, $B_T = 50$.

whose maximum gap from that of Ranz and Marshall is about 12.5 %. In contrast, the inclusion of the blowing effect reduces the Nusselt number significantly, especially for large values of B_T, which correspond to droplet temperatures near the critical point: here, the correlations of Yuen and Chen (Nu5) and that of Renksizbulut and Yuen (Nu6) give very small Nu. The correction factor of El Wakil *et al.* results in Nusselt value which actually lies between the curves Nu1 and Nu4, depending on the ratio $\dot{Q}_{evap}/\dot{Q}_{gas}$. The correlations proposed by Abramzon and Sirignano (Nu7 and Nu8) also lie within this range, with the exception of that in conjunction with the correlation of Clift *et al.* (Nu8) for low heat-transfer numbers. It is also clear that the correction factor of Abramzon and Sirignano gives a relatively small sensitivity to the heat-transfer number, which is about 12 % between the two B_T values used here.

From these figures, the Nu correlations can be divided in two main groups. One consists of the correlations of Ranz and Marshall, Rowe *et al.* and Pruppacher *et al.* which are essentially for conditions of low or zero evaporation and are therefore, not applicable in Diesel engine conditions. The other group comprises the correlations accounting for the blowing effect and they can be further subdivided into three groups based on the correction function they use, which may be one of $\mathcal{F}$, B_T or B'_T.

All the three subgroups have been used in Diesel spray calculations. In particular, Tabrizi [280], Kralj [171], Ikonomou [143] and Bai [29] among others used the factor of El Wakil *et al.* to correct the Ranz and Marshall correlation. Some researchers used the same correlation but corrected by the factor of Abramzon and Sirignano (see e.g. Daidžić *et al.* [75], Varnavas and Assanis [294], Hohmann *et al.* [137]). The latter correction factor has also been employed by Ayoub and Reitz [27]. Finally, the correlation proposed by Renksizbulut and Yuen has been used by Renksizbulut and Bussmann [247] and Aggarwal and Peng [4] among others. In this study three representative correlations will be adopted. One is the widely-employed Ranz and Marshall correlation, given by Eq. (3.80) and corrected by $\mathcal{F}$, Eq. (3.86). The second is that of Renksizbulut and Yuen, given by Eq. (3.89). The third is again that of

Ranz and Marshall but corrected according to Eq. (3.92) as proposed by Abramzon and Sirignano.

If the temperature within the droplet is uniform, the energy equation reduces to a simple overall energy balance, given below. According to Daidžić *et al.* [75] and Ayoub and Reitz [27], this approach is valid when the Biot number, defined by:

$$Bi = \frac{hR_d}{k_d} \,, \tag{3.96}$$

is smaller than 0.1. This condition may be satisfied when, for example either the liquid conductivity is very large or the internal circulation is strong. However, in Diesel sprays, Bi typically varies from 1 to 100 and consequently, the low Bi assumption is not applicable. Nevertheless, according to Hohmann *et al.* [137], the low Bi assumption does not result in appreciable deviations from the real case, when applied to entire Diesel spray, because of the high evaporation rates and the wide distribution of droplet sizes. Thus, in this study both low Bi and 'arbitrary' Bi cases are considered. Due to the different nature they give to the droplet energy equation, they will be examined individually.

Energy conservation equation for very low Bi

If the droplet temperature, T_d, is assumed to be always uniform, it may be calculated from an overall energy balance. To this end, Eq. (3.75) is integrated over the droplet volume and then, Eq. (3.76c) is inserted into it to yield:

$$m_d c_{p,d} \frac{dT_d}{dt} = \dot{Q}_{gas} + \dot{Q}_{evap} \,. \tag{3.97}$$

The LHS of the above equation represents the rate of internal energy change of *both* the liquid droplet and the vapour formed. The RHS expresses the net rate of energy given to the system consisting of the droplet and the vapour.

By defining a heat-transfer relaxation time as:

$$\tau_e = \frac{m_d c_{p,d}}{4\pi R_d^2 h + \dfrac{\dot{m}_d L(T_d)}{T - T_d}} \,, \tag{3.98}$$

Eq. (3.97) can be recast into the following simple form:

$$\frac{dT_d}{dt} = \frac{T - T_d}{\tau_e} \ . \tag{3.99}$$

The physical meaning of the heat-transfer relaxation time is that for large values ($\tau_e \to \infty$), the droplet is practically adiabatic, whereas for small values ($\tau_e \to 0$), it reaches the ambient temperature rapidly.

Energy conservation equation for 'arbitrary' Bi

As already noted, for $Bi > 0.1$, Eq. (3.75) must be solved to calculate the temperature field within the droplet.

Since the droplet radius decreases due to evaporation, an appropriate transformation of coordinates is applied to fix the boundaries. Also, all variables in Eq. (3.75) are non-dimensionalised for convenience. Thus, following Landis and Mills [176], the following variables are introduced:

$$\Theta = \frac{T_d - T}{T_{d,0} - T} \ ; \quad \tau = \frac{\alpha_d t}{R_{d,0}^2} \ ; \quad \omega = \frac{r}{R_d(t)} \ ; \quad \zeta = \frac{R_d(t)}{R_{d,0}} \ . \tag{3.100}$$

Here, $R_{d,0}$ denotes the initial droplet radius, while R_d is the time-varying instantaneous radius. Also, α_d is the thermal diffusivity given by:

$$\alpha_d = \frac{k_d}{\rho_d c_{p,d}} \ . \tag{3.101}$$

The variables Θ, ω and ζ vary from 0 to 1. Introduction of these variables into Eq. (3.75) allows it to be recast into:

$$\frac{1}{\omega^2 \zeta^2(\tau)} \frac{\partial}{\partial \omega} \left[\omega^2 \frac{\partial \Theta(\omega, \tau)}{\partial \omega} \right] - \frac{\omega}{\zeta(\tau)} \frac{d\zeta(\tau)}{d\tau} \frac{\partial \Theta(\omega, \tau)}{\partial \omega} = \frac{\partial \Theta(\omega, \tau)}{\partial \tau} \ . \tag{3.102}$$

In the derivation of the above expression, the widely-adopted (see e.g. Landis and Mills [176], Law [181], Ayoub and Reitz [27], Al Omari [7]) assumption that the thermal conductivity is constant*, was used. The initial and boundary conditions

*Actually, the thermal conductivity is a function of temperature and as the temperature changes along the radius, k_d changes as well. Usually, the thermal conductivity of liquids decreases linearly with increasing temperature [198]. However, the change is not big (for a temperature range of $100\,K$, all the values of k_d are within about $10\,\%$ of the mean value for this temperature range [198]) and it can be neglected. For instance, for n-heptane, $k_d = 0.15\,\frac{W}{mK}$ for $T_d = 300\,K$ and $k_d = 0.10\,\frac{W}{mK}$ for $T_d = 540\,K$.

are also transformed, thus,

$$\Theta(\omega,\, 0) = 1 \;, \tag{3.103a}$$

$$\frac{\partial \Theta(0,\, \tau)}{\partial \omega} = 0 \;, \tag{3.103b}$$

$$\frac{\partial \Theta(1,\, \tau)}{\partial \omega} = -Bi\Theta(1,\, \tau) + \mathcal{Q} \;, \tag{3.103c}$$

where $\mathcal{Q}$ is the non-dimensional evaporation energy, defined by:

$$\mathcal{Q} = \frac{\dot{Q}_{evap}}{4\pi R_d k_d \left(T_{d,0} - T\right)} \;. \tag{3.104}$$

Eq. (3.102) is non-linear with non-homogeneous boundary conditions and therefore, can only be solved numerically. This approach has been used by Landis and Mills [176], Hubbard *et al.* [140], Kneer *et al.* [165] and Hohmann *et al.* [137] among many others. Although, the calculations are not very expensive in terms of computer resources when a single droplet is considered*, they introduce considerable computer overheads when they are applied to a spray simulation, which usually involves many thousands droplets. In this study, a simple profile method is developed, as will be explained later, which requires fewer calculations. The accuracy of this method is assessed by reference to a semi-analytical method which will now be explained.

Semi-analytical method

The analytical solution of the conduction equation for a solid sphere with constant properties and conditions on its surface, expressed in a Fourier series, can be found in many relevant classical books (see e.g. Carslaw and Jaeger [57], Arpaci [26], Özişik [226], Poulikakos [235]). However, in the case of a Diesel droplet, not only are the boundaries moving due to evaporation, but also the properties of the droplet change with the temperature. In addition, as the droplet moves through the gas, the conditions on its surface vary. Here, a semi-analytical solution is obtained which combines the analytical solution with a time-marching numerical technique. Thus, within a

*Hohmann *et al.* [137] used 10 grid points in each droplet, but Kneer *et al.* [165] employed a uniform mesh of 100 grid points, although they claimed that it could be reduced to 20 with only minor deviations of the solution.

fine enough time step, $\delta\tau$, the droplet properties and radius as well as the conditions on its surface are assumed to be constant. With these assumptions, the term containing the gradient $d\zeta/d\tau$ in Eq. (3.102) vanishes and the analytical solution can be used. Based on the temperature field at the end of $\delta\tau$, new thermophysical properties, radius and conditions are calculated. These updated values are used to obtain the temperature field in the next $\delta\tau$ assuming again that the droplet properties, radius and conditions on its surface are constant. Note that for constant properties and very low evaporation rate, this solution corresponds to the exact solution and therefore, can be used to assess the accuracy of the profile method.

Assuming that the initial temperature of the droplet is uniform, the dimensionless temperature distribution* at time τ reads:

$$\Theta(\omega,\,\tau) = \sum_{n=1}^{\infty} \frac{2\left(\sin\lambda_n - \lambda_n\cos\lambda_n\right)}{\lambda_n\left(\lambda_n - \sin\lambda_n\cos\lambda_n\right)} e^{-\lambda_n^2\tau/\zeta^2}\frac{\sin\left(\lambda_n\omega\right)}{\omega}\,. \tag{3.105}$$

In the above expression, the λ_n are characteristic values satisfying the boundary condition on the droplet surface (see Appendix B.1 for details).

Although the above expression describes the temperature field at time τ for constant droplet thermophysical properties and conditions on its surface, it does not represent the general case. This is because at the end of the time $\delta\tau$, the droplet thermophysical properties (density, specific heat capacity, thermal conductivity etc.) should be updated and the new calculation should commence with non-uniform 'initial' temperature distribution from the previous step. Thus, in this case the temperature field is given by (see Appendix B.1):

$$\Theta(\omega,\,\tau) = \sum_{n=1}^{\infty}\left\{\frac{\lambda_n\Theta_1\sum_{m=1}^{\infty}\left[\frac{\sin\left(\lambda_m\xi-\lambda_n\right)}{\lambda_m\xi-\lambda_n} - \frac{\sin\left(\lambda_m\xi+\lambda_n\right)}{\lambda_m\xi+\lambda_n}\right]\alpha_m e^{-\lambda_m^2\xi^2\delta\tau^o/\zeta^2}}{\xi\left(\lambda_n - \sin\lambda_n\cos\lambda_n\right)} + \frac{2\Theta_2\left(\sin\lambda_n-\lambda_n\cos\lambda_n\right)}{\lambda_n\left(\lambda_n-\sin\lambda_n\cos\lambda_n\right)}\right\} e^{-\lambda_n^2\tau/\zeta^2}\frac{\sin\left(\lambda_n\omega\right)}{\omega}\,. \tag{3.106}$$

*The derivation of this is given in Appendix B.1.

Here, α_m and λ_m are the coefficients of the infinite series and the characteristic values, respectively, at the previous time step, $\delta\tau^o$. Also, the variables Θ_1, Θ_2 and ξ, whose definitions are given in Appendix B.1, are introduced to allow for changes of the droplet radius and the conditions on its surface.

A parametric study based on the solutions given by Eqs. (3.105) and (3.106) will now be performed. In this study, a single droplet is considered, whose properties are assumed constant. In addition, evaporation is suppressed and consequently, the above temperature distributions, Eqs. (3.105) and (3.106), represent the exact* solution.

Firstly, a case with low Biot number ($Bi = 0.1$) is considered. The dimensionless temperature distribution within the droplet at various dimensionless times, τ, is shown in Fig. 3.13. As can be seen, the temperature profile is almost uniform with

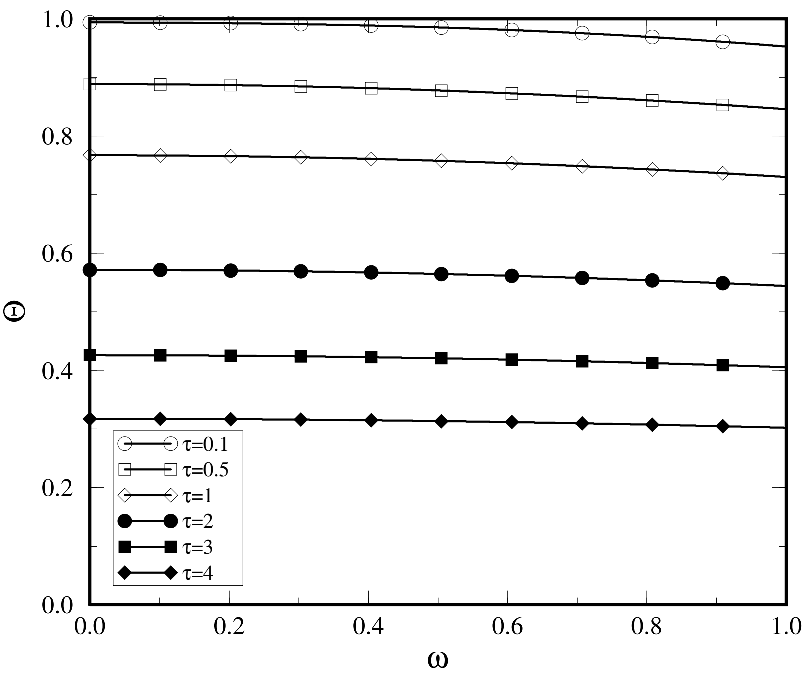

Figure 3.13: Dimensionless temperature distributions for $Bi = 0.1$.

*It should be noted that the exact solution requires the summation in Eqs. (3.105) and (3.106) of infinite number of terms. Here, the first 100 terms of the series are considered keeping the error below 10^{-8} %.

maximum temperature difference between the centre of the droplet and its surface less than 4 %. As the time elapses, the droplet is heated up almost uniformly until it reaches the ambient temperature. The latter is shown in Fig. 3.14 which describes the surface temperature.

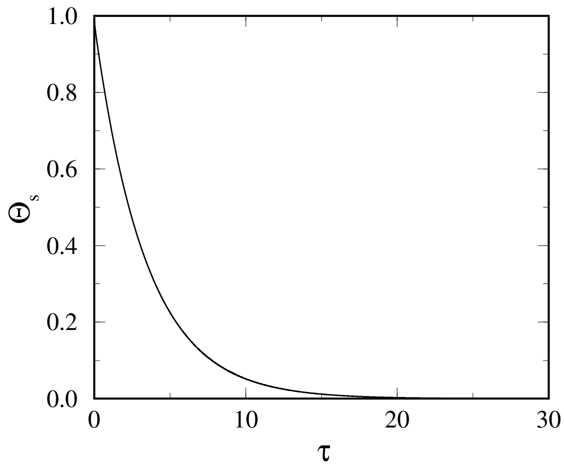

Figure 3.14: Temporal variation of dimensionless surface temperature for $Bi = 0.1$.

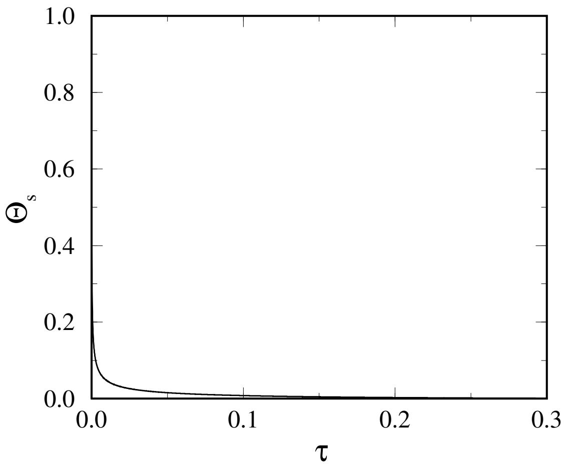

Figure 3.15: Temporal variation of dimensionless surface temperature for $Bi = 100$.

In contrast, for large values of Biot number, the surface temperature rapidly reaches the ambient temperature, as shown in Fig. 3.15 for $Bi = 100$, while the droplet interior is still cold, resulting in a very non-uniform temperature distribution. This is shown in Fig. 3.16 giving the dimensionless temperature distribution at various times. The temperature on the droplet surface increases rapidly while it is significantly lower in the droplet interior. Relatively soon, the surface temperature reaches the ambient temperature and remains there until the whole droplet acquires this temperature. The overall result is that the temperature gradient on the droplet surface decreases, as can be clearly seen in Fig. 3.16.

Profile method

An approximate method of solving Eq. (3.102) will now be presented. The temperature distribution within the droplet can be approximated by a polynomial function. Thus, the problem reduces to the finding of the coefficients of this function. For a

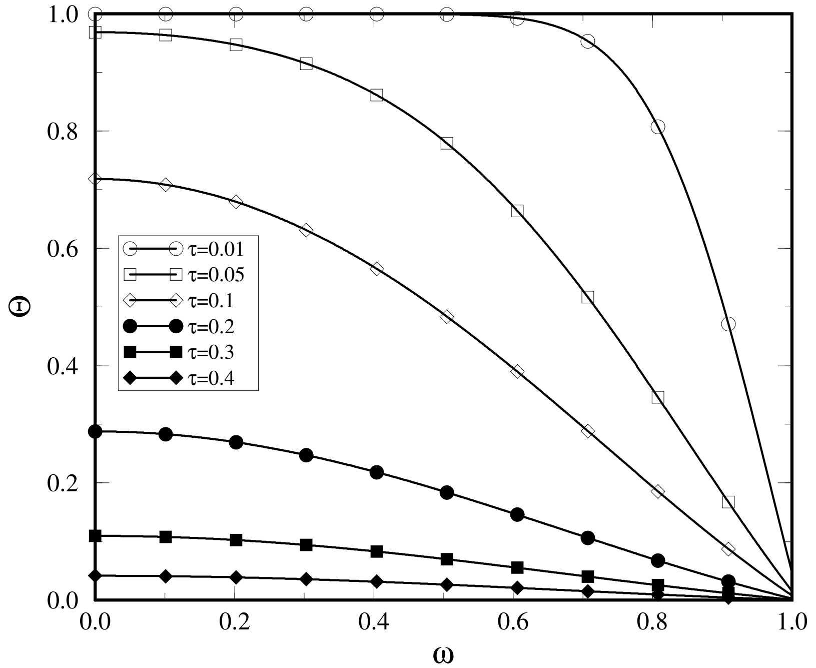

Figure 3.16: Dimensionless temperature distributions for $Bi = 100$.

polynomial of n^{th} degree, $n+1$ equations are required to calculate the $n+1$ coefficients. However, here, there is an additional unknown which defines the position from which the polynomial profile is valid. This is necessary because although the surface temperature increases rapidly, the heat needs some time to reach the droplet centre due to the finite conductivity. Thus, in the early stages, the heat penetrates to a depth ε and from this point to the droplet centre the temperature is uniform and equal to the initial value (see Fig. 3.16 at $\tau = 0.01$). Here, four equations are readily available (the differential equation, the initial condition and the two boundary conditions), thus, a polynomial of 2^{nd} degree seems the obvious choice*. It is

*A higher degree polynomial can be used by deriving additional equations, for instance, higher moments of the conduction equation. However, the problem becomes complicated and no attempt will be done in this study, since the simplicity of the methodology is of main importance in order to be applicable to a large number of droplets in a spray calculation. On the other hand, a lower degree polynomial can be used, i.e. linear function, by neglecting one of the two boundary conditions. Obviously, this approach is less accurate.

therefore assumed that the temperature distribution is described by:

$$\Theta(\omega,\,\tau) = \begin{cases} \eta_1(\tau)\,, & \text{for } \omega < \delta(\tau)\ , \\ \eta_1(\tau) + \eta_2(\tau)\,[\omega - \delta(\tau)] + \eta_3(\tau)\,[\omega - \delta(\tau)]^2\ , & \text{for } \omega \geq \delta(\tau)\ , \end{cases} \tag{3.107}$$

where $\delta(\tau) = 1 - \varepsilon(\tau)/R_d(\tau)$. Note that $\delta(0) = 1$ due to the uniform initial profile.

The problem is described by the conduction equation, Eq. (3.102), the initial condition, Eq. (3.103a) and the boundary condition on the droplet surface, Eq. (3.103c) while the boundary condition at the centre moves to $\delta(\tau)$, i.e.

$$\frac{\partial\Theta(\delta,\,\tau)}{\partial\omega} = 0\ . \tag{3.108}$$

Introducing Eq. (3.107) into the initial condition, given by Eq. (3.103a), the coefficient $\eta_1(0)$ is obtained:

$$\eta_1(\tau) = 1\ . \tag{3.109}$$

This coefficient is constant until $\delta(\tau) = 0$. Also, substitution of Eq. (3.107) into Eq. (3.108), results in $\eta_2(\tau) = 0$. Hence, the profile solution, Eq. (3.107), simplifies to:

$$\Theta(\omega,\,\tau) = \begin{cases} 1\,, & \text{for } \omega < \delta(\tau)\ , \\ 1 + \eta_3(\tau)\,[\omega - \delta(\tau)]^2\ , & \text{for } \omega \geq \delta(\tau)\ . \end{cases} \tag{3.110}$$

Substitution of the above in the boundary condition on the droplet surface, expressed by Eq. (3.103c), yields:

$$\eta_3(\tau) = \frac{-Bi + \mathcal{Q}}{[1 - \delta(\tau)]\,\{2 + Bi\,[1 - \delta(\tau)]\}}\ . \tag{3.111}$$

The above expression involves two unknowns, $\eta_3(\tau)$ and $\delta(\tau)$ and therefore, one more equation is required to close the system. This is supplied by the conduction equation, Eq. (3.102), into which the temperature profile, expressed by Eq. (3.110), is substituted. Then, integration is performed over the ω field in order to eliminate ω and reduce the number of independent variables to one. The result is the following equation:

$$\begin{aligned} &\eta_3(\tau)\left\{\frac{6}{\zeta^2}\,[1 - \delta(\tau)] + \frac{4}{\zeta^2}\delta(\tau)\ln\delta(\tau) - \frac{2}{\zeta}\frac{d\zeta}{d\tau}\left[\frac{1}{3} - \frac{\delta(\tau)}{2} + \frac{\delta^3(\tau)}{6}\right]\right\} \\ =&\frac{d\eta_3(\tau)}{d\tau}\frac{[1 - \delta(\tau)]^3}{3} - \eta_3(\tau)\,[1 - \delta(\tau)]^2\,\frac{d\delta(\tau)}{d\tau}\ . \end{aligned} \tag{3.112}$$

Substitution of Eq. (3.111) into the above gives a first-order ordinary differential equation for $\delta(\tau)$:

$$\frac{6}{\zeta^2}\left[1-\delta(\tau)\right]+\frac{4}{\zeta^2}\delta(\tau)\ln\delta(\tau)-\frac{2}{\zeta}\frac{d\zeta}{d\tau}\left[\frac{1}{3}-\frac{\delta(\tau)}{2}+\frac{\delta^3(\tau)}{6}\right]$$
$$=-\left[1-\delta(\tau)\right]^2\left\{\frac{4+Bi\left[1-\delta(\tau)\right]}{3\left\{2+Bi\left[1-\delta(\tau)\right]\right\}}\right\}\frac{d\delta(\tau)}{d\tau}\,. \tag{3.113}$$

The differential term in the above is discretised in the first-order Euler form as follows:

$$\frac{d\delta(\tau)}{d\tau}=\frac{\delta-\delta^o}{\delta\tau}\,, \tag{3.114}$$

where $\delta\tau$ is a dimensionless time step. For accuracy this must be appreciably smaller than a characteristic time $\tau_{p,T}$, which is the time required for δ to become zero. This characteristic time is evaluated by setting $\delta=0$ in Eq. (3.113). Hence,

$$\tau_{p,T}=\frac{4+Bi}{6+3Bi}\frac{\delta^o}{\dfrac{6}{\zeta^2}-\dfrac{2}{3\zeta}\dfrac{d\zeta}{d\tau}}\,. \tag{3.115}$$

With the help of Eq. (3.140) the above can be recast into:

$$\tau_{p,T}=\frac{4+Bi}{6+3Bi}\frac{\delta^o}{\dfrac{6}{\zeta^2}+\dfrac{2R_dR_{d,0}}{9\zeta\alpha_d\tau_m}}\,, \tag{3.116}$$

where τ_m is a characteristic time whose definition and meaning will be explained later (see Eq. (3.139)). Eq. (3.113) is solved implicitly at each time step, using the Newton-Raphson method. The iteration is stopped when the δ difference between two successive iterations is less than 10^{-6}.

As soon as the heat reaches the droplet centre, the profile shape, Eq. (3.107), becomes:

$$\Theta(\omega,\,\tau)=\eta_1(\tau)+\eta_2(\tau)\omega+\eta_3(\tau)\omega^2\,. \tag{3.117}$$

When this is introduced into the boundary condition, Eq. (3.103b), $\eta_2(\tau)$ is obtained:

$$\eta_2(\tau)=0\,. \tag{3.118}$$

Also, substitution of Eq. (3.117) into Eq. (3.103c) gives a relation between $\eta_1(\tau)$ and $\eta_3(\tau)$:

$$\eta_1(\tau)=\frac{\mathcal{Q}-(2+Bi)\,\eta_3(\tau)}{Bi}\,. \tag{3.119}$$

Substitution of Eq. (3.117) into Eq. (3.102) and integration over ω field yields:

$$\eta_3(\tau)\left(\frac{6}{\zeta^2}-\frac{2}{3\zeta}\frac{d\zeta}{d\tau}\right)=\frac{d\eta_1(\tau)}{d\tau}+\frac{1}{3}\frac{d\eta_3(\tau)}{d\tau}\,. \tag{3.120}$$

When Eq. (3.119) is introduced into the above equation, a first-order ordinary differential equation for $\eta_3(\tau)$ is generated:

$$\eta_3(\tau)\left(\frac{6}{\zeta^2}-\frac{2}{3\zeta}\frac{d\zeta}{d\tau}\right)=-\frac{6+2Bi}{3Bi}\frac{d\eta_3(\tau)}{d\tau}\,. \tag{3.121}$$

The above equation can be integrated analytically to give:

$$\eta_3(\tau)=\eta_4\exp\left(-\frac{\dfrac{6}{\zeta^2}-\dfrac{2}{3\zeta}\dfrac{d\zeta}{d\tau}}{\dfrac{6+2Bi}{3Bi}}\tau\right)\,, \tag{3.122}$$

where η_4 is the integration constant defined by the initial condition, as will be explained later. By substituting Eq. (3.122) into Eq. (3.119), $\eta_1(\tau)$ is also obtained. Then, substitution of both $\eta_1(\tau)$ and $\eta_3(\tau)$ into Eq. (3.117), gives the following temperature distribution:

$$\begin{aligned}\Theta(\omega,\,\tau)=&\frac{\mathcal{Q}}{Bi}\\ &+\eta_4\exp\left(-\frac{\dfrac{6}{\zeta^2}-\dfrac{2}{3\zeta}\dfrac{d\zeta}{d\tau}}{\dfrac{6+2Bi}{3Bi}}\tau\right)\left(\omega^2-\frac{2+Bi}{Bi}\right)\,.\end{aligned} \tag{3.123}$$

The 'initial' temperature distribution for the current step is known from the previous time step, $\delta\tau^o$. This should also be satisfied by the above equation. Hence, the constant η_4 can be calculated:

$$\eta_4=\frac{\mathcal{Q}}{2}-\frac{Bi}{2}\left[\Theta_1\Theta^o(1,\,\delta\tau^o)+\Theta_2\right]\,, \tag{3.124}$$

where $\Theta^o(1,\,\delta\tau^o)$ is the surface temperature at the previous time step. Also, Θ_1 and Θ_2, whose expressions are given by Eq. (B.18), have been introduced to allow for changes of the gas temperature. Note that if the gas temperature does not change, Θ_1 and Θ_2 are 1 and 0, respectively.

Hence, the final temperature distribution reads:

$$
\begin{aligned}
\Theta(\omega,\,\tau) = & \frac{\mathcal{Q}}{Bi} \\
& + \left\{ \frac{\mathcal{Q}}{2} - \frac{Bi}{2} \left[\Theta_1 \Theta^o(1,\,\delta\tau^o) + \Theta_2 \right] \right\} \\
& \exp\left(- \frac{\dfrac{6}{\zeta^2} - \dfrac{2}{3\zeta}\dfrac{d\zeta}{d\tau}}{\dfrac{6+2Bi}{3Bi}} \tau \right) \left(\omega^2 - \frac{2+Bi}{Bi} \right) \,.
\end{aligned}
\tag{3.125}
$$

Accuracy of the profile solution

The accuracy of the profile method will now be assessed by comparing it with the semi-analytical one presented earlier. A single droplet is considered and in order to simplify matters the properties of the droplet are assumed constant. Also, evaporation is not considered (i.e. $\mathcal{Q} = 0$) consequently, the semi-analytical solution approximates the exact solution with an error less than $10^{-8}\,\%$ caused by the finite number of terms in the Fourier series.

In preliminary computations, different time steps were used in the profile method to ensure time-step independent results. It was found that the maximum difference in the dimensionless temperature distributions for $\delta\tau = 10^{-4}$ and $\delta\tau = 10^{-5}$ is less than $0.05\,\%$ and consequently, the latter time step is adopted.

Firstly, the case with low Biot number, $Bi = 0.1$, is examined. The dimensionless temperature distribution at various times, obtained with both the analytical and the profile method, is shown in Fig. 3.17. As can be seen, here the maximum difference with the *exact* solution is less than $2\,\%$. For higher Biot numbers, the error increases. This can be seen in Fig. 3.18 which presents the dimensionless temperature distribution for $Bi = 100$. Although the shapes of the temperature distributions are well captured, the maximum gap between the two methods is up to $12\,\%$. However, it should be emphasised that in spray applications, the surface temperature is of greatest importance, because it plays the dominant role in energy exchange between the two phases and it also controls the evaporation rate. As can be seen in Figs. 3.19 and 3.20, which show the temporal variations of the dimensionless

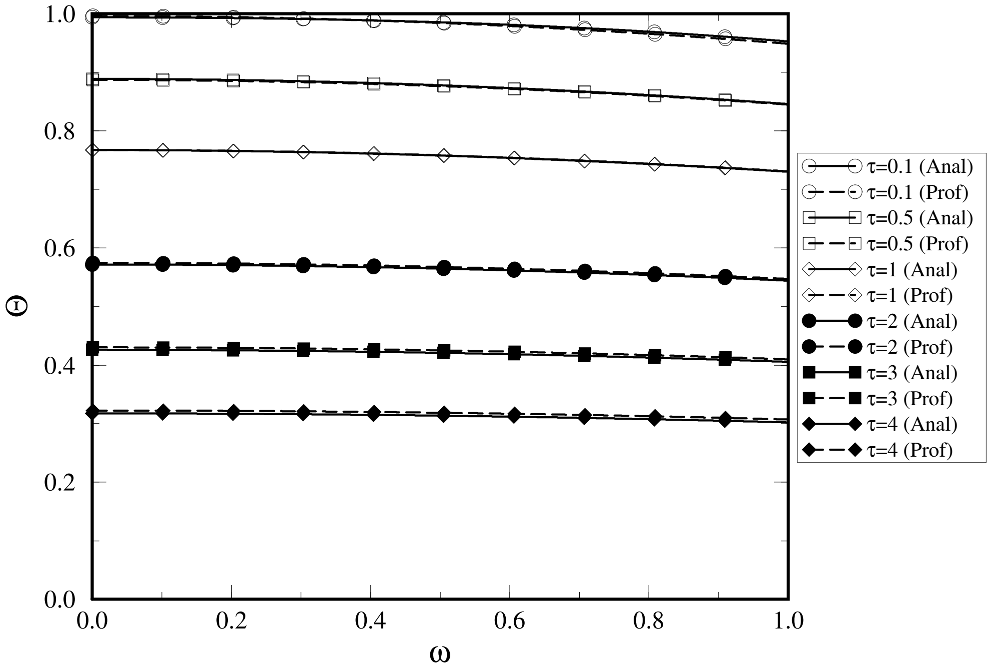

Figure 3.17: Comparison between profile and analytical solutions of dimensionless temperature distributions for $Bi = 0.1$.

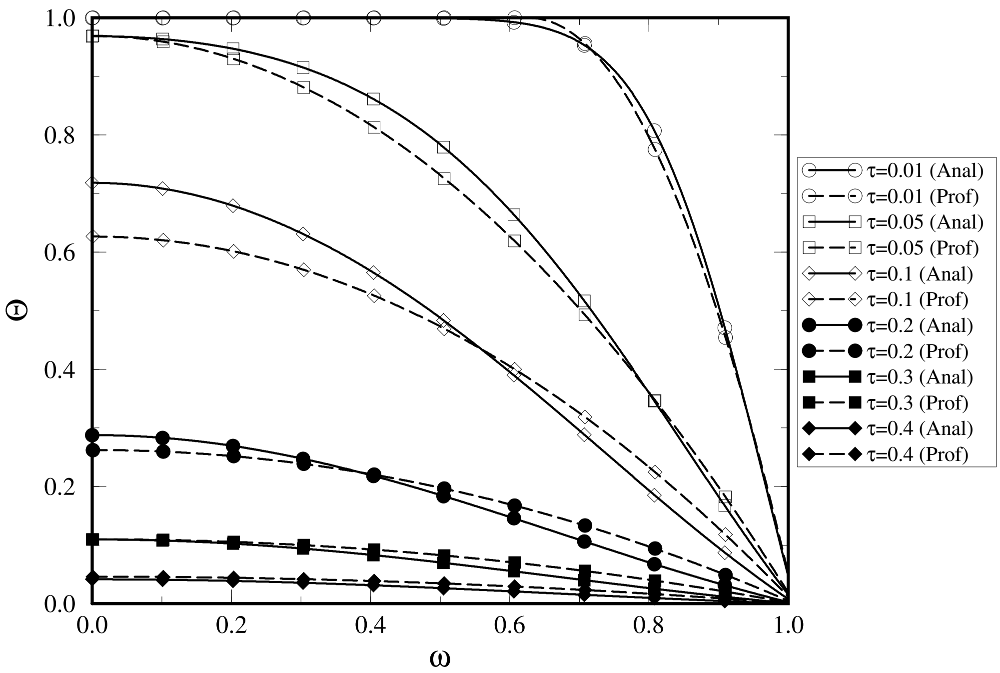

Figure 3.18: Comparison between profile and analytical solutions of dimensionless temperature distributions for $Bi = 100$.

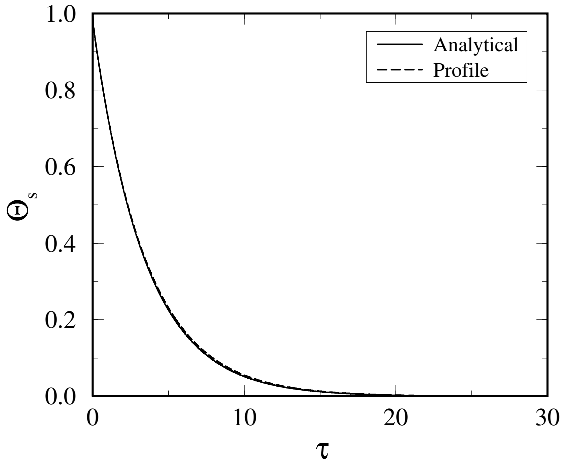

Figure 3.19: Comparison between profile and analytical solutions of the temporal dimensionless surface temperature for $Bi = 0.1$.

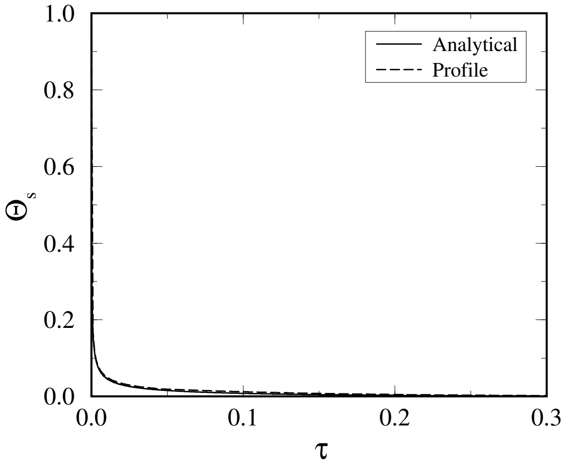

Figure 3.20: Comparison between profile and analytical solutions of the temporal dimensionless surface temperature for $Bi = 100$.

temperature at the droplet surface for $Bi = 0.1$ and $Bi = 100$, respectively, the predictions of the profile method are very close to the exact solution. Considering the satisfactory accuracy of the profile method at the droplet surface and taking also into account its simplicity and economy, in respect of computer resources, it is adopted in this study.

Effective conductivity

The external flow may induce flow, including recirculation, inside the droplet as illustrated in Fig. 3.21 (see Wong and Lin [310]). The higher the velocity of the external flow the stronger the internal circulation. This produces strong convective

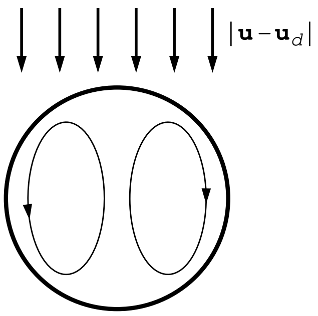

Figure 3.21: Schematic of a droplet with internal recirculations.

transport, inside the droplet, compared to conduction and hence, the isotherms may in the limit be expected to coincide with the streamlines (Aggarwal [3], Abramzon and Sirignano [1]). This situation is modelled by the *vortex* model of Tong and Sirignano [291] who introduced a relevant parameter in the two-dimensional energy equation. This parameter is the Peclet number, Pe_d, defined below, which measures the relative importance of convection and conduction (see Eq. (3.127)). Although this model offers increased accuracy, it requires substantial additional computational time and therefore, in Diesel spray calculations, where many thousands droplets are considered, it is impractical to use.

A simplified approach has been suggested by Jin and Borman [150] and Talley and Yao [283]. It employs the 'ordinary' conduction model, but uses an *effective* value of the liquid thermal conductivity inside the droplet, $k_{\mathit{eff}} = \chi k_d$, where χ is a factor greater than unity. Such an idea was first introduced by Kronig and Brink [172] who investigated mass transfer inside droplets for Hill's type of internal circulation at high Peclet numbers. They found that the overall heat or mass transfer rate between the droplet interior and the surface is 2.72 times higher than that of a solid sphere. Talley and Yao [283] found that $\chi = 2.25$ fits well the vortex-model results. In this study, the following simple correlation for χ, proposed by Abramzon and Sirignano [1], is adopted:

$$\chi = 1.86 + 0.86 \tanh\left[2.245 \log_{10}\left(\frac{Pe_d}{30}\right)\right] . \tag{3.126}$$

As can be seen, this correlation is a function of the Peclet number which is defined as:

$$Pe_d = \frac{Re_d}{Pr_d} . \tag{3.127}$$

The Reynolds and Prandtl numbers are respectively given by:

$$Re_d = \frac{\rho_d U_s D_d}{\mu_d} , \tag{3.128}$$

$$Pr_d = \frac{\mu_d c_{p,d}}{k_d} . \tag{3.129}$$

Here, U_s is the maximum velocity at the droplet surface given by:

$$U_s = \frac{1}{32}|\hat{\mathbf{u}} - \mathbf{u}_d|\frac{\mu_m}{\mu_d} Re_\infty C_F , \tag{3.130}$$

where

$$Re_\infty = \frac{\rho_m |\hat{\mathbf{u}} - \mathbf{u}_d| D_d}{\mu_m} \; . \tag{3.131}$$

Also, C_F is the friction drag coefficient given by Renksizbulut and Yuen [249] for an evaporating droplet as:

$$C_F = \frac{14.5}{Re^{0.71}\,(1 + B_M)} \; . \tag{3.132}$$

Here, in analogy to the heat-transfer number, B_M is the mass-transfer number, given by:

$$B_M = \frac{Y_{v,s} - Y_v}{1 - Y_{v,s}} \; . \tag{3.133}$$

The correlation of Abramzon and Sirignano, Eq. (3.126), gives $\chi = 1$ for very low Pe_d, i.e. the conduction limit, while for high Pe_d it approaches the value reported by Kronig and Brink [172], i.e. $\chi = 2.72$. The latter essentially lowers Bi by a factor of 2.72. The dependence of χ on Pe_d is illustrated in Fig. 3.22.

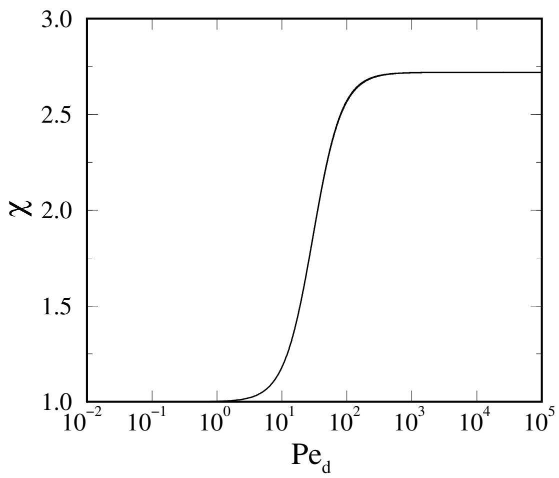

Figure 3.22: Factor for effective thermal conductivity of droplet with internal circulation.

Energy contribution to the gas phase

The exchange of energy between the droplet and the gas generates an additional source term, S_e^d, in the gas energy conservation equation, Eq. (2.74). This is given by:

$$S_e^d(\mathbf{x}) = -\lim_{\substack{\Delta t \to 0 \\ \delta V \to 0}} \frac{1}{\Delta t \delta V} \int_{\delta V} \left\{ \sum_{p=1}^{N_p} \int_t^{t+\Delta t} \delta\left(\mathbf{x} - \mathbf{x}_p\right) \frac{d}{dt} \left[m_p c_{p,d} \left(T_p - T_{ref} \right) \right] dt \right\} dV \;, \tag{3.134}$$

where $T_{ref} = 298\,K$ is the reference temperature.

3.6.3 Mass conservation equation

Attention is now turned to mass transfer within the droplet and between this and the gas. A single-component fuel can be treated as a special case of the general one, but because of its simple mathematical formulation it will be considered separately. Then, the multicomponent diffusion equation will be analysed.

Single-component

In this case, the concentration within the droplet is uniform and only the mass transfer at the surface needs to be considered. Following Borman and Johnson [48], the evaporation rate is expressed as:

$$\frac{dm_d}{dt} = -\pi D_d \mathcal{D}_f Sh \rho_f \ln \frac{1 - \chi_v}{1 - \chi_{v,s}} \;, \tag{3.135}$$

where $\mathcal{D}_f$ is the mass diffusivity evaluated at the film temperature and $\chi_{v,s}$ and χ_v are the fuel vapour molar concentrations at the droplet surface and far from it, respectively. The latter is obtained from the solution of the fuel vapour conservation equation, Eq. (2.72). The fuel vapour molar concentration at the droplet surface is calculated from phase equilibrium. For ideal mixtures, the equilibrium is described by Raoult's law, which reads:

$$\chi_{v,s} = \frac{p_{v,s}}{p} \chi_{d,s} \;. \tag{3.136}$$

Here, p is the total pressure of gas mixture and $p_{v,s}$ and $\chi_{d,s}$ are the partial fuel vapour pressure and fuel liquid concentration, respectively, at the droplet surface. In the present circumstances $\chi_{d,s} = 1$. Also, in Eq. (3.135), the gas density ρ_f is calculated from the ideal gas law at the film temperature and composition, which represent the arithmetic mean of the gas properties and those of the droplet surface. Further, Sh is the Sherwood number, a dimensionless mass transfer coefficient, given by correlations similar to those for heat transfer. Since, in this study, as mentioned in §3.6.2, the correlations of Ranz and Marshall [237, 238] corrected by the factor of El Wakil *et al.* [85] and that of Abramzon and Sirignano [1] and the correlation of Renksizbulut and Yuen [248] are adopted, the corresponding Sh correlations read:

$$Sh = \left(2 + 0.6 Re^{1/2} Sc^{1/3}\right) \mathcal{F} , \tag{3.137a}$$

$$Sh = 2 + \frac{0.6 Re^{1/2} Sc^{1/3}}{\mathcal{F}_M} , \tag{3.137b}$$

$$Sh = \frac{2 + 0.57 Re^{1/2} Sc^{1/3}}{(1 + B_M)^{0.7}} , \tag{3.137c}$$

where $\mathcal{F}_M$ is obtained by replacing B'_T in Eq. (3.90) with B_M. Also, Sc is the Schmidt number, given by:

$$Sc = \frac{\mu_f}{\rho_m \mathcal{D}_f} . \tag{3.138}$$

An evaporation relaxation time can be defined using Eq. (3.135) as:

$$\tau_m = \frac{m_d}{\pi D_d \mathcal{D}_f Sh \rho_f \ln \dfrac{1 - \chi_v}{1 - \chi_{v,s}}} = \frac{\rho_d D_d^2}{6 \mathcal{D}_f Sh \rho_f \ln \dfrac{1 - \chi_v}{1 - \chi_{v,s}}} , \tag{3.139}$$

resulting in:

$$\frac{dm_d}{dt} = -\frac{m_d}{\tau_m} . \tag{3.140}$$

The physical meaning of the evaporation relaxation time is that for large values ($\tau_m \to \infty$), the droplet is practically non-evaporating, whereas for small values ($\tau_m \to 0$), it evaporates very rapidly.

Multicomponent

An important aspect of the Diesel sprays is that they involve the evaporation of a multicomponent fuel. Aggarwal [3] distinguished three main differences between single-component and multicomponent fuels:

1. The effect of transient heat transport inside the droplet is probably not important* in predicting the droplet behaviour of a single-component fuel. However, for the multicomponent case, the transient thermal and mass transfer may be the rate-controlling processes and must be considered in modelling.

2. In the multicomponent case, the volatile component may be trapped inside the droplet due to high mass diffusional resistance, where it may be heated beyond its boiling point. This can start homogeneous nucleation leading to microexplosion (see also Law [181]).

3. Certain regions of the chamber may be relatively rich in the volatile fuel while others may have a high concentration of the less volatile fuel. The non-uniform fuel distribution may significantly influence not only the ignition, flame stability and pollutant formation, but also the dominant burning mechanism itself.

Renksizbulut and Bussmann [247] studied the evaporation of a binary hydrocarbon droplet, consisting of decane and hexadecane, in air at $1000\,K$ and $10\,atm$ for $Re = 100$, using numerical methods. They included all transient effects including droplet size and velocity variations, heat and mass transfer within the liquid phase and thermophysical property variations with temperature and concentration in both phases. They concluded that the existing drag coefficient, Sherwood number and Nusselt number correlations originally developed for single-component droplets can be used for multicomponent droplets as well.

Mass diffusion in the droplet is described by a differential equation similar to that for heat conduction, Eq. (3.75). Following Law and Law [182], the general transient-diffusion equation for the concentration, $Y_{d,i}$, of species i reads:

$$\frac{\mathcal{D}_{d,i}}{r^2}\frac{\partial}{\partial r}\left(r^2\frac{\partial Y_{d,i}}{\partial r}\right) = \frac{\partial Y_{d,i}}{\partial t}\ , \tag{3.141}$$

where $\mathcal{D}_{d,i}$ denotes the diffusion coefficient of the i^{th} component. The initial condition is given by the assumption of uniform initial concentration, i.e.

$$Y_{d,i}(r,\,0) = Y_{d,i,0}\ , \tag{3.142a}$$

*As shown earlier, this strictly is true only for low Bi.

while the boundary conditions at the droplet centre and its surface are respectively expressed by:

$$\frac{\partial Y_{d,i}(0,\, t)}{\partial r} = 0 \,, \tag{3.142b}$$

$$4\pi R_d^2 \rho_d \mathcal{D}_{d,i} \frac{\partial Y_{d,i}(R_d,\, t)}{\partial r} = \dot{m}_d \left[Y_{d,i}(R_d,\, t) - \frac{\dot{m}_{d,i}}{\dot{m}_d} \right] \,. \tag{3.142c}$$

In the above, $\dot{m}_{d,i}$ is given by:

$$\dot{m}_{d,i} = -\pi D_d \mathcal{D}_{f,i} Sh_i \rho_f \ln \frac{1 - \chi_{v,i}}{1 - \chi_{v,i,s}} \,, \tag{3.143}$$

while $\dot{m}_d$ is the summation of the individual surface mass-transfer rates, i.e.

$$\dot{m}_d = \sum_{i=1}^{N} \dot{m}_{d,i} \,. \tag{3.144}$$

Note that in the above, $\chi_{v,i,s}$ is calculated from Raoult's law, as explained in the single-component case. However here, $\chi_{d,i,s}$ is not unity but it is now obtained from the solution of the diffusion equation, Eq. (3.141), where the following conversion formulae are also used:

$$Y_i = \frac{\chi_i M_i}{\sum\limits_{i=1}^{N} \chi_i M_i} \,, \tag{3.145a}$$

$$\chi_i = \frac{Y_i / M_i}{\sum\limits_{i=1}^{N} Y_i / M_i} \,. \tag{3.145b}$$

In the above, M denotes the molecular weight.

By introducing the dimensionless variables τ, ω and ζ, defined by Eq. (3.100), the diffusion equation recasts into:

$$\frac{1}{\omega^2 \zeta^2(\tau) Le_i} \frac{\partial}{\partial \omega} \left[\omega^2 \frac{\partial Y_{d,i}(\omega,\, \tau)}{\partial \omega} \right] - \frac{\omega}{\zeta(\tau)} \frac{d\zeta(\tau)}{d\tau} \frac{\partial Y_{d,i}(\omega,\, \tau)}{\partial \omega} = \frac{\partial Y_{d,i}(\omega,\, \tau)}{\partial \tau} \,, \tag{3.146}$$

where Le_i is the Lewis number defined as:

$$Le_i = \frac{\alpha_d}{\mathcal{D}_{d,i}} \,. \tag{3.147}$$

Also, the initial and boundary conditions, now become into:

$$Y_{d,i}(\omega,\,0) = Y_{d,i,0}\ , \tag{3.148a}$$

$$\frac{\partial Y_{d,i}(0,\,\tau)}{\partial \omega} = 0\ , \tag{3.148b}$$

$$\frac{\partial Y_{d,i}(1,\,\tau)}{\partial \omega} = \mathcal{M}\left[Y_{d,i}(1,\,\tau) - \frac{\dot{m}_{d,i}}{\dot{m}_d}\right]\ , \tag{3.148c}$$

where $\mathcal{M}$ is the dimensionless evaporation rate, given by:

$$\mathcal{M} = \frac{\dot{m}_d}{4\pi R_d \rho_d \mathcal{D}_{d,i}}\ . \tag{3.149}$$

The similarity of the diffusion equation and its initial and boundary conditions with the conduction equation and its corresponding initial and boundary conditions suggests the solutions are also similar. Hence, the profile method* is applied here as well and since the method has already been presented earlier, the details are omitted and only the final results are given.

In the early stages ($\delta(\tau) > 0$), the concentration distribution can be approximated by:

$$Y_{d,i}(\omega,\,\tau) = \begin{cases} Y_{d,i,0}\ , & \text{for } \omega < \delta(\tau)\ , \\ Y_{d,i,0} + \eta_3(\tau)\left[\omega - \delta(\tau)\right]^2\ , & \text{for } \omega \geq \delta(\tau)\ , \end{cases} \tag{3.150}$$

where $\delta(\tau)$ is obtained by integrating the following first-order ordinary differential equation:

$$\begin{aligned} &\frac{6}{\zeta^2 Le_i}\left[1-\delta(\tau)\right] + \frac{4}{\zeta^2 Le_i}\delta(\tau)\ln\delta(\tau) - \frac{2}{\zeta}\frac{d\zeta}{d\tau}\left[\frac{1}{3} - \frac{\delta(\tau)}{2} + \frac{\delta^3(\tau)}{6}\right] \\ &= -\left[1-\delta(\tau)\right]^2\left\{\frac{4-\mathcal{M}\left[1-\delta(\tau)\right]}{6-3\mathcal{M}\left[1-\delta(\tau)\right]}\right\}\frac{d\delta(\tau)}{d\tau}\ . \end{aligned} \tag{3.151}$$

The solution of the above can be obtained numerically as explained in §3.6.2. The differential term is discretised according to Eq. (3.114) while the initial condition is $\delta(0) = 1$. It is also noted that the time step must be smaller than a characteristic time, $\tau_{p,m}$, as explained in §3.6.2 (see Eq. (3.116)). Here, this characteristic time

*The semi-analytical solution can also be obtained in the same manner as it was obtained for the conduction equation (see §3.6.2). However, here, the established profile method is adopted.

reads:

$$\tau_{p,m} = \frac{4-\mathcal{M}}{6-3\mathcal{M}} \frac{\delta^o}{\dfrac{6}{\zeta^2 Le_i} + \dfrac{2R_d R_{d,0}}{9\zeta\alpha_d\tau_m}} \,. \tag{3.152}$$

Finally, in Eq. (3.150), $\eta_3(\tau)$ is evaluated from:

$$\eta_3(\tau) = \frac{\mathcal{M}\left(Y_{d,i,0} - \dfrac{\dot{m}_{d,i}}{\dot{m}_d}\right)}{\left[1-\delta(\tau)\right]\left\{2-\mathcal{M}\left[1-\delta(\tau)\right]\right\}} \,. \tag{3.153}$$

As soon as $\delta(\tau) = 0$, the concentration distribution becomes:

$$Y_{d,i}(\omega,\,\tau) = \frac{\dot{m}_{d,i}}{\dot{m}_d} + \frac{\mathcal{M}}{2}\left[Y^o_{d,i}(1,\,\delta\tau^o) - \frac{\dot{m}_{d,i}}{\dot{m}_d}\right] \exp\left(\frac{\dfrac{6}{\zeta^2 Le_i} - \dfrac{2}{3\zeta}\dfrac{d\zeta}{d\tau}}{\dfrac{6-2\mathcal{M}}{3\mathcal{M}}}\tau\right) \left(\omega^2 + \frac{2-\mathcal{M}}{\mathcal{M}}\right) \,, \tag{3.154}$$

where $Y^o_{d,i}(1,\,\delta\tau^o)$ is the surface concentration at the previous time step, $\delta\tau^o$.

Just as for heat transfer, the internal circulation in the droplet leads to an enhanced diffusivity. The effective diffusivity can be calculated in the same way as the effective conductivity was calculated in §3.6.2. Thus,

$$\mathcal{D}_{d,i,\mathit{eff}} = \chi\mathcal{D}_{d,i} \,, \tag{3.155}$$

where χ is evaluated from Eq. (3.126).

Finally, it is noted that non-condensible gas solubility in the droplet can also be taken into account by simply considering $N+1$ components, where the additional component is the gas.

Mixing rules

The properties of a mixture are not necessarily a linear combination of the properties of each component. In this study, the properties of a multicomponent mixture, consisting of N components, are obtained following the recommendations of Reid *et al.* [241], as outlined below.

The liquid mixture viscosity is calculated by the method of Grunberg and Nissan [114]:

$$\ln \mu_{d,mix} = \sum_{i=1}^{N} \chi_{d,i} \ln \mu_{d,i} + \sum_{i=1}^{N} \sum_{\substack{j=1 \\ j \neq i}}^{N} \chi_{d,i} \chi_{d,j} G_{ij} \ , \tag{3.156}$$

where $\chi_{d,i}$ and $\mu_{d,i}$ are the mole fractions and the dynamic viscosity of the i^{th} component, respectively and G_{ij} is an interaction parameter which is a function of the nature of the components i and j, as well as the temperature and in some cases, the composition. For a hydrocarbon mixture, G_{ij} is evaluated at a reference temperature, $298\,K$, by:

$$G_{ij}(298) = \sum \Delta_i - \sum \Delta_j + \frac{0.3161\,(N_i - N_j)^2}{N_i + N_j} - 0.1188\,(N_i - N_j) \ , \tag{3.157}$$

where N is the number of carbon atoms in each component and the subscript 'i' denotes that with the most carbon atoms. Also, $\sum \Delta$ is calculated based on the number of groups that each component comprises, where the value of each group is given in Table 3.3. The temperature dependence of G_{ij} is obtained from the

Table 3.3: Group contributions for G_{ij} at $298\,K$.

Group	Value of Δ
$-CH_3$	-0.100
$>CH_2$	0.096
$>CH-$	0.204
$>C<$	0.433

correlation of Isdale *et al.* [144]:

$$G_{ij}(T_d) = 1 - [1 - G_{ij}(298)]\,\frac{573 - T_d}{275} \ . \tag{3.158}$$

For the calculation of the thermal conductivity, the Li method [189] is used:

$$k_{d,mix} = \sum_{i=1}^{N} \sum_{j=1}^{N} \phi_i \phi_j k_{ij} \ , \tag{3.159}$$

where ϕ_i and k_{ij} are respectively given by:

$$\phi_i = \frac{\chi_{d,i} V_i}{\sum_{j=1}^{N} \chi_{d,j} V_j} \ , \tag{3.160}$$

$$k_{ij} = \frac{2}{\dfrac{1}{k_{d,i}} + \dfrac{1}{k_{d,j}}} \ . \tag{3.161}$$

Here, V_i is the molar volume of the pure component i.

When vapour of component i diffuses into a multicomponent gas mixture, the diffusion coefficient is given by the Blanc's law [45], which reads:

$$\mathcal{D}_i = \left(\sum_{\substack{j=1 \\ j \neq i}}^{N} \frac{\chi_{v,j}}{\mathcal{D}_{ij}} \right)^{-1} , \tag{3.162}$$

where $\mathcal{D}_{ij}$ is the binary diffusion coefficient of i into j. In cases of liquids, there are no convenient and simple estimation methods for multicomponent diffusion coefficients. Here, this coefficient is evaluated based on the assumption that the mixture is homogeneous. Hence, binary diffusion of the component i to the homogeneous mixture is assumed. Following the suggestion of Perkins and Geankoplis [232], the diffusion coefficient is evaluated from:

$$\mathcal{D}_{d,i,mix} \mu_{d,mix}^{0.8} = \sum_{\substack{j=1 \\ j \neq i}}^{N} \chi_{d,j} \mathcal{D}_{d,ij}^{o} \mu_{d,j}^{0.8} \ . \tag{3.163}$$

Here, $\mathcal{D}_{d,ij}^{o}$ is the infinite dilution binary diffusion coefficient of solute i into the solvent j. This, for normal paraffin solutions, is given by the Hayduk and Minhas correlation [123]:

$$\mathcal{D}_{d,ij}^{o} = 9.859426 \cdot 10^{-14} \, T_d^{1.47} \, (1000 \mu_{d,j})^{\varepsilon_i} \, \rho_{d,i}^{0.71} \ , \tag{3.164}$$

where $\varepsilon_i = 0.0102 \rho_{d,i} - 0.791$.

The recommendation of Hadden [117] is adopted to calculate the mixture surface tension:

$$\sigma_{d,mix} = \sum_{i=1}^{N} \chi_{d,i,s} \sigma_{d,i} \ , \tag{3.165}$$

where $\chi_{d,i,s}$ is the mole fraction on the droplet surface.

Finally, the boiling and pseudocritical temperature as well as the pseudocritical pressure are calculated by a simple mole-fraction averaging method often called

Kay's rule [160]:

$$T_{b,mix} = \sum_{i=1}^{N} \chi_{d,i} T_{b,i} \ , \tag{3.166a}$$

$$T_{c,mix} = \sum_{i=1}^{N} \chi_{d,i} T_{c,i} \ , \tag{3.166b}$$

$$p_{c,mix} = \sum_{i=1}^{N} \chi_{d,i} p_{c,i} \ . \tag{3.166c}$$

Following Varnavas and Assanis [294], in the use of the above, the properties of each component are evaluated at the volume-mean temperature, $T_{d,m}$, defined by:

$$T_{d,m} = \frac{1}{V_d} \int_{V_d} T_d(r)\, dV_d = \frac{3}{R_d^3} \int_0^{R_d} T_d(r) r^2\, dr \ , \tag{3.167}$$

where V_d denotes the volume of the droplet with radius R_d. This practice is not, however, followed for the surface tension coefficient and latent heat of vapourisation, which by definition are evaluated at the surface temperature.

Mass contribution to the gas phase

The exchange of mass between the droplet and the gas gives rise to an associated source term, S_m^d, in the mass conservation equation of gas, Eq. (2.71), given by:

$$S_m^d(\mathbf{x}) = - \lim_{\substack{\Delta t \to 0 \\ \delta V \to 0}} \frac{1}{\Delta t \delta V} \int_{\delta V} \left[\sum_{p=1}^{N_p} \int_t^{t+\Delta t} \delta\left(\mathbf{x} - \mathbf{x}_p\right) \frac{dm_p}{dt} dt \right] dV \ . \tag{3.168}$$

The source due to the evaporation rate of a particular component i is given by:

$$S_{Y_{v,i}}^d(\mathbf{x}) = - \lim_{\substack{\Delta t \to 0 \\ \delta V \to 0}} \frac{1}{\Delta t \delta V} \int_{\delta V} \left[\sum_{p=1}^{N_p} \int_t^{t+\Delta t} \delta\left(\mathbf{x} - \mathbf{x}_p\right) \frac{dm_{p,i}}{dt} dt \right] dV \ . \tag{3.169}$$

3.7 Breakup

3.7.1 Introduction

The phenomenon of disintegration of droplets into smaller ones due to aerodynamic forces is called *breakup*. The relative motion between the droplet and the surrounding gas causes a non-uniform distribution of pressure and shear stress on the droplet surface. These external forces deform the droplet and cause it to disintegrate when they overcome the opposing force of surface tension. The new droplets may undergo further breakup until a stable diameter is reached for which the surface tension force is stronger than the external forces*.

Dimensionless numbers, expressing the ratio of the aforementioned forces, are used in correlations of the various breakup regimes. Hinze [132] reported that the breakup regime transitions are mainly functions of the Weber number, We and the Ohnesorge number, Oh. Both of them have been defined in Section 3.3, however, here their mathematical formulae are redefined to read for a particular droplet as follows:

$$We = \frac{\rho_m |\hat{\mathbf{u}} - \mathbf{u}_d|^2 D_d}{\sigma_d} \,, \tag{3.170}$$

$$Oh = \frac{\mu_d}{\sqrt{\rho_d D_d \sigma_d}} \,. \tag{3.171}$$

Kitscha *et al.* [164] stated that the combination of Kelvin-Helmholtz and Rayleigh-Taylor instability theories can describe droplet breakup. They predicted that it occurs when the growth rate of interfacial waves on the front is faster than the rate at which waves propagate around the interface to the side. Expressions for the propagation speed and the growth factor can be derived assuming the perturbed flow is irrotational. The growth factor determines the degree of amplification or damping.

Pilch and Erdman [233] collected data in a wide literature search for various fluids and categorised droplet breakup into five distinct mechanisms described below and illustrated schematically in Fig. 3.23:

1. **Vibrational breakup** ($We \leq 12$): A few large fragments are produced. The overall breakup time is long compared to the other breakup mechanisms. Hence, this mechanism is usually not considered important in droplet breakup studies.

*A recent comprehensive literature review on this subject can be found in Faeth [95].

2. **Bag breakup** ($12 < We \leq 50$): A thin hollow bag is blown downstream while it is attached to a more massive toroidal rim. The bag forms a large number of small fragments, whereas the rim, a short time later, produces a small number of large fragments.

3. **Bag-and-stamen breakup** ($50 < We \leq 100$): This mode is similar to bag breakup. A thin bag is blown downstream while being anchored to a massive toroidal rim. A column of liquid (stamen) is formed along the drop axis parallel to the approaching flow. The bag bursts first and the disintegration of rim and stamen follows.

4. **Sheet stripping** ($100 < We \leq 350$): A thin sheet is continuously drawn from the periphery of the deforming drop. The sheet disintegrates a short distance downstream from the drop. A coherent residual drop exists during the entire breakup process.

5. **Wave crest stripping followed by catastrophic breakup** ($350 < We$): Waves with large amplitude and small wavelength are formed on the windward surface of the drop. The wave crests are continuously eroded by the action of the flow field over the surface of the drop. Waves with large amplitude and long wavelength ultimately penetrate the drop creating several large fragments. This is referred to as catastrophic breakup.

Similar observations have been reported by Krzeczkowski [173] who indicated four typical cases of liquid droplet breakup listed below:

1. Bag mechanism, for $10 < We \leq 20$;

2. Bag jet mechanism, for $20 < We \leq 30$;

3. Transition mechanism, for $30 < We \leq 65$;

4. Shear (or stripping off) mechanism, for $65 < We$.

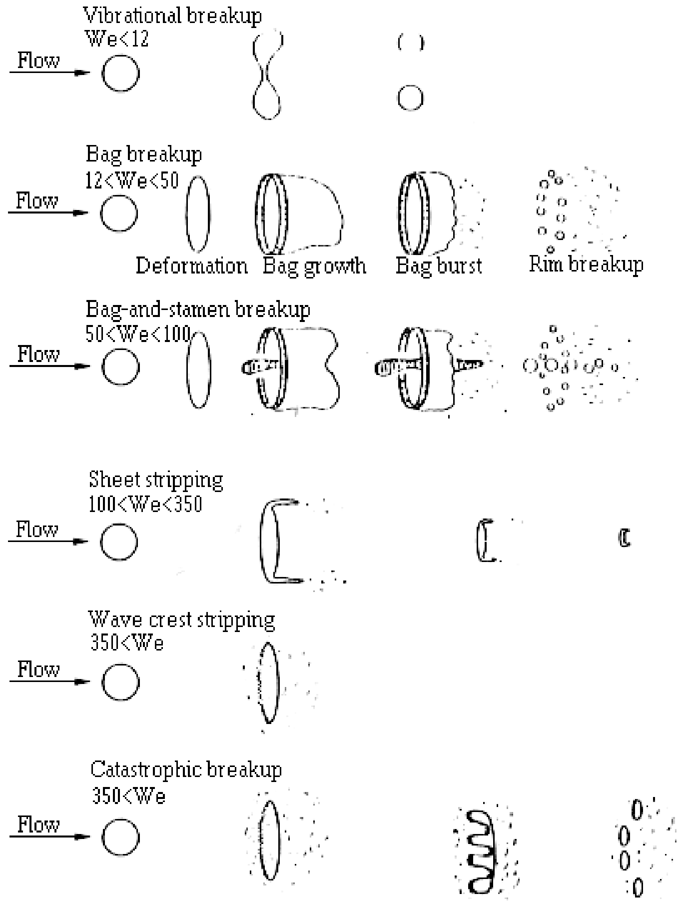

Figure 3.23: Breakup mechanisms, adapted from Pilch and Erdman [233].

Krzeczkowski's investigations were carried out for six liquids of various viscosities and he also noted an influence of the liquid viscosity on the breakup mechanism for $Oh > 0.1$. His results have been confirmed recently by Hsiang and Faeth [139] as shown in Fig. 3.24.

Wierzba and Takayama [307] investigated experimentally, applying holographic interferometry, the stripping type of droplet breakup. They used water droplets of diameter $1030\,\mu m$ and $4300\,\mu m$ and gas Mach numbers from 1.3 to 1.5. The Weber number under these conditions was in the range of 600 to 7600. They established a four-stage mechanism for stripping breakup. In the first, disruption of the liquid surface, manifested by the formation of a small lip on the leeward surface, takes place. During the second stage, droplet deformation occurs and the process of the stripping of microdrops from the surface of parent droplet is initiated. The third stage is

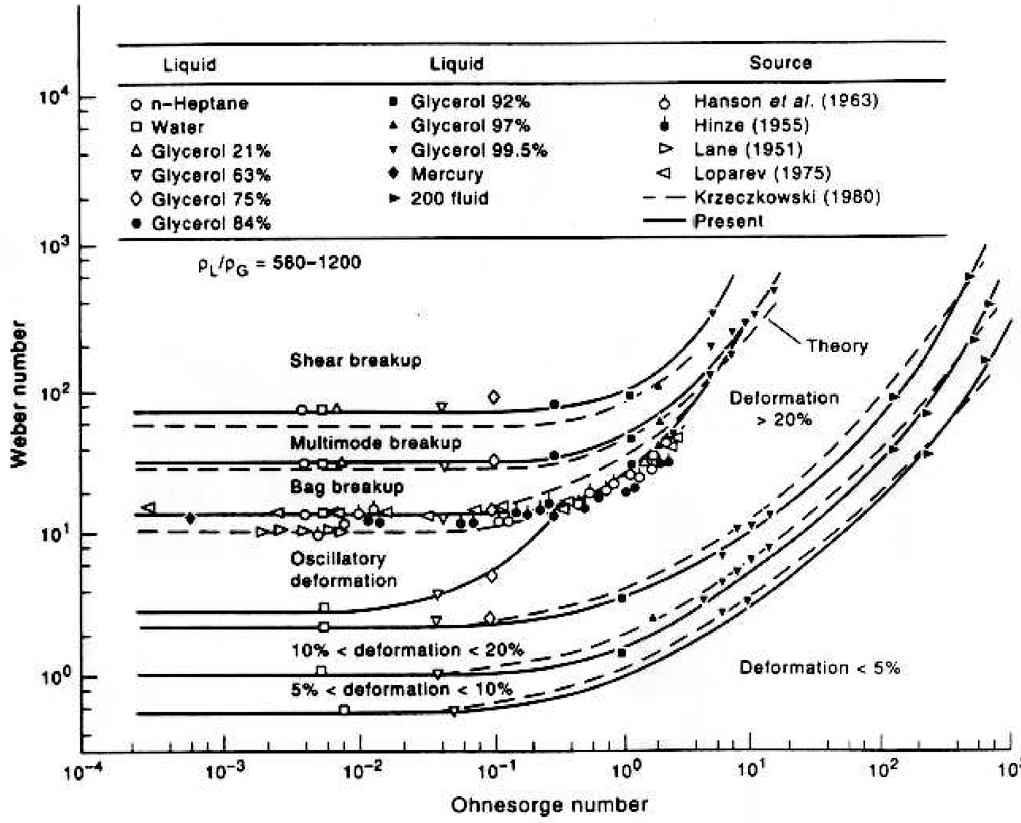

Figure 3.24: Droplet deformation and breakup regime, taken from Hsiang and Faeth [139].

characterised by continuous stripping of the microdrops and continuous deformation of the parent droplet until its lateral deformation reaches a maximum. At the end of this stage, the remaining part of the droplet breaks up into comparatively large fragments. During the fourth stage, the secondary stripping of microdrops from these fragments takes place.

In this study, three breakup models are adopted, designated as Reitz-Diwakar [245, 246], Pilch-Erdman [233] and Hsiang-Faeth [138]. All the three models are based on empirical correlations which provide criteria for the breakup modes and in case of the onset breakup, equations for the stable diameter and the breakup time. It is noted here, that the breakup process is applied only to secondary droplets while the primary droplets participate only in the atomisation process as described in Section 3.3.

Details of the abovementioned models are given below.

3.7.2 Reitz-Diwakar model

This model is based on the correlations given by Nicholls [210] and reported by Reitz and Diwakar [245, 246] and Reitz [243]. Two different types of breakup are considered:

1. Bag breakup:
$$We > C_{bag} \; ; \tag{3.172}$$

2. Stripping breakup:
$$\frac{We}{\sqrt{Re}} > C_{strip} \; , \tag{3.173}$$

where C_{bag} and C_{strip} are coefficients of the model given in Table 3.4.

According to this model, breakup occurs when either of the two abovementioned criteria is satisfied. The stable diameter is then evaluated from:

$$D_{st} = \begin{cases} C_{bag} \dfrac{\sigma_d}{\rho_m |\hat{\mathbf{u}} - \mathbf{u}_d|^2} \, , & \text{for bag breakup,} \\[2ex] C_{strip}^2 \dfrac{\sigma_d^2}{\rho_m |\hat{\mathbf{u}} - \mathbf{u}_d|^3 \mu_m} \, , & \text{for stripping breakup.} \end{cases} \tag{3.174}$$

The rate of change of the droplet diameter is given by:

$$\frac{dD_d}{dt} = -\frac{D_d - D_{st}}{\tau_b} \; , \tag{3.175}$$

where τ_b is the characteristic breakup time determined by:

$$\tau_b = \begin{cases} C_b D_d \sqrt{\dfrac{\rho_d D_d}{\sigma_d}} \, , & \text{for bag breakup,} \\[2ex] \dfrac{C_s D_d}{|\hat{\mathbf{u}} - \mathbf{u}_d|} \sqrt{\dfrac{\rho_d}{\rho_m}} \, , & \text{for stripping breakup,} \end{cases} \tag{3.176}$$

where C_b and C_s are coefficients given in Table 3.4. There is an uncertainty regarding the coefficient C_s and various values have been proposed in the literature. Nicholls [210] used $C_s = 4$, Reitz and Diwakar [246] proposed $C_s = 10$ and O'Rourke and Amsden [224] recommended $C_s = \sqrt{3}/2$. In this study, the value proposed by the model developers (i.e. Reitz and Diwakar [246]) is adopted.

Table 3.4: Coefficients of the Reitz-Diwakar breakup model.

C_{bag}	C_{strip}	C_b	C_s
12	1	$\pi/4$	10

The characteristic breakup time indicates the tendency of the droplet to break up. For large values ($\tau_b \to \infty$), the droplet resists the forces leading to breakup. In contrast, for small values ($\tau_b \to 0$), it easily breaks up until it reaches the stable diameter.

During the breakup process the droplet mass and total energy, comprising the kinetic and the surface energy, are conserved. Thus, each of the three velocity components of the droplet are reduced by a factor δu, given by Reitz and Diwakar [245] as:

$$\delta u = 1 - \left(\frac{D_d}{D_d^n} - 1 \right) \frac{3\sigma_d}{2\rho_d D_d u_d^2} \,, \tag{3.177}$$

where the subscript 'n' denotes condition after breakup. For consistency, the droplet momentum loss is added to the gas momentum.

3.7.3 Pilch-Erdman model

Pilch and Erdman [233] distinguished five different breakup regimes as described in §3.7.1. The characteristic breakup time is given by:

$$\tau_b = T_b \frac{D_d}{|\hat{\mathbf{u}} - \mathbf{u}_d|} \sqrt{\frac{\rho_d}{\rho_m}} \,, \tag{3.178}$$

where T_b is called the *dimensionless breakup time* and for each regime, it is estimated from the following correlations:

$$T_b = \begin{cases} 6\,(We - 12)^{-0.25} \,, & \text{for } 12 < We \leq 18 \,, \\ 2.45\,(We - 12)^{0.25} \,, & \text{for } 18 < We \leq 45 \,, \\ 14.1\,(We - 12)^{-0.25} \,, & \text{for } 45 < We \leq 351 \,, \\ 0.766\,(We - 12)^{0.25} \,, & \text{for } 351 < We \leq 2670 \,, \\ 5.5 \,, & \text{for } 2670 < We \,. \end{cases} \tag{3.179}$$

As We increases, the droplet is expected to break up easier because the stabilising surface tension forces decrease. Therefore, a monotonic decrease of T_b with We would be expected. However, the above correlations have been extracted from a number of experimental results performed by various researchers for various liquids and conditions and they represent best fits in each regime. Consequently, the variation of T_b with We is not monotonic, as illustrated in Fig. 3.25.

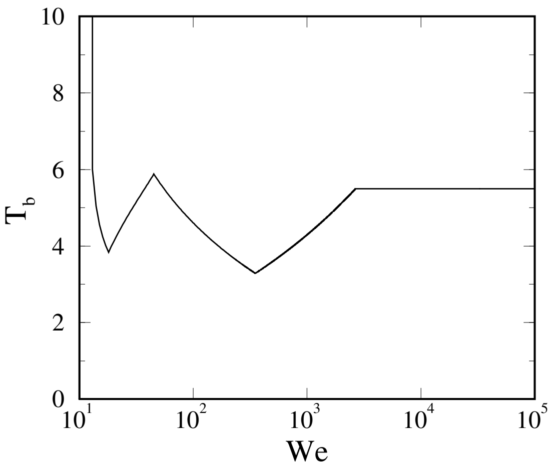

Figure 3.25: Dimensionless breakup time.

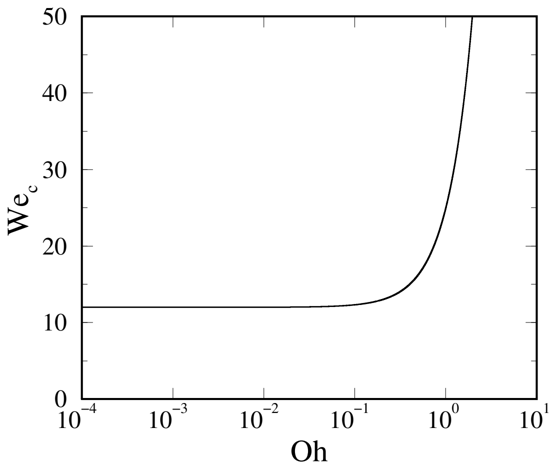

Figure 3.26: Critical Weber number.

The stable diameter is determined, for all the abovementioned regimes, by the following expression:

$$D_{st} = We_c \frac{\sigma_d}{\rho_m |\hat{\mathbf{u}} - \mathbf{u}_d|^2} \left(1 - \frac{V_d}{|\hat{\mathbf{u}} - \mathbf{u}_d|}\right)^{-2} , \tag{3.180}$$

where We_c is the critical Weber number below which breakup does not occur. An empirical correlation for this, for gas/liquid systems, is given by Brodkey [54]:

$$We_c = 12 \left(1 + 1.077 Oh^{1.6}\right) . \tag{3.181}$$

The critical Weber number is approximately 12 when the Ohnesorge number is small ($Oh < 0.1$), as depicted in Fig. 3.26. Also, in Eq. (3.180), V_d is the velocity of the fragment cloud when all breakup processes cease, expressed by:

$$V_d = |\hat{\mathbf{u}} - \mathbf{u}_d| \sqrt{\frac{\rho_m}{\rho_d}} \left(B_1 T_b + B_2 T_b^2\right) . \tag{3.182}$$

In the above expression, the values of the coefficients B_1 and B_2, given in Table 3.5, were chosen to fit experimental data obtained by Kauffman and Nicholls [159], for the time required by a fragmenting droplet behind a shock wave to reach 60 % of the flow field velocity.

Table 3.5: Coefficients of the Pilch-Erdman breakup model.

B_1	B_2
0.375	0.2274

The droplet diameter change is obtained from Eq. (3.175).

3.7.4 Hsiang-Faeth model

Hsiang and Faeth [138] suggested a breakup model which is valid for $We < 1000$ and $Oh < 3.5$. This range covers all the types of breakup mentioned earlier. The stable diameter and the characteristic breakup time are respectively given by:

$$D_{st} = 6.2 D_d \left(\frac{\rho_d}{\rho_m}\right)^{1/4} \sqrt{\frac{\mu_d}{\rho_d D_d |\hat{\mathbf{u}} - \mathbf{u}_d|}} \,, \tag{3.183}$$

$$\tau_b = \frac{35}{7 - Oh} \frac{D_d}{|\hat{\mathbf{u}} - \mathbf{u}_d|} \sqrt{\frac{\rho_d}{\rho_m}} \,. \tag{3.184}$$

When breakup occurs, the droplet diameter rate of change is given by Eq. (3.175).

3.8 Droplet/droplet collision

3.8.1 Introduction

Comprehensive analyses of dense spray phenomena by O'Rourke and Bracco [225], Kuo and Bracco [174] and Bracco [51] pointed out the importance of the effect of droplet collisions. In particular, during the collision process, the droplets exchange mass momentum and energy and coalescence may also occur. The last leads to droplet growth and consequently, is a competitive mechanism of breakup.

The model adopted in this study follows that of O'Rourke [223] which is based on the proposals of Brazier-Smith *et al.* [53] for computing collision processes in rain clouds by the statistical discrete particle method. It distinguishes three types of collision outcome, shown schematically in Fig. 3.27. Here, they are listed in order of decreasing impact velocity:

1. **Separation**: A number of smaller droplets are produced.
2. **Permanent coalescence**: The two colliding droplets form a single droplet.
3. **Bouncing**: The two droplets involved in collision simply exchange momentum (not mass).

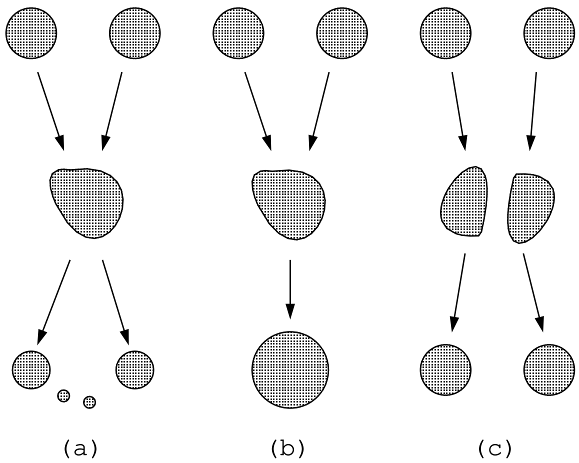

Figure 3.27: Types of collision: (a) Separation, (b) Permanent coalescence, (c) Bouncing.

In accordance with the assumption that all the droplets included in a parcel have common properties, they are not allowed to interact with other droplets in the same parcel.

A statistical approach is used to avoid increasing the total number of parcels*. Once the type of collision has been determined, all the droplets of the parcel with the

*More details are given by Kralj [171] who implemented the model in SPEED code.

bigger diameter, called collector, undergo collisions with the droplets of the other parcel. In some cases during coalescence, the droplets with the smaller diameter are all absorbed and the number of parcels is reduced by one.

3.8.2 Probability of collision

It is assumed that for each pair of parcels, collision may occur only if they lie in the same computational cell. This is a deficiency of the model, since collision between two neighbouring parcels located in different computational cells is *a priori* excluded*. This feature of the collision model is a source of mesh dependency in the spray simulation.

The droplets in parcels are considered to be uniformly distributed within the cell where the parcel resides. The collision frequency ν of the collector droplets (the droplets with the bigger diameter) with all droplets in another parcel is given by:

$$\nu = \frac{\pi}{4}\left(D_{d,1} + D_{d,2}\right)^2 \left|\mathbf{u}_{d,1} - \mathbf{u}_{d,2}\right| E_{12} \frac{N_{d,2}}{\delta V} \,, \tag{3.185}$$

where the subscripts 1 and 2 refer to the collector and the droplet, respectively and δV denotes the cell volume. This expression for the collision frequency is borrowed from the kinetic theory of gases where the collision efficiency, E_{12}, is introduced to allow for the effects of the differences between droplet and molecular collisions. This takes into account the fact that the droplets do not follow straight-line trajectories, since they interact with the surrounding gas. Langmuir [177] showed E_{12} is given by:

$$E_{12} = \begin{cases} \left[1 + 0.75 \dfrac{\ln(2K)}{K - 1.214}\right]^{-2} , & \text{for } K > 1.214 \,, \\ 0 \,, & \text{for } K \leq 1.214 \,, \end{cases} \tag{3.186}$$

*Collision between two parcels should be decided based on the distance between them (see e.g. Berlemont *et al.* [37]), however, this introduces computational overheads because it requires calculation of the distance for each parcel from all the other parcels, i.e. for N_p parcels, $(N_p - 1)!$ calculations are required. On the other hand, this treatment would be consistent only if the trajectory of each parcel is continuously followed so that, when it crosses the trajectory of another parcel at the same time, collision occurs. However, the parcel position is calculated every discrete time steps, δt, as will be explained in Chapter 4. Therefore, two parcels do not collide if their interdistance is large, despite, that at some time earlier, their locations were close each other. Thus, for simplicity, parcels are allowed to collide only if they reside at the same cell.

where K is the so-called dimensionless stopping distance, defined as:

$$K = \frac{\rho_{d,2}|\mathbf{u}_{d,1} - \mathbf{u}_{d,2}|D_{d,2}^2}{9\mu_m D_{d,1}} \, . \tag{3.187}$$

Langmuir [177] found that when $K << 1$, then $E_{12} \approx 0$ because the small droplet is carried around the larger one by the gas flow and consequently, collision does not occur. In the opposite extreme, when $K >> 1$ then $E_{12} \approx 1$.

The probability that the collector droplet undergoes n collisions with the droplets within a time interval δt, follows a Poisson distribution:

$$P_n = \frac{\bar{n}^n}{n!} e^{-\bar{n}} \, , \tag{3.188}$$

with mean value $\bar{n} = \nu \delta t$. The probability of no collisions, i.e. $n = 0$, is $P_0 = e^{-\bar{n}}$. A random number $Y_{r,1}$ in the interval [0, 1] is chosen to determine whether collision takes place between the droplets in considered parcels. If $Y_{r,1} < P_0$, collision does not occur.

3.8.3 Separation

The experiment of Brazier-Smith *et al.* [53] showed that when droplets of nearly equal size collide and the impact parameter exceeds some critical value, the droplets will break up (separation). Usually, two or three smaller satellite droplets are produced. In their theoretical study, they found that in order for separation to occur, the rotational energy must exceed the additional surface energy required to form the initial droplets from the coalescence drop-pair. This is expressed by:

$$E \geq E_{coal} \, , \tag{3.189}$$

where E and E_{coal} are the coalescence efficiency and its critical value, respectively, defined by:

$$E = \left(\frac{2X}{D_{d,1} + D_{d,2}}\right)^2 \, , \tag{3.190}$$

$$E_{coal} = \min\left[\frac{2.4 f(\gamma)}{We_d}, 1\right] \, , \tag{3.191}$$

where γ is the ratio of the collector diameter to the droplet diameter,

$$\gamma = \frac{D_{d,1}}{D_{d,2}} \tag{3.192}$$

and $f(\gamma)$ is the following function:

$$f(\gamma) = \gamma^3 - 2.4\gamma^2 + 2.7\gamma \; . \tag{3.193}$$

Also, in the above expressions, X is the distance between the centres of the droplets perpendicular to the relative velocity vector (see Fig. 3.28) and We_d is the droplet Weber number, given by:

$$We_d = \frac{\rho_{d,2}|\mathbf{u}_{d,1} - \mathbf{u}_{d,2}|^2 D_{d,2}}{2\sigma_{d,2}} \; . \tag{3.194}$$

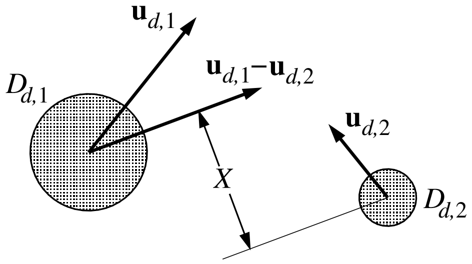

Figure 3.28: Droplet collision; subscript '1' indicates the collector and '2' the droplet.

A random number $Y_{r,2}$ in the interval [0, 1] is chosen to decide about the collision type. If $Y_{r,2} \geq E_{coal}$, separation occurs. This condition is equivalent to $X \geq X_c$, where X_c is the critical distance between the droplets for which separation is still possible. This is evaluated from Eqs. (3.189) and (3.190):

$$X_c = \frac{D_{d,1} + D_{d,2}}{2}\sqrt{E_{coal}} \; ; \tag{3.195}$$

and X is the randomly chosen distance given by:

$$X = \frac{D_{d,1} + D_{d,2}}{2}\sqrt{Y_{r,2}} \; . \tag{3.196}$$

O'Rourke [223] derived expressions for the droplet velocities after separation (denoted by the superscript 'n') from the conservation of linear and angular momentum and energy, under the assumption that the droplets retain their original size:

$$\begin{aligned}\mathbf{u}_{d,1}^n &= \frac{(m\mathbf{u})_{d,1} + (m\mathbf{u})_{d,2} + m_{d,2}\left(\mathbf{u}_{d,1} - \mathbf{u}_{d,2}\right) f_{\mathbf{u}}}{m_{d,1} + m_{d,2}} \ , \\ \mathbf{u}_{d,2}^n &= \frac{(m\mathbf{u})_{d,1} + (m\mathbf{u})_{d,2} - m_{d,2}\left(\mathbf{u}_{d,1} - \mathbf{u}_{d,2}\right) f_{\mathbf{u}}}{m_{d,1} + m_{d,2}} \ ,\end{aligned} \tag{3.197}$$

where

$$f_{\mathbf{u}} = \frac{\sqrt{Y_{r,2}} - \sqrt{E_{coal}}}{1 - \sqrt{E_{coal}}} \ . \tag{3.198}$$

3.8.4 Coalescence

If separation does not occur, the collision outcome is either permanent coalescence or bouncing. Coalescence occurs when the kinetic energy of the collided droplets is high enough to overcome the resistance of the air film trapped between them. This is expressed by:

$$Y_{r,2} < E_{boun} \ , \tag{3.199}$$

where E_{boun} is the bouncing efficiency defined by Jayaratne and Mason [147] as:

$$E_{boun} = \left[\frac{We_d}{2.4 f(\gamma)}\right]^{1/3} \ . \tag{3.200}$$

The number of droplets, M, which take part in coalescence with each collector droplet is evaluated from:

$$\sum_{i=0}^{M-1} P_i < Y_{r,2} < \sum_{i=0}^{M} P_i \ ; \tag{3.201}$$

and they are removed from their initial parcel until the complete depletion of the parcel. Then, M is recomputed so that all droplets participate in coalescence. The remaining number of droplets in the parcel 2, $N_{d,2}^n$, is obtained by:

$$N_{d,2}^n = N_{d,2} - M N_{d,1} \ . \tag{3.202}$$

All the other droplet properties do not change.

The new properties of the collector droplet are determined from mass, momentum and energy conservation. Thus,

$$m_{d,1}^n = m_{d,1} + M m_{d,2} \ , \tag{3.203}$$

$$(m\mathbf{u})_{d,1}^{n} = (m\mathbf{u})_{d,1} + M\,(m\mathbf{u})_{d,2} \ , \tag{3.204}$$

$$(mc_pT)_{d,1}^{n} = (mc_pT)_{d,1} + M\,(mc_pT)_{d,2} \ . \tag{3.205}$$

The number of droplets in the collector does not change and the droplet diameter after coalescence, is calculated based on the new mass.

3.8.5 Bouncing

If neither separation nor coalescence occurs, the collision result is bouncing (see flowchart in Fig. 3.29). Bouncing occurs at low droplet velocities and is accompanied by deformation of each of the approaching droplet pair, approximately into the shape of an oblate spheroid due to the air film trapped between them.

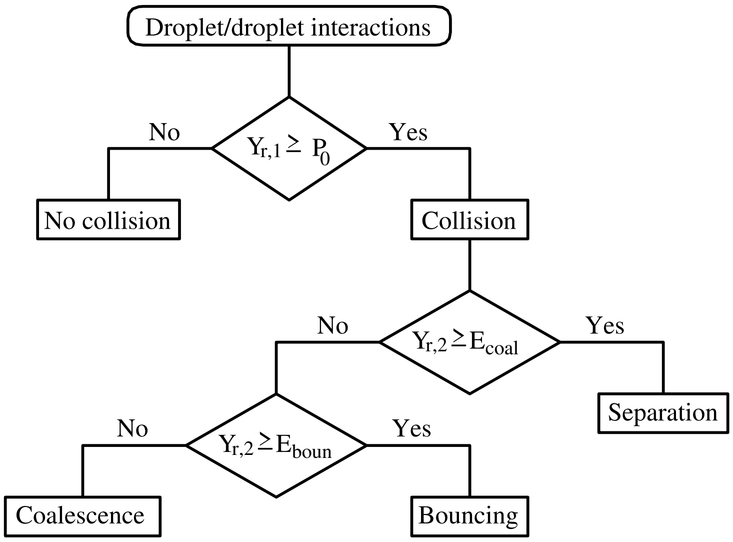

Figure 3.29: Droplet/droplet collisions.

The droplets involved in bouncing do not exchange mass and internal energy, but only momentum. The droplet velocities are determined as in separation by Eq. (3.197), however, the coefficient $f_{\mathbf{u}}$ is now given by:

$$f_{\mathbf{u}} = \frac{\sqrt{Y_{r,2}} - \sqrt{E_{boun}}}{1 - \sqrt{E_{boun}}} \ . \tag{3.206}$$

3.9 Impingement

3.9.1 Introduction

Another process taking place in Diesel engines, especially in small DI engines where the distance between the injector and the piston is short, is spray impingement on the walls. This interaction has been found to affect combustion since it controls the droplet size distribution and the vapour formation near the wall (see Senda [262], Bai and Gosman [30], Arcoumanis and Cutter [20], Stanton and Rutland [273], Guerrassi and Champoussin [115]). Although it creates some negative effects (e.g. incomplete evaporation leading to increase unburned hydrocarbons and soot formation [195]), some engine designs exploit this by deliberately impinging the fuel on the bowl wall (Naber [205]). For these and also due to the recent tendency for high injection pressures and consequently, unavoidable impingement, the study of impinging sprays and the consequent liquid film formation has become of major importance.

A number of experimental works (see e.g. Engel [88, 89], Hobbs and Alkezweeny [135], Hobbs and Osheroff [136], Levin [187], Levin and Hobbs [188], Stow and Stainer [275]) show that the outcome of impingement is correlated to the impact velocity, the droplet size, the liquid surface tension, the roughness and curvature of the target surface and the thickness of the liquid film accumulated on the wall. The effect of the wall temperature was recently studied by Arcoumanis and Chang [18] who found that with increasing wall temperature, the output droplets have higher velocity tangential to the wall and smaller diameter.

The modelling of the liquid jet impinging on a wall surface is usually based on the wall temperature and the liquid Weber number, whose values determine the type of the interaction, which might be one of the following (see Naber and Reitz [206], Bai and Gosman [30] and Stanton and Rutland [273]):

1. Sticking, in which the droplet sticks on the wall;

2. Rebounding, in which the droplet is reflected;

3. Spreading, in which the droplet breaks up and sticks on the wall forming a film;

4. Splashing, in which the droplet breaks up and all the newly formed droplets are reflected.

The sticking and spreading of droplets form a film of liquid on the wall. The liquid film influences the impingement of subsequent droplets, since it changes the wall characteristics. On the other hand, when a droplet impinges on the film it may cause liquid to be ejected. Recently, attempts have been made to model the film formation by deriving and solving mass, momentum and energy conservation equations for it (see Bai and Gosman [31], Ahmadi-Befrui *et al.* [6] and Bai [29]).

In this study, the film formation is not modelled, but a droplet/wall interaction model, developed at the Max-Planck Institut by Obermeier and Chaves [218] is adopted. The model, presented below, is based on droplet impingement experiments performed by Obermeier and his colleagues [212, 213, 215, 216] for various ambient pressures and temperatures, fuels, incidence angles, wall temperatures and wall roughnesses.

3.9.2 MPI model

The MPI model [58, 218, 312] takes into account multiple droplet impacts (i.e. droplet chains) but neglects the effects of wall roughness and curvature, possible liquid film formation and heat transfer between the droplet and the wall. It distinguishes between three different regimes, shown schematically in Fig. 3.30:

1. **Splashing**: The incident droplet breaks up into smaller droplets, which are reflected with characteristic velocity magnitude and direction.

2. **Fragmentation**: The droplet is fragmented into smaller droplets, which stick on the wall.

3. **Sticking**: The droplet does not break up but simply sticks on the wall.

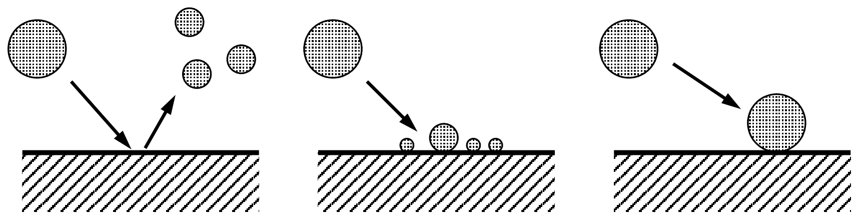

(a) (b) (c)

Figure 3.30: Schematic of various outcomes of droplet/wall interactions: (a) Splashing, (b) Fragmentation, (c) Sticking.

The relevant forces are the inertial, surface tension and viscous forces. The dimensionless criteria determining the onset of each regime, involving these forces, are the droplet incidence Weber number, We_d and the Ohnesorge number, Oh. The latter has already been defined by Eq. (3.171) while the former is given by:

$$We_d = \frac{\rho_d D_d u_{d,n}^2}{\sigma_d} \ , \tag{3.207}$$

where $u_{d,n}$ is the normal component of the droplet velocity relative to the wall (see Fig. 3.31).

Splashing

Splashing occurs when $We_d > We_{spl}$, where We_{spl} is evaluated from the empirical relation of Wachters and Westerling [296]:

$$We_{spl} = \begin{cases} 2.5 \cdot 10^3 \, (Oh)^{0.4} \ , & \text{for } T_W \leq T_{Leid} \ , \\ 7.9 \cdot 10^{10} \, (Oh)^{2.8} \ , & \text{for } T_W > T_{Leid} \ . \end{cases} \tag{3.208}$$

Here, T_W and T_{Leid} are the wall and Leidenfrost temperature*, respectively.

When splashing occurs, the impinging droplet breaks up into two parts. One part remains on the wall whereas the other is reflected as a *cloud* of droplets (splashed

*The Leidenfrost temperature is the temperature for which the droplet levitates above a cushion of its own vapour and is not in direct contact with the wall.

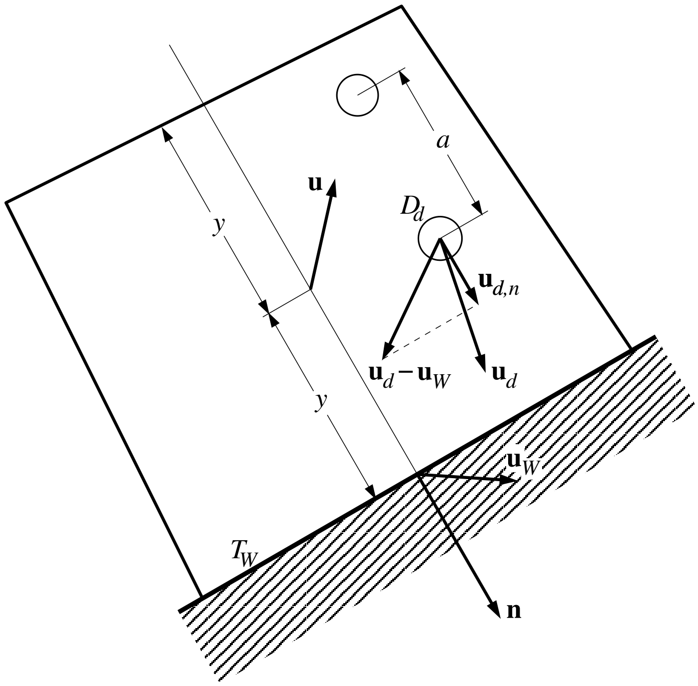

Figure 3.31: Droplet/wall interaction.

droplets). The total volume of the splashed droplets, V_s, is given by:

$$\frac{V_s}{V_d} = \begin{cases} 0\,, & \text{for } Ch < 2000\,, \\ 5.3\cdot 10^{-4} Ch - 1.06\,, & \text{for } 2000 \leq Ch \leq 3500\,, \\ 0.8\,, & \text{for } Ch > 3500\,, \end{cases} \tag{3.209}$$

where V_d is the volume of impinging droplet and Ch is a dimensionless characteristic number defined as:

$$Ch = \frac{We_d^{2/3} Re_d^{1/3}}{St_d}\,. \tag{3.210}$$

Here, Re_d and St_d are the droplet Reynolds and Strouhal numbers defined by:

$$Re_d = \frac{\rho_d u_{d,n} D_d}{\mu_d}\,, \tag{3.211}$$

$$St_d = f\frac{D_d}{u_{d,n}} = \frac{D_d}{a}\,, \tag{3.212}$$

where f is the frequency of impingement and a is the average distance, normal to the wall, between impinging droplets (see Fig. 3.31). This distance is calculated assuming that the droplets in the impinging parcel are uniformly distributed in the cell adjacent to the wall where they reside, i.e.

$$a = 2yN_d^{-1/3}\,. \tag{3.213}$$

In the above expression, y is the normal distance of cell centre from the wall (see Fig. 3.31) and N_d the number of droplets in the parcel.

The diameter of the splashed droplets, D_s and their number, N_s, are calculated from an empirical correlation and mass conservation, thus,

$$D_s = 0.12 D_d \ , \tag{3.214}$$

$$N_s = \frac{6V_s}{\pi D_s^3} \ . \tag{3.215}$$

The remaining mass, $\rho_d(V_d - V_s)$, remains on the wall. This mass is expected to form a film: however, this process is not modelled so the remaining liquid mass is assumed to form a spherical droplet with diameter D_d^n calculated from mass conservation:

$$D_d^n = \left[\frac{6}{\pi}\left(V_d - V_s\right)\right]^{1/3} \ . \tag{3.216}$$

The tangential velocity of the splashed droplets is assumed to be equal to that of the impinging droplet. The magnitude of the other component is assumed to be equal to $u_{d,n}$ and its direction is taken randomly within the wall and a cone determined by the angle α_s, i.e. $\alpha = Y_r \alpha_s$ (see Fig. 3.32) where Y_r is a random number in the range [0, 1]. Here, α_s is the maximum reflection angle given by the empirical correlation:

$$\alpha_s = \begin{cases} \dfrac{Ch - 2000}{1500} 60^\circ \ , & \text{for } 2000 \leq Ch \leq 3500 \ , \\ \\ 60^\circ \ , & \text{for } Ch > 3500 \ . \end{cases} \tag{3.217}$$

All splashed droplets from the considered parcel are divided into two computational parcels, each containing half* the total number of splashed droplets, N_s. Their diameters, D_s, are taken to be equal while their velocities are expressed by:

$$\mathbf{u}_{s,1} = \mathbf{u}'_{s,1} + \mathbf{u}_W = u_{d,t}\mathbf{t}_1 + u_{d,n}\mathbf{t}_2 + \mathbf{u}_W \ , \tag{3.218a}$$

$$\mathbf{u}_{s,2} = \mathbf{u}'_{s,2} + \mathbf{u}_W = u_{d,t}\mathbf{t}_1 + u_{d,n}\mathbf{t}'_2 + \mathbf{u}_W \ , \tag{3.218b}$$

where $\mathbf{t}_1$, $\mathbf{t}_2$ and $\mathbf{t}'_2$ are unit vectors, defined in Fig. 3.32.

*The splashed droplets are ejected from the wall forming an irregular cone cloud. Here, this cone is simulated with only two directions to limit the number of newly-formed parcels because of the demands on computer time and memory.

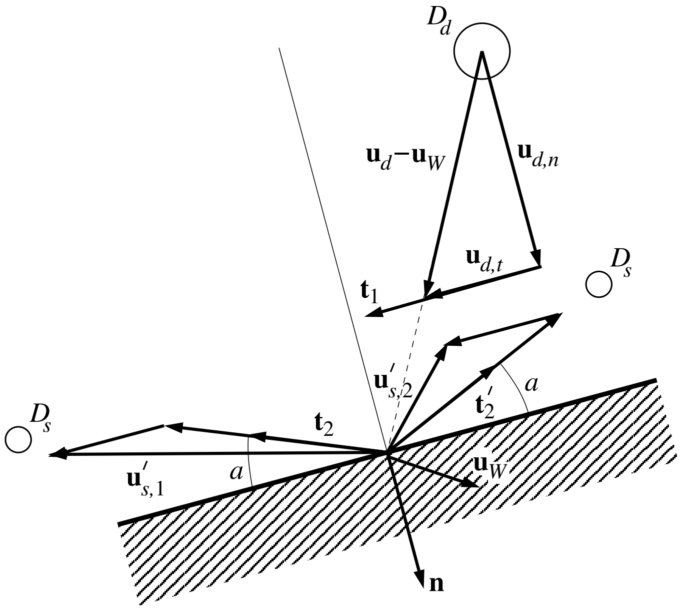

Figure 3.32: Droplet splashing.

Fragmentation

Fragmentation occurs when the droplet Weber number and the wall temperature satisfy the following conditions:

$$\begin{aligned} 80 < We_d < We_{spl} \;, \\ T_W > T_{Leid} \;. \end{aligned} \tag{3.219}$$

The wall temperature in Diesel engines is usually lower than the Leidenfrost temperature and consequently, fragmentation does not happen. Here it is modelled for the sake of completeness. The diameter of fragmented droplets, D_{frg}, is assumed to be:

$$D_{frg} = \frac{D_d}{3} \; . \tag{3.220}$$

All the droplets formed by fragmentation adhere to the wall and evaporate there.

Sticking

If neither splashing nor fragmentation occurs, the droplet sticks to the wall. The sticking droplets are assumed to keep their spherical shape and are not allowed to exchange heat with the wall. However, they evaporate, exchanging mass and energy with the surrounding gas in the same manner as an ordinary droplet.

3.10 Initial conditions

This section describes the spray initial conditions required to calculate all the spray processes described in the previous sections.

Assuming that the type of fuel and its temperature have been defined, the injection flow rate history is necessary to be able to define the instantaneous fuel flow rate.

The total fuel mass injected in the time interval $(t,\, t+\Delta t)$ is distributed over a prespecified number of parcels, N_p. Thus, the mass of each parcel is given by:

$$m_p = \frac{1}{N_p}\rho_d \frac{\dot{Q}(t) + \dot{Q}(t+\Delta t)}{2}\Delta t \;, \tag{3.221}$$

where $\dot{Q}$ is the volumetric flow rate. The accuracy of spray predictions is affected by N_p, thus, a large value should ideally be used for the best representation of the spray. However, the computational overhead is directly proportional to N_p. Tabrizi [280] and Kralj [171] suggested that the optimum value is $1\,\mathrm{parcel}/\mu s$.

The number of droplets, N_d, that each parcel contains is calculated from mass conservation, thus,

$$N_d = \frac{m_p}{\rho_d}\frac{6}{\pi D_d^3} \;, \tag{3.222}$$

where the initial droplet diameter, D_d, is assumed to be equal to the nozzle diameter.

The initial droplet location corresponds to the location of the nozzle exit and its velocity is determined from the injection flow rate as follows:

$$u_d(t) = \frac{\dot{Q}(t) + \dot{Q}(t+\Delta t)}{2}\frac{4}{\pi D_d^2}\frac{1}{C_{ch}} \;. \tag{3.223}$$

Here, the nozzle exit area contraction ratio, C_{ch}, is calculated from the nozzle cavitation model described in Section 3.2, for which the nozzle wall roughness, k_r and the entrance area contraction ratio, C_c, must be given. The direction of the droplet velocity is randomly sampled within the spray cone angle, which must be supplied if the MPI atomisation model, described in §3.3.3, is employed, or internally calculated by the Huh atomisation model, described in §3.3.2, when this is used. In the latter model, the discharge coefficient, c_d, is required.

3.11 Closure

A complete model of the spray has been presented in this chapter. For this purpose the stochastic discrete droplet method has been used in which a computational parcel comprises a number of droplets of the same properties.

The mathematical description of the spray commences from the nozzle whose effective exit area may be smaller than the geometrical one due to cavitation. The MPI cavitation model, described in Section 3.2, simulates this phenomenon.

As soon as the liquid jet leaves the nozzle it atomises into individual droplets. For this purpose, two atomisation models have been described in Section 3.3. The Huh model attributes atomisation to the turbulence developed in the nozzle hole, while the MPI model assumes that the cavitation is responsible for the jet atomisation.

The droplet trajectory is computed in a Lagrangian manner, as described in Section 3.4. The effect of turbulence is also taken into account by a stochastic treatment.

Ordinary differential equations describe the mass, momentum and energy of the computational parcel and express the interaction with the ambient gas. Droplet deformation due to aerodynamic forces is taken into account for the evaluation of the drag coefficient in the momentum equation, as explained in Section 3.5. The mass and energy equations presented in Section 3.6 allow for multicomponent fuel and for both infinite and finite conductivity. An inexpensive, in respect of computer requirements, profile method has been developed and applied to the conduction and diffusion equations.

As described in Section 3.7, the aerodynamic forces lead the droplet not only to deform but also to break up. The latter phenomenon was described by three different models, namely Reitz-Diwakar, Pilch-Erdman and Hsiang-Faeth. All the models calculate the rate of breakup based on correlations for the stable diameter.

In addition, during its life, a droplet may collide with other droplets or hit the wall. The former phenomenon is simulated by the model of O'Rourke, presented in Section 3.8, which distinguishes three possible outcomes of collision, namely separation, permanent coalescence and bouncing. The spray impingement is modelled according to the recommendations of Max-Planck Institut. This model has been presented in Section 3.9 and it allows for splashing, fragmentation and sticking.

Finally, the initial conditions of the spray and the variables that must be known in advance for the spray calculation have been listed in Section 3.10.

With this chapter the mathematical description of the two phases has been completed. The next chapter will deal with the integration and discretisation of the differential gas and spray equations.

Chapter 4

Discretisation

4.1 Introduction

In the previous chapters, the mathematical models of both gaseous and liquid phases have been presented. In Chapter 2 the conservation equations of mass, fuel vapour mass fraction, momentum and energy were described along with the turbulence equations and constitutive relations to set a closed problem. The spray modelling was presented in Chapter 3 describing the mass, momentum and energy conservation of a droplet. Submodels were explained for simulating the physical processes of the liquid such as cavitation in the nozzle, atomisation, breakup and droplet interaction with neighbouring droplets or walls. All these mathematical expressions together with the boundary and initial conditions as well as the source terms allowing for the interphase coupling form a well-posed problem, for which the solution is unique and non-trivial. However, this non-linear system of differential equations cannot be solved analytically and therefore, a numerical procedure must be employed.

The continuous function of the dependent variable ϕ in a differential equation can be approximated by a discrete function consisting of the numerical values of this variable at a finite number of points, called *nodes*, in the solution domain. Algebraic relations between the values of ϕ at the nodes are extracted based on the differential equation. This procedure is called *discretisation* and it is the aim of this chapter to discretise and transform the differential equations of the gas and liquid into a set of simultaneous algebraic equations whose solution approximates the exact solution to a required order of accuracy.

Various suitable discretisation methods have been proposed which can be grouped into three main categories, namely the finite difference (FDM) (Smith [267]), finite element (FEM) (Gallagher *et al.* [99] and Zienkiewicz and Taylor [316]) and finite volume (FVM) (Patankar [228], Hirsch [134]). The efficiency and the accuracy of discretisation methods strongly depend on the spatial and temporal resolution of the computational domain. Therefore, mesh generation techniques are of main importance. However, they will not be dealt in this study and for information on these, the reader is referred to the works of Thompson [289], Theodoropoulos [288] and Sarantinos [257].

In this chapter, the discretisation of the differential equations is outlined. The FVM adopted in this study is presented in Section 4.2. The discretisation of the general transport equation is explained in Section 4.3 and the discretised governing equations of the gas are obtained in Section 4.4. The differential equations of the spray are of ordinary type and therefore, their discretisation is much simpler. Their discretisation, which combines analytical and numerical methods, is presented in Section 4.5. Finally, the treatment of the boundary conditions is presented in Section 4.6 followed by the closure of this chapter in Section 4.7.

4.2 Basis of the finite volume method

The finite volume method was established in the field of computational fluid dynamics by the works of Gosman *et al.* [113] and McDonald [196] among others, because of some important advantages it offers over the other alternatives (see Kralj [171]). The most important feature which is of particular interest in fluid flow problems is the natural enforcement of the conservation law in volumes of arbitrary shape and size within the computational domain [295].

The computational domain is defined by the space and time coordinates. The space domain is divided into a finite number of contiguous non-overlapping control volumes or cells. In this study, an unstructured mesh, whose points cannot be identified with coordinate lines (see Hirsch [134]), is formed by a number of hexahedral cells. The collocated arrangement is adopted according to which the representative values of all the variables are located in the cell centres. This reduces the storage requirements and simplifies the computer programming (Perić [231]). Also, Cartesian coordinates are used and each cell face can only be shared by the two neighbouring cells*. The cell faces can move in time to follow the moving boundaries of the domain.

The time domain is divided into a finite number of time intervals, named time steps, which must be small enough to assure the required temporal resolution.

The governing transport equation is integrated over each control volume in the space domain and over a finite increment of time, Δt. The individual differential terms are replaced by algebraic approximations by using presumed spatial and temporal interpolation functions which evaluate the facial value of the dependent variables in the discretised computational domain. By applying the discretised transport equation to each control volume, a set of simultaneous algebraic equations is generated. The number of unknowns, which are the values of the dependent variables in the cells, is equal to the number of the algebraic equations so that a closed problem is obtained. Obviously, the accuracy of the numerical solution is affected by the fineness of the mesh and temporal resolution.

Three main temporal approximation schemes, namely *explicit*, *implicit* and their combination, *semi-implicit* have been distinguished by Patankar [228]. Implicit differencing is adopted in this study although the resulting coefficient matrix is not diagonal and its inversion requires more complex algorithms compared to that of the explicit differencing. However, this disadvantage is compensated for by an absence

*An interpolation scheme can be applied to the fluxes between the cells at that face to overcome this restriction (see e.g. [69]).

of stability and convergence limitations on the time step, whereas the explicit differencing requires a small enough time step to satisfy the Courant-Friedrichs-Lewy condition (see Courant *et al.* [71] and Hirsch [134]) to ensure stability. On the other hand, semi-implicit differencing does not guarantee solutions which are physically plausible or without oscillations (see Patankar and Baliga [229]). More information about temporal schemes can be found in the works of Patankar [228], Begleris [35] and Hirsch [134].

Further information on different aspects of the finite volume method can be found in Patankar [228], Hirsch [134] and Versteeg and Malalasekera [295]. The particular practices employed in the present study were described in detail in Theodoropoulos [288], Kralj [171] and Leskovšek [186], whose notation will mainly be followed in this chapter.

4.2.1 Notation

A typical cell arrangement and notation is shown in Fig. 4.1. The letter P denotes the considered cell with faces denoted by $\mathcal{S}_f^P$, where f takes any of the values $\{\pm 1, \pm 2, \pm 3\}$ indicating the face of the cell in the considered direction. The indices f and $-f$ indicate two opposite faces of the cell P. The neighbouring cell of P in the direction f is denoted by $N(f)$ and NN represents neighbours of N other than P.

Each cell is defined by its eight vertices whose locations are given by the position vectors $\mathbf{r}_i$, $(i = 1, 2, ..., 8)$ in the global Cartesian coordinate system. The cell centre, $\mathbf{r}_P$ and the centre of the face f, $\mathbf{r}_f$, are defined as the arithmetic means of the position vectors of all cell vertices and all vertices which belong to the considered face f, respectively:

$$\mathbf{r}_P = \frac{1}{8} \sum_{\{i\}_P} \mathbf{r}_i \; , \tag{4.1a}$$

$$\mathbf{r}_f = \frac{1}{4} \sum_{\{i\}_f} \mathbf{r}_i \; . \tag{4.1b}$$

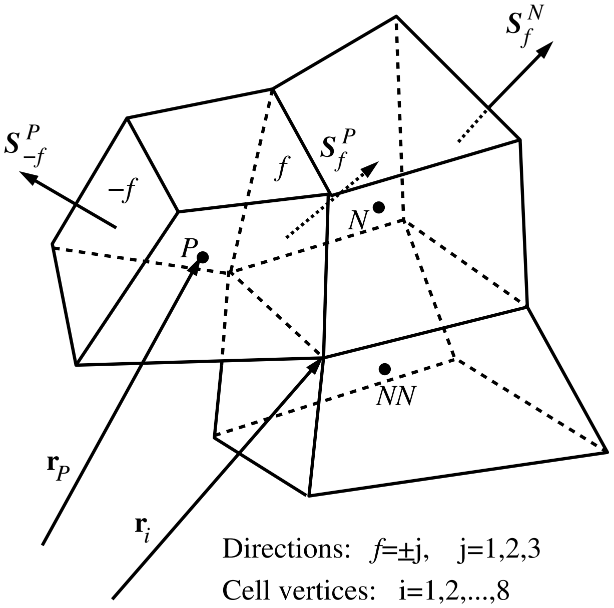

Figure 4.1: Cell notation.

The face vector $\mathcal{S}_f^P$ is calculated via the vector product of the two face diagonals and it points outwards. The cell volume V_P is calculated from the volumes of the six pyramids whose bases are the cell faces and apexes are the cell centre P:

$$V_P = \frac{1}{3} \sum_{\{f\}_P} \mathcal{S}_f^P \cdot (\mathbf{r}_f - \mathbf{r}_P) \ , \tag{4.2}$$

where $\sum_{\{f\}_P}$ denotes summation over all six directions in the cell P.

The values of the dependent variables, ϕ and other gas properties such as viscosity, at the cell faces are estimated from the following spatial interpolation scheme:

$$\phi_f = \lambda_f^P \phi_P + \left(1 - \lambda_f^P\right) \phi_N \ , \tag{4.3}$$

where λ_f^P represents the interpolation factor of the cell P in the direction f, defined in Fig. 4.2 and ϕ_P and ϕ_N denote the values of ϕ at the cells P and N, respectively.

In the governing equations, the nabla operator, ∇, appears frequently. This can be expressed in terms of the face value by applying the Gauss' divergence theorem which for a vector field $\mathbf{u}$ reads:

$$\int_V \nabla \cdot \mathbf{u} \, dV = \int_S d\mathcal{S} \cdot \mathbf{u} \ , \tag{4.4a}$$

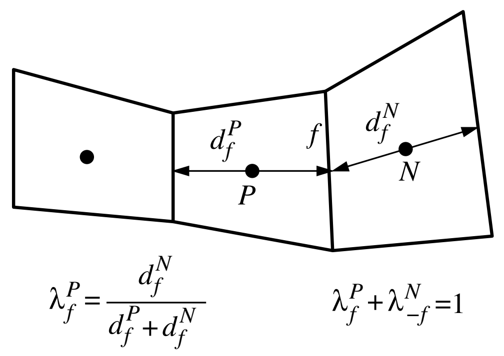

Figure 4.2: Definition of the interpolation factors.

where S indicates the surface of the volume V. Hence,

$$\nabla \cdot \mathbf{u} \approx \frac{1}{V} \sum_{\{f\}} \mathcal{S}_f \cdot \mathbf{u}_f \ . \tag{4.4b}$$

Considering the above theorem as well as the expression for the face value, Eq. (4.3), the finite-volume counterparts of the gradient of an arbitrary scalar field ϕ, the divergence and gradient of a vector field $\mathbf{u}$ and the divergence of a tensor field $\mathbf{T}$, are respectively given by the following formulae:

$$\begin{aligned}(\nabla\phi)_P &\approx (\mathcal{N}\phi)_P \\ &= \frac{1}{V_P} \sum_{\{f\}_P} \mathcal{S}_f^P \left[\lambda_f^P \phi_P + \left(1 - \lambda_f^P\right) \phi_N\right] \ ;\end{aligned} \tag{4.5a}$$

$$\begin{aligned}(\nabla\cdot\mathbf{u})_P &\approx (\mathcal{N}\cdot\mathbf{u})_P \\ &= \frac{1}{V_P} \sum_{\{f\}_P} \mathcal{S}_f^P \cdot \left[\lambda_f^P \mathbf{u}_P + \left(1 - \lambda_f^P\right) \mathbf{u}_N\right] \ ;\end{aligned} \tag{4.5b}$$

$$\begin{aligned}(\nabla\mathbf{u})_P &\approx (\mathcal{N}\mathbf{u})_P \\ &= \frac{1}{V_P} \sum_{\{f\}_P} \mathcal{S}_f^P \left[\lambda_f^P \mathbf{u}_P + \left(1 - \lambda_f^P\right) \mathbf{u}_N\right] \ ;\end{aligned} \tag{4.5c}$$

$$\begin{aligned}(\nabla\cdot\mathbf{T})_P &\approx (\mathcal{N}\cdot\mathbf{T})_P \\ &= \frac{1}{V_P} \sum_{\{f\}_P} \mathcal{S}_f^P \cdot \left[\lambda_f^P \mathbf{T}_P + \left(1 - \lambda_f^P\right) \mathbf{T}_N\right] \ .\end{aligned} \tag{4.5d}$$

4.3 General transport equation discretisation

The general transport equation, Eq. (2.77), when integrated over a control volume V reads:

$$\int_V \frac{\partial \rho\phi}{\partial t}\, dV + \int_V \nabla\cdot\rho\mathbf{u}\phi\, dV - \int_V \nabla\cdot\rho\Gamma_{\phi,\mathit{eff}}\nabla\phi\, dV = \int_V \left(S_\phi + S_\phi^d\right)\, dV\ . \tag{4.6}$$

Applying Gauss' divergence theorem, Eq. (4.4a), this becomes:

$$\int_V \frac{\partial \rho\phi}{\partial t}\, dV + \int_S d\mathcal{S}\cdot\rho\mathbf{u}\phi - \int_S d\mathcal{S}\cdot\rho\Gamma_{\phi,\mathit{eff}}\nabla\phi = \int_V \left(S_\phi + S_\phi^d\right)\, dV\ . \tag{4.7}$$

In domains with moving boundaries and therefore moving coordinates, the control volume must obey the *space conservation law* (Warsi [299], Demirdžić and Perić [80]), which reads:

$$\frac{d}{dt}\int_V \rho\phi\, dV = \int_V \frac{\partial \rho\phi}{\partial t}\, dV + \int_S d\mathcal{S}\cdot\rho\mathbf{u}_b\phi\ , \tag{4.8}$$

where $\mathbf{u}_b$ is the velocity of the boundary of the control volume. Gauss' theorem, Eq. (4.4a), has been applied to the second term on the RHS of the above equation. Substituting this formula in Eq. (4.7), the following form of the transport conservation law in the Eulerian/Lagrangian frame of reference is obtained:

$$\frac{d}{dt}\int_V \rho\phi\, dV + \int_S d\mathcal{S}\cdot\left(\rho\mathbf{u}_r\phi - \rho\Gamma_{\phi,\mathit{eff}}\nabla\phi\right) = \int_V \left(S_\phi + S_\phi^d\right)\, dV\ . \tag{4.9}$$

Here, $\mathbf{u}_r$ denotes the relative velocity of the gas velocity, $\mathbf{u}$, with respect to the velocity of the reference frame, $\mathbf{u}_b$, i.e.

$$\mathbf{u}_r = \mathbf{u} - \mathbf{u}_b\ . \tag{4.10}$$

Each term of the general transport equation will individually be considered in the following subsections.

4.3.1 The unsteady term

In order to discretise this term, it is assumed that (Kralj [171]):

$$\int_{V_P} \rho\phi\, dV \approx (\rho\phi V)_P \approx (\rho V)_P\, \phi_P\ ; \tag{4.11}$$

and the local rate of change of ϕ can be approximated by an average change during the finite time step Δt. Thus, the discretised unsteady term reads:

$$\frac{d}{dt}\int_{V_P}\rho\phi\, dV \approx \frac{(\rho V)_P\,\phi_P - (\rho V)_P^o\,\phi_P^o}{\Delta t}\ , \tag{4.12}$$

where superscript 'o' denotes the 'old' time values.

4.3.2 The convection/diffusion term

The second term on the LHS of Eq. (4.9) represents the total flux of ϕ through the entire cell surface S_P which is equal to the sum of the fluxes over all faces of the cell P:

$$\int_{S_P} d\mathcal{S}\cdot(\rho\mathbf{u}_r\phi - \rho\Gamma_{\phi,\mathit{eff}}\nabla\phi) = \sum_{\{f\}_P}\int_{S_f} d\mathcal{S}\cdot(\rho\mathbf{u}_r\phi - \rho\Gamma_{\phi,\mathit{eff}}\nabla\phi) = \sum_{\{f\}_P} F_f\ . \tag{4.13}$$

Assuming that the total flux of ϕ through a face, F_f, can be approximated by the average flux through the face and some representative average values of ϕ and $\nabla\phi$, the following expression is obtained (Kralj [171]):

$$F_f \approx \mathcal{S}_f\cdot\left[(\rho\mathbf{u}_r\phi)_f - (\rho\Gamma_{\phi,\mathit{eff}}\nabla\phi)_f\right]\ . \tag{4.14}$$

The convective flux of ϕ can be recast into:

$$\begin{aligned}\mathcal{S}_f\cdot(\rho\mathbf{u}_r\phi)_f &\approx \mathcal{S}_f\cdot(\rho\mathbf{u}_r)_f\,\phi_f\\ &\approx \mathcal{C}_f\left[w_f\phi_P + (1-w_f)\,\phi_N\right]\ ,\end{aligned} \tag{4.15}$$

where $\mathcal{C}_f$ is the mass flux, defined as:

$$\mathcal{C}_f = \mathcal{S}_f\cdot(\rho\mathbf{u}_r)_f \tag{4.16}$$

and w_f is a weighting factor whose definition will be given in §4.3.4.

The diffusion flux vector $(\rho\Gamma_{\phi,\mathit{eff}}\nabla\phi)_f$ is resolved into the *normal diffusion*, $\mathbf{d}_f^n(\phi)$ and *cross diffusion*, $\mathbf{d}_f^c(\phi)$, components (Theodoropoulos [288]):

$$(\rho\Gamma_{\phi,\mathit{eff}}\nabla\phi)_f = \mathbf{d}_f^n(\phi) + \mathbf{d}_f^c(\phi)\ . \tag{4.17}$$

In the normal diffusion component only the contributions to the diffusive flux across the faces $+f$ and $-f$ are considered. Hence,

$$\mathbf{d}_f^n(\phi) \approx \overline{\mathcal{S}_f}^P \left(\phi_N - \phi_P\right) \ , \tag{4.18a}$$

where

$$\overline{\mathcal{S}_f}^P = \lambda_f^P \left(1 - \lambda_f^P\right) \left[\left(\mathcal{S}_f^P - \mathcal{S}_{-f}^P\right) \left(\frac{\rho\Gamma_{\phi,\mathit{eff}}}{V}\right)_P + \left(\mathcal{S}_f^P + \mathcal{S}_f^N\right) \left(\frac{\rho\Gamma_{\phi,\mathit{eff}}}{V}\right)_N\right] \ . \tag{4.18b}$$

The above equation* involves only the ϕ values at P and its nearest neighbour N, which allows a fully implicit treatment of the normal diffusion term without an increase of the size of the *computational molecule*†. In the cross diffusion term the neighbours NN of the neighbour N are present, leading to the enlargement of the computational molecule. This contribution is treated explicitly, using the currently-available values via the following formula:

$$\begin{aligned}\mathbf{d}_f^c(\phi) \approx\ & \lambda_f^P \left(\frac{\rho\Gamma_{\phi,\mathit{eff}}}{V}\right)_P \sum_{\{l \neq \pm f\}_P} \mathcal{S}_l \left[\lambda_l \phi_P + \left(1 - \lambda_l\right) \phi_N\right] \\ & + \left(1 - \lambda_f^P\right) \left(\frac{\rho\Gamma_{\phi,\mathit{eff}}}{V}\right)_N \sum_{\{l \neq \pm f\}_N} \mathcal{S}_l \left[\lambda_l \phi_N + \left(1 - \lambda_l\right) \phi_{NN}\right] \ .\end{aligned} \tag{4.19}$$

The combination of Eqs. (4.14) to (4.19) allows a compact expression of the total flux through the face f as:

$$\begin{aligned}F_f \approx\ & \left(\mathcal{C}_f w_f + \mathcal{D}_f^{\phi,n}\right) \phi_P \\ & - \left[\mathcal{C}_f \left(w_f - 1\right) + \mathcal{D}_f^{\phi,n}\right] \phi_N \\ & - \mathcal{D}_f^{\phi,c} \ ,\end{aligned} \tag{4.20a}$$

where

$$\mathcal{D}_f^{\phi,n} = \mathcal{S}_f \cdot \overline{\mathcal{S}_f}^P \ , \tag{4.20b}$$

$$\mathcal{D}_f^{\phi,c} = \mathcal{S}_f \cdot \mathbf{d}_f^c(\phi) \ . \tag{4.20c}$$

*See Appendix C.1 for derivation.

†A computational molecule is composed of all the nodes participating in evaluation of the terms in Eq. (4.9).

4.3.3 The source term

The source term in Eq. (4.9), S_ϕ, is in general a non-linear function of ϕ. However, its linearisation is beneficial for the diagonal dominance of the resulting matrix and for the numerical stability (see Patankar [228], Theodoropoulos [288]). Therefore, it is split into the explicit, $S_{\mathcal{U}}^{\phi}$ and implicit, $S_{\mathcal{P}}^{\phi}\phi_P$, counterparts, as follows:

$$\int_{V_P} S_\phi \, dV \approx \left(S_{\mathcal{U}}^{\phi}\right)_P + \left(S_{\mathcal{P}}^{\phi}\right)_P \phi_P \, . \tag{4.21}$$

The same approach is adopted for the source expressing the spray contribution to the gas phase:

$$\int_{V_P} S_\phi^d \, dV \approx \left(S_{\mathcal{U}}^{\phi,d}\right)_P + \left(S_{\mathcal{P}}^{\phi,d}\right)_P \phi_P \, . \tag{4.22}$$

The coefficient $S_{\mathcal{P}}^{\phi}$ must be non-positive to ensure the numerical stability and the physical plausibility of results. It should be noted that $S_{\mathcal{P}}$ is always a scalar, whereas, $S_{\mathcal{U}}$ must be a tensor of the same order as ϕ.

4.3.4 Convective flux differencing scheme

Patankar [228] pointed out the importance of a suitable interpolation practice, or *differencing scheme*, for the convective fluxes for the successful application of the FVM to fluid flow problems. The main properties that a differencing scheme must preserve are physical plausibility of results, consistency between the discretised and differential equations and numerical stability (Begleris [35]).

Numerous different schemes can be found in the literature (see Patankar [228], Collins [68]). Following the author's predecessors (Kralj [171] and Leskovšek [186]), in the present study the self-filtered central differencing scheme (SFCD) of Ziman [317] is adopted. Details of the scheme are given below.

Self-filtered central differencing scheme

SFCD is a conservative, second-order-accurate discretisation scheme which switches, depending on the local distribution of ϕ, between central differencing (CD), upwind differencing (UD) and a non-linear blend of UD and linear upwind differencing (LUD). This switching between various differencing schemes reduces the numerical diffusion and prevents unphysical oscillations. A brief description of the scheme is given below.

The evaluation of ϕ at a face f, ϕ_f, depends, as illustrated in Fig. 4.3, on the ϕ gradients and the sign of the convective flux:

If $\mathcal{C}_f \geq 0$:

$$\phi_f = \phi_P + \beta_f \left(1 - \lambda_f^P\right) \left(\phi_P - \phi_{N(-f)}\right) \ , \tag{4.23a}$$

$$\beta_f = \max \left[0, \ \min \left(\frac{\phi_N - \phi_P}{\phi_P - \phi_{N(-f)}}, \ \beta_{max}\right)\right] \ ; \tag{4.23b}$$

If $\mathcal{C}_f < 0$:

$$\phi_f = \phi_N + \beta_f \lambda_f^P \left(\phi_N - \phi_{NN(f)}\right) \ , \tag{4.23c}$$

$$\beta_f = \max \left[0, \ \min \left(\frac{\phi_N - \phi_P}{\phi_{NN(f)} - \phi_N}, \ \beta_{max}\right)\right] \ . \tag{4.23d}$$

Thus, when $0 < \beta_f < \beta_{max}$, corresponding to cases (b) and (c) in Fig. 4.3, the above expressions for all $\mathcal{C}_f$ yield the CD scheme:

$$\phi_f = \lambda_f^P \phi_P + \left(1 - \lambda_f^P\right) \phi_N \ . \tag{4.24}$$

When the normalised gradient of ϕ, i.e. the ratio of the differences of ϕ in Eqs. (4.23b) and (4.23d), exceeds the parameter β_{max}, the scheme reduces to a non-linear blend of UD and LUD in order to prevent unphysical oscillations in the solutions. Thus,

$$\phi_f = \begin{cases} \phi_P + \beta_{max} \left(1 - \lambda_f^P\right) \left(\phi_P - \phi_{N(-f)}\right) \ , & \text{for } \mathcal{C}_f \geq 0 \ , \\ \phi_N + \beta_{max} \lambda_f^P \left(\phi_N - \phi_{NN(f)}\right) \ , & \text{for } \mathcal{C}_f < 0 \ . \end{cases} \tag{4.25}$$

Hence, β_{max} plays a role of an upper limit of acceptable gradients, as well as being a weight of the LUD scheme.

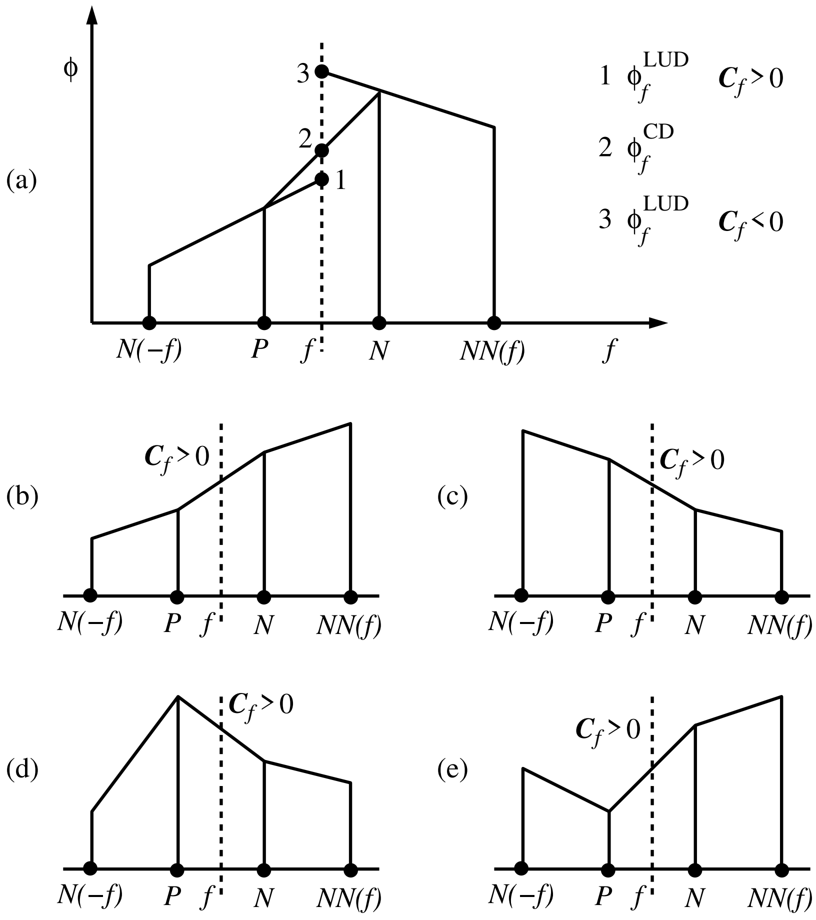

Figure 4.3: SFCD scheme.

In the third case, when local extrema occur as in cases (d) and (e) in Fig. 4.3, $\beta_f = 0$ and therefore, the UD scheme is retrieved:

$$\phi_f = \begin{cases} \phi_P\,, & \text{for } \mathcal{C}_f \geq 0\,, \\ \phi_N\,, & \text{for } \mathcal{C}_f < 0\,. \end{cases} \tag{4.26}$$

Depending on the local ϕ distribution, mesh spacing and β_{max}, one of the above mentioned modes will be employed. For a given flow field and mesh, β_{max} has the following meanings: if $\beta_{max} = 0$, the SFCD scheme reduces to UD. If $\beta_{max} \to \infty$, it is equivalent to CD. If $\beta_{max} = 1$, SFCD behaves as a blend of UD and LUD; only when $\beta_f = 1$ does SFCD yield the LUD scheme. Based on the experience of the author's predecessors, $\beta_{max} = 5$ is found to offer the advantage of extensive use of CD in most parts of the computational domain without inducing convergence problems or oscillations in solutions. Consequently, it is adopted in this study.

Implementation of SFCD

In the general case, the SFCD uses the values of ϕ at the next-nearest neighbours NN and therefore, an implicit treatment would expand the computational molecule. In order to avoid this, a partially-explicit method is implemented according to which, the upwind part of the convective flux, ϕ_P for $\mathcal{C}_f \geq 0$ and ϕ_N for $\mathcal{C}_f < 0$, is treated implicitly, while the remaining contributions are evaluated from the currently available values of ϕ and added to the source term in the explicit fashion (Kralj [171] and Leskovšek [186]). The evaluation of convective flux is obtained as follows (Kralj [171]):

1. Evaluation of the flux term F_f, given by Eq. (4.20a), according to the UD scheme, i.e. with the following factor:

$$w_f = 1 + \min\left[0, \, \mathrm{sign}(\mathcal{C}_f)\right] \ . \tag{4.27}$$

2. Calculation of the explicit part according to:

$$\left(S_{\mathcal{U}}^{\phi}\right)_P^{\mathrm{S}} = -\sum_f \phi'_f \mathcal{C}_f \ , \tag{4.28a}$$

where ϕ'_f is defined by:

$$\phi'_f = \begin{cases} \beta_f \left(1 - \lambda_f^P\right) \left(\phi_P - \phi_{N(-f)}\right) \ , & \text{for } \mathcal{C}_f \geq 0 \ , \\ \beta_f \lambda_f^P \left(\phi_N - \phi_{NN(f)}\right) \ , & \text{for } \mathcal{C}_f < 0 \ ; \end{cases} \tag{4.28b}$$

and addition to the overall source term.

4.3.5 Discretised form of the general transport equation

Substitution of Eqs. (4.12), (4.20a) and (4.21) into Eq. (4.9) results in:

$$\begin{aligned} &\frac{(\rho V)_P \, \phi_P - (\rho V)_P^o \, \phi_P^o}{\Delta t} \\ &+ \sum_N \left\{ \left[\mathcal{C}_f w_f + \mathcal{D}_f^{\phi,n}\right] \phi_P - \left[\mathcal{C}_f \left(w_f - 1\right) + \mathcal{D}_f^{\phi,n}\right] \phi_N - \mathcal{D}_f^{\phi,c} \right\} \\ = &\left(S_{\mathcal{U}}^{\phi}\right)_P + \left(S_{\mathcal{P}}^{\phi}\right)_P \phi_P + \left(S_{\mathcal{U}}^{\phi}\right)_P^{\mathrm{S}} + \left(S_{\mathcal{U}}^{\phi,d}\right)_P + \left(S_{\mathcal{P}}^{\phi,d}\right)_P \phi_P \ , \end{aligned} \tag{4.29}$$

where the subscript 'N' in the summation denotes a neighbour across the face f. The counterpart of the above equation for the mass conservation equation, Eq. (2.71), is:

$$\frac{(\rho V)_P}{\Delta t} = \frac{(\rho V)_P^o}{\Delta t} - \sum_N \mathcal{C}_f + \left(S_m^d\right)_P \ . \tag{4.30}$$

When the latter equation is multiplied by ϕ_P and substituted in Eq. (4.29), the following result is obtained:

$$\begin{aligned} &\frac{(\rho V)_P^o \, \phi_P - (\rho V)_P^o \, \phi_P^o}{\Delta t} \\ &+ \sum_N \left\{ \left[\mathcal{C}_f \left(w_f - 1\right) + \mathcal{D}_f^{\phi,n}\right] \phi_P - \left[\mathcal{C}_f \left(w_f - 1\right) + \mathcal{D}_f^{\phi,n}\right] \phi_N - \mathcal{D}_f^{\phi,c} \right\} \\ = &\left(S_{\mathcal{U}}^\phi\right)_P + \left(S_{\mathcal{P}}^\phi\right)_P \phi_P + \left(S_{\mathcal{U}}^\phi\right)_P^{\mathrm{S}} + \left(S_{\mathcal{U}}^{\phi,d}\right)_P + \left(S_{\mathcal{P}}^{\phi,d}\right)_P \phi_P - \left(S_m^d\right)_P \phi_P \ . \end{aligned} \tag{4.31}$$

Equations of the above form may be written for all N_c cells in the solution domain, giving a system of N_c non-linear algebraic equations. Thus,

$$\mathcal{A}_P^\phi \phi_P = \sum_N \mathcal{A}_N^\phi \phi_N + b_P^\phi \ , \quad P = 1, ..., N_c \ , \tag{4.32a}$$

where $\mathcal{A}_P^\phi$ and $\mathcal{A}_N^\phi$ are the diagonal and off-diagonal coefficients of the system, respectively and b_P^ϕ is the source term, given by:

$$\mathcal{A}_P^\phi = \sum_N \mathcal{A}_N^\phi + \frac{(\rho V)_P^o}{\Delta t} - \left(S_{\mathcal{P}}^\phi\right)_P - \left(S_{\mathcal{P}}^{\phi,d}\right)_P + \left(S_m^d\right)_P \ , \tag{4.32b}$$

$$\mathcal{A}_N^\phi = \left[\mathcal{C}_f \left(w_f - 1\right) + \mathcal{D}_f^{\phi,n}\right] \ , \tag{4.32c}$$

$$b_P^\phi = \frac{(\rho V)_P^o}{\Delta t} \phi_P^o + \sum_N \mathcal{D}_f^{\phi,c} + \left(S_{\mathcal{U}}^\phi\right)_P + \left(S_{\mathcal{U}}^\phi\right)_P^{\mathrm{S}} + \left(S_{\mathcal{U}}^{\phi,d}\right)_P \ . \tag{4.32d}$$

Eq. (4.32a) can also be expressed in a matrix form as:

$$\mathbf{A}^\phi \boldsymbol{\phi} = \mathbf{b}^\phi \ , \tag{4.33}$$

where $\mathbf{A}^\phi$ is the $N_c \times N_c$ sparse coefficient matrix and $\boldsymbol{\phi}$ and $\mathbf{b}^\phi$ are the column vectors of the unknowns and the source, respectively.

4.4 Discretised gas equations

Based on the discretised form of the general transport equation given by Eq. (4.32), in this section, the governing equations of the gas phase are presented in their final form, together with detailed descriptions of their source terms.

4.4.1 Mass conservation equation

The discretisation of the continuity equation, Eq. (2.71), results in:

$$\frac{(\rho V)_P - (\rho V)_P^o}{\Delta t} + \sum_N \mathcal{C}_f = \left(S_m^d\right)_P \ . \tag{4.34}$$

The fuel evaporation rate, given by Eq. (3.168), is now:

$$\left(S_m^d\right)_P = -\frac{1}{\Delta t}\int_{V_P}\left[\sum_{p=1}^{N_p}\sum_{i=1}^{N_s}\delta\left(\mathbf{x}-\mathbf{x}_p^i\right)\left(m_p^i - m_p^{i-1}\right)\right] dV \ , \tag{4.35}$$

where the superscripts 'i' and '$i-1$' denote the values at the time $t+\delta t$ and t, respectively and the subcycling time step, δt, is defined as $\Delta t/N_s$ (see Section 4.5).

The fuel vapour mass conservation equation, Eq. (2.72), is discretised as follows:

$$\mathcal{A}_P^{Y_{v,i}}\left(Y_{v,i}\right)_P = \sum_N \mathcal{A}_N^{Y_{v,i}}\left(Y_{v,i}\right)_N + b_P^{Y_{v,i}} \ , \tag{4.36a}$$

where

$$\mathcal{A}_P^{Y_{v,i}} = \sum_N \mathcal{A}_N^{Y_{v,i}} + \frac{(\rho V)_P^o}{\Delta t} + \left(S_m^d\right)_P \ , \tag{4.36b}$$

$$\mathcal{A}_N^{Y_{v,i}} = \left[\mathcal{C}_f\left(w_f - 1\right) + \mathcal{D}_f^{Y_{v,i},n}\right] \ , \tag{4.36c}$$

$$b_P^{Y_{v,i}} = \frac{(\rho V)_P^o}{\Delta t}\left(Y_{v,i}\right)_P^o + \sum_N \mathcal{D}_f^{Y_{v,i},c} + \left(S_{\mathcal{U}}^{Y_{v,i}}\right)_P^{\mathrm{S}} + \left(S_{Y_{v,i}}^d\right)_P \ . \tag{4.36d}$$

The evaporation rate of the fuel component j, expressed by Eq. (3.169), becomes:

$$\left(S_{Y_{v,j}}^d\right)_P = -\frac{1}{\Delta t}\int_{V_P}\left[\sum_{p=1}^{N_p}\sum_{i=1}^{N_s}\delta\left(\mathbf{x}-\mathbf{x}_p^i\right)\left(m_{p,j}^i - m_{p,j}^{i-1}\right)\right] dV \ . \tag{4.37}$$

4.4.2 Momentum conservation equation

The momentum conservation equation, Eq. (2.73), when discretised reads:

$$\mathcal{A}_P^{\mathbf{u}}\mathbf{u}_P = \sum_N \mathcal{A}_N^{\mathbf{u}}\mathbf{u}_N + \mathbf{b}_P^{\mathbf{u}} - (\vartheta V \mathcal{N} p)_P + \left(\mathbf{S}_{\mathcal{U}}^{\mathbf{u},d}\right)_P \ , \tag{4.38a}$$

where

$$\mathcal{A}_P^{\mathbf{u}} = \sum_N \mathcal{A}_N^{\mathbf{u}} + \frac{(\rho V)_P^o}{\Delta t} - \left(S_{\mathcal{P}}^{\mathbf{u},d}\right)_P + \left(S_m^d\right)_P \ , \tag{4.38b}$$

$$\mathcal{A}_N^{\mathbf{u}} = \left[\mathcal{C}_f\left(w_f - 1\right) + \mathcal{D}_f^{\mathbf{u},n}\right] \ , \tag{4.38c}$$

$$\mathbf{b}_P^{\mathbf{u}} = \frac{(\rho V)_P^o}{\Delta t}\mathbf{u}_P^o + \sum_N \mathcal{D}_f^{\mathbf{u},c} + (\mathbf{S}_{\mathcal{U}}^{\mathbf{u}})_P + (\mathbf{S}_{\mathcal{U}}^{\mathbf{u}})_P^{\mathrm{S}} \ . \tag{4.38d}$$

In anticipation of the derivation of the pressure equation in the next chapter, the pressure gradient and the spray source terms are separated from the rest of the source term. The diffusive flux in the momentum equation does not conform to the standard form of this term because parts of the stress tensor cannot be cast in the compact gradient form. Therefore, these parts are treated as explicit source terms, as follows:

$$\begin{aligned}(\mathbf{S}_{\mathcal{U}}^{\mathbf{u}})_P = &\left\{V\mathcal{N}\cdot\left[\rho\nu_{\mathit{eff}}\left(\mathcal{N}\mathbf{u}^o\right)^{\mathrm{T}}\right]\right\}_P \\ &-\frac{2}{3}\left[V\mathcal{N}\cdot\left(\rho\nu_{\mathit{eff}}\mathcal{N}\cdot\mathbf{u}^o\mathbf{I}\right)\right]_P \\ &-\frac{2}{3}\left[V\mathcal{N}\cdot\left(\rho k^o\mathbf{I}\right)\right]_P \ .\end{aligned} \tag{4.39}$$

The spray momentum contribution to the gas, given by Eq. (3.73), when integrated over the cell volume, reads:

$$\left(\mathbf{S}_{\mathbf{u}}^d\right)_P = -\frac{1}{\Delta t}\int_{V_P}\left\{\sum_{p=1}^{N_p}\sum_{i=1}^{N_s}\delta\left(\mathbf{x}-\mathbf{x}_p^i\right)\left[\left(m_p\mathbf{u}_p\right)^i - \left(m_p\mathbf{u}_p\right)^{i-1}\right]\right\}dV \ . \tag{4.40}$$

Linearisation of this term according to Eq. (4.21) results in (see Section 4.5):

$$\begin{aligned}\left(\mathbf{S}_{\mathcal{U}}^{\mathbf{u},d}\right)_P = -\frac{1}{\Delta t}\int_{V_P}\Bigg\{&\sum_{p=1}^{N_p}\sum_{i=1}^{N_s}\delta\left(\mathbf{x}-\mathbf{x}_p^i\right) \\ &\left\{m_p^i\left[\mathbf{u}''\left(\mathbf{x}_p^{i-1}\right) - \left[\mathbf{u}''\left(\mathbf{x}_p^{i-1}\right) - \mathbf{u}_p^{i-1}\right]e^{-\delta t/\tau_{\mathbf{u}}^{i-1}}\right]\right. \\ &\left. - \left(m_p\mathbf{u}_p\right)^{i-1}\right\}\Bigg\}dV \ ,\end{aligned} \tag{4.41a}$$

$$\left(S_{\mathcal{P}}^{\mathbf{u},d}\right)_P = -\frac{1}{\Delta t}\int_{V_P}\left\{\sum_{p=1}^{N_p}\sum_{i=1}^{N_s}\delta\left(\mathbf{x}-\mathbf{x}_p^i\right)\left[m_p^i\left(1 - e^{-\delta t/\tau_{\mathbf{u}}^{i-1}}\right)\right]\right\}dV \ . \tag{4.41b}$$

The SFCD source term, $(\mathbf{S}_{\mathcal{U}}^{\mathbf{u}})_P^{\mathrm{S}}$, is given by Eq. (4.28).

4.4.3 Energy conservation equation

The discrete form of the energy conservation equation, Eq. (2.74), is:

$$\mathcal{A}_P^e e_P = \sum_N \mathcal{A}_N^e e_N + b_P^e \; , \tag{4.42a}$$

where

$$\mathcal{A}_P^e = \sum_N \mathcal{A}_N^e + \frac{(\rho V)_P^o}{\Delta t} - \left(S_{\mathcal{P}}^{e,d}\right)_P + \left(S_m^d\right)_P \; , \tag{4.42b}$$

$$\mathcal{A}_N^e = \left[\mathcal{C}_f \left(w_f - 1\right) + \mathcal{D}_f^{e,n}\right] \; , \tag{4.42c}$$

$$b_P^e = \frac{(\rho V)_P^o}{\Delta t} e_P^o + \sum_N \mathcal{D}_f^{e,c} + (S_{\mathcal{U}}^e)_P + (S_{\mathcal{U}}^e)_P^{\mathrm{S}} + \left(S_{\mathcal{U}}^{e,d}\right)_P \; . \tag{4.42d}$$

The pressure work term must be approximated using the mean value of the pressure during the computational time step Δt in order to ensure reversibility of this term during expansion and compression (Watkins [301]). Thus, the pressure work source term reads:

$$(S_{\mathcal{U}}^e)_P = -\frac{(p + p^o)_P}{2} \left\{\mathcal{N}\cdot\left[\vartheta \mathbf{u} + (1-\vartheta)\,\mathbf{u}_l\right]\right\}_P V_P \; . \tag{4.43}$$

From Gauss' theorem, Eq. (4.4a), the term $\mathcal{N}\cdot(\vartheta\mathbf{u})_P V_P$ can be written as:

$$\mathcal{N}\cdot(\vartheta\mathbf{u})_P V_P = \sum_{\{f\}_P} \mathcal{S}_f\cdot(\vartheta\mathbf{u})_f \; . \tag{4.44}$$

Taking into account Eqs. (4.10) and (4.16), the above expression becomes:

$$\mathcal{N}\cdot(\vartheta\mathbf{u})_P V_P = \sum_{\{f\}_P} \mathcal{C}_f \left(\frac{\vartheta}{\rho}\right)_f + \mathcal{N}\cdot(\vartheta\mathbf{u}_b)_P V_P \; . \tag{4.45}$$

The term $\mathcal{N}\cdot[(1-\vartheta)\,\mathbf{u}_l]_P V_P$ in Eq. (4.43) is derived by discretising expression (2.31), taking into account the discretised fuel evaporation rate given by Eq. (4.35) and also considering the general case of a moving boundary. Therefore,

$$\begin{aligned}\mathcal{N}\cdot[(1-\vartheta)\,\mathbf{u}_l]_P V_P =& \frac{(\vartheta - \vartheta^o)_P}{\Delta t} V_P \\ &+ \frac{1}{\Delta t}\int_{V_P} \left[\sum_{p=1}^{N_p}\sum_{i=1}^{N_s} \delta\left(\mathbf{x} - \mathbf{x}_p^i\right)\left(\frac{m_p^i - m_p^{i-1}}{\rho_p^i}\right)\right] dV \\ &+ \mathcal{N}\cdot[(1-\vartheta)\,\mathbf{u}_b]_P V_P \; .\end{aligned} \tag{4.46}$$

Substituting Eqs. (4.45) and (4.46) into Eq. (4.43), the source term $(S^e_{\mathcal{U}})_P$ is obtained:

$$
\begin{aligned}
(S^e_{\mathcal{U}})_P = -\frac{(p+p^o)_P}{2} \Bigg\{ & \sum_{\{f\}_P} \mathcal{C}_f \left(\frac{\vartheta}{\rho}\right)_f + \frac{(\vartheta-\vartheta^o)_P}{\Delta t} V_P \\
& + \frac{1}{\Delta t} \int_{V_P} \left[\sum_{p=1}^{N_p} \sum_{i=1}^{N_s} \delta\left(\mathbf{x}-\mathbf{x}_p^i\right) \left(\frac{m_p^i - m_p^{i-1}}{\rho_p^i} \right) \right] dV \\
& + \mathcal{N}\cdot(\mathbf{u}_b)_P \, V_P \Bigg\} \; . \qquad (4.47)
\end{aligned}
$$

The spray contribution to the gas energy, expressed by Eq. (3.134), when integrated over the cell volume, reads:

$$
\begin{aligned}
\left(S^d_e\right)_P = -\frac{1}{\Delta t} \int_{V_P} \Bigg\{ & \sum_{p=1}^{N_p} \sum_{i=1}^{N_s} \delta\left(\mathbf{x}-\mathbf{x}_p^i\right) \\
& c_{p,d}^{i-1} \left\{ \left[m_p\left(T_p - T_{ref}\right)\right]^i - \left[m_p\left(T_p - T_{ref}\right)\right]^{i-1} \right\} \Bigg\} dV \; . \qquad (4.48)
\end{aligned}
$$

Linearisation of this term according to Eq. (4.21) results in (see Section 4.5):

$$
\left(S^{e,d}_{\mathcal{U}}\right)_P = \frac{1}{\Delta t} \int_{V_P} \left\{ \sum_{p=1}^{N_p} \sum_{i=1}^{N_s} \delta\left(\mathbf{x}-\mathbf{x}_p^i\right) c_{p,d}^{i-1} \left(m_p^i T_{ref} + m_p^{i-1} T_p^{i-1} \right) \right\} dV \; , \qquad (4.49a)
$$

$$
\left(S^{e,d}_{\mathcal{P}}\right)_P = -\frac{1}{e_P^o} \frac{1}{\Delta t} \int_{V_P} \left\{ \sum_{p=1}^{N_p} \sum_{i=1}^{N_s} \delta\left(\mathbf{x}-\mathbf{x}_p^i\right) c_{p,d}^{i-1} \left(m_p^i T_p^i + m_p^{i-1} T_{ref} \right) \right\} dV \; . \qquad (4.49b)
$$

The above expressions for the source term are valid for all forms of the energy equation for the droplet (for infinite, finite and effective conductivity and analytical and profile method) derived in Chapter 3. However, for the cases of finite and effective conductivity, the temperature T_p of the ‘droplet’ must be replaced by the droplet mean temperature, given by Eq. (3.167).

4.4.4 Turbulence equations

Turbulence kinetic energy

The turbulence kinetic energy conservation equation, Eq. (2.75), is discretised as:

$$\mathcal{A}_P^k k_P = \sum_N \mathcal{A}_N^k k_N + b_P^k \ , \tag{4.50a}$$

where

$$\mathcal{A}_P^k = \sum_N \mathcal{A}_N^k + \frac{(\rho V)_P^o}{\Delta t} - \left(S_{\mathcal{P}}^k\right)_P - \left(S_{\mathcal{P}}^{k,d}\right)_P + \left(S_m^d\right)_P \ , \tag{4.50b}$$

$$\mathcal{A}_N^k = \left[\mathcal{C}_f\left(w_f - 1\right) + \mathcal{D}_f^{k,n}\right] \ , \tag{4.50c}$$

$$b_P^k = \frac{(\rho V)_P^o}{\Delta t} k_P^o + \sum_N \mathcal{D}_f^{k,c} + \left(S_{\mathcal{U}}^k\right)_P + \left(S_{\mathcal{U}}^k\right)_P^{\mathrm{S}} + \left(S_{\mathcal{U}}^{k,d}\right)_P \ . \tag{4.50d}$$

The gas-related source terms are expressed by:

$$\left(S_{\mathcal{U}}^k\right)_P = G_t + \frac{2}{3}\left(\rho k^o V\right)_P \max\left[0,\ \left(\mathcal{N}\cdot\mathbf{u}\right)_P\right] \ , \tag{4.51a}$$

$$\begin{aligned}\left(S_{\mathcal{P}}^k\right)_P = & -C_\mu \left(\rho k^o V\right)_P \left[\frac{2}{3}\frac{1}{\varepsilon^o}\left(\mathcal{N}\cdot\mathbf{u}\right)^2 + \frac{1}{\nu_t}\right]_P \\ & + \frac{2}{3}\left(\rho V\right)_P \min\left[0,\ \left(\mathcal{N}\cdot\mathbf{u}\right)_P\right] \ ,\end{aligned} \tag{4.51b}$$

where

$$G_t = \left(\rho \nu_t V\right)_P \left\{\left[\mathcal{N}\mathbf{u} + \left(\mathcal{N}\mathbf{u}\right)^{\mathrm{T}}\right] : \mathcal{N}\mathbf{u}\right\}_P \ . \tag{4.51c}$$

Here the term $2/3\rho(\nabla\cdot\mathbf{u})k$ is split into implicit and explicit source parts according to the sign of $\nabla\cdot\mathbf{u}$.

The same approach is used for the spray-related source terms, Eq. (2.68), i.e.

$$\left(S_{\mathcal{U}}^{k,d}\right)_P = \max\left[0,\ \left(\dot{S}_k^d\right)_P\right] \ , \tag{4.52a}$$

$$\left(S_{\mathcal{P}}^{k,d}\right)_P = \frac{1}{k_P^o}\min\left[0,\ \left(\dot{S}_k^d\right)_P\right] \ , \tag{4.52b}$$

where

$$\begin{aligned}\left(\dot{S}_k^d\right)_P = -\frac{1}{\Delta t}\int_{V_P} & \left\{\sum_{p=1}^{N_p}\sum_{i=1}^{N_s}\delta\left(\mathbf{x}-\mathbf{x}_p^i\right)\mathbf{u}''\left(\mathbf{x}_p^i\right)\delta t\right. \\ & \left\{\left(m_p\mathbf{u}_p\right)^i - \left(m_p\mathbf{u}_p\right)^{i-1}\right. \\ & \left.\left. - \left[\mathbf{u}\left(\mathbf{x}_p^i\right) - \frac{1}{2}\mathbf{u}''\left(\mathbf{x}_p^i\right)\right]\left(m_p^i - m_p^{i-1}\right)\right\}\right\} dV \ .\end{aligned} \tag{4.52c}$$

Turbulence dissipation

The discretisation of the turbulence dissipation conservation equation, Eq. (2.76), results in:

$$\mathcal{A}_P^\varepsilon \varepsilon_P = \sum_N \mathcal{A}_N^\varepsilon \varepsilon_N + b_P^\varepsilon \ , \tag{4.53a}$$

where

$$\mathcal{A}_P^\varepsilon = \sum_N \mathcal{A}_N^\varepsilon + \frac{(\rho V)_P^o}{\Delta t} - (S_\mathcal{P}^\varepsilon)_P - \left(S_\mathcal{P}^{\varepsilon,d}\right)_P + \left(S_m^d\right)_P \ , \tag{4.53b}$$

$$\mathcal{A}_N^\varepsilon = \left[\mathcal{C}_f\,(w_f - 1) + \mathcal{D}_f^{\varepsilon,n}\right] \ , \tag{4.53c}$$

$$b_P^\varepsilon = \frac{(\rho V)_P^o}{\Delta t}\varepsilon_P^o + \sum_N \mathcal{D}_f^{\varepsilon,c} + (S_\mathcal{U}^\varepsilon)_P + (S_\mathcal{U}^\varepsilon)_P^{\mathrm{S}} + \left(S_\mathcal{U}^{\varepsilon,d}\right)_P \ . \tag{4.53d}$$

Following a similar approach to that for turbulence energy, the source terms are treated as follows:

$$\begin{aligned}(S_\mathcal{U}^\varepsilon)_P = {} & C_{\varepsilon 1} G_t \left(\frac{\varepsilon^o}{k^o}\right)_P \\ & + \left(C_{\varepsilon 3} - \frac{2}{3}C_{\varepsilon 1}\right)(\rho\varepsilon^o V)_P \min\left[0,\ (\mathcal{N}\cdot\mathbf{u})_P\right] \ ,\end{aligned} \tag{4.54a}$$

$$\begin{aligned}(S_\mathcal{P}^\varepsilon)_P = {} & -\left(\frac{\rho V}{k^o}\right)_P \left[\frac{2}{3}C_{\varepsilon 1}\nu_t\,(\mathcal{N}\cdot\mathbf{u})^2 + C_{\varepsilon 2}\varepsilon^o\right]_P \\ & + \left(C_{\varepsilon 3} - \frac{2}{3}C_{\varepsilon 1}\right)(\rho V)_P \max\left[0,\ (\mathcal{N}\cdot\mathbf{u})_P\right] \ .\end{aligned} \tag{4.54b}$$

In the above expressions, the fact that $C_{\varepsilon 3} - 2C_{\varepsilon 1}/3$ is always negative (see Table 2.2) is taken into account. The spray source term, Eq. (2.70), reads:

$$\left(S_\mathcal{U}^{\varepsilon,d}\right)_P = C_{\varepsilon 4}\frac{\varepsilon_P^o}{k_P^o}\max\left[0,\ \left(\dot{S}_k^d\right)_P\right] \ , \tag{4.55a}$$

$$\left(S_\mathcal{P}^{\varepsilon,d}\right)_P = C_{\varepsilon 4}\frac{1}{k_P^o}\min\left[0,\ \left(\dot{S}_k^d\right)_P\right] \ . \tag{4.55b}$$

4.5 Discretised spray equations

The spray equations are ordinary differential equations and therefore, they are discretised in first-order Euler form. Some of the spray equations can be integrated analytically provided that the coefficients of the differential equation are constant.

This has already been exploited in Section 3.6 where the conduction and diffusion equations were integrated analytically but *only* within a fine enough time step during which, the coefficients were assumed to be constant. The same remedy will now be applied to all the remaining spray equations presented in Chapter 3. Thus, each of the spray differential equations is integrated analytically* within a small time step, δt, whose meaning is explained next, assuming that the coefficients of the equation are constant. These coefficients are updated at the beginning of each time step based on the values obtained at the end of the previous time step. Before the presentation of the integrated spray equations, the definition of the time step δt and the spatial interpolation, employed in spray equations, are explained.

4.5.1 Temporal subcycling

The physical processes of the spray usually have smaller time scales than the time step Δt, used for the gas phase. Thus, a droplet subcycling time step, δt, is introduced, which is defined as the smallest characteristic time among all the time scales of the spray processes, i.e.

$$\delta t = \min\left(\Delta t,\ \tau_{\mathbf{u}},\ \tau_{osc},\ \tau_e,\ \tau_m,\ \tau_b,\ \tau_c,\ \frac{\tau_{p,T} R_{d,0}^2}{\alpha_d},\ \frac{\tau_{p,m} R_{d,0}^2}{\alpha_d}\right)\ , \tag{4.56}$$

where all the time scales have been defined in Chapter 3, apart from τ_{osc} and τ_c. The former is the characteristic time of the droplet distortion model and will be given later (see Eq. (4.69)), while the latter is the parcel residence time in the current cell†, evaluated from:

$$\tau_c = \frac{L_c}{|\mathbf{u}_p|}\ , \tag{4.57}$$

where L_c is the characteristic cell length, evaluated from the cell volume, V_P, by:

$$L_c = V_P^{1/3}\ . \tag{4.58}$$

The parcel residence time is included in Eq. (4.56) in order to ensure that the parcel does not traverse more than one computational cell in one subcycling time step. This

*The term *semi-analytical* can be recalled since a combination of the analytical solution and the time-marching technique is employed.

†In order to find the cell in which the droplet resides, each cell is locally transformed into an orthogonal parallelepiped [316].

is essential for the accuracy of the coupling between the two phases since the source terms representing mass, momentum and energy exchange between a parcel and the surrounding gas are evaluated at the end of each subcycling time step and added to the corresponding gas conservation equations of the cell in which the parcel resides. Consequently, for a relatively large subcycling time step, the abovementioned spray source terms are not considered in intermediate cells located in the parcel path*.

The subcycling time step δt, is further reduced so that $N_s = \Delta t/\delta t$ is an integer. Then, a number of iterations N_s, are performed on the spray equations.

4.5.2 Spatial interpolation

The gas properties are used in the calculation of droplet-related quantities like the drag coefficient, evaporation rate etc. and must be evaluated at the droplet locations. Linear interpolation is used between the values of the gas property ϕ at the six faces† of the cell in which the parcel resides, to obtain property $\phi(\mathbf{x}_p)$, at the parcel location $\mathbf{x}_p$. Thus,

$$\phi(\mathbf{x}_p) = \frac{\sum\limits_{\{f\}_P} \left(\dfrac{1}{|\mathbf{x}_p - \mathbf{r}_f|} \phi_f \right)}{\sum\limits_{\{f\}_P} \left(\dfrac{1}{|\mathbf{x}_p - \mathbf{r}_f|} \right)} \,. \tag{4.59}$$

4.5.3 Spray governing equations

In the following, the superscript '$i-1$' indicates a value at the time t and the superscript 'i' at the time $t + \delta t$.

---

*The expression $|\mathbf{u}_p|\delta t/L_c$ is called *parcel Courant number* in analogy to the well-known Courant number of the gas (see §5.2.3 and Eq. (5.25)).

†Here, the values at the faces are considered rather than the values at the neighbouring cells. The latter can be also used but it causes problems at cells adjacent to a boundary whose contribution could not taken into account consistently.

Nozzle flow

The equations describing the boundary layer in the nozzle, Eqs. (3.8a) and (3.8d), are both of the form:

$$\frac{d\overline{R}_\delta}{d\overline{x}} = F\left(\overline{R}_\delta\right) \ , \tag{4.60}$$

which is discretised explicitly as:

$$\overline{R}_\delta^i = \overline{R}_\delta^{i-1} + F\left(\overline{R}_\delta^{i-1}\right)\Delta\overline{x} \ . \tag{4.61}$$

The above is integrated with $\Delta\overline{x}$ of the order of 10^{-4}, which guarantees that the total error is of the order of 10^{-3} [204], since both $\overline{x}$ and $\overline{R}_\delta$ are dimensionless.

Atomisation

The droplet diameter rate-of-change equation of the Huh atomisation model, given by Eq. (3.27), is approximated as:

$$D_d^i = D_d^{i-1} - 2\left(\frac{L_A}{\tau_A}\right)^{i-1}\frac{\delta t'}{C_5} \ , \tag{4.62}$$

where the integration is performed by a separate subcycling time step, $\delta t' = \tau_A/10$, because the extent of atomisation is calculated at the beginning of each time step, prior to the solution of the gas transport equations and the rest spray equations.

Parcel trajectory

The parcel trajectory equation, Eq. (3.59), is discretised explicitly as:

$$\mathbf{x}_p^i = \mathbf{x}_p^{i-1} + \mathbf{u}_p^{i-1}\delta t \ . \tag{4.63}$$

Parcel momentum conservation equation

The momentum conservation equation, Eq. (3.63), is integrated and discretised implicitly to yield:

$$\mathbf{u}_p^i = \hat{\mathbf{u}}\left(\mathbf{x}_p^{i-1}\right) - \left[\hat{\mathbf{u}}\left(\mathbf{x}_p^{i-1}\right) - \mathbf{u}_p^{i-1}\right] e^{-\delta t/\tau_{\mathbf{u}}^{i-1}} \ . \tag{4.64}$$

The equation describing the distortion of the droplet surface due to aerodynamic forces, Eq. (3.69), is a second-order ordinary differential equation and its solution within a time step δt can be obtained analytically if the coefficients are assumed constant during this time step. Therefore, the solution is expressed by:

$$y^i = e^{\mathcal{R}^{i-1}\delta t}\left\{\left(y^{i-1} - \frac{\beta_3^{i-1}}{\beta_2^{i-1}}\right)\cos\left(\mathcal{I}^{i-1}\delta t\right) + \left[\frac{\dot{y}^{i-1} - \left(y^{i-1} - \frac{\beta_3^{i-1}}{\beta_2^{i-1}}\right)\mathcal{R}^{i-1}}{\mathcal{I}^{i-1}}\right]\sin\left(\mathcal{I}^{i-1}\delta t\right)\right\} + \frac{\beta_3^{i-1}}{\beta_2^{i-1}}\,, \tag{4.65}$$

where the coefficients β_1^{i-1}, β_2^{i-1} and β_3^{i-1}, given by

$$\beta_1^{i-1} = \frac{20\mu_d}{\rho_d D_d^2}\,, \tag{4.66a}$$

$$\beta_2^{i-1} = \frac{64\sigma_d}{\rho_d D_d^3}\,, \tag{4.66b}$$

$$\beta_3^{i-1} = \frac{8}{3}\frac{\rho_m}{\rho_d}\frac{\left(\hat{\mathbf{u}} - \mathbf{u}_d\right)^2}{D_d^2}\,, \tag{4.66c}$$

are evaluated using the values of the properties of the previous subcycling time step and they are updated in the beginning of each subcycling time step. Also, in Eq. (4.65), $\mathcal{R}^{i-1}$ and $\mathcal{I}^{i-1}$ are the real and imaginary parts of the roots of the characteristic equation, respectively, given by:

$$\mathcal{R}^{i-1} = -\frac{\beta_1^{i-1}}{2}\,, \tag{4.67a}$$

$$\mathcal{I}^{i-1} = \sqrt{\beta_2^{i-1} - \frac{\left(\beta_1^{i-1}\right)^2}{4}}\,. \tag{4.67b}$$

Finally, $\dot{y}^{i-1}$ in Eq. (4.65) represents the time-derivative of y given by:

$$\dot{y}^{i-1} = \mathcal{R}^{i-2}e^{\mathcal{R}^{i-2}\delta t^o}\left\{\left(y^{i-2} - \frac{\beta_3^{i-2}}{\beta_2^{i-2}}\right)\cos\left(\mathcal{I}^{i-2}\delta t^o\right) + \left[\frac{\dot{y}^{i-2} - \left(y^{i-2} - \frac{\beta_3^{i-2}}{\beta_2^{i-2}}\right)\mathcal{R}^{i-2}}{\mathcal{I}^{i-2}}\right]\sin\left(\mathcal{I}^{i-2}\delta t^o\right)\right\}$$

$$
+\mathcal{I}^{i-2} e^{\mathcal{R}^{i-2}\delta t^o} \left\{ - \left(y^{i-2} - \frac{\beta_3^{i-2}}{\beta_2^{i-2}} \right) \sin\left(\mathcal{I}^{i-2}\delta t^o\right) \right.
$$

$$
\left. + \left[\frac{\dot{y}^{i-2} - \left(y^{i-2} - \frac{\beta_3^{i-2}}{\beta_2^{i-2}} \right) \mathcal{R}^{i-2}}{\mathcal{I}^{i-2}} \right] \cos\left(\mathcal{I}^{i-2}\delta t^o\right) \right\} . \quad (4.68)
$$

As can be seen from Eq. (4.65), the solution of the equation describing the droplet distortion, is a sinusoidal function with period equal to $2\pi/\mathcal{I}$. Although this could represent the characteristic time τ_{osc}, the latter is taken to be the one fourth of the period in order to capture the maxima and minima of the oscillation, i.e.

$$
\tau_{osc} = \frac{\pi}{2\mathcal{I}} \; . \quad (4.69)
$$

Evaporation

The integration and discretisation of the conduction and diffusion equations have already been presented in Section 3.6. Here, only the remaining evaporation-related equations are discretised.

Integration and discretisation of the parcel mass conservation equation for a single-component fuel, Eq. (3.140), yield:

$$
m_p^i = m_p^{i-1} e^{-\delta t/\tau_m^{i-1}} \; . \quad (4.70)
$$

The energy equation with infinite conductivity, Eq. (3.99), when integrated and discretised, reads:

$$
T_p^i = T\left(\mathbf{x}_p^i\right) - \left[T\left(\mathbf{x}_p^i\right) - T_p^{i-1}\right] e^{-\delta t/\tau_e^{i-1}} \; . \quad (4.71)
$$

Breakup

When Eq. (3.175) is integrated and discretised, the following expression for the droplet diameter is obtained:

$$
D_d^i = D_{st}^{i-1} - \left[D_{st}^{i-1} - D_d^{i-1}\right] e^{-\delta t/\tau_b^{i-1}} \; . \quad (4.72)
$$

4.6 Boundary conditions

The discretised source terms presented in the previous sections are valid for all internal cells. A modified treatment is imposed for cells with a face lying on the boundary. In particular, the corresponding coefficient $\mathcal{A}_N^\phi$ is set to zero and an additional boundary 'source' term, $\left(S^\phi\right)_P^b$, which contains the boundary condition, is introduced. The linearisation of this term is in accord to Eq. (4.21):

$$\left(S^\phi\right)_P^b = \left(S_\mathcal{U}^\phi\right)_P^b + \left(S_\mathcal{P}^\phi\right)_P^b \phi_P \; ; \tag{4.73}$$

and the terms $\left(S_\mathcal{U}^\phi\right)_P^b$ and $\left(S_\mathcal{P}^\phi\right)_P^b$ are added to the source terms $\left(S_\mathcal{U}^\phi\right)_P$ and $\left(S_\mathcal{P}^\phi\right)_P$, respectively.

The source terms generated by the boundary conditions will be discussed in this section. Two types of boundary conditions can be distinguished:

1. The value of the dependent variable is known and the boundary face fluxes are calculated from these values and the values at the nodes adjacent to the boundary.

2. The fluxes are known and therefore, they are directly imposed on the cell face adjacent to the boundary.

The specific practices adopted for each of the boundary types are given below.

4.6.1 Wall boundaries

The various boundary conditions applying at walls given in §2.5.1 require different implementation as will be explained.

Velocities

From Eqs. (2.79b) and (2.86) the wall shear stress in the tangential direction to the wall gives rise to a boundary momentum sink given by:

$$(\mathbf{S}^{\mathbf{u}})^b_P = (F^{\mathbf{u}}_w)_P \left\{ \mathbf{u}_P - \mathbf{u}_W - \left[(\mathbf{u}_P - \mathbf{u}_W) \cdot \frac{\mathcal{S}_b}{|\mathcal{S}_b|^2} \mathcal{S}_b \right] \right\} |\mathcal{S}_b| \, , \tag{4.74}$$

where $\mathcal{S}_b$ is the cell face vector at the boundary. Decomposition of this term according to Eq. (4.73) yields, in component form, (Theodoropoulos [288]):

$$\begin{aligned} (S^{u_i}_{\mathcal{U}})^b_P = & -(F^{\mathbf{u}}_w)_P \left[|\mathcal{S}_b| - \frac{(\mathcal{S}_b \cdot \mathbf{e}_i)^2}{|\mathcal{S}_b|} \right] u_{i,W} \\ & - (F^{\mathbf{u}}_w)_P \frac{\mathcal{S}_b \cdot \mathbf{e}_i}{|\mathcal{S}_b|} \left[\sum_{j \neq i} (u_{j,P} - u_{j,W}) \, \mathcal{S}_b \cdot \mathbf{e}_j \right] \, , \end{aligned} \tag{4.75a}$$

$$(S^{u_i}_{\mathcal{P}})^b_P = (F^{\mathbf{u}}_w)_P \left[|\mathcal{S}_b| - \frac{(\mathcal{S}_b \cdot \mathbf{e}_i)^2}{|\mathcal{S}_b|} \right] \, , \tag{4.75b}$$

where $\mathbf{e} = (\mathbf{e}_1, \mathbf{e}_2, \mathbf{e}_3)$ is a unit base vector in the global coordinate system and subscripts i and j denote the coordinate directions ($i, j = 1, 2, 3$).

Energy

In the case of heat transfer at a wall, the wall heat flux, Eq. (2.87), is expressed in 'source' form for the boundary cell as follows:

$$\begin{aligned} (S^e)^b_P &= \mathcal{S}_b \cdot (-\mathbf{q}_W) \\ &= -|\mathcal{S}_b| \, (F^e_w)_P \, (e_W - e_P) \ . \end{aligned} \tag{4.76}$$

Linearisation of this term according to Eq. (4.73) results in:

$$(S^e_{\mathcal{U}})^b_P = -|\mathcal{S}_b| \, (F^e_w)_P \, e_W \, , \tag{4.77a}$$

$$(S^e_{\mathcal{P}})^b_P = |\mathcal{S}_b| \, (F^e_w)_P \ . \tag{4.77b}$$

For an adiabatic wall, both $(S^e_{\mathcal{U}})^b_P$ and $(S^e_{\mathcal{P}})^b_P$ are set to zero.

Turbulence parameters

In the cells adjacent to the wall, the average energy dissipation rate over the control volume in the k equation, Eq. (2.75), is calculated using the wall functions (Launder and Spalding [180], Begleris [35]). Thus,

$$\varepsilon_P^k = \frac{1}{V_P}\int_{V_P} \varepsilon \, dV \approx C_\mu^{3/4} k_P^{3/2} \frac{u_P^+}{y_P} \, , \tag{4.78}$$

where u_P^+ is calculated from Eq. (2.84). This is achieved by evaluating the $S_{\mathcal{P}}^k$ term in §4.4.4, replacing the turbulent viscosity, ν_t, with the effective viscosity, ν_{eff}, (Theodoropoulos [288]). The latter is expressed by:

$$\nu_{\mathit{eff}} = \begin{cases} \nu_m \, , & \text{for } y_P^+ \leq y_c^+ \, , \\ \dfrac{C_\mu^{1/4} k^{1/2} \kappa y_P}{\ln\left(E y_P^+\right)} \, , & \text{for } y_P^+ > y_c^+ \, . \end{cases} \tag{4.79}$$

Also, the part of the generation term caused by the work of the wall shear stress, τ_W, is modified. According to the Couette flow assumptions of §2.5.1, the turbulence kinetic energy generation rate in the cell adjacent to the wall, $(G_w)_P$, is calculated as a volume integral of Eq. (2.80):

$$(G_w)_P = \int_{V_P} \tau_W \frac{\partial u_P'}{\partial y} \, dV \, . \tag{4.80}$$

Substitution of Eq. (2.86) in the above formula and approximation result in (Kralj [171]):

$$(G_w)_P \approx -\frac{F_w^{\mathbf{u}}}{y_P} \mathbf{u}_P' \cdot \mathbf{u}_P' V_P \, . \tag{4.81}$$

Finally, the diffusion flux of k near walls is assumed to be zero, (Launder and Spalding [180]) and therefore,

$$\left(S_{\mathcal{U}}^k\right)_P^b = \left(S_{\mathcal{P}}^k\right)_P^b = 0 \, . \tag{4.82}$$

The dissipation rate in the near-wall cells is given by Eq. (2.92) and its discretised counterpart reads:

$$\varepsilon_P = \frac{C_\mu^{3/4} k_P^{3/2}}{\kappa y_P} \, . \tag{4.83}$$

This value is enforced by setting the boundary source term, according to Eq. (4.73), to:

$$(S_{\mathcal{U}}^{\varepsilon})_P^b = L\frac{C_\mu^{3/4}k_P^{3/2}}{\kappa y_P} \ , \tag{4.84a}$$

$$(S_{\mathcal{P}}^{\varepsilon})_P^b = -L \ , \tag{4.84b}$$

where $L \gg \varepsilon_P$. In the present study $L = 10^{30}$ is adopted.

It should be noted that the above treatment of the cells adjacent to the wall replaces the usual practices adopted for interior cells for both k and ε equations.

4.6.2 Inflow and outflow surfaces

Here, it is assumed that the mass flow rate $\dot{m}_b$ through the inflow or outflow boundary is known. In the cells adjacent to such boundaries, the linearised boundary source term components read:

Inflow ($\dot{m}_b \leq 0$):

$$\left(S_{\mathcal{U}}^{\phi}\right)_P^b = -\dot{m}_b\phi_b \ , \tag{4.85a}$$

$$\left(S_{\mathcal{P}}^{\phi}\right)_P^b = \dot{m}_b \ ; \tag{4.85b}$$

Outflow ($\dot{m}_b > 0$):

$$\left(S_{\mathcal{U}}^{\phi}\right)_P^b = 0 \ , \tag{4.85c}$$

$$\left(S_{\mathcal{P}}^{\phi}\right)_P^b = 0 \ , \tag{4.85d}$$

for $\phi = Y_{v,i}$, $\mathbf{u}$, e, k, ε, where ϕ_b denotes the value of ϕ at the cell face b. In the present study, the only flow boundaries, as already mentioned in §2.5.2, in engine simulation are valve curtains.

4.6.3 Symmetry planes

At a symmetry plane, the fluxes are zero (see §2.5.3) and therefore, the boundary source term for all the properties there is set to zero:

$$\left(S_{\mathcal{U}}^{\phi}\right)_P^b = \left(S_{\mathcal{P}}^{\phi}\right)_P^b = 0 \ , \quad \text{for } \phi = Y_{v,i},\ \mathbf{u},\ e,\ k,\ \varepsilon \ . \tag{4.86}$$

4.6.4 Cyclic boundaries

As mentioned in §2.5.4, the flow repeats itself on each side of a domain enclosed between the cyclic boundaries. Considering the cell P, shown in Fig. 4.4, it can be treated as an ordinary internal cell if a fictitious cell N is added as a neighbour

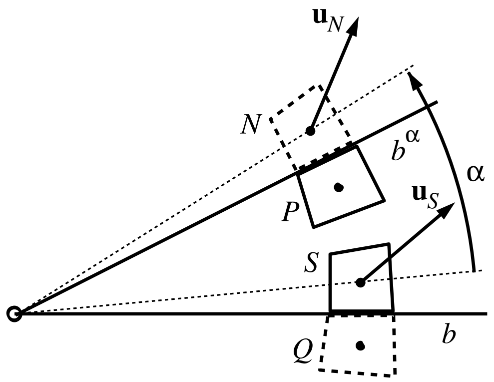

Figure 4.4: Cells at the cyclic boundaries.

across the boundary b^α, with the scalar properties equal to those in the cell S and gas velocity equal to the rotated velocity in the same cell for the angle α:

$$\phi_N = \phi_S \ , \quad \text{for } \phi = Y_{v,i},\ e,\ k,\ \varepsilon \ , \tag{4.87a}$$

$$\mathbf{u}_N = \mathbf{R}^\alpha \cdot \mathbf{u}_S \ , \tag{4.87b}$$

where $\mathbf{R}^\alpha$ is a rotational matrix. The same treatment can be applied for the cell S. A fictitious cell Q can be considered as a neighbour of the cell S with the scalar properties taken from P and gas velocity equal to the rotated velocity in the cell P for the angle $-\alpha$.

4.7 Closure

The discretised counterparts of the gas transport equations given in Chapter 2 and the spray governing equations described in Chapter 3 have been presented in this chapter.

The FVM has been adopted for the discretisation of the gas transport equations because it ensures conservation as explained in Section 4.2. The method has been applied to an arbitrary unstructured mesh consisting of hexahedral cells. The collocated variable arrangement has been chosen to decrease the storage requirement. A fully-implicit temporal discretisation practice has been used to ensure linear stability of the solution for an arbitrary time-step size.

The detailed discretisation of the general transport equation has been given in Section 4.3 along with the SFCD differencing scheme. The discretised governing equations of the gaseous phase have been presented in Section 4.4.

The spray equations have been discretised in Section 4.5 by combining analytical and numerical methods. A subcycling time step has been introduced to allow for the smaller time scales of the spray processes.

Finally, Section 4.6 dealt with the treatment of the boundary conditions.

The final result of discretisation is a system of simultaneous non-linear algebraic equations. The solution procedure for the solution of this system must be efficient in respect of the computational time and storage as well as robustness. The selection of a suitable solution method will be the scope of the next chapter.

Chapter 5

Solution Procedure

5.1 Introduction

The discretised and linearised transport equations, as explained in the previous chapter, form a system of algebraic equations. The solution procedure for solving this system of mutually coupled equations is the aim of this chapter.

The procedure comprises three main stages described in Section 5.2. Firstly, a global adjustment to the cylinder thermodynamic properties is performed. Then, a predictor-corrector sequence with fully embedded spray equations is applied to the gas properties. Finally, the turbulence parameters are calculated at the end of the corrector sequence in their own predictor-corrector, because of their strong coupling, according to the method of Theodoropoulos [288].

The systems of the algebraic equations are solved by conjugate gradient methods with preconditioning as is explained in Section 5.3. The convergence criteria are discussed in §5.3.2. Finally, the closure of the present chapter is presented in Section 5.4.

5.2 Solution algorithm

The solution sequence comprises three stages. The first is the *bulk adjustment*, which is required to separate the large-scale changes in pressure, density and temperature of the in-cylinder charge due to global effects (piston motion, valve flow etc.) from the smaller variations induced by the flow field. Then, the spray processes and the flow field are calculated by the predictor-corrector solution procedure. In the third stage, the droplet/droplet interactions and the turbulence properties are calculated but they are not allowed to affect the flow field in the current time step.

The main feature of the second stage is the algorithm for the simultaneous satisfaction of the continuity and momentum conservation equations. In low Mach number flows compressibility effects are weak and using the continuity equation to evaluate the density and from the density to calculate the pressure is not effective (Leskovšek [186]). Instead, the momentum and continuity equations are combined to generate an equation whose main dependent variable is the pressure. In the present study the Lagged-Operator Nonorthogonal-Grid Pressure-Implicit with Splitting of Operators (LONG-PISO) method of Theodoropoulos [288], modified by Kralj [171] who embedded the spray processes in the algorithm, has been chosen. The LONG-PISO method is an extension of the EPISO algorithm of Begleris [35], who applied the well known non-iterative PISO algorithm of Issa [145] to engine calculations.

The LONG-PISO algorithm uses an operator splitting technique to temporarily decouple the flow equations, in order to allow solution of the governing equations sequentially. These are linearised, assuming that their coefficients, evaluated from the currently available values of the required properties, are constant. The algorithm predicts initial approximations of all the flow field variables. A corrector sequence is then performed in which the coupling of the equations is taken into account by updating the coefficients of each set of governing equations. The pressure equation, based on the continuity equation, enforces mass conservation. The corrector sequence is repeated until the required accuracy of the solution is reached.

The complete solution algorithm is depicted in the flow chart shown in Fig. 5.1

and the description of its particular blocks can be summarised as follows.

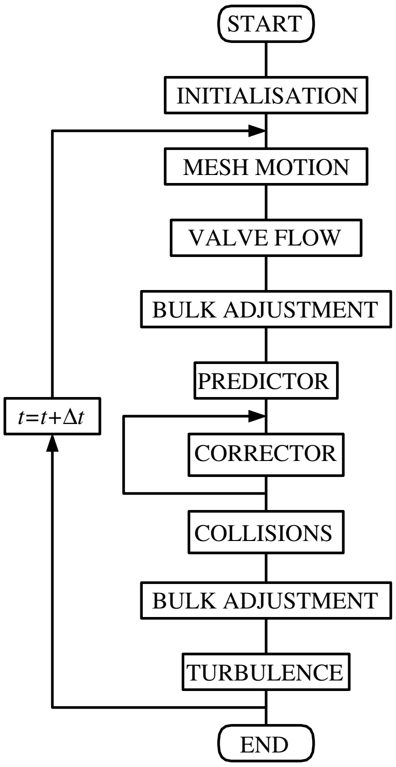

Figure 5.1: Flow chart of the solution algorithm.

1. **Initialisation**

   All the dependent variables at time $t = t_0$ are set to their initial values which are denoted by the superscript 'o'.

2. **Mesh motion**

   The vertices of the mesh are moved in a prescribed fashion and removal or addition of layers is arranged to avoid extreme values of aspect ratio. Mesh-related properties, such as cell volumes, cell face area vectors and spatial interpolation factors are calculated.

3. **Valve flow**

   The inlet/outlet mass and energy fluxes through the valves are determined by the orifice equations, energy conservation and perfect gas law. All the flow properties on the valve curtain boundaries such as $\mathbf{u}$, p, ρ, T, $Y_{v,i}$, k and ε are set in accord with the input data.

4. **Bulk adjustment**

   The pressure p is split into the cylinder averaged or 'reference' value, p_{cyl} and the local relative value, p':

$$p_P = p_{cyl} + p'_P \; . \tag{5.1}$$

   p_{cyl}, p', ρ, ϑ, ν_{eff}, T and e are updated to account for the mesh motion, valve flow and heat transfer through the walls. These updated values will be hereafter denoted by superscript '(1)', except for the reference pressure, the void fraction, the internal energy and the temperature whose updated values are intermediate and thus, denoted by superscript '($\prime$)'. The void fraction will be further updated in the predictor stage by solving the spray equations while the reference pressure will be updated considering the presence of the liquid phase. The other two properties will be updated by solving the internal energy conservation equation. At the end of the predictor step all the updated properties will be then denoted by superscript '(1)'. Therefore, at the end of the bulk adjustment, the following properties are known: $(p')^{(1)}$, $\rho^{(1)}$, $\nu_{\mathit{eff}}^{(1)}$ and $p_{cyl}^{(\prime)}$, $\vartheta^{(\prime)}$, $T^{(\prime)}$ and $e^{(\prime)}$.

5. **Predictor**

   The spray contributions to the gas mass, momentum and energy conservation equations are calculated. The fuel vapour mass fraction and the energy equations are assembled and solved to obtain $Y_{v,i}^{(1)}$ and $e^{(1)}$. The temperature $T^{(1)}$ is calculated from $e^{(1)}$. The reference pressure $p_{cyl}^{(\prime)}$ is then further updated to take into account variations due to compression provoked by the liquid phase to yield $p_{cyl}^{(1)}$. At the end of this stage the equations for the three components of momentum are assembled and solved from the currently available pressure, density, mass fluxes and turbulence kinetic energy. Approximations of velocities $\mathbf{u}^{(1)}$ are thus, obtained.

6. **Corrector**

   The spray contributions to the gas are corrected and a new estimate of the pressure field $(p')^{(2)}$ is calculated. The mass fluxes and $\rho^{(2)}$ are updated and the gas velocities are corrected to yield $\mathbf{u}^{(2)}$. Then, the fuel vapour mass fraction and energy equations are assembled and solved to obtain $Y_{v,i}^{(2)}$ and $e^{(2)}$. $p_{cyl}^{(2)}$ is updated as in the predictor stage.

This step is repeated until the convergence criterion given in Section 5.3.2 is satisfied.

7. **Droplet/droplet interactions**

   The collisions among the droplets are calculated. The liquid phase properties are modified; however, the gas phase is not allowed to be affected by collisions in the current time step.

8. **Bulk adjustment**

   In order to remove possible inconsistencies that may arise during the corrections in the previous stage, the pressure and the density are adjusted in accord to the mass conservation and the perfect gas law.

9. **Turbulence calculation**

   The k and ε equations are assembled and solved. The effective viscosity is also updated.

All the field values obtained from the above sequence are denoted by the superscript 'n' and they represent the numerical solution of the governing equations at the time $t = t_0 + \Delta t$. These values are used as initial values of the next time step and the sequence is repeated until the required time is reached.

A detailed description of the solution algorithm is given next.

5.2.1 Bulk adjustment

The bulk adjustment stage estimates the average (bulk) properties, namely the cylinder pressure, p_{cyl} and density, ρ_{cyl}. Then, based on these averages, it adjusts the local pressure and density.

Average properties

The piston motion, valve flow and heat transfer arise pressure changes which are large compared to the changes induced by the flow field. In order to separate these large-scale changes from the smaller due to the flow field, the local pressure is decomposed into the average pressure and the relative one where the average pressure is calculated from overall conservation balances using a zero-dimensional analysis as follows.

The global calculation of the average properties, p_{cyl} and ρ_{cyl}, is based on the cylinder mass and enthalpy balances:

Mass:

$$\rho_{cyl}^{(1)} = \frac{\rho_{cyl}^o V_{cyl}^o - \dot{m}_v \Delta t}{V_{cyl}} \; ; \tag{5.2}$$

Enthalpy:

$$p_{cyl}^{(\prime)} = \frac{\left[\left(\frac{c_p}{R}\right)_{cyl} - 1\right] \overline{V}_{cyl} p_{cyl}^o + \left(\dot{Q}_b - e_v \dot{m}_v\right) \Delta t}{\left[\left(\frac{c_p}{R}\right)_{cyl} - 1\right] \overline{V}_{cyl} + \left(\frac{c_p}{R}\right)_{cyl} \left(V_{cyl} - V_{cyl}^o\right)} \, , \tag{5.3}$$

where $(c_p/R)_{cyl}$ is the volume-averaged of c_p/R defined by:

$$\left(\frac{c_p}{R}\right)_{cyl} = \frac{1}{V_{cyl}} \sum_{P=1}^{N_c} \frac{c_p(T_P)}{R_P} V_P \; . \tag{5.4}$$

Also, in Eqs. (5.2) and (5.3), $\dot{m}_v$ and e_v are the mass flow rate (negative $\dot{m}_v$ means inflow) and specific internal energy of the valve flow, respectively. Finally, $\dot{Q}_b$ stands for the total heat transfer rate at the cylinder surface and $\overline{V}_{cyl}$ is the average cylinder volume given by:

$$\overline{V}_{cyl} = \frac{V_{cyl}^o + V_{cyl}}{2} \; . \tag{5.5}$$

The first term of the numerator on the RHS in Eq. (5.3) represents the effect of the cylinder volume change and the second term the effects of the heat transfer and the valve flow on the bulk cylinder pressure.

Local corrections

Firstly, since the mesh has been moved and distorted, the droplets may no longer reside in the same cell as were found at the end of the previous time step. Therefore, the void fraction is recalculated and the density is updated as:

$$\rho_P^{(\prime)} = \frac{\rho_P^o}{\vartheta_P^o}\vartheta_P^{(\prime)} \; . \tag{5.6}$$

Then, due to the changes of the average density and pressure, as explained earlier, the local microscopic density and relative pressure are uniformly* adjusted in each cell $P = 1, 2..., N_c$ as:

$$\rho_P^{(1)} = \rho_P^{(\prime)} + \rho^+ \vartheta_P^{(\prime)} \; , \tag{5.7}$$

$$\left(p'_P\right)^{(1)} = \left(p'_P\right)^o + p^+ \; , \tag{5.8}$$

where the corrections, denoted by the superscript '+' are evaluated from the requirements for consistency between the overall and the individual field values:

$$\sum_{P=1}^{N_c} \rho_P^{(1)} V_P = \sum_{P=1}^{N_c} \left(\rho_P^{(\prime)} + \rho^+ \vartheta_P^{(\prime)}\right) V_P = \rho_{cyl}^{(1)} V_{cyl} \; , \tag{5.9}$$

$$\sum_{P=1}^{N_c} \left[p_{cyl}^{(\prime)} + \left(p'_P\right)^{(1)}\right] \vartheta_P^{(\prime)} V_P = \sum_{P=1}^{N_c} \left[p_{cyl}^{(\prime)} + \left(p'_P\right)^o + p^+\right] \vartheta_P^{(\prime)} V_P = p_{cyl}^{(\prime)} \sum_{P=1}^{N_c} \vartheta_P^{(\prime)} V_P \; . \tag{5.10}$$

Thus,

$$\rho^+ = \frac{\rho_{cyl}^{(1)}}{\vartheta_{cyl}^{(\prime)}} - \frac{1}{\vartheta_{cyl}^{(\prime)} V_{cyl}} \sum_{P=1}^{N_c} \rho_P^{(\prime)} V_P \; , \tag{5.11}$$

$$p^+ = -\frac{1}{\vartheta_{cyl}^{(\prime)} V_{cyl}} \sum_{P=1}^{N_c} \left(p'_P\right)^o \vartheta_P^{(\prime)} V_P \; , \tag{5.12}$$

where

$$\vartheta_{cyl}^{(\prime)} = \frac{1}{V_{cyl}} \sum_{P=1}^{N_c} \vartheta_P^{(\prime)} V_P \; . \tag{5.13}$$

The local gas temperature is updated using the perfect gas law:

$$T_P^{(\prime)} = \frac{\vartheta_P^{(\prime)} \left[p_{cyl}^{(\prime)} + \left(p'_P\right)^{(1)}\right]}{R_P \rho_P^{(1)}} \; . \tag{5.14}$$

*It should be emphasised that the microscopic and *not* the macroscopic density is uniformly adjusted because the gas mass change is distributed in the volume occupied by the gas and *not* the total volume.

The above values are used to update the specific internal energy of the gas and the effective viscosity:

$$e_P^{(\prime)} = e\left(T_P^{(\prime)},\, Y_{v,i,P}^o\right)\ , \tag{5.15}$$

$$\nu_{\mathit{eff},P} = \nu_{m,P} + C_\mu \frac{(k_P^o)^2}{\varepsilon_P^o}\ . \tag{5.16}$$

5.2.2 Predictor stage

The predictor stage consists of the spray predictor and the gas predictor as shown in Fig. 5.2. During the spray predictor, the spray equations are solved to determine the local void fraction, $\vartheta_P^{(1)}$ and the source terms which represent the spray contributions to the gas phase, $(S_m^d)_P^{(1)}$, $(S_{Y_{v,i}}^d)_P^{(1)}$, $(\mathbf{S}_{\mathcal{U}}^{\mathbf{u},d})_P^{(1)}$, $(S_{\mathcal{P}}^{\mathbf{u},d})_P^{(1)}$, $(S_{\mathcal{U}}^{e,d})_P^{(1)}$ and $(S_{\mathcal{P}}^{e,d})_P^{(1)}$. A subcycling time step is used to solve the spray equations during which the gas fields are kept *frozen*.

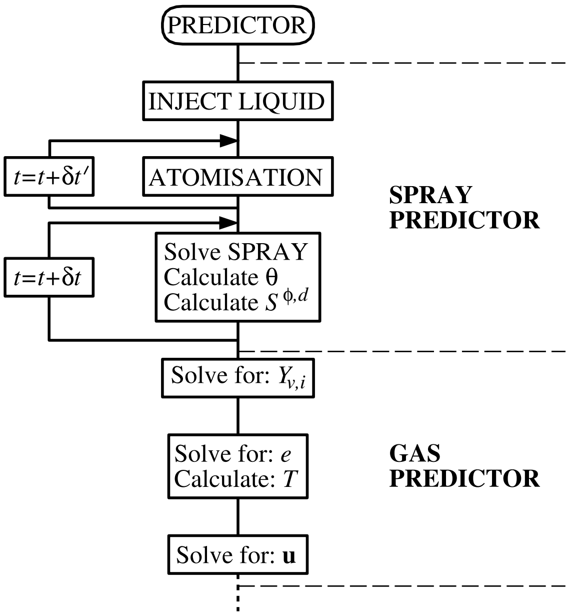

Figure 5.2: Flow chart of the predictor stage.

In the gas predictor, the coefficients matrices of the conservation equations for the fuel vapour mass fraction, energy and momentum are assembled and solved implicitly, including the void fraction and the spray source terms calculated in the spray predictor, as follows. The discretised fuel vapour mass fraction and energy equations, respectively, read:

$$\mathcal{A}_P^{Y_{v,i}} \left(Y_{v,i}\right)_P^{(1)} = \sum_N \mathcal{A}_N^{Y_{v,i}} \left(Y_{v,i}\right)_N^{(1)} + \left(b_P^{Y_{v,i}}\right)^{(1)} , \tag{5.17}$$

$$\mathcal{A}_P^e e_P^{(1)} = \sum_N \mathcal{A}_N^e e_N^{(1)} + \left(b_P^e\right)^{(1)} . \tag{5.18}$$

In high load cases (when a large amount of fuel is injected) and when the time step, Δt, is relatively large, the temporal changes of the void fraction may be large, especially in a fine mesh. Therefore, the pressure work term in the energy equation changes as well. However, at this stage this leads to inconsistent results because the velocity field has not been predicted yet. This could lead to unrealistic energy field resulting in numerical instability. To avoid this, the source term expressing the pressure work of the previous time step, given by Eq. (4.47), is used in the calculation of $(b_P^e)^{(1)}$, given by Eq. (4.42d). However, this term must be corrected by the new gas volume in order to be consistent with the other terms of Eq. (4.42). Thus,

$$\left(S_{\mathcal{U}}^e\right)_P^{(1)} = \frac{\vartheta_P^{(1)} V_P}{\vartheta_P^o V_P^o} \left(S_{\mathcal{U}}^e\right)_P^o . \tag{5.19}$$

Then, the local gas temperature is calculated from the internal energy via the inverse function:

$$T_P^{(1)} = e^{-1}\left(e_P^{(1)}, Y_{v,i,P}^{(1)}\right) . \tag{5.20}$$

The heat and mass transfer between the phases and the changes of the void fraction result in changes of the average cylinder pressure. Therefore, p_{cyl} is updated once again, based on the perfect gas law:

$$p_{cyl}^{(1)} = \frac{1}{\vartheta_{cyl}^{(1)} V_{cyl}} \sum_{P=1}^{N_c} \left(\rho V R T\right)_P^{(1)} , \tag{5.21}$$

where

$$\vartheta_{cyl}^{(1)} = \frac{1}{V_{cyl}} \sum_{P=1}^{N_c} \vartheta_P^{(1)} V_P . \tag{5.22}$$

The momentum equation is now solved to obtain a first estimate of velocities, $\mathbf{u}_P^{(1)}$:

$$\mathcal{A}_P^{\mathbf{u}} \mathbf{u}_P^{(1)} = \sum_N \mathcal{A}_N^{\mathbf{u}} \mathbf{u}_N^{(1)} + \mathbf{b}_P^{\mathbf{u}} + \left(\mathbf{S}_{\mathcal{U}}^{\mathbf{u},d}\right)_P^{(1)} - \left[V \vartheta^{(1)} \mathcal{N}\left(p'\right)^{(1)}\right]_P . \tag{5.23}$$

At the end of this stage, provisional values of all the variables have been obtained. However, the predicted velocity field does not necessarily satisfy the continuity equation. Consequently, new pressure and velocity fields have to be calculated until all the governing equations are satisfied to the required tolerance.

5.2.3 Corrector stage

The corrector stage comprises the correction of the spray and the gas field. The correction procedure is repeated, as illustrated in Fig. 5.3, until a convergence criterion is reached.

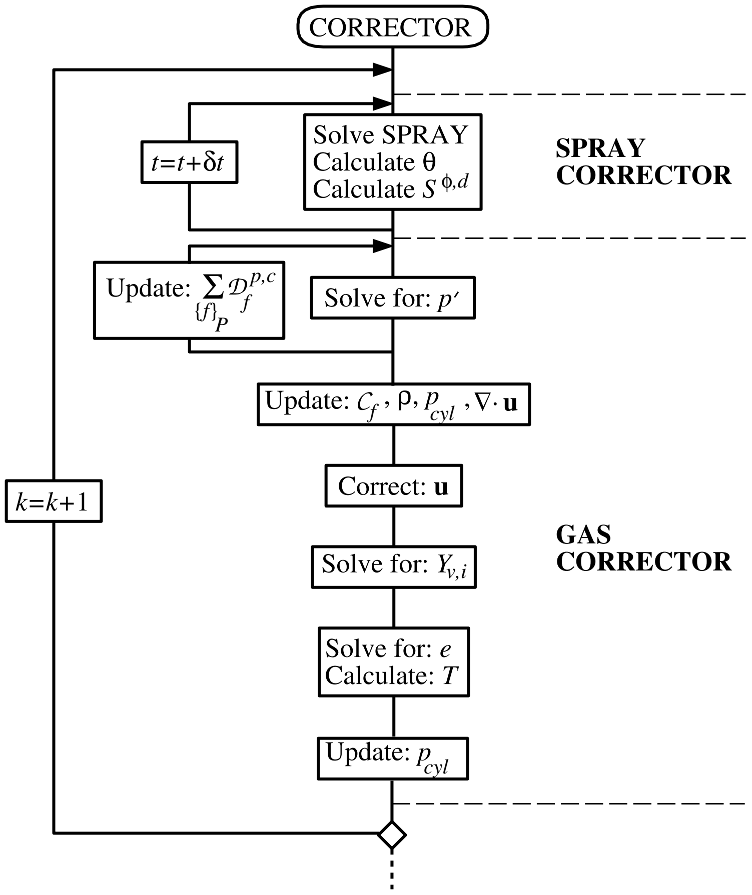

Figure 5.3: Flow chart of the corrector stage.

The iteration step (k), where $k = 2$ represents the first correction, starts with the correction of the spray field determining the corrected local void fraction, $\vartheta_P^{(k)}$

and the spray-related source terms, $(S_m^d)_P^{(k)}$, $(S_{Y_{v,i}}^d)_P^{(k)}$, $(\mathbf{S}_{\mathcal{U}}^{\mathbf{u},d})_P^{(k)}$, $(S_{\mathcal{P}}^{\mathbf{u},d})_P^{(k)}$, $(S_{\mathcal{U}}^{e,d})_P^{(k)}$ and $(S_{\mathcal{P}}^{e,d})_P^{(k)}$. However, in high load cases and when a relatively large time step Δt is used, the spray source terms become large compared to the other terms of the general transport equation, Eq. (4.32), because the void fraction, which multiplies all the terms except the spray source terms is small and the only term which is not multiplied by the void fraction, i.e. the term with the old time value, is divided by the time step which as mentioned above is relatively large. Consequently, the spray source terms play an important role in the gas equations. In addition, the spray field might change substantially between two successive correctors due to the large time step, leading to the possibility that the parcels move to different cells. Since the spray source terms are not smooth functions but Dirac functions taking values based on the parcel positions, this can affect the convergence of the flow field. In order to reduce the discrepancies of the source terms between two successive correctors and consequently, improve the convergence of the code, underrelaxation factors, F_u, are introduced in the spray source terms, as follows:

$$\left(S^{\phi,d}\right)_P^{(k)} = F_u \left(S^{\phi,d}\right)_P^{(k)} + (1 - F_u) \left(S^{\phi,d}\right)_P^{(k-1)} . \tag{5.24}$$

In order to assess the effect of these underrelaxation factors, a high load case is set up. A cylindrical pressure chamber is used with pressure $50\,bar$ and temperature $800\,K$. Six nozzles with diameter $200\,\mu m$ are located very close to the chamber axis on the top wall injecting downward. During the entire run, $36\,mg$ of n-heptane of temperature $300\,K$, equally distributed among the six nozzles, is injected according to the simple volumetric flow rate schedule, shown in Fig. 5.4. The time step is $\Delta t = 10\,\mu s$ and three different values of F_u are used. Fig. 5.5 presents the normalised residual (see §5.3.2) of the pressure equation, given next by Eq. (5.26), at the time $t = 60\,\mu s$. At this time the minimum void fraction in the last corrector stage is $\vartheta^{(30)} = 59\,\%$ and the maximum Courant number*, Co, defined by:

$$Co = \frac{|\mathbf{u}^o|\Delta t}{\Delta x} , \tag{5.25}$$

*Explicit differencing is known to suffer from a stability-imposed numerical time step restriction [228] expressed by the Courant number. For example, in an unsteady one-dimensional convection problem the stability of an explicit scheme is only ensured with the Courant-Friedrich-Lewy condition $Co \leq 1$ [35, 134].

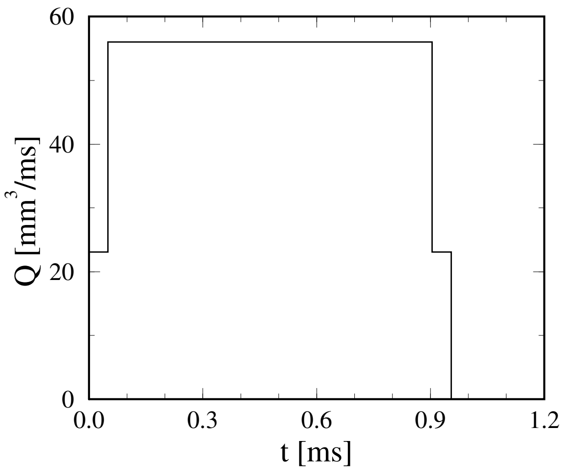

Figure 5.4: Volumetric flow rate.

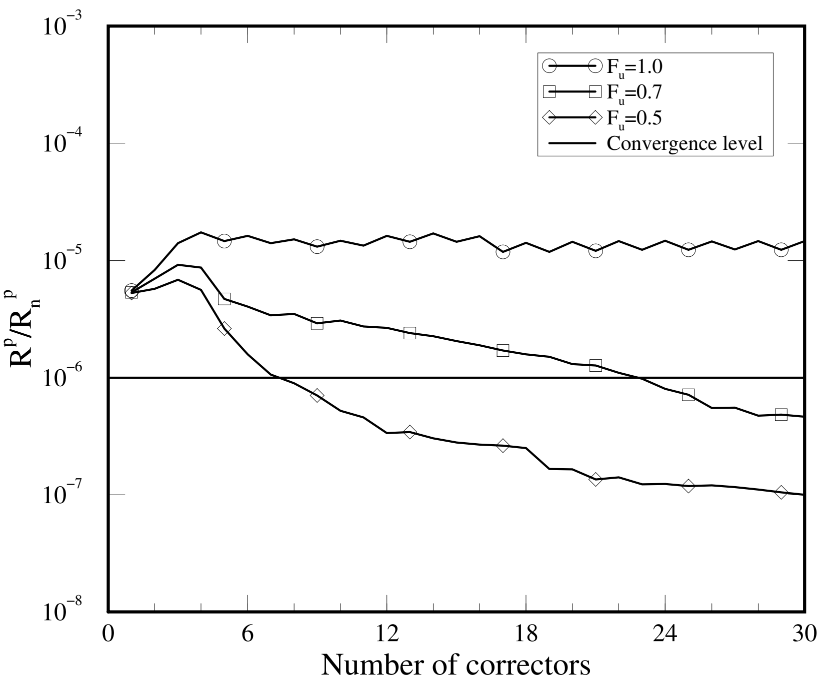

Figure 5.5: Normalised residual of the pressure equation at $t = 60\,\mu s$.

where Δx is a characteristic length of the cell, is $Co = 0.83$. The convergence criterion is set to $\lambda = 10^{-6}$ (see §5.3.2). In the case in which underrelaxation factors are not used (i.e. $F_u = 1.0$), convergence is unreachable since an oscillation of the residual takes place. In contrast, when underrelaxation is used, convergence is obtained and notably, reducing F_u speeds convergence up. An extreme case is depicted in Fig. 5.6, which presents the normalised residual of the pressure equation

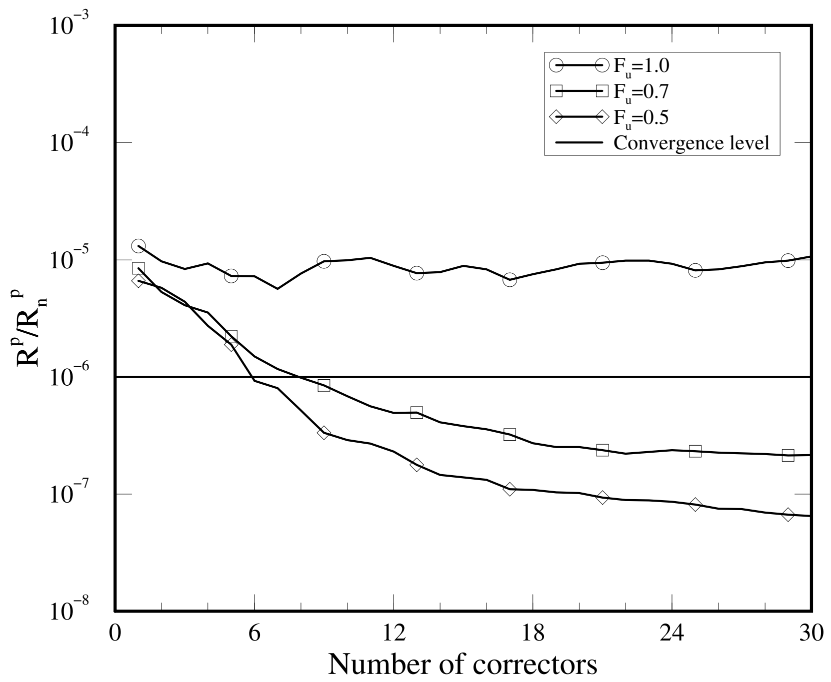

Figure 5.6: Normalised residual of the pressure equation at $t = 80\,\mu s$.

for the same case as above but at a later time, $t = 80\,\mu s$. At this time the minimum void fraction is extremely low, $\vartheta^{(30)} = 14\,\%$ and the maximum Courant number is $Co = 2.38$. Again*, it is clear that the case without underrelaxation does not converge, whereas the other two cases show that underrelaxation guarantees convergence even for extreme cases. It should be noted that for low load cases, in which convergence can be obtained even without underrelaxation, small values of F_u slow

*It should be noted that the residuals in the first corrector in Fig. 5.6 are not the same for the three cases because in earlier time ($t = 60\,\mu s$, see Fig. 5.5) convergence was not achieved for $F_u = 1.0$ and therefore, the initial fields for $t = 80\,\mu s$ are different.

down the convergence rate. Therefore, as a compromise in this study, $F_u = 0.5$ is used in order to ensure convergence without substantially increasing the number of correctors in low-load cases.

After the spray field is corrected, the gas corrector sequence starts, in which the pressure correction p' is calculated by solving the pressure equation, derived from the combination of the mass and momentum conservation equations*:

$$\mathcal{A}_P^p \left(p'\right)_P^{(k)} = \sum_N \mathcal{A}_N^p \left(p'\right)_N^{(k)} + \left(b_P^p\right)^{(k)} \ , \tag{5.26a}$$

where

$$\mathcal{A}_P^p = \sum_N \mathcal{A}_N^p + \frac{1}{\Delta t} \vartheta_P^{(k)} \left(\frac{V}{RT}\right)_P^{(k-1)} \ , \tag{5.26b}$$

$$\mathcal{A}_N^p = \left(\mathcal{D}_f^{p,n}\right)^{(k-1)} \ , \tag{5.26c}$$

$$\begin{aligned} \left(b_P^p\right)^{(k)} = & - \sum_{\{f\}_P} \mathcal{S}_f \cdot \rho_f^{(k-1)} \left(\mathcal{H}^{(k-1)} - \mathbf{u}_b\right)_f \\ & + \left(S_m^d\right)_P^{(k)} - \frac{1}{\Delta t} \vartheta_P^{(k)} \left(\frac{V p_{cyl}}{RT}\right)_P^{(k-1)} \\ & + \frac{(\rho V)_P^o}{\Delta t} + \sum_{\{f\}_P} \mathcal{D}_f^{p,c} \ . \end{aligned} \tag{5.26d}$$

Here $\mathcal{H}^{(k-1)}$ is defined as:

$$\mathcal{H}_P^{(k-1)} = \frac{1}{\mathcal{A}_P^{\mathbf{u}}} \left[\sum_N \mathcal{A}_N^{\mathbf{u}} \mathbf{u}_N^{(k-1)} + \left(\mathbf{b}_P^{\mathbf{u}}\right)^{(k-1)} + \left(\mathbf{S}_{\mathcal{U}}^{\mathbf{u},d}\right)_P^{(k)} \right] \ . \tag{5.27}$$

The convective fluxes are updated by:

$$\mathcal{C}_f^{(k-1)} = \mathcal{S}_f \cdot \left\{ \rho_f^{(k-1)} \left[\mathcal{H}^{(k-1)} - \mathbf{u}_b - \frac{1}{\mathcal{A}_P^{\mathbf{u}}} \vartheta^{(k)} V \mathcal{N} \left(p'\right)^{(k)} \right]_f \right\} \ . \tag{5.28}$$

Next, the density is updated from the continuity equation, (4.34), here rewritten as:

$$\rho_P^{(k)} = \frac{\Delta t}{V_P} \left[\frac{(\rho V)_P^o}{\Delta t} + \left(S_m^d\right)_P^{(k)} - \sum_{\{f\}_P} \mathcal{C}_f^{(k-1)} \right] \ . \tag{5.29}$$

Then, the velocity field is corrected by the relation:

$$\mathbf{u}_P^{(k)} = \left(\frac{\rho^{(k-1)}}{\rho^{(k)}}\right)_P \left[\mathcal{H}_P^{(k-1)} - \frac{1}{\mathcal{A}_P^{\mathbf{u}}} \vartheta_P^{(k)} \sum_{\{f\}_P} \mathcal{S}_f \left(p'\right)_f^{(k)} \right] \ . \tag{5.30}$$

*The derivation of the pressure equation is given in Appendix D.1.

Finally, the fuel vapour mass fraction and the energy conservation equations are assembled and solved:

$$\mathcal{A}_P^{Y_{v,i}} \left(Y_{v,i}\right)_P^{(k)} = \sum_N \mathcal{A}_N^{Y_{v,i}} \left(Y_{v,i}\right)_N^{(k)} + \left(b_P^{Y_{v,i}}\right)^{(k)} , \tag{5.31}$$

$$\mathcal{A}_P^e e_P^{(k)} = \sum_N \mathcal{A}_N^e e_N^{(k)} + \left(b_P^e\right)^{(k)} , \tag{5.32}$$

with coefficient matrices calculated from the latest available values.

5.2.4 Turbulence calculation

At the end of the corrector loop, all the variables fields satisfy the governing equations apart from the turbulence equations. The k and ε equations are solved in their own predictor-corrector sequence, in which care is taken to allow for the strong coupling between these equations via their source terms. In particular, the system of the two coupled k-ε equations is solved for each cell* as follows. The description given below is divided into the cases of internal cells and of cells adjacent to the wall because of their different treatment. This predictor-corrector sequence proposed by Theodoropoulos [288] and modified by Kralj [171] to account for the additional spray source terms is adopted in this study.

Turbulence predictor

In the turbulence predictor stage, identified by the superscript '$(j = 1)$', the source terms of k and ε equations are evaluated based on the old time values of k and ε and the current values of all the other variables involved. Then, their respective transport equations are assembled and solved:

$$\mathcal{A}_P^k k_P^{(1)} = \sum_N \mathcal{A}_N^k k_N^{(1)} + \left(b_P^k\right)^{(1)} , \tag{5.33}$$

$$\mathcal{A}_P^\varepsilon \varepsilon_P^{(1)} = \sum_N \mathcal{A}_N^\varepsilon \varepsilon_N^{(1)} + \left(b_P^\varepsilon\right)^{(1)} . \tag{5.34}$$

*Note that each of all the other transport equations is solved, as described previously, in the whole space domain before the procedure moves to another equation. Here, both k and ε equations are solved cell by cell.

The corrector sequence iteratively corrects the sources $(b_P^k)^{(1)}$ and $(b_P^\varepsilon)^{(1)}$ until the required tolerance is reached.

Algebraic turbulence corrector for internal cells

Multiplying the discretised k equation, Eq. (4.50), by $\varepsilon_P^{(j)}$ and the discretised ε equation, Eq. (4.53), by $k_P^{(j)}$ the following system of equations is obtained for the j^{th} corrector ($j > 1$) (Theodoropoulos [288]):

$$a_0^k k_P^{(j)} \varepsilon_P^{(j)} = a_1^k \left(\varepsilon_P^{(j)}\right)^2 + a_2^k \varepsilon_P^{(j)} + a_3^k k_P^{(j)} \ , \tag{5.35}$$

$$a_0^\varepsilon k_P^{(j)} \varepsilon_P^{(j)} = a_1^\varepsilon \left(\varepsilon_P^{(j)}\right)^2 + a_2^\varepsilon k_P^{(j)} \ . \tag{5.36}$$

The coefficients are given by:

$$\begin{aligned} a_0^k = & \sum_N \mathcal{A}_N^k + \frac{(\rho V)_P^o}{\Delta t} - \frac{1}{k_P^{(j-1)}} \min\left(0, \sum_{\{f\}_P} \mathcal{D}_f^{k,c}\right) \\ & + \frac{2}{3} C_\mu \left[\frac{\rho V k^{(j-1)}}{\varepsilon^{(j-1)}} (\mathcal{N} \cdot \mathbf{u})^2\right]_P \\ & - \frac{1}{k_P^{(j-1)}} \min\left[0, \left(\dot{S}_k^d\right)_P\right] + \left(S_m^d\right)_P \ , \end{aligned} \tag{5.37a}$$

$$a_1^k = \left[\frac{2}{3} \frac{k_P^{(j-1)}}{\varepsilon_P^{(j-1)}} \min(0, \mathcal{N} \cdot \mathbf{u})_P - 1\right] (\rho V)_P \ , \tag{5.37b}$$

$$\begin{aligned} a_2^k = & \sum_N \mathcal{A}_N^k k_N^{(j-1)} + \frac{(\rho V)_P^o}{\Delta t} k_P^o + \max\left(0, \sum_{\{f\}_P} \mathcal{D}_f^{k,c}\right) \\ & + \frac{2}{3} \left(\rho V k^{(j-1)}\right)_P \max(0, \mathcal{N} \cdot \mathbf{u})_P + \left(S_{\mathcal{U}}^k\right)_P^{\mathrm{S}} + \max\left[0, \left(\dot{S}_k^d\right)_P\right] \ , \end{aligned} \tag{5.37c}$$

$$a_3^k = C_\mu \left(\rho V k^{(j-1)}\right)_P \left\{\left[\mathcal{N}\mathbf{u} + (\mathcal{N}\mathbf{u})^{\mathrm{T}}\right] : \mathcal{N}\mathbf{u}\right\}_P \ ; \tag{5.37d}$$

and

$$\begin{aligned} a_0^\varepsilon = & \sum_N \mathcal{A}_N^\varepsilon + \frac{(\rho V)_P^o}{\Delta t} - \frac{1}{\varepsilon_P^{(j-1)}} \min\left(0, \sum_{\{f\}_P} \mathcal{D}_f^{\varepsilon,c}\right) \\ & + \frac{2}{3} C_{\varepsilon 1} C_\mu \left[\rho V \frac{k^{(j-1)}}{\varepsilon^{(j-1)}} \left(\mathcal{N} \cdot \mathbf{u}^2\right)\right]_P \\ & - C_{\varepsilon 4} \frac{1}{k_P^{(j-1)}} \min\left[0, \left(\dot{S}_k^d\right)_P\right] + \left(S_m^d\right)_P \ , \end{aligned} \tag{5.37e}$$

$$a_1^\varepsilon = \left(C_{\varepsilon 3} - \frac{2}{3}C_{\varepsilon 1}\right)\left[\rho V \frac{k^{(j-1)}}{\varepsilon^{(j-1)}} \max\left(0, \mathcal{N}\cdot\mathbf{u}\right)\right]_P - C_{\varepsilon 2}\left(\rho V\right)_P \ , \tag{5.37f}$$

$$\begin{aligned} a_2^\varepsilon = & \sum_N \mathcal{A}_N^\varepsilon \varepsilon_N^{(j-1)} + \frac{(\rho V)_P^o}{\Delta t}\varepsilon_P^o + \max\left(0, \sum_{\{f\}_P} \mathcal{D}_f^{\varepsilon,c}\right) \\ & + C_{\varepsilon 1} C_\mu \left(\rho V k^{(j-1)}\right)_P \left\{\left[\mathcal{N}\mathbf{u} + (\mathcal{N}\mathbf{u})^{\mathrm{T}}\right] : \mathcal{N}\mathbf{u}\right\}_P \\ & + \left(C_{\varepsilon 3} - \frac{2}{3}C_{\varepsilon 1}\right)\left(\rho V \varepsilon^{(j-1)}\right)_P \min\left(0, \mathcal{N}\cdot\mathbf{u}\right)_P \\ & + \left(S_\mathcal{U}^\varepsilon\right)_P^{\mathrm{S}} + C_{\varepsilon 4}\frac{\varepsilon_P^{(j-1)}}{k_P^{(j-1)}} \max\left[0, \left(\dot{S}_k^d\right)_P\right] \ . \end{aligned} \tag{5.37g}$$

Theodoropoulos [288] showed that both equations (5.35) and (5.36) represent hyperbolas in the $k-\varepsilon$ space and they always have a non-trivial single positive solution obtained from the combination of these equations which results in:

$$k_P^{(j)} = \frac{A_2^k \varepsilon_P^{(j)} + \left(A_1^k - A_1^\varepsilon\right)\left(\varepsilon_P^{(j)}\right)^2}{A_2^\varepsilon - A_3^k} \ , \tag{5.38}$$

where

$$A_i^\phi = \frac{a_i^\phi}{a_0^\phi} \ , \quad \text{for} \begin{cases} i = 1, 2, 3, & \text{for } \phi = k \ , \\ i = 1, 2, & \text{for } \phi = \varepsilon \ . \end{cases} \tag{5.39}$$

Substitution of this equation into Eq. (5.35) yields:

$$\varepsilon_P^{(j)}\left[B_1\left(\varepsilon_P^{(j)}\right)^2 + B_2 \varepsilon_P^{(j)} + B_3\right] = 0 \ , \tag{5.40}$$

where

$$B_1 = A_1^k - A_1^\varepsilon \ , \tag{5.41a}$$

$$B_2 = A_2^k - A_1^k A_2^\varepsilon + A_3^k A_1^\varepsilon \ , \tag{5.41b}$$

$$B_3 = -A_2^k A_2^\varepsilon \ . \tag{5.41c}$$

The positive root of this equation is given by (Theodoropoulos [288]):

$$\varepsilon_P^{(j)} = \frac{-B_2 + \sqrt{B_2^2 - 4B_1 B_3}}{2B_1} \ . \tag{5.42}$$

Algebraic turbulence corrector for near-wall cells

For cells adjacent to the wall, ε is calculated via the algebraic expression (4.83), replacing the corresponding transport equation for ε, which for the j^{th} turbulence corrector reads:

$$\varepsilon_P^{(j)} = C_\mu^{3/4} \frac{\left(k_P^{(j)}\right)^{3/2}}{\kappa y_P} \ . \tag{5.43}$$

Although k is still calculated from Eq. (4.50), for cells adjacent to the wall, the coefficients are modified because the turbulent viscosity in this region is calculated based on the formula (4.79).

If the node lies within the viscous sublayer, i.e. $y_P^+ \leq y_c^+$, Eqs. (4.50) and (4.79) can be rearranged into (Theodoropoulos [288]):

$$a_{v,1}^k \left(k_P^{(j)}\right)^2 + a_{v,2}^k k_P^{(j)} + a_{v,3}^k = 0 \ , \tag{5.44a}$$

where

$$a_{v,1}^k = C_\mu \left(\frac{\rho V}{\nu_m}\right)_P \ , \tag{5.44b}$$

$$\begin{aligned} a_{v,2}^k = & \sum_N \mathcal{A}_N^k + \frac{(\rho V)_P^o}{\Delta t} - \frac{1}{k_P^{(j-1)}} \min\left(0, \sum_{\{f\}_P} \mathcal{D}_f^{k,c}\right) \\ & + \frac{2}{3}\left[\nu_m \rho V \frac{(\mathcal{N}\cdot\mathbf{u})^2}{k^{(j-1)}}\right]_P - \frac{2}{3}(\rho V)_P \min(0, \mathcal{N}\cdot\mathbf{u})_P \\ & - \frac{1}{k_P^{(j-1)}} \min\left[0, \left(\dot{S}_k^d\right)_P\right] + \left(S_m^d\right)_P \ , \end{aligned} \tag{5.44c}$$

$$\begin{aligned} a_{v,3}^k = -\Bigg\{ & \sum_N \mathcal{A}_N^k k_N^{(j-1)} + \frac{(\rho V)_P^o}{\Delta t} k_P^o + \max\left(0, \sum_{\{f\}_P} \mathcal{D}_f^{k,c}\right) \\ & + \left\{\nu_m \rho V \left[\mathcal{N}\mathbf{u} + (\mathcal{N}\mathbf{u})^{\mathrm{T}}\right] : \mathcal{N}\mathbf{u}\right\}_P \\ & + \frac{2}{3}\left(\rho V k^{(j-1)}\right)_P \max(0, \mathcal{N}\cdot\mathbf{u})_P \\ & + \left(S_{\mathcal{U}}^k\right)_P^{\mathrm{S}} + \max\left[0, \left(\dot{S}_k^d\right)_P\right] \Bigg\} \ . \end{aligned} \tag{5.44d}$$

The only positive root of Eq. (5.44a) is given by:

$$k_P^{(j)} = \frac{-a_{v,2}^k + \sqrt{\left(a_{v,2}^k\right)^2 - 4 a_{v,1}^k a_{v,3}^k}}{2 a_{v,1}^k} \ . \tag{5.45}$$

Then, the corresponding ε is calculated from Eq. (5.43).

If the node lies in the inertial sublayer, i.e. $y_P^+ > y_c^+$, again considering Eq. (4.79), the k equation, Eq. (4.50), reads:

$$a_{i,1}^k \left(q_P^{(j)}\right)^2 + a_{i,2}^k q_P^{(j)} + a_{i,3}^k = 0 \ , \tag{5.46a}$$

where

$$q_P^{(j)} = \left(k_P^{(j)}\right)^{1/2} \ , \tag{5.46b}$$

$$\begin{aligned} a_{i,1}^k = &\sum_N \mathcal{A}_N^k + \frac{(\rho V)_P^o}{\Delta t} - \frac{1}{k_P^{(j-1)}} \min\left(0, \sum_{\{f\}_P} \mathcal{D}_f^{k,c}\right) \\ &- \frac{2}{3} (\rho V)_P \min(0, \mathcal{N}\cdot\mathbf{u})_P \\ &+ \left[\frac{C_\mu^{3/4} \ln(Ey^+)}{\kappa y} \rho V \left(k^{(j-1)}\right)^{1/2}\right]_P \\ &- \frac{1}{k_P^{(j-1)}} \min\left[0, \left(\dot{S}_k^d\right)_P\right] + \left(S_m^d\right)_P \ , \end{aligned} \tag{5.46c}$$

$$\begin{aligned} a_{i,2}^k = &\frac{2}{3}\left[\frac{C_\mu^{1/4}\kappa y}{\ln(Ey^+)} \rho V (\mathcal{N}\cdot\mathbf{u})^2\right]_P \\ &- \left\{\frac{C_\mu^{1/4}\kappa y}{\ln(Ey^+)} \rho V \left[\mathcal{N}\mathbf{u} + (\mathcal{N}\mathbf{u})^{\mathrm{T}}\right] : \mathcal{N}\mathbf{u}\right\}_P \ , \end{aligned} \tag{5.46d}$$

$$\begin{aligned} a_{i,3}^k = - &\left\{\sum_N \mathcal{A}_N^k k_N^{(j-1)} + \frac{(\rho V)_P^o}{\Delta t} k_P^o + \max\left(0, \sum_{\{f\}_P} \mathcal{D}_f^{k,c}\right)\right. \\ &+ \frac{2}{3}\left(\rho V k^{(j-1)}\right)_P \max(0, \mathcal{N}\cdot\mathbf{u})_P \\ &\left. + \left(S_{\mathcal{U}}^k\right)_P^{\mathrm{S}} + \max\left[0, \left(\dot{S}_k^d\right)_P\right]\right\} \ . \end{aligned} \tag{5.46e}$$

The positive root of Eq. (5.46a) is given by:

$$q_P^{(j)} = \frac{-a_{i,2}^k + \sqrt{\left(a_{i,2}^k\right)^2 - 4a_{i,1}^k a_{i,3}^k}}{2a_{i,1}^k} \ . \tag{5.47}$$

Now, $k_P^{(j)}$ and $\varepsilon_P^{(j)}$ can be calculated using Eqs. (5.46b) and (5.43), respectively.

Summary of the turbulence predictor-corrector algorithm

In the predictor stage, k and ε are calculated from Eqs. (5.33) and (5.34). Then, in the corrector stage, iteration over the following steps is performed for each cell P

until convergence has been reached:

1. Calculate coefficients A_i^{ϕ} and B_i from Eqs. (5.39) and (5.41), respectively.
2. Calculate $\varepsilon_P^{(j)}$ from Eq. (5.42) or Eq. (5.43) depending on the cell type (internal or adjacent to the wall).
3. Calculate $k_P^{(j)}$ from Eq. (5.38) or Eq. (5.45) or Eqs. (5.46b) and (5.47) depending on the cell type and for cells adjacent to the wall, on the node distance from the wall as well.
4. If not converged return to step 1.

Note that in the above algebraic equations the cross diffusion terms of the k and ε transport equations are omitted because the experience of the author's predecessors shows that this improves the convergence of this iterative scheme with an acceptable loss of accuracy (Leskovšek [186]).

5.3 Solution of linear algebraic equations

Many different methods have been proposed in the literature for solving a system of simultaneous linear algebraic equations such as the resultant system of the discretised and linearised transport equations. The choice of method depends on the characteristics of the coefficient matrix $\mathbf{A}^{\phi}$ in Eq. (4.33). Reid [240] proposed the conjugate gradient method (CG) to be the optimum for solving a system of equations for which the coefficient matrix $\mathbf{A}^{\phi}$ is sparse, asymmetric and strongly diagonally dominant.

5.3.1 Conjugate gradient method

The CG method was proposed by Hestenes and Stiefel [130] to solve a symmetric system of N_c linear equations. The procedure starts with an arbitrary solution and is able to find the *exact* solution in at most N_c iterations. Many different methods have been developed to extend the CG method to asymmetric systems. The bi-conjugate gradient method (BiCG) of Fletcher [97] is used in this study.

In a typical CFD calculation where N_c is of the order of $10^4 - 10^5$ the number of iterations could be very large and therefore, a technique must be applied to reduce the number of iterations and render the method efficient. The convergence rate depends on the spectral radius and the dispersion of the eigenvalues of the matrix $\mathbf{A}^\phi$. Thus, by reducing the spectral radius or the *spectral condition number*, being the ratio of the largest to the smallest eigenvalue, the convergence rate increases. This is achieved by preconditioning which transforms the linear system into an equivalent one with reduced spectral condition number.

In this study, the incomplete Cholesky decomposition (Kershaw [162]) applied to the CG method, is used for solving the pressure equation which is symmetric, while for all the other transport equations, the BiCG method with diagonal preconditioning is used. For more details on the methods the reader is referred to Theodoropoulos [288] who implemented the solvers in SPEED code and to Leskovšek [186].

5.3.2 Convergence criteria

At each time step three repetitive cycles can be distinguished in the present solution procedure. The repetitive correction sequence is required to resolve the non-linearities in the system and determine the number of corrector steps in the LONG-PISO algorithm. The non-orthogonal iteration is employed in solving the pressure correction equation to improve the convergence rate of the outer iteration. The inner iteration is required to solve individual equation sets.

In the present study the convergence of the inner iteration is assumed to be reached when the normalised sum over all cells of the absolute residual, R^ϕ, defined as:

$$R^\phi = \sum_{P=1}^{N_c} |R_P^\phi| \,, \tag{5.48}$$

where

$$R_P^\phi = \sum_N \mathcal{A}_N^\phi \phi_N + b_P^\phi - \mathcal{A}_P^\phi \phi_P \; , \tag{5.49}$$

decreases below a prespecified small level λ from its initial value at the current time step (Begleris [35]):

$$\frac{R^\phi}{R_n^\phi} < \lambda \; . \tag{5.50}$$

The appropriate value of λ depends on the choice of the normalisation factor and experience. In the present study $\lambda = 10^{-7}$ has been used for all equations.

The normalisation factors R_n^ϕ in Eq. (5.50) are taken to be proportional to a characteristic rate of change of the total mass in the cylinder, m_{cyl} and some reference value of the property, ϕ_{ref}:

$$R_n^\phi = \frac{m_{cyl}}{\tau_{ref}} \phi_{ref} \; . \tag{5.51}$$

The reference time scale τ_{ref} is taken to be equal to the computational time step Δt. The choice of ϕ_{ref} depends on ϕ. For the momentum equations u_{ref} is chosen to be the mean piston speed* (Theodoropoulos [288]). For the pressure equation the characteristic mass flow rate already reflects the characteristic time scale of the pressure change and therefore, $p_{ref} \equiv 1$† [288]. The reference specific internal energy is taken to be $e_{ref} = c_v(\Phi, T_{ref})T_{ref}$ [288], where T_{ref} is assumed to be the normal temperature, i.e. $300\,K$ and Φ is the equivalence ratio of the mixture, based on the total fuel mass. Thus, for a fuel of N components, it reads:

$$\Phi = \frac{Y_v}{Y_{v,s}} = \frac{\left(\sum_{i=1}^{N} m_{v,i}/m_{air} \right)}{\left(\sum_{i=1}^{N} m_{v,i}/m_{air} \right)_s} \; , \tag{5.52}$$

where Y_v is the fuel/air mass ratio and the subscript 's' denotes the stoichiometric value. The fuel reference concentration, $Y_{v,ref}$, is assumed to be the same for all the fuel components and is taken to be the stoichiometric fuel/air mass ratio, $Y_{v,s}$.

*In cases of stationary geometries, which are considered in this study (see Chapter 6), u_{ref} is set to $3\,m/s$. This value is of the order of mean piston velocities in engine cases.

†p_{ref} should not be confused with the reference or cylinder average pressure p_{cyl} introduced in Section 5.2.

The turbulence kinetic energy reference value is assumed to be $k_{ref} = u_{ref}^2$ and its dissipation rate $\varepsilon_{ref} = k_{ref}^{3/2}/0.1\,L_{ref}$, where the reference length scale is taken to be a characteristic dimension of the cylinder, given by $L_{ref} = V_{cyl}^{1/3}$ (Kralj [171]). Table 5.1 shows all the abovementioned normalisation factors.

Table 5.1: Normalisation factors for transport equation residuals.

ϕ	R_n^ϕ
$\mathbf{u}$	$u_{ref}\dfrac{m_{cyl}}{\tau_{ref}}$
p'	$\dfrac{m_{cyl}}{\tau_{ref}}$
e	$c_v(\Phi, T_{ref})T_{ref}\dfrac{m_{cyl}}{\tau_{ref}}$
$Y_{v,i}$	$Y_{v,s}\dfrac{m_{cyl}}{\tau_{ref}}$
k	$u_{ref}^2\dfrac{m_{cyl}}{\tau_{ref}}$
ε	$\dfrac{u_{ref}^3}{0.1V_{cyl}^{1/3}}\dfrac{m_{cyl}}{\tau_{ref}}$

The convergence criteria for the non-orthogonal and LONG-PISO iteration loops are both based on the absolute residual sum in the pressure equation at the beginning of each corrector step. In the k^{th} corrector iteration, convergence is taken to be reached when the following condition is satisfied:

$$\frac{\left(R^{p'}\right)^{(k)}}{R_n^{p'}} < \lambda_c \ , \tag{5.53}$$

where the convergence tolerance is set to $\lambda_c = 10\lambda = 10^{-6}$.

The convergence criteria for the calculation of the turbulence parameters are taken to be (Theodoropoulos [288]):

$$\left(r^\phi\right)^{(j)} < \lambda_t \ , \quad \phi = k,\, \varepsilon \ , \tag{5.54}$$

where $\lambda_t = 10^{-3}$ [171] and the normalised residuals are defined as [171, 288]:

$$\left(r^\phi\right)^{(j)} = \frac{1}{N_c}\sum_{P=1}^{N_c}\frac{\phi_P^{(j)} - \phi_P^{(j-1)}}{\max\left(\phi_P^{(j)},\, \phi_P^{(j-1)}\right)} \ , \quad \phi = k,\, \varepsilon \ . \tag{5.55}$$

5.4 Closure

In this chapter, the solution procedure for assembling and solving the system of the discretised algebraic equations has been presented. The procedure comprises three main stages described in Section 5.2. Firstly, a global adjustment to the cylinder thermodynamic properties is performed. Then, a predictor-corrector sequence, which incorporates the spray equations as well, is applied to all the gas variables apart from the turbulence parameters. The latter are calculated at the end of the corrector sequence in their own predictor-corrector according to the method of Theodoropoulos [288].

The systems of the algebraic equations for all the gas variables are solved by the BiCG method with diagonal factorisation apart from the pressure equation which is solved by the CG solver with incomplete Cholesky decomposition as explained in Section 5.3. Finally, the convergence criteria have been discussed in §5.3.2.

With this chapter the numerical solution of the gas and spray equations has been completed. The next chapter will present parametric and validation studies to assess the presented methodology and the various submodels.

Chapter 6

Validation

6.1 Introduction

The present chapter deals with the application of the complete mathematical model for the gas and spray to various test cases for which experimental data are available, in order to assess its validity.

Four test cases will be considered. The first one relates to the evaporation of single droplets. Obviously, in this test case, the evaporation process is isolated and therefore, it is suitable for detailed investigation of this particular process without the influence of other physical processes, described in Chapter 3. The experimental results have been obtained at Centre National de la Recherche Scientifique, Orleans and Université d' Orléans, Orleans by Gökalp *et al.* [100], Birouk [42] and Birouk *et al.* [43]. These consist of measurements of the size of droplets exposed in an air stream at atmospheric pressure and temperatures up to $449\,K$. In these experiments, single droplets of pure n-heptane and n-decane were used with initial diameter $1.3\,mm$. Also, a bi-component fuel combining the abovementioned components was employed. This test case is exploited here to investigate the performance of three different Nusselt and Sherwood correlations, as discussed in Section 3.6, in order to choose the most appropriate for Diesel spray calculations. Also, comparisons are performed using the infinite, finite and effective conductivity model versions, as presented in §3.6.2. Finally, the combined energy and diffusion equations are solved for the bi-component fuel.

The second test case is pulsed injection under atmospheric conditions. The investigation of this case commences with sensitivity studies of the mesh, time step and parcel introduction rate. Then, the experimental results of Paál [227], which comprise spray penetration, tip and droplet velocities and Sauter mean diameter at three locations, are used to examine the performance of various spray submodels. In particular, the Huh and MPI atomisation models, presented in Section 3.3, are considered first. Then, results using the drag coefficient correlation for distorted droplets are compared against those using a spherical droplet correlation (see Section 3.5). Also, the performance of the Reitz-Diwakar, Pilch-Erdman and Hsiang-Faeth breakup models, described in Section 3.7, are examined. Finally, the effect of collision is also investigated.

The third test case concerns pulsed injection in a constant-volume pressure chamber under conditions similar to those prevailing in Diesel engines. The experimental results have been obtained at Rheinisch Westfälische Technische Hochschule (RWTH), Aachen, by Koss *et al.* [168, 169] and they comprise liquid and vapour penetration and fuel vapour mass fraction at six locations. As in the previous test case, this one also starts with sensitivity studies of the mesh, time step and parcel introduction rate. Then, comparisons between the infinite, finite and effective conductivity treatments are presented. Investigation of the performance of the two drag coefficient correlations and the two atomisation models is also considered.

The final test case deals with a real Diesel engine, namely a Volkswagen four-cylinder DI 1.9 l engine with transparent flat piston, for which measurements are available from Hentschel *et al.* [124, 126–129] and Arcoumanis and Whitelaw [24]. Four different operating points are considered and for each point a single combination of spray submodels is employed.

Each of these test cases is considered in an individual section which commences with the description of the case. Then, the results are presented and discussed. The section closes with a synopsis of the findings. Before the presentation of these test cases, various definitions of physical quantities, used in the comparisons, are given in the following section. Then, the single-droplet test case is considered in Section 6.3. The free spray and the pressure chamber cases are presented in Sections 6.4 and 6.5, respectively. The engine case is examined in Section 6.6. Finally, the closure of this chapter is given in Section 6.7.

In all calculations the fuel properties are evaluated based on the data reported by Daubert and Danner [77], American Petroleum Institute (API) [10] and National Bureau of Standards [208].

6.2 Definitions

Some physical quantities like the fuel vapour distribution and the droplet temperature and concentration cannot readily be measured, but their values are easily provided by the mathematical models. On the other hand, there are some quantities, such as the spray penetration, which are not uniquely defined. Obviously, these introduce a number of uncertainties in the validation of the spray calculations. The definitions of all the quantities monitored in this study will now be given, following the corresponding definitions used in experiments and calculations as widely appear in the literature.

Spray penetration

The instantaneous fuel vapour penetration is defined as the farthest point from the injector where the fuel vapour mass fraction has the value 0.05. This definition has been used by Kralj [171].

For the liquid penetration three different definitions will be used. The first one is the so-called *leading droplet* penetration, defined as the distance between the farthest (leading) droplet and the injector. This definition has been used by many researchers (see Karlsson and Chomiak [158], Ikonomou [143]). Obviously, this quantity is not in general representative, because a particular droplet might be far away (carried by the flow) while all the remaining spray is much behind. Moreover it is unlikely that this droplet will be detected in experiments. Therefore, a second penetration definition is introduced, defined as the distance between the injector and the farthest point at which the void fraction is 99 %, as used by Kralj [171]. From now on, this will be called as 99 % *void* definition. Although this is more representative than the previous one, it is obviously, mesh-dependent. For instance, for a coarse mesh, the liquid may never occupy the 1 % of the cell volume. To this end, a third definition is introduced, being the distance between the injector and the point behind which 99 % of the total liquid mass is included. This will be referred to as 99 % *mass* definition, as used by Hohmann *et al.* [137].

In order to be consistent with the experiments, the penetration is calculated along the measured direction. Thus, for example, for the cases of the atmospheric spray and the Aachen pressure chamber, the penetration point is located on the injector axis. In contrast, for the Volkswagen engine, this point is projected on a plane parallel to the cylinder head.

Finally, it should be mentioned that these penetration definitions are arbitrary, but widely used in the literature (see Kralj [171], Hohmann *et al.* [137]). Of course, in comparisons between various submodels, using the same definitions, the arbitrariness is not so important.

Cumulative evaporated mass

As its name implies, the cumulative evaporated mass is defined as the ratio of the cumulative fuel vapour mass to the cumulative injected fuel mass. In mathematical terms:

$$\mathrm{CEM}(t) = 1 - \frac{\sum_{p=1}^{N_p} m_p}{\sum_{i=1}^{N_t} \rho_{d,inj} \frac{\dot{Q}_i + \dot{Q}_{i+1}}{2} \Delta t_i} , \tag{6.1}$$

where N_t is the total number of time steps Δt from the start of injection, SOI, to the current time, t.

Mean diameter

A number of definitions can be used to characterise the mean diameter of the whole droplet population (see Lefebvre [185]). However, the most popular choice in the literature (see O'Rourke and Bracco [225], Reitz and Diwakar [245], Paál [227], Takenaka *et al.* [282], Sommerfeld [269], Faeth [94], Kralj [171]) is the Sauter mean diameter, SMD, which reads:

$$\mathrm{SMD} = \frac{\sum_{p=1}^{N_p} N_{d,p} D_p^3}{\sum_{p=1}^{N_p} N_{d,p} D_p^2} . \tag{6.2}$$

It can be seen from the above that the SMD is the diameter of the droplet whose volume-to-surface ratio is equal to that of the entire spray.

Local spray values

In this study, the droplet velocities and sizes at some points are compared to measurements. Obviously, the droplet properties cannot be simply defined at a point because on the one hand, the spray is not a continuum and consequently, its local values cannot be obtained by interpolation and on the other, the droplet is not a 'point'. Therefore, a control volume* around the considered point is assumed and the droplet properties are calculated based on the droplets captured in this volume during a time window equal to that used in the experiment, which is usually $100\,\mu s$ (see Paál [227]). The mean, $u_{d,mean}$ and RMS, $u_{d,rms}$, velocities are respectively calculated as:

$$u_{d,mean} = \frac{\sum_{i=1}^{N_i} N_{d,i} |\mathbf{u}_{d,i}|}{\sum_{i=1}^{N_i} N_{d,i}} , \tag{6.3a}$$

*For consistency, the dimensions of the control volume are equal to those used in the experiments. In the case of the phase Doppler anemometry, the volume length is $227\,\mu m$.

$$u_{d,rms} = \sqrt{\frac{\sum_{i=1}^{N_i} N_{d,i} \left(u_{d,mean} - |\mathbf{u}_{d,i}|\right)^2}{\sum_{i=1}^{N_i} N_{d,i}}}\,, \tag{6.3b}$$

where N_i is the total number of parcels captured in the considered control volume during the considered time window. The local Sauter mean diameter is calculated using Eq. (6.2) in which the summations are performed over N_i and not N_p.

Local field values

Comparison with experimental data is made for some gas properties, particularly, the fuel vapour mass fraction at certain points. Linear interpolation is used between grid-node values.

6.3 Single droplets

This section is devoted to the investigation of the evaporation process. In order to isolate it from other physical phenomena such as atomisation, breakup, collisions and impingement, single droplets are considered. Both single-component and bi-component fuels are examined and comparisons are made with experimental results obtained at Centre National de la Recherche Scientifique, Orleans and Université d' Orléans, Orleans and reported by Gökalp *et al.* [100], Birouk [42] and Birouk *et al.* [43].

6.3.1 Description

The experimental setup consists of a vertical wind tunnel providing electrically heated air. The droplet is suspended $3\,cm$ above the exit section of the tunnel by a quartz fibre of $0.2\,mm$ diameter. Droplets with initial diameters in the range between $1\,mm$ to $2\,mm$ were investigated.

The instantaneous droplet diameter was measured by a CCD camera at 10000 frames per second. The surrounding air pressure was atmospheric while its temperature was varied from room value up to 449 K.

6.3.2 Single-component fuel

Four different conditions are examined for n-heptane and n-decane, as summarised in Tables 6.1 and 6.2, respectively. These tables also include some relevant characteristic dimensionless numbers which have been evaluated at the initial conditions. The initial droplet temperature is not reported and therefore, it is assumed to be room temperature, i.e. equal to the air flow temperature. In cases of heated air, the initial droplet temperature is assumed to be 300 K.

Table 6.1: The n-heptane test cases.

Case	p $[atm]$	T $[K]$	$\lvert\mathbf{u}\rvert$ $[m/s]$	$D_{d,0}$ $[mm]$	$T_{d,0}$ $[K]$	Re	Bi	Pe	B_T	B_M
H1	1	300	2.00	1.3	300	167	1.2	1310	0	0.25
H2	1	304	1.22	1.3	304	100	1.0	742	0	0.31
H3	1	372	1.45	1.3	300	90	1.0	848	0.36	0.25
H4	1	449	2.01	1.3	300	95	1.1	1273	0.82	0.25

Table 6.2: The n-decane test cases.

Case	p $[atm]$	T $[K]$	$\lvert\mathbf{u}\rvert$ $[m/s]$	$D_{d,0}$ $[mm]$	$T_{d,0}$ $[K]$	Re	Bi	Pe	B_T	B_M
D1	1	300	2.00	1.3	300	164	1.1	1374	0	0.01
D2	1	303	1.22	1.3	303	98	0.9	765	0	0.01
D3	1	372	1.45	1.3	300	88	0.9	889	0.38	0.01
D4	1	449	2.01	1.3	300	93	1.0	1336	0.85	0.01

Since only evaporation is considered, a small computer code has been constructed which solves only the droplet conduction and diffusion equations, described in Section 3.6, in order to save computational time. The coupling between the two phases is not taken into account, i.e. it is assumed that the surrounding air conditions are constant. This is reasonable, since the flow conditions are controlled by the wind tunnel and also, the air carries away the fuel vapour from the evaporating droplet.

The predictions are affected by three elements. Firstly, as mentioned in Section 3.6, various correlations for the Nusselt and Sherwood numbers have been proposed in the literature. In these calculations, three different sets of correlations will be employed, as summarised in Table 6.3, in order to investigate their influence on the predictions of droplet evaporation.

Table 6.3: Nusselt and Sherwood correlations.

Designation	Correlation
EW/RM	El Wakil *et al.*/Ranz-Marshall, Eqs. (3.86), (3.80), (3.137a)
AS/RM	Abramzon-Sirignano/Ranz-Marshall, Eqs. (3.92), (3.80), (3.137b)
RY	Renksizbulut-Yuen, Eqs. (3.89), (3.137c)

Another element influencing the results is the treatment of the temperature within the droplet. In Section 3.6, two cases were examined based on the Biot number. Here, this number is of the order of unity (see Tables 6.1 and 6.2) and therefore, the 'low-Bi' treatment, which assumes uniform temperature, is not valid. For a non-uniform temperature calculation, the effective conductivity should be considered when strong internal circulation takes place (see Section 3.6). Here, the Peclet number is up to 1374 (see Tables 6.1 and 6.2) and as illustrated in Fig. 3.22, the effect of internal circulation should not be neglected.

Finally, the third element affecting the predictions is the time-step size, $\delta\tau$. In order to get time-step independent results a sensitivity study is performed on the case which physically has the smallest time scale and therefore, it requires the finest time step. This is the Case H4, in which the highest temperature and velocity of the free stream are applied to the most volatile fuel, leading to the highest evaporation rate. Four different time steps are tested using the effective conductivity treatment and employing the EW/RM correlations (see Table 6.3). The results will now be presented.

The droplet evaporation history for Case H4, depicted in Fig. 6.1, is shown in terms of the squared diameter normalised by the initial one, $\mathcal{E}$:

$$\mathcal{E} = \frac{D_d^2}{D_{d,0}^2} \, . \tag{6.4}$$

Also, the time is normalised by the characteristic time, t_d, defined as:

$$t_d = \frac{100 D_{d,0}^2}{\nu_m} \, , \tag{6.5}$$

where the kinematic viscosity is calculated at the free stream temperature. Here, the

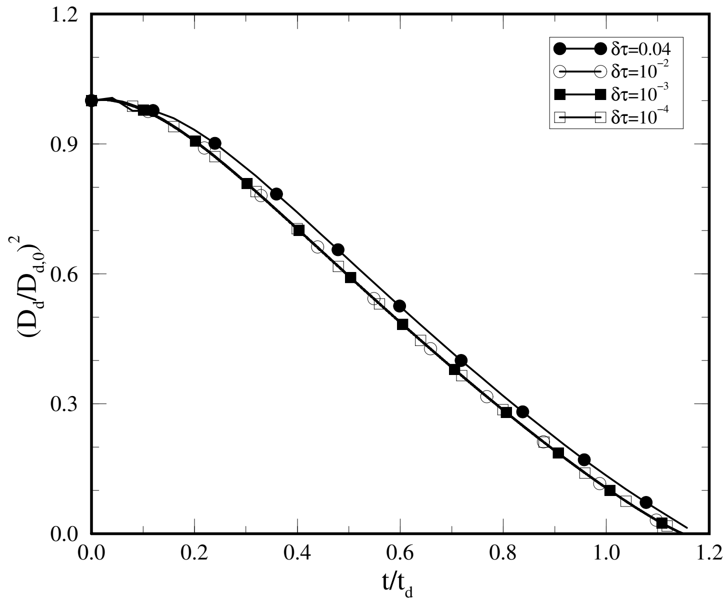

Figure 6.1: Effect of the computational time step, $\delta\tau$, on the evaporation history for Case H4 ($449\,K$, $2.01\,m/s$).

characteristic time $\tau_{p,T}$ (see Eq. (3.116)) is about 0.09. As evidenced, the time step is still too large when it is 0.04, but it does not lead to appreciable differences for values less than 10^{-2}. The maximum difference between the evaporation histories obtained using $\delta\tau = 10^{-2}$ and $\delta\tau = 10^{-3}$ is about $0.7\,\%$ and reduces to $0.4\,\%$ when a comparison between those for $\delta\tau = 10^{-3}$ and $\delta\tau = 10^{-4}$ is made. Thus, $\delta\tau = 10^{-3}$, which approximately corresponds to $5\,ms$, is considered to be fine enough and is adopted for the remaining calculations.

Having decided to adopt $\delta\tau = 10^{-3}$ and the effective conductivity treatment, the three different Nusselt and Sherwood correlations listed in Table 6.3 will now be used for all the n-heptane and n-decane cases. The droplet evaporation history will be shown mainly in terms of $\mathcal{E}$, while the time axis will be normalised either by t_d or by the square of the droplet initial diameter.

The temporal variations of $\mathcal{E}$ for Cases H1–H4 are shown in Figs. 6.2–6.5, respectively. The lowest evaporation rate is always obtained from the Renksizbulut

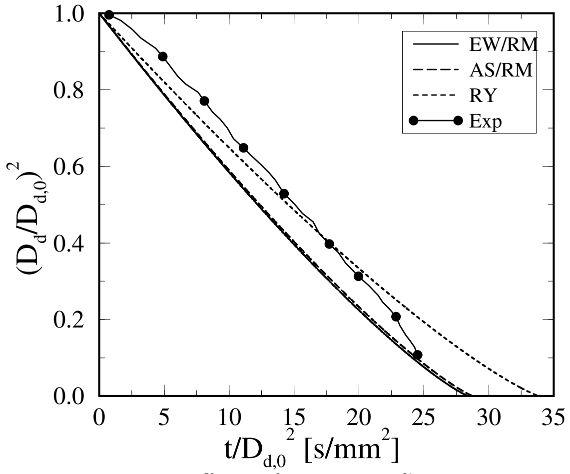

Figure 6.2: Effect of Nu and Sh correlations on the evaporation history for Case H1 ($300\,K$, $2.00\,m/s$).

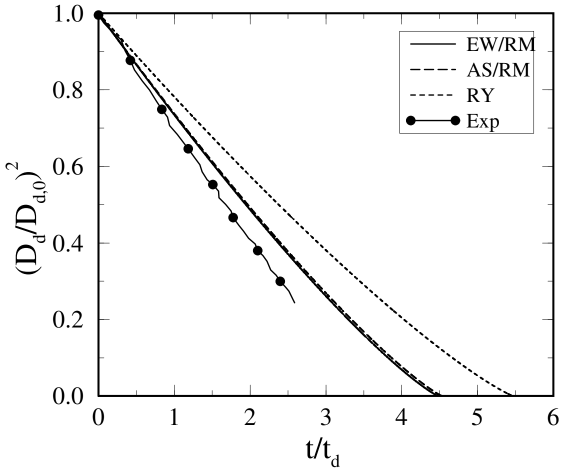

Figure 6.3: Effect of Nu and Sh correlations on the evaporation history for Case H2 ($304\,K$, $1.22\,m/s$).

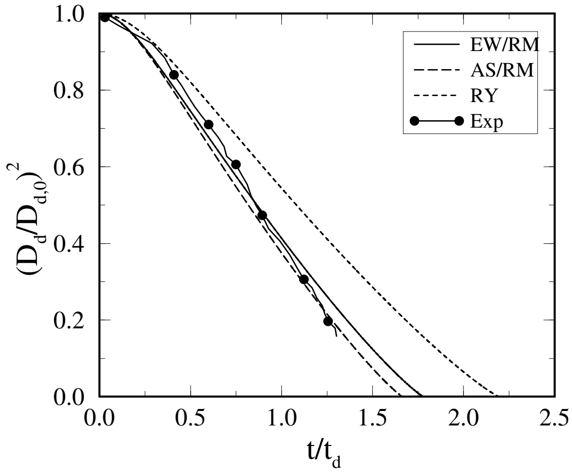

Figure 6.4: Effect of Nu and Sh correlations on the evaporation history for Case H3 ($372\,K$, $1.45\,m/s$).

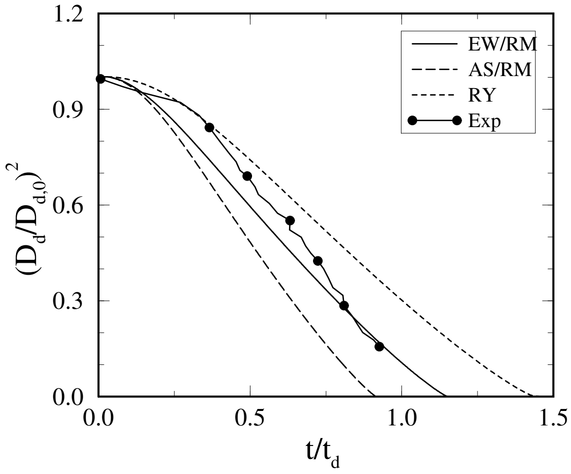

Figure 6.5: Effect of Nu and Sh correlations on the evaporation history for Case H4 ($449\,K$, $2.01\,m/s$).

and Yuen correlations. The correction factor of El Wakil *et al.* shows a similar performance to that of Abramzon and Sirignano for low evaporation rates (Cases H1 and H2). However, increasing the free stream temperature and velocity, causes the difference to increase, since AS/RM seems to be more sensitive to these, resulting in the highest evaporation rate of the three.

Comparing the predictions with the measurements, it can be seen in Fig. 6.2 that for room temperature, good agreement is obtained using RY. However, for lower air velocity (Fig. 6.3) all the calculations underpredict the evaporation rate. Evidently, by increasing the free stream temperature and velocity, the droplet evaporates faster in both predictions and measurements (see Figs. 6.4 and 6.5), as expected. However, it seems that the predictions are more sensitive to these conditions than are the measurements. Hence, although all the sets of correlations result in underprediction of the evaporation rate for low temperature and velocity of the surrounding air (Case H2), the curves move closer to the experimental results as the air temperature and velocity increase. Thus, very good agreement is observed in Fig. 6.4 using both EW/RM and AS/RM, while they lead to overprediction of the evaporation rate for Case H4. However, the agreement between predictions obtained by EW/RM and measurements is not too bad. The correlations of Renksizbulut and Yuen give good predictions in the early stages whereas later, the evaporation rate is underpredicted. In contrast, the Ranz and Marshall correlations (in conjunction with either the correction factor of El Wakil *et al.* or that of Abramzon and Sirignano) fail to reproduce the experimental data in the beginning but later on the slope of $\mathcal{E}$ follows that of the measurements.

Concerning the shape of the predicted curves, a slight increase of the droplet diameter in the beginning ($t/t_d < 0.1$) is observed in Fig. 6.5. The exposure of the droplet in a high-temperature environment ($T = 449\,K$), results in a rapid increase of the droplet temperature leading to lower density and subsequently, larger volume. The rate of increase of the droplet volume is higher than the evaporation rate at this time resulting in this small increase of the diameter. Obviously, after a while, the droplet temperature does not increase rapidly and the rate of decrease of its diameter due to evaporation becomes higher. In contrast, for lower air temperature, Case H3, the evaporation rate is higher than the rate of increase of the volume and therefore, the diameter decreases continuously. This effect is clearly shown for n-decane whose evaporation rate is smaller than that of n-heptane and consequently, the initial increase of the diameter is higher (see Figs. 6.8 and 6.9).

Similar observations and trends apply to the n-decane results as can be seen in Figs. 6.6–6.9, which present $\mathcal{E}$ for Cases D1–D4, respectively. However, here,

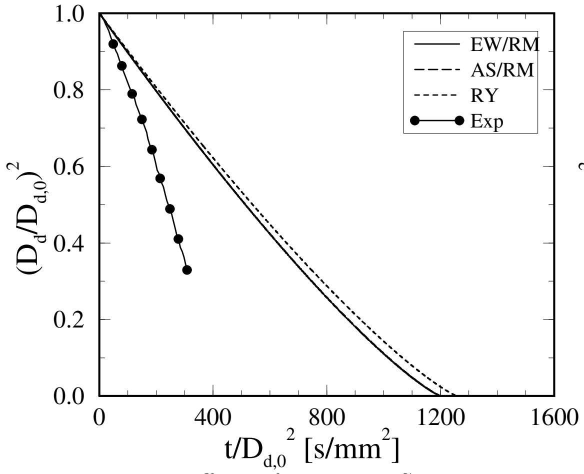

Figure 6.6: Effect of Nu and Sh correlations on the evaporation history for Case D1 ($300\,K$, $2.00\,m/s$).

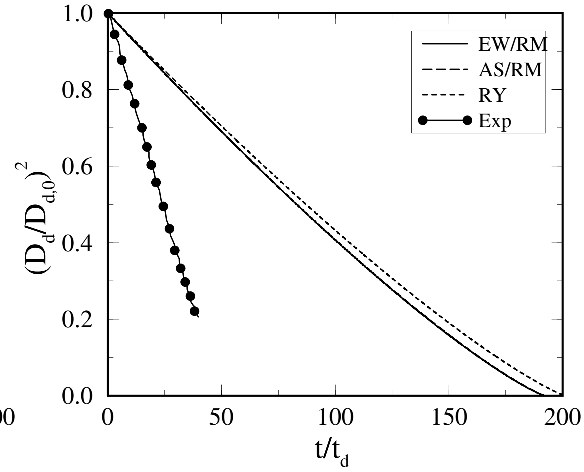

Figure 6.7: Effect of Nu and Sh correlations on the evaporation history for Case D2 ($303\,K$, $1.22\,m/s$).

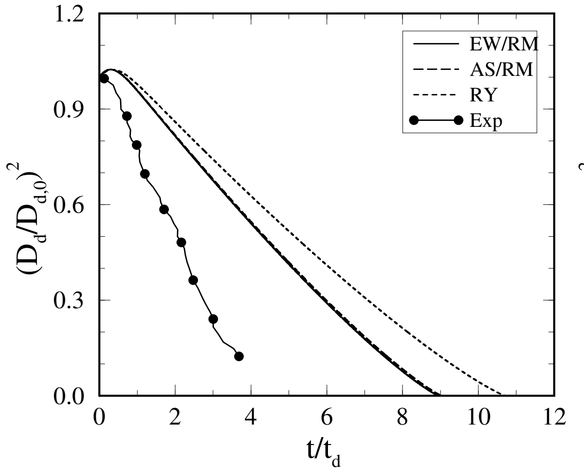

Figure 6.8: Effect of Nu and Sh correlations on the evaporation history for Case D3 ($372\,K$, $1.45\,m/s$).

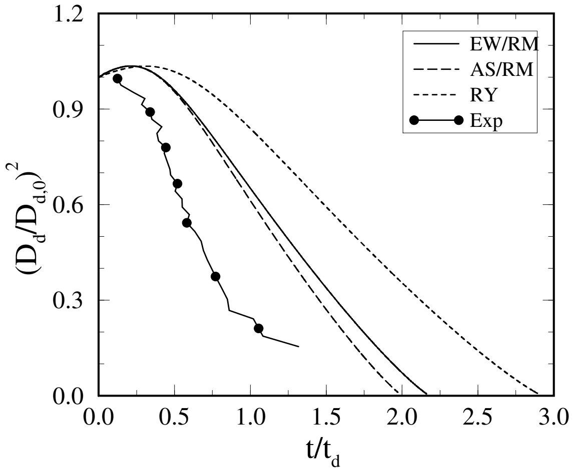

Figure 6.9: Effect of Nu and Sh correlations on the evaporation history for Case D4 ($449\,K$, $2.01\,m/s$).

the evaporation rate is significantly underpredicted, especially for cases which correspond to room-temperature conditions (Cases D1 and D2).

As can be seen in all the figures for n-decane cases, poor agreement between predictions and measurements is observed. This cannot be attributed to the Nusselt and Sherwood correlations, since the predictions do not seem to be as sensitive to these in comparison to the gap between them and the measurements. The thermophysical properties data cannot be responsible for the poor agreement because for pure components, the properties are well-established with minor uncertainties.

In an attempt, at least to justify the predictions, the following procedure is used. In Cases H1 and D1, for which the air temperature is low, the heat transfer is negligible; and considering also that the surface temperature rapidly reaches the wet bulb temperature and remains there, the evaporation rate is mainly controlled by Eq. (3.135). Hence, the ratio of the evaporation rates of the two fuels, $\mathcal{R}$, is expected to be closely approximated by:

$$\mathcal{R} = \frac{\left(\mathcal{D}_f Sh \rho_f \ln \dfrac{1-\chi_v}{1-\chi_{v,s}}\right)_{\text{heptane}}}{\left(\mathcal{D}_f Sh \rho_f \ln \dfrac{1-\chi_v}{1-\chi_{v,s}}\right)_{\text{decane}}} . \tag{6.6}$$

All the variables involved in the above are well-known for the given conditions except from Sh. In this study, three different correlations for Sh have been employed, namely EW/RM, AS/RM and RY, given by Eqs. (3.137a), (3.137b) and (3.137c), respectively. These correspond to $\mathcal{R} = 39.3$, $\mathcal{R} = 38.8$ and $\mathcal{R} = 34.6$, respectively. These numbers are compared with the ratios of the slopes of curves in Fig. 6.2 to the corresponding ones in Fig. 6.6, since according not only to the experimentalists involved in this work (see Gökalp *et al.* [100], Birouk [42]) but also to other researchers (see Law and Law [182], Lefebvre [185]), the evaporation rate can be approximated by the rate of change of the squared droplet diameter. These ratios are 42.1, 41.6 and 37.1 for EW/RM, AS/RM and RY, respectively and they are very close to the corresponding values of $\mathcal{R}$ estimated above. In contrast, the ratio of the evaporation rates obtained by experiment is only 17.1. Here, it is noted that the slopes of the curves in Figs. 6.2 and 6.6 have been evaluated between $\mathcal{E} = 0.9$ and $\mathcal{E} = 0.4$ in order to exclude transient effects in the beginning of the process (which would not allow comparison of the ratios of the evaporation rates with $\mathcal{R}$) and effects due to the quartz fibre which deforms the droplet when its radius is comparable to that of the fibre (see Birouk [42]).

The discussion here, reveals that the predicted ratio of the evaporation rates of the two fuels depends on the Sherwood correlation. However, none of the correlations employed here results in a good agreement with the measurements. It would be interesting to estimate the Sherwood number for both measurements and predictions in order to quantify the difference. To this end, the droplet mass conservation equation, Eq. (3.135), is solved for Sh and dm_d/dt is expressed in terms of dD_d^2/dt. The latter represents the slope of the curves in Figs. 6.2 and 6.6. Hence,

$$Sh = -\frac{\rho_d \dfrac{dD_d^2}{dt}}{6\mathcal{D}_f \rho_f \ln \dfrac{1-\chi_v}{1-\chi_{v,s}}} \,. \tag{6.7}$$

The estimated values of Sh for both fuels (Cases H1 and D1) and for both measurements and predictions are listed in Table 6.4. It is clear that for n-heptane

Table 6.4: Estimated Sherwood number.

	n-heptane (H1)	n-decane (D1)
EW/RM	7.14	7.66
AS/RM	7.05	7.65
RY	5.99	7.29
Exp	6.87	18.18

all the predictions produce similar Sh to that of the measurements. In contrast, for n-decane the measured Sh is more than two times larger than the predictions, which are close to each other. It is also noteworthy that the correlations used here cover a wide range of the proposed correlations in the literature and particularly, those of Ranz and Marshall in conjunction with either the correction factor of El Wakil *et al.* or that of Abramzon and Sirignano are widely employed in Diesel spray calculations. Hence, it can be claimed that the predictions are consistent with the expectations resulting from the existing theory and concerning the poor agreement with measurements, uncertainties and ambiguities of the latter should not be excluded.

The effect on the predictions of the different treatments of the droplet conductivity will now be examined. To this end, the cases with high air temperature (Cases H3, H4, D3 and D4) are calculated using the finite, effective and infinite conductivity treatments. The Ranz and Marshall correlations corrected by the factor of El Wakil *et al.* (see Table 6.3) are employed. The results are shown in Figs. 6.10, 6.11, 6.12 and 6.13 for Cases H3, H4, D3 and D4, respectively.

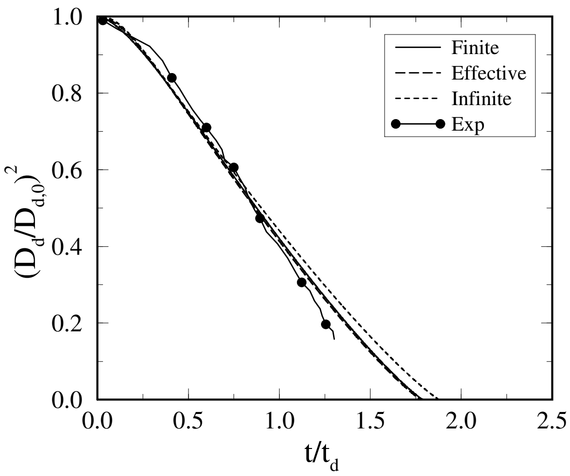

Figure 6.10: Effect of conductivity treatment on the evaporation history for Case H3 ($372\,K$, $1.45\,m/s$).

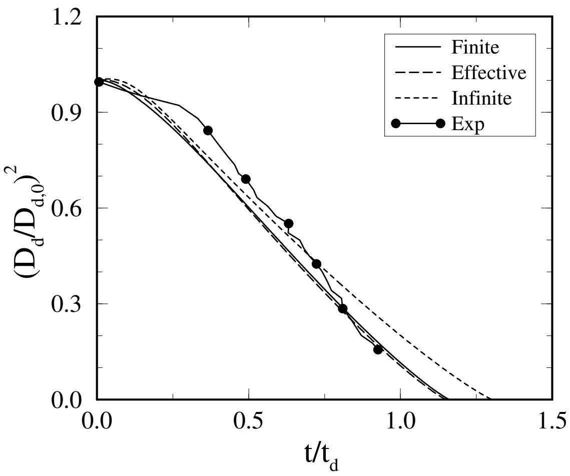

Figure 6.11: Effect of conductivity treatment on the evaporation history for Case H4 ($449\,K$, $2.01\,m/s$).

As can be seen, none of the conductivity treatments changes the predictions for n-decane appreciably. Indeed, for low evaporation rates (see Fig. 6.12) all the conductivity treatments present similar performance. However, if the evaporation rate is increased, either by increasing the air temperature (or velocity) (Case D4) or by using fuel with higher volatility (Case H3), the infinite conductivity assumption leads to a lower evaporation rate compared to those of the other two. This is because both the finite and effective conductivity treatments rapidly lead to higher temperature on the droplet surface and subsequently, higher vapour pressure with consequences on the evaporation rate.

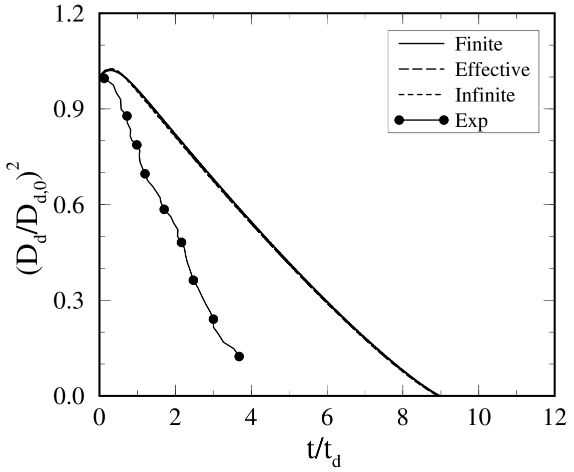

Figure 6.12: Effect of conductivity treatment on the evaporation history for Case D3 ($372\,K$, $1.45\,m/s$).

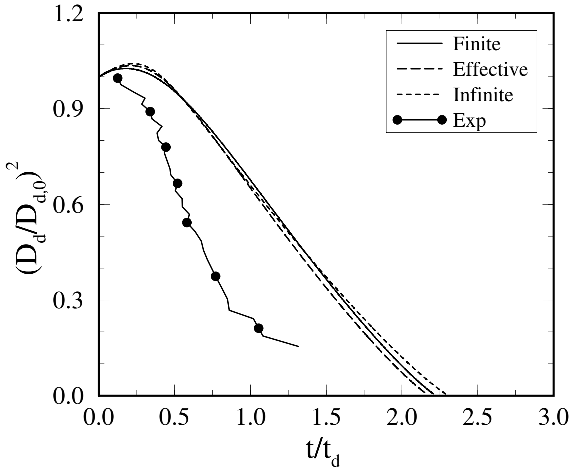

Figure 6.13: Effect of conductivity treatment on the evaporation history for Case D4 ($449\,K$, $2.01\,m/s$).

Surprisingly, only little effect of internal circulation, as reflected in the effective conductivity is observed. This can be explained with the help of Figs. 6.14 and 6.15, which present the droplet surface temperature histories for n-heptane and n-decane,

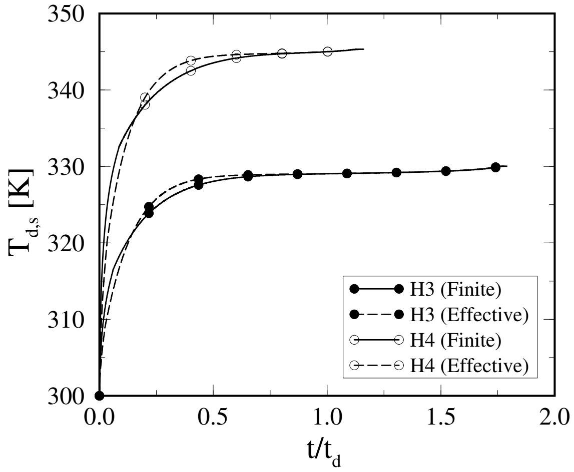

Figure 6.14: Effect of conductivity treatment on the droplet surface temperature for Cases H3 and H4.

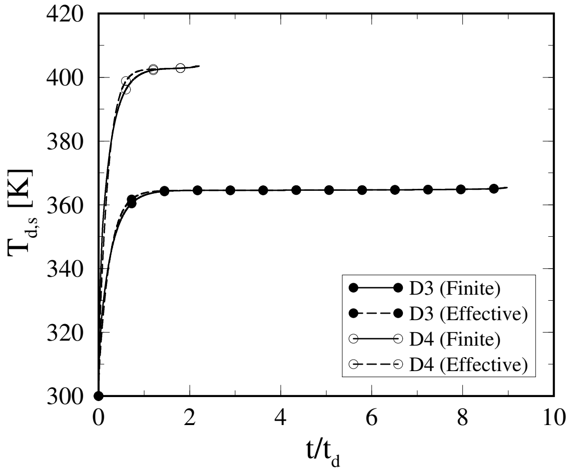

Figure 6.15: Effect of conductivity treatment on the droplet surface temperature for Cases D3 and D4.

respectively. In the beginning, the finite conductivity results in higher surface temperatures than the effective one does. This also leads to higher evaporation rates (see Figs. 6.11 and 6.13). However, the surface temperature, which mainly controls the evaporation rate, reaches the wet bulb temperature very quickly. Thereafter, there is no effect of the thermal conductivity on the evaporation rate since the surface temperature is constant. Consequently, the evaporation rates for the two conductivity treatments are similar.

Finally, it is interesting to compare the relative performance of the two fuels used here in order to be able to explain the behaviour of the bi-component fuel cases. The instantaneous droplet surface temperatures for both n-heptane and n-decane are plotted in Fig. 6.16 for Cases H3, H4, D3 and D4. In all these cases, the Ranz

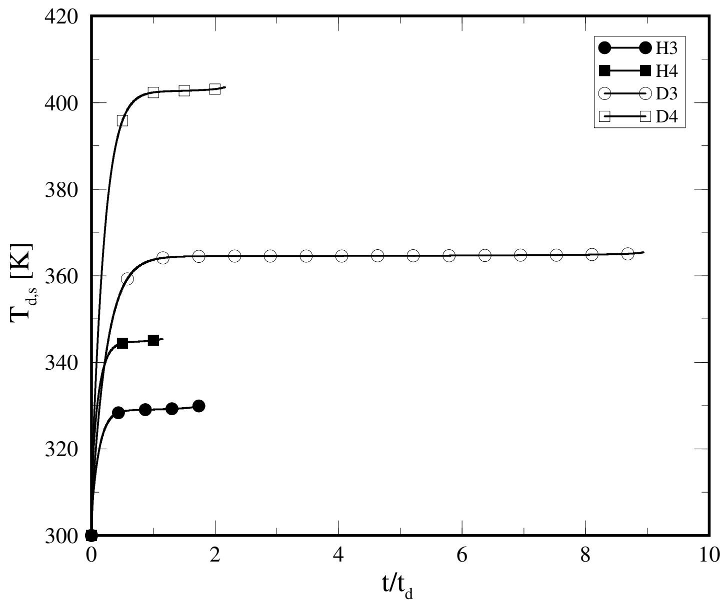

Figure 6.16: Instantaneous droplet surface temperature for Cases H3, H4, D3 and D4.

and Marshall correlations corrected by the factor of El Wakil *et al.* are employed together with the effective conductivity treatment. It is observed that in all cases the surface temperature increases due to the heat transfer until it reaches the wet bulb temperature. For both air conditions, it can be confirmed that the wet bulb temperature for n-heptane is lower than the corresponding for n-decane because the latter extracts more heat for temperature increase and less for evaporation, since its evaporation process is slower. Thus, for $T = 372\,K$, the wet bulb temperature for n-heptane is $330\,K$, while for n-decane it is $365\,K$, which is very close to the surrounding air temperature. This indicates that the evaporation rate of n-decane is relatively low and indeed, its total evaporation time (defined as the time at which $\mathcal{E}$ becomes less than 10^{-3}) is about 4 times longer than that of the n-heptane droplet. For the higher air temperature ($T = 449\,K$), the wet bulb temperature is also higher. In particular, the wet bulb temperature for n-heptane is $345\,K$ and for n-decane $404\,K$. It is noteworthy that the air temperature has a stronger effect on the evaporation rate of n-decane than on that of n-heptane, reducing the difference between the total evaporation times of the two fuels. This is attributed to the higher boiling temperature of n-decane, which results in significantly lower evaporation rates for low temperatures.

6.3.3 Bi-component fuel

The bi-component fuel evaporation performance will now be investigated. The mixture consists of n-heptane and n-decane and two different compositions are considered, particularly, 80 % and 20 % by volume. All the cases with their individual parameters are tabulated in Table 6.5.

Table 6.5: The bi-component test cases.

Case	p $[atm]$	T $[K]$	$\|\mathbf{u}\|$ $[m/s]$	$D_{d,0}$ $[mm]$	$T_{d,0}$ $[K]$	n-heptane	n-decane
B1	1	304	1.22	1.3	304	$80\,\%\,vol.$	$20\,\%\,vol.$
B2	1	372	1.45	1.3	300	$80\,\%\,vol.$	$20\,\%\,vol.$
B3	1	449	2.01	1.3	300	$80\,\%\,vol.$	$20\,\%\,vol.$
B4	1	372	1.45	1.3	300	$20\,\%\,vol.$	$80\,\%\,vol.$
B5	1	449	2.01	1.3	300	$20\,\%\,vol.$	$80\,\%\,vol.$

As explained in the investigation of the pure-component fuels, the Ranz-Marshall correlations in conjunction with the factor of El Wakil *et al.* give the best agreement, of all the correlations employed, with the experimental results. Therefore, these are adopted in all the calculations of the bi-component fuel cases. Also, the effective conductivity treatment is employed for a better representation of the simulated cases despite the fact that, as shown earlier, it does not result in appreciable differences in comparison with the finite one. Last, the smallest characteristic time of the diffusion equation, $\tau_{p,m}$, (see Eq. (3.152)) is 1.72, which is larger than $\tau_{p,T}$ (see §6.3.2) and therefore, the time step used for the single-component calculations, i.e. $\delta\tau = 10^{-3}$, is fine enough and is adopted here as well. In contrast to the conduction equation, the smallest time scale for the diffusion equation is that of the room-temperature case, since it produces the biggest difference between the evaporation rates of the two components, as discussed earlier, resulting in the largest concentration gradients.

The results for Case B1 are plotted in Fig. 6.17. In both measurements and predictions, two slopes can clearly be distinguished. The largest evaporation rate is observed in the beginning because at this stage, the surface concentration of the volatile component (n-heptane, hereafter denoted by the subscript '1') is high. However, this results in a rapid decrease of the concentration of n-heptane on the droplet surface, as demonstrated in Fig. 6.18. Then, the evaporation rate of n-decane

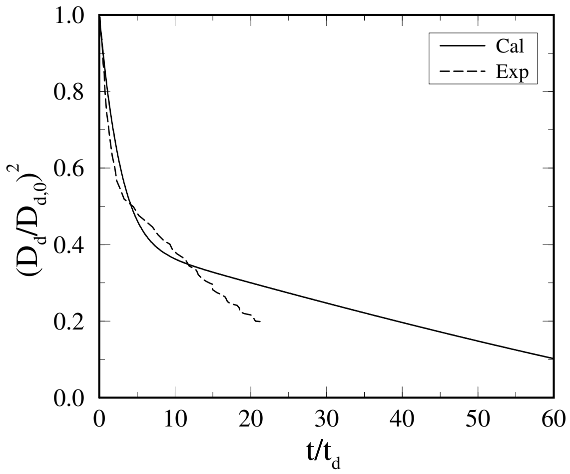

Figure 6.17: Evaporation history for Case B1 ($304\,K$, $1.22\,m/s$).

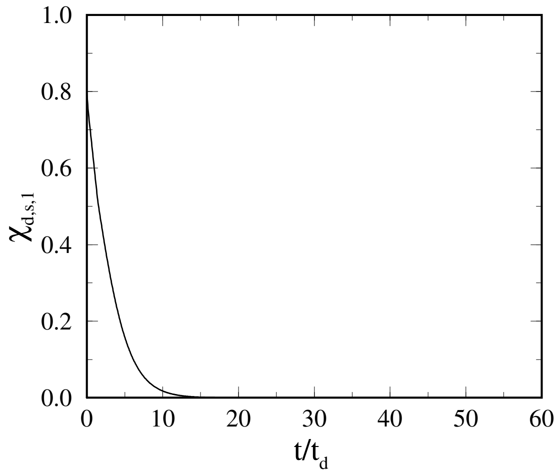

Figure 6.18: Molar fraction of n-heptane on the droplet surface for Case B1.

becomes dominant; and since it is smaller than that of n-heptane, as shown earlier, the total evaporation rate lowers significantly, resulting in two distinguishable slopes in Fig. 6.17.

Comparing the predictions with the measurements, it is once again clear that the former give slower evaporation in cases in which the free stream is at room temperature. The underprediction for n-heptane is small (see Fig. 6.3) and therefore, a good agreement is observed in the beginning. However, afterwards, when the evaporation rate of n-decane is dominant, $\mathcal{E}$ is significantly underpredicted, in consistency with the findings for the single-component cases (see Fig. 6.7).

The results for higher air velocity and temperature are plotted in Fig. 6.19. The high temperature reduces the difference between the evaporation rates of the

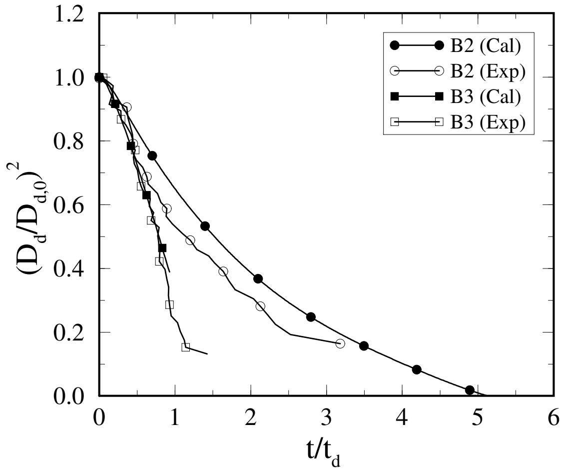

Figure 6.19: Evaporation history for Cases B2 ($372\,K$, $1.45\,m/s$) and B3 ($449\,K$, $2.01\,m/s$).

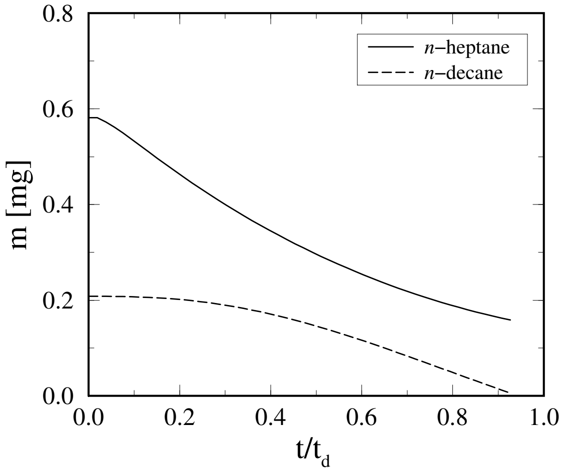

Figure 6.20: Mass temporal variation for n-heptane and n-decane for Case B3 ($449\,K$, $2.01\,m/s$).

two components, as mentioned earlier and consequently, two clearly distinguishable slopes are no longer observed. In particular, for Case B2, only a gradual reduction of the evaporation rate with time can be observed, while for higher temperature (Case B3) a nearly constant slope appears. For the latter case, it can be observed in Fig. 6.20 that for $t/t_d < 0.4$, n-heptane evaporates faster than n-decane because on the one hand, the droplet temperature is still low and on the other, the n-heptane concentration on the surface is higher. However, as its concentration decreases, the two components evaporate with similar rates and since the n-decane mass is smaller it disappears faster. Hence, the boiling temperature of the mixture approaches that of the pure n-heptane and as soon as the entire droplet temperature becomes higher than the mixture boiling point, the whole droplet suddenly evaporates, as shown in

Fig. 6.19.

It can be seen that increasing the air temperature, causes the predictions to move closer to the measurements. This conforms with the observations for the single-component calculations. Thus, the agreement between predictions and measurements for Case B2 is not bad; and it is very good for Case B3.

When the initial concentration of n-heptane is decreased to 20 %, the evaporation rate decreases. This can be seen in Fig. 6.21, which presents the results for

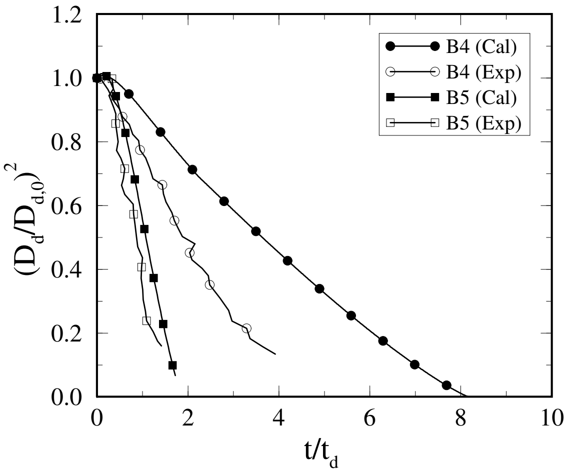

Figure 6.21: Evaporation history for Cases B4 ($372\,K$, $1.45\,m/s$) and B5 ($449\,K$, $2.01\,m/s$).

Cases B4 and B5. Since the concentration of n-decane is now higher than that for Cases B2 and B3, the agreement between predictions and measurements at a given air temperature becomes worse. In particular, significant underprediction of the evaporation rate is obtained for Case B4. Improved agreement is observed for higher temperature (Case B5) in consistency with the earlier findings. Regarding the nature of the evaporation process in Cases B4 and B5, the earlier explanation also applies here.

6.3.4 Summary

The evaporation of single droplets of mono- and bi-component fuel exposed to atmospheric pressure air stream of velocity up to $2.01\,m/s$ and temperature up to $449\,K$

was considered.

Three sets of Nusselt and Sherwood number correlations were examined. The correlations of Ranz and Marshall in conjunction with the correction factor of El Wakil *et al.*, Eqs. (3.86), (3.80), (3.137a), showed the best agreement with the measurements. It was also observed that the correction factors of El Wakil *et al.*, Eq. (3.86) and Abramzon and Sirignano, Eq. (3.92), have similar performance for low evaporation rates. However, for high air temperatures, the latter tends to overpredict the evaporation rate. In contrast, the correlations of Renksizbulut and Yuen, Eqs. (3.89) and (3.137c), consistently underpredict the evaporation rate.

The effective conductivity model was found to have minor effect on the evaporation rate, despite the fact that Pe is relatively high. The explanation is that the droplet reaches the wet bulb temperature in a relatively short period and thereafter, the conductivity does not affect the evaporation rate. The infinite conductivity assumption results in lower evaporation rates, especially for high air temperatures and for fuels with high volatility. This is because the temperature of the droplet surface is lower than that for the finite conductivity treatment, with consequences on the evaporation rate.

Although very good agreement between predictions and measurements was observed for n-heptane (in both single-component and bi-component cases when in the latter n-heptane was dominant), the results for n-decane were disappointing. It was shown that this disagreement cannot be attributed to the Nusselt and Sherwood correlations because three different correlations were employed here and all predict similar evaporation rates which are much lower than the measured ones. Experimental uncertainties must therefore be considered as a possible cause of the discrepancies. Fortunately, when the air temperature is increased, the agreement between the predictions and measurements is significantly improved. This is very important, since the main focus of the present study is the assessment of the spray methodology under Diesel engine conditions, where the prevailing gas temperature is high.

Finally, the profile method can be claimed to produce encouraging results for both conduction and diffusion equations.

6.4 Atmospheric sprays

6.4.1 Description

Sprays injected under atmospheric pressure and temperature are nominally called *atmospheric* or *free* sprays. Here, the experimental results of Paál [227], for pulsed Diesel sprays, are used for validation purposes under such conditions. In this experiment, the spatial and temporal characteristics of a Diesel spray were investigated. A five-hole injector was used, one of whose jets was measured in the experiment while the other four sprays were captured by a special device. The hole diameter was $0.18\,mm$ and length $0.7\,mm$, resulting in a length-to-diameter ratio of 3.89.

Combinations of two different total injection volumes and pump speeds were used resulting in four cases. These cases are designated here according to the practice adopted by Paál [227] and the details are tabulated in Table 6.6. It should be noted

Table 6.6: Atmospheric spray test cases.

Case	p $[atm]$	T $[K]$	Total volume $[mm^3]$	Injection duration $[ms]$	Pump speed $[rpm]$	$T_{d,inj}$ $[K]$
A	1	300	11.75	0.88	600	300
B	1	300	23.5	1.3	600	300
C	1	300	11.75	0.84	1200	300
D	1	300	23.5	1.25	1200	300

that the temperature of the air and the fuel are not given and therefore, assumed here to be $300\,K$. The higher pump speed (Cases C and D) leads to steeper increase of the injection flow rate in the beginning and consequently, shorter injection duration for the same total amount of injected fuel. This can clearly be seen in Fig. 6.22 where the total injection flow rate, measured by a Bosch/Lucas fuel rate indicator,

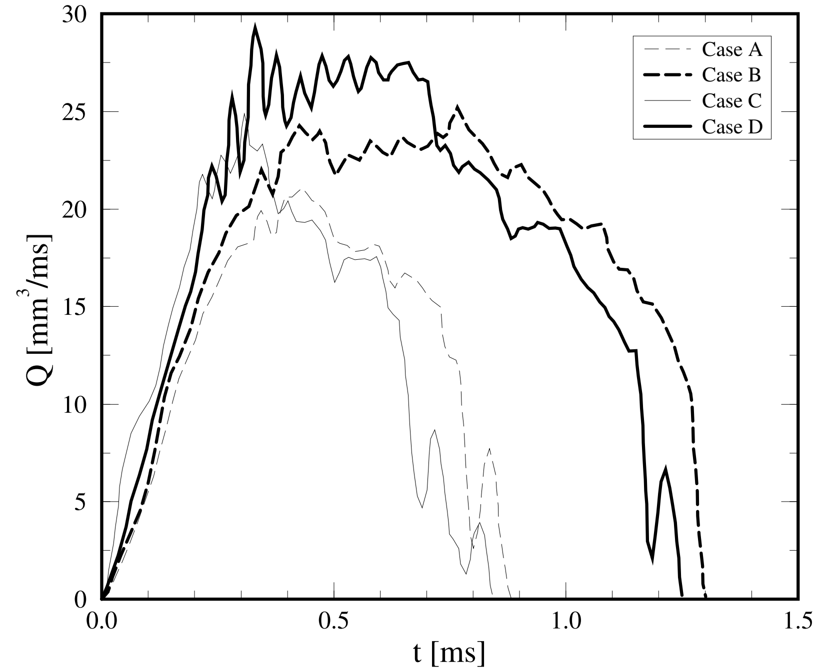

Figure 6.22: Injection flow rate histories.

is plotted for all the cases. The measurements also showed that this flow is divided nearly equally (typical deviation less than 5 %) between the holes.

The fuel used in the experiment was Shell gas oil with density $844\,kg/m^3$ and kinematic viscosity $3.5\,cSt$ at $313\,K$. In an attempt to simulate this fuel with a pure component fuel*, n-dodecylbenzene whose density and kinematic viscosity at the same temperature are close to the reported ones (in particular, $839.19\,kg/m^3$ and $4.08\,cSt$, respectively) is adopted in the calculations. It is noted that this density difference is minor, resulting in negligible mass difference of less than 0.6 %.

The two-beam technique was used to measure spray penetration and phase Doppler anemometry (PDA) was employed to obtain droplet velocity and size at specific locations. The axial, z and radial, r, distances of the measuring locations from the nozzle are given in Table 6.7 and the available types of data for each case

*As presented in §3.6.3, a multicomponent fuel could be used for exact simulation of Shell gas oil, however, its composition consists of a number of components and additives resulting in a complicated problem. On top of that, the exact composition of this fuel is not given.

are tabulated in Table 6.8. It is noted that following the dynamic range of the PDA device (see Paál [227]), the local droplet velocities and SMD in calculations are evaluated from droplets with diameter between 3.1 μm and 108.5 μm.

Table 6.7: Measurement locations.

Designation	z [mm]	r [mm]
P_{10}	10	0
P_{30}	30	0
P_{60}	60	0

Table 6.8: Available experimental data.

Experimental data	Case A	Case B	Case C	Case D
Penetration	$\surd$	$\surd$	$\surd$	$\surd$
Tip velocity	$\surd$	$\surd$	$\surd$	$\surd$
Droplet Velocity & SMD at P_{10}	$\surd$	$\surd$	$\surd$	$\surd$
Droplet Velocity & SMD at P_{30}	$\surd$	$\surd$	$\surd$	$\surd$
Droplet Velocity & SMD at P_{60}	$\surd$	$\surd$	$\surd$	–

6.4.2 Computational mesh

A vertical cylindrical domain of radius 50 mm and height 200 mm is used to simulate the injection in the atmosphere. The dimensions of the cylinder are arbitrary but large enough to eliminate the effect of the wall on the spray. For the same reason, the injector is located 10 mm below the top wall injecting vertically downwards. The symmetry of the problem is exploited and the calculations are performed in a sector of 30° of one computational cell thickness.

A number of different meshes are used to investigate the effect of the grid density. To this end, six meshes are built by varying the number of cells and the aspect ratio*. In the axial direction, the spray penetrates to a substantial depth as shown by the

*The aspect ratio is defined as the ratio between the maximum to the minimum cell length in the considered direction.

measurements and consequently, a uniform grid is used in all meshes. In contrast, the spray half-width is less than $5\,mm$ and therefore, fine resolution is required only in this region whereas the grid density far away is not important. Thus, the number of cells in the radial direction is kept constant in order to minimise the computational requirements while the effect of the grid is investigated by uniformly expanding the spacing to create a finer mesh in the spray region and coarser far away. The parameters of the meshes are listed in Table 6.9.

Table 6.9: Parameters of computational meshes.

Mesh	Axial direction			Radial direction		
	Number of cells	Aspect ratio	min(Δz) [mm]	Number of cells	Aspect ratio	min(Δr) [mm]
M1	100	1.00	2.00	60	5.72	0.31
M2	150	1.00	1.33	60	5.72	0.31
M3	200	1.00	1.00	60	5.72	0.31
M4	200	1.00	1.00	60	3.22	0.44
M5	200	1.00	1.00	60	1.80	0.61
M6	200	1.00	1.00	60	1.00	0.83

It should be noted that there is a lower limit on cell size imposed by the requirement that the local void fraction should not become too small. This would violate the assumption that the gas phase is continuum, although as presented in §2.3.4 and §5.2.3, the methodology developed here, can numerically cope with smaller ϑ. It should also be noted that the cell size should be larger than the maximum droplet diameter (typically $\sim 200\,\mu m$), since according to the present methodology, the source terms representing the exchange of mass, momentum and energy are added to the cell in which the droplet centre is located. Therefore, a finer mesh in the radial direction than M3 would not fulfill the methodology assumptions.

Computational parameters

As discussed above, the void fraction sets a lower limit to the cell size. Hence, in this parametric study, the case with the tendency to generate the smallest void fraction is employed. This is the Case D, which has the highest injection flow rate.

Two further important computational parameters which could affect the results are the size of the time step, Δt and the parcel introduction rate, $\dot{N}_p$. Their effect will be illustrated later, but at present, a fine enough Δt and a large enough $\dot{N}_p$ are chosen to eliminate their effects. Thus, the time step is chosen to be $2\,\mu s$, following Beshay [38] who suggested this value based on a droplet trajectory analysis. On the other hand, considering the recommendations of Dukowicz [83] and Tabrizi [280] who found that the spray is not very sensitive to variations of $\dot{N}_p$ when it is bigger than $2\,\text{parcels}/\Delta t$, a rate of $2\,\text{parcels}/\mu s$ is selected in these calculations.

Also, in this study, the MPI cavitation model and the Huh atomisation model are employed. As mentioned in Section 3.10, the entrance area contraction ratio, C_c and the nozzle wall roughness, k_r, are required for the former one, while the latter needs the discharge coefficient, c_d and the value of the coefficient C_5 in the breakup rate equation, Eq. (3.27). Unfortunately, data are not available for C_c and k_r for this nozzle and therefore, typical values for Diesel injectors, i.e. $C_c = 0.7$ and $k_r = 1\,\mu m$, are used. The average discharge coefficient calculated by Arcoumanis *et al.* [19] from the injection pressure history, the injected volume and the injection duration was found to be about 0.62 for all the cases. All the injector specifications are gathered in Table 6.10. Finally, following the original work of Huh and Gosman [141], C_5 is set to 1 while a parametric study for various values of C_5 will be performed later.

Table 6.10: Injector specifications.

Length, L $[mm]$	0.7
Diameter, D $[mm]$	0.18
Discharge coefficient, c_d	0.62

In preliminary computations, it was found that the total evaporated mass after $2\,ms$ is less than $0.02\,\%$. Hence, to reduce the computational overheads, the evaporation model is switched off in all these calculations. As observed from these preliminary computations, the effect of the evaporation on the SMD is less than $5\,\%$

while on the penetration it is about 3 %. All submodels and correlations employed in the present parametric study along with the values of their relevant parameters are listed in Table 6.11.

Table 6.11: Spray submodels.

Spray process	Submodel/correlation
Cavitation	MPI
C_c	0.7
k_r $[\mu m]$	1
Atomisation	Huh
c_d	0.62
C_5	1
Drag coefficient	Yuen-Chen, Eq. (3.66)
Breakup	Hsiang-Faeth
Collision	O'Rourke

The initial values of the flow-field variables must be defined as well. Since the experiment took place in a quiescent free atmosphere, a zero initial velocity field is assumed while the turbulence parameters are set to low values. Following Ikonomou [143], who simulated the same experiment, k is set to $10^{-3}\,m^2/s^2$ and ε to $4{\cdot}10^{-4}\,m^2/s^3$ to ensure that the initial turbulent viscosity is not too large compared to the molecular one. It is also noted that according to O'Rourke and Bracco [225], the spray predictions are rather insensitive to the initial values of k and ε when they are small. All the initial values of the flow field along with the spray characteristics are summarised in Table 6.12.

Results and discussion

The presentation of the results starts with the penetration, based on the 99 % mass definition, which however, results in similar predictions to that of the leading droplet and the 99 % void definitions. This can be seen in Fig. 6.23 which presents the penetrations obtained with the finest mesh, M3. In this figure, the 99 % void definition does not give a smooth line because when the front droplets move from the current

Table 6.12: Initial flow field and injection characteristics.

Ambient gas	air
$\mathbf{u}$ $[m/s]$	0
p $[atm]$	1
T $[K]$	300
k $[m^2/s^2]$	10^{-3}
ε $[m^2/s^3]$	$4 \cdot 10^{-4}$
Fuel	n-dodecylbenzene
Case	D
Volume $[mm^3]$	4.7
$T_{d,inj}$ $[K]$	300
SOI $[ms]$	0
EOI $[ms]$	1.25

cell with 99 % void fraction to the next one, the threshold value may not be met in any of these cells and the 'apparent' penetration becomes smaller.

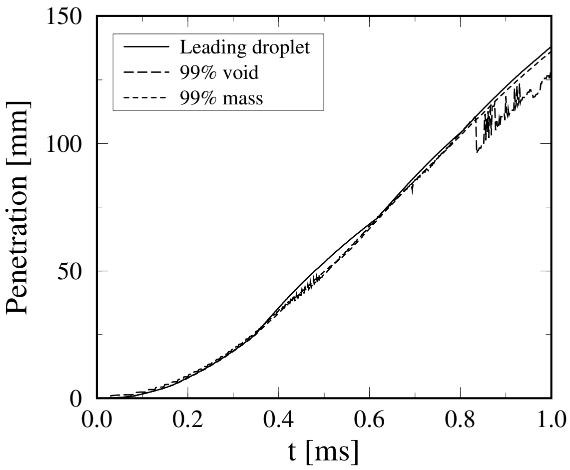

Figure 6.23: Comparison of three different definitions of spray penetration.

Figs. 6.24 and 6.25 show the effect of the grid density on spray penetration. It is observed that changing the axial distribution of the cells within the present range does not introduce appreciable effect on the spray penetration. In contrast, it is influenced by the radial cell size as can be seen in Fig. 6.25. Notably, decreasing the cell size causes the penetration to increase after about $0.35\,ms$. This can be explained as follows. By decreasing the radial cell size, the void fraction decreases

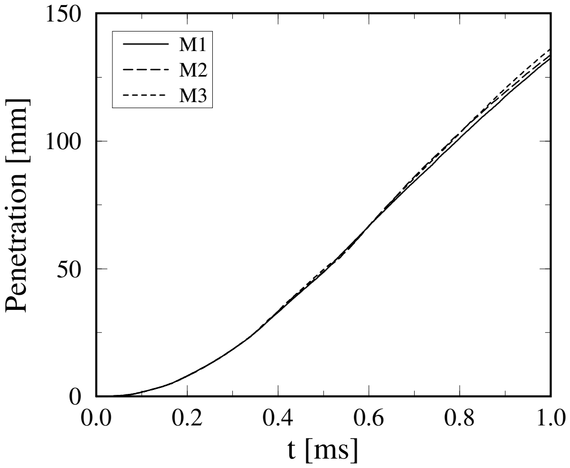

Figure 6.24: Effect of the axial grid density on spray penetration.

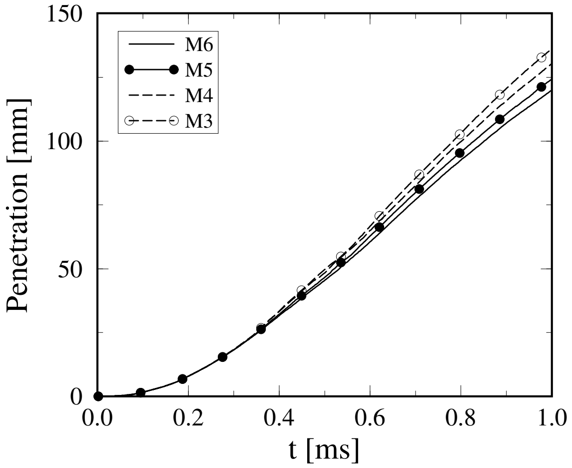

Figure 6.25: Effect of the radial grid density on spray penetration.

because the liquid is mainly accumulated near the axis and hence, only the gas mass in this cell decreases. This results in relatively larger spray-related source terms, leading to higher induced gas velocities. Therefore, the following droplets will experience a smaller drag force resulting in higher penetration. This also explains why the difference is not observed until some time after the start of injection. In contrast, the axial changes of the cell size do not have such an effect, because the void fraction is not influenced and consequently, the gas field is not affected. Hence, grid-independent results could only be obtained with radial refinement only if a fine enough mesh is employed so that the void fraction changes gradually and *not* suddenly along the radius, as occurs in the axial direction. However, this is impossible in the present test case because the smallest radial dimension of the cells near the injection axis is already of a similar size to the largest droplets. Also, the smallest void fraction for the finest mesh is 0.27 and there is a little scope for further reduction. Therefore, the mesh M3 (see Fig. 6.26), which is the finest comprising 12000 cells, will be used for all the remaining calculations for atmospheric sprays. However, it is worthwhile investigating the effect of this compromise on other spray characteristics, as follows.

The SMD as a function of time is depicted in Fig. 6.27 for various axial mesh spacings and in Fig. 6.28 for the radial refinement. As can be seen in the latter,

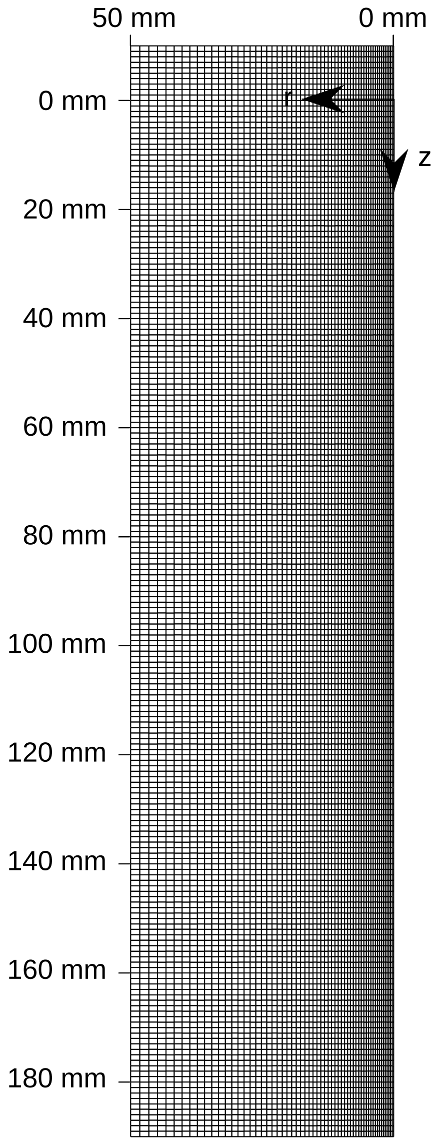

Figure 6.26: The computational mesh (M3 in Table 6.9) used for the atmospheric spray calculations.

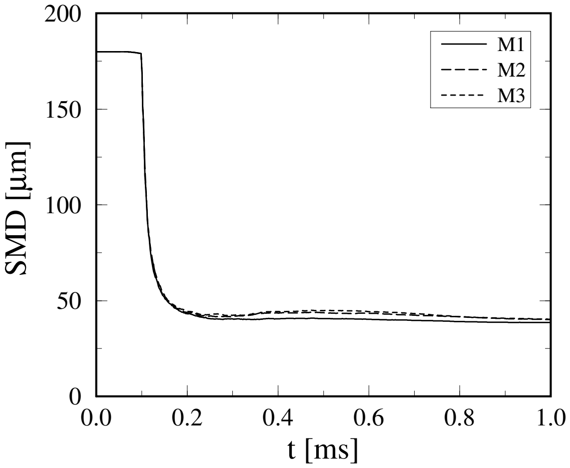

Figure 6.27: Effect of the axial grid density on the SMD.

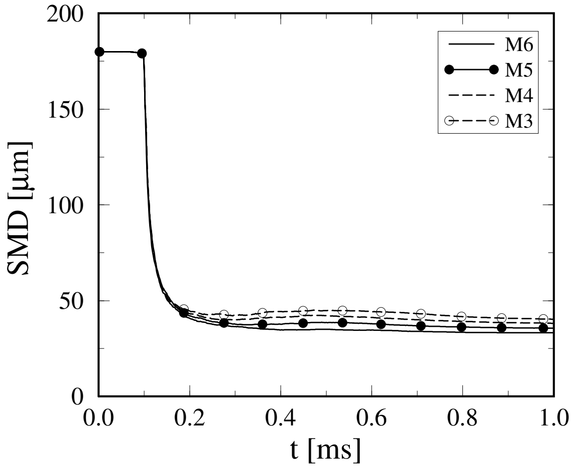

Figure 6.28: Effect of the radial grid density on the SMD.

decreasing the cell size produces larger droplets. This is consistent with the afore-given explanation, since the finer mesh results in higher gas velocities (closer to the droplet velocities) and consequently, the aerodynamic forces become weaker, reducing the droplet breakup rate (see Section 3.7). The effect of the axial grid density on the SMD decreases as the mesh becomes finer. The maximum difference between M1 and M2 is about 7 % whereas it is less than 2 % between M2 and M3. For radial refinement, the maximum difference of SMD between M5 and M4 is about 8.5 % and it decreases to 6 % between M4 and M3.

The effect of the grid density on the tip velocity is shown in Fig. 6.29 for the axial refinement and in Fig. 6.30 for the radial. The tip velocity here is evaluated from the temporal differentiation of the penetration curve. Faster droplets behind the tip may overtake the latter due not only to their higher injection velocity but also because they experience smaller drag force since they are in the wake of the front droplets. This change of the front droplets results in the irregular behaviour shown in these figures. Nevertheless, the tip velocities predicted with meshes M1, M2 and M3 have very similar trends. On the other hand, once again, the radial grid density has a larger effect. Although the evidence is not clear, it can be seen that between 30 mm and 50 mm away from the nozzle the finer the mesh, the higher is the tip velocity. This is in accord with the effect on the penetration.

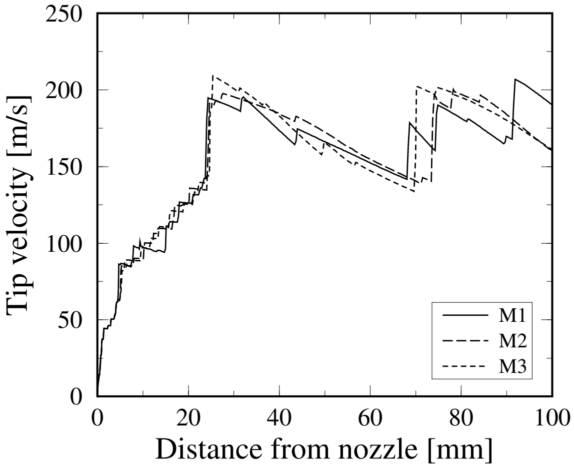

Figure 6.29: Effect of the axial grid density on tip velocity.

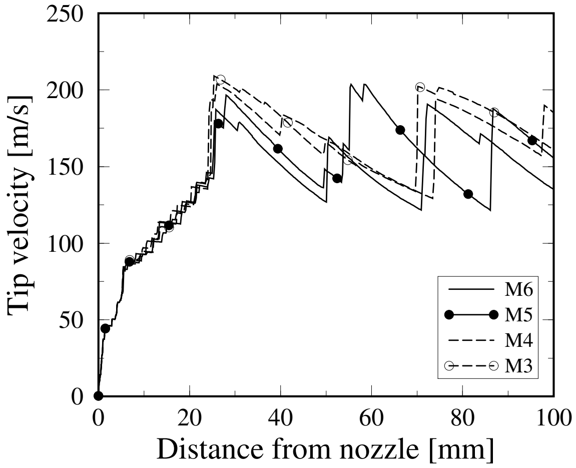

Figure 6.30: Effect of the radial grid density on tip velocity.

Finally, the effect of mesh refinement on local droplet velocities and SMD for a representative point is also investigated. Here, the point P_{30} is chosen, since it lies between the other two points at which measurements have been obtained (see Table 6.7). Figs. 6.31 and 6.32 show the effect of the axial and radial grid densities,

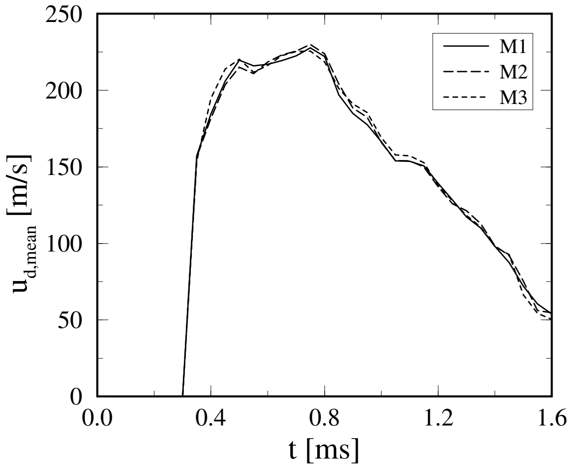

Figure 6.31: Effect of the axial grid density on droplet velocities at P_{30}.

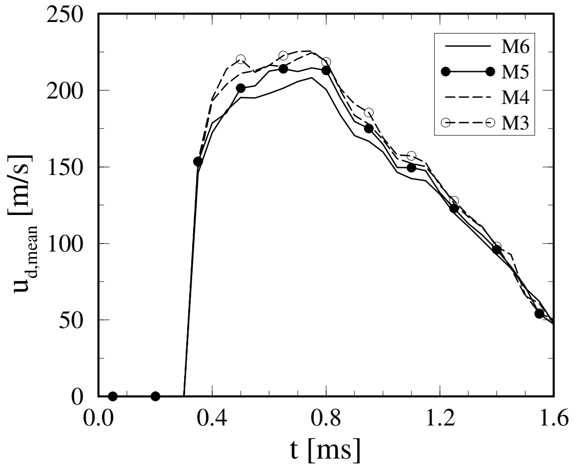

Figure 6.32: Effect of the radial grid density on droplet velocities at P_{30}.

respectively, on the droplet velocities. Recall that these data are averaged over a time window of 100 μs and values are extracted at 50 μs intervals. As a consequence, the predicted curves are not smooth. As can be seen again, the effect of the axial grid density is minor with a maximum difference between M2 and M3 of less than 0.2 %. In contrast, as the radial size of the cell decreases, the droplet velocity increases presenting a maximum difference between M3 and M4 about 2 %. These observations are consistent with those for the penetration and tip velocity.

The effect of the axial grid density on the SMD at the same point is shown in Fig. 6.33 and the effect of the radial one in Fig. 6.34. It is once again observed

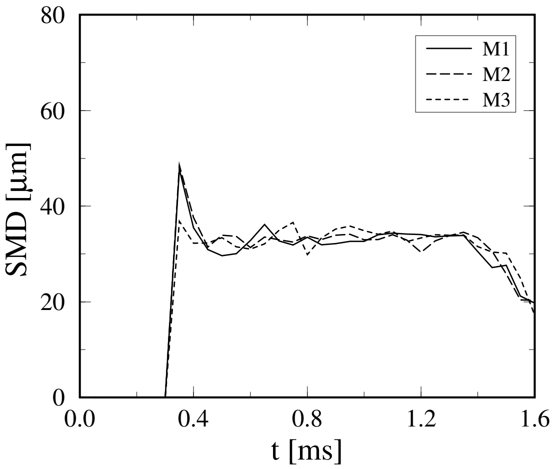

Figure 6.33: Effect of the axial grid density on the SMD at P_{30}.

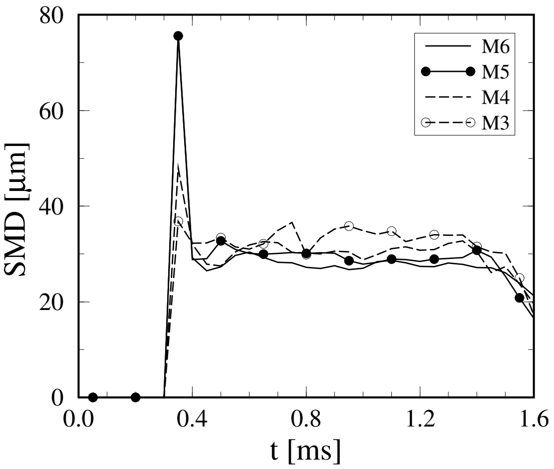

Figure 6.34: Effect of the radial grid density on the SMD at P_{30}.

that the axial grid density shows minor effects which lie within the irregularities of the results. Nevertheless, all the curves have similar trends. In contrast, the finer the mesh in the radial direction, the larger the SMD. This conforms with the observations for the SMD in the total spray. It can also be seen here that the first time at which droplets are captured at the measuring location, large differences among the different meshes are observed. These are attributed to the small sample of droplets available at this time which is not statistically representative.

6.4.3 Effect of the time step

Mesh M3 is now used to investigate the effect of the time-step size on the predictions. Three different Δt are used as listed in Table 6.13, while all the other parameters remain the same as before.

The effect of Δt on the spray penetration is shown in Fig. 6.35 and as can be seen it is not appreciable for values less than $8\,\mu s$. The maximum difference between

Table 6.13: Effect of the time step.

Designation	Δt $[\mu s]$
T8	8
T4	4
T2	2

$\Delta t = 2\,\mu s$ and $\Delta t = 4\,\mu s$ is less than $3\,\%$. Although some effect is encountered in Fig. 6.36, which presents the tip velocity as a function of the distance from the nozzle, it is not clear whether it is due to the time-step size or the scattering of the results. Minor effect of Δt is also observed in Fig. 6.37 which presents the SMD.

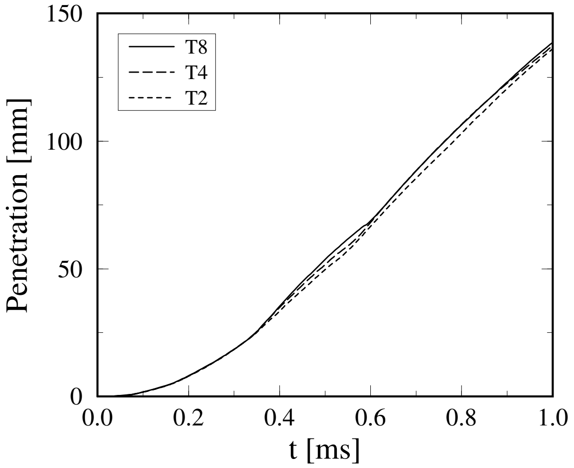

Figure 6.35: Effect of the time step on spray penetration.

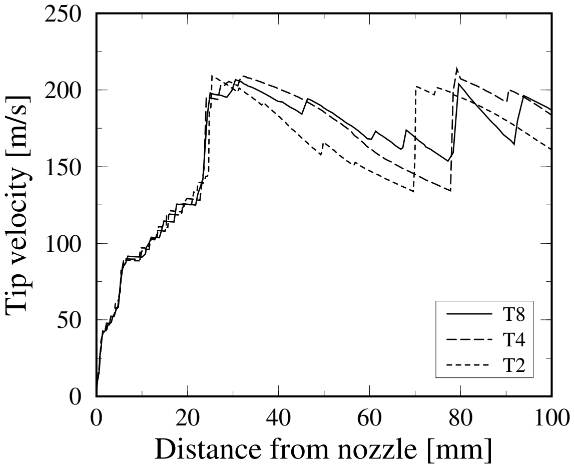

Figure 6.36: Effect of the time step on tip velocity.

The above observations can also be seen in Figs. 6.38 and 6.39 in which the droplet velocity and SMD at P_{30} are respectively plotted. Here, the maximum difference between T4 and T2 is less than $4\,\%$.

Considering that the effect of the time-step size between T4 and T2 is less than $4\,\%$ for all the results and bearing also in mind that reducing the time step by half, the computational time is more than doubled* because of the larger number of parcels generated by the atomisation model, $\Delta t = 4\,\mu s$ is taken to be a fair

*During calculations, it was observed that the computational time for $\Delta t = 2\,\mu s$ was four times larger than that for $\Delta t = 4\,\mu s$.

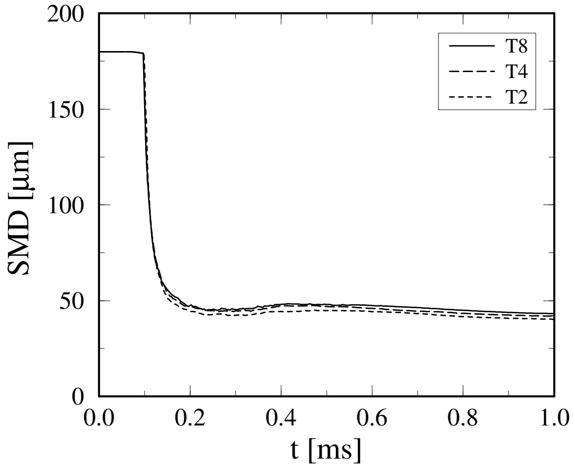

Figure 6.37: Effect of the time step on the SMD.

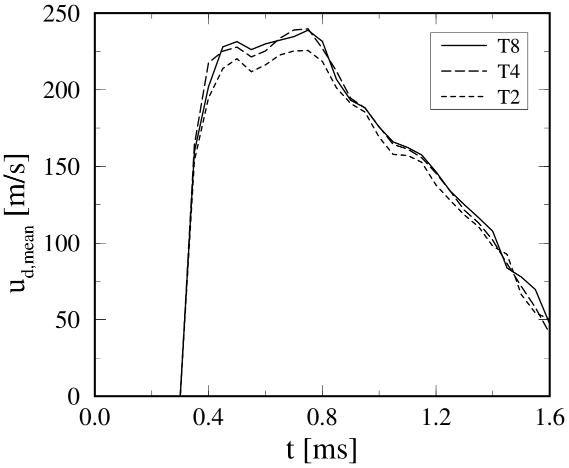

Figure 6.38: Effect of the time step on droplet velocities at P_{30}.

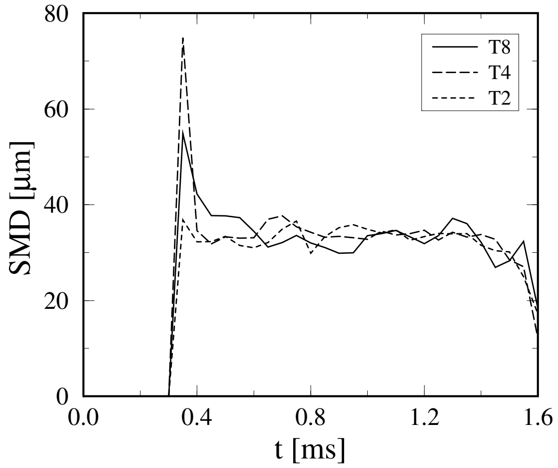

Figure 6.39: Effect of the time step on the SMD at P_{30}.

compromise and is used in all further calculations.

6.4.4 Effect of the parcel introduction rate

Another computational parameter affecting the predictions is the number of parcels introduced per time step, $\dot{N}_p$. Obviously, a large number is desirable for best representation of the spray: however, this implies larger computer overheads as well. Therefore, an optimum parcel introduction rate should be determined. To this end, three different rates are investigated as listed in Table 6.14.

Table 6.14: Effect of the parcel introduction rate.

Designation	$\dot{N}_p$ [parcels/μs]
N1	1
N2	2
N4	4

The effect of $\dot{N}_p$ on the spray penetration is shown in Fig. 6.40. It can be seen that the maximum difference between N1 and N2 is about 2.7 % while it decreases to less than 2 % between N2 and N4. Clear conclusions about the effect of $\dot{N}_p$ on the tip velocity cannot be drawn since this is based on few droplets at the tip and is not statistically representative. Nevertheless, the curves shown in Fig. 6.41 follow similar trends. Fig. 6.42 presents the effect of the parcel introduction rate on the

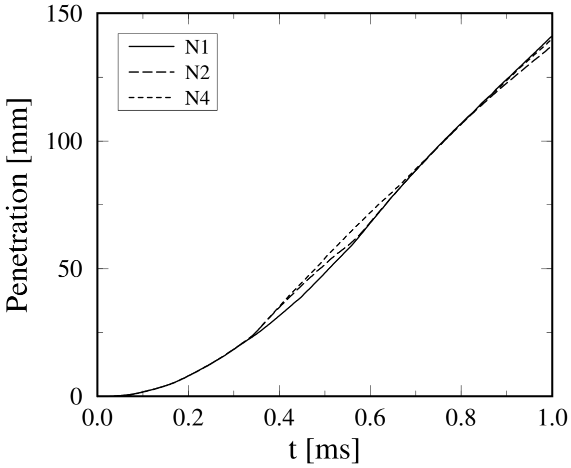

Figure 6.40: Effect of the parcel introduction rate on spray penetration.

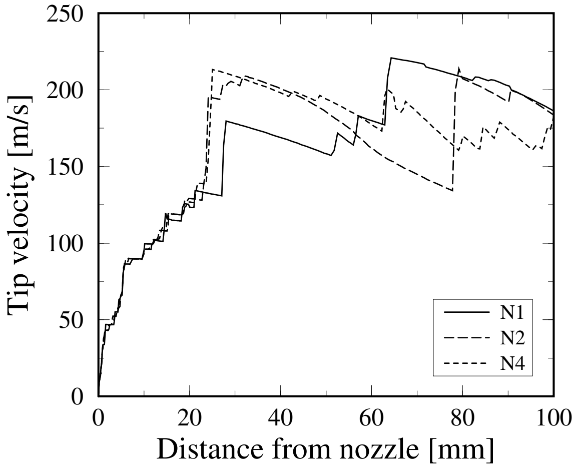

Figure 6.41: Effect of the parcel introduction rate on tip velocity.

SMD. The maximum difference between N1 and N2 is about 13 %. However, it reduces to about 5 % between N2 and N4 due to the better representation of the spray.

Figs. 6.43 and 6.44 show the effect of the parcel introduction rate on the droplet velocity and SMD, respectively, at P_{30}. In both figures, it can be seen that the effect is minor.

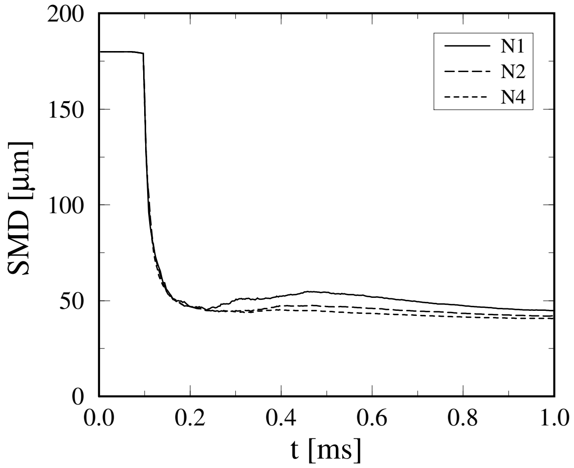

Figure 6.42: Effect of the parcel introduction rate on the SMD.

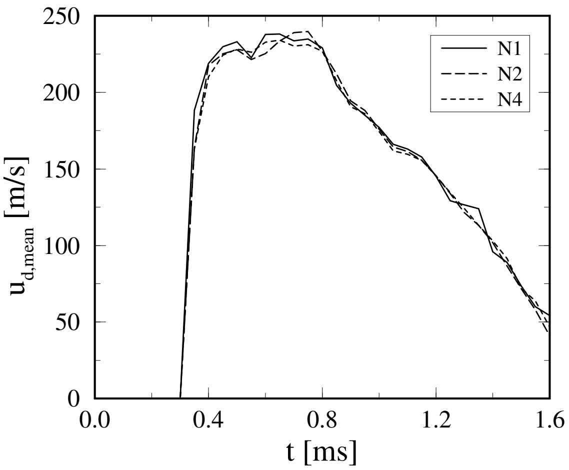

Figure 6.43: Effect of the parcel introduction rate on droplet velocities at P_{30}.

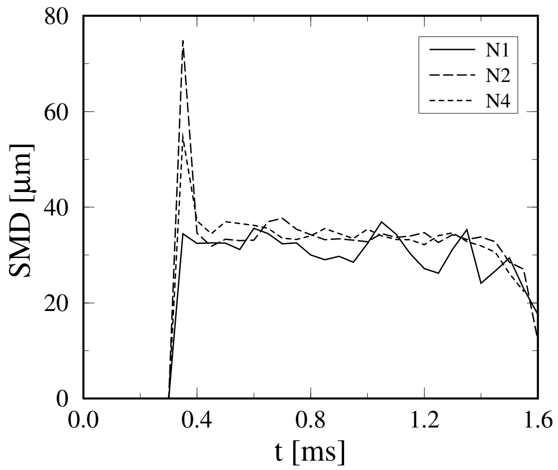

Figure 6.44: Effect of the parcel introduction rate on the SMD at P_{30}.

The effect of the parcel introduction rate on the local droplet RMS velocities is presented in Fig. 6.45. Although it cannot be clearly seen, there is a tendency for larger RMS velocities when the parcel introduction rate increases due to the larger sample. The maximum difference between N2 and N4 is as much as 23 %.

Since the differences between N2 and N4 are less than 5 % for all the results but the RMS velocities and taking also into account that the computational overheads increase with $\dot{N}_p$, 2 parcels/μs is considered to give an acceptable representation of the spray and is used hereafter. However, it should be borne in mind that the

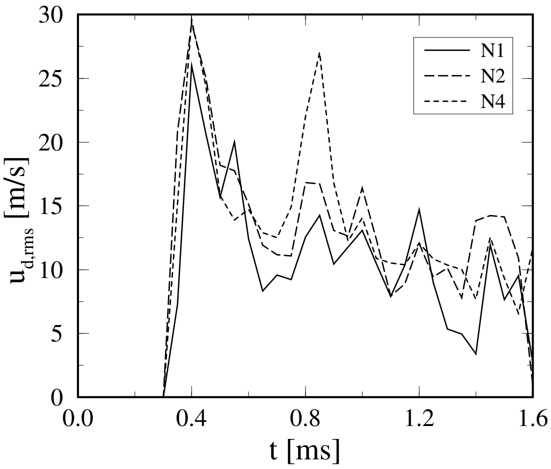

Figure 6.45: Effect of the parcel introduction rate on droplet RMS velocities at P_{30}.

droplet RMS velocities are expected to be underestimated.

For each of the four cases comparisons will now be made between predictions using various spray models and experimental results. In particular for Case A, the Huh and MPI atomisation models are examined. Case B is used to investigate the effect of the increased drag coefficient due to the droplet surface oscillations. Case C is devoted to examining the breakup models presented in Section 3.7. Finally, Case D is used to determine the effect of collisions.

The results for Case A will be explained in detail, showing the spray and gas development at certain times. For the remaining cases, emphasis will be given on the comparison between predictions and measurements.

6.4.5 Case A

Here, the two atomisation models presented in Section 3.3 are compared. Each of these models has one input parameter which needs to be specified from the experimental setup. Two different values of each parameter will be used to investigate its effect on the results. Specifically, the Huh model requires the value of the coefficient

C_5 in Eq. (3.27)* while the MPI model needs the spray semi-cone angle, α_{exp}. The values of C_5 are chosen to be 1 and 0.1, since the former was originally proposed by the developers of the Huh model (see Huh and Gosman [141]), while the latter was employed by Kralj [171] and Ikonomou [143] in Diesel spray calculations. Concerning the value of α_{exp}, unfortunately no information has been supplied from the experimental work. However, it can be estimated from the correlation of Varde [293] which gives the value of the spray cone angle, θ, as follows:

$$\tan\theta = A_1 \left(\frac{\rho_m}{\rho_{d,inj}}\right)^{1/3} Re^{1/3} We^{A_2} \; . \tag{6.8}$$

Here, the Reynolds and Weber numbers are evaluated using the liquid properties at injection conditions. Also, A_1 and A_2 are functions of the length-to-diameter ratio of the nozzle, given respectively by:

$$A_1 = \begin{cases} 10^{-4}\,(L/D)^5 \; , & \text{for } L/D < 6 \; , \\ 0.7 \, , & \text{for } L/D > 6 \; , \end{cases} \tag{6.9a}$$

$$A_2 = \frac{3 - L/D}{3L/D} \; . \tag{6.9b}$$

The above correlation is valid for atmospheric densities up to $40\,kg/m^3$ and it has been derived based on experimental results from many fuels and various types of nozzles. Here, α_{exp} is the maximum spray semi-cone angle and therefore, the maximum injection velocity (see Fig. 6.22) is used to calculate the Reynolds and Weber numbers. This results in $\theta = 4.04°$ and hence, $\alpha_{exp} = 2°$ is chosen. In order to examine its effect on spray characteristics, an additional calculation is performed with a different value of α_{exp}. Here, it is arbitrarily chosen to be five times larger than 2°, so that its effect can easily be detected, despite the fact that according to the above analysis 10° is not realistic. The values of both C_5 and α_{exp} used in this study are tabulated in Table 6.15. All the other spray submodels as well as the initial conditions of the flow field are the same as in §6.4.2 (see Tables 6.11 and 6.12). The injection characteristics are given in Table 6.16.

*The reader is reminded that the smaller the value of C_5, the higher the breakup rate of the primary droplets.

Table 6.15: Designation of the calculations for Case A.

Designation	Atomisation model	C_5	α_{exp} [°]
Huh1	Huh	1	-
Huh2	Huh	0.1	-
MPI1	MPI	-	2
MPI2	MPI	-	10

Table 6.16: Injection characteristics.

Fuel	n-dodecylbenzene
Volume [mm^3]	2.35
$T_{d,inj}$ [K]	300
SOI [ms]	0
EOI [ms]	0.88

Results and discussion

A detailed analysis of the spray structure will firstly be given using the Huh atomisation model with $C_5 = 1$ (i.e. Huh1 in Table 6.15). The spray development is shown in Fig. 6.46 where the droplet velocities are plotted at selected times. Unfortunately, the spray is too dense and details cannot be seen. Nevertheless, this picture provides qualitative informations on spray penetration and the droplet velocity distribution. It can be seen that during injection ($t = 0.3\,ms$ and $t = 0.6\,ms$), the largest velocities are encountered close to the injector since further downstream the droplets are decelerated due to the drag force. After the end of injection, the droplets with the highest velocity overtake the remaining droplets. Hence, after $t = 0.9\,ms$, the tip of the spray has the highest velocity. However, this decreases in time due to drag. Although the maximum injection velocity based on the injection flow rate and the nozzle geometrical area is about $165\,m/s$ (see Fig. 6.47), the droplet velocities reach up to $200\,m/s$. This increase is attributed to cavitation, since according to the predictions, it reduces the nozzle effective area to as low as $78\,\%$ of the geometrical area, as shown in Fig. 6.48.

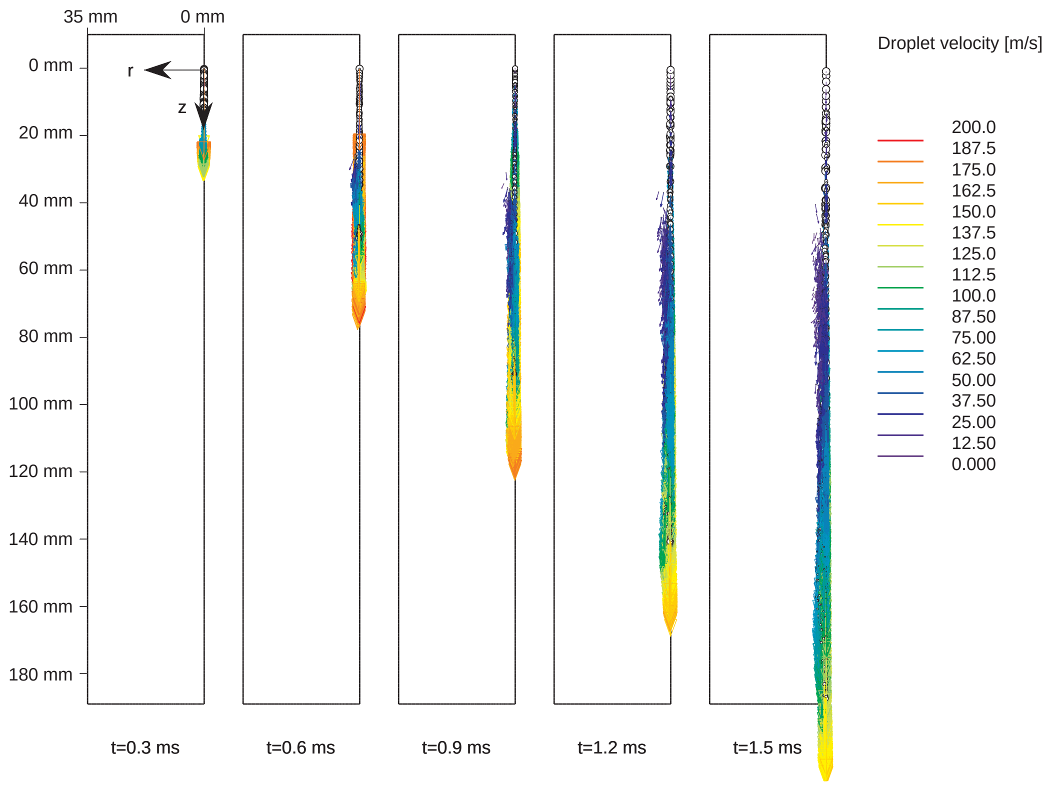

Figure 6.46: Droplet velocity at various times.

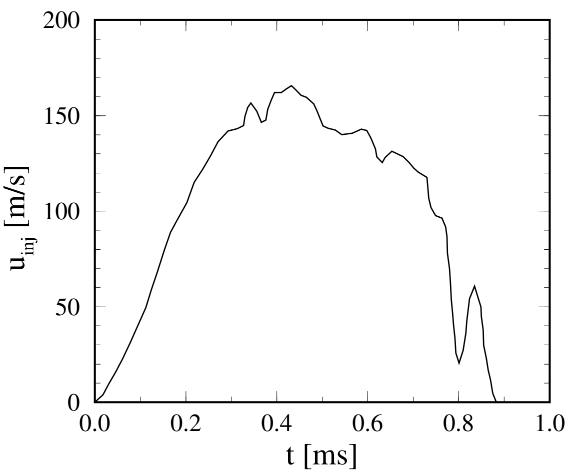

Figure 6.47: Injection velocity based on the nozzle geometrical area.

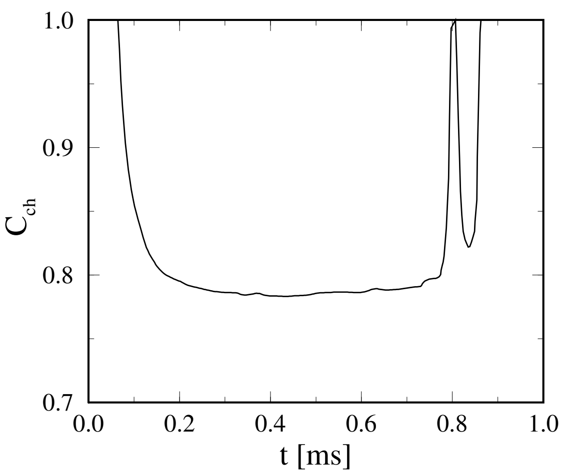

Figure 6.48: Effective to geometrical area ratio.

Fig. 6.49 presents the gas velocity fields at the same times as the previous plot. Since this motion is induced by the spray, the maximum value is found on the axis of the latter. After the end of injection, the location of the maximum velocity moves downstream following the droplets with the highest velocity (see Fig. 6.46). The induced velocity gives rise to local generation of turbulence kinetic energy, as shown in Fig. 6.50. The order of magnitude of the latter implies that the initial values of turbulence parameters are not important because they are very small by comparison (see Table 6.12).

The spray penetration based on the 99 % mass definition is shown in Fig. 6.51, along with the experimental data. The predictions have similar behaviour but they lie well below the experimental data. This leads to the suspicion that there might be some inconsistencies in timings (e.g. for SOI) and this possibility is discussed below. According to the measurements, the spray penetration is $7.15\,mm$ at $t = 0.08\,ms$. This requires an average tip velocity of $89.38\,m/s$. However, according to the injection velocity history (see Fig. 6.47) the injection velocity at this time is only $34.24\,m/s$ and before this time it is even smaller. This leads to the conclusion that the true start of injection in the experiment was somewhat earlier than the reported time. The start of injection was probably defined based on the needle lift because the latter can be measured directly (Nagwaney [207]): however, the exact definition is not given. Hence, some liquid may have issued from the nozzle before the needle lift reaches the threshold value resulting in this 'apparent' high penetration. This difference between the predicted and the measured penetration was also encountered by Ikonomou [143] who simulated the same experiment. Following his remedy, the decision is taken to adjust the start of injection time by $0.14\,ms$ to produce a more plausible initial penetration, as shown in Fig. 6.52. The necessity for this adjustment is confirmed by the local droplet velocities, as will be seen later, by comparing the timings of the predicted peak values to those of the measurements. Hereafter, all experimental results for all cases will be plotted in this shifted time frame. The fact that this time is the same for all cases implies that it is related to the geometrical characteristics of the injector as well as the definition of the SOI.

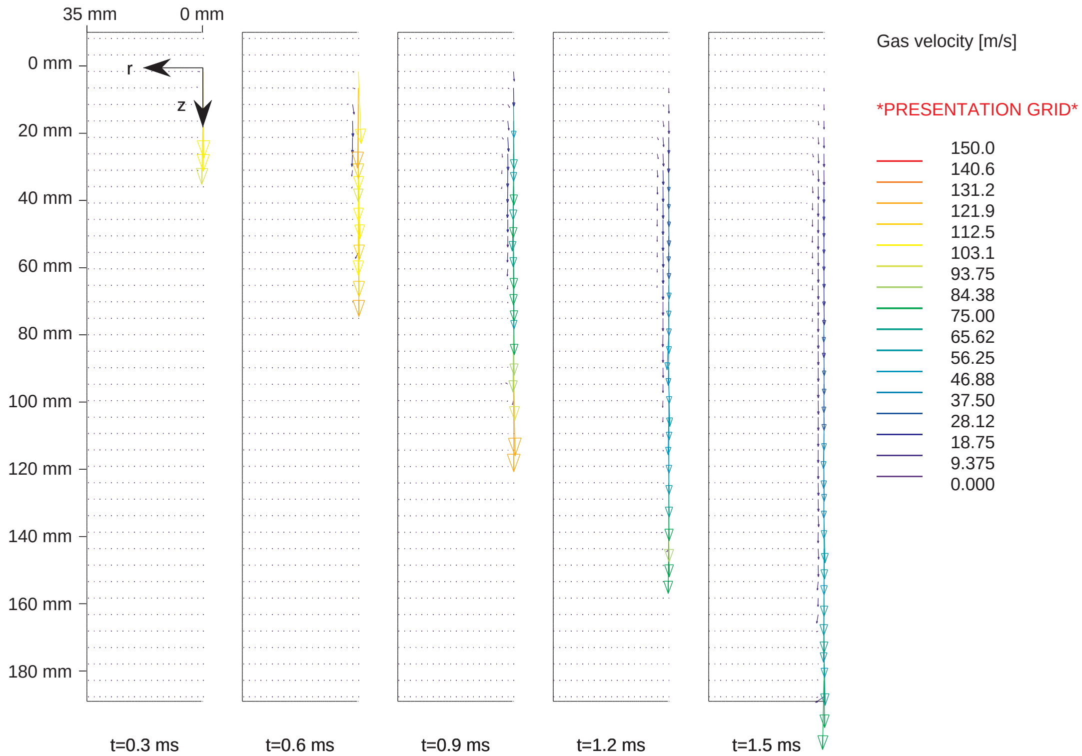

Figure 6.49: Gas velocity field at axial section at various times.

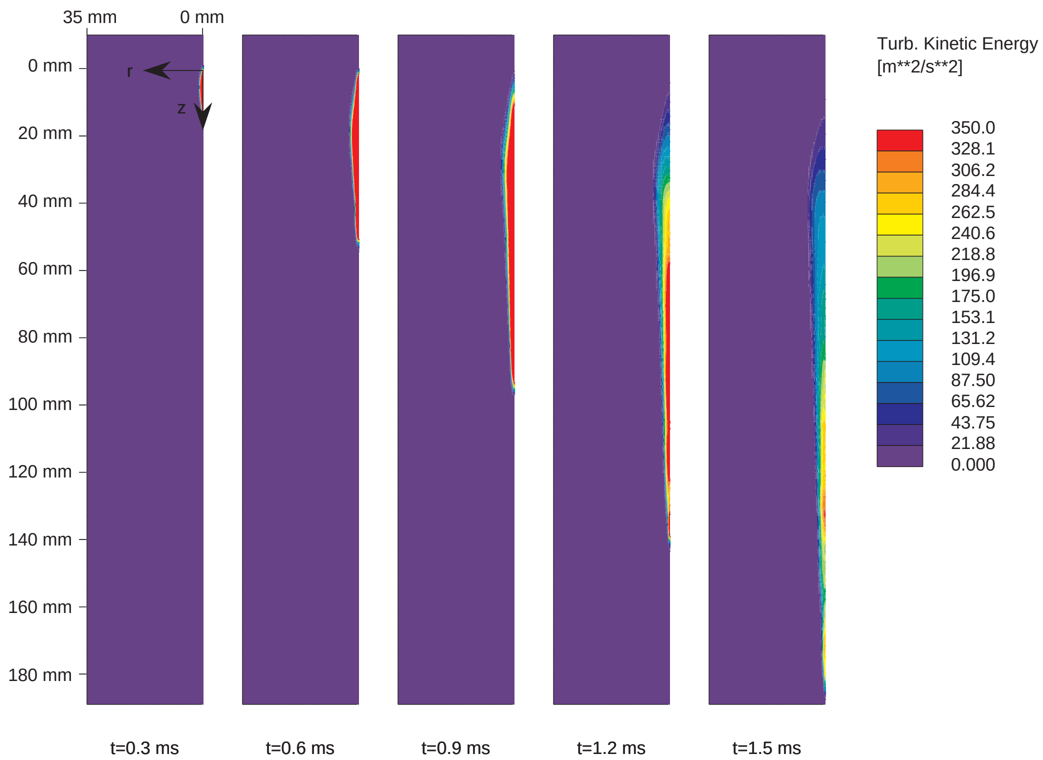

Figure 6.50: Turbulence kinetic energy field at axial section at various times.

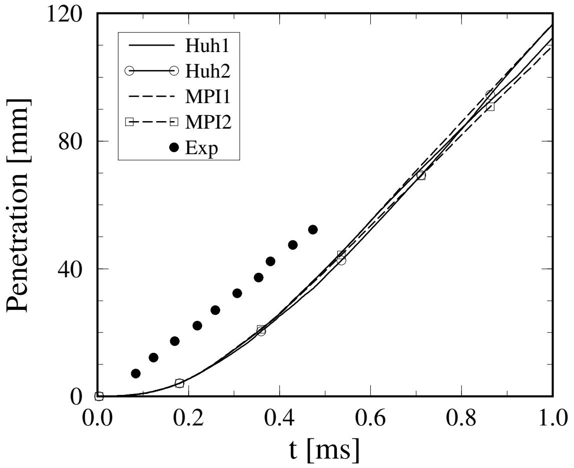

Figure 6.51: Effect of the atomisation model on the spray penetration.

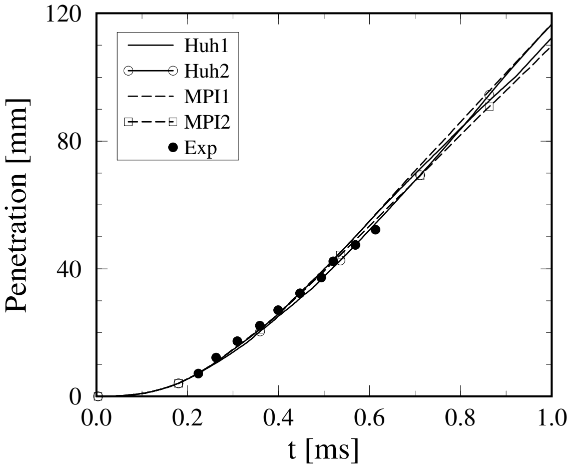

Figure 6.52: Spray penetration based on the 99 % mass definition with time-shifted experimental data.

Another one interesting point is that in reality, the needle lifts when the line pressure reaches a certain value (opening pressure) and hence, the liquid is initially injected with a relatively high velocity. Unfortunately, this cannot be modelled here due to the lack of informations. However, it is clear that underestimated droplet velocities may be expected.

The performance of the atomisation models and their parameters will now be discussed. As can be seen in Fig. 6.52, the penetration shows some sensitivity to the parameter C_5. A ten-fold change in the latter produces a maximum difference in penetration of 8.2 %. When C_5 is decreased the penetration decreases, because the breakup rate increases (see Eq. (3.27)) resulting in smaller droplets which decelerate faster. This can also be seen in both Figs. 6.53 and 6.54 which present the tip velocity and the SMD, respectively, although the evidence in the former is not clear. In Fig. 6.54 the maximum difference between Huh1 and Huh2 is 33.5 %. Just prior the end of injection atomisation ceases and the droplet size afterwards is mainly controlled by breakup and coalescence. It seems that the latter mechanism causes the SMD produced by Huh2 to be higher than for Huh1. This enhances the penetration as well.

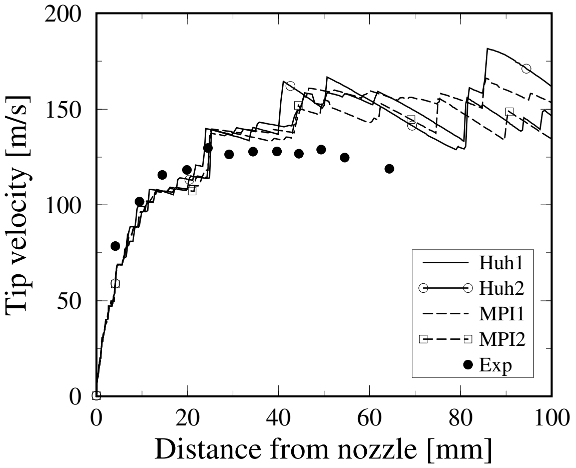

Figure 6.53: Effect of the atomisation model on tip velocity.

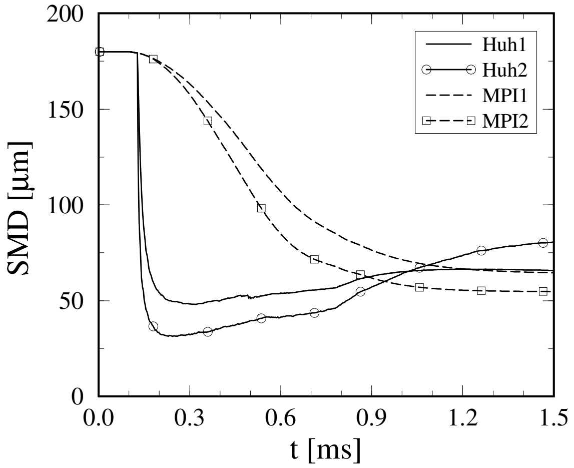

Figure 6.54: Effect of the atomisation model on the SMD.

Concerning the MPI model predictions, it can be seen in Fig. 6.52 that by increasing the spray semi-cone angle, α_{exp}, from 2° (MPI1) to 10° (MPI2), the penetration decreases, presenting a maximum difference about 6 %. This reduction is attributed to the fact that the spray is spread in a bigger volume and hence, more mass of the surrounding gas participates in momentum exchange. The latter results in lower induced velocities with consequences on drag. The effect on the axial droplet velocity is also shown in Fig. 6.53.

Comparing the penetrations produced by the two atomisation models, it can be seen that for $\alpha_{exp} = 2°$ (MPI1), the penetration is similar to that produced by the Huh model (Huh1) with a maximum difference about 3 %. It is noted that this angle is relatively close to the one predicted by the Huh model which is around 0.6° as shown in Fig. 6.55.

As can be seen in Fig. 6.53 for both atomisation models, the tip velocity is overpredicted beyond $40\,mm$ from the injector. This is consistent with the penetration. The main difference between the behaviours of the two models is the droplet size. As shown in Fig. 6.54, atomisation commences at $0.13\,ms$ for both models, because at this time the injection velocity is such that it satisfies the criterion for atomisation onset, given in Section 3.3. Shortly afterwards, the Huh model produces droplets

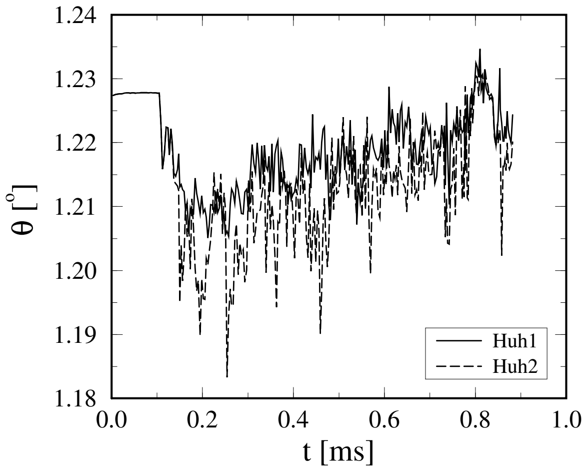

Figure 6.55: Spray cone angle predicted by the Huh atomisation model.

of about 50 μm SMD while after the end of injection, SMD increases due to coalescences. In contrast, the SMD produced by the MPI model with $\alpha_{exp} = 2°$ (MPI1) gradually approaches the value produced by Huh1 which is about 65 μm. The case with larger α_{exp} (MPI2) leads to smaller SMD than that of MPI1 because the spray is more dilute resulting in stronger breakup rate and lower collision frequency. The increasing value of the SMD when the Huh atomisation model is employed, was also observed by Müller [203] who studied the atomisation process under atmospheric conditions. Also, Müller [203] used a constant injection velocity of 200 m/s and nozzle diameter 100 μm to investigate the PDF of the secondary droplets. He found that the majority of them had a diameter of less than 5 μm leading to low further breakup rate. Hence, coalescence resulted in an increasing SMD.

The temporal variation of the local SMD at locations P_{10}, P_{30} and P_{60} (see Table 6.7) is plotted in Figs. 6.56, 6.57 and 6.58, respectively. It can be seen that moving downstream the measurements show a slight decrease of the SMD while a slight increase is indicated by the predictions using the Huh atomisation model. The latter is attributed to coalescence. It is interesting that no droplets are encountered at P_{10} when the MPI model is used. This is because at this location all the droplets are larger than the threshold value of 108.5 μm (see also Fig. 6.54) while further downstream the SMD decreases. Although the MPI model reproduces the trends of

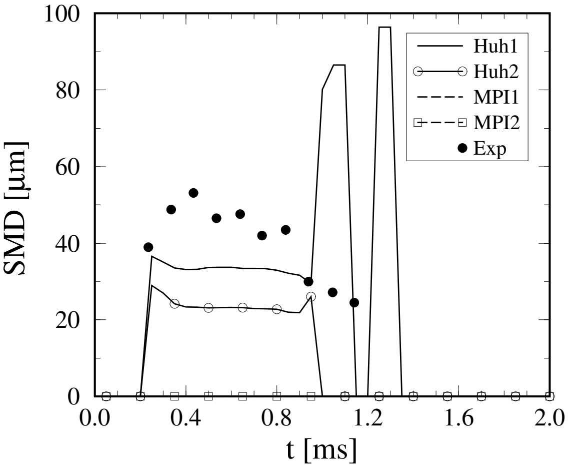

Figure 6.56: SMD at P_{10}.

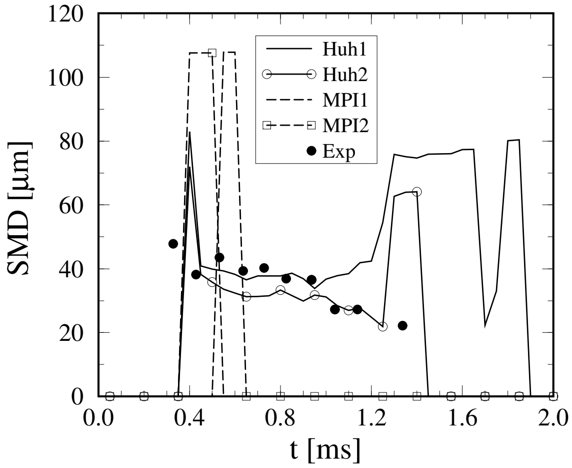

Figure 6.57: SMD at P_{30}.

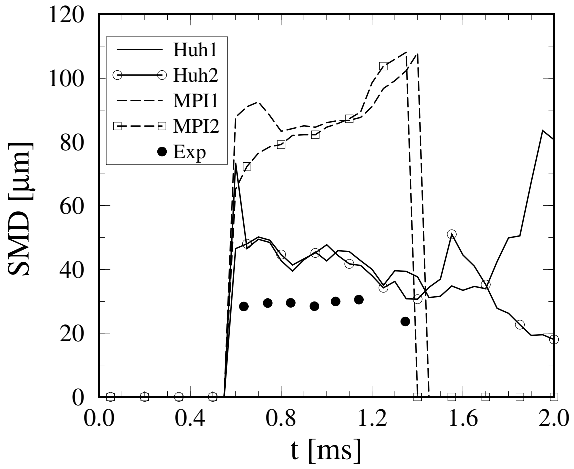

Figure 6.58: SMD at P_{60}.

the measurements (i.e. decreasing SMD with distance), it overpredicts the level. In contrast, the Huh model gives a very good agreement at P_{30}, while the differences at the other two locations are not substantial. Finally, concerning the effect of the coefficient C_5, it seems that at distances close to the injector (P_{10}) it gives smaller SMD when it is reduced. However, further downstream its effect is minor, since the SMD there is mainly controlled by the combination of breakup and coalescence. It is also noted that the scattering of the predictions at some cases is due to the small sample.

The temporal variation of the mean droplet velocity at the three measurement locations is shown in Figs. 6.59–6.61. It is encouragingly observed that the predictions follow the trends of the measurements. Also, by comparing the timings of the predicted peak values to the corresponding measured ones, the shifting, in time, of the experimental results is further justified. Another observation in these figures is that the effect of C_5 on the local droplet velocities is negligible.

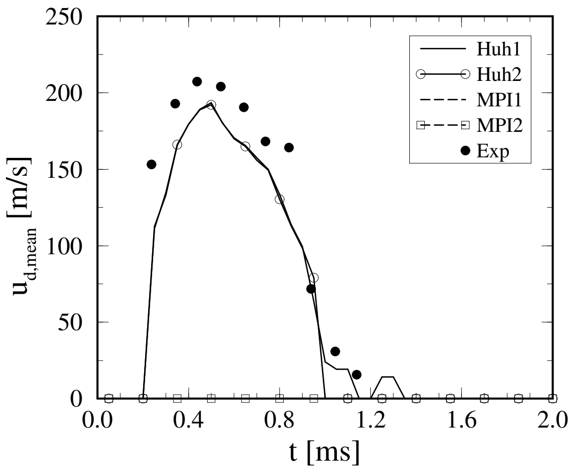

Figure 6.59: Droplet mean velocity at P_{10}.

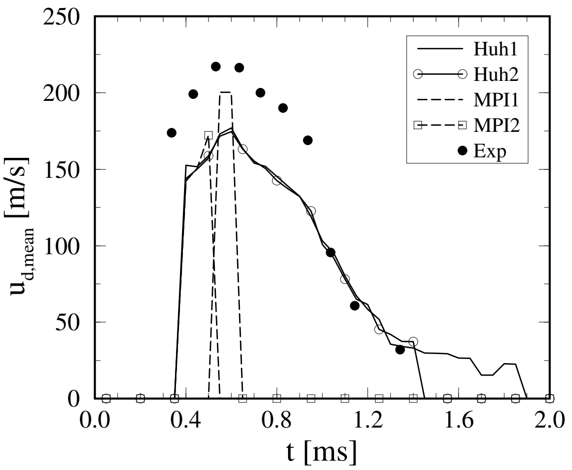

Figure 6.60: Droplet mean velocity at P_{30}.

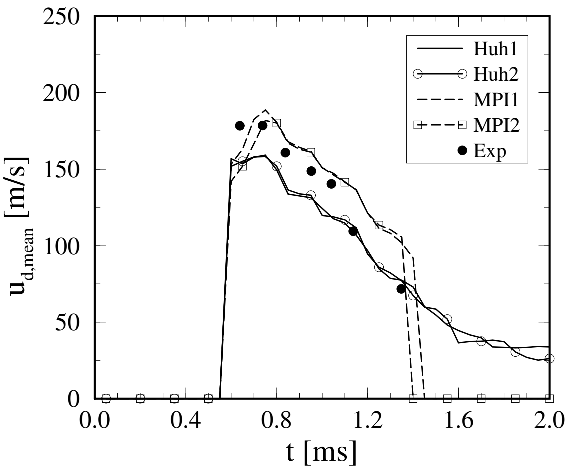

Figure 6.61: Droplet mean velocity at P_{60}.

Concerning the agreement between the calculated and measured droplet mean velocities, it can be seen that the Huh model results in underprediction while the MPI model gives higher velocities, which are closer to the measurements, due to the larger size of the droplets. It should, however, be noted that the predicted values lie within the measured ones ±RMS* (see Figs. 6.62–6.64) for both atomisation models and hence, an acceptable agreement can be claimed in both cases. The RMS levels are significantly underpredicted, probably due to the insufficient sample (see

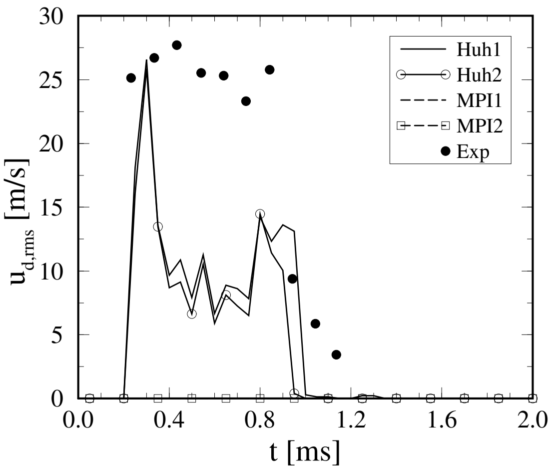

Figure 6.62: Droplet RMS velocity at P_{10}.

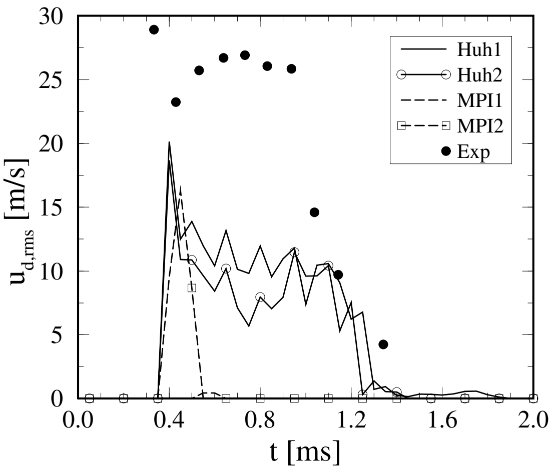

Figure 6.63: Droplet RMS velocity at P_{30}.

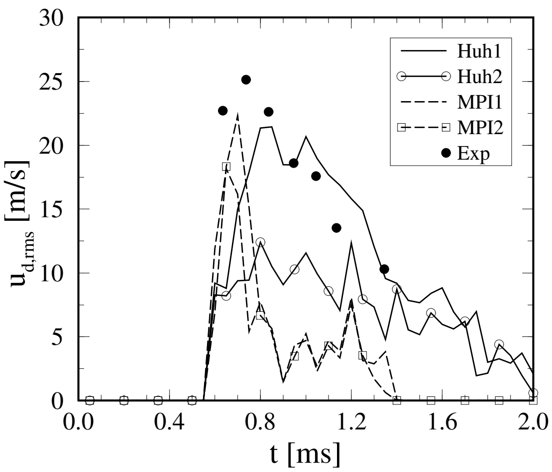

Figure 6.64: Droplet RMS velocity at P_{60}.

§6.4.4). It should also be noted that in sprays the RMS droplet velocity represents not only the turbulent fluctuations, as is the case in the continuous phase, but also

*Note that according to statistics the confidence interval for the real mean value of a normal distribution, as is the case here (see Paál [227]), to lie within the measured one ±RMS is only 68 % [258].

the variations due to the different sizes and histories of the droplets passing through the location in question.

6.4.6 Case B

Case B is used to investigate the effect of the choice of drag coefficient correlation on the spray characteristics. Specifically, the correlation of Yuen and Chen [313], Eq. (3.66), for spherical droplets will be compared to the correction proposed by Patterson *et al.* [230], Eq. (3.72), for dynamically-distorting droplets. The two calculations are designated according to Table 6.17. All the other spray submodels

Table 6.17: Designation of the calculations for Case B.

Designation	Drag coefficient
Sph	Yuen-Chen, Eq. (3.66)
Dist	Patterson *et al.*, Eq. (3.72)

as well as the initial conditions of the flow field remain the same as used in §6.4.2 (see Tables 6.11 and 6.12) while the injection characteristics are given in Table 6.18.

Table 6.18: Injection characteristics.

Fuel	n-dodecylbenzene
Volume $[mm^3]$	4.7
$T_{d,inj}$ $[K]$	300
SOI $[ms]$	0
EOI $[ms]$	1.3

Results and discussion

The spray penetration based on the 99 % mass definition is plotted in Fig. 6.65. Although the spherical droplets have lower drag coefficients than the distorted ones,

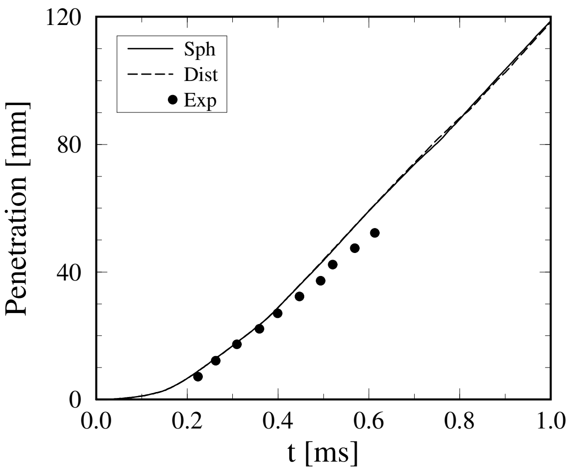

Figure 6.65: Effect of the drag coefficient on spray penetration.

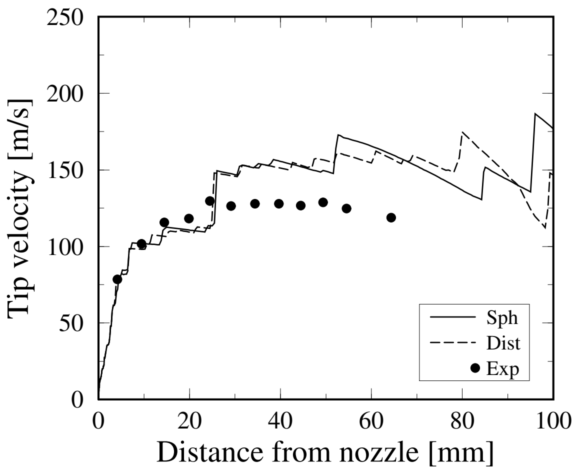

Figure 6.66: Effect of the drag coefficient on tip velocity.

there is negligible effect on the penetration. This is in accord with the tip velocity behaviour shown in Fig. 6.66, although some discrepancies at distances greater than $50\,mm$ from the nozzle are observed. Nevertheless, these do not give clear evidence about which of the two correlations produces the larger velocities. Similar observations have been reported by Liu *et al.* [190], who found that the spray penetration is insensitive to the drag coefficient level even when the latter is multiplied by a factor of 16. Their explanation was that the higher drag coefficient lowers the relative velocity between the droplet and the surrounding air, which results in larger droplets (according to the breakup model) with higher momentum. However, as can be seen in Fig. 6.67 which presents the temporal variation of the overall SMD, this is the case only after $0.7\,ms$. Therefore, the explanation of Liu *et al.* [190] is not enough to justify the non-sensitivity of the penetration. Another possible explanation is that the higher drag coefficient results in greater momentum given to the gas and hence, smaller drag force acting on the following droplets.

The comparison of the predictions with the experimental results shows that the tip velocity is overpredicted for distances greater than $30\,mm$, with a maximum difference about $17\,\%$. This leads to penetration overprediction as well, whereas below this distance, very good agreement is obtained for both the penetration and tip velocity.

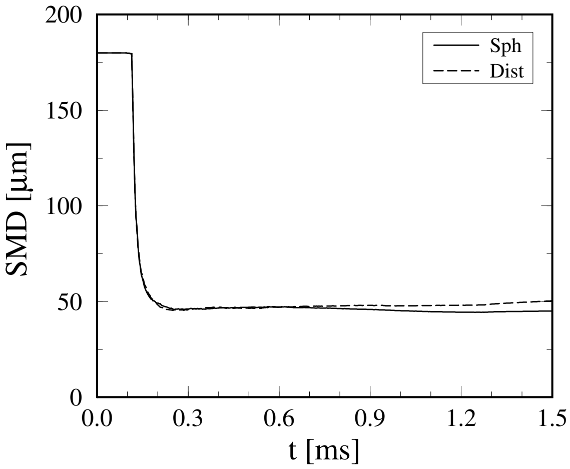

Figure 6.67: Effect of the drag coefficient on the SMD.

As can be seen in Fig. 6.68, the drag coefficient also does not much affect the local droplet velocities. Although the region around the measured peak velocity is very well captured by the predictions, this is not true later on, when underprediction occurs. This cannot be explained by the RMS velocity levels shown in Fig. 6.69, although at some times the predicted mean velocity is within the RMS variation of the measured one.

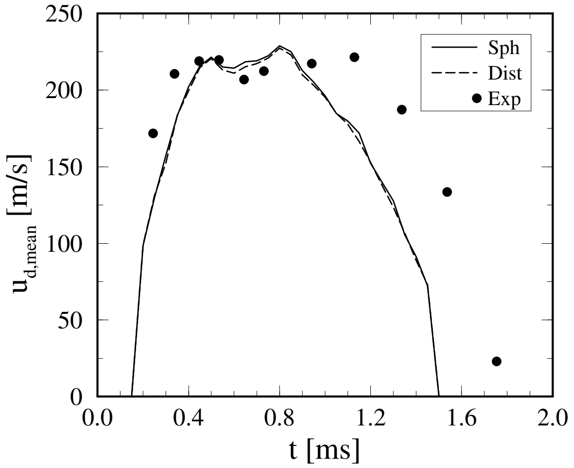

Figure 6.68: Droplet mean velocity at P_{10}.

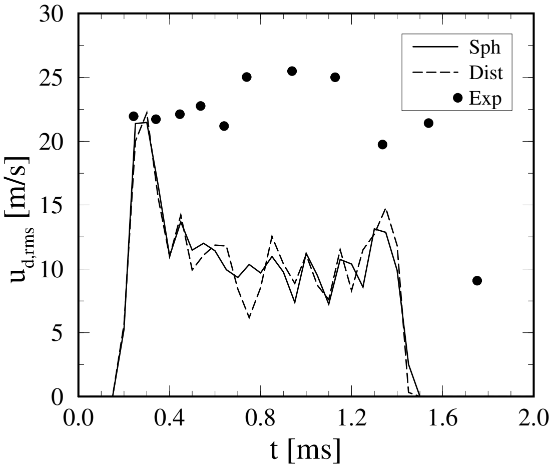

Figure 6.69: Droplet RMS velocity at P_{10}.

Despite the promising predictions of the droplet velocity, the SMD is significantly underestimated as shown in Fig. 6.70. However, moving farther from the injector, the gap between the predictions and the measurements decreases as can be

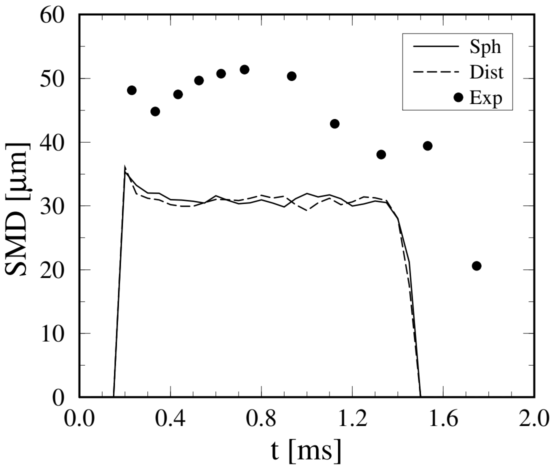

Figure 6.70: SMD at P_{10}.

observed in Figs. 6.71 and 6.72 at distances $30\,mm$ and $60\,mm$, respectively. This is because the measured SMD decreases moving downstream, while the predicted level is relatively constant. This is probably due to the atomisation model, which immediately produces small droplets whose further breakup rate is small. Nevertheless, the droplet size also depends on both breakup and coalescence. These mechanisms will be individually investigated in the remaining two cases.

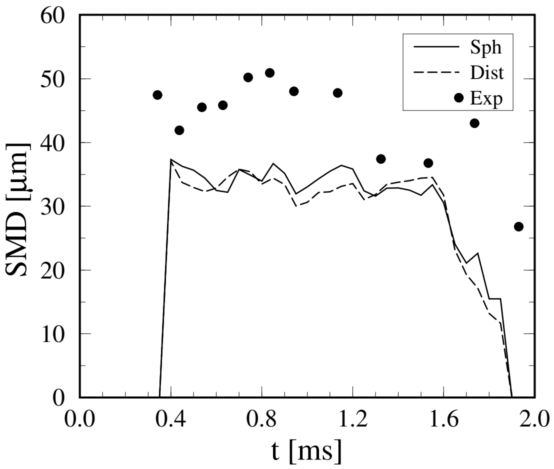

Figure 6.71: SMD at P_{30}.

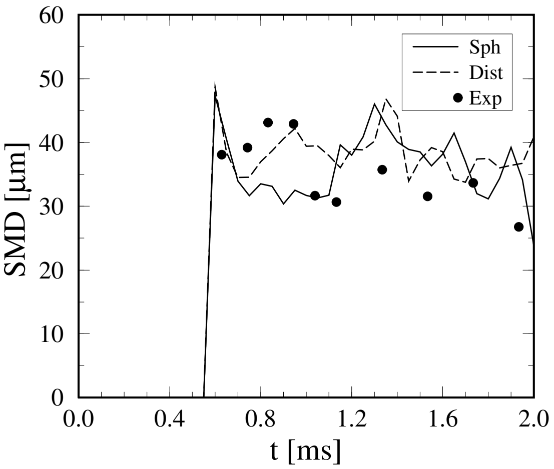

Figure 6.72: SMD at P_{60}.

Moving downstream, the droplet mean velocity decreases according to both measurements and predictions, as depicted in Figs. 6.73 and 6.74 for distances $30\,mm$ and $60\,mm$, respectively. However, at both locations, the predicted peak levels are

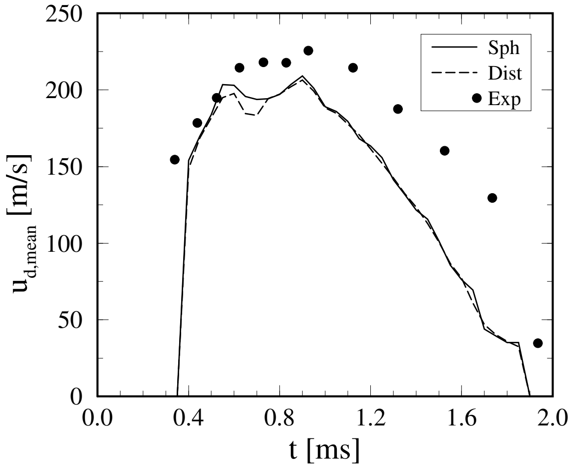

Figure 6.73: Droplet mean velocity at P_{30}.

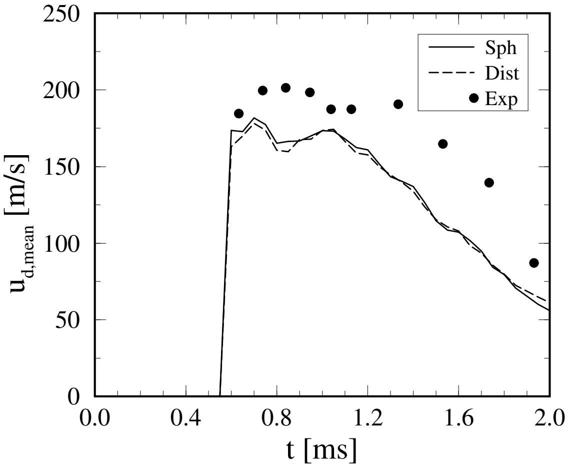

Figure 6.74: Droplet mean velocity at P_{60}.

lower than the measured ones by about 11 % and 17 %, respectively. Nevertheless, these differences are of the order of the RMS velocities shown in Figs. 6.75 and 6.76.

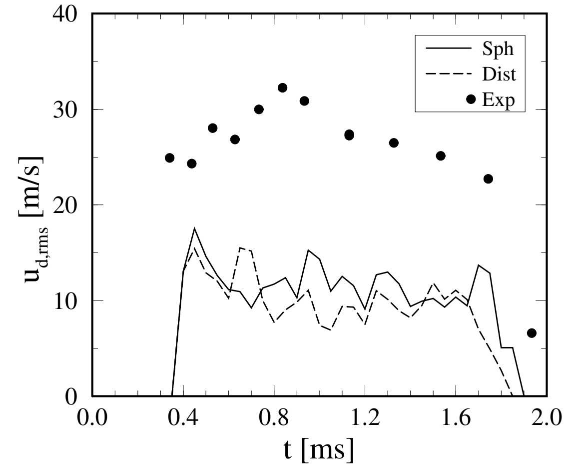

Figure 6.75: Droplet RMS velocity at P_{30}.

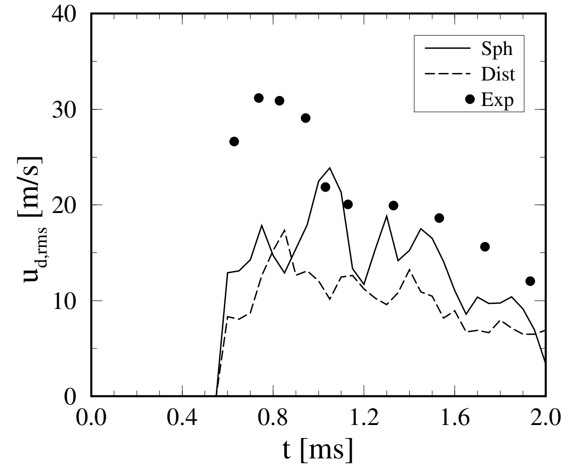

Figure 6.76: Droplet RMS velocity at P_{60}.

An important conclusion is therefore, that the local droplet velocity and SMD as well as the spray penetration and global SMD are rather insensitive to the choice of drag coefficient correlation.

6.4.7 Case C

The effect of the breakup on the spray structure will be examined using Case C. Results using three breakup models presented in Section 3.7 will be compared each other and the experimental data. Also, one additional calculation will be performed in which the breakup model is switched off. The calculations are designated as listed in Table 6.19. All the other spray submodels as well as the initial conditions

Table 6.19: Designation of the calculations for Case C.

Designation	Breakup model
RD	Reitz-Diwakar
HF	Hsiang-Faeth
PE	Pilch-Erdman
NO	None

of the flow field are the same as those used in §6.4.2 (see Tables 6.11 and 6.12). The injection characteristics are given in Table 6.20.

Table 6.20: Injection characteristics.

Fuel	n-dodecylbenzene
Volume $[mm^3]$	2.35
$T_{d,inj}$ $[K]$	300
SOI $[ms]$	0
EOI $[ms]$	0.84

Results and discussion

Fig. 6.77 shows the spray penetration based on the 99 % mass definition. It is observed that there is no appreciable difference among the penetrations using any of the three breakup models. However, in the absence of breakup, the penetration increases, because the droplets are larger, with greater inertia relative to drag. They, therefore, have higher velocity, as can be seen in Fig. 6.78 which displays the tip

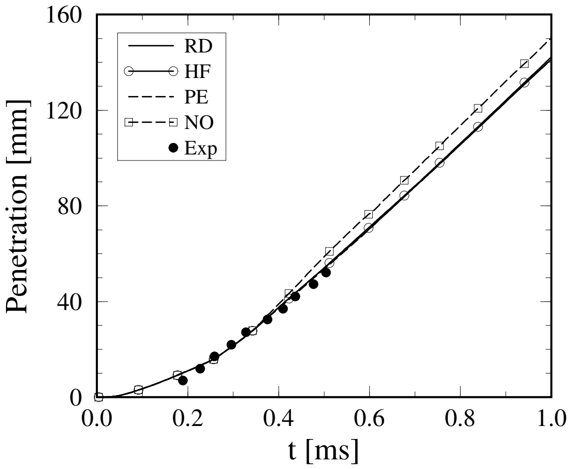

Figure 6.77: Effect of breakup on spray penetration.

velocity. However, the evidence is not clear about whether any particular model produces higher velocity. This is in accord with the penetration curve.

The choice of model does however, affect the SMD, as can be clearly seen in Fig. 6.79. If there is no breakup model, the only mechanism controlling the droplet size after the end of injection is collision. As can be seen in this figure, the main output of collision is coalescence, since the SMD increases after the EOI ($0.84\,ms$). It is also observed that until EOI, the controlling mechanism of the droplet size is the atomisation, while afterwards, the differences in the SMD between the models become stronger. Thus, at $1.2\,ms$, the Hsiang-Faeth model produces a SMD about $16\,\%$ smaller than that obtained by switching breakup off. A further reduction of the SMD is observed with the Pilch-Erdman model, to about $24\,\%$. The Reitz-Diwakar model produces the largest reduction, of $36\,\%$. The fact that this model predicts a smaller stable diameter than the Pilch-Erdman one, was also noted by the developers of the latter (see Pilch and Erdman [233]).

Concerning the comparison of the predictions to the measurements, the effect of the breakup on penetration is to produce better agreement for all models, as can be seen in Fig. 6.77. Improved agreement is also obtained for the tip velocity, as can be seen in Fig. 6.78.

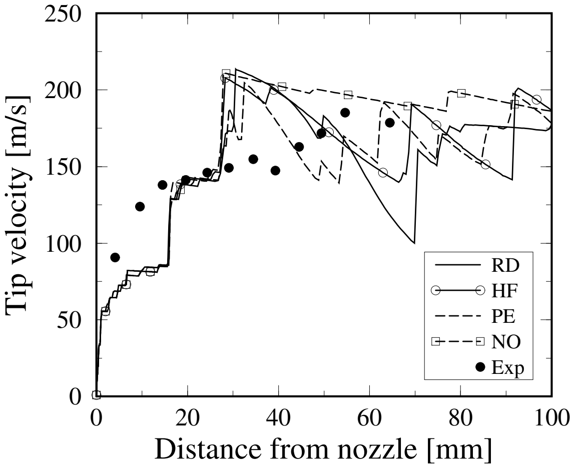

Figure 6.78: Effect of breakup on tip velocity.

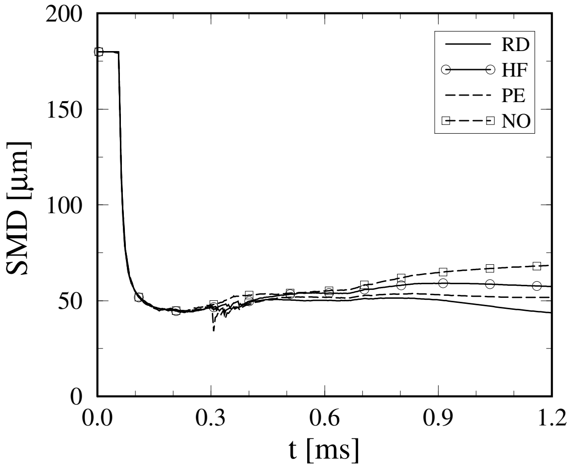

Figure 6.79: Effect of breakup on the SMD.

Fig. 6.80 shows that the effect of breakup on local droplet velocities at $10\,mm$ from the nozzle is minor. In all cases the mean velocity is underpredicted by about $7\,\%$ at the peak value. However, this difference is of the order of the RMS velocity shown in Fig. 6.81. The same comments apply to the other two locations, for which

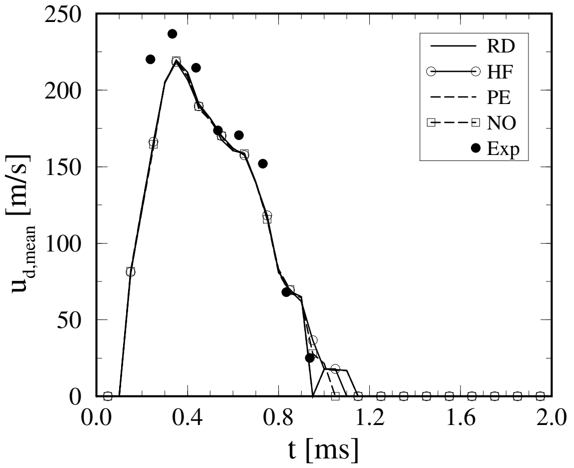

Figure 6.80: Droplet mean velocity at P_{10}.

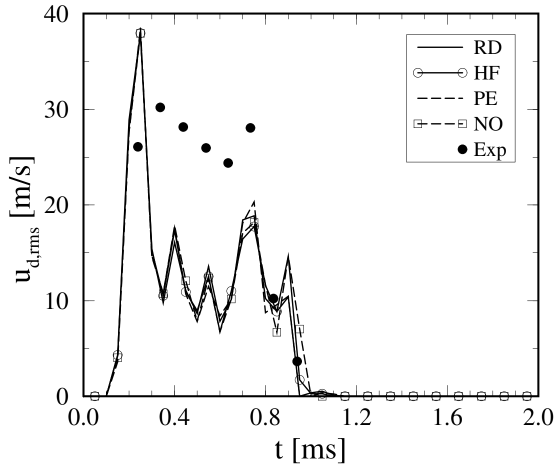

Figure 6.81: Droplet RMS velocity at P_{10}.

the mean velocities are shown in Figs. 6.82 and 6.83 and the RMS levels in Figs. 6.84 and 6.85.

The SMD at $10\,mm$ distance from the nozzle is shown in Fig. 6.86. The effect of breakup seems to be minor, probably because this location is close to the nozzle and the droplet size is mainly controlled by the atomisation model. Further

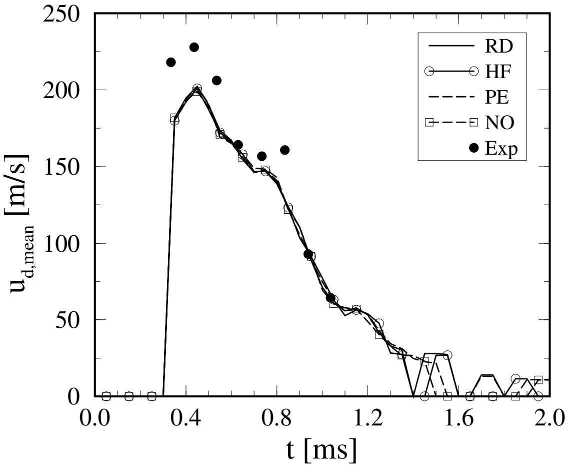

Figure 6.82: Droplet mean velocity at P_{30}.

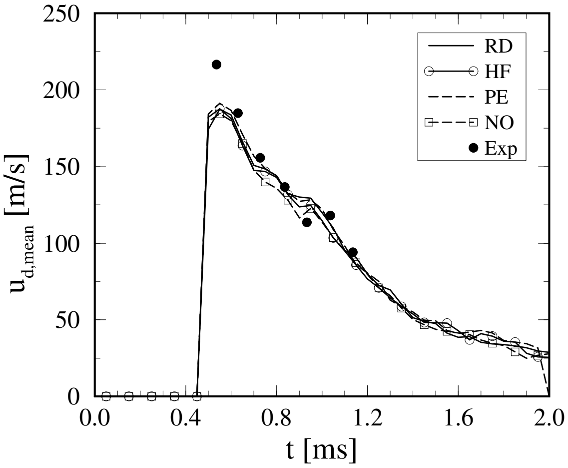

Figure 6.83: Droplet mean velocity at P_{60}.

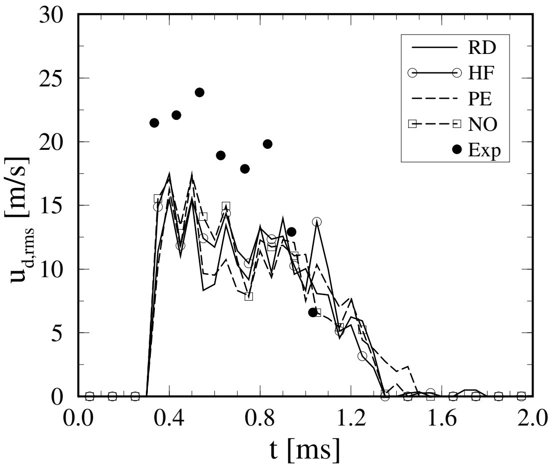

Figure 6.84: Droplet RMS velocity at P_{30}.

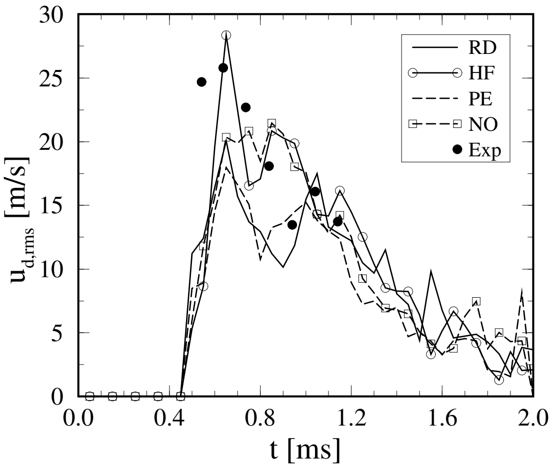

Figure 6.85: Droplet RMS velocity at P_{60}.

downstream, some differences can be observed between the SMD predictions of the models, with Hsiang-Faeth one perhaps producing larger droplets (see Figs. 6.87 and 6.88). However, surprisingly when the breakup model is switched off, slightly smaller droplets are produced despite the fact that in Fig. 6.79 the inverse tendency was observed. This can be attributed to coalescence which probably occurs at the spray axis, where the spray is dense, with higher frequency than elsewhere. Nevertheless, the differences with and without breakup are not pronounced. Good agreement is obtained between predictions and measurements at 30 mm from the nozzle while underprediction is observed at 10 mm and overprediction at 60 mm.

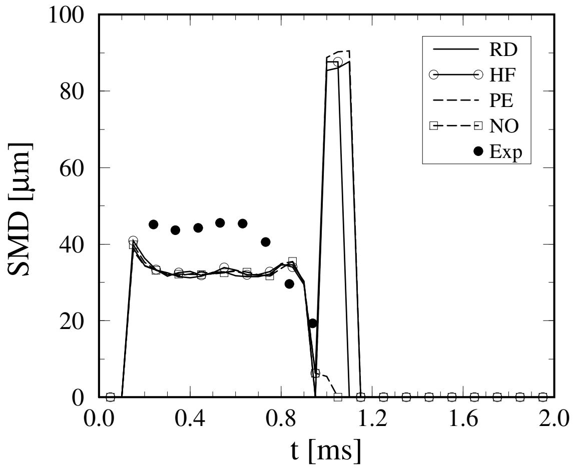

Figure 6.86: SMD at P_{10}.

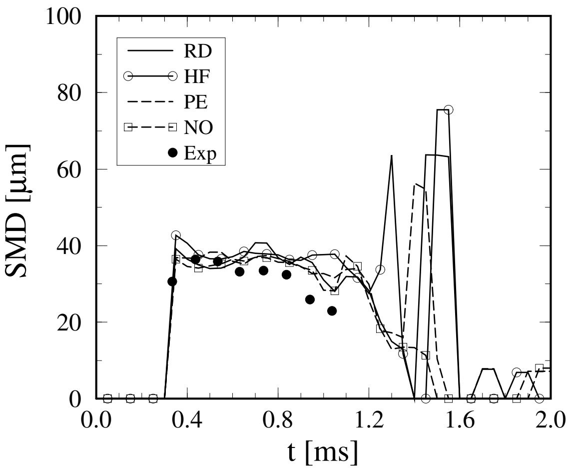

Figure 6.87: SMD at P_{30}.

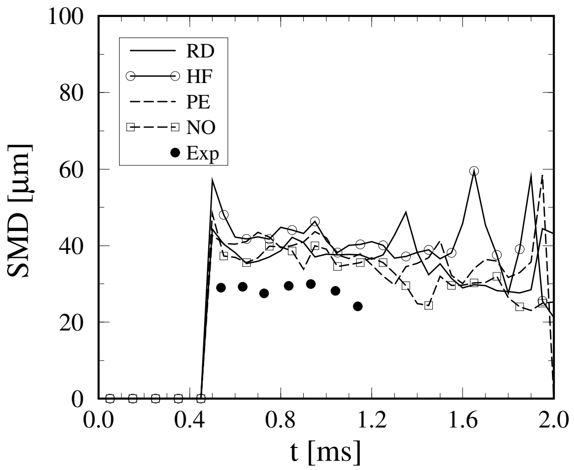

Figure 6.88: SMD at P_{60}.

6.4.8 Case D

This case is used to explore the effect of collision and coalescence on the spray characteristics. Two calculations are performed with the collision model described in Section 3.8 switched on and off, as designated in Table 6.21. All the other spray submodels and the initial conditions of the flow field remain the same as in §6.4.2 (see Tables 6.11 and 6.12). The injection data are given in Table 6.22.

Table 6.21: Designation of the calculations for Case D.

Designation	Collision model
ON	Switched on
OFF	Switched off

Table 6.22: Injection characteristics.

Fuel	n-dodecylbenzene
Volume $[mm^3]$	4.7
$T_{d,inj}$ $[K]$	300
SOI $[ms]$	0
EOI $[ms]$	1.25

Results and discussion

The temporal variation of the SMD is plotted in Fig. 6.89. As shown, the SMD increases when collisions are included. This implies that the main output of collision is coalescence. According to the modelling of this phenomenon (see §3.8.4), when

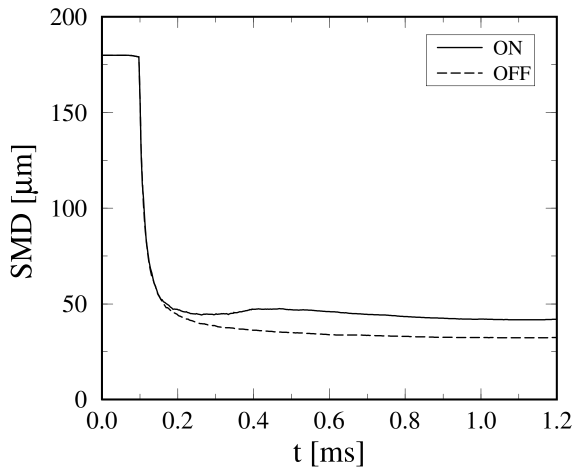

Figure 6.89: Effect of collisions on the SMD.

coalescence occurs the total momentum of the colliding droplets is conserved (see Eq. (3.204)). Thus, the newly-formed droplet always has a velocity smaller than or equal to the larger of the two colliding droplet velocities. Consequently, coalescence reduces tip velocity and penetration. These trends are shown in Figs. 6.90 and 6.91.

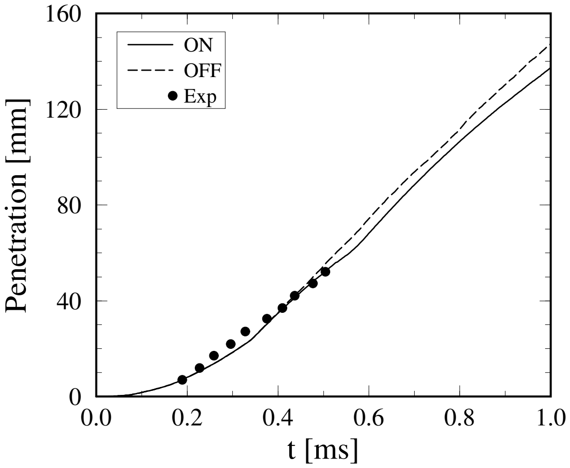

Figure 6.90: Effect of collisions on spray penetration.

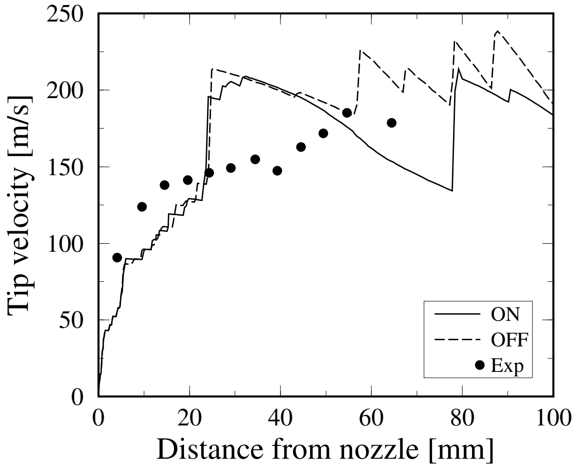

Figure 6.91: Effect of collisions on tip velocity.

The maximum difference in penetration between the two calculations is about 7 %, but unfortunately, experimental data are not available at the stage at which the two differ, i.e. beyond 0.5 ms: it is therefore not clear whether the effect of coalescences on prediction accuracy is positive or negative.

The effect of coalescence on the local SMD at P_{10} and P_{30} can be seen in Figs. 6.92 and 6.93, respectively. At the first location, it results in a 5.7 % larger SMD, while further downstream, the gap increases up to 16.6 %. It is interesting to note that

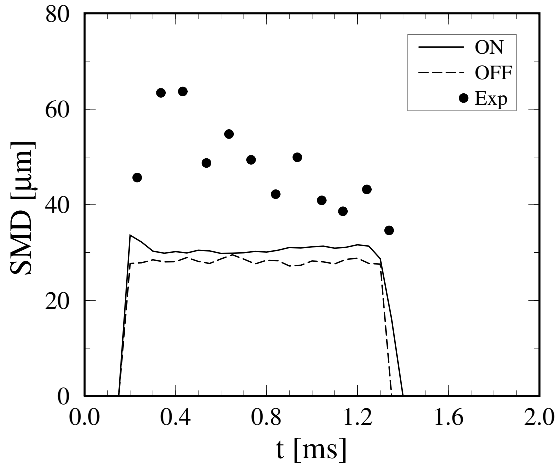

Figure 6.92: SMD at P_{10}.

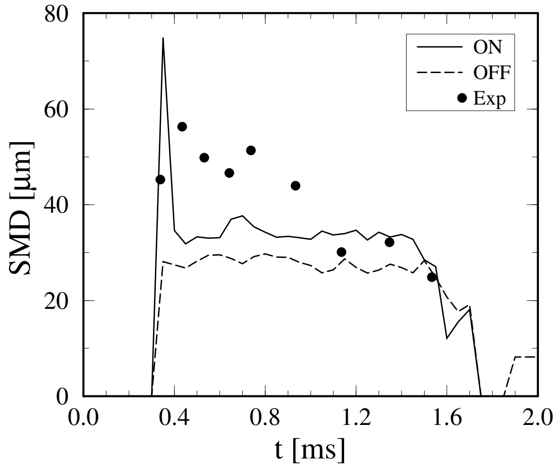

Figure 6.93: SMD at P_{30}.

when collision is switched off, the SMD remains relatively constant. This implies that the rate of droplet breakup is rather small. Comparing the predictions with the measurements, a significant difference is observed at P_{10}. However, this decreases further downstream. It can also be seen that the effect of coalescence is beneficial to the agreement. The same comment applies to the droplet mean velocities at $10\,mm$ and $30\,mm$ away from the nozzle plotted in Figs. 6.94 and 6.95, respectively. It is

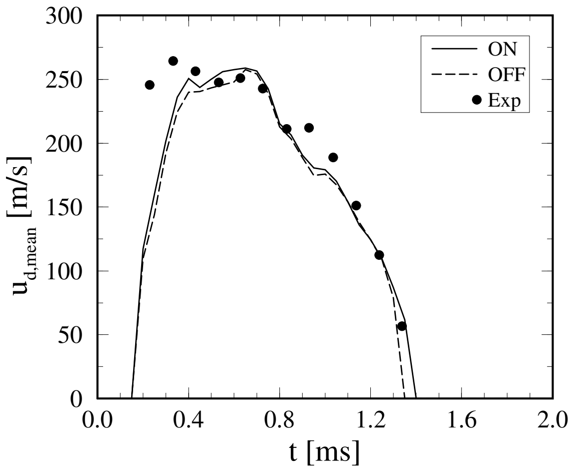

Figure 6.94: Droplet mean velocity at P_{10}.

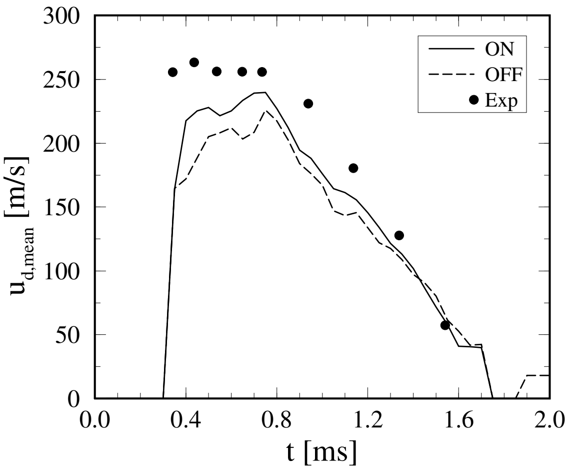

Figure 6.95: Droplet mean velocity at P_{30}.

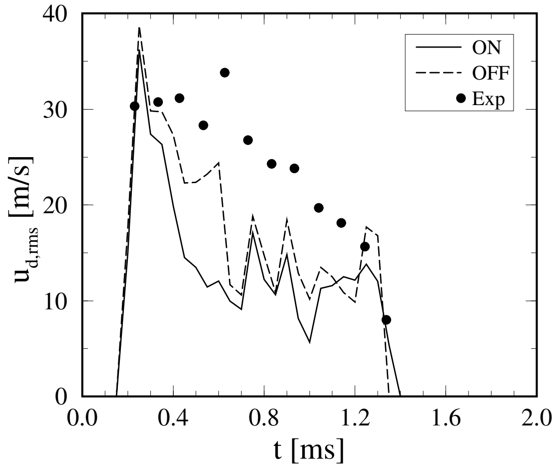

Figure 6.96: Droplet RMS velocity at P_{10}.

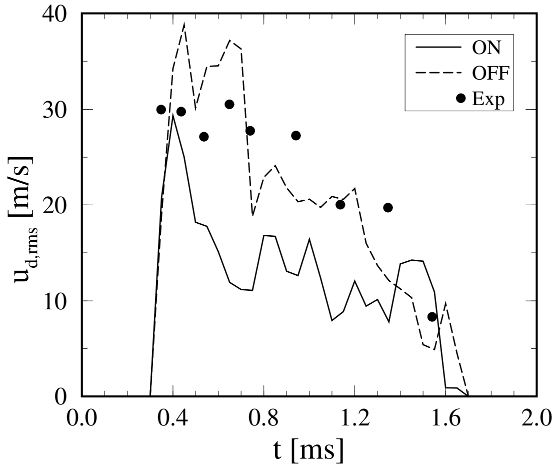

Figure 6.97: Droplet RMS velocity at P_{30}.

noteworthy that the droplet velocities at the former location are very well predicted compared with the measurements. However, farther from the injector the predictions show a reduction, which is attributed to the drag force, while the measurements are rather constant. At this location, the coalescences result in a 6.3 % smaller peak velocity compared with the measured level, while when the collision model is switched off, the difference increases to 11.7 %. However, it is once again pointed out that the differences between the predicted and the measured mean velocities are of the order of the RMS, plotted in Figs. 6.96 and 6.97 for the two locations.

6.4.9 Summary

This section has reported tests of the methodology for sprays at atmospheric conditions. The effects of grid density, time step and parcel introduction rate were investigated and additional investigations were made into the effects of atomisation, drag coefficient, breakup and collision treatments.

It was found that the spray predictions are rather insensitive to the axial size of the grid cells. In contrast, the radial size influences the results because the void fraction variation is not well resolved in the radial direction. In particular, as the radial size of the cells is decreased, the penetration, SMD and local droplet velocities become larger. This is attributed to the fact that the smaller the radial spacing, the smaller the void fraction until the latter is adequately resolved. Hence, the spray-related source terms are relatively larger leading to higher induced velocity of the gas. This leads to smaller drag force and breakup rate. However, the effect of the radial cell size decreases with refinement.

The parametric study of the effect of the time-step size on the spray results showed that nearly Δt-independent results are obtained for values less than $4\,\mu s$, since the differences in spray penetration, local droplet velocities and SMD between $\Delta t = 2\,\mu s$ and $\Delta t = 4\,\mu s$ are less than 4 %.

The parametric study of the parcel introduction rate revealed that between 2 parcels/μs and 4 parcels/μs substantial differences of up to 23 % are observed in the local droplet RMS velocities. However, for all the other spray results examined here, the difference is less than 5 % and consequently, $\dot{N}_p = 2\,\text{parcels}/\mu s$ is considered to provide an acceptable representation of the spray.

The Huh atomisation model was found to predict very well the spray penetration and reasonably well the droplet sizes. However, it underpredicts the local droplet velocity, despite the fact that the cavitation model produces a more than 20 % increase in the injection velocity. This is possibly because the droplet size is underpredicted near the injector, leading to faster deceleration. Nevertheless, the differences between the predicted and the measured local droplet velocities are of the order of the RMS velocities. The MPI atomisation model gives higher local droplet velocities than the Huh model, but it significantly overpredicts the SMD. Similar penetrations are produced by the two atomisation models.

The parameters of the two atomisation models investigated here were found not to affect the spray results significantly. In particular, the coefficient C_5 used in the primary droplet breakup rate in the Huh atomisation model resulted in only about 8 % reduction of the spray penetration when it was decreased ten times. This coefficient also produced some effect on the SMD, while the local droplet velocities were rather insensitive. Using the MPI atomisation model, the spray semi-cone angle was found to little affect the spray results. In fact when it is increased, the penetration is slightly decreased because the spray momentum is distributed over a wider angle.

The choice of drag coefficient correlation was found to have a minor effect on the spray results because the higher drag force calculated for distorted droplets is balanced by their higher momentum due to the smaller relative velocity and hence, smaller breakup rate. In addition, the higher momentum transferred from the leading droplets to the surrounding gas lowers the drag force acting on the trailing droplets. These observations are in accord to the findings of other researchers, who found that the spray penetration is insensitive to this input even when the drag coefficient is increased by an order of magnitude (see Liu *et al.* [190]).

Breakup seems to be beneficial to the accuracy of spray penetration predictions, with all the models tested giving similar results. The local droplet velocity is rather insensitive to the choice of breakup model. In contrast, different SMD levels were obtained from different models. The Hsiang-Faeth model gives the largest SMD and the Reitz-Diwakar the smallest one. However, these differences are not dramatic.

Coalescence was found to be the main output of collision under the conditions of the tests here. Thus, collision results in larger SMD. The spray penetration decreases due to coalescence, since the droplet velocity decreases in order to conserve the momentum of the colliding droplets. It was also observed that the agreement between predictions and measurements for both local SMD and droplet mean velocities is enhanced when collision is considered.

From the overall picture of all the test cases, it can be claimed that the penetration is very well predicted compared with the measurements. The local droplet velocities are slightly underpredicted, which may be attributed to the fact that the atomisation model produces too small droplets which decelerate too quickly. Although this may be true for the Huh atomisation model, the local droplet velocities are still underpredicted when the MPI model, which produces significantly larger droplets, is used. Concerning the local SMD, it was observed that the measurements show a reduction of the SMD moving downstream for all the cases. In contrast, the predictions show an increase of the SMD. The latter is due to coalescence, on the one hand and a relatively low breakup rate, on the other. Concerning the latter phenomenon, three different models were used, but none of them produced the trend of the measurements. This is probably because the Huh atomisation model produces small droplets which cannot further break up and the only size change mechanism is coalescence. The MPI atomisation model gives results which follow the trend of the measurements, because the initial droplet size is significantly overpredicted, allowing the breakup model to further reduce their size with a larger rate than the rate of coalescence. This discussion leads to the conclusion that a better atomisation model may be necessary, which produces an SMD between the values predicted by the Huh and MPI models. However, this may not be sufficient, since in some of the cases examined here good agreement was obtained between the predicted and the measured SMD at P_{30} whereas at the farthest point the SMD was overpredicted. Obviously, after the point P_{30} the atomisation model is not important and the droplet size is controlled by the breakup and collision models. Therefore, some improvements of these models may also be necessary. Of course, it should be noted here that some differences between the predictions and the measurements at P_{60} may be due to the different properties that the fuels used in calculations and experiments may have.

Last but not least, errors and ambiguities of the measurements should also be considered, since the various combinations of models used in this study consistently present similar trends.

Finally, it is emphasised that the experimental results were shifted in time by $0.14\,ms$. This was necessary due to the unrealistic measured penetration. The necessity was also confirmed by comparing the timings of the predicted and measured peak values of the local droplet mean velocities. This difference is probably due to the definition of the time of the start of injection, which unfortunately, was not given by the experimentalist.

6.5 Pressure chamber

6.5.1 Description

In this section, sprays injected into a pressure chamber under Diesel engine conditions will be investigated. The pressure chamber in question was used by investigators at the Rheinisch Westfälische Technische Hochschule (RWTH), Aachen within the IDEA and IDEA-EFFECT projects and is illustrated in Fig. 6.98. It is specially designed to allow optical access for non-intrusive measurement techniques. Compressed air enters via two heaters and passes through straightening blades into the observation area of the chamber. The peak temperature and pressure attainable are $900\,K$ and $60\,bar$, respectively. The mean velocity of the air flow is lower than $0.1\,m/s$ as measured by Schmidt *et al.* [260], thus, it can be considered as nearly quiescent compared to the axial velocities of the injected fuel spray.

The main part of the observation chamber is a measuring section which can

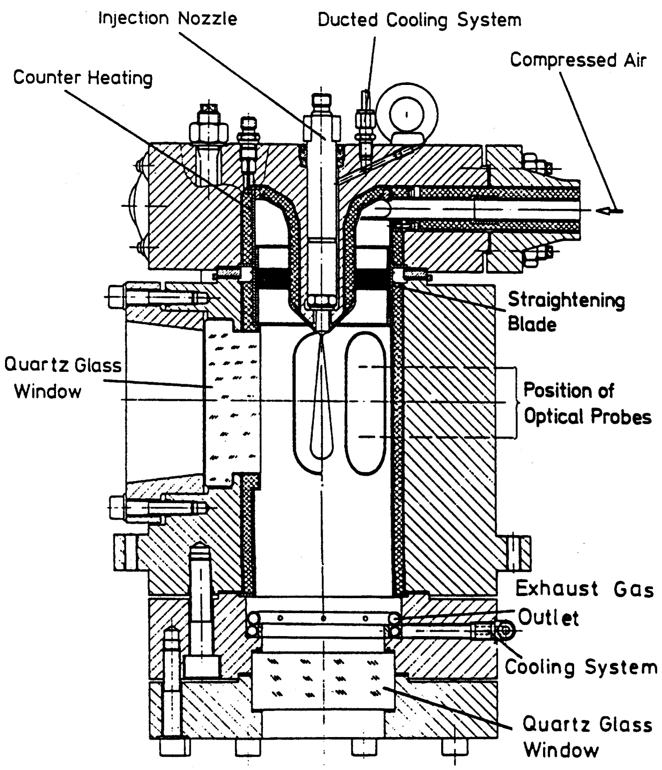

Figure 6.98: Aachen pressure chamber, taken from Schmidt *et al.* [261].

accommodate up to four quartz glass windows of 100 mm length and 40 mm width. The distance between the windows is 90 mm, so the wall influences on the spray are negligible. Also, all the walls of the chamber are adiabatic. Other details of the geometry of the chamber can be found in Schmidt *et al.* [260].

The injection system comprises an in-line injection pump (Bosch Type PES 4 MW 80), an injection line and a Bosch commercial single-hole nozzle of 0.8 mm length and 0.2 mm diameter. The injector is located at the centre of the top wall injecting downwards along the chamber axis and is water-cooled. The injector specifications are summarised in Table 6.23 and further details can be found in Koss *et al.* [169].

The fuel used in the IDEA project was n-heptane (C_7H_{16}) and three different operating points that were investigated will be simulated in this study. The conditions for these are summarised in Table 6.24. The fuel injection flow rate histories, shown in Fig. 6.99, were deduced by Koss *et al.* [169] from measurements of the needle lift,

Table 6.23: Injector specifications.

Length, L $[mm]$	0.8
Diameter, D $[mm]$	0.2
Discharge coefficient, c_d	0.66

Table 6.24: Operating points of the Aachen pressure chamber.

No.	p $[bar]$	T $[K]$	Total mass $[mg]$	Fuel
1	50	800	6	n-heptane
3	50	800	10	n-heptane
4	30	600	6	n-heptane

the injection line pressure and the nozzle discharge coefficient. The last has been measured at a constant pressure difference of $100\,bar$ as a function of the needle lift using Diesel fuel. The fuel temperature was not measured but is estimated to be $295\,K$.

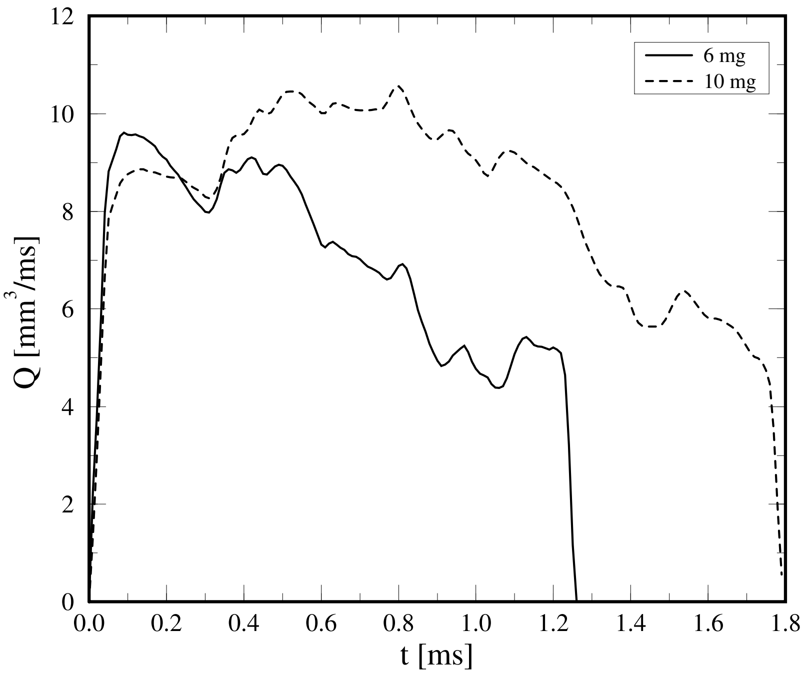

Figure 6.99: Injection flow rate histories.

Measurements were obtained for the vapour and liquid penetrations as well as the fuel vapour mass fraction, Y_v, at six locations whose axial, z and radial, r, coordinates are given in Table 6.25 (see also Fig. 6.100). The spray penetration was

Table 6.25: Measurement locations.

Designation	z $[mm]$	r $[mm]$
P_{30}	30	0
P_{34}	30	4
P_{40}	40	0
P_{44}	40	4
P_{50}	50	0
P_{54}	50	4

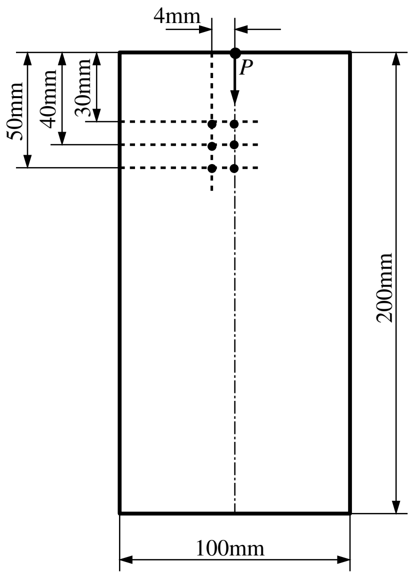

Figure 6.100: Measurement locations.

deduced from high-speed cinematographic films in combination with the Schlieren technique (Bäcker and Wiartalla [28]). The temporal variations of the fuel vapour mass fraction at the six locations were measured by Raman spectroscopy. The experimental data are reported in Koss *et al.* [168, 169] and they represent the ensemble average of approximately 50 samples. The available types of data for each operating point are summarised in Table 6.26.

Table 6.26: Available experimental data.

Experimental data	Operating point		
	No. 1	No. 3	No. 4
Vapour penetration	$\surd$	$-$	$\surd$
Liquid penetration	$\surd$	$-$	$\surd$
Y_v at P_{30}	$-$	$\surd$	$\surd$
Y_v at P_{34}	$\surd$	$\surd$	$\surd$
Y_v at P_{40}	$\surd$	$\surd$	$\surd$
Y_v at P_{44}	$\surd$	$\surd$	$\surd$
Y_v at P_{50}	$\surd$	$\surd$	$\surd$
Y_v at P_{54}	$\surd$	$\surd$	$\surd$

6.5.2 Computational mesh

The calculation domain is taken to be a longitudinal wedge section of a cylinder of 200 mm height and 100 mm diameter. The walls of this domain are unlikely to influence the spray because the experimental results show that it penetrates less than 100 mm and has a half-width of less than 10 mm. These characteristics are also taken into account in the mesh design. Thus, a fine mesh is used close to the injector in both the radial and axial directions, while a coarser mesh is employed in the remaining regions. As mentioned in the previous section, the grid density affects the spray predictions and in order to examine this effect, seven different meshes with various distributions have been used.

The calculations are performed in a 30° sector with one computational cell in the angular direction. The grid density in the spray region influences the results, but far away it is not very important. Thus, in the other two directions, the number of cells is kept constant for all the meshes while refinement in the injector vicinity is achieved at the expense of the grid density far away, using uniform expansion factors. The details of all the meshes are tabulated in Table 6.27.

Table 6.27: Parameters of computational meshes.

Mesh	Axial direction			Radial direction		
	Number of cells	Aspect ratio	$\min(\Delta z)$ $[mm]$	Number of cells	Aspect ratio	$\min(\Delta r)$ $[mm]$
M1	90	1.00	2.22	60	5.72	0.31
M2	90	2.42	1.38	60	5.72	0.31
M3	90	5.83	0.81	60	5.72	0.31
M4	90	13.88	0.45	60	5.72	0.31
M5	90	13.88	0.45	60	3.22	0.44
M6	90	13.88	0.45	60	1.80	0.61
M7	90	13.88	0.45	60	1.00	0.83

Computational parameters

As explained in Section 6.4, the void fraction sets a limit to the size of the smallest cell. Therefore, a locally finer mesh than M4 could not be employed, as will be discussed later. Also, in this mesh study, the highest load case, i.e. operating point No. 3, which is expected to produce the smallest void fraction, is used.

Based on the discussion in §6.4.2, the time step is set to $1\,\mu s$. Bearing in mind that the high-temperature environment results in high evaporation rates, a relatively large parcel introduction rate is chosen to keep a large parcel population in the computational domain, for a better statistical representation of the spray. Thus, $\dot{N}_p$ is set to $20\,\text{parcels}/\mu s$. The effects of both the time step and the parcel introduction rate will be examined later.

The spray submodels used in this study are summarised in Table 6.28. The MPI cavitation model is adopted with entrance area contraction ratio assumed to be 0.7 and nozzle wall roughness to be $1\,\mu m$. The Huh atomisation model is employed with the coefficient C_5 set to 1 and discharge coefficient to 0.66 as measured by Koss *et al.* [169]. The Ranz and Marshall correlations corrected by the factor of El Wakil *et al.* are used for the Nusselt and Sherwood numbers and the infinite conductivity assumption (uniform temperature profile within the droplet) is adopted to reduce the computational time.

Table 6.28: Spray submodels.

Spray process	Submodel/correlation
Cavitation	MPI
C_c	0.7
k_r $[\mu m]$	1
Atomisation	Huh
c_d	0.66
C_5	1
Drag coefficient	Yuen-Chen, Eq. (3.66)
Evaporation	
Conductivity	Infinite
Nu and Sh	El Wakil *et al.*/Ranz-Marshall, Eqs. (3.86), (3.80), (3.137a)
Breakup	Hsiang-Faeth
Collision	O'Rourke

Following Kralj [171] who simulated the same experiment, a zero initial velocity field and low values of the turbulence parameters are assumed, since the initial flow is quiescent. Regarding the turbulence parameters, it was observed in §6.4.5, that when they are small, they do not affect the spray because the induced values due to the latter are much larger (see also the relevant discussion in §6.4.2). All the initial values of the flow field, along with the spray characteristics, are summarised in Table 6.29.

Table 6.29: Initial flow field and injection characteristics.

Ambient gas	air
$\mathbf{u}$ $[m/s]$	0
p $[bar]$	50
T $[K]$	800
k $[m^2/s^2]$	10^{-3}
ε $[m^2/s^3]$	$7{\cdot}10^{-4}$
Fuel	n-heptane
Mass $[mg]$	10
$T_{d,inj}$ $[K]$	295
SOI $[ms]$	0
EOI $[ms]$	1.79

Results and discussion

The effects of the axial and radial grid density on the liquid penetration are plotted in Figs. 6.101 and 6.102, respectively. Here, the liquid penetration is based on the 99 % void definition. The decision for this was based on the experimental results which show zero penetration even before the end of injection. This implies that the liquid penetration could be detected only when the spray is dense and the other two definitions for the liquid penetration given in Section 6.2 do not provide the ability to distinguish a dense spray. Thus, despite the fact that as has already been explained the 99 % void definition is mesh-dependent, it is adopted here.

As can be seen in Figs. 6.101 and 6.102, the effect of the radial cell distribution is stronger than that of the axial spacing, as was also found in the atmospheric spray study. In both directions (radial and axial), the effect decreases with mesh refinement. However, the smallest void fraction in the finest mesh, M4, is 0.19, which is about the limit for refinement for the reasons explained in §6.4.2.

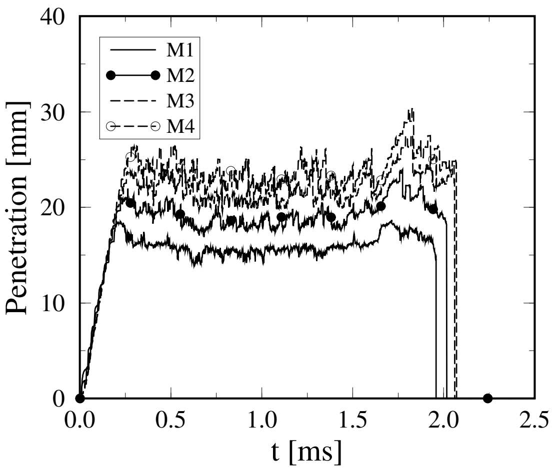

Figure 6.101: Effect of the axial grid density on liquid penetration.

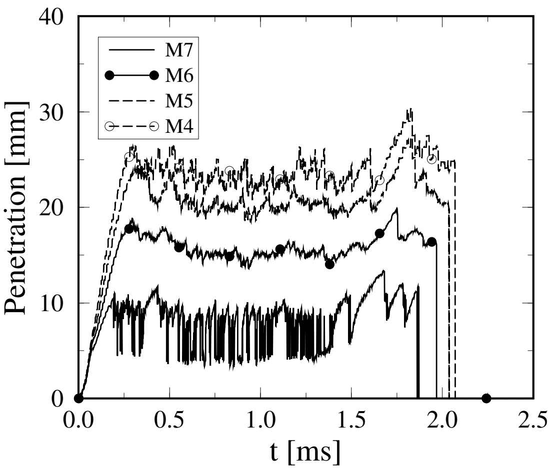

Figure 6.102: Effect of the radial grid density on liquid penetration.

Decreasing effect of the mesh is also observed for the vapour penetration shown in Figs. 6.103 and 6.104.

The effect of the mesh on the cumulative evaporated mass, CEM, is presented in Figs. 6.105 and 6.106, for the axial and radial refinement, respectively. As can

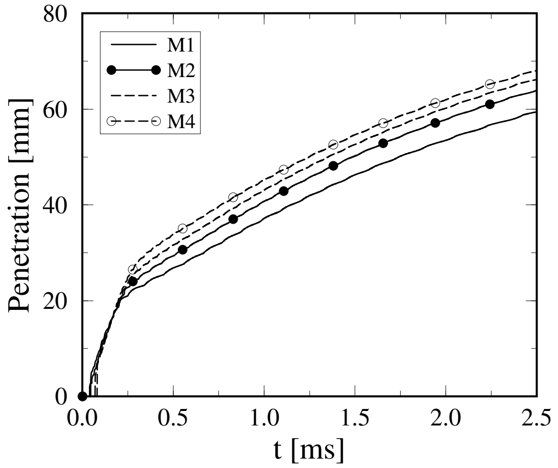

Figure 6.103: Effect of the axial grid density on vapour penetration.

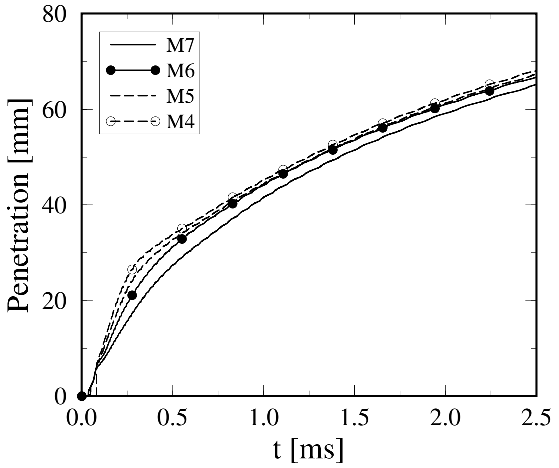

Figure 6.104: Effect of the radial grid density on vapour penetration.

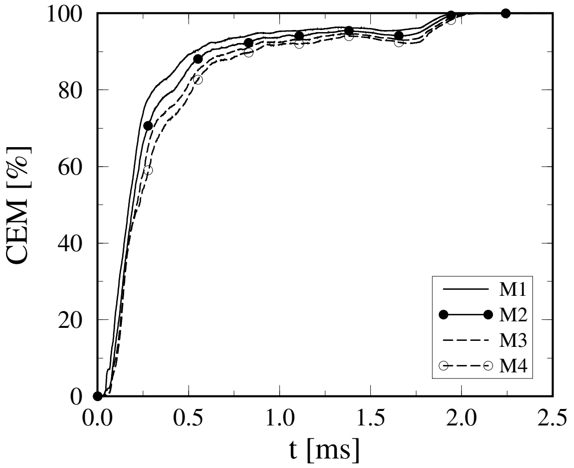

Figure 6.105: Effect of the axial grid density on the cumulative evaporated mass.

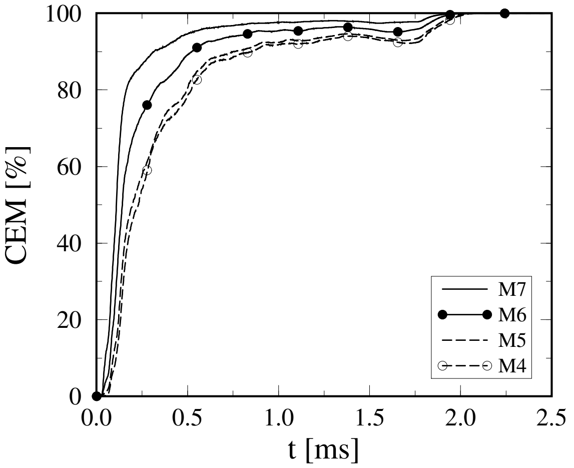

Figure 6.106: Effect of the radial grid density on the cumulative evaporated mass.

be seen, the finer the mesh, the lower is the evaporation rate. This is because when the cell size decreases, i.e. the void fraction decreases, the vapour concentration in this cell increases leading to lower evaporation rate. It is again observed that the radial cell spacing has a stronger effect than the axial one. However, the finer the mesh, the smaller the effect, in both directions.

The effect of the mesh on the SMD is consistent with that on the penetration and the cumulative evaporated mass. Thus, as can be seen in Figs. 6.107 and 6.108, the SMD increases when the cell size is decreased.

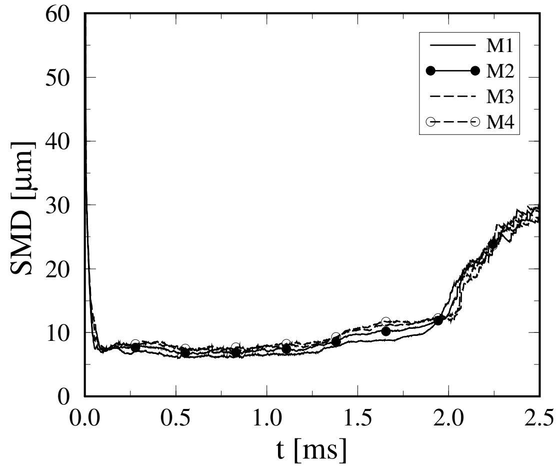

Figure 6.107: Effect of the axial grid density on the SMD.

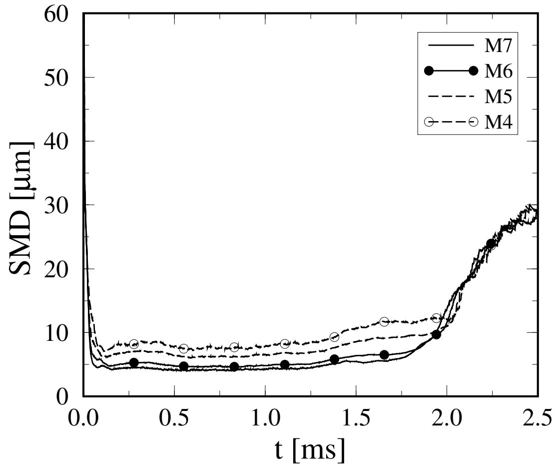

Figure 6.108: Effect of the radial grid density on the SMD.

Finally, the effect of the mesh spacing on the fuel vapour mass fraction at specific locations is examined. Two representative points have been chosen, P_{40} and P_{44}, which lie between the locations at which measurements have been obtained (see Table 6.25). Figs. 6.109 and 6.110 show the effect of the axial and radial cell size, respectively, on the results at the former point. Figs. 6.111 and 6.112 show those for the off-axis location. Consistent with the vapour penetration behaviour, as the

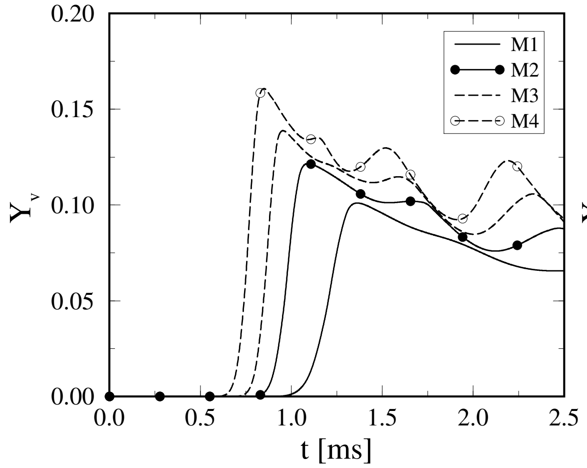

Figure 6.109: Effect of the axial grid density on Y_v at P_{40}.

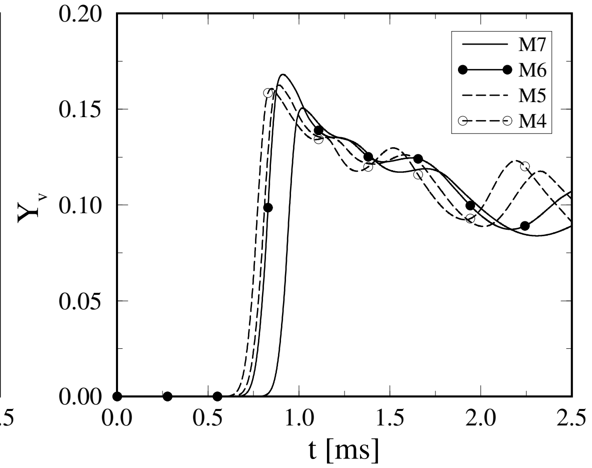

Figure 6.110: Effect of the radial grid density on Y_v at P_{40}.

cell size is decreased, fuel vapour is detected earlier at both points. Also, the axial refinement leads to higher vapour concentration, whereas the effect of the radial spacing is much weaker. This is because the cumulative evaporated mass is not substantially affected by the axial spacing (see Fig. 6.105) and since similar amounts of vapour are produced by all meshes, the larger the cell size, the lower is the vapour concentration. In contrast, CEM is significantly affected by the radial spacing (see Fig. 6.106). Thus, the coarser the mesh the larger the amount of vapour produced. However, the mass of air in the cells of the coarser mesh is also larger, leading to minor differences of the vapour concentration between various meshes. Nevertheless, the effect of the mesh decreases with refinement in both directions.

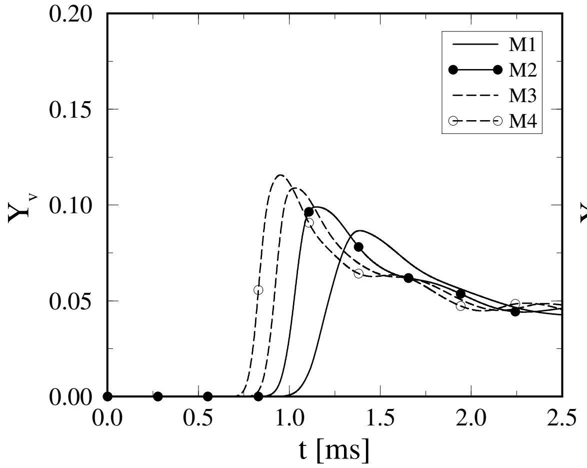

Figure 6.111: Effect of the axial grid density on Y_v at P_{44}.

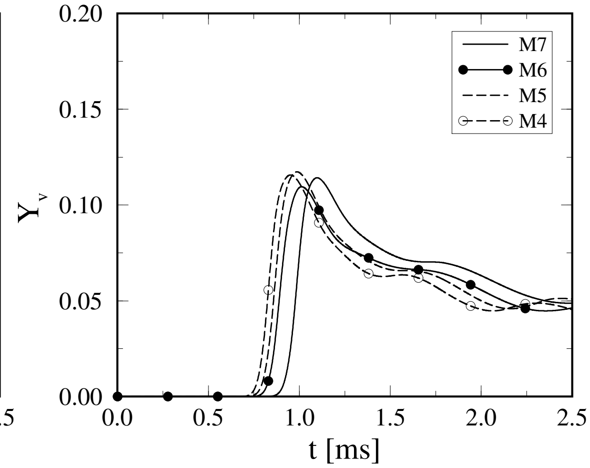

Figure 6.112: Effect of the radial grid density on Y_v at P_{44}.

Evidently, the effects of the grid density on all the properties examined here, diminishes with refinement. However, a finer mesh than M4 could not be employed due to restrictions set by the discrete droplet methodology, as explained in the section presenting the atmospheric spray. Hence, in the following calculations, the finest mesh, M4, shown in Fig. 6.113, will be used.

6.5.3 Effect of the time step

Here, the effect of the time step on spray results is examined for the same operating point, No. 3. Three different time steps are used, as listed in Table 6.30 while all the other parameters including initial conditions and submodels have been given in §6.5.2.

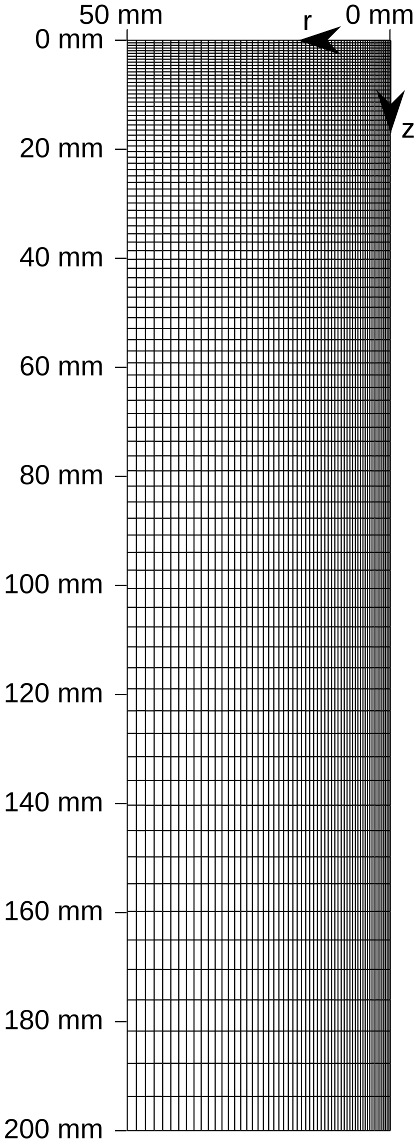

Figure 6.113: The computational mesh (M4 in Table 6.27) used for the pressure chamber calculations.

Table 6.30: Effect of the time step.

Designation	Δt [μs]
T4	4
T2	2
T1	1

As can be seen in Figs. 6.114 and 6.115, the effect of the time step on both liquid and vapour penetrations is negligible, for values smaller than $2\,\mu s$. Notably, the effect decreases when the time step is reduced.

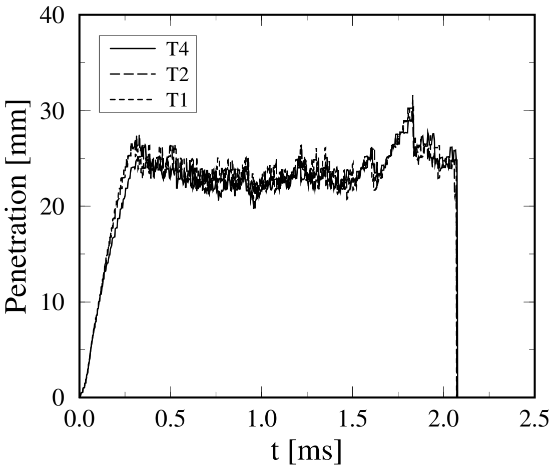

Figure 6.114: Effect of the time step on liquid penetration.

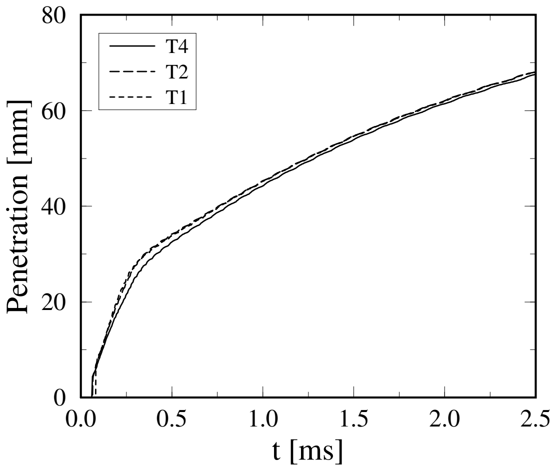

Figure 6.115: Effect of the time step on vapour penetration.

The effect of Δt on the cumulative evaporated mass and the SMD is also small as shown in Figs. 6.116 and 6.117, respectively. It can be seen that the smaller the time step the smaller is the effect, eventually leading to time-step independent results.

Finally, the effect of the time step on local vapour concentrations is shown in Figs. 6.118 and 6.119. Again, it can be claimed that the sensitivity is minor and decreases by reducing Δt.

Evidently, in all the results shown here, the effect of the time step is minor and is getting smaller by reducing the time-step size. It can be claimed that time-step

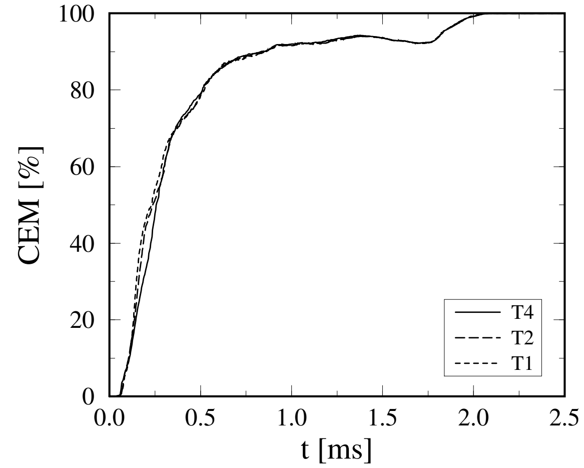

Figure 6.116: Effect of the time step on the cumulative evaporated mass.

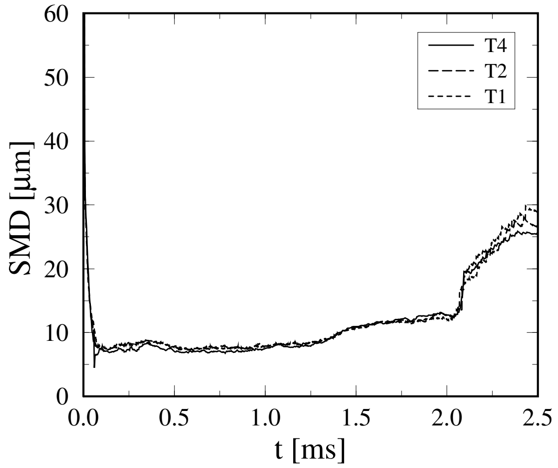

Figure 6.117: Effect of the time step on the SMD.

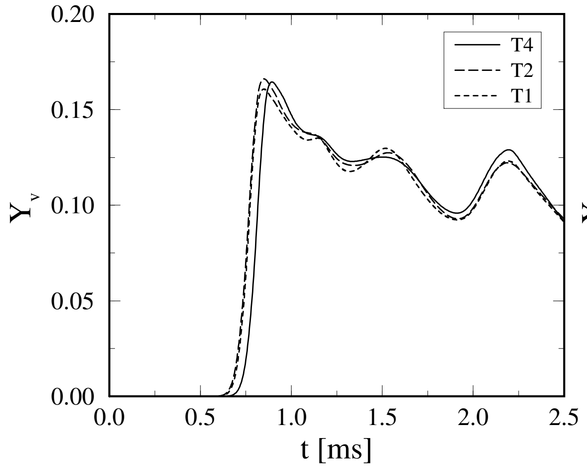

Figure 6.118: Effect of the time step on Y_v at P_{40}.

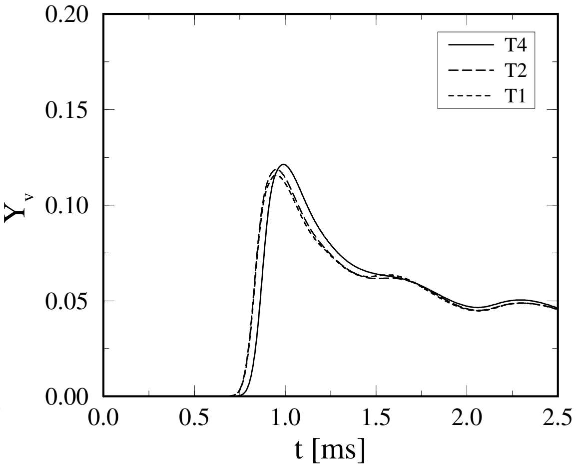

Figure 6.119: Effect of the time step on Y_v at P_{44}.

independent results are almost obtained when $\Delta t = 1\,\mu s$ and further reduction of Δt is not necessary. Thus, this value is used for all the remaining calculations.

6.5.4 Effect of the parcel introduction rate

Last, the effect on the predictions of the number of parcels introduced per time step, $\dot{N}_p$, is investigated. To this end, three different rates are used as listed in Table 6.31 while all the other computational parameters and submodels are the same as in §6.5.2.

Table 6.31: Effect of the parcel introduction rate.

Designation	$\dot{N}_p$ [parcels/μs]
N5	5
N10	10
N20	20
N40	40

The liquid and vapour penetrations for the different $\dot{N}_p$ are shown in Figs. 6.120 and 6.121, respectively. As can be seen, both penetrations are rather insensitive to the parcel introduction rate.

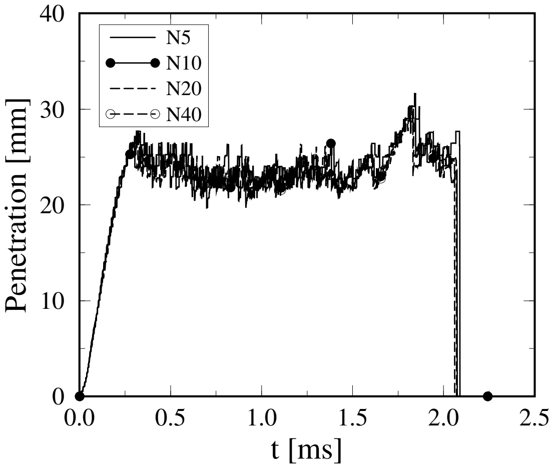

Figure 6.120: Effect of the parcel introduction rate on liquid penetration.

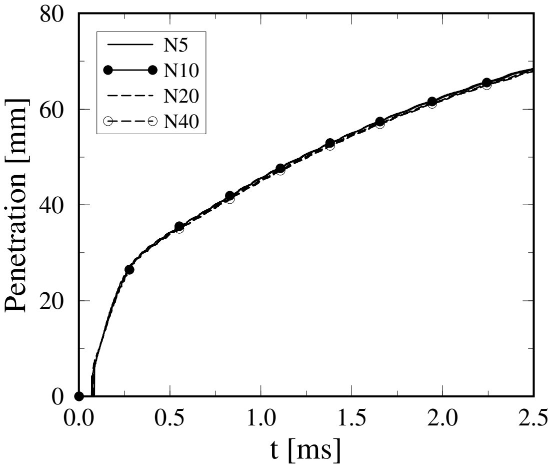

Figure 6.121: Effect of the parcel introduction rate on vapour penetration.

The cumulative evaporated mass shown in Fig. 6.122 similarly exhibits negligible sensitivity to $\dot{N}_p$. However, it has some effect on the SMD (Fig. 6.123) mainly at the latter stage. This is probably due to the small number of parcels participating in the calculations at this stage, due to evaporation. This also justifies the large parcel introduction rate used in the investigation of the mesh effect in this study, compared to the value used in the atmospheric spray calculations.

Relatively larger effects of the parcel introduction rate are observed on the local vapour concentration as shown in Figs. 6.124 and 6.125. In particular, the lowest rate, N5, shows some discrepancies which are attributed to the too small number of

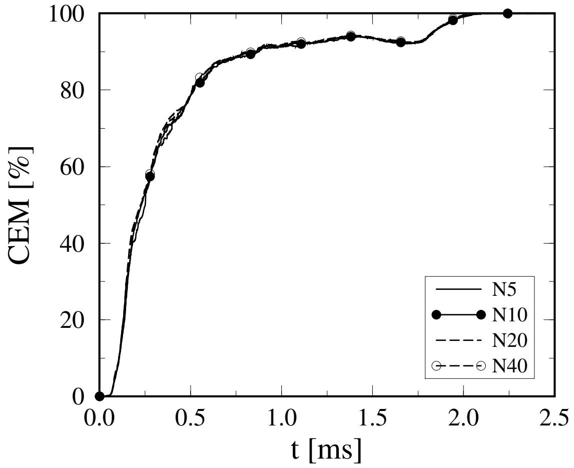

Figure 6.122: Effect of the parcel introduction rate on the cumulative evaporated mass.

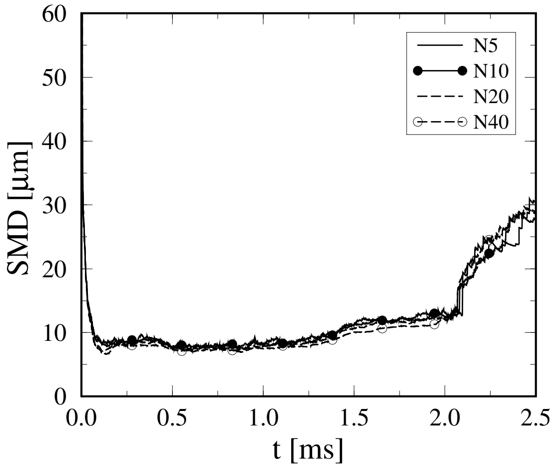

Figure 6.123: Effect of the parcel introduction rate on the SMD.

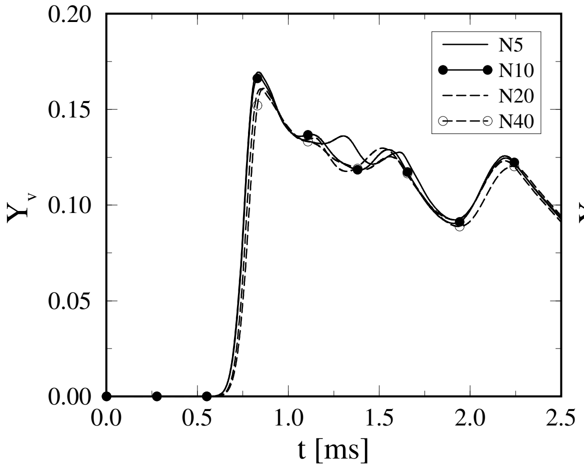

Figure 6.124: Effect of the parcel introduction rate on Y_v at P_{40}.

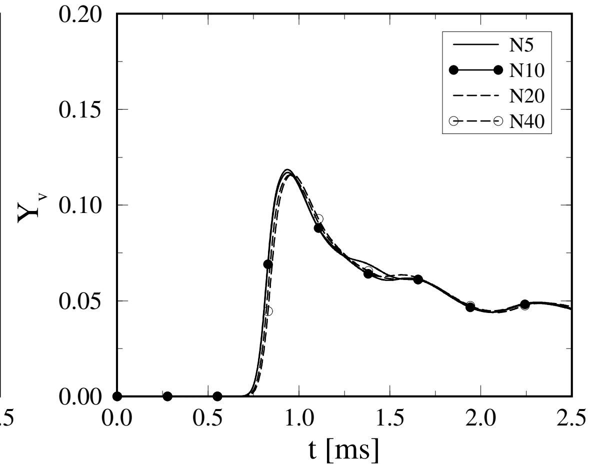

Figure 6.125: Effect of the parcel introduction rate on Y_v at P_{44}.

droplets which cannot statistically represent the spray.

Nevertheless, the effect of the parcel introduction rate seems to be very small, especially for values larger than 10 parcels/μs. Hence, the rate 20 parcels/μs is adopted for all the further calculations.

6.5.5 Operating point No. 1

The first operating point is devoted to the investigation of the effect of the liquid conductivity treatment. Three models have been presented in Section 3.6 and the results here are designated according to Table 6.32. All the other spray submodels

Table 6.32: Designation of the calculations for operating point No. 1.

Designation	Conductivity
INF	Infinite
FIN	Finite
EFF	Effective

as well as the initial flow field remain the same as used in the mesh sensitivity study (see Tables 6.28 and 6.29). The injection characteristics of this operating point are summarised in Table 6.33.

Table 6.33: Injection characteristics.

Fuel	n-heptane
Mass $[mg]$	6
$T_{d,inj}$ $[K]$	295
SOI $[ms]$	0
EOI $[ms]$	1.26

Results and discussion

Before the presentation of the comparisons between the predictions and the measurements, a detailed analysis of the predicted spray development and its interaction with the surrounding gas will be given, based on the results obtained with the infinite conductivity treatment.

The spray temporal development is shown in Fig. 6.126. As can be seen, the liquid penetration increases until an almost constant penetration value of around

$25\,mm$ is reached, which persists until around $1.2\,ms$. Higher penetration cannot occur because the droplets at the tip cannot survive longer, since their temperature is close to the critical temperature of n-heptane, i.e. $540\,K$ and their size is small. Unfortunately, the latter cannot be seen because for clarity the 'droplets' are given the same size in Fig. 6.126. However, greater penetration is observed at $1.5\,ms$, because the droplets appearing there have been injected towards the end of injection and consequently, have experienced, on the one hand, less drag force and on the other, smaller evaporation rate. The former is caused by the fact that the surrounding gas has an induced motion due to the momentum exchange with earlier-injected droplets. This is clearly shown in the gas velocity plots of Fig. 6.127. The increased gas velocity reduces the convective transfer coefficient resulting in less evaporation. The latter is further decreased because the evaporation of earlier-injected droplets has not only cooled the gas down but also increased the vapour concentration. An additional effect of the induced gas velocity is that it reduces the breakup rate, leading to larger droplets with higher momentum and hence, farther penetration.

The fuel vapour mass fraction at the same times is plotted in Fig. 6.128. The highest vapour concentration at each instant is around the tip of the spray, where the droplets have relatively small size and high temperature, leading to high evaporation rates. Although the liquid does not penetrate more than $30\,mm$, the vapour penetrates to $50\,mm$ at $1.5\,ms$, since it is convected by the gas flow (see Fig. 6.127). The shape of the isotherms, shown in Fig. 6.129, follows those of the fuel vapour mass fraction contours. It is clear that the droplet evaporation cools the vapour/air mixture. This is because energy is extracted for both vapour formation and heating the liquid up.

Attention will now be focussed on comparison between predictions and measurements, as well as on the effect of the conductivity treatment. It can be seen in Fig. 6.130, which presents the liquid penetration, that up to $0.2\,ms$, very good agreement is observed between predictions and measurements. Later on, the experiments show that the penetration decreases, resulting in zero levels even at $0.16\,ms$ before the end of injection, probably because the spray is too dilute to be detected.

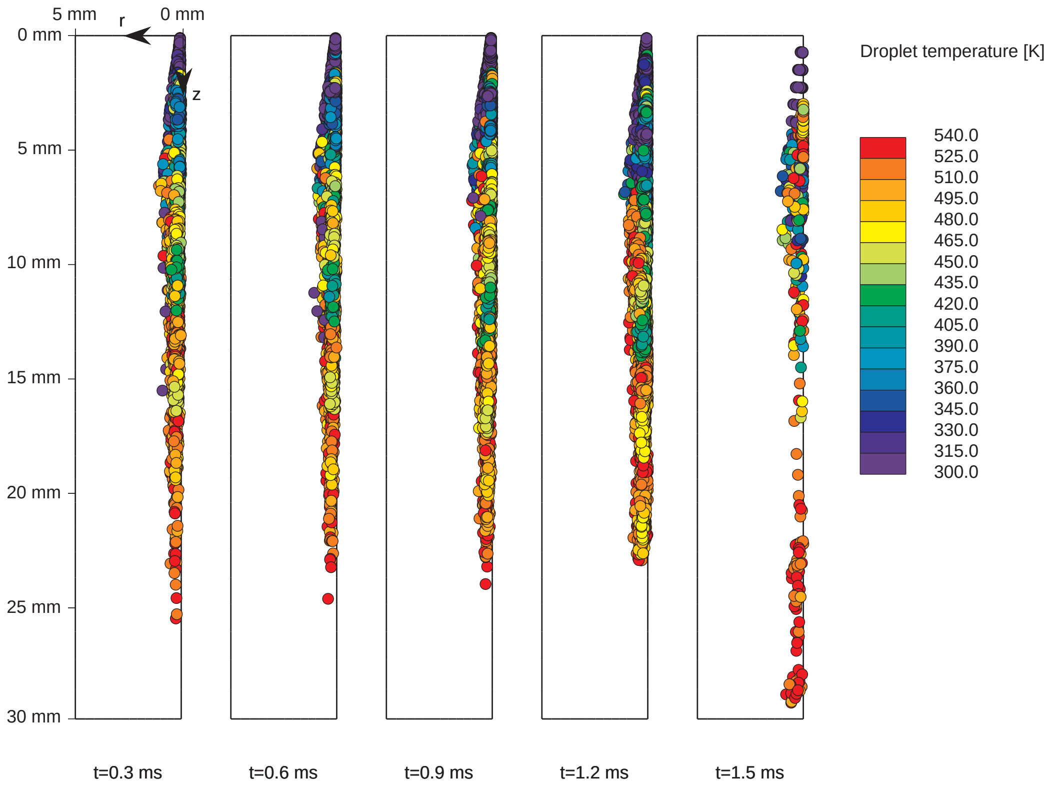

Figure 6.126: Droplet temperature at various times.

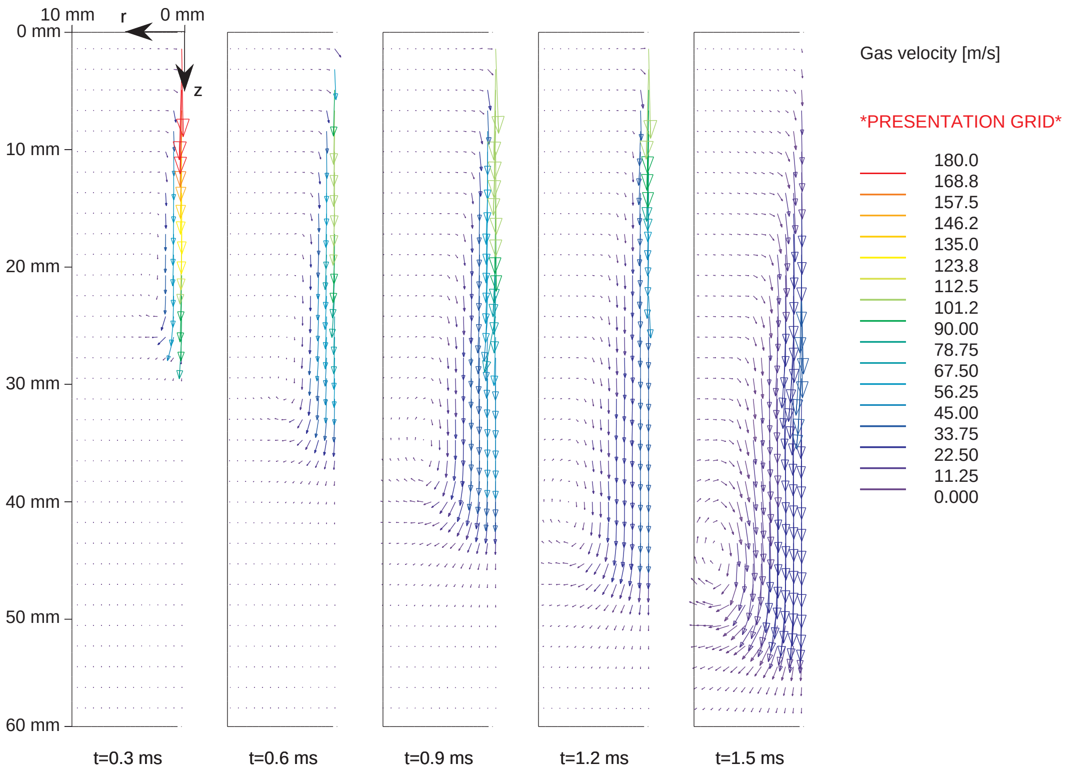

Figure 6.127: Gas velocity field at axial section at various times.

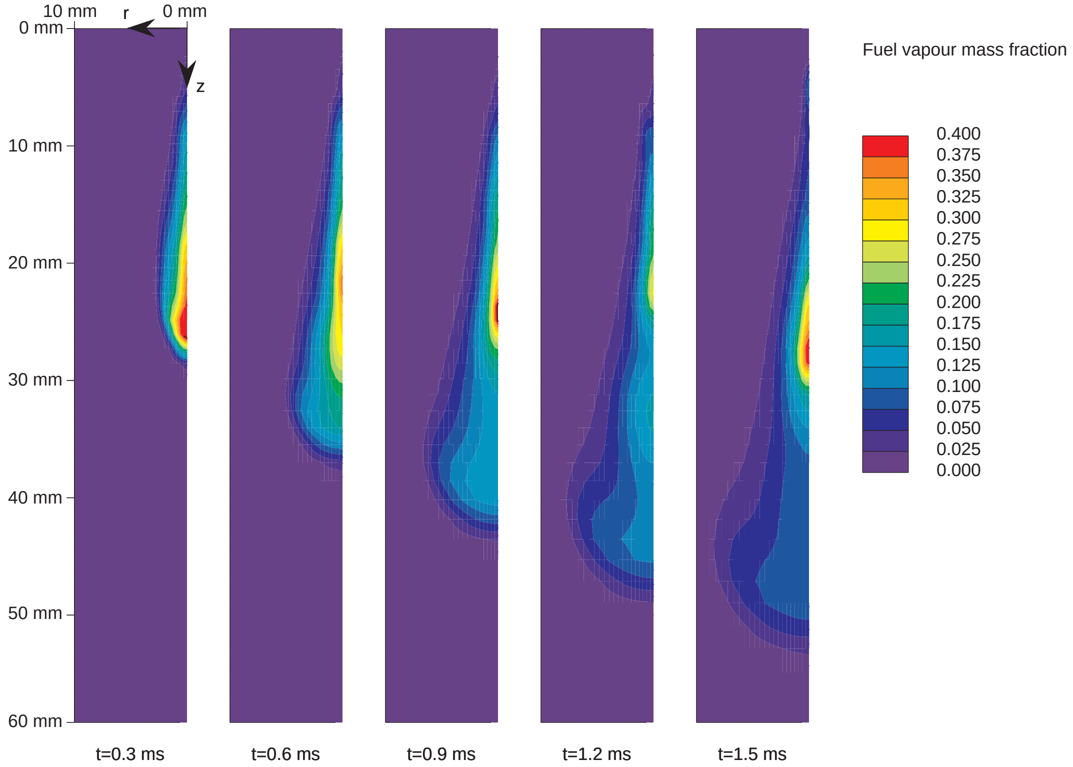

Figure 6.128: Fuel vapour mass fraction at axial section at various times.

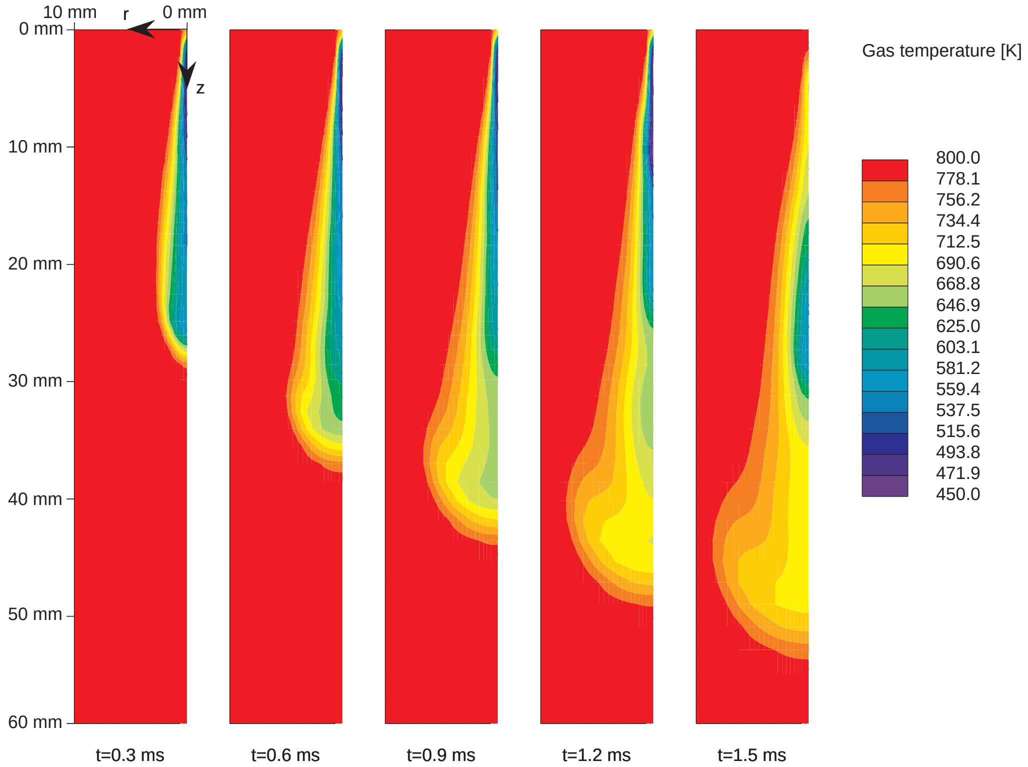

Figure 6.129: Gas temperature field at axial section at various times.

However, this is not expected and probably represents the level of the experimental uncertainty. Another possible reason for overprediction is perhaps an overestimate of the droplet size, by the atomisation model, leading to higher liquid velocity. Comparisons among the predictions reveal that the effective conductivity treatment results in slightly larger penetration. This is probably because the evaporation rate is lower, allowing higher momentum to the droplets.

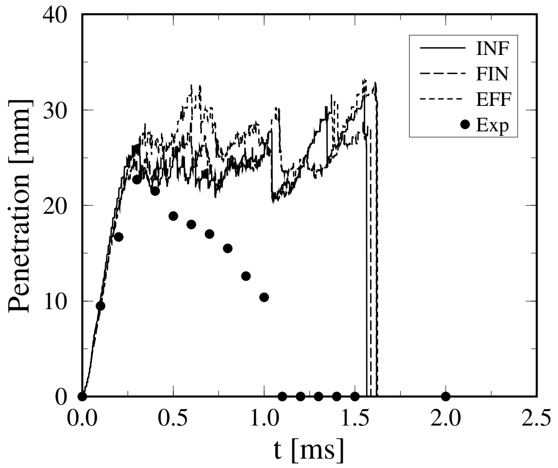

Figure 6.130: Effect of the conductivity model on liquid penetration.

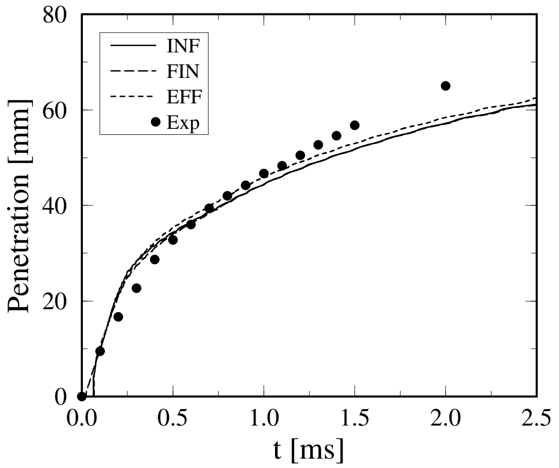

Figure 6.131: Effect of the conductivity model on vapour penetration.

The results are more clear for the vapour penetration, presented in Fig. 6.131. Consistent with the liquid penetration, the effective conductivity model results in the highest penetration. Nevertheless, the differences between the predicted penetrations are less than $2\,\%$. However, all calculations overpredict the penetration until $0.5\,ms$ while afterwards, they underpredict it. Until $0.3\,ms$ the vapour follows the liquid, exhibiting relatively large velocities while later on, the slope of the vapour penetration gradually decreases, since the vapour is convected by the gas. The gap between the measured and predicted penetrations at $0.3\,ms$ is about $20\,\%$ and decreases to $10\,\%$ at $2\,ms$. However, according to the experiment, ignition* occurs at $1.63\,ms$ and therefore, the comparison after this time is not meaningful. Although after ignition, the predictions cannot represent reality, because this phenomenon is not modelled here, the calculations are performed until $2.5\,ms$ for a

*The ignition delay was measured by Wiartalla *et al.* [306] based on the light emission and represents the average from 256 injection cycles.

better representation of the effect of the conductivity model.

The cumulative evaporated mass is plotted in Fig. 6.132. As can be seen the finite conductivity model produces the highest evaporation rate, at least up to $0.5\,ms$, whereas the infinite conductivity treatment gives the lowest evaporation rate, because the droplet surface temperature is also the lowest. However, later on, the

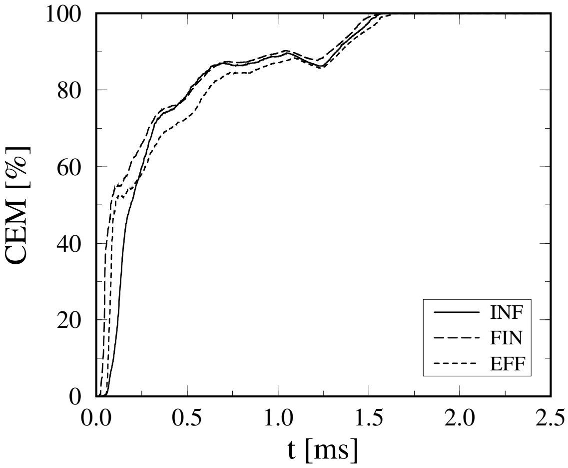

Figure 6.132: Effect of the conductivity model on the cumulative evaporated mass.

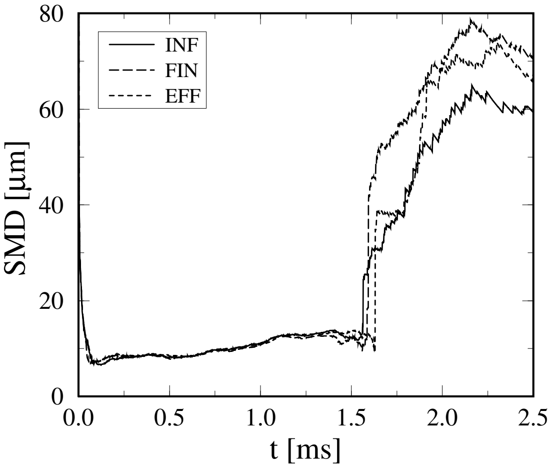

Figure 6.133: Effect of the conductivity model on the SMD.

evaporation rate for this treatment reaches the level of that predicted using the finite conductivity model, because the droplets have been warmed up. In the beginning, the evaporation rate using the effective conductivity treatment lies between those obtained from the other two models, as expected. However, afterwards, it gives the lowest evaporation rate, which supports the earlier discussions concerning the penetrations.

Despite the differences in the cumulative evaporated mass among the three conductivity models, the SMD, shown in Fig. 6.133, seems to be rather insensitive until $1.5\,ms$. After this time, some differences are observed but they are very scattered, since the droplet population is small because the small droplets have evaporated. The latter also explains why SMD increases.

The fuel vapour mass fraction at $30\,mm$ downstream and $4\,mm$ off the spray axis is depicted in Fig. 6.134. Here, the measurements are presented with error-bars whose half-lengths represent the standard deviation due to cycle-to-cycle variations. Very good agreement with measurements using the effective conductivity model is obtained until $1.2\,ms$ while the other two overpredict the vapour concentration. However, afterwards, the calculations underpredict the concentration for all conductivity treatments, although the trends of the curves follow those of the measurements (see the local maximum at $1.75\,ms$). Further downstream, the vapour concentra-

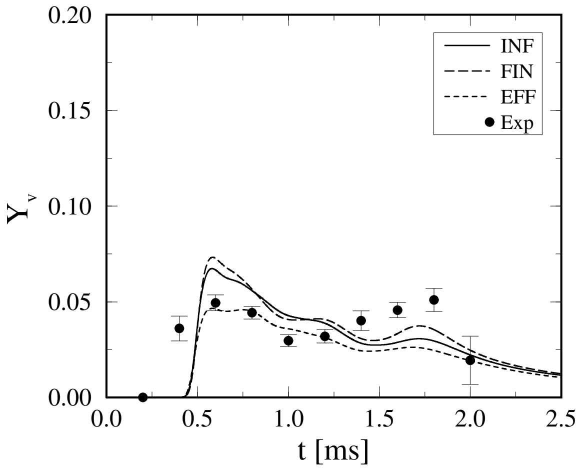

Figure 6.134: Effect of the conductivity model on Y_v at P_{34}.

tion is overpredicted as shown in Figs. 6.135–6.138. Consistent with the vapour penetration, shown in Fig. 6.131, the vapour arrives at $z = 40\,mm$ and $z = 50\,mm$ earliest when the effective conductivity model is used. It is also observed that at $z = 50\,mm$ the predicted vapour tip reaches the measurement location earlier than the measured one, which is in contradiction with the vapour penetration results in Fig. 6.131. This is clearly shown in Fig. 6.139 which presents the measured penetration and that evaluated from the measurements of the vapour concentration. This inconsistency reveals an uncertainty in the measurements.

As shown in Figs. 6.135–6.138, the vapour concentration is overpredicted at all measurement locations. The reasons for this disagreement are discussed below.

It could be claimed that the mathematical model produces higher evaporation rates than those of the experiment. However, as shown in Section 6.3 the evaporation rate for single droplets is well predicted for n-heptane, while for other fuels

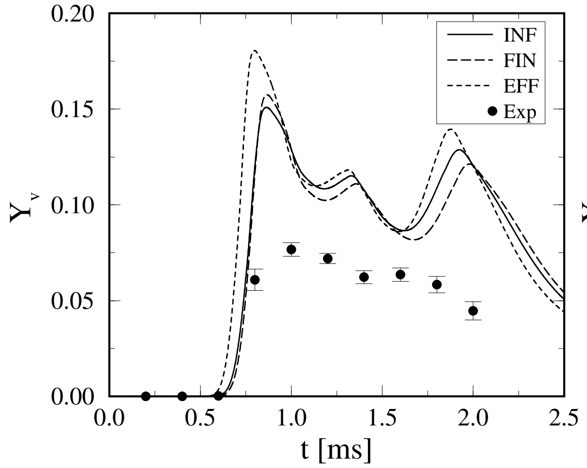

Figure 6.135: Effect of the conductivity model on Y_v at P_{40}.

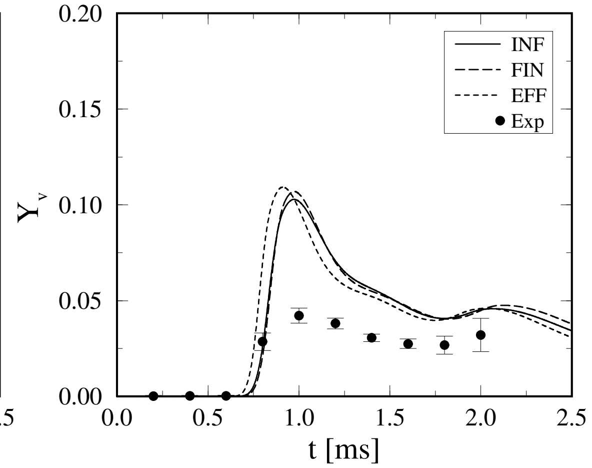

Figure 6.136: Effect of the conductivity model on Y_v at P_{44}.

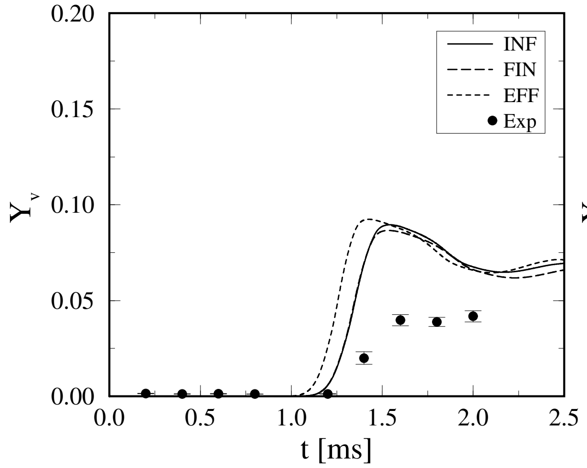

Figure 6.137: Effect of the conductivity model on Y_v at P_{50}.

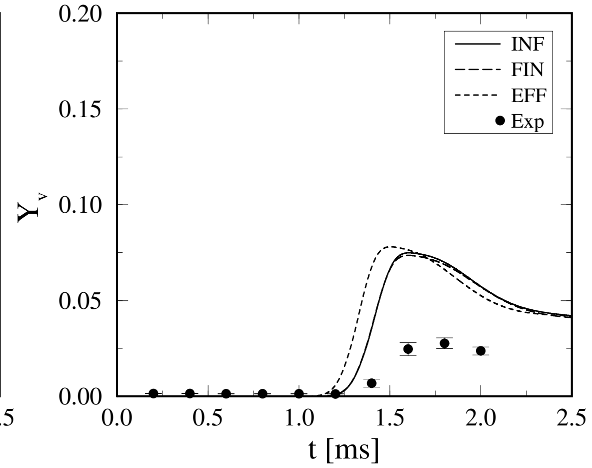

Figure 6.138: Effect of the conductivity model on Y_v at P_{54}.

(e.g. n-decane) it is even underpredicted. In the same section, it was also shown that various Nusselt and Sherwood correlations that were employed here do not produce significantly different evaporation rates. Of course the rate also depends on the droplet size and since here, this is determined by the atomisation model, over-estimated evaporation rate may be expected simply due to underestimated droplet size. If the latter is true, it is in contradiction with the explanation given earlier for the liquid penetration, indicating that the disagreement is purely due to the measurements. Unfortunately, measurements of the evaporation rate and SMD are not available here and the above statement cannot be confirmed. The effect of the

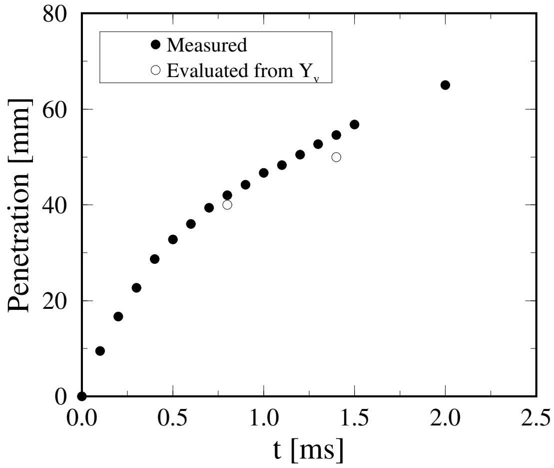

Figure 6.139: Measured and evaluated vapour penetration.

atomisation model will be examined later in operating point No. 4.

A second explanation could be that the predictions underestimate the radial spread of the vapour, leading to high concentrations. In order to investigate this, the radial distribution of vapour at two planes, $z = 40\,mm$ and $z = 50\,mm$, is plotted in Figs. 6.140 and 6.141, respectively, at three different times using the infinite

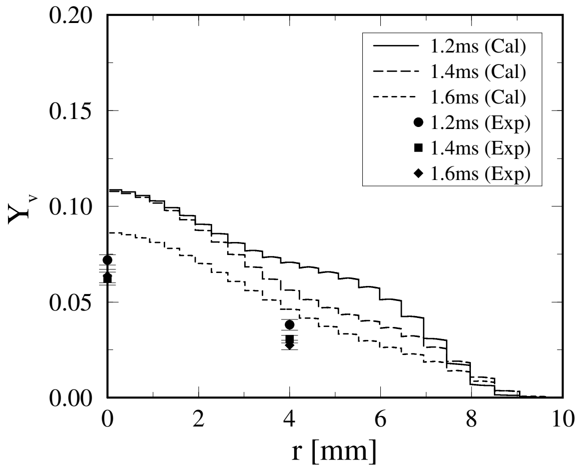

Figure 6.140: Radial distribution of Y_v at $z = 40\,mm$ at various times using infinite conductivity.

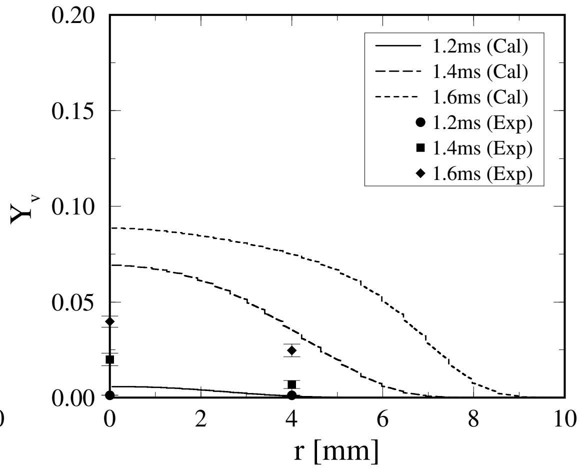

Figure 6.141: Radial distribution of Y_v at $z = 50\,mm$ at various times using infinite conductivity.

conductivity model. Unfortunately, the vapour concentration was only measured at one point $4\,mm$ off axis. Nevertheless, it seems, judging from the shape of the predicted curves, that the calculated vapour concentration is higher than the measured one even off axis. This was investigated by reducing the turbulent Schmidt number, $\sigma_{Y_{v,i}}$, in the fuel vapour mass fraction conservation equation, Eq. (2.72), from 1 (see Table 2.1) to the value 0.5, which is appropriate for turbulent jets* [142] and repeating the calculations, using the infinite conductivity model. The results for the five locations are given in Figs. 6.142–6.146. As can be seen the agreement between predictions and measurements is significantly improved, especially at locations on the spray axis. However, the vapour concentration is still somewhat overpredicted.

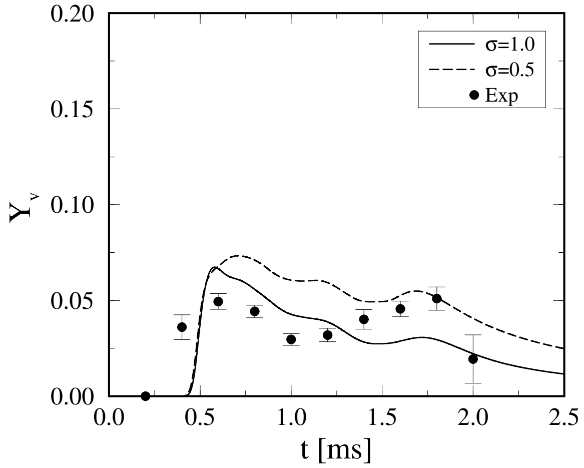

Figure 6.142: Effect of the turbulent Schmidt number on Y_v at P_{34}.

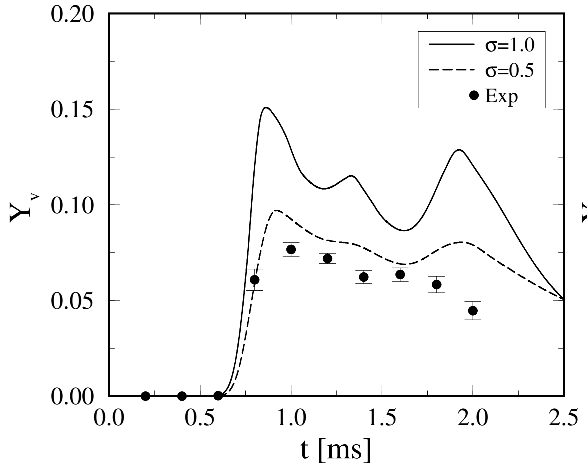

Figure 6.143: Effect of the turbulent Schmidt number on Y_v at P_{40}.

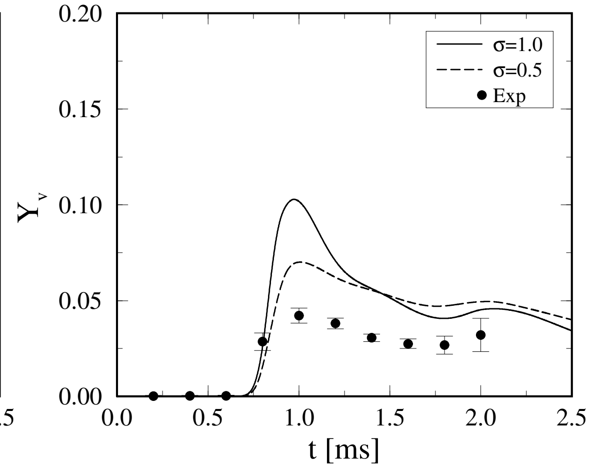

Figure 6.144: Effect of the turbulent Schmidt number on Y_v at P_{44}.

*In free shear flows most researchers use values of $\sigma_{Y_{v,i}}$ ranging from 0.5 to 0.7 [179]. Here, the lowest value is employed in order to investigate its effect on the local vapour concentration.

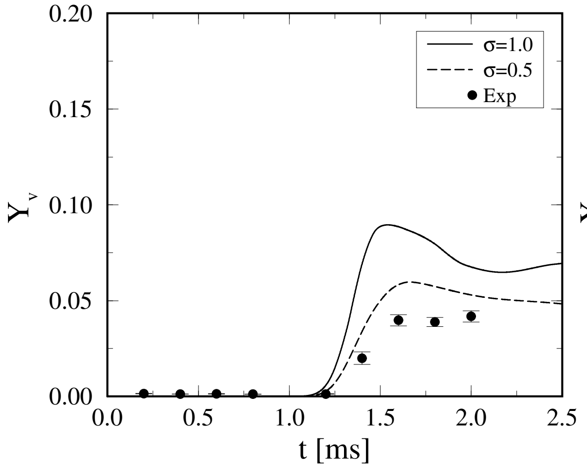

Figure 6.145: Effect of the turbulent Schmidt number on Y_v at P_{50}.

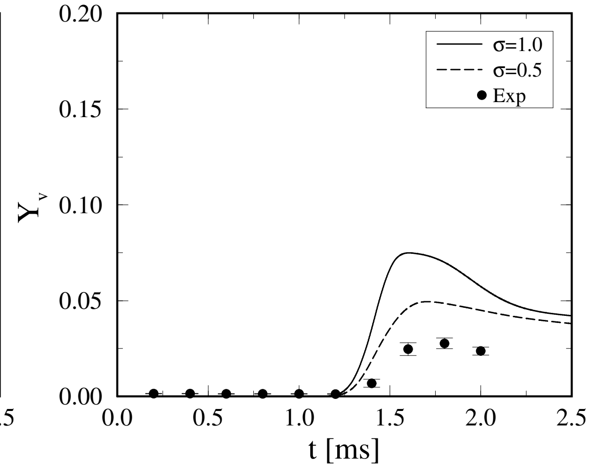

Figure 6.146: Effect of the turbulent Schmidt number on Y_v at P_{54}.

It should be mentioned that other researchers who simulated the same experiment, observed similar levels of overprediction (see Leduc and Karlsson [184] and Kralj [171]). In contrast, better agreement was obtained by Hohmann *et al.* [137], at least at one location presented in their report. However, in their mathematical model the coupling between the two phases is incomplete, since the void fraction does not appear in the conservation equations of the gas phase. Also, the atomisation process was not modelled and thus, arbitrary spray angle and initial distribution of droplet size were given. Finally, as explained earlier, grid-independent results cannot be obtained and in particular, the coarser the mesh in the axial direction, the lower the local vapour concentration (see Fig. 6.109). Hohmann *et al.* used a uniform axial cell size of 1.17 mm in their calculations whereas here, the smallest axial cell size is 0.45 mm (see Table 6.27).

Finally, it is noted that experimental errors and uncertainties should also be investigated.

6.5.6 Operating point No. 3

This operating point is used to investigate the effect of the drag coefficient submodel on the spray development. It should be recalled that this effect was found to be minor in atmospheric sprays (see Section 6.4). The predictions are designated as in Table 6.34. All the other spray submodels and initial conditions of the flow field are the same as used in §6.5.2 (see Tables 6.28 and 6.29).

Table 6.34: Designation of the calculations for operating point No. 3.

Designation	Drag coefficient
Sph	Yuen-Chen, Eq. (3.66)
Dist	Patterson *et al.*, Eq. (3.72)

Although measurements of liquid and vapour penetration are not available for this operating point, both are nonetheless presented here. As can be seen in Figs. 6.147 and 6.148, higher penetration is obtained by employing the distorted

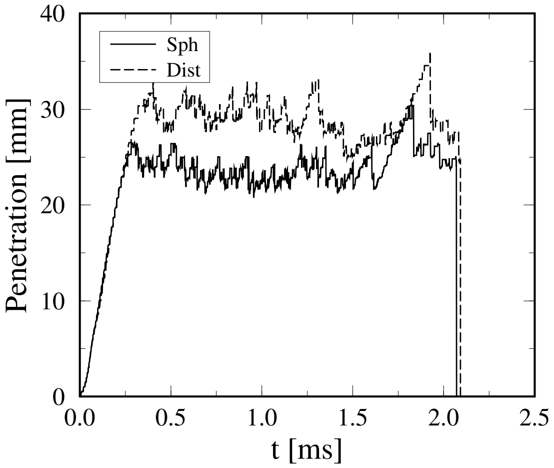

Figure 6.147: Effect of the drag coefficient model on liquid penetration.

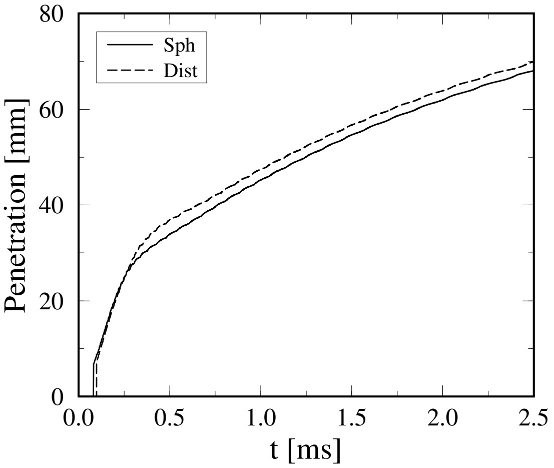

Figure 6.148: Effect of the drag coefficient model on vapour penetration.

droplet model. In the atmospheric spray calculations, it was observed that the drag coefficient correlation does not affect appreciably the liquid penetration because as was explained there, the higher drag of the distorted droplets is balanced by their higher momentum due to the reduced breakup rate. The latter is due to the lower relative velocity between the droplet and the surrounding gas. Here, the distorted droplets achieve higher penetration than the spherical ones. This is because the lower relative velocity not only reduces the breakup rate but also lowers the evaporation rate. Both mechanisms lead to larger SMD. These effects are clearly shown in Figs. 6.149 and 6.150 which present the cumulative evaporated mass and the SMD, respectively.

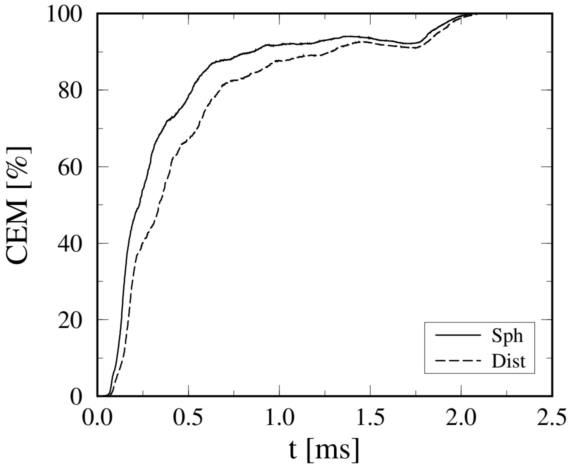

Figure 6.149: Effect of the drag coefficient model on the cumulative evaporated mass.

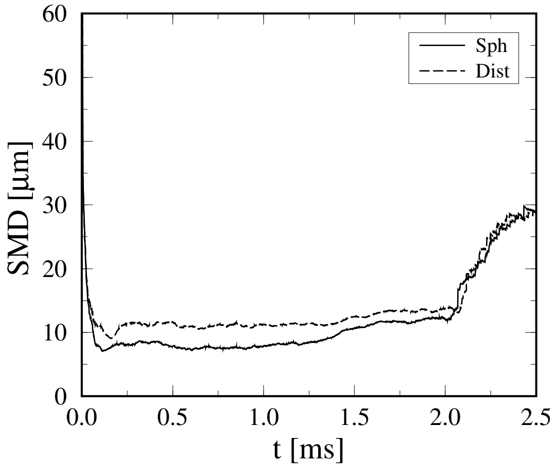

Figure 6.150: Effect of the drag coefficient model on the SMD.

The distorted droplet model produces higher vapour concentrations than the spherical one at P_{30} (see Fig. 6.151). The scattering of the results is due to droplets which reach the critical temperature, resulting in rapid evaporation. At this location both models overpredict the vapour concentration, whereas $4\,mm$ off axis, the experimental data lie between the two curves. Here, the highest concentration is now predicted by the spherical model. Note that ignition occurs at $1.8\,ms$ (Wiartalla *et al.* [305]) and therefore, after this time, the predictions do not represent reality. Further downstream, the concentration is overpredicted at all locations as can be seen in Figs. 6.153–6.156. However, better agreement is expected if lower value of $\sigma_{Y_{v,i}}$ is used. Overall, the distorted droplet model gives the best results at the locations off axis. However, it nevertheless consistently overpredicts the concentration. On the other hand, the spherical droplet model gives better results at the points on axis.

The conclusion here is that both models for drag coefficient tend to result in overprediction of the vapour concentration as observed in the previous operating

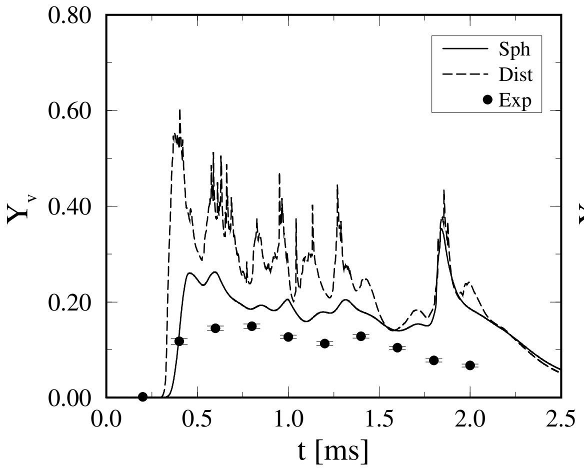

Figure 6.151: Effect of the drag coefficient model on Y_v at P_{30}.

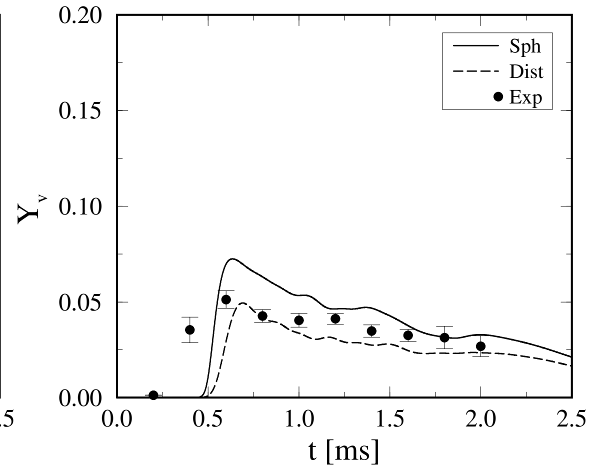

Figure 6.152: Effect of the drag coefficient model on Y_v at P_{34}.

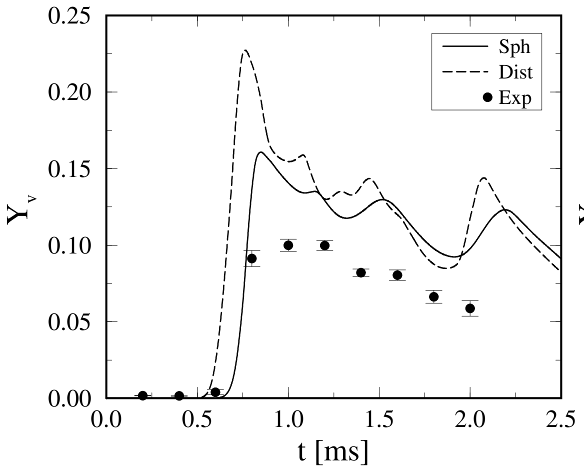

Figure 6.153: Effect of the drag coefficient model on Y_v at P_{40}.

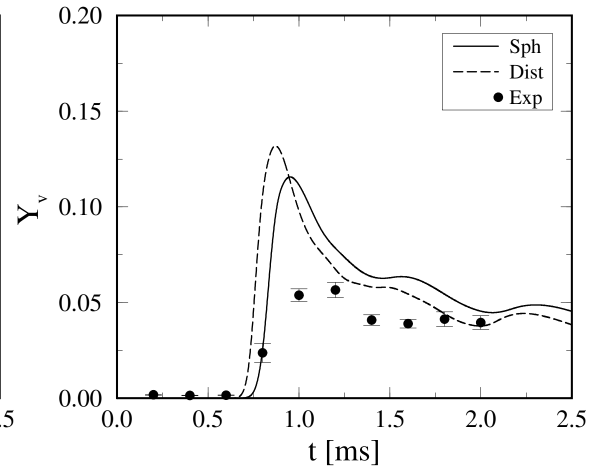

Figure 6.154: Effect of the drag coefficient model on Y_v at P_{44}.

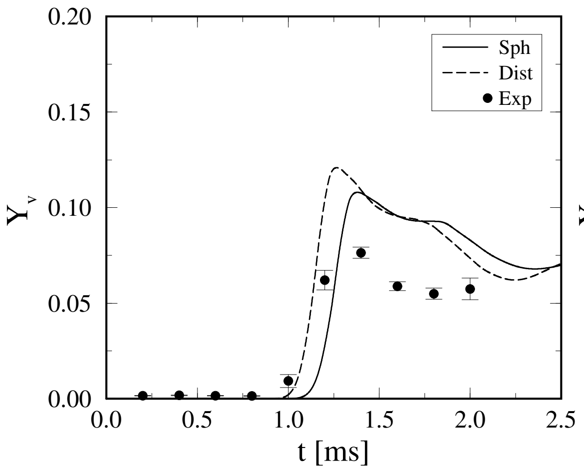

Figure 6.155: Effect of the drag coefficient model on Y_v at P_{50}.

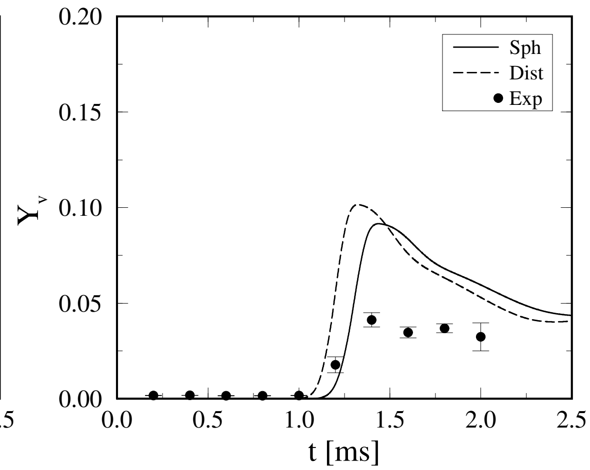

Figure 6.156: Effect of the drag coefficient model on Y_v at P_{54}.

point as well. However, improved agreement could be obtained by reducing the value of $\sigma_{Y_{v,i}}$ from 1 to a more appropriate one in the range 0.5 to 0.7. The gap in vapour penetrations between the two models is only about 3 %, but it is bigger in liquid penetration. However, these quantities were not measured and it is not clear which model gives the best results.

6.5.7 Operating point No. 4

The performance of the two atomisation models, presented in Section 3.3, is investigated for this case. The spray semi-cone angle, α_{exp}, required by the MPI atomisation model was not measured in the experiment and hence, it is estimated by applying the correlation of Varde [293] given by Eq. (6.8). This results in $\theta = 25.04°$ and hence, $\alpha_{exp} = 12.5°$ is chosen. The same value was used by Hohmann *et al.* [137] who simulated the same experiment, while Kralj [171] used two different values, $\alpha_{exp} = 6.5°$ and $\alpha_{exp} = 10°$. Here, another calculation with $\alpha_{exp} = 5°$ is performed in order to investigate its effect on the results. Also, the two values of the coefficient C_5 of the Huh model, used in the atmospheric spray calculations are employed here as well. The calculations are designated according to Table 6.35.

Table 6.35: Designation of the calculations for operating point No. 4.

Designation	Atomisation model	C_5	α_{exp} [°]
Huh1	Huh	1	-
Huh2	Huh	0.1	-
MPI1	MPI	-	5
MPI2	MPI	-	12.5

The liquid penetration is plotted in Fig. 6.157. Although the results are scattered, it can be seen that the larger the input angle for the MPI model, the smaller the penetration. As explained in §6.4.5, this is due to the larger region in which the spray is distributed leading to lower induced gas velocity and hence, stronger drag. The measured penetration is lower than the predicted ones and as explained for operating point No. 1, this is probably because the spray is dilute in the tip vicinity and consequently, cannot be detected in the experiments. In the same discussion it was also conjectured that the Huh atomisation model may produce excessively large droplets leading to overprediction. Here, it is clear that for both models and for all parameters examined, the liquid penetration is overpredicted and the differences among the predictions are much smaller than the differences between the predictions and the measurements.

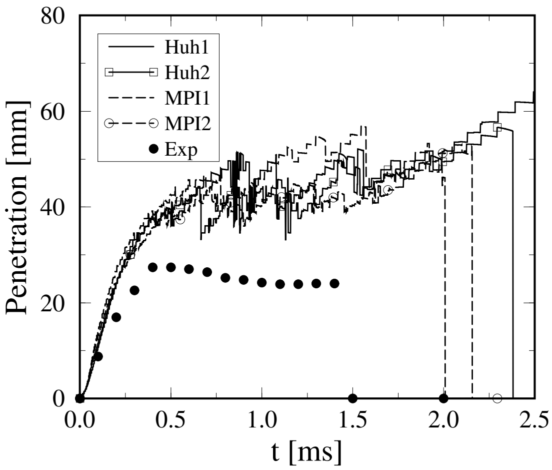

Figure 6.157: Effect of the atomisation on liquid penetration.

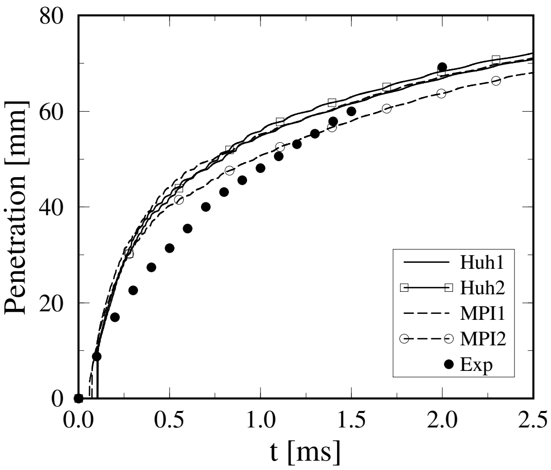

Figure 6.158: Effect of the atomisation on vapour penetration.

The vapour penetration, shown in Fig. 6.158, shows similar trends. Thus, the MPI2 produces the smallest penetration while all the other predicted curves are close to each other. Disagreement between the predictions and the measurements is observed up to $1.5\,ms$. The calculated curves have a higher initial slope which gradually reduces. As explained for operating point No. 1, this is because the vapour penetration follows the liquid penetration until around $40\,mm$. Then, the liquid length becomes constant and the vapour is further convected by the induced gas velocity. Since the latter has lower velocity than the liquid, the slope of the penetration curve decreases.

As can be seen in Fig. 6.159, the MPI model results in faster evaporation than the Huh model. It is also observed that increasing the angle α_{exp} causes the evaporation rate to increase because the spray is spread over a wider angle, resulting in lower vapour concentration around each droplet. The effect on the cumulative evaporated mass is consistent with that on the SMD depicted in Fig. 6.160. Thus, the larger the α_{exp}, the smaller the SMD, while MPI produces smaller SMD than those of the Huh model. However, the difference between the MPI atomisation model and the Huh model is negligible and both lead to relatively small SMD rapidly, whereas in the atmospheric spray calculations the MPI was found to reduce the SMD gradually. Although the reduction of C_5 leads to smaller initial droplet diameter, this is not

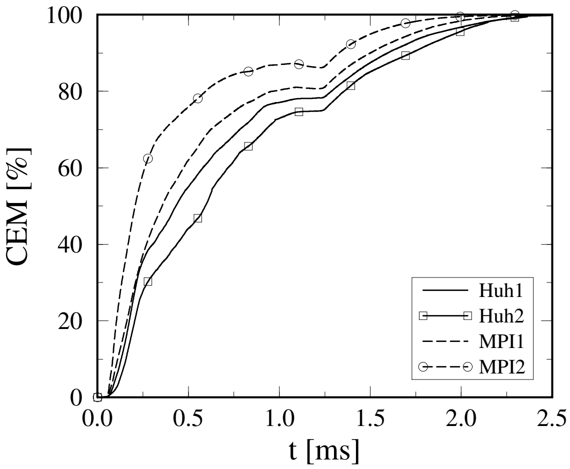

Figure 6.159: Effect of the atomisation on the cumulative evaporated mass.

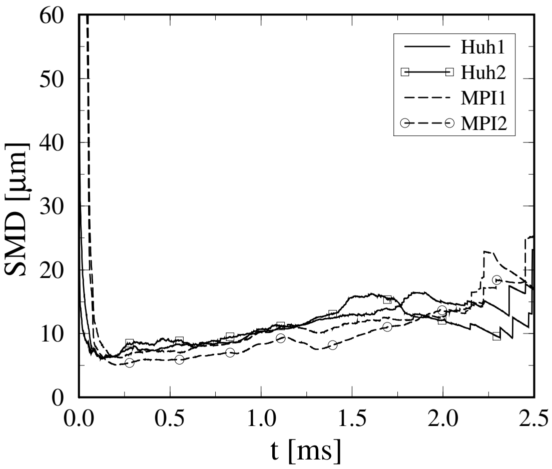

Figure 6.160: Effect of the atomisation on the SMD.

visible in Fig. 6.160. This is because the smaller droplets have lower relative velocity with the gas, leading to slower evaporation (see Fig. 6.159) and hence, larger droplets. Note that in the atmospheric spray, the decrease of C_5 clearly reduces SMD as was observed in Fig. 6.54 because the opposing mechanism of evaporation did not take place there.

The local vapour concentration at the six measurement locations is shown in Figs. 6.161–6.166. The differences among all predictions apart from those for MPI2 are small. Overprediction is observed at all locations on axis as was also found in the previous operating points. Better agreement is obtained off axis at 30 mm and 40 mm downstream. It is noteworthy that the measurements surprisingly show earlier vapour arrival off axis rather than on axis at 30 mm downstream. This implies some experimental uncertainties.

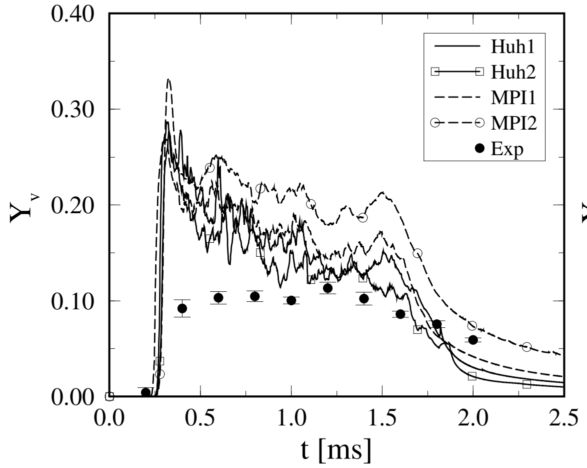

Figure 6.161: Effect of the atomisation on Y_v at P_{30}.

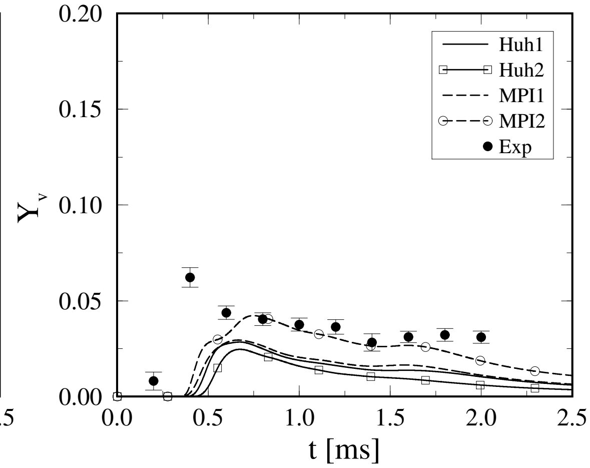

Figure 6.162: Effect of the atomisation on Y_v at P_{34}.

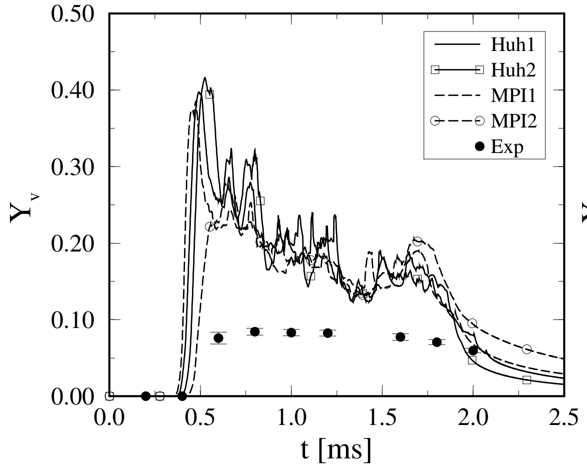

Figure 6.163: Effect of the atomisation on Y_v at P_{40}.

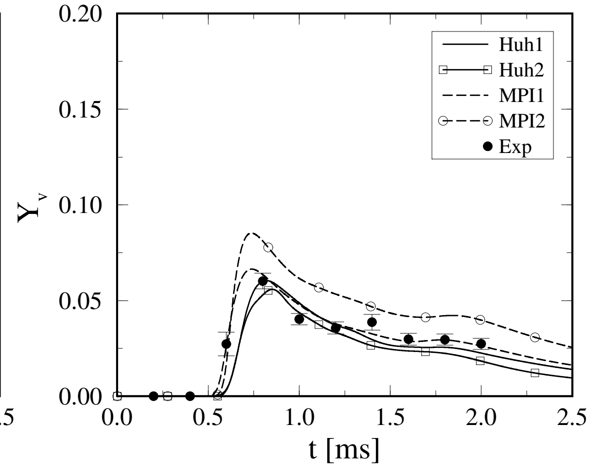

Figure 6.164: Effect of the atomisation on Y_v at P_{44}.

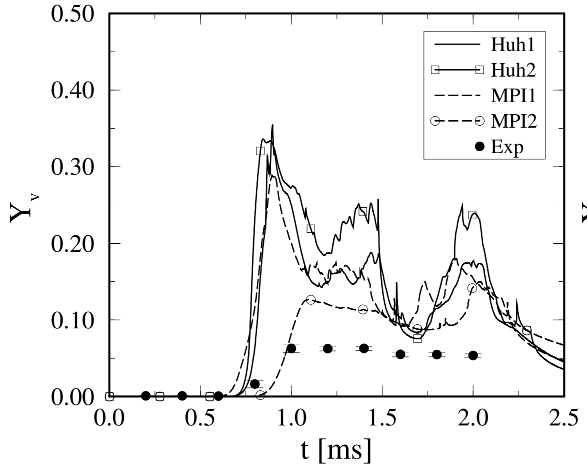

Figure 6.165: Effect of the atomisation on Y_v at P_{50}.

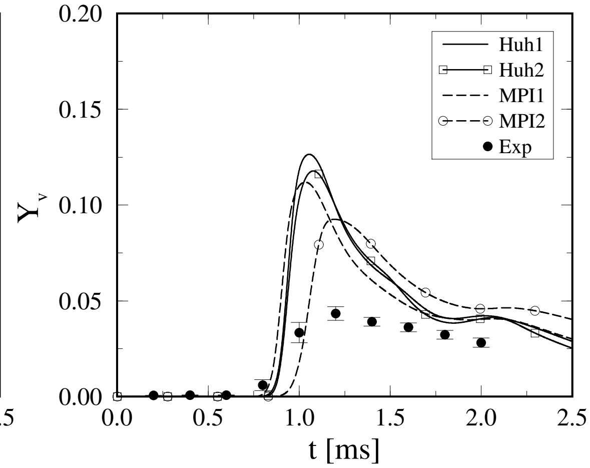

Figure 6.166: Effect of the atomisation on Y_v at P_{54}.

6.5.8 Summary

The spray methodology was assessed in this section under high pressure and temperature conditions. The effects of the mesh, time step and parcel introduction rate were examined and particular investigations were performed for individual submodels.

The effects of the time step and the parcel introduction rate were found to be negligible for values smaller than $2\,\mu s$ and larger than $10\,\text{parcels}/\mu s$, respectively. In contrast, the grid density, especially in the radial direction, substantially influences the predictions, as was also observed for the atmospheric spray. However, it was found that the mesh effect decreases with refinement, although a truly grid-independent result cannot be obtained since a limit is set by the maximum allowable void fraction.

Three different treatments for the internal temperature distribution in the droplet were examined. They were found to produce closely similar results. Similar observations have been reported by Hohmann *et al.* [137] who found that although there is a substantial difference between the finite and infinite conductivity models when the evaporation of a single droplet is studied, the difference is much less pronounced when are applied to a whole spray.

It was surprisingly observed that the higher is the drag coefficient, the higher are the liquid and vapour penetrations, although the increase is relatively small. This was attributed to the fact that the higher drag coefficient lowers the relative velocity between the droplets and the surrounding gas resulting in lower breakup and evaporation rates. These lead to larger droplets with higher momentum.

Regarding the atomisation models, it was found that the spray results are rather insensitive to the value of the coefficient C_5 in the Huh model. For the MPI model, it was observed that the higher is the spray semi-cone angle, the lower is the penetration. This is due to the larger region in which the spray is distributed leading to lower induced gas velocities and higher evaporation rates. It was also observed that both atomisation models rapidly produce a relatively small SMD whereas in the atmospheric spray calculations, it was found that the MPI model gradually reaches the value produced by the Huh model.

Comparison of the predictions with experimental results revealed that the liquid penetration is overpredicted for all combinations of submodels used in this study. Also, the vapour penetration is overpredicted in the beginning because it follows the liquid, whereas afterwards, the liquid reaches a steady state and the vapour is convected by the induced gas velocity. Thus, the vapour velocity decreases gradually. The overprediction of the liquid part was attributed to the fact that the measuring technique can only detect dense sprays. The hypothesis that this overprediction may be due to the atomisation model, producing relatively large droplets with high momentum, was found to be in contradiction with the results for the local vapour concentration. In particular, the latter is overpredicted, implying that the droplets are too small, leading to high evaporation rates.

The overprediction of the local evaporation rate could also be attributed directly to the evaporation model (Nusselt and Sherwood correlations), however, as was found in the investigation of single droplet evaporation, the Nu and Sh correlations are in a good agreement with the measurements, at least for n-heptane.

Another reason that could be invoked to explain the overprediction of the vapour concentration is that the predictions underestimate the rate of spread of the vapour jet. However, it was found that even when the turbulent Schmidt number is reduced by a factor of two, Y_v is still overpredicted although an improved agreement is obtained. Nevertheless, the latter statement leads to the conclusion that in turbulent jets the turbulent Schmidt number should be lower than 1, in agreement with the relevant literature (see Launder and Spalding [179] and Ideriah [142]).

Last but not least, it has to be mentioned that overprediction of the same order was also reported by Leduc and Karlsson [184] and Kralj [171] who simulated the same experiment. Hence, experimental errors and uncertainties should also be explored.

6.6 Volkswagen engine

The spray methodology assessed in the previous sections of the current chapter will now be tested in a real Diesel engine. For this purpose, the Volkswagen four-cylinder DI 1.9 l engine, which was the research engine of the IDEA and IDEA-EFFECT projects, is chosen. During these projects measurements were obtained at Volkswagen AG, Wolfsburg and at Imperial College of Science, Technology and Medicine, London. The results of the former research group are reported by Hentschel *et al.* [124, 126–129], while those of the latter one are reported by Arcoumanis and Whitelaw [24], Arcoumanis [15] and Arcoumanis *et al.* [21].

6.6.1 Description

The Volkswagen four-cylinder DI 1.9 l engine is a modified version of the commercial one. The original omega-shape bowl-in-piston is modified to a transparent flat one to allow optical access for experimental investigation of the in-cylinder flow, spray, autoignition and combustion processes. A diagram of the engine is illustrated in Fig. 6.167. The engine comprises one inlet (IV) and one exhaust (EV) valve as

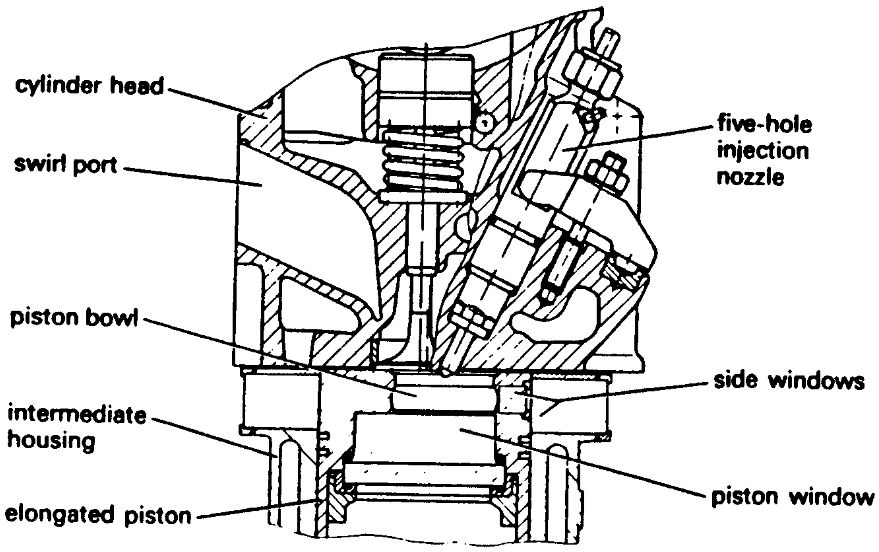

Figure 6.167: Diagram of the Volkswagen DI 1.9 l transparent engine, taken from Arcoumanis *et al.* [17].

depicted in Fig. 6.168. With respect to the coordinate system defined in this figure where the centre is located on the cylinder axis and the cylinder head, the bowl axis is $7\,mm$ off x axis and $1.7\,mm$ off y axis. The engine geometrical specifications are listed in Table 6.36.

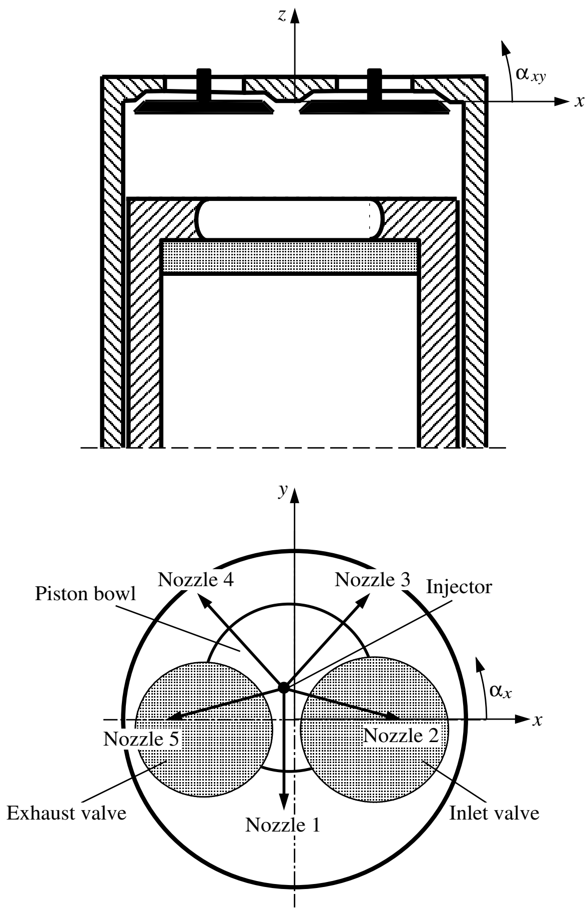

Figure 6.168: Coordinate system for Volkswagen DI $1.9\,l$ transparent engine simulation.

The injection system comprises a distributor pump and an inclined injector with five holes, located slightly off the bowl axis. The holes are asymmetric with respect to the injector axis and their exit position along with their direction of injection are tabulated in Table 6.37. In this table, the angle α_{xy} is the angle between the plane $x - y$ and the injection direction while the angle α_x is the angle between the x axis and the injection direction (see Fig. 6.168). Since the injector is not symmetric, the lengths of the nozzles are unequal, however, here, the holes are assumed to

Table 6.36: Engine geometrical specifications.

Displacement [l]	1.9
Bore [mm]	79.5
Stroke [mm]	95.5
Connecting rod [mm]	144.0
Compression ratio	19.5
Inlet valve:	
Diameter [mm]	36.0
Open (IVO) [$^\circ CA$ BTDC]	21.0
Close (IVC) [$^\circ CA$ ABDC]	63.0
Exhaust valve:	
Diameter [mm]	31.5
Open (EVO) [$^\circ CA$ BBDC]	71.0
Close (EVC) [$^\circ CA$ ATDC]	30.0

Table 6.37: Injector holes locations and injection directions.

Hole No.	x [mm]	y [mm]	z [mm]	α_{xy} [$^\circ$]	α_x [$^\circ$]
1	−1.900	6.379	−2.351	−14.01	270.0
2	−0.458	7.396	−2.543	−14.636	339.0
3	−0.901	9.039	−2.983	−15.78	52.0
4	−2.899	9.039	−2.983	−15.78	128.0
5	−3.342	7.396	−2.543	−14.636	201.0

have the same dimensions, given in Table 6.38. The asymmetry of the injector results also in different discharge coefficients between the nozzles with consequences on the volumetric flow rates. The latter were not measured individually for each

Table 6.38: Injector specifications.

Length, L [mm]	0.8
Diameter, D [mm]	0.184
Discharge coefficient, c_d	0.70

nozzle, so there is no direct way of knowing them. However, in order to match the penetrations, in this study, unequal volumetric flow rates are considered using an *ad hoc* adjustment, based on the angle between the injector axis and nozzle axis, ϕ, making the individual flow rates proportional to $1 + \cos\phi$.

Various operating points have been investigated, as summarised in Table 6.39. This follows the designation adopted by Volkswagen AG (VW). In the experiments,

Table 6.39: Engine operating points.

	EOP1a	EOP1c	EOP2	EOP4a
Engine speed $[rpm]$	2000	2000	1000	2000
Fuel type	Diesel	Diesel	Diesel	Diesel
Fuel mass injected $[mg]$	8	8	5	30
$T_{d,inj}$ $[K]$	300	300	300	300
SOI $[^\circ CA]$	358.2	352.5	357.5	352.2
EOI $[^\circ CA]$	365.7	360.0	361.1	369.5

Diesel fuel was used, while here, it is simulated with n-dodecane, following the practice of Takenaka *et al.* [281], Kong *et al.* [167], Kralj [171] and Ikonomou [143]. The fuel volumetric flow schedules were supplied by Volkswagen AG [276] and are shown in Fig. 6.169, for all four operating points. They apparently smoothed approximations to the real schedules.

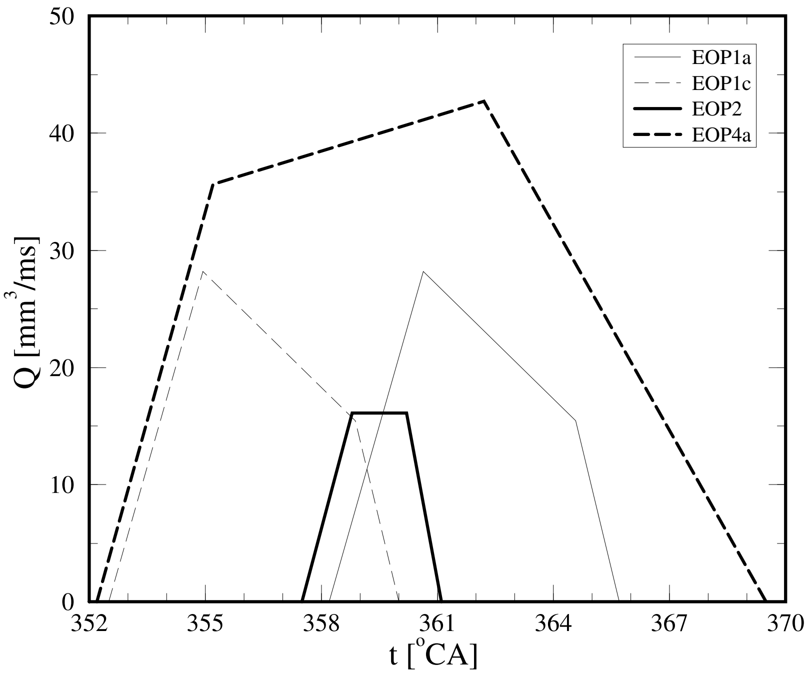

Figure 6.169: Injection flow rate histories.

The measurements of spray penetration obtained at VW were evaluated from high-speed films and each data point represents the ensemble average over a number of cycles. Specifically, 38 [127], 16 [127] and 48 [126] cycles were averaged for EOP1a, EOP1c and EOP2, respectively. The spray penetration was also measured at Imperial College (IC) for two operating points, using a high-speed camera [24]. Droplet radial velocities at five locations were also obtained at IC by LDV [24]. Four of these positions are located close to the axis of nozzle No. 4, while the fifth one is close to the nozzle No. 1 axis. The exact locations of the five points are given in Table 6.40. The coordinates are as defined in Fig. 6.168, except for r which indicates the radial distance from the injector centre. The available experimental data for each operating point are indicated in Table 6.41.

Table 6.40: Locations of droplet velocity measurements.

Location	r $[mm]$	α_x [°]	z $[mm]$
A	7.4	126.0	−4.0
B	9.2	126.0	−4.5
C	11.2	126.0	−5.0
D	14.0	126.0	−5.5
E	10.0	270.0	−4.0

Table 6.41: Summary of available experimental data.

Experimental data	Operating point			
	EOP1a	EOP1c	EOP2	EOP4a
Spray penetration (VW)	$\surd$	$\surd$	$\surd$	$\surd$
Spray penetration (IC)	$\surd$	−	$\surd$	−
Droplet velocities at A	−	−	$\surd$	−
Droplet velocities at B	−	−	$\surd$	−
Droplet velocities at C	$\surd$	−	$\surd$	−
Droplet velocities at D	$\surd$	−	$\surd$	−
Droplet velocities at E	−	−	$\surd$	−

6.6.2 Computational mesh

Accommodation of the piston and the valve motions can lead to distortion of the computational mesh. For highly-squashed cells, which can happen during the compression and exhaust strokes, or highly-elongated cells, which can occur during the induction and expansion strokes, the convergence of the numerical algorithm may be slowed down or even prevented (see Theodoropoulos [288]). In addition, as the piston ascends the mesh resolution becomes finer whereas a coarser mesh results when the piston descends.

The abovementioned problems are overcome by adding or removing cell layers as appropriate. Hence, when the piston ascends, layers of cells adjacent to the piston are removed when they are squeezed more than a prespecified threshold value, whereas new layers are added when the piston descends*. This action results in a varying number of cells but with relatively uniform grid density. It is also noted that during this action all the extensive gas properties are conserved, while the void fraction is recalculated based on the droplet positions in the new mesh.

The computational mesh, generated by Sarantinos [257], follows the chamber geometry in substantial detail, including head recesses and piston cut-outs for the valves. Figs. 6.170 and 6.171 illustrate the mesh at 180° CA and 360° CA, respectively. In the former case, it comprises 148663 cells and in the latter case, this reduces to 26895. It is noted that the average cell size is about $1\,mm$ and according to the discussion in §6.5.2, an even finer mesh should be employed. However, the available computer capacity would not allow this.

6.6.3 Initial and boundary conditions

The calculations commence at -32° CA (before the inlet valve starts to open) and here, a brief description of the initial and boundary conditions is given, while for details, the reader is referred to Kralj [171].

*This feature was developed and implemented in the SPEED code by Mr. B. Adamson.

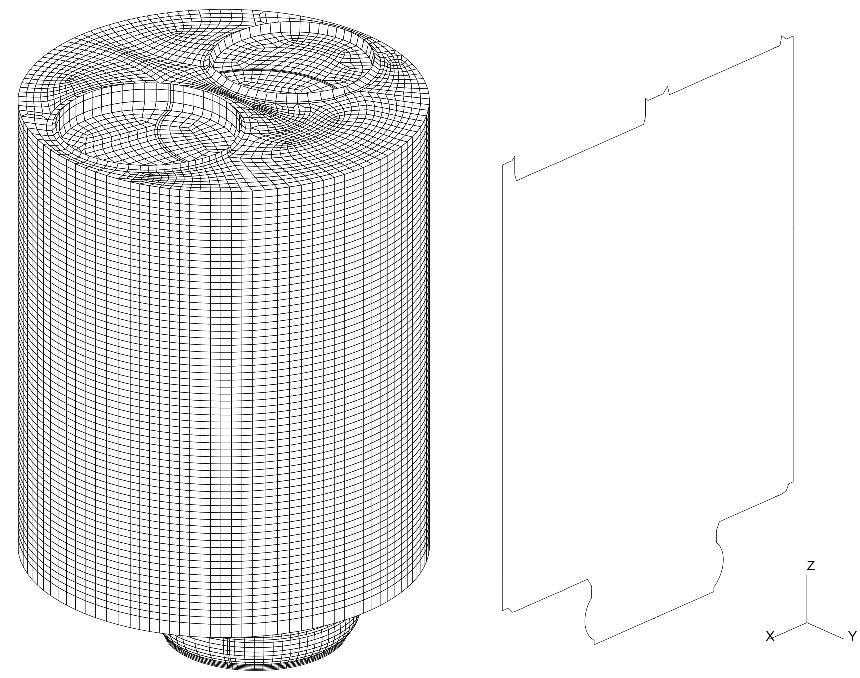

Figure 6.170: View and cross section through the cylinder axis of the VW engine computational mesh at 180° CA.

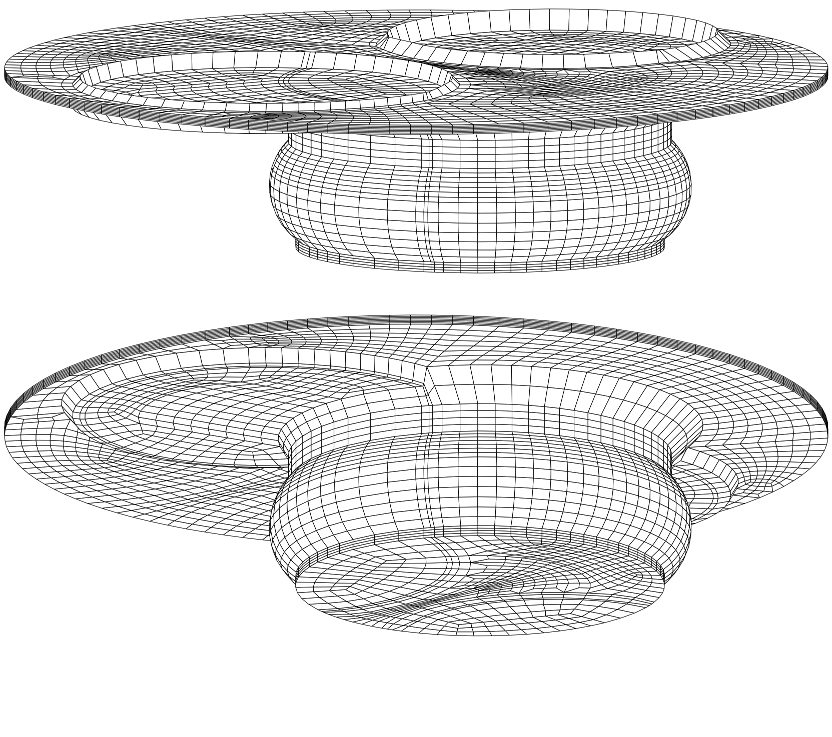

Figure 6.171: Views of the VW engine computational mesh at 360° CA.

Uniform initial temperature and pressure in the cylinder are assumed with values $300\,K$ and $0.833\,bar$, respectively. The initial values of k and ε are set to $2\,m^2/s^2$ and $800\,m^2/s^3$, respectively. A uniform initial swirl velocity around the cylinder axis is also assumed while the other two velocity components are zero.

Data from the experimental studies of Arcoumanis and Whitelaw [23] and Arcoumanis *et al.* [25] were used to specify the inlet conditions. In these experiments, measurements were obtained under steady-flow conditions at four fixed valve lifts of the velocity distribution in the valve curtain* and the discharge coefficient. In the velocity measurements all three components were determined at several points in the valve gap at six circumferential positions. In the calculations, the velocities were linearly interpolated in both space and time†. At the exhaust valve, a uniform velocity profile was assumed.

In the absence of experimental data, the turbulence kinetic energy and its dissipation rate at the valve curtain were evaluated according to the practices of Ahmadi-Befrui [5] and Begleris [35] based on some characteristic properties of the valve flow. Thus,

$$k_v = K_v^k u_{v,r}^2 \ , \tag{6.10}$$

$$\varepsilon_v = C_\mu^{3/4} \frac{k_v^{3/2}}{l_v} \ . \tag{6.11}$$

Here, $u_{v,r}$ is the average radial inlet velocity ($u_{v,r} = \dot{Q}_v / S_v$, where $\dot{Q}_v$ is the volumetric flow rate through the valve curtain and S_v is the cross-sectional area of the valve curtain) and l_v is a characteristic turbulence length scale ($l_v = K_v^\varepsilon L_v$, where L_v is the valve lift). Also, K_v^k and K_v^ε are coefficients given in Table 6.42. It is, however, emphasised that the in-cylinder turbulence level is rather insensitive to these boundary conditions since most of the turbulence production in the cylinder is generated by the shear layers at the edges of the incoming jet (see Ahmadi-Befrui [5]).

*In principle the SPEED calculation domain could have been extended to include the inlet port, obviating the need for these measurements, however this would have substantially increased the computing mesh requirements.

†The measured velocities were obtained as functions of the valve lift and they were converted into functions of time based on the valve lift profile (see Kralj [171]).

Finally, the pressure and temperature in the inlet and outlet ports are tabulated in Table 6.42.

Table 6.42: Inlet and outlet conditions.

Property	Inlet port	Outlet port
Pressure [bar]	0.833	1.167
Temperature [K]	291	340
K_v^k	0.01	0.01
K_v^ε	0.045	0.045

The wall temperatures at the various parts of the engine were not measured, however, they were specified according to experience and directions given by VW. A uniform temperature was assumed on each part whereas from part to part the temperature was varying in the range of $340\,K$ to $400\,K$ (see Kralj [171]).

6.6.4 Operating point EOP1a

The spray submodels employed in the simulation of the operating point EOP1a, are listed in Table 6.43. The time step is set to $0.024°\,CA$, which corresponds to $2\,\mu s$. As was found in §6.5.3*, when it is below this value, its effect on the predictions is negligible. Also, the parcel introduction rate is set to 5 parcels/μs for each nozzle. In Section 6.5, the parcel introduction rate used was 20 parcels/μs but here, it would lead to a very large number of droplets, due to the five nozzles, resulting in excessive computing requirements. Nevertheless, when the parcel introduction rate is 5 parcels/μs the effect on the spray predictions is negligible (see §6.5.4) and the results can be considered statistically representative.

*Note that the prevailing conditions of the gas during the injection are similar to those of the pressure chamber case. In particular, for motored conditions, the pressure and temperature at $360°\,CA$ for $2000\,rpm$ are $43\,bar$ and $892\,K$, respectively. For $1000\,rpm$, these values are $38\,bar$ and $862\,K$, respectively.

Table 6.43: Spray submodels for EOP1a.

Spray process	Submodel/correlation
Cavitation	MPI
C_c	0.7
k_r [μm]	1
Atomisation	Huh
c_d	0.7
C_5	1
Drag coefficient	Yuen-Chen, Eq. (3.66)
Evaporation	
Conductivity	Infinite
Nu and Sh	El Wakil *et al.*/Ranz-Marshall, Eqs. (3.86), (3.80), (3.137a)
Breakup	Hsiang-Faeth
Collision	O'Rourke

Results and discussion

A detailed analysis of the spray development will be presented for this operating point only. For the other operating points, only comparisons between predictions and measurements will be given.

Top and side views of the spray development* are depicted in Fig. 6.172, at 360° CA, 364° CA, 368° CA, 372° CA, 376° CA and 380° CA. Here, it should be noted that the ignition delay is 6.8° CA [127] and consequently, the predictions after 365° CA do not represent reality, since ignition and combustion are excluded in the present study. However, here, the calculations are performed until 380° CA for the sake of a better presentation of the spray development. As can be seen in this figure, the penetration rates are unequal, because of the non-uniform partitioning of the injected flow among the holes. Other spray characteristics are the nearly straight paths during the early part of injection, followed by the clear evidence of deflection of the tip by the swirling motion in the latter stages (see Figs. 6.176 and 6.177) and the impingement on the bowl wall, leading to some droplet breakup due to splashing.

Although the evaporation process is not evident in Fig. 6.172, since the droplets

*Note that for clarity, the droplets are not scaled according to their size.

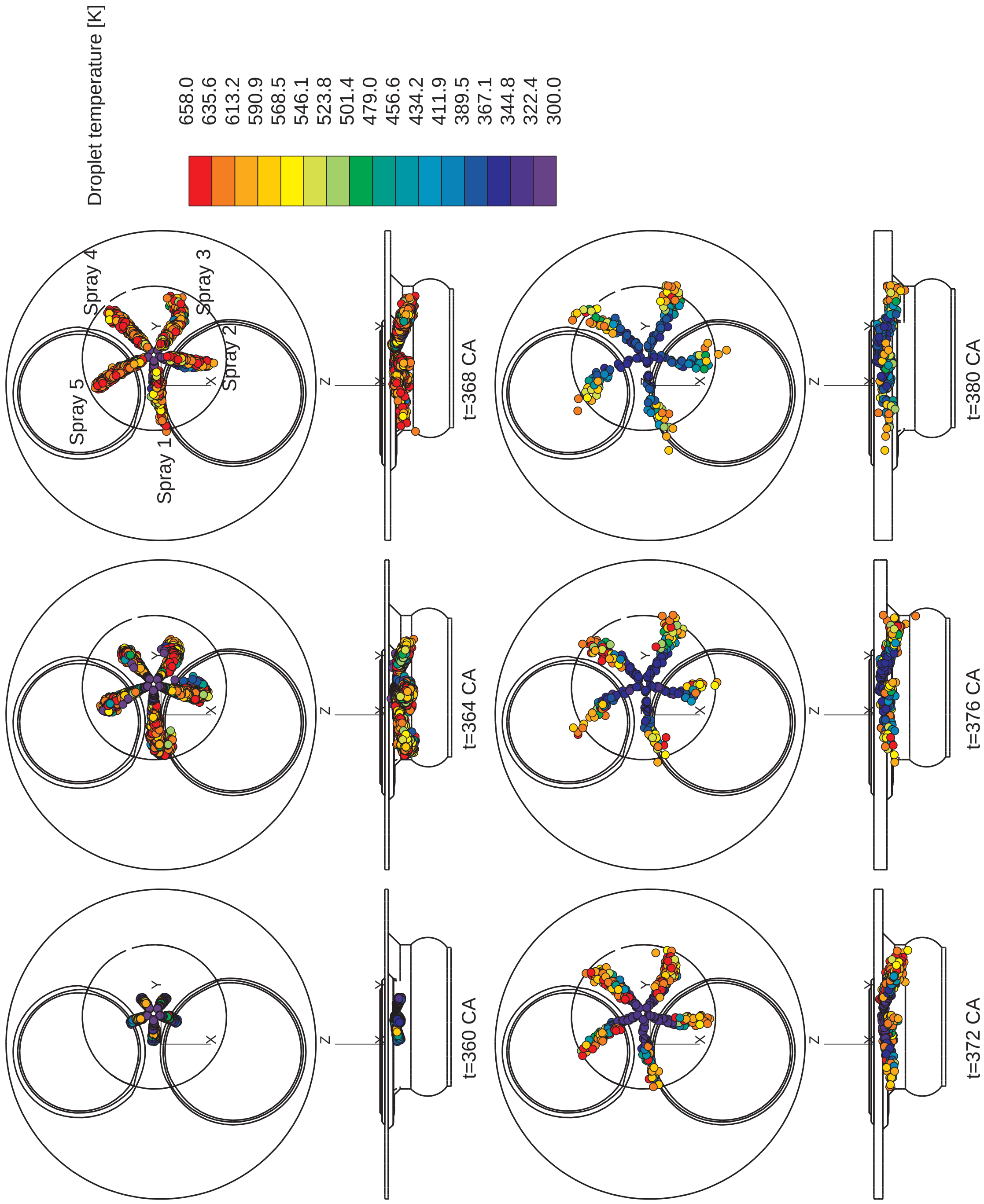

Figure 6.172: Top and side views of droplet temperature field at 360° *CA*, 364° *CA*, 368° *CA*, 372° *CA*, 376° *CA* and 380° *CA*.

are not scaled according to their size, its presence can clearly be seen in Fig. 6.173 which presents the cumulative evaporated mass. After the end of injection, most

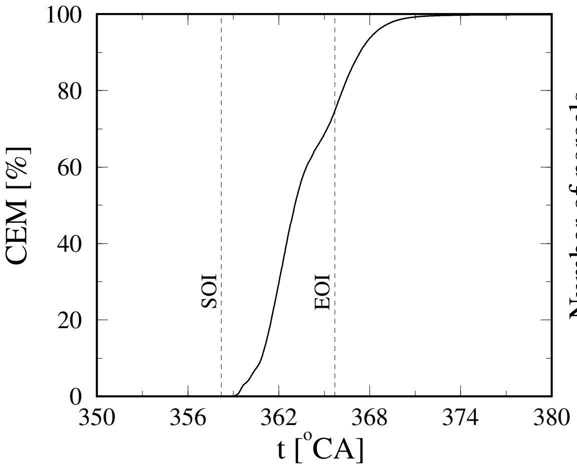

Figure 6.173: Cumulative evaporated mass for EOP1a.

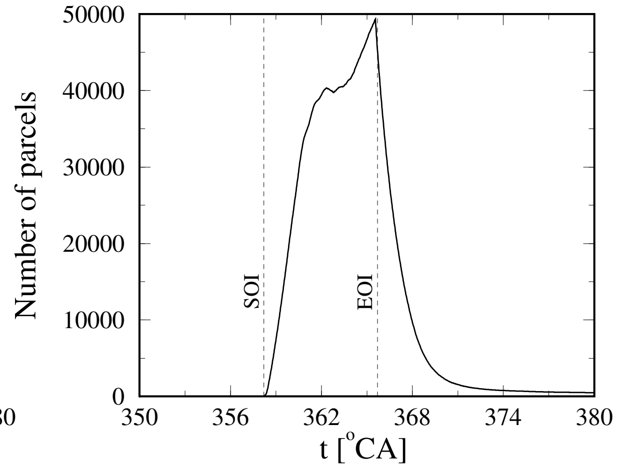

Figure 6.174: Number of computational parcels for EOP1a.

of the droplets evaporate rapidly (see Fig. 6.174) and thus, only those that have been injected just prior the EOI remain. These have low velocity (see Fig. 6.169) and they travel in an environment of relatively high vapour concentration and low temperature, due to the earlier-injected droplets, resulting in low evaporation levels. Hence, on the one hand, their surface regression rate is low and on the other, their temperature is relatively low, as evident in Fig. 6.172.

Since soon after the EOI the majority of the droplets evaporate and the remaining droplets evaporate slowly and do not break up, the Sauter mean diameter increases, as can be seen in Fig. 6.175.

The gas velocity fields at 360° CA, 364° CA, 368° CA, 372° CA, 376° CA and 380° CA are plotted in Figs. 6.176 and 6.177. Note that for clarity the velocity vectors have been mapped onto a regular presentation grid that is somewhat coarser than that used in the computations. In these figures, two horizontal planes, 3 mm and 8 mm below the cylinder head and one vertical plane passing through the axes of the cylinder and nozzle No. 1 are shown. At TDC a dominant swirling motion emerges caused by the deliberately-designed helical inlet port (see Bo *et al.* [47]).

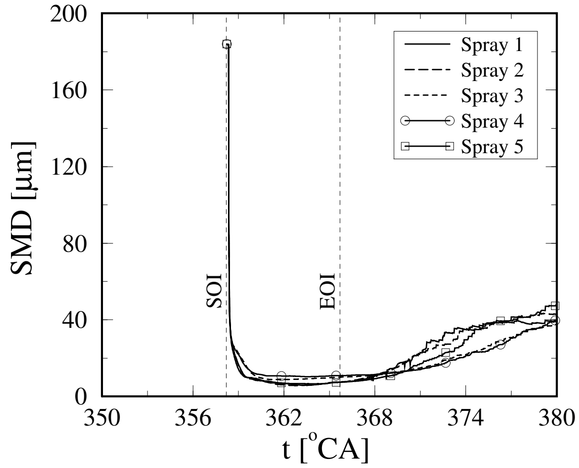

Figure 6.175: Sauter mean diameter for EOP1a.

As soon as the expansion stroke commences reverse squish flows develop (asymmetrically, due to the piston bowl offset) and these, on the one hand, induce a toroidal vortex in the bowl and on the other, modify the swirl distribution. Also evident in Fig. 6.176 are the effects of the spray on the gas flow, mainly manifested as strong induced velocities in the direction of the spray motion.

The distribution of evaporated fuel at the same planes and crank angles is shown in Figs. 6.178 and 6.179. Before the droplets reach the bowl wall the highest concentrations occur near the spray axes, while afterwards these are found in the impingement zone, where the droplets are the smallest, due to the combined effects of evaporation, breakup due to aerodynamic forces and splashing.

The temperature field contours, shown in Figs. 6.180 and 6.181, mainly follow those of the fuel vapour mass fraction. Thus, low temperature is observed in regions with high vapour concentration, due to the heat absorbed for evaporation. Significant cooling of the gas takes place at the spray vicinity due to the heat exchange, as can be seen in Fig. 6.180 at 360° CA and 364° CA. As the piston descends, a global reduction of the gas temperature, caused by expansion, is also observed.

Detailed comparisons between the predictions and the measurements will now be given. Fig. 6.182 presents the penetration of spray No. 1. In this figure, the computed liquid penetration is represented by both the leading droplet and the

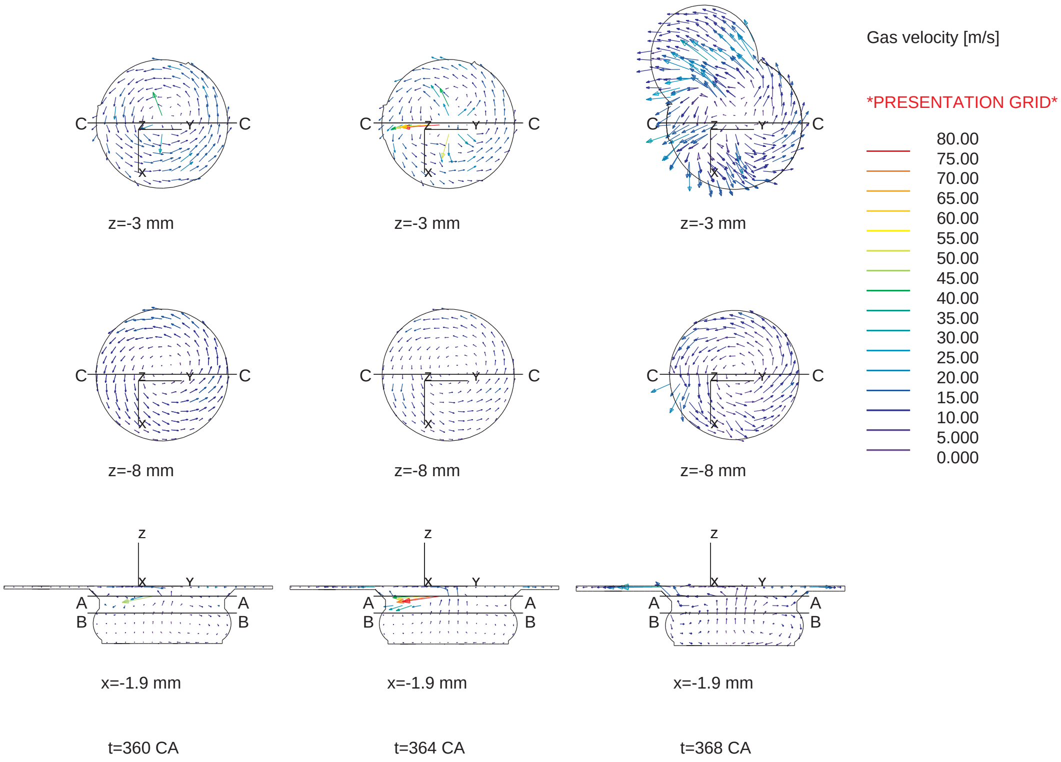

Figure 6.176: Velocity field at horizontal planes AA, $z = -3\,mm$ and BB, $z = -8\,mm$ and vertical plane CC, passing through the axis of nozzle No. 1, at $360°\ CA$, $364°\ CA$ and $368°\ CA$.

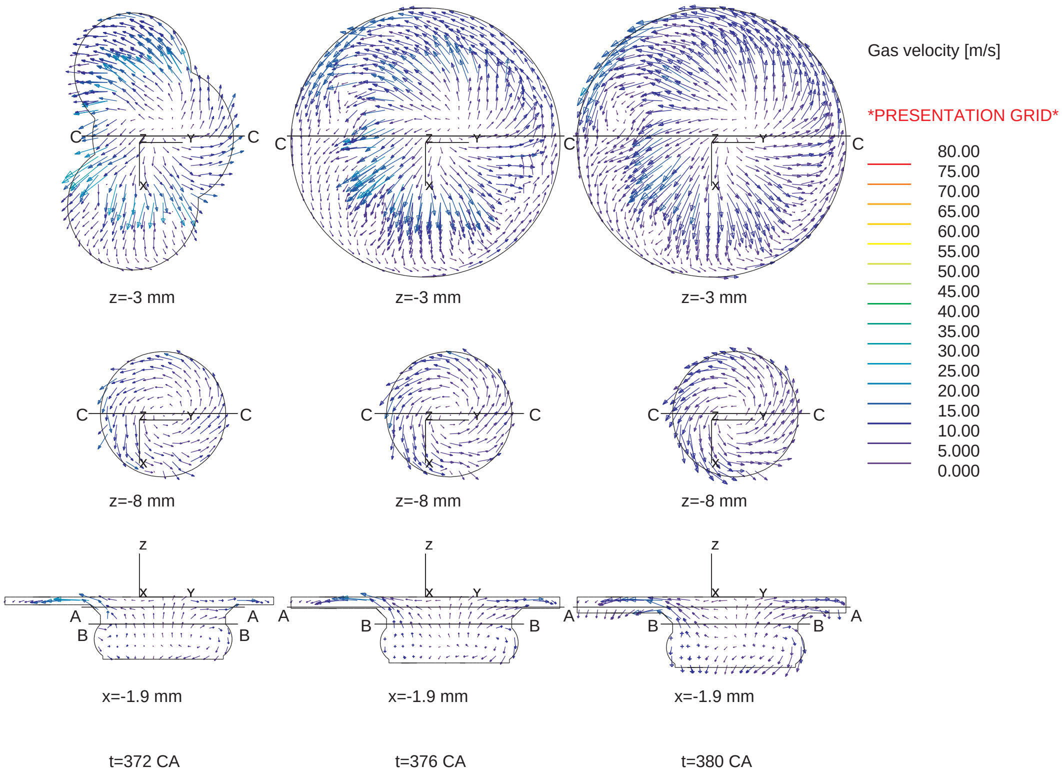

Figure 6.177: Velocity field at horizontal planes AA, $z = -3\,mm$ and BB, $z = -8\,mm$ and vertical plane CC, passing through the axis of nozzle No. 1, at $372°\ CA$, $376°\ CA$ and $380°\ CA$.

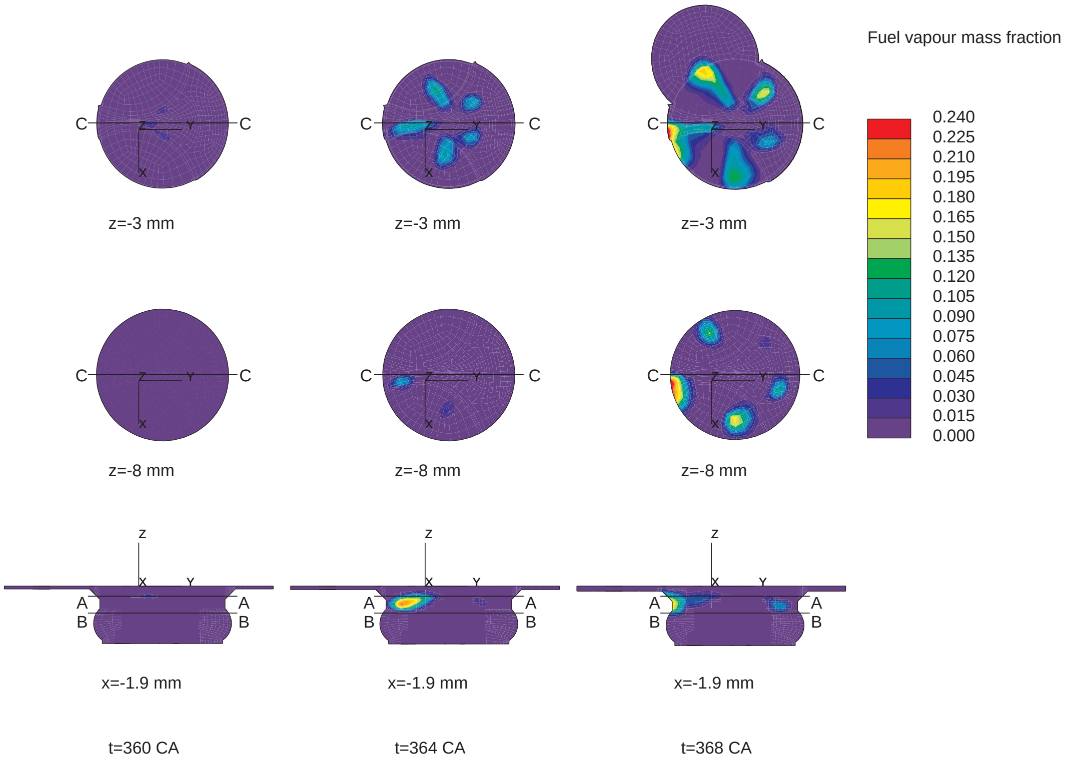

Figure 6.178: Fuel vapour mass fraction at horizontal planes AA, $z = -3\,mm$ and BB, $z = -8\,mm$ and vertical plane CC, passing through the axis of nozzle No. 1, at $360°\ CA$, $364°\ CA$ and $368°\ CA$.

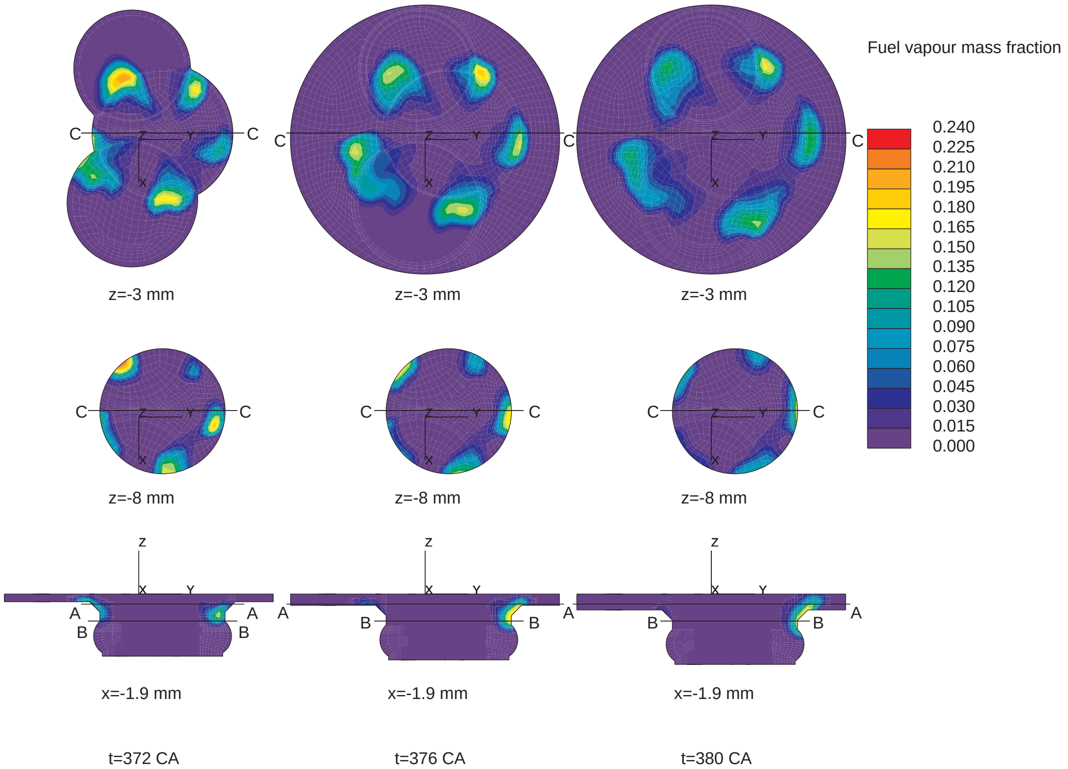

Figure 6.179: Fuel vapour mass fraction at horizontal planes AA, $z = -3\,mm$ and BB, $z = -8\,mm$ and vertical plane CC, passing through the axis of nozzle No. 1, at $372°\ CA$, $376°\ CA$ and $380°\ CA$.

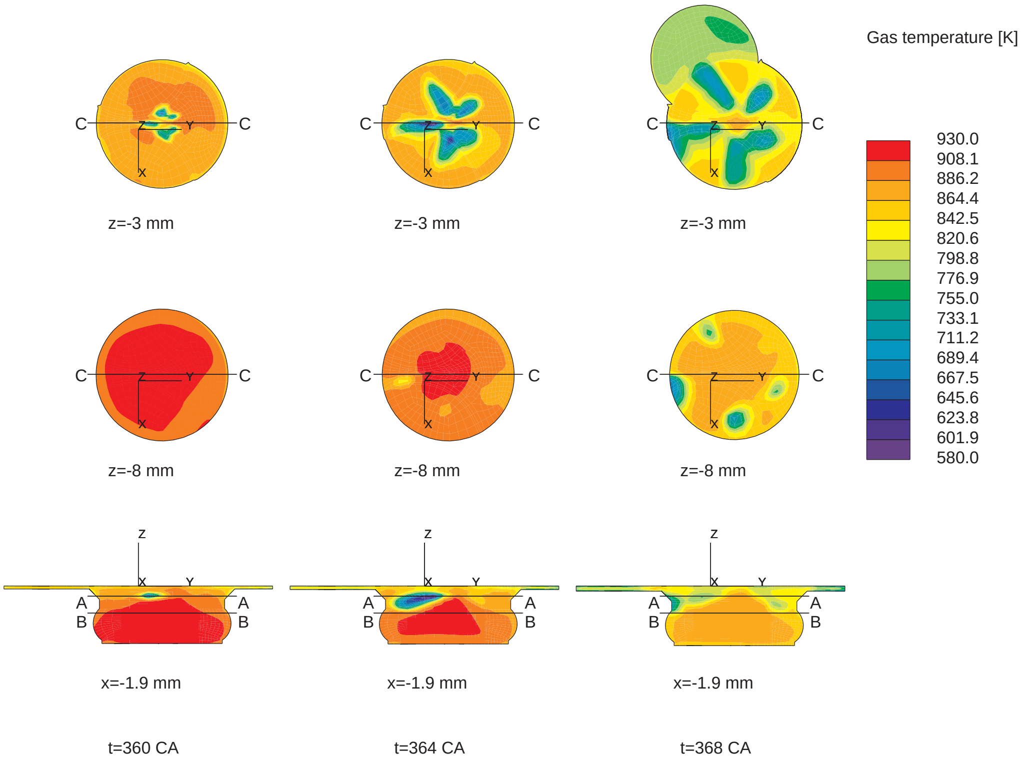

Figure 6.180: Temperature field at horizontal planes AA, $z = -3\,mm$ and BB, $z = -8\,mm$ and vertical plane CC, passing through the axis of nozzle No. 1, at $360°\ CA$, $364°\ CA$ and $368°\ CA$.

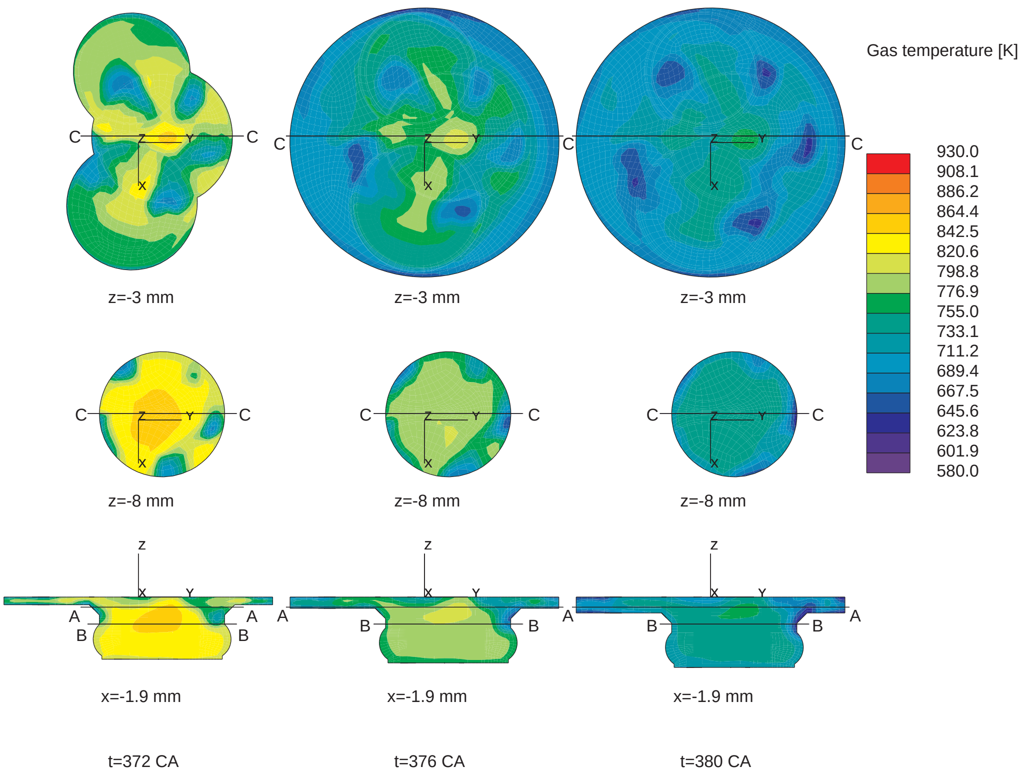

Figure 6.181: Temperature field at horizontal planes AA, $z = -3\,mm$ and BB, $z = -8\,mm$ and vertical plane CC, passing through the axis of nozzle No. 1, at $372°\ CA$, $376°\ CA$ and $380°\ CA$.

99 % mass definitions. The vapour penetration is also plotted. For this operating point, experimental results have been obtained at both VW and IC and they broadly agree. Although the slopes of the computed penetrations are similar to that of the measured ones, significant underprediction is observed due, it is believed, to incorrect start of injection time. Thus, careful inspection of the experimental results reveals that 0.297° CA after the SOI, the spray penetrates 7.03 mm, which requires a mean tip velocity of 284 m/s. However, from the injection volumetric flow rate (see Fig. 6.169) the calculated injection velocity at this time is only 25.8 m/s, based on the assumption that the fuel is equally distributed among the five nozzles. However, it should be noted that even if the whole amount of fuel is delivered through one nozzle, the corresponding velocity is only 129 m/s. The same situation was also found in Section 6.4 and as explained there, this is attributed to the fact that the experimentalists define the SOI as the time at which the needle lift reaches a certain level (see Hentschel and Röpke [125]). This means that at the 'SOI' the spray might have already entered the cylinder. Hence, a shifting of the experimental results is justifiable. For this operating point, the measurements are shifted for 1.8° CA (0.15 ms) and the resulting comparison is shown in Fig. 6.183. As can be seen, reasonable agreement between the predictions and measurements is now obtained.

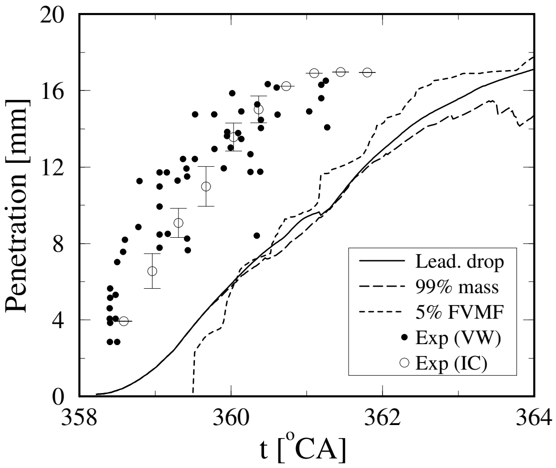

Figure 6.182: Penetration of spray No. 1 for EOP1a.

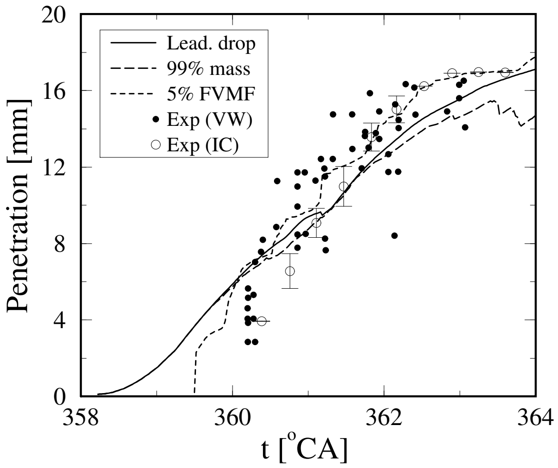

Figure 6.183: Penetration of spray No. 1 for EOP1a with shifted experimental data.

It is also noted that in the first stages of the injection, the liquid penetration is larger than that of the vapour penetration while later, the latter overtakes because it is convected by the gas, as in the pressure chamber cases. The measured penetrations were evaluated from high-speed films which do not provide the ability to distinguish a dense vapour region from a dilute liquid one. Thus, the measured penetration probably represents the maximum between that of the vapour and that of the liquid and as such, the maximum between the predicted values should be compared with the measurements.

The spray penetrations from the remaining four nozzles are plotted in Figs. 6.184–6.187, respectively. In all these figures, the measurements have also been shifted by $1.8^\circ\, CA$. Although reasonable agreement is observed, it can be seen that the slopes of the predicted penetrations are slightly lower than those of the measured ones. As was also mentioned in the atmospheric spray calculations, the underprediction can be attributed to the fact that, in reality, the needle lifts when the line pressure is above a threshold value (opening pressure) and therefore, the fuel injection starts with a relatively high velocity. Another reason for the penetration underprediction is perhaps the relatively small size of droplets produced by the atomisation and/or breakup and/or evaporation models, leading to fast deceleration.

Fig. 6.188 compares the calculated and measured temporal variations of the ensemble-average droplet velocities at locations C and D, whose coordinates were given in Table 6.40. According to the predictions, the spray reaches the point C about $2.2^\circ\, CA$ earlier than point D, which is located some $2.84\, mm$ downstream. This implies that the average spray velocity between these two points is about $15.5\, m/s$. This is consistent with the fact that the first droplets arriving at C are travelling at about $20\, m/s$ while at D their speed is reduced to $15\, m/s$ due to drag. In contrast, the measurements show similar velocities at the two points, about $25\, m/s$ and apparent arrival at D before C. According to the measured velocity at these locations, the spray should have reached point C about $1.37^\circ\, CA$ earlier than point D, implying that the experimental uncertainty is about $1.67^\circ\, CA$. These anomalies should be borne in mind in assessing the accuracy of the predictions. A probable contributor to the uncertainties are the high levels of the root mean square

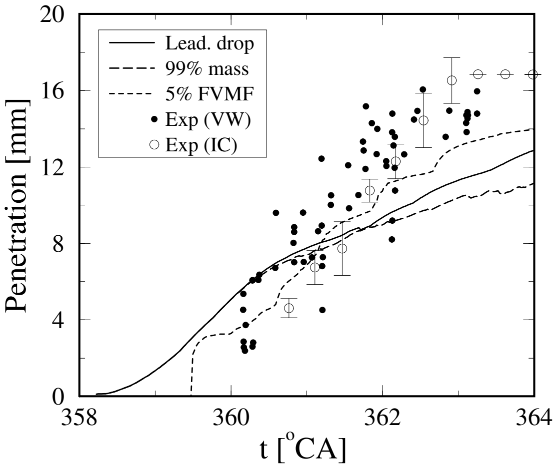

Figure 6.184: Penetration of spray No. 2 for EOP1a.

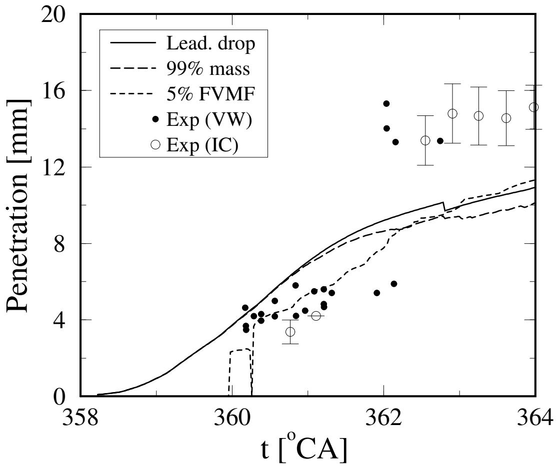

Figure 6.185: Penetration of spray No. 3 for EOP1a.

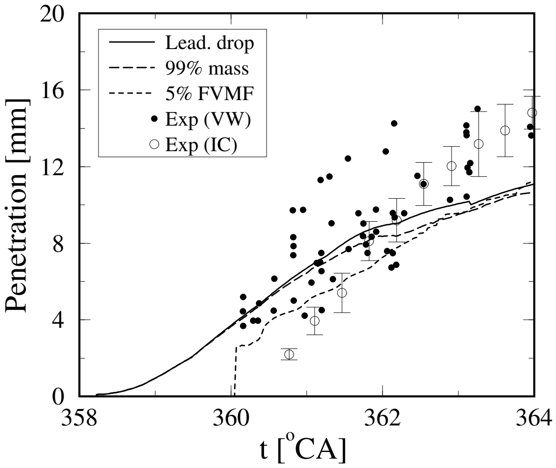

Figure 6.186: Penetration of spray No. 4 for EOP1a.

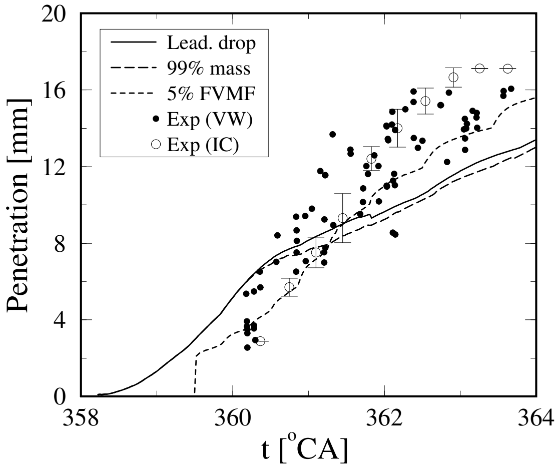

Figure 6.187: Penetration of spray No. 5 for EOP1a.

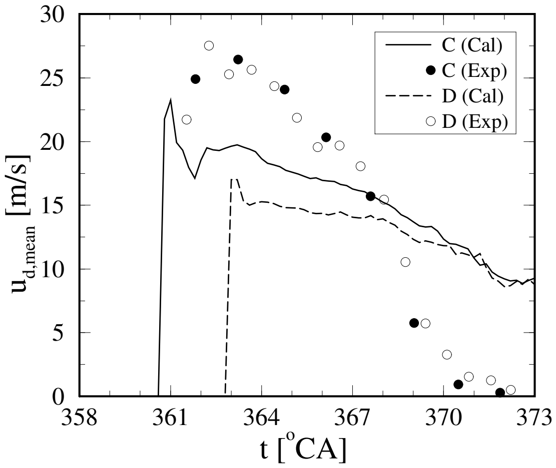

Figure 6.188: Droplet mean velocities along spray No. 4 for EOP1a.

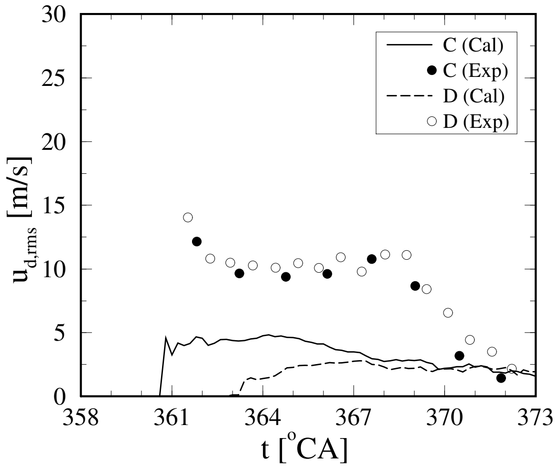

Figure 6.189: Droplet RMS velocities along spray No. 4 for EOP1a.

variations in the droplet velocity, displayed in Fig. 6.189. The principal cause of these is probably the distribution of droplet size, resulting in different levels of drag and hence, velocities. The predicted levels are much lower than the measured ones, probably because the calculation sample is not enough and perhaps, the breakup rate is overpredicted resulting in small and relatively uniform SMD. The latter explains also the underprediction of the mean velocities in the beginning and the overprediction later on, since the small droplets can be carried by the gas.

6.6.5 Operating point EOP1c

Table 6.44 lists all the spray submodels, used for the simulation of the operating point EOP1c. The time step and the parcel introduction rate are the same as those used in EOP1a, i.e. 0.024° CA and 5 parcels/μs, respectively.

Table 6.44: Spray submodels for EOP1c.

Spray process	Submodel/correlation
Cavitation	MPI
C_c	0.7
k_r [μm]	1
Atomisation	Huh
c_d	0.7
C_5	1
Drag coefficient	Yuen-Chen, Eq. (3.66)
Evaporation	
Conductivity	Infinite
Nu and Sh	El Wakil *et al.*/Ranz-Marshall, Eqs. (3.86), (3.80), (3.137a)
Breakup	Reitz-Diwakar
Collision	O'Rourke

Results and discussion

The ignition delay for this operating point was found to be 7.4° CA [127] allowing comparison of the predictions with the measurements up to 359.9° CA. The spray penetrations for the sprays Nos. 1–5 are shown in Figs. 6.190–6.194, respectively.

Here, the experimental results have been shifted for $1.1° \, CA$ $(0.09 \, ms)$ due to the reasons explained earlier. As can be seen, the agreement between the predictions and the measurements is similar to that for operating point EOP1a, although a different breakup model is employed here (all the other spray submodels remain the same, see Tables 6.43 and 6.44). This is consistent with the findings in §6.4.7, where it was observed that all the breakup models examined in the present study produce almost the same penetration.

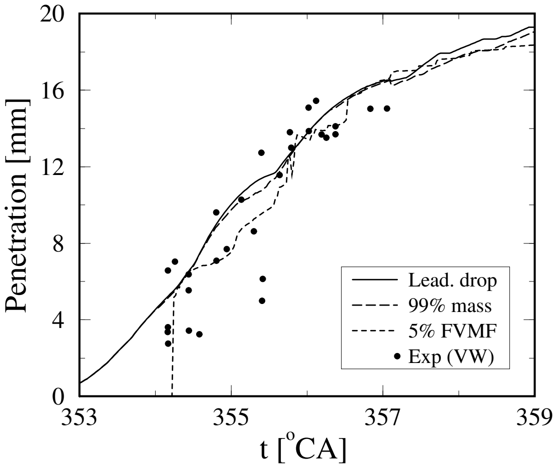

Figure 6.190: Penetration of spray No. 1 for EOP1c.

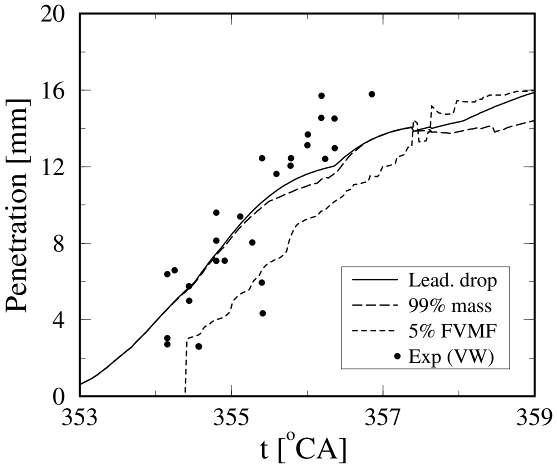

Figure 6.191: Penetration of spray No. 2 for EOP1c.

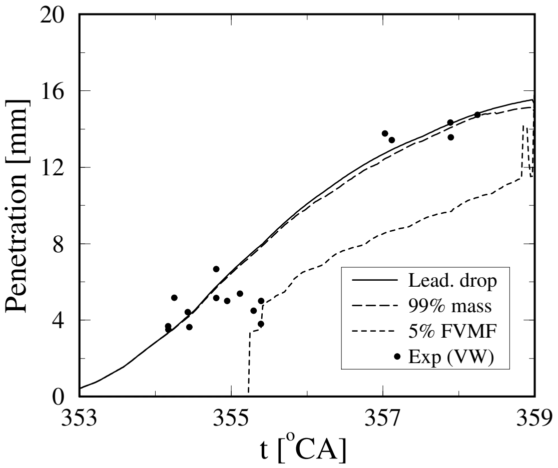

Figure 6.192: Penetration of spray No. 3 for EOP1c.

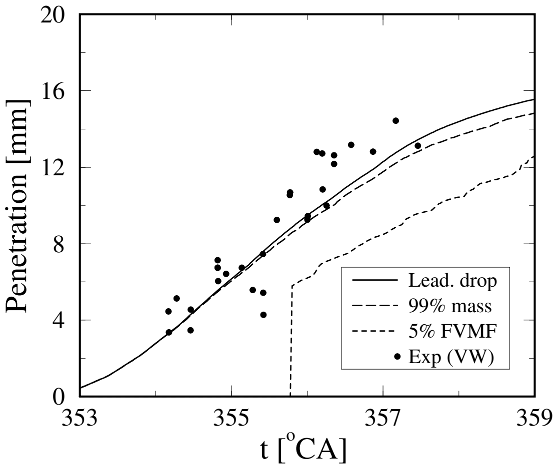

Figure 6.193: Penetration of spray No. 4 for EOP1c.

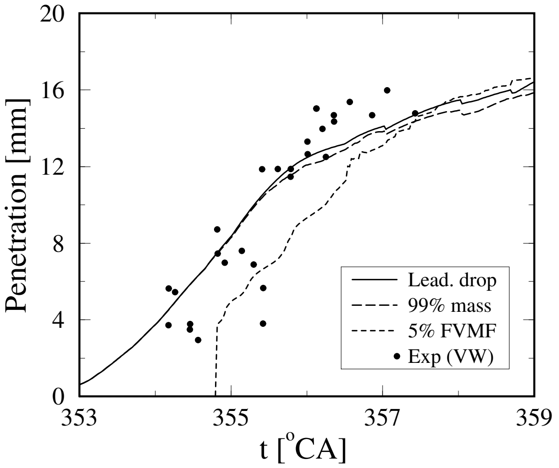

Figure 6.194: Penetration of spray No. 5 for EOP1c.

6.6.6 Operating point EOP2

All the spray submodels employed for the simulation of the operating point EOP2 are gathered in Table 6.45. The time step and the parcel introduction rate are the same as those used in the previous operating points, i.e. 0.024° CA and 5 parcels/μs, respectively. However, this time step is equivalent to 4 μs whereas in the previous cases, it was 2 μs due to the different engine speed. Here, the same time step (in CA) is chosen in order to avoid the production of a huge number of computational parcels* which would introduce heavy computational overheads. This value, however, does not introduce appreciable errors, since the effect of the time-step size on the spray results was found in §6.5.3 to be minor for values up to 4 μs.

Results and discussion

According to Hentschel and Schindler [128], the ignition delay for operating point EOP2 is 5.2° CA and therefore, the predictions can be compared with the measurements until 362.7° CA.

The spray penetrations from nozzles Nos. 1–5 are plotted in Figs. 6.195–6.199,

*Note that the atomisation model allows the generation of one secondary parcel per primary one per time step.

Table 6.45: Spray submodels for EOP2.

Spray process	Submodel/correlation
Cavitation	MPI
C_c	0.7
k_r $[\mu m]$	1
Atomisation	Huh
c_d	0.7
C_5	1
Drag coefficient	Patterson *et al.*, Eq. (3.72)
Evaporation	
Conductivity	Effective
Nu and Sh	El Wakil *et al.*/Ranz-Marshall, Eqs. (3.86), (3.80), (3.137a)
Breakup	Hsiang-Faeth
Collision	O'Rourke

respectively. The experimental results have also been shifted for this operating point, here by $1.5^\circ\, CA$ ($0.25\, ms$). As can be seen, the previous observations apply

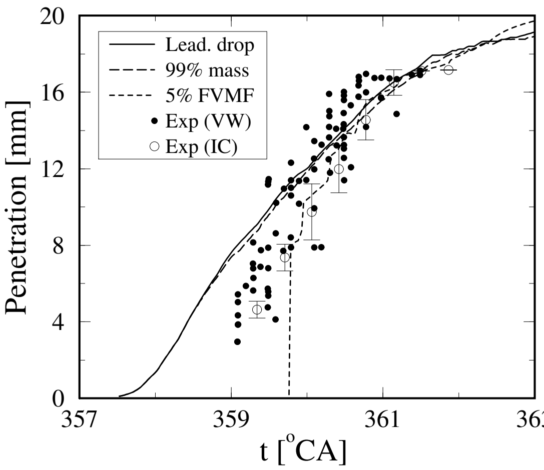

Figure 6.195: Penetration of spray No. 1 for EOP2.

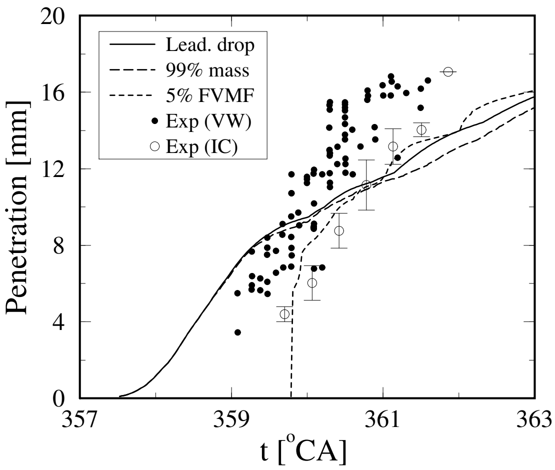

Figure 6.196: Penetration of spray No. 2 for EOP2.

here. Thus, the slopes of the predicted curves are lower than the corresponding measured ones, except for sprays No. 1 and No. 5 for which reasonable agreement is observed. It is however, noted that for sprays No. 3 and No. 4, disagreement also occurs between the two experiments. This provides an indication of the experimental uncertainty which should also be considered in assessing the predictions.

Comparison between the predicted and measured droplet mean velocities at the

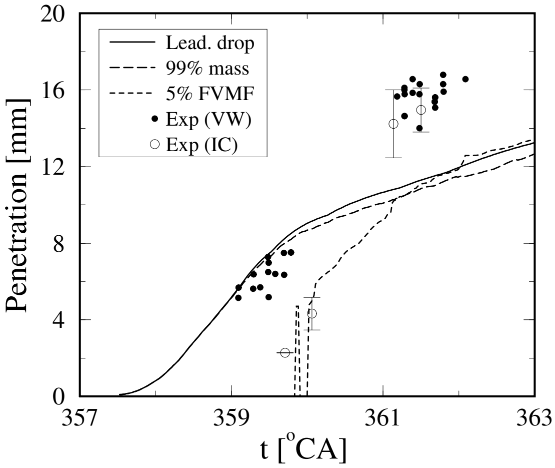

Figure 6.197: Penetration of spray No. 3 for EOP2.

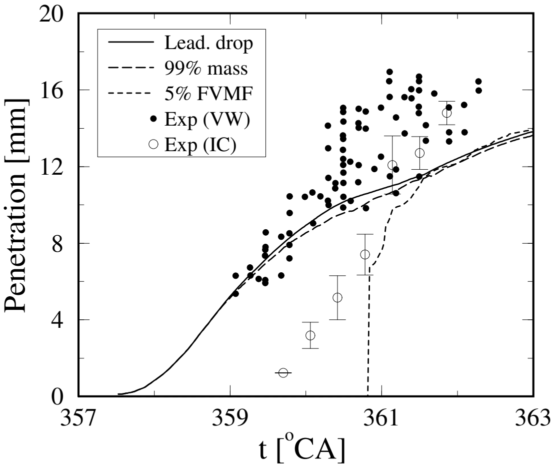

Figure 6.198: Penetration of spray No. 4 for EOP2.

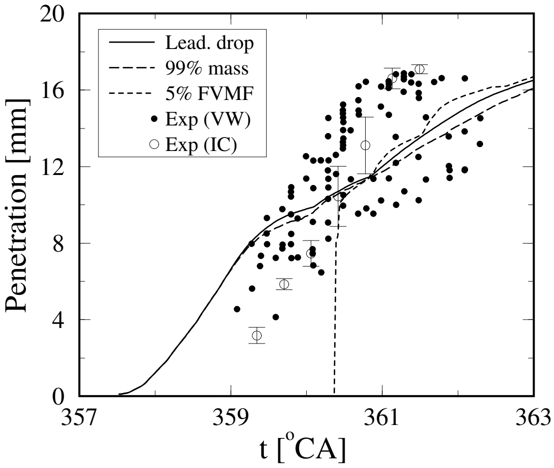

Figure 6.199: Penetration of spray No. 5 for EOP2.

five locations listed in Table 6.40 is shown in Fig. 6.200. As was also observed for EOP1a, the predictions show that the droplet velocities decrease along the axis of nozzle No. 4 (points A, B, C and D) due to the combined effects of drag and evaporation. In contrast, the measurements indicate that the droplet velocities are nearly uniform in space. Higher droplet velocities are indicated by both predictions and measurements at point E. This is consistent with the penetration curves, since higher penetration is obtained from spray No. 1 than from spray No. 4. Also, at point E the droplet velocities are overpredicted, whereas the opposite occurs at all other points along spray No. 4, at least until $364° \ CA$. These observations conform with

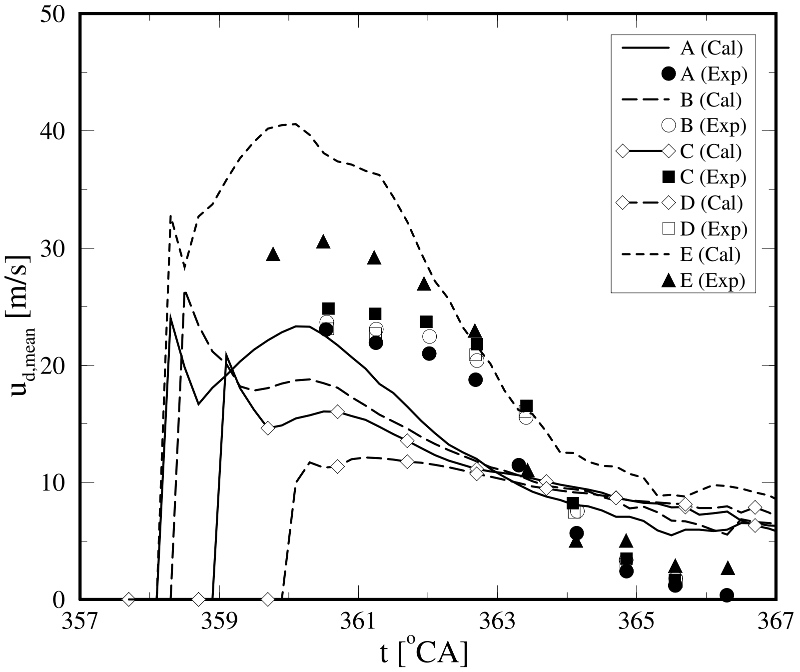

Figure 6.200: Droplet mean velocities at various locations for EOP2.

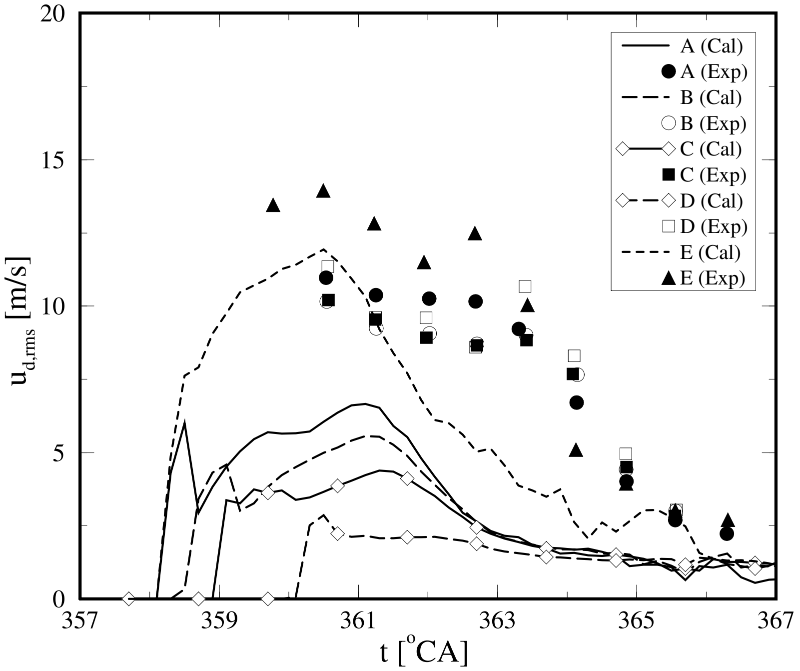

Figure 6.201: Droplet RMS velocities at various locations for EOP2.

the spray penetration behaviour, since a significant underprediction of penetration is observed in Fig. 6.198 for spray No. 4. Perhaps, the *ad hoc* adjustment of the fuel flow among the injector holes used here results in higher flow rate than the real one in hole No. 1, at the expense of the flow rates in the remaining holes. Of course, the high RMS levels of the droplet velocities, presented in Fig. 6.201, should be taken into account when comparisons are made between predictions and measurements.

6.6.7 Operating point EOP4a

Table 6.46 tabulates all the spray submodels employed for the simulation of the last operating point, EOP4a. Measurements of the spray semi-cone angles, required by the MPI atomisation model, have been reported by Hentschel and Schindler [128]. The fact that the MPI atomisation model produces fewer parcels than the Huh

Table 6.46: Spray submodels for EOP4a.

Spray process	Submodel/correlation
Cavitation	MPI
C_c	0.7
k_r [μm]	1
Atomisation	MPI
$\alpha_{exp,1}$ [°]	13.40
$\alpha_{exp,2}$ [°]	19.05
$\alpha_{exp,3}$ [°]	16.60
$\alpha_{exp,4}$ [°]	16.85
$\alpha_{exp,5}$ [°]	14.75
Drag coefficient	Patterson *et al.*, Eq. (3.72)
Evaporation	
Conductivity	Infinite
Nu and Sh	El Wakil *et al.*/Ranz-Marshall, Eqs. (3.86), (3.80), (3.137a)
Breakup	Hsiang-Faeth
Collision	O'Rourke

model, is exploited to set the values for the time step and the parcel introduction rate to the same as those adopted for the pressure chamber calculations. Thus, the time step is chosen to be $0.012^\circ\, CA$ and the parcel introduction rate, to be $20\,$parcels/μs per nozzle.

Results and discussion

The predictions for this operating point may be compared with the measurements until 363.1° CA since the ignition delay was found to be 10.9° CA [128]. The spray penetrations from nozzles Nos. 1–5 are plotted in Figs. 6.202–6.206, respectively. Here, the experimental data have been shifted by 1° CA (0.04 ms). Clearly better agreement between predictions and measurements is obtained in this case compared to the previous operating points.

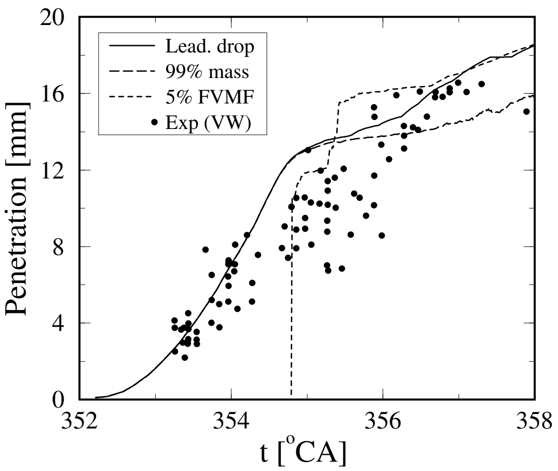

Figure 6.202: Penetration of spray No. 1 for EOP4a.

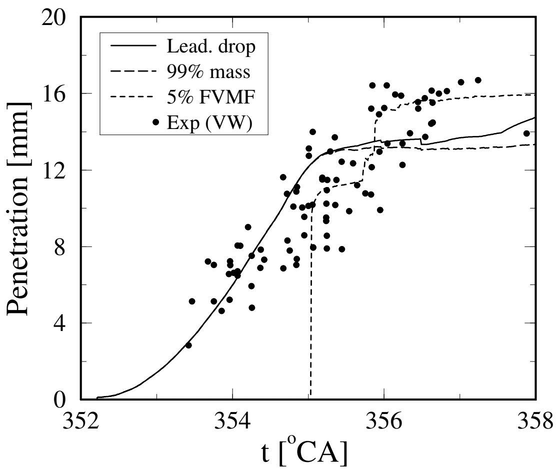

Figure 6.203: Penetration of spray No. 2 for EOP4a.

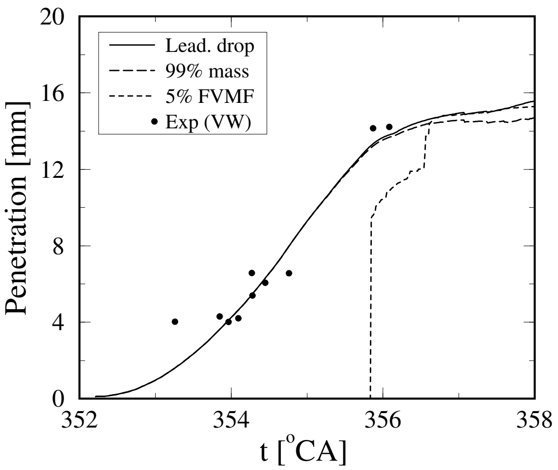

Figure 6.204: Penetration of spray No. 3 for EOP4a.

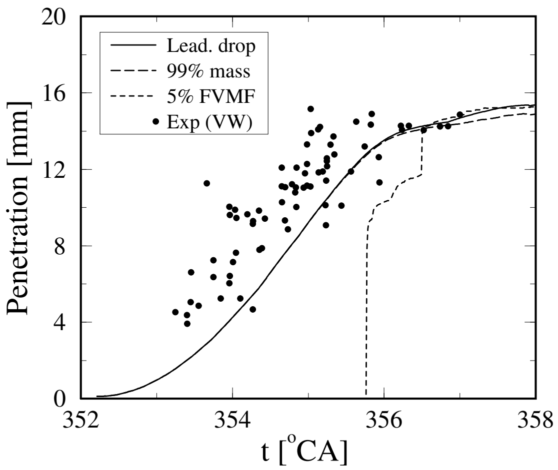

Figure 6.205: Penetration of spray No. 4 for EOP4a.

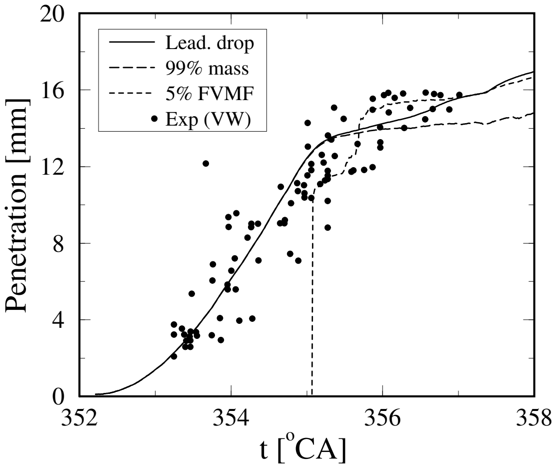

Figure 6.206: Penetration of spray No. 5 for EOP4a.

6.6.8 Summary

In the last test case of this study, data for a real DI Diesel engine with a five-hole injector have been used. Four operating points were examined and various combinations of spray submodels were employed for the simulation. Comparisons between predictions and measurements were made for the spray penetrations and droplet velocities measured at five locations.

In general, the penetrations and the droplet velocities were somewhat under-predicted. The disagreement between predictions and measurements was partly attributed to the performance of the atomisation model which perhaps produces excessively small droplets resulting in fast deceleration and partly to the fact that in reality, the initial liquid velocity is relatively high due to the threshold value of the opening pressure.

Another factor resulting in disagreement between predictions and measurements are experimental uncertainties. Some of them have been revealed in some cases by comparing the measurements obtained by two different groups of experimentalists and pointing out that they do not agree. Additional experimental uncertainties were observed in the local droplet velocities. In these, earlier droplet arrival at the farther point was apparently shown. The *loose* definition of the start of injection introduces additional ambiguities. All these uncertainties should be considered in the assessment of the predictions.

6.7 Closure

In this chapter, the mathematical framework for Diesel spray simulation presented in previous chapters has been assessed by comparison with experiment. This has been accomplished by performing sensitivity studies for four different test cases for which measurements were available.

The first test case, presented in Section 6.3, was exploited to investigate the modelling of the evaporation process. Single droplets of mono- and bi-component fuel evaporating in atmospheric air streams of velocity up to $2.01\,m/s$ and temperature up to $449\,K$ were considered. Three sets of widely-employed Nusselt and Sherwood correlations were examined. The Ranz and Marshall correlations corrected by the factor of El Wakil *et al.* for the blowing effect were found to give the best agreement with the experimental data for the temporal variation of droplet size.

The droplet effective conductivity treatment was found not to appreciably influence the results, despite the fact that Pe was relatively large. This was due to the fact that the droplet surface quickly reaches the wet bulb temperature, for both finite and effective conductivity treatments; and after this, the conductivity has little influence on the evaporation process. In contrast, the infinite conductivity treatment was found to produce lower evaporation rates than those of the finite and effective ones, due to the lower temperature it produces for the droplet surface.

Although the predictions for n-heptane were in a very good agreement with the measurements, those for n-decane showed an underprediction of the evaporation rate. This was also observed for the bi-component fuel, when n-decane was the main component. However, it was found that the predictions are consistent with the existing theory and consequently, it is concluded that experimental errors and uncertainties may be responsible for at least part of the discrepancy.

Finally, this test case allowed the assessment of the profile method of solution for the internal temperature and concentration distributions. Satisfactory results were obtained for both the conduction and diffusion equations. Solution of the latter for bi-component fuels produced the two distinguishable slopes of the evaporation rate history, the gap between which decreases with the gas temperature, in accord with the experimental observations.

Section 6.4 presented the atmospheric spray calculations. Experimental results for four different operating points were available. These were utilised to investigate the effects of atomisation, drag coefficient correlation, breakup and collision. Also, sensitivity studies for the mesh, the time step and the parcel introduction rate were performed.

It was found that the axial grid density has a minor effect on the results, whereas these are appreciably influenced by the radial cell size, since the void fraction variation is not adequately resolved. Thus, the smaller the cell, the larger the penetration, the SMD and the droplet velocities, because higher gas velocities are induced. The time step and the parcel introduction rate were found to have minor effects on most features of spray calculations when they are smaller than $4\,\mu s$ and larger than $2\,\text{parcels}/\mu s$, respectively. However, the latter is not enough as far as the local droplet RMS velocities are concerned, since it results in underestimation due to inadequate sampling.

Satisfactory spray penetration and SMD predictions were obtained from the Huh atomisation model which, however, produces underprediction of the droplet velocities, even when the effective injection velocity is deduced using the MPI nozzle flow model, which allows for cavitation. The error in local droplet velocities was reduced, but not eliminated when the MPI atomisation model was used, due to the larger SMD it produces. The fact that the droplet velocities were still underpredicted is probably due to experimental uncertainties. The latter was also responsible for the necessity to shift in time the experimental data, in order to get a plausible spray penetration behaviour. The main difference between the two atomisation models was the temporal variation of the SMD. In particular, it was observed that the SMD produced from the Huh model rapidly decreases to a value which is gradually approached when the MPI model is employed. Best agreement with the experimental data for local SMD was obtained from the Huh model.

In this test case, the spray was also found to be rather insensitive to the choice of drag coefficient correlation.

The breakup process was found to reduce the spray penetration due to the smaller SMD it produces. Three different breakup models were tested and were found to result in the same penetration, although they produce about 20 % different SMD. In particular, the Hsiang-Faeth model was found to give the largest SMD and the Reitz-Diwakar model the smallest one.

Under the atmospheric conditions prevailing here, the main output of collision was found to be coalescence, resulting in higher SMD and lower penetration due to momentum conservation. Coalescence improved the agreement between the predictions and measurements.

In the third case, a constant-volume pressure chamber simulated Diesel engine conditions, as presented in Section 6.5. Here, experimental data for the liquid and vapour penetrations and local fuel vapour concentration were available for three operating points. This test case enabled the investigation of the effect of the internal droplet conductivity treatment. Two atomisation models and two droplet drag coefficient correlations were also examined. Sensitivity studies for the mesh, the time step and the parcel introduction rate were performed for this test case as well.

In accord with the observations for the atmospheric spray, the radial cell size was found to significantly affect the results. However, it was also found that this effect decreases with decreasing cell size, although a truly grid-independent result cannot be obtained, since a limit is set by the lowest allowable void fraction (here, successful calculations were performed with ϑ as low as 20 %) and the largest droplet diameter (200 μm). Minor effects of the time step and the parcel introduction rate were obtained for values smaller than 2 μs and larger than 10 parcels/μs, respectively.

The spray characteristics were found to be rather insensitive to the conductivity treatment, probably because of the wide droplet size distribution and high evaporation rates. This is in accord with the findings of Hohmann *et al.* [137].

In contrast to the observation in the atmospheric spray cases, the drag coefficient correlation does affect the spray penetration; however, not dramatically. In particular, the higher drag coefficient leads to higher penetration, due to the lower relative velocity between the droplets and the gas, leading to lower evaporation and breakup rates.

The two atomisation models resulted in similar predictions, whereas in the atmospheric spray calculations, the MPI model was found to gradually reach the SMD value produced by the Huh model.

All submodel combinations overpredicted the liquid and vapour penetrations. The former was attributed in part to the fact that the spray tip is probably too dilute to be detected by the measuring technique. Overprediction was also observed for the local fuel vapour concentration. This was mainly attributed to the fact that the predictions result in an excessively narrow spray. Significantly improved agreement between the predictions and measurements was obtained when the turbulent Schmidt number was reduced from 1 to 0.5, which is appropriate for turbulent jets [142, 179].

The last test case concerned a real Diesel engine. As presented in Section 6.6, data for the Volkswagen four-cylinder DI 1.9 l transparent engine were used. Measurements for four operating points were available and various combinations of spray submodels were employed.

It was found that generally, the spray penetration and the local droplet velocities were slightly underpredicted. However, in this case it is difficult to pinpoint weaknesses of the modelling, due to large experimental uncertainties. These comprise the *loose* definition of the start of injection, which resulted in implausibly-large droplet velocities deduced from the penetration. Also, the measurements of the local droplet velocities apparently showed earlier droplet arrival at locations which are farther from the nozzle. Furthermore, in some cases, substantial disagreement was observed between the spray penetrations measured by two different experimental groups.

The following, final, chapter will summarise the main findings and conclusions of this work and give suggestions for future research.

Chapter 7

Closure

7.1 Introduction

The current chapter summarises, in the following section, the main achievements and conclusions drawn from this research. Also, based on the experience acquired, some suggestions for future research will be given in Section 7.3.

7.2 Conclusions

The results of the present study have been extensively discussed in detail in earlier chapters. Here, only the main findings are presented, as follows:

- The robustness of the spray simulation methodology has been extended and improvements in stability and accuracy have been achieved. These have been accomplished by the careful rederivation of the conservation equations of multiphase flows and by some local restructuring of the overall solution algorithm. The former revealed that an additional term, representing the interphase pressure work, must be added to the energy equation of the gas, while the latter included the introduction of underrelaxation factors in the spray-related source term calculations. The restructuring also comprised consistent calculation of the pressure work term in the predictor stage based on the value of the previous time step. These enable successful calculations of high-load cases and cases with relatively large time steps ($Co > 1$) which result in extremely low void fractions.

- An efficient, in terms of computational time and storage requirements, profile method has been developed and successfully employed for solving the one-dimensional conduction and diffusion equations within the droplet. These developments improve the simulation of the evaporation process and enable it to be applied to multicomponent fuels.

- The grid spacing, especially in the radial direction, influences the spray predictions. The grid effect decreases with refinement: however, a truly mesh-independent result cannot be obtained, since the void fraction sets a lower limit to the cell size, for both physical and numerical reasons. In this study, successful calculations have been performed with void fractions as low as 20 %.

  It was found that the smaller the cell size, the higher the penetration, the local droplet velocities and the SMD. This is because the exchanges of mass, momentum and energy between a droplet and the surrounding gas have larger influences for a small cell, because it contains less gas. Therefore, larger induced velocity, higher vapour concentration and lower temperature (due to the relatively cold droplet) are obtained. These reduce both the breakup and the evaporation rates, leading to larger droplets with higher momentum.

- The effect of the time-step size on the spray results is negligible for values smaller than $2\,\mu s$. This corresponds to a maximum Courant number of about 0.8.

- Statistically representative results for atmospheric sprays are obtained for parcel introduction rates greater than $2\,\text{parcels}/\mu s$. However, higher rates, up to $10\,\text{parcels}/\mu s$, are required for calculations under Diesel engine conditions, due to evaporation, which reduces the droplet population. Even larger parcel introduction rates are required for the calculation of the local droplet RMS velocities.

- It has been confirmed that in sprays (where the jet is turbulent), the turbulent Schmidt number should be lower than 1. In particular, a value of 0.5 has been found to be more appropriate, in conformity with earlier studies of gas jets.

- Three different droplet conductivity treatments have been considered, namely infinite, finite and effective. The first one is valid for low Biot numbers ($Bi < 0.1$), while the last one takes into approximate account droplet internal circulation induced by the gas flow field. In single droplet calculations, the infinite conductivity treatment results in the lowest evaporation rate, since it leads to the lowest temperature on the droplet surface. However, in spray calculations, the conductivity treatment was found not to significantly influence the spray characteristics. This finding is in accord with that of Hohmann *et al.* [137].

- Three sets of Nusselt and Sherwood correlations have been employed. The best agreement with the experimental results for single droplets is obtained with the correlations of Ranz and Marshall [237, 238] in conjunction with the correction factor of El Wakil *et al.* [85] for the blowing effect. These correlations overpredict the evaporation rate when the blowing effect is considered according to the suggestion of Abramzon and Sirignano [1]. Significant underprediction of the evaporation rate is obtained from the correlations of Renksizbulut and Yuen [248].

- Little difference in the predicted spray penetrations is observed with the two atomisation models used in this study. However, the Huh atomisation model gives better agreement with measurements than the MPI for the SMD but worse for the local droplet velocities. In particular, smaller SMD and droplet velocities are predicted by the Huh model, as was found in the atmospheric spray calculations. However, similar SMD values are produced by the two models under Diesel-engine-like conditions.

The breakup rate of the primary droplets in the Huh atomisation model little affects the SMD and its effect on penetration and droplet velocities is negligible.

Increasing the initial semi-cone angle, needed as input by the MPI model, causes the penetration to decrease because the spray-related source terms are distributed over a wider region and therefore, the induced gas velocity is smaller.

- It is confirmed that the breakup process results in smaller SMD and hence, penetration. However, all the breakup models considered here produce spray penetrations very close to each other. The local droplet velocities are also rather insensitive to the breakup model. In respect of the SMD, the Reitz-Diwakar model produces the smallest droplets and the Hsiang-Faeth the largest, with differences of about 20 %.

- The drag coefficient has only minor effect on the spray characteristics under atmospheric conditions, because the momentum loss due to the higher drag coefficient is balanced by the gain due to the lower breakup rate. This observation is in accord with that of Liu *et al.* [190]. However, in Diesel engine conditions, the distorted droplet model of Patterson *et al.* [230] results in higher vapour penetration due to the lower evaporation rate which results in larger droplets with higher momentum.

- It was found that under atmospheric conditions, the main output of the collision model is coalescence. This phenomenon increases the SMD and lowers the penetration. It was also observed that the inclusion of this model improves the agreement between the predictions and measurements for the spray penetration and local droplet velocities and SMD.

- The extensive validation has revealed some experimental uncertainties that should be borne in mind in the assessment of the modelling. In particular, it was found that the start of injection is often loosely defined, leading to inconsistency between the spray penetration and the injection velocity data. In this study, a time-shifting of the experimental data was frequently necessary in order to obtain plausible results. Apparent inconsistencies were also observed in in-cylinder droplet velocity measurements. Finally, substantial disagreements were observed between the spray penetrations obtained in the Volkswagen DI Diesel engine by two different research groups. These could have been due to a number of causes about which it is pointless to speculate: however, they emphasise the difficulties of relying on such data for model assessment.

7.3 Suggestions for future research

The present study has revealed that there is still room for improvement in the CFD simulation of the spray processes in Diesel engines. However, it is also of vital importance to emphasise that the assessment and improvement of the modelling requires the availability of carefully-obtained experimental data. Also, experiments with single-component fuels, whose properties are well known, will further reduce the uncertainties. Some inconsistencies between experimental and computational definitions encountered in this study can only be resolved when a close collaboration between experimentalists and computationalists is established.

It is not the object of this work to give detailed suggestions to the experimentalists, since the author is far from being an expert in experimental methods. Thus, the following list of tasks, in author's view regarded to be of the highest priority, is mainly directed towards researchers in the field of numerical simulation.

- Extensive validation studies of the present spray model with various combinations of its individual submodels against comprehensive experimental data for wide ranges of operating conditions. The usage of data for single-component fuel with known properties is recommended.

- A fine mesh is desirable in the spray region and regions with large spatial gradients of the field variables. Adaptive mesh refinement would increase the spatial resolution in these particular regions without introducing additional overheads due to needlessly fine mesh in regions of lesser importance.

- One of the achievements in the present study is the ability to successfully calculate dense sprays using relatively fine meshes. However, this implies that the droplet size is of the same order of the cell size and hence, a droplet may occupy more than one cell. Ideally, the source terms for mass, momentum and energy due to this particular droplet should be distributed to all cells in which it resides, rather than to be given to the cell in which the droplet centre is located.

- In dense spray calculations the current methodology may cause the void fraction to become extremely small or even negative, since in the usual Lagrangian formulation, each droplet does not 'recognise' the proximity of other droplets. A model, perhaps based on the local void fraction, could be derived to handle this undesirable situation by displacing droplets to neighbouring cells.

- More accurate modelling of the fuel flow in the injector, from the sac volume to the nozzle exit, also comprising the cavitation process, will reduce the uncertainties concerning the injection velocities. These are important since they determine the initial conditions which affect the results further downstream.

- For a better mathematical description of the in-cylinder processes in Diesel engines, where the pressure may be higher than 100 bar, a real gas state equation should be employed, accounting for compressibility effects, as was suggested by Hohmann *et al.* [137]. This should also be considered in the evaporation model for the calculation of the phase equilibrium, since the fugacity coefficient is smaller than unity.

- Small high-speed DI Diesel engines have recently become very attractive for automotive applications, especially for urban driving, owing to their lower fuel consumption compared to their IDI counterparts. In these engines, the fuel is likely to impinge the wall and therefore, the modelling of film formation there is important, since it controls the droplet size distribution and vapour formation near the wall, as was found by Bai and Gosman [30], Stanton and Rutland [273], Guerrassi and Champoussin [115] among others.

7.4 Closure

This study was concentrated with the improvement, extension and validation of the spray modelling in an existing engine simulation computer code, called SPEED. The work presented in this thesis was being developed in parallel with similar efforts for modelling of Diesel ignition and combustion as well as of premixed combustion, knock and emission processes; hence, SPEED code represents the current state of the art of engine simulation. Thus, this thesis should be regarded as a step towards perfection of CFD tools for engine designers.

It is the author's hope that this work has accelerated the pace towards a comprehensive understanding of the relevant physical phenomena, eventually leading to engines with higher performance, better fuel exploitation and lower emissions. The author also hopes that future researchers will benefit from his work to improve the CFD methodology and modelling and hence develop an even better computational tool than SPEED.

Appendix A

A.1 Relations between average quantities

The instantaneous value of a property ϕ and the macroscopic density ρ can be decomposed as:

$$\phi = \overline{\phi} + \phi' \ , \tag{A.1}$$

$$\rho = \overline{\rho} + \rho' \ . \tag{A.2}$$

Multiplying Eq. (A.1) by Eq. (A.2) and applying the ensemble average technique, the following relation is obtained:

$$\overline{\rho\phi} = \overline{\rho}\,\overline{\phi} + \overline{\rho'\phi'} \ . \tag{A.3}$$

According to the density-weighted average technique, the instantaneous value of ϕ can be decomposed as:

$$\phi = \widetilde{\phi} + \phi'' \ , \tag{A.4}$$

where

$$\widetilde{\phi} = \frac{\overline{\rho\phi}}{\overline{\rho}} \ . \tag{A.5}$$

Substitution of Eq. (A.3) into Eq. (A.5), provides:

$$\widetilde{\phi} = \overline{\phi} + \frac{\overline{\rho'\phi'}}{\overline{\rho}} \ . \tag{A.6}$$

Substituting $\widetilde{\phi}$ from Eq. (A.6) into Eq. (A.4), the instantaneous value of ϕ can be expressed by:

$$\phi = \overline{\phi} + \frac{\overline{\rho'\phi'}}{\overline{\rho}} + \phi'' \ . \tag{A.7}$$

By applying the ensemble average technique to the above equation, the following relation is obtained:

$$\overline{\phi''} = -\frac{\overline{\rho'\phi'}}{\overline{\rho}} \ . \tag{A.8}$$

Multiplying Eq. (A.7) by ρ and applying the ensemble averaging, the following expression is obtained:

$$\overline{\rho\phi} = \overline{\rho}\overline{\phi} + \overline{\rho'\phi'} + \overline{\rho\phi''} \ . \tag{A.9}$$

Substitution of Eq. (A.3) into the above expression yields:

$$\overline{\rho\phi''} = 0 \ . \tag{A.10}$$

Multiplying Eq. (A.4) by ρ and ensemble-averaging, the following relation is derived:

$$\overline{\rho\phi} = \overline{\rho}\tilde{\phi} + \overline{\rho}\overline{\phi''} + \overline{\rho'\phi''} \ . \tag{A.11}$$

Substitution of Eq. (A.5) into the above equation yields:

$$\overline{\rho}\overline{\phi''} = -\overline{\rho'\phi''} \ . \tag{A.12}$$

The combination of the above equation and Eq. (A.8) yields:

$$\overline{\rho'\phi''} = \overline{\rho'\phi'} \ . \tag{A.13}$$

The density-weighted average of the ensemble average of ϕ is expressed by:

$$\tilde{\overline{\phi}} = \frac{\overline{\rho\overline{\phi}}}{\overline{\rho}} = \overline{\phi} \ . \tag{A.14}$$

Similarly, the ensemble average of the density-weighted average of ϕ is given by:

$$\overline{\tilde{\phi}} = \overline{\left(\frac{\overline{\rho\phi}}{\overline{\rho}}\right)} = \frac{\overline{\rho\phi}}{\overline{\rho}} = \frac{\overline{\rho}\tilde{\phi}}{\overline{\rho}} = \tilde{\phi} \ . \tag{A.15}$$

Appendix B

B.1 Analytical solution of the conduction equation

After the introduction of $d\zeta/d\tau = 0$ in Eq. (3.102), the corresponding particular solutions are Bessel functions of the first kind of order 1/2, $J_{1/2}$ and $J_{-1/2}$, [26]. In order to reduce the spherical Laplacian to the Cartesian Laplacian whose solution is expressible in terms of circular functions [26], the transformation

$$\Theta(\omega,\, \tau) = \frac{\Psi(\omega,\, \tau)}{\omega} \tag{B.1}$$

is introduced. Then, Eq. (3.102), becomes into:

$$\frac{1}{\zeta^2(\tau)} \frac{\partial^2 \Psi(\omega,\, \tau)}{\partial \omega^2} = \frac{\partial \Psi(\omega,\, \tau)}{\partial \tau} \; . \tag{B.2}$$

Also, the initial and boundary conditions read:

$$\Psi(\omega,\, 0) = \omega \; , \tag{B.3a}$$

$$\Psi(0,\, \tau) = 0 \; , \tag{B.3b}$$

$$\frac{\partial \Psi(1,\, \tau)}{\partial \omega} + (Bi - 1)\, \Psi(1,\, \tau) = \mathcal{Q} \; . \tag{B.3c}$$

The method of separation of variables [268] is used to solve Eq. (B.2). Thus, it is assumed that the solution can be expressed as the product of two functions, each of which depends on only one of the independent variables ω and τ:

$$\Psi(\omega,\, \tau) = \mathcal{A}(\omega) \cdot \mathcal{B}(\tau) \; . \tag{B.4}$$

Substituting this solution in Eq. (B.2) and dividing both sides by the product $\mathcal{A}(\omega)\cdot\mathcal{B}(\tau)$ yield:

$$\frac{1}{\zeta^2}\frac{1}{\mathcal{A}(\omega)}\frac{d^2\mathcal{A}(\omega)}{d\omega^2} = \frac{1}{\mathcal{B}(\tau)}\frac{d\mathcal{B}(\tau)}{d\tau}\ . \tag{B.5}$$

The problem can now be resolved into two problems. The first one is described by the second-order ordinary differential equation:

$$\frac{d^2\mathcal{A}(\omega)}{d\omega^2} + \lambda^2\mathcal{A}(\omega) = 0\ , \tag{B.6}$$

with boundary conditions given by:

$$\mathcal{A}(0) = 0\ , \tag{B.7a}$$

$$\frac{d\mathcal{A}(1)}{d\omega} + (Bi - 1)\,\mathcal{A}(1) = \frac{\mathcal{Q}}{\mathcal{B}(\tau)}\ . \tag{B.7b}$$

The second problem is expressed by the first-order ordinary differential equation:

$$\frac{d\mathcal{B}(\tau)}{d\tau} + \frac{\lambda^2}{\zeta^2}\mathcal{B}(\tau) = 0\ . \tag{B.8}$$

At this point it is appropriate to note that for an evaporating droplet, the boundary condition (B.7b) is not homogeneous, since the function $\mathcal{B}(\tau)$ appears. In contrast, for a non-evaporating droplet, the term which contains this function is absent. A special treatment is introduced here to eliminate $\mathcal{B}(\tau)$ from Eq. (B.7b). Taking into account Eqs. (B.1) and (B.4), it can be expressed as:

$$\mathcal{B}(\tau) = \frac{\omega\Theta}{\mathcal{A}(\omega)}\ . \tag{B.9}$$

Substitution of this into Eq. (B.7b) yields:

$$\frac{d\mathcal{A}(1)}{d\omega} + (Bi - 1)\,\mathcal{A}(1) = \mathcal{Q}\frac{T_{d,0} - T}{T_d(1,\,\tau) - T}\mathcal{A}(1)\ . \tag{B.10}$$

However, the surface temperature $T_d(1,\,\tau)$ is not known at this stage and an iterative procedure must be used to calculate the correct temperature. From experience, one iteration is enough to keep the error below 0.05 %.

The solution of Eq. (B.6), is given by:

$$\mathcal{A}(\omega) = C_n\sin\left(\lambda_n\omega\right)\ , \tag{B.11}$$

where $\sin(\lambda_n \omega)$ is the characteristic function. The characteristic value λ_n must be such as the boundary condition, Eq. (B.10), is satisfied. By substituting Eq. (B.11) into Eq. (B.10), the following equation is obtained:

$$\tan \lambda_n + \frac{\lambda_n}{Bi - 1 - \mathcal{Q}\dfrac{T_{d,0} - T}{T_d(1,\, \tau) - T}} = 0 \ . \tag{B.12}$$

The solution of Eq. (B.8), is given by:

$$\mathcal{B}(\tau) = C_n e^{-\lambda_n^2 \tau/\zeta^2} \ . \tag{B.13}$$

The product solution can be expressed in a Fourier series:

$$\Psi(\omega,\, \tau) = \sum_{n=1}^{\infty} \alpha_n e^{-\lambda_n^2 \tau/\zeta^2} \sin\left(\lambda_n \omega\right) \ , \tag{B.14}$$

where the coefficients α_n are determined by:

$$\alpha_n = \frac{\displaystyle\int_0^1 \Psi(\omega,\, 0) \sin\left(\lambda_n \omega\right) d\omega}{\displaystyle\int_0^1 \sin^2\left(\lambda_n \omega\right) d\omega} \tag{B.15a}$$

$$= \frac{2\left(\sin \lambda_n - \lambda_n \cos \lambda_n\right)}{\lambda_n\left(\lambda_n - \sin \lambda_n \cos \lambda_n\right)} \ . \tag{B.15b}$$

Thus, the dimensionless temperature field within the droplet is expressed by:

$$\Theta(\omega,\, \tau) = \sum_{n=1}^{\infty} \frac{2\left(\sin \lambda_n - \lambda_n \cos \lambda_n\right)}{\lambda_n\left(\lambda_n - \sin \lambda_n \cos \lambda_n\right)} e^{-\lambda_n^2 \tau/\zeta^2} \frac{\sin\left(\lambda_n \omega\right)}{\omega} \ . \tag{B.16}$$

It is noted that the above solution does not represent the general case because it is based on the assumption that the initial temperature field is uniform. This may be true only at the time that the droplet enters the chamber. However, afterwards, the initial temperature for each calculation in a time step $\delta\tau$ is given from the solution of the previous time step $\delta\tau^o$. Thus, the new $\Psi(\omega,\, 0)$ reads:

$$\Psi(\omega,\, 0) = \Theta_1 \sum_{m=1}^{\infty} \alpha_m e^{-\lambda_m^2 \xi^2 \delta\tau^o/\zeta^2} \frac{\sin\left(\lambda_m \omega \xi\right)}{\xi} + \omega\Theta_2 \ , \tag{B.17}$$

where the subscript 'm' denotes the values of the previous time step, $\delta\tau^o$. Also, the variable $\xi = R_d/R_d^o$ is introduced to allow for the droplet surface regression.

In addition, the change of the gas temperature is considered via Θ_1 and Θ_2, given respectively, by:

$$\Theta_1 = \frac{T_{d,0} - T^o}{T_{d,0} - T} , \tag{B.18a}$$

$$\Theta_2 = \frac{T^o - T}{T_{d,0} - T} . \tag{B.18b}$$

In all the above, the subscript 'o' denotes conditions of the previous time step. Note that if the gas temperature is constant, Θ_1 and Θ_2 are 1 and 0, respectively.

Now, by substituting Eq. (B.17) into Eq. (B.15a), the new coefficients of the series are obtained:

$$\begin{aligned} \alpha_n =& \frac{\lambda_n \Theta_1 \sum_{m=1}^{\infty} \left[\frac{\sin(\lambda_m \xi - \lambda_n)}{\lambda_m \xi - \lambda_n} - \frac{\sin(\lambda_m \xi + \lambda_n)}{\lambda_m \xi + \lambda_n} \right] \alpha_m e^{-\lambda_m^2 \xi^2 \delta\tau^o / \zeta^2}}{\xi \left(\lambda_n - \sin\lambda_n \cos\lambda_n \right)} \\ &+ \frac{2\Theta_2 \left(\sin\lambda_n - \lambda_n \cos\lambda_n \right)}{\lambda_n \left(\lambda_n - \sin\lambda_n \cos\lambda_n \right)} . \end{aligned} \tag{B.19}$$

Hence, the new dimensionless temperature field reads:

$$\begin{aligned} \Theta(\omega,\, \tau) = \sum_{n=1}^{\infty} \Bigg\{ & \frac{\lambda_n \Theta_1 \sum_{m=1}^{\infty} \left[\frac{\sin(\lambda_m \xi - \lambda_n)}{\lambda_m \xi - \lambda_n} - \frac{\sin(\lambda_m \xi + \lambda_n)}{\lambda_m \xi + \lambda_n} \right] \alpha_m e^{-\lambda_m^2 \xi^2 \delta\tau^o / \zeta^2}}{\xi \left(\lambda_n - \sin\lambda_n \cos\lambda_n \right)} \\ & + \frac{2\Theta_2 \left(\sin\lambda_n - \lambda_n \cos\lambda_n \right)}{\lambda_n \left(\lambda_n - \sin\lambda_n \cos\lambda_n \right)} \Bigg\} e^{-\lambda_n^2 \tau / \zeta^2} \frac{\sin(\lambda_n \omega)}{\omega} . \end{aligned} \tag{B.20}$$

Note that in the above temperature distribution, all the variables including the dimensionless Θ, ω and ζ are updated at the end of the previous time step $\delta\tau^o$. The latter indicates also, $\tau = 0$.

Appendix C

C.1 The normal diffusion

Applying Eq. (4.3) to the diffusion flux vector, its value at the face f between two neighbouring cells P and N is obtained:

$$\begin{aligned}
\left(\rho\Gamma_{\phi,\mathit{eff}}\nabla\phi\right)_f &= \lambda_f^P \left(\rho\Gamma_{\phi,\mathit{eff}}\nabla\phi\right)_P + \left(1-\lambda_f^P\right)\left(\rho\Gamma_{\phi,\mathit{eff}}\nabla\phi\right)_N && \text{(C.1a)}\\
&\approx \lambda_f^P \left(\rho\Gamma_{\phi,\mathit{eff}}\right)_P \left(\nabla\phi\right)_P + \left(1-\lambda_f^P\right)\left(\rho\Gamma_{\phi,\mathit{eff}}\right)_N \left(\nabla\phi\right)_N \ . && \text{(C.1b)}
\end{aligned}$$

Substituting $\nabla\phi$ from Eq. (4.5a), the above approximation becomes:

$$\begin{aligned}
\left(\rho\Gamma_{\phi,\mathit{eff}}\nabla\phi\right)_f \approx{}& \lambda_f^P \left(\frac{\rho\Gamma_{\phi,\mathit{eff}}}{V}\right)_P \sum_{\{l\}_P} \mathcal{S}_l^P \left[\lambda_l^P\phi_P + \left(1-\lambda_l^P\right)\phi_N\right]\\
&+ \left(1-\lambda_f^P\right)\left(\frac{\rho\Gamma_{\phi,\mathit{eff}}}{V}\right)_N \sum_{\{l\}_N} \mathcal{S}_l^N \left[\lambda_l^N\phi_N + \left(1-\lambda_l^N\right)\phi_{NN}\right] \ . \qquad \text{(C.2)}
\end{aligned}$$

According to Eq. (4.17), the diffusion flux vector is resolved into the normal and cross diffusion components, where the former comprises only the contributions to the diffusive flux across the faces $+f$ and $-f$. Therefore, from Eq. (C.2) it follows that:

$$\begin{aligned}
\mathbf{d}_f^n(\phi) \approx{}& \lambda_f^P \left(\frac{\rho\Gamma_{\phi,\mathit{eff}}}{V}\right)_P\\
&\left\{\mathcal{S}_f^P\left[\lambda_f^P\phi_P + \left(1-\lambda_f^P\right)\phi_{N(f)}\right] + \mathcal{S}_{-f}^P\left[\lambda_{-f}^P\phi_P + \left(1-\lambda_{-f}^P\right)\phi_{N(-f)}\right]\right\}\\
&+ \left(1-\lambda_f^P\right)\left(\frac{\rho\Gamma_{\phi,\mathit{eff}}}{V}\right)_N
\end{aligned}$$

$$\left\{\mathcal{S}_f^N\left[\lambda_f^N\phi_{N(f)}+\left(1-\lambda_f^N\right)\phi_{NN(f)}\right]\right.$$
$$\left.+\,\mathcal{S}_{-f}^N\left[\lambda_{-f}^N\phi_{N(f)}+\left(1-\lambda_{-f}^N\right)\phi_{NN(-f)}\right]\right\}\ . \tag{C.3}$$

In order to eliminate $\phi_{N(-f)}$ and $\phi_{NN(f)}$, a linear variation of ϕ over cells is assumed. Therefore,

$$\left(1-\lambda_{-f}^P\right)\left(\phi_{N(-f)}-\phi_P\right)=-\left(1-\lambda_f^P\right)\left(\phi_{N(f)}-\phi_P\right)\ , \tag{C.4a}$$
$$\left(1-\lambda_f^N\right)\left(\phi_{NN(f)}-\phi_{N(f)}\right)=-\left(1-\lambda_{-f}^N\right)\left(\phi_{NN(-f)}-\phi_{N(f)}\right)\ . \tag{C.4b}$$

Substituting the above expressions in Eq. (C.3) and taking also into account the equivalencies:

$$\phi_{NN(-f)}\equiv\phi_P\ , \tag{C.5a}$$
$$\mathcal{S}_{-f}^N\equiv-\mathcal{S}_f^P\ , \tag{C.5b}$$
$$1-\lambda_{-f}^N\equiv\lambda_f^P\ , \tag{C.5c}$$

the following expression is generated:

$$\begin{aligned}\mathbf{d}_f^n(\phi)\approx\lambda_f^P&\left(\frac{\rho\Gamma_{\phi,\mathit{eff}}}{V}\right)_P\\&\left\{\mathcal{S}_f^P\left[\lambda_f^P\phi_P+\left(1-\lambda_f^P\right)\phi_{N(f)}\right]+\mathcal{S}_{-f}^P\left[\phi_P-\left(1-\lambda_f^P\right)\left(\phi_{N(f)}-\phi_P\right)\right]\right\}\\&+\left(1-\lambda_f^P\right)\left(\frac{\rho\Gamma_{\phi,\mathit{eff}}}{V}\right)_N\\&\left\{\mathcal{S}_f^N\left[\phi_{N(f)}+\lambda_f^P\left(\phi_{N(f)}-\phi_P\right)\right]-\mathcal{S}_f^P\left[\left(1-\lambda_f^P\right)\phi_{N(f)}+\lambda_f^P\phi_P\right]\right\}\ .\end{aligned} \tag{C.6}$$

For the sake of factorisation, the following approximations are assumed:

$$\mathcal{S}_{-f}^P\phi_P\approx-\mathcal{S}_f^P\phi_P\ , \tag{C.7a}$$
$$\mathcal{S}_f^N\phi_{N(f)}\approx\mathcal{S}_f^P\phi_{N(f)}\ . \tag{C.7b}$$

Hence, Eq. (C.6) becomes:

$$\begin{aligned}\mathbf{d}_f^n(\phi)\approx\lambda_f^P&\left(1-\lambda_f^P\right)\left(\phi_{N(f)}-\phi_P\right)\\&\left\{\left(\mathcal{S}_f^P-\mathcal{S}_{-f}^P\right)\left(\frac{\rho\Gamma_{\phi,\mathit{eff}}}{V}\right)_P+\left(\mathcal{S}_f^P+\mathcal{S}_f^N\right)\left(\frac{\rho\Gamma_{\phi,\mathit{eff}}}{V}\right)_N\right\}\ .\end{aligned} \tag{C.8}$$

Appendix D

D.1 The pressure equation

The pressure equation is generated from the combination of the continuity and momentum equations.

The velocity in a cell P can be extracted from the discretised momentum equation, Eq. (4.38), as:

$$\mathbf{u}_P = \mathcal{H}_P - \frac{1}{\mathcal{A}_P^{\mathbf{u}}} \left(\vartheta V \mathcal{N} p\right)_P \ , \tag{D.1a}$$

where

$$\mathcal{H}_P = \frac{1}{\mathcal{A}_P^{\mathbf{u}}} \left[\sum_N \mathcal{A}_N^{\mathbf{u}} \mathbf{u}_N + \mathbf{b}_P^{\mathbf{u}} + \left(\mathbf{S}_{\mathcal{U}}^{\mathbf{u},d}\right)_P \right] \ . \tag{D.1b}$$

If the usual spatial interpolation for the velocity at the cell face is applied for the evaluation of the convective fluxes, Eq. (4.16), in the discretised continuity equation, Eq. (4.34), possible oscillations can arise (Patankar [228]). Theodoropoulos [288] applied to an unstructured non-orthogonal mesh, the remedy of Rhie and Chow [252] who proposed the convective fluxes to be calculated from the following formula:

$$\sum_{\{f\}_P} \mathcal{C}_f = \sum_{\{f\}_P} \mathcal{S}_f \cdot \rho_f \left(\mathcal{H} - \mathbf{u}_b\right)_f - \sum_{\{f\}_P} \mathcal{S}_f \cdot \left(\frac{1}{\mathcal{A}_P^{\mathbf{u}}} \rho \vartheta V \mathcal{N} p \right)_f \ . \tag{D.2}$$

Substitution of the above equation into the continuity equation, Eq. (4.34), yields the pressure equation:

$$\frac{1}{\Delta t} \left(\frac{\vartheta V p'}{RT} \right)_P - \sum_{\{f\}_P} \mathcal{S}_f \cdot \left(\frac{1}{\mathcal{A}_P^{\mathbf{u}}} \rho \vartheta V \mathcal{N} p' \right)_f = - \sum_{\{f\}_P} \mathcal{S}_f \cdot \rho_f \left(\mathcal{H} - \mathbf{u}_b\right)_f$$

$$
\begin{aligned}
&+\left(S_m^d\right)_P - \frac{1}{\Delta t}\left(\frac{\vartheta V p_{cyl}}{RT}\right)_P \\
&+\frac{(\rho V)_P^o}{\Delta t} \ ,
\end{aligned}
\tag{D.3}
$$

where account has been taken that $\mathcal{N} p_{cyl} = 0$ and the density is expressed via the perfect gas state equation:

$$
\rho = \vartheta \frac{p}{RT} = \vartheta \frac{p_{cyl} + p'}{RT} \ . \tag{D.4}
$$

In order not to extend the computational molecule beyond the nearest neighbours, the second term on the LHS of the pressure equation is split into the orthogonal and non-orthogonal counterparts as in Eq. (4.17), in §4.3.2, with $\Gamma_{\phi,eff} = \vartheta V / \mathcal{A}_P^{\mathbf{u}}$, i.e.

$$
\sum_{\{f\}_P} \mathcal{S}_f \cdot \left(\frac{1}{\mathcal{A}_P^{\mathbf{u}}} \rho \vartheta V \mathcal{N} p'\right)_f = \sum_{\{f\}_P} \mathcal{D}_f^{p,n} \left(p'_N - p'_P\right) + \sum_{\{f\}_P} \mathcal{D}_f^{p,c} \ . \tag{D.5}
$$

Thus, the pressure equation becomes:

$$
\mathcal{A}_P^p p'_P = \sum_N \mathcal{A}_N^p p'_N + b_P^p \ , \tag{D.6a}
$$

where

$$
\mathcal{A}_P^p = \sum_N \mathcal{A}_N^p + \frac{1}{\Delta t}\left(\frac{\vartheta V}{RT}\right)_P \ , \tag{D.6b}
$$

$$
\mathcal{A}_N^p = \mathcal{D}_f^{p,n} \ , \tag{D.6c}
$$

$$
\begin{aligned}
b_P^p = &- \sum_{\{f\}_P} \mathcal{S}_f \cdot \rho_f \left(\mathcal{H} - \mathbf{u}_b\right)_f \\
&+ \left(S_m^d\right)_P - \frac{1}{\Delta t}\left(\frac{\vartheta V p_{cyl}}{RT}\right)_P \\
&+ \frac{(\rho V)_P^o}{\Delta t} + \sum_{\{f\}_P} \mathcal{D}_f^{p,c} \ .
\end{aligned}
\tag{D.6d}
$$

This equation is a Poisson type equation and written for all N_c cells in the domain, the coefficients matrix is real, symmetric and diagonally dominant. These properties are desirable for iterative solution and must be preserved when boundary conditions are applied. It follows from Eq. (D.1a) that the zero-gradient boundary condition must be applied to the wall since the normal component of velocity there is zero, see Section 4.6. This is achieved by setting the corresponding $\mathcal{A}_N^p$ coefficient to zero. At the inflow/outflow boundaries, the mass fluxes are taken into account as additional contributions to the flux term $\mathcal{S}_f \cdot \rho_f \left(\mathcal{H} - \mathbf{u}_b\right)_f$ in Eq. (D.6d).

References

[1] Abramzon B. and Sirignano W. A. *Droplet Vaporization Model for Spray Combustion Calculations.* International Journal of Heat and Mass Transfer, Vol. 32, No. 9, pages 1605–1618, 1989.

[2] Adamson B., Gosman A. D., Marooney C. J., Nasseri B. and Theodoropoulos T. *A New Unstructured-Mesh Method for Flow Prediction in Internal Combustion Engines.* In International Symposium on Diagnostics and Modeling of Combustion in Internal Combustion Engines, COMODIA, Kyoto, Japan, 1990.

[3] Aggarwal S. K. *Modeling of a Dilute Vaporizing Multicomponent Fuel Spray.* International Journal of Heat and Mass Transfer, Vol. 30, No. 9, pages 1949–1961, 1987.

[4] Aggarwal S. K. and Peng F. *A Review of Droplet Dynamics and Vaporization Modeling for Engineering Calculations.* ASME Journal of Engineering for Gas Turbines and Power, Vol. 117, pages 453–461, July 1995.

[5] Ahmadi-Befrui B. *Analysis of Flow Evolution in the Cylinders of Motored Reciprocating Engines.* Ph.D. thesis, Imperial College of Science, Technology and Medicine, University of London, May 1985.

[6] Ahmadi-Befrui B., Uchil N., Gosman A. D. and Issa R. I. *Modeling and Simulation of Thin Liquid Films Formed by Spray-Wall Interaction.* SAE Technical paper series, No. 960627, 1996.

[7] Al Omari S. A. B. *Numerical Simulation of Transient Liquid Fuel Sprays Vaporization under Engine-Like Conditions Using Diffusion Limit and Well Mixed Vaporization Models.* SAE Technical paper series, No. 960877, 1996.

[8] Alexander D. R., Wiles K. J., Schaub S. A. and Seeman M. P. *Effects of Non-Spherical Drops on a Phase Doppler Spray Analyser.* In Particle Sizing and Spray Analysis, N. Chigier and G. W. Stewart, editors, pages 67–72, 1985.

[9] Alkidas A. C. *Heat Transfer Characteristics of a Spark-Ignition Engine.* Journal of Heat Transfer, Vol. 102, pages 189–193, 1980.

[10] American Petroleum Institute (API). *Technical Data Book – Petroleum Refining*, 1981.

[11] Amsden A. A. *KIVA-3 – A KIVA Program with Block Structured Mesh for Complex Geometries.* Report LA-12503-MS, Los Alamos National Laboratory, Los Alamos, New Mexico, 1993.

[12] Amsden A. A., O'Rourke P. J. and Butler T. D. *KIVA-II: A Computer Program for Chemically Reactive Flows with Sprays.* Report LA-11560-MS, Los Alamos National Laboratory, Los Alamos, New Mexico, 1989.

[13] Amsden A. A., Ramshaw J. D., O'Rourke P. J. and Dukowicz J. K. *KIVA: A Computer Program for Two- and Three-Dimensional Fluid Flows with Chemical Reactions and Fuel Sprays.* Report LA-10245-MS, Los Alamos National Laboratory, Los Alamos, New Mexico, February 1985.

[14] Anderson Jr. J. D. *Modern Compressible Flow*, 2^{nd} ed. Aerospace Series. McGraw-Hill Book Company, New York, 1990.

[15] Arcoumanis C. *Spray Characterization in Direct-Injection Diesel Engines.* In International Symposium on Advanced Spray Combustion, Hiroshima, Japan, pages 91–108, 6–8 July 1994.

[16] Arcoumanis C. *Combustion and Emissions.* In Flow, Combustion and Emissions in Passenger Car Engines, Imperial College of Science, Technology and Medicine, University of London, London, 2–3 November 1995.

[17] Arcoumanis C., Bae C., Nagwaney A. and Whitelaw J. H. *Effect of EGR on Combustion Development in a 1.9 l DI Diesel Optical Engine.* SAE Technical paper series, No. 950850, 1995.

[18] Arcoumanis C. and Chang J. C. *Flow and Heat Transfer Characteristics of Impinging Transient Diesel Sprays.* SAE Technical paper series, No. 940678, 1994.

[19] Arcoumanis C., Cossali E., Paal G. and Whitelaw J. H. *Transient Characteristics of Multi-Hole Diesel Sprays.* SAE Technical paper series, No. 900480, 1990.

[20] Arcoumanis C. and Cutter P. A. *Flow and Heat Transfer Characteristics of Impinging Diesel Sprays under Cross-Flow Conditions.* SAE Technical paper series, No. 950448, 1995.

[21] Arcoumanis C., Hu Z. and Whitelaw J. H. *Droplet Velocity Measurements in a Four-Cylinder Optical DI Diesel Engine.* In The Third International Symposium on Diagnostics and Modeling of Combustion in Internal Combustion Engines, COMODIA 94, Yokohama, Japan, pages 205–211, 11–14 July 1994.

[22] Arcoumanis C. and Whitelaw J. H. *Fluid Mechanics of Internal Combustion Engines – A Review.* In Proceedings of the Institution of Mechanical Engineers (IMechE), Vol. 201, 1987.

[23] Arcoumanis C. and Whitelaw J. H. *Experiments on Spray Development and Combustion in DI Diesel Engines.* In Periodic Report No. 7 for the period 01.01.1992 – 30.06.1992, K.-P. Schindler, editor, IDEA, Subprogramme C3, Imperial College of Science, Technology and Medicine, London, pages 264–287, 1992.

[24] Arcoumanis C. and Whitelaw J. H. *Measurement of Velocities, Droplet/Soot Concentration and Wall Film Thickness in Diesel Engines.* In Second Periodic Report for the period 01.07.1993 – 31.12.1993, O. Haahtela, editor, IDEA-EFFECT, Subprogramme FM.4, Imperial College of Science, Technology & Medicine, London, pages 95–131, 1993.

[25] Arcoumanis C., Whitelaw J. H., Hentschel W. and Schindler K.-P. *Flow and Combustion in a Transparent 1.9 Litre Direct Injection Diesel Engine.* In Proceedings of the Institution of Mechanical Engineers (IMechE), Vol. 208, pages 191–205, 1994.

[26] Arpaci V. S. *Conduction Heat Transfer.* Addison-Wesley Series in Mechanics and Thermodynamics. Addison-Wesley Publishing Company, Massachusetts, 1966.

[27] Ayoub N. S. and Reitz R. D. *Multidimensional Computation of Multicomponent Spray Vaporization and Combustion.* SAE Technical paper series, No. 950285, 1995.

[28] Bäcker H. and Wiartalla A. *Pressure Chamber Measurement Data.* In Additional Report, Rheinisch Westfälische Technische Hochschule, Aachen, December 1992.

[29] Bai C. *Modelling of Spray Impingement Processes.* Ph.D. thesis, Imperial College of Science, Technology and Medicine, University of London, May 1996.

[30] Bai C. and Gosman A. D. *Development of Methodology for Spray Impingement Simulation.* SAE Technical paper series, No. 950283, 1995.

[31] Bai C. and Gosman A. D. *Mathematical Modelling of Wall Films Formed by Impinging Sprays.* SAE Technical paper series, No. 960626, 1996.

[32] Beard K. V. and Pruppacher H. R. *A Wind Tunnel Investigation of the Rate of Evaporation of Small Water Drops Falling at Terminal Velocity in Air.* Journal of Atmospheric Sciences, Vol. 28, pages 1455–1464, 1971.

[33] Beatrice C., Belardini P., Bertoli C., Cameretti M. C. and Cirillo N. C. *Fuel Jet Models for Multidimensional Diesel Combustion Calculation: An Update.* SAE Technical paper series, No. 950086, 1995.

[34] Beattie J. A. *Thermodynamic Properties of Real Gases and Mixtures of Real Gases.* In High Speed Aerodynamics and Jet Propulsion, Volume I – Thermodynamics and Physics of Matter, F. D. Rossini, editor, Geoffrey Cumberlege, Oxford University Press, London, 1955.

[35] Begleris P. *Three-Dimensional Flow Predictions in Motored Diesel Engines.* Ph.D. thesis, Imperial College of Science, Technology and Medicine, University of London, December 1986.

[36] Berlad A. and Hibbard R. *Effect of radiant energy on vaporization and combustion of liquid fuels.* RME-52109, NACA, 1952.

[37] Berlemont A., Benoist F. and Gouesbet G. *Influence of Collisions on Particle Fluctuating Velocities Using a Lagrangian Approach.* In Numerical Methods in Multiphase Flows, Vol. 185, ASME, pages 23–28, 1994.

[38] Beshay K. R. *Computer Modelling of Diesel Spray Dispersion and Evaporation.* Ph.D. thesis, Imperial College of Science, Technology and Medicine, University of London, 1985.

[39] Beshay K. R., Gosman A. D. and Watkins A. P. *Assessments of Multidimensional Diesel Spray Predictions.* SAE Technical paper series, No. 861570, 1986.

[40] Bilger R. W. *Turbulent Jet Diffusion Flames.* Progress in Energy and Combustion Science, Vol. 1, No. 2/3, page 87, 1976.

[41] Bird R. B., Stewart W. E. and Lightfoot E. N. *Transport Phenomena.* John Wiley & Sons, Singapore, 1960.

[42] Birouk M. *Influence de la Turbulence Homogène et Isotrope sur la Vaporisation et la Combustion de Gouttes de Combustibles Liquides.* Ph.D. thesis, Université d' Orléans, Orleans, 1996.

[43] Birouk M., Chauveau C. and Gökalp I. *Turbulence Effects on the Vaporization of Single Droplets.* In 32nd AIAA/ASME/SAE/ASEE Joint Propulsion Conference, AIAA Paper, No. 96-2626, Lake Buena Vista, 1–3 July 1996.

[44] Birouk M., Chauveau C., Sarh B., Quilgars A. and Gökalp I. *Turbulence Effects on the Vaporization of Monocomponent Single Droplets.* Combustion Science and Technology, Vol. 113-114, pages 413–428, 1996.

[45] Blanc A. Journal of Physics, Vol. 7, page 825, 1908.

[46] Bland R., Boretti A. A., Lisbona M. G. and Nebuloni P. *Spark-Ignition Engine Combustion Chamber Design with Three-Dimensional Flow Computations.* In Proceedings of the 3rd International Conference, Innovation and Reliability in Automotive Design and Testing, Vol. 2, Associazione Tecnica dell' Automobile (ATA) & Dipartimento di Meccanica e Tecnologie Industriali (DMTI), Florence, Italy, pages 663–677, 8–10 April 1992.

[47] Bo T., Clerides D., Gosman A. D. and Theodossopoulos P. *Prediction of the Flow and Spray Processes in an Automobile DI Diesel Engine.* SAE Technical paper series, No. 970882, 1997.

[48] Borman G. L. and Johnson J. H. *Unsteady Vaporization Histories and Trajectories of Fuel Drops Injected into Swirling Air.* SAE Technical paper series, No. 598C, 1962.

[49] Boussinesq J. *Théorie de l' Écoulement Tourbillant.* Mem. Présentés par Divers Savants Acad. Sci. Inst. Fr., Vol. 23, pages 46–50, 1877.

[50] Bracco F. V. *Application of Steady State Spray Equations to Combustion Modelling.* AIAA Journal, Vol. 12, pages 1534–1540, 1976.

[51] Bracco F. V. *Modelling of Engine Sprays.* SAE Technical paper series, No. 850394, 1985.

[52] Bradshaw P. *An Introduction into Turbulence and its Measurements.* Pergamon Press, London, 1971.

[53] Brazier-Smith P. R., Jennings S. G. and Latham J. *The Interaction of Falling Water Drops: Coalescence.* In Proc. R. Soc. London, Vol. A326, pages 393–408, 1972.

[54] Brodkey R. S. *The Phenomena of Fluid Motions.* Addison-Wesley Publishing Company, Reading, Massachusetts, 1969.

[55] Bruni G., Fiore A., Laforgia D. and Fiorentino L. *3-D Analysis of the Flow Through a Multihole V.C.O. Nozzle for D.I. Diesel Engine.* SAE Technical paper series, No. 950085, 1995.

[56] Butler T. D., Cloutman L. D., Dukowicz J. K. and Ramshaw J. D. *CONCHAS: An Arbitrary Lagrangian-Eulerian Computer Program for Multicomponent Chemically Reactive Fluid Flow at All Speeds.* Report LA-8929-MS, Los Alamos National Laboratory, Los Alamos, New Mexico, 1979.

[57] Carslaw H. S. and Jaeger J. C. *Conduction of Heat in Solids*, 2$^{\text{nd}}$ ed. Oxford University Press, London, 1959.

[58] Chaves H., Hentschel W., Obermeier F., Schindler K. P. and Weiss D. *Fuel Spray in Diesel Engines, Part II: Spray Propagation and Wall Interaction.* In Proceedings of the 3$^{\text{rd}}$ International Conference, Innovation and Reliability in Automotive Design and Testing, Vol. 2, Associazione Tecnica dell' Automobile (ATA) & Dipartimento di Meccanica e Tecnologie Industriali (DMTI), Florence, Italy, pages 761–772, 8–10 April 1992.

[59] Chaves H., Knapp M., Kubitzek A., Obermeier F. and Schneider T. *Experimental Study of Cavitation in the Nozzle Hole of Diesel Injectors Using Transparent Nozzles.* SAE Technical paper series, No. 950290, 1995.

[60] Chaves H. and Obermeier F. *Modelling the Effect of Modulations of the Injection Velocity on the Structure of Diesel Sprays.* SAE Technical paper series, No. 961126, 1996.

[61] Cheroudi B., Onuma Y., Chen S.-H. and Bracco F. V. *On the Intact Core of Full-Cone Sprays.* SAE Technical paper series, No. 850126, 1985.

[62] Chiang G. H., Raju M. S. and Sirignano W. A. *Numerical Analysis of Convecting, Vaporizing Fuel Droplets with Variable Properties.* International Journal of Heat and Mass Transfer, 1991.

[63] Chou P. Y. *On the Velocity Correlations and the Solution of the Equations of Turbulent Fluctuation.* Quarterly of Applied Mathematics, Vol. 3, page 38, 1945.

[64] Chung T. *Finite Element Analysis in Fluid Dynamics.* McGraw-Hill Book Company, New York, 1978.

[65] Clerides D. A., Papadakis G. and Bergeles G. C. *Numerical Investigation of the Isothermal Two-Phase Flow Inside a Pressurized Pulverized Coal Combustor.* In Proceedings of the Florence World Energy Research Symposium, FLOWERS'94, E. Carnevale, G. Manfrida, and F. Martelli, editors, Florence, Italy, pages 835–843, 6–8 July 1994.

[66] Clift R., Grace J. R. and Weber M. E. *Bubbles, Drops and Particles.* Academic Press, New York, 1978.

[67] Clift R. and Grauvin W. H. *Motion of Entrained Particles in Gas Stream.* The Canadian Journal of Chemical Engineering, Vol. 49, page 439, 1971.

[68] Collins P. J. *Prediction of Turbulent Flow of Inelastic Shear-Thinning Fluids in Ducts and Mixing Vessels.* Ph.D. thesis, Imperial College of Science, Technology and Medicine, University of London, 1990.

[69] Computational Dynamics Ltd., London. *STAR-CD Manual, Version 2.3*, 1995.

[70] Computational Dynamics Ltd., London. *SPEED/PROSPEED User's Manual, Release 2.302*, May 1996.

[71] Courant R., Friedrichs K. O. and Lewy H. *Uber die Partiellen Differenzgleichungen der Mathematischen Physik.* Mathematische Annalen, Vol. 100, pages 32–74, 1928. English translation in IBM Journal, pages 215–234, 1967.

[72] Crowe C. T. *A Computational Model for the Gas-Droplet Flow Field in the Vicinity of an Atomiser.* In 11$^{\text{th}}$ JANAF Symposium, No. 74-23, The Combustion Institute, 1974.

[73] Crowe C. T. *Review – Numerical Models for Dilute Gas-Particle Flows.* ASME Journal of Fluids Engineering, Vol. 104, pages 297–303, 1982.

[74] Crowe C. T., Sharma H. P. and Stock D. E. *The Particle-Source-In-Cell (PSI-Cell) Model for Gas/Droplet Flows.* ASME Journal of Fluids Engineering, pages 325–332, 1977.

[75] Daidžić N., Kohnen G. and Sommerfeld M. *A New Spray Evaporation Model Based on Droplet Interface Phenomena.* In Proceedings of The Second International Conference on Multiphase Flow '95-Kyoto, Vol. 1, Kyoto, Japan, pages SP23–SP30, 3–7 April 1995.

[76] Dandy D. S. and Dwyer H. A. *A Sphere in a Shear Flow at Finite Reynolds Number: Effect of Shear on Particle Lift, Drag and Heat Transfer.* Journal of Fluid Mechanics, Vol. 216, pages 381–410, 1990.

[77] Daubert T. E. and Danner R. P. *Data Compilation Tables of Properties of Pure Compounds.* Design Institute for Physical Property Data, American Institute of Chemical Engineers (AIChE), 1985.

[78] Davidov B. I. *On the Statistical Dynamics of an Incompressible Fluid.* Doklady Akademiya Nauk SSSR, Vol. 136, page 47, 1961.

[79] Delplanque J.-P. and Sirignano W. A. *Numerical Study of the Transient Vaporization of an Oxygen Droplet at Sub- and Super-Critical Conditions.* International Journal of Heat and Mass Transfer, Vol. 36, No. 2, pages 303–314, 1993.

[80] Demirdžić I. and Perić M. *Space Conservation Law in Finite Volume Calculations of Fluid Flow.* International Journal for Numerical Methods in Fluids, Vol. 8, pages 1037–1050, 1988.

[81] Di Giorgio F., Laforgia D. and Damiani V. *Investigation of Drop Size Distribution in the Spray of a Five-Hole, V.C.O. Nozzle at High Feeding Pressure.* SAE Technical paper series, No. 950087, 1995.

[82] Diwakar R., Anderson J. D., Griffin M. D. and Jones E. *Inviscid Solutions of the Flowfield in an Internal Combustion Engine.* AIAA Journal, Vol. 14, No. 12, page 1667, 1976.

[83] Dukowicz J. K. *A Particle-Fluid Numerical Model for Liquid Sprays.* Journal of Computational Physics, Vol. 35, pages 229–253, 1980.

[84] El Tahry S. H. *k-ε Equations for Compressible Reciprocating Engine Flows.* AIAA Journal of Energy, Vol. 7, pages 345–353, 1983.

[85] El Wakil M. M., Uyehara O. A. and Myers F. S. *A Theoretical Investigation of the Heating-up Period of Injected Fuel Droplets Vaporizing in Air.* Technical Note 3179, NACA, 1954.

[86] Elghobashi S. E. and Abou-Arab T. W. *A Two-Equation Turbulence Model for Two-Phase Flows.* Physics of Fluids, Vol. 26, pages 931–938, 1983.

[87] Elghobashi S. E., Abou-Arab T. W. and Mostafa A. *Prediction of the Particle-Laden Jet with a Two-Equation Turbulence Model.* International Journal of Multiphase Flow, Vol. 10, pages 697–710, 1984.

[88] Engel O. G. *Water Drop Collisions with Solid Surfaces.* National Bureau of Standards, Journal of Research, Vol. 54, pages 281–298, 1955.

[89] Engel O. G. *Crater Depth in Fluid Impacts.* Journal of Applied Physics, Vol. 37, pages 1798–1808, 1966.

[90] Faeth G. M. *Current status of droplet and liquid combustion.* Progress in Energy and Combustion Science, Vol. 3, pages 191–224, 1977.

[91] Faeth G. M. *Evaporation and Combustion of Sprays.* Progress in Energy and Combustion Science, Vol. 9, pages 1–76, 1983.

[92] Faeth G. M. *Mixing, Transport and Combustion in Sprays.* Progress in Energy and Combustion Science, Vol. 13, pages 293–345, 1987.

[93] Faeth G. M. *Structure and Atomization Properties of Dense Turbulent Sprays.* In Twenty-Third Symposium (International) on Combustion, The Combustion Institute, pages 1345–1352, 1990.

[94] Faeth G. M. *Spray Combustion: A Review.* In Proceedings of The Second International Conference on Multiphase Flow '95-Kyoto, Vol. 1, Kyoto, Japan, 3–7 April 1995.

[95] Faeth G. M., Hsiang L.-P. and Wu P.-K. *Structure and Breakup Properties of Sprays.* International Journal of Multiphase Flow, Vol. 21, pages 99–127, 1995.

[96] Favre A. *Statistical Equations of Turbulent Gases.* In Problems of Hydrodynamics and Continuum Mechanics, Soc. Indust. Appl. Math., pages 231–266, 1969.

[97] Fletcher R. *Conjugate Gradient Methods for Indefinite Systems.* In Proc. Dundee Conference on Numerical Analysis, G. A. Watson, editor, Springer-Verlag, 1976.

[98] FLUENT Inc., Centerra Resource Park, Lebanon, NH 03766, USA. *FLUENT User's Guide, Version 4.25*, 1995.

[99] Gallagher R. H., Zienkiewicz O. C., Oden J. T., Morandi Cecchi M. and Taylor C., editors. *Finite Elements in Fluids*, Vol. 3. John Wiley & Sons, 1978.

[100] Gökalp I., Chauveau C., Berrekam H. and Ramos-Arroyo N. A. *Vaporization of Miscible Binary Fuel Droplets under Laminar and Turbulent Convective Conditions.* Atomization and Sprays, Vol. 4, pages 661–676, 1994.

[101] Gökalp I., Chauveau C., Simon O. and Chesneau X. *Mass Transfer from Liquid Fuel Droplets in Turbulent Flow.* Combustion and Flame, Vol. 89, pages 286–298, 1992.

[102] Gonzalez D. M. A., Borman G. L. and Reitz R. D. *A Study of Diesel Cold Starting Using Both Cycle Analysis and Multidimensional Calculations.* SAE Technical paper series, No. 910180, 1991.

[103] Gonzalez D. M. A., Lian Z. W. and Reitz R. D. *Modeling Diesel Engine Spray Vaporization and Combustion.* SAE Technical paper series, No. 920579, 1992.

[104] Gosman A. D. *Computer Modelling of Flow and Heat Transfer in Engines – Progress and Prospects.* In Proc. Int. Symp. on Diagnostics and Modelling of Combustion in Reciprocating Engines, Tokyo, 1985.

[105] Gosman A. D. *Flow Processes in Cylinders.* In The Thermodynamics and Gas Dynamics of Internal Combustion Engines, J. H. Horlock and D. E. Winterbone, editors, Vol. 2, Clarendon-Press, Oxford, 1986.

[106] Gosman A. D., Huh K. Y. and Zhang Q. *Development and Evaluation of a Three-Dimensional Fuel Spray Model for Reciprocating Engines.* In Progress Report for Joint Research Committee of European Automobile Manufacturers, Internal report, Imperial College of Science, Technology and Medicine, London, May 1989.

[107] Gosman A. D. and Ioannides E. *Aspects of Computer Simulation of Liquid-Fuelled Combustors.* AIAA Journal of Energy, Vol. 7, No. 6, pages 482–490, 1983.

[108] Gosman A. D., Ioannides E., Lever D. A. and Cliffe K. A. *A Comparison of 'Continuum' and 'Discrete Droplet' Finite-Difference Models Used in the Calculation of Spray Combustion in Swirling, Turbulent Flows.* Report TP 865, Imperial College of Science, Technology and Medicine, University of London, 1980.

[109] Gosman A. D. and Johns R. J. R. *Computer Analysis of Fuel-Air Mixing in Direct-Injection Engines.* SAE Technical paper series, No. 800091, 1980.

[110] Gosman A. D., Kralj C., Marooney C. J. and Theodossopoulos P. *The Development of the SPEED Code for Diesel Combustion Simulation.* In Proceedings of the 3rd International Conference, Innovation and Reliability in Automotive Design and Testing, Vol. 2, Associazione Tecnica dell' Automobile (ATA) & Dipartimento di Meccanica e Tecnologie Industriali (DMTI), Florence, Italy, pages 653–662, 8–10 April 1992.

[111] Gosman A. D., Kralj C., Marooney C. J. and Theodossopoulos P. *Development Strategies for Diesel Combustion Simulation Using the SPEED Code.* In Proceedings of the Institution of Mechanical Engineers (IMechE), No. C448/035, 1992.

[112] Gosman A. D. and Marooney C. J. *Development and Validation of Computer Models of the Cylinder Flow and Combustion in Diesel and Spark Ignition

Engines. In Proceedings of the Institution of Mechanical Engineers (IMechE), No. C399/19, 1989.

[113] Gosman A. D., Pun W. N., Runchal A. K., Spalding D. and Wolfstein M. *Heat and Mass Transfer in Recirculating Flows.* Academic Press, 1969.

[114] Grunberg L. and Nissan A. H. Nature, Vol. 164, page 799, 1949.

[115] Guerrassi N. and Champoussin J. C. *Experimental Study and Modeling of Diesel Spray/Wall Impingement.* SAE Technical paper series, No. 960864, 1996.

[116] Haagen-Smit A. J. *Chemistry and Physiology of Los Angeles Smog.* Industrial & Engineering Chemistry, Vol. 44, page 1342, 1952.

[117] Hadden S. T. Hydrocarbon Processing and Petroleum Refiner, Vol. 45, No. 10, page 161, 1966.

[118] Haenlein A. *Disintegration of a Liquid Jet.* TN 659, NACA, 1932.

[119] Hamady F. J., Hahn J. P., Hellman K. H. and Gray C. L. *High-Speed/High-Resolution Imaging of Fuel Sprays from Various Injector Nozzles for Direct Injection Engines.* SAE Technical paper series, No. 950289, 1995.

[120] Harlow F. H. and Amsden A. A. *Numerical Calculation of Multiphase Fluid Flow.* Journal of Computational Physics, Vol. 17, pages 19–52, 1975.

[121] Harlow F. H. and Nakayama P. I. *Transport of Turbulence Energy Decay Rate.* Report LA-3854, Los Alamos Sci. Lab., University of California, 1968.

[122] Haselman L. C. and Westbrook C. K. *A Theoretical Model for Two-Phase Fuel Injection in Stratified Charge Engines.* SAE Technical paper series, No. 780318, 1978.

[123] Hayduk W. and Minhas B. S. The Canadian Journal of Chemical Engineering, Vol. 60, page 295, 1982.

[124] Hentschel W., Hesse A. and Schindler K.-P. *Experimental Investigation of Spray Formation and Combustion in a Real Diesel Engine.* In Periodic Report for the period 01.11.1988 – 30.04.1989, K.-P. Schindler, editor, IDEA, Subprogramme C4, Volkswagen AG, Wolfsburg, pages 180–203, August 1989.

[125] Hentschel W. and Röpke S. *Influence of Exhaust Gas Recirculation on Diesel Combustion.* In Second Periodic Report for the period 01.07.1993 – 31.12.1993, O. Haahtela, editor, IDEA-EFFECT, Subprogramme A.3, Volkswagen AG, Wolfsburg, pages 557–576, 1993.

[126] Hentschel W. and Schindler K.-P. *Experimental Investigation of Spray Formation and Combustion in a Real Diesel Engine.* In Periodic Report No. 5 for the period 01.01.1991 – 30.06.1991, K.-P. Schindler, editor, IDEA, Subprogramme C4, Volkswagen AG, Wolfsburg, pages 331–350, September 1991.

[127] Hentschel W. and Schindler K.-P. *Experimental Investigation of Spray Formation and Combustion in a Real Diesel Engine.* In Periodic Report No. 6 for the period 01.07.1991 – 31.12.1991, K.-P. Schindler, editor, IDEA, Subprogramme C4, Volkswagen AG, Wolfsburg, pages 303–334, December 1991.

[128] Hentschel W. and Schindler K.-P. *Experimental Investigation of Spray Formation and Combustion in a Real Diesel Engine.* In Periodic Report No. 7 for the period 01.01.1992 – 30.06.1992, K.-P. Schindler, editor, IDEA, Subprogramme C4, Volkswagen AG, Wolfsburg, pages 288–322, 1992.

[129] Hentschel W. and Schindler K.-P. *Experimental Investigation of Spray Formation and Combustion in a Real Diesel Engine.* In Eighth Periodic Report for the period 01.07.1992 – 31.12.1992, K.-P. Schindler, editor, IDEA, Subprogramme C4, Volkswagen AG, Wolfsburg, May 1993.

[130] Hestenes M. R. and Stiefel E. L. *Method of Conjugate Gradients for Solving Linear Systems.* National Bureau of Standards, Journal of Research, Vol. 29, pages 409–436, 1952.

[131] Heywood J. B. *Internal Combustion Engine Fundamentals.* Automotive Technology Series. McGraw-Hill Book Company, Singapore, 1988.

[132] Hinze J. O. *Fundamentals of the Hydrodynamic Mechanism of Splitting in Dispersion Processes.* AIChE Journal, Vol. 1, No. 3, pages 289–295, 1955.

[133] Hinze J. O. *Turbulence*, 2nd ed. McGraw-Hill Book Company, Inc., New York, 1975.

[134] Hirsch C. *Numerical Computation of Internal and External Flows, Volume 1: Fundamentals of Numerical Discretization.* Wiley Series in Numerical Methods in Engineering. John Wiley & Sons, Chichester, 1992.

[135] Hobbs P. V. and Alkezweeny A. J. *Splashing of Water Drop.* Science, Vol. 155, pages 1112–1114, 1967.

[136] Hobbs P. V. and Osheroff T. *Splashing of Drops on Shallow Liquids.* Science, Vol. 158, pages 1184–1186, 1967.

[137] Hohmann S., Klingsporn M. and Renz U. *An Improved Model to Describe Spray Evaporation under Diesel-Like Conditions.* SAE Technical paper series, No. 960630, 1996.

[138] Hsiang L.-P. and Faeth G. M. *Near-Limit Drop Deformation and Secondary Breakup.* International Journal of Multiphase Flow, Vol. 18, No. 5, pages 635–652, 1992.

[139] Hsiang L.-P. and Faeth G. M. *Drop Deformation and Breakup due to Shock Wave and Steady Disturbances.* International Journal of Multiphase Flow, Vol. 21, No. 4, pages 545–560, 1995.

[140] Hubbard G. L., Denny V. E. and Mills A. F. *Droplet Evaporation: Effects of Transients and Variable Properties.* International Journal of Heat and Mass Transfer, Vol. 18, pages 1003–1008, 1975.

[141] Huh K. Y. and Gosman A. D. *A phenomenological model of diesel spray atomization.* In Proceedings of The International Conference on Multiphase Flows, Vol. 2, Tsukuba, pages 515–518, 1991.

[142] Ideriah F. J. K. *Turbulent Natural and Forced Convection in Plumes and Cavities.* Ph.D. thesis, Imperial College of Science, Technology and Medicine, University of London, June 1977.

[143] Ikonomou E. *A Computational Study of Diesel Sprays and Combustion.* Ph.D. thesis, Imperial College of Science, Technology and Medicine, University of London, October 1995.

[144] Isdale J. D., MacGillivray J. C. and Cartwright G. *Prediction of Viscosity of Organic Liquid Mixtures by a Group Contribution Method.* In Natl. Eng. Lab. Rept., East Kilbride, Glasgow, Scotland, 1985.

[145] Issa R. I. *Solution of the Implicitly Discretised Fluid Flow Equations by Operator-Splitting.* Journal of Computational Physics, Vol. 62, pages 40–65, 1985.

[146] Issa R. I., Gosman A. D. and Watkins A. P. *The Computation of Compressible and Incompressible Recirculating Flows by a Non-Iterative Implicit Scheme.* Journal of Computational Physics, Vol. 62, No. 1, pages 66–82, January 1986.

[147] Jayaratne O. W. and Mason B. J. *The Coalescence and Bouncing of Water Drops at an Air/Water Interface.* In Proc. R. Soc. London, Vol. A280, pages 545–565, 1964.

[148] Jayatilleke C. L. V. *The Influence of Prandtl Number and Surface Roughness on the Resistance of the Laminar Sublayer to Momentum and Heat Transfer.* Progress in Heat and Mass Transfer, Vol. 1, 1969.

[149] Jia H. and Gogos G. *High Pressure Droplet Vaporization; Effects of Liquid-Phase Gas Solubility.* International Journal of Heat and Mass Transfer, Vol. 36, No. 18, pages 4419–4431, 1993.

[150] Jin J. D. and Borman G. L. *A Model for Multicomponent Droplet Vaporization at High Ambient Pressures.* SAE Technical paper series, No. 850264, 1985.

[151] Jones J. B. and Hawkins G. A. *Engineering Thermodynamics, An Introductory Textbook*, 2^{nd} ed. John Wiley & Sons, Inc., New York, 1986.

[152] Jones P. M. and Junday J. S. *Full Cycle Computational Fluid Dynamics Calculations in a Motored Four Valve Pent Roof Combustion Chamber and Comparison with Experiments.* SAE Technical paper series, No. 950286, 1995.

[153] Jones W. P. *Models for Turbulent Flows with Variable Density and Combustion.* In Lecture Series 1979-2, Von Kármán Institute for Fluid Dynamics, Rhode-Saint-Genèse, Belgium, 1979.

[154] Jones W. P. and Launder B. E. *The Prediction of Laminarization with a Two-Equation Model of Turbulence.* International Journal of Heat and Mass Transfer, Vol. 15, pages 301–314, 1972.

[155] Jones W. P. and Launder B. E. *The Calculation of Low-Reynolds-Number Phenomena with a Two-Equation Model of Turbulence.* International Journal of Heat and Mass Transfer, Vol. 16, pages 1119–1130, 1973.

[156] Kakaç S. and Yener Y. *Convective Heat Transfer*, 2$^{\text{nd}}$ ed. CRC Press, Inc., Boca Raton, Florida, 1995.

[157] Karasawa T., Shiga S., Tanaka M., Nakamura H. and Kurabayashi T. *Relationship between Atomization Behavior and the Nozzle Inlet-Shape of a Steady-Jet.* In International Symposium on Advanced Spray Combustion, Hiroshima, Japan, pages 25–32, 6–8 July 1994.

[158] Karlsson J. A. J. and Chomiak J. *Calculations with the SPICE Code.* In Second Periodic Report for the period 01.07.1993 – 31.12.1993, O. Haahtela, editor, IDEA-EFFECT, Subprogramme C.3, Chalmers University of Technology, Göteborg, pages 507–514, 1993.

[159] Kauffman C. W. and Nicholls J. A. *Shock-Wave Ignition of Liquid Fuel Drops.* AIAA Journal, Vol. 9, 1971.

[160] Kay W. B. Industrial & Engineering Chemistry, Vol. 28, page 1014, 1936.

[161] Kegl B. *An Improved Mathematical Model of Conventional FIE Processes.* SAE Technical paper series, No. 950079, 1995.

[162] Kershaw D. S. *The Incomplete Cholesky Conjugate Gradient Method for the Iterative Solution of Systems of Linear Equations.* Journal of Computational Physics, Vol. 26, pages 43–65, 1978.

[163] Khalil E. E. and Whitelaw J. H. *Aerodynamic and Thermodynamic Characteristics of Kerosene Spray Flames.* In Sixteenth Symposium (International) on Combustion, The Combustion Institute, pages 569–576, 1977.

[164] Kitscha J. and Kocamustafaogullari G. *Breakup Criteria for Fluid Particles.* International Journal of Multiphase Flow, Vol. 15, No. 4, pages 573–588, 1989.

[165] Kneer R., Schneider M., Noll B. and Wittig S. *Diffusion Controlled Evaporation of a Multicomponent Droplet: Theoretical Studies on the Importance of Variable Liquid Properties.* International Journal of Heat and Mass Transfer, Vol. 36, No. 9, pages 2403–2415, 1993.

[166] Kong S.-C., Ayoub N. and Reitz R. D. *Modeling Combustion in Compression Ignition Homogeneous Charge Engines.* SAE Technical paper series, No. 920512, 1992.

[167] Kong S.-C., Han Z. and Reitz R. D. *The Development and Application of a Diesel Ignition and Combustion Model for Multidimensional Engine Simulation.* SAE Technical paper series, No. 950278, 1995.

[168] Koss H. J. and Brüggemann D. *Results from Fuel/Air Ratio Measurements in an n-Heptane Injection Spray.* In Periodic Report No. 7 for the period 01.01.1992 – 30.06.1992, K.-P. Schindler, editor, IDEA, Subprogramme A2, Rheinisch Westfälische Technische Hochschule, Aachen, pages 117–124, 1993.

[169] Koss H. J., Brüggemann D., Wiartalla A., Bäcker H. and Breuer A. *Results from Fuel/Air Ratio Measurements in an n-Heptane Injection Spray.* In Eighth Periodic Report for the period 01.07.1992 – 31.12.1992, K.-P. Schindler, editor, IDEA, Subprogramme A2, Rheinisch Westfälische Technische Hochschule, Aachen, May 1993.

[170] Kowalewicz A. *Combustion Systems of High-Speed Piston I.C. Engines.* Elsevier Science Publishers, Amsterdam, 1984.

[171] Kralj C. *Numerical Simulation of Diesel Spray Processes.* Ph.D. thesis, Imperial College of Science, Technology and Medicine, University of London, October 1995.

[172] Kronig R. and Brink J. C. *On the Theory of Extraction from Falling Droplets.* In Appl. Scient. Res. A2, pages 142–154, 1951.

[173] Krzeczkowski S. A. *Measurement of Liquid Droplet Disintegration Mechanisms.* International Journal of Multiphase Flow, Vol. 6, pages 227–239, 1980.

[174] Kuo T. W. and Bracco F. V. *On the scaling of Transient Laminar, Turbulent and Spray Jets.* SAE Technical paper series, No. 820038, 1982.

[175] Lahey Jr. R. T. *The CFD Analysis of Multidimensional Phenomena in Multiphase Flow.* In Proceedings of The Second International Conference on Multiphase Flow '95-Kyoto, Vol. 3, Kyoto, Japan, 3–7 April 1995.

[176] Landis R. B. and Mills A. F. *Effect of Internal Diffusional Resistance on the Evaporation of Binary Droplets.* In Proceedings of The Fifth International Heat Transfer Conference, Vol. IV, The Science Council of Japan, Tokyo, Japan, pages 345–349, 3–7 September 1974.

[177] Langmuir I. *The Production of Rain by a Chain Reaction in Cumulus Clouds at Temperatures above Freezing.* Journal of Meteorology, Vol. 5, No. 5, pages 175–192, October 1948.

[178] Launder B. E. and Sharma B. I. *Application of the Energy Dissipation Model of Turbulence to the Calculation of Flow near a Spinning Disc.* Letters in Heat and Mass Transfer, Vol. 1, No. 2, pages 131–138, 1974.

[179] Launder B. E. and Spalding D. B. *Mathematical Models of Turbulence.* Academic Press, London, 1972.

[180] Launder B. E. and Spalding D. B. *The Numerical Computation of Turbulent Flows.* Computer Methods in Applied Mechanics and Engineering, Vol. 3, pages 269–289, 1974.

[181] Law C. K. *Internal Boiling and Superheating in Vaporizing Multicomponent Droplets.* AIChE Journal, Vol. 24, No. 4, pages 626–632, July 1978.

[182] Law C. K. and Law H. K. *A d^2-Law for Multicomponent Droplet Vaporization and Combustion.* AIAA Journal, Vol. 20, No. 4, pages 522–527, April 1982.

[183] Lebrère L. and Dillies B. *Engine Flow Calculations Using a Reynolds Stress Model in the Kiva-II Code.* SAE Technical paper series, No. 960636, 1996.

[184] Leduc J.-F. and Karlsson J. A. J. *Comparison between Different Atomization Models and Experimental Data.* In ICLASS-94, Rouen, France, 18–22 July 1994.

[185] Lefebvre A. H. *Atomization and Sprays.* Combustion Series. Hemisphere Publishing Corporation, 1989.

[186] Leskovšek D. *Predictions of Combustion in Spark-Ignition Engines.* Ph.D. thesis, Imperial College of Science, Technology and Medicine, University of London, July 1996.

[187] Levin Z. *Splashing of Water Drops: A Study of the Hydrodynamics and Charge Separation.* Ph.D. thesis, University of Washington, Seattle, 1970.

[188] Levin Z. and Hobbs P. V. *Splashing of Water Drops on Solid and Wetted Surfaces: Hydrodynamics and Charge Separation.* In Phil. Trans. Roy. Soc. London, Vol. A269, pages 555–585, 1971.

[189] Li C. C. AIChE Journal, Vol. 22, page 927, 1976.

[190] Liu A. B., Mather D. and Reitz R. D. *Modeling the Effects of Drop Drag and Breakup on Fuel Sprays.* SAE Technical paper series, No. 930072, 1993.

[191] Lock G. S. H. *Latent Heat Transfer, An Introduction to Fundamentals.* Oxford Engineering Science Series. Oxford University Press, Oxford, 1994.

[192] Lozinski D. and Matalon M. *Vaporization of a Spinning Fuel Droplet.* In Twenty-Fourth Symposium (International) on Combustion, The Combustion Institute, pages 1483–1491, 1992.

[193] Maly R. R. *Applied Flow and Combustion Diagnostics for IC Engines.* In Computational Fluid Dynamics '94, S. Wagner, J. Périaux, and E. H. Hirschel, editors, John Wiley & Sons, 1994.

[194] Mao C.-P., Wakamtsu Y. and Faeth G. M. *Simplified Model of High Pressure Combustion.* In Eighteenth Symposium (International) on Combustion, The Combustion Institute, pages 337–347, 1981.

[195] Matsui Y. and Sugihara K. *Sources of Hydrocarbon Emissions from a Small Direct Injection Diesel Engine.* JSAE Review, Vol. 7, pages 4–11, 1986.

[196] McDonald P. W. *The Computation of Transonic Flow through Two-Dimensional Gas Turbine Cascade.* ASME, 71-GT-89, 1971.

[197] McLandress A., Emerson R., McDowell P. and Rutland C. *Intake and In-Cylinder Flow Modeling Characterization of Mixing and Comparison with Flow Bench Results.* SAE Technical paper series, No. 960635, 1996.

[198] McLaughlin E. *Theory of Thermal Conductivity of Fluids.* In Thermal Conductivity, R. P. Tye, editor, Vol. 2, Academic Press, London, pages 1–64, 1969.

[199] Mei R. *An Approximate Expression for the Shear Lift Force on a Spherical Particle at Finite Reynolds Number.* International Journal of Multiphase Flow, Vol. 18, No. 1, pages 145–147, 1992.

[200] Moler T. and Mansour N. *Modeling of Turbulence in Rapidly Compressed Flows.* SAE Technical paper series, No. 820040, 1982.

[201] Mostafa A. A. and Mongia H. C. *On the Modeling of Turbulent Evaporating Sprays: Eulerian Versus Lagrangian Approach.* International Journal of Heat and Mass Transfer, Vol. 30, pages 2583–2593, 1987.

[202] Mostafa A. A. and Mongia H. C. *On the Interaction of Particles and Turbulent Fluid Flow.* International Journal of Heat and Mass Transfer, Vol. 31, pages 2063–2075, 1988.

[203] Müller K. *A Study of Atomisation of Sprays under High Injection Pressure.* Master's thesis, Imperial College of Science, Technology and Medicine, University of London, September 1996.

[204] Myskis A. D. *Introductory Mathematics for Engineers.* In Lectures in Higher Mathematics, MIR Publisher, Moskow, 1975.

[205] Naber J. D. *Droplet Impingement on a Heated Surface.* Ph.D. thesis, University of Wisconsin, Madison, 1992.

[206] Naber J. D. and Reitz R. D. *Modeling Engine Spray/Wall Impingement.* SAE Technical paper series, No. 880107, 1988.

[207] Nagwaney A. Private communication, December 1996.

[208] National Bureau of Standards.

[209] Newman J. A. and Brzustowski T. *Behavior of a Liquid Jet near the Thermodynamic Critical Region.* AIAA Journal, Vol. 9, pages 1595–1602, 1971.

[210] Nicholls J. *Stream and Droplet Breakup by Shock Waves.* D. T. Harrje and F. H. Reardon, editors, NASA SP-194, pages 126–128, 1972.

[211] Nigmatulin R. I. *Dynamics of Multiphase Media*, Revised and Augmented ed., Vol. 1. Hemisphere Publishing Corporation, New York, 1991. Originally published by Nauka Moscow under the title: Dinamika Mnogofaznykh Sred.

[212] Obermeier F. *Deposition and Re-Evaporation of Fuel at the Wall of a Diesel Combustion Chamber.* In Periodic Report No. 4 for the period 01.07.1990 – 31.12.1990, K.-P. Schindler, editor, IDEA, Subprogramme A3, Max-Planck Institut für Strömungsforschung, Göttingen, pages 90–103, January 1991.

[213] Obermeier F. *Deposition and Re-Evaporation of Fuel at the Wall of a Diesel Combustion Chamber.* In Periodic Report No. 5 for the period 01.01.1991 – 30.06.1991, K.-P. Schindler, editor, IDEA, Subprogramme A3, Max-Planck Institut für Strömungsforschung, Göttingen, pages 118–132, August 1991.

[214] Obermeier F. *Study of Pressure Fluctuations, Flow Separation and Cavitation in the Nozzle and their Influence on Spray Formation.* In Periodic Report No. 5 for the period 01.01.1991 – 30.06.1991, K.-P. Schindler, editor, IDEA, Subprogramme A1, Max-Planck Institut für Strömungsforschung, Göttingen, pages 76–94, August 1991.

[215] Obermeier F. *Deposition and Re-Evaporation of Fuel at the Wall of a Diesel Combustion Chamber.* In Periodic Report No. 6 for the period 01.07.1991 – 31.12.1991, K.-P. Schindler, editor, IDEA, Subprogramme A3, Max-Planck Institut für Strömungsforschung, Göttingen, pages 114–124, February 1992.

[216] Obermeier F. *Deposition and Re-Evaporation of Fuel at the Wall of a Diesel Combustion Chamber.* In Periodic Report No. 7 for the period 01.01.1992 – 30.06.1992, K.-P. Schindler, editor, IDEA, Subprogramme A3, Max-Planck Institut für Strömungsforschung, Göttingen, pages 125–137, 1992.

[217] Obermeier F. *Study of Pressure Fluctuations, Flow Separation and Cavitation in the Nozzle and their Influence on Spray Formation.* In Periodic Report No. 6 for the period 01.07.1991 – 31.12.1991, K.-P. Schindler, editor, IDEA, Subprogramme A1, Max-Planck Institut für Strömungsforschung, Göttingen, pages 67–88, March 1992.

[218] Obermeier F. *Deposition and Re-Evaporation of Fuel at the Wall of a Diesel Combustion Chamber.* In Eighth Periodic Report for the period 01.07.1992 – 31.12.1992, K.-P. Schindler, editor, IDEA, Subprogramme A3, Max-Planck Institut für Strömungsforschung, Göttingen, May 1993.

[219] Obermeier F. *Experimental and Theoretical study of the Influence of Unsteady High Frequency Flow Conditions on Flow Separation and Cavitation within a Nozzle and on Spray Formation of Fuel Injectors under Diesel Engine Conditions.* In Second Periodic Report for the period 01.07.1993 – 31.12.1993, O. Haahtela, editor, IDEA-EFFECT, Subprogramme FM.1, Institut für Angewandte Mechanik und Strömungsphysik der Georg August Universität, Göttingen, pages 45–62, 1993.

[220] Obermeier F. *Modelling of Atomisation.* Additional report, Max-Planck Institut für Strömungsforschung, Göttingen, March 1993.

[221] Obermeier F. *Modelling of Nozzle Flow.* Additional report, Max-Planck Institut für Strömungsforschung, Göttingen, March 1993.

[222] Obermeier F. *Study of Pressure Fluctuations, Flow Separation and Cavitation in the Nozzle and their Influence on Spray Formation.* In Eighth Periodic Report for the period 01.07.1992 – 31.12.1992, K.-P. Schindler, editor, IDEA, Subprogramme A1, Max-Planck Institut für Strömungsforschung, Göttingen, May 1993.

[223] O'Rourke P. J. *Collective Drop Effects on Vaporizing Liquid Sprays.* Ph.D. thesis, University of Princeton, 1981.

[224] O'Rourke P. J. and Amsden A. A. *The Tab Method for Numerical Calculation of Spray Droplet Breakup.* SAE Technical paper series, No. 872089, 1987.

[225] O'Rourke P. J. and Bracco F. V. *Modelling of Drop Interactions in Thick Sprays and a Comparison with Experiments.* In Conference on Stratified Charge Automotive Engines, No. C404/80, Institution of Mechanical Engineers (IMechE), pages 101–116, November 1980.

[226] Özişik M. N. *Heat Conduction.* John Wiley & Sons, Inc., New York, 1980.

[227] Paál G. *Transient Characteristics of Diesel Engine Sprays.* Ph.D. thesis, Imperial College of Science, Technology and Medicine, University of London, March 1992.

[228] Patankar S. V. *Numerical Heat Transfer and Fluid Flow.* Series in Computational Methods in Mechanics and Thermal Sciences. McGraw-Hill Book Company, New York, 1980.

[229] Patankar S. V. and Baliga B. R. *A New Finite-Difference Scheme for Parabolic Differential Equations.* Numerical Heat Transfer, Vol. 1, pages 27–37, 1978.

[230] Patterson M. A., Kong S.-C., Hampson G. J. and Reitz R. D. *Modeling the Effects of Fuel Injection Characteristics on Diesel Engine Soot and NOx Emissions.* SAE Technical paper series, No. 940523, 1994.

[231] Perić M. *A Finite Volume Method for the Prediction of Three-Dimensional Flow in Complex Ducts.* Ph.D. thesis, Imperial College of Science, Technology and Medicine, University of London, 1985.

[232] Perkins L. R. and Geankoplis C. J. Chemical Engineering Science, Vol. 24, page 1035, 1969.

[233] Pilch M. and Erdman C. A. *Use of Breakup Time Data and Velocity History Data to Predict the Maximum Size of Stable Fragments for Acceleration-Induced Breakup of a Liquid Drop.* International Journal of Multiphase Flow, Vol. 13, No. 6, pages 741–757, 1987.

[234] Potz D., Kreh A. and Warga J. *Variable Orifice Geometry Verified on the Two-Phase Nozzle (VRD).* SAE Technical paper series, No. 950081, 1995.

[235] Poulikakos D. *Conduction Heat Transfer.* Prentice-Hall, Englewood Cliffs, New Jersey, 1994.

[236] Pruppacher H. R. and Rasmussen R. *A Wind Tunnel Investigation of the Rate of Evaporation of Large Water Drops Falling at Terminal Velocity in Air.* Journal of Atmospheric Sciences, Vol. 36, pages 1255–1260, 1979.

[237] Ranz W. E. and Marshall Jr. W. R. *Evaporation from Drops; Part I.* Chemical Engineering Progress, Vol. 48, No. 3, pages 141–146, March 1952.

[238] Ranz W. E. and Marshall Jr. W. R. *Evaporation from Drops; Part II.* Chemical Engineering Progress, Vol. 48, No. 4, pages 173–180, April 1952.

[239] Rayleigh L. *On the Instability of Jets.* In Proc. London Math. Soc., Vol. 10, pages 4–13, 1878.

[240] Reid J. K. *On the Method of Conjugate Gradients for the Solution of Large Sparse System of Linear Equations.* In Large Sparse Sets of Linear Equations, J. K. Reid, editor, Academic Press, New York, 1971.

[241] Reid R. C., Prausnitz J. M. and Poling B. E. *The Properties of Gases and Liquids*, 4^{th} ed. McGraw-Hill Book Company, Inc., New York, 1987.

[242] Reitz R. D. *Atomization and Other Breakup Regimes of a Liquid Jet.* Ph.D. thesis, Princeton University, 1978.

[243] Reitz R. D. *Modeling Atomization Processes in High-Pressure Vaporizing Sprays.* Atomisation and Spray Technology, Vol. 3, pages 309–337, 1987.

[244] Reitz R. D. *Assessment of Wall Heat Transfer Models for Premixed-Charge Engine Combustion Computations.* SAE Technical paper series, No. 910267, 1991.

[245] Reitz R. D. and Diwakar R. *Effect of Drop Breakup on Fuel Sprays.* SAE Technical paper series, No. 860469, 1986.

[246] Reitz R. D. and Diwakar R. *Structure of High-Pressure Fuel Sprays.* SAE Technical paper series, No. 870598, 1987.

[247] Renksizbulut M. and Bussmann M. *Multicomponent Droplet Evaporation at Intermediate Reynolds Numbers.* International Journal of Heat and Mass Transfer, Vol. 36, No. 11, pages 2827–2835, 1993.

[248] Renksizbulut M. and Yuen M. C. *Experimental Study of Droplet Evaporation in a High-Temperature Air Stream.* ASME Journal of Heat Transfer, Vol. 105, pages 384–388, May 1983.

[249] Renksizbulut M. and Yuen M. C. *Numerical Study of Droplet Evaporation in a High-Temperature Stream.* ASME Journal of Heat Transfer, Vol. 105, pages 389–397, May 1983.

[250] Renner G. and Maly R. R. *Spray Structures of Automotive Injectors.* In International Symposium on Advanced Spray Combustion, Hiroshima, Japan, pages 45–53, 6–8 July 1994.

[251] Reynolds A. J. *Turbulence Flows in Engineering.* John Wiley & Sons, London, 1974.

[252] Rhie C. M. and Chow W. L. *A Numerical Study of the Turbulent Flow Past an Isolated Airfoil with Trailing Edge Separation.* AIAA Paper, No. 820998, 1982.

[253] Ricart L. M. and Reitz R. D. *Visualization and Modeling of Pilot Injection and Combustion in Diesel Engines.* SAE Technical paper series, No. 960833, 1996.

[254] Rowe P. N., Claxton K. T. and Lewis J. B. *Heat and Mass Transfer from a Single Sphere in an Extensive Flowing Fluid.* In Transactions of the Institute of Chemical Engineers, Vol. 43, pages T14–T31, 1965.

[255] Saffman P. G. *The Lift on a Small Sphere in a Slow Shear Flow.* Journal of Fluid Mechanics, Vol. 22, No. 2, pages 385–400, 1965.

[256] Saffman P. G. *Corrigendum: The Lift on a Small Sphere in a Slow Shear Flow.* Journal of Fluid Mechanics, Vol. 31, page 624, 1968.

[257] Sarantinos M. G. *Mesh Generation and Visualisation Tools for Computational Fluid Dynamics.* Ph.D. thesis, Imperial College of Science, Technology and Medicine, University of London, June 1994.

[258] Scheaffer R. L. and McClave J. T. *Probability and Statistics for Engineers,* 4$^{\text{th}}$ ed. Duxbury Press, Belmont, California, 1995.

[259] Schindler K.-P. *Emissions and the Environment.* In Flow, Combustion and Emissions in Passenger Car Engines, Imperial College of Science, Technology and Medicine, University of London, London, 2–3 November 1995.

[260] Schmidt T., Esser-Schmittmann W., Roosen P., Hassel E., Xu H., Reuter U. and Scheid E. *Pressure Chamber Experiments for Fuel Spray Model Development.* In Final Report, JRC, Contract No. EN3E-0102-D, Rheinisch Westfälische Technische Hochschule, Aachen, October 1988.

[261] Schmidt T., Roosen P., Brüggemann D., Xu H., Scheid E. and Breuer A. *Investigation of the Influence of Turbulence and Type of Fuel on the Evaporation and Mixture Formation in Fuel-Sprays.* In Periodic Report No. 2 for the period 01.05.1989 – 30.09.1989, K.-P. Schindler, editor, IDEA, Subprogramme A2, Rheinisch Westfälische Technische Hochschule, Aachen, pages 33–49, July 1990.

[262] Senda J. *Characteristics of Diesel Spray Impinging on a Flat Wall.* In International Symposium on Advanced Spray Combustion, Hiroshima, Japan, pages 55–69, 6–8 July 1994.

[263] Shearer A. J. and Faeth G. M. *Combustion of Liquid Spray at High Pressures.* Technical Report CR-135210, NASA, 1977.

[264] Shearer A. J., Tamura H. and Faeth G. M. *Evaluation of Locally Homogeneous Flow Model of Spray Evaporation.* AIAA Paper, No. 78-1042R, 1978.

[265] Shuen J. S., Solomon A. S. P., Zhang Q. F. and Faeth G. M. *A Theoretical and Experimental Study of Turbulent Particle-Laden Jets.* Report CR-168293, NASA, 1983.

[266] Sirignano W. A. *The Formulation of Spray Combustion Models: Resolution Compared to Droplet Spacing.* ASME Journal of Heat Transfer, Vol. 108, pages 633–639, August 1986.

[267] Smith G. D. *Numerical Solution of Partial Differential Equations: Finite Difference Methods.* Oxford University Press, 1985.

[268] Sokolnikoff I. S. and Redheffer R. M. *Mathematics of Physics and Modern Engineering.* McGraw-Hill Book Company, New York, 1958.

[269] Sommerfeld M. *The Importance of Detailed Measurements for the Validation of Numerical Models and Methods for Dispersed Two-Phase Flows.* In Experimental and Computational Aspects of Validation of Multiphase Flow CFD Codes, I. Celik, Y. Hassan, D. Huges, R. Johnson, and M. Sommerfeld, editors, Vol. 180, ASME, pages 1–14, 1994.

[270] Soo S. L. *Multiphase Fluid Dynamics.* Science Press, Beijing, 1990.

[271] Soteriou C., Andrews R. and Smith M. *Direct Injection Diesel Sprays and the Effect of Cavitation and Hydraulic Flip on Atomization.* SAE Technical paper series, No. 950080, 1995.

[272] Soteriou C. C. E., Smith M. and Andrews R. J. *Cavitation Hydraulic Flip and Atomization in Direct Injection Diesel Sprays.* In Proceedings of the Institution of Mechanical Engineers (IMechE), No. C465/051/93, pages 45–65, 1993.

[273] Stanton D. W. and Rutland C. J. *Modeling Fuel Film Formation and Wall Interaction in Diesel Engines.* SAE Technical paper series, No. 960628, 1996.

[274] Stephenson P. W., Claybaker P. J. and Rutland C. J. *Modeling the Effects of Intake Generated Turbulence and Resolved Flow Structures on Combustion in DI Diesel Engines.* SAE Technical paper series, No. 960634, 1996.

[275] Stow C. D. and Stainer R. D. *The Physical Products of a Splashing Water Drop.* Journal of the Meteorological Society of Japan, Vol. 55, No. 5, pages 518–531, October 1977.

[276] Strauss T. S. Private communication, November 1995.

[277] Strauss T. S., Schweimer G. W. and Ritscher U. *Combustion in a Swirl Chamber Diesel Engine Simulation by Computation of Fluid Dynamics.* SAE Technical paper series, No. 950280, 1995.

[278] Su T. F., Farrell P. V. and Nagarajan R. T. *Nozzle Effect on High Pressure Diesel Injection.* SAE Technical paper series, No. 950083, 1995.

[279] Syed S. A. and Bracco F. V. *Further Comparison of Computed and Measured Divided-Chamber Engine Combustion.* SAE Technical paper series, No. 790247, 1979.

[280] Tabrizi B. S. *Three-Dimensional Diesel Spray Predictions in Combustion Chamber Flows.* Ph.D. thesis, Imperial College of Science, Technology and Medicine, University of London, June 1991.

[281] Takenaka Y., Aoyagi Y., Tsuji Y. and Joko I. *3D Numerical Simulation of Fuel Injection and Combustion Phenomena in DI Diesel Engines.* SAE Technical paper series, No. 890668, 1989.

[282] Takenaka Y., Kudo Y., Kakegawa T., Shiozaki T. and Aoyagi Y. *The Spray Models and Their Influence on Ignition.* SAE Technical paper series, No. 950279, 1995.

[283] Talley D. G. and Yao S. C. *A Semi-Empirical Approach to Thermal and Composition Transients inside Vaporizing Fuel Droplets.* In Twenty-First Symposium (International) on Combustion, The Combustion Institute, pages 609–616, 1986.

[284] Taylor A. M. K. P., editor. *Instrumentation for Flows with Combustion.* Academic Press, 1993.

[285] Taylor G. I. *Generation of Ripples by Wind Blowing over a Viscous Fluid.* In Scientific Papers of Sir G. I. Taylor, G. Batchelor, editor, Vol. 3, Cambridge Press, pages 244–254, 1963.

[286] Tennekes H. and Lumley J. L. *A First Course in Turbulence*, 15$^{\text{th}}$ ed. The MIT Press, Cambridge, Massachusetts, 1994.

[287] Theodorakakos A. and Bergeles G. *Predictions of the In-Cylinder Fluid Flow of a Motored Internal Combustion Engine.* Entropie, No. 174/175, pages 7–14, 1993.

[288] Theodoropoulos T. *Prediction of Three-Dimensional Engine Flow on Unstructured Meshes.* Ph.D. thesis, Imperial College of Science, Technology and Medicine, University of London, June 1990.

[289] Thompson J. F. *A Survey of Grid Generation Techniques in Computational Fluid Dynamics.* AIAA Journal, Vol. 22, pages 1505–1523, 1984.

[290] Thring M. W. and Newby M. P. *Combustion Length of Enclosed Turbulent Jet Flames.* In Fourth Symposium (International) on Combustion, The Williams & Wilkins Company, Baltimore, pages 789–796, 1953.

[291] Tong A. Y. and Sirignano W. A. *Analysis of Vaporizing Droplet with Slip, Internal Circulation and Unsteady Liquid-Phase and Quasi-Steady Gas-Phase Heat Transfer.* In ASME/JSME Thermal Engng Joint Conf. Proc., Vol. 2, pages 481–487, 1983.

[292] Travis J. R., Harlow F. H. and Amsden A. A. *Numerical Calculation of Two-Phase Flows.* Nuclear Science and Engineering, Vol. 61, pages 1–10, 1976.

[293] Varde K. S. *Spray Cone Angle and its Correlation in a High Pressure Fuel Spray.* The Canadian Journal of Chemical Engineering, Vol. 63, pages 183–187, April 1985.

[294] Varnavas C. and Assanis D. N. *A High Temperature and High Pressure Evaporation Model for the KIVA-3 Code.* SAE Technical paper series, No. 960629, 1996.

[295] Versteeg H. K. and Malalasekera W. *An Introduction to Computational Fluid Dynamics – The Finite Volume Method.* Longman Scientific & Technical, Essex, 1995.

[296] Wachters L. H. J. and Westerling N. A. J. *The Heat Transfer from a Hot Wall to Impinging Water Drops in the Spheroidal State.* Chemical Engineering Science, Vol. 21, pages 1047–1056, 1966.

[297] Wallis G. B. *One-Dimensional Two-Phase Flow.* McGraw-Hill Book Company, 1969.

[298] Wark K. *Thermodynamics*, 4^{th} ed. McGraw-Hill Book Company, Inc., New York, 1983.

[299] Warsi Z. U. A. *Conservation Form of the Navier-Stokes Equations in General Nonsteady Coordinates.* AIAA Journal, Vol. 19, pages 240–242, 1976.

[300] Watkins A. P. *Calculation of Flow and Heat Transfer in the Combustion Chamber of a Reciprocating Engine.* Master's thesis, Imperial College of Science, Technology and Medicine, University of London, 1973.

[301] Watkins A. P. *Flow and Heat Transfer in Piston/Cylinder Assemblies.* Ph.D. thesis, Imperial College of Science, Technology and Medicine, University of London, 1977.

[302] Weller H. G., Uslu S., Gosman A. D., Maly R. R., Herweg R. and Heel B. *Prediction of Combustion in Homogeneous-Charge Spark-Ignition Engines.* In International Symposium COMODIA 94, The Japan Society of Mechanical Engineers, 1994.

[303] White F. M. *Viscous Fluid Flow.* McGraw-Hill Book Company, 1974.

[304] White F. M. *Fluid Mechanics*, 2^{nd} ed. McGraw-Hill Book Company, Inc., Singapore, 1986.

[305] Wiartalla A., Bäcker H., Koss H. J. and Brüggemann D. *Influence of Spray Development and Fuel Quality on Soot Formation and Oxidation.* In Periodic Report No. 7 for the period 01.01.1992 – 30.06.1992, K.-P. Schindler, editor, IDEA, Subprogramme D6, Rheinisch Westfälische Technische Hochschule, Aachen, pages 431–467, 1992.

[306] Wiartalla A., Bäcker H., Koss H. J. and Brüggemann D. *Influence of Spray Development and Fuel Quality on Soot Formation and Oxidation.* In Eighth Periodic Report for the period 01.07.1992 – 31.12.1992, K.-P. Schindler, editor, IDEA, Subprogramme D6, Rheinisch Westfälische Technische Hochschule, Aachen, May 1993.

[307] Wierzba A. and Takayama K. *Experimental Investigation of the Aerodynamic Breakup of Liquid Drops.* AIAA Journal, Vol. 26, No. 11, pages 1329–1335, November 1988.

[308] Wilcox D. C. *Turbulence Modeling for CFD.* DCW Industries, California, 1993.

[309] Williams A. *Combustion of Sprays of Liquid Fuels.* Elek Science, London, 1976.

[310] Wong S.-C. and Lin A.-C. *Internal Temperature Distributions of Droplets Vaporizing in High-Temperature Convective Flows.* Journal of Fluid Mechanics, Vol. 237, pages 671–687, 1992.

[311] Yamamoto H. and Niimura K. *Characteristics of Fuel Sprays from Specially Shaped and Impinging Flow Nozzles.* SAE Technical paper series, No. 950082, 1995.

[312] Yarin A. L. and Weiss D. A. *Impact of Drops on Solid Surfaces: Self-Similar Capillary Waves and Splashing as a New Type of Kinematic Discontinuity.* Journal of Fluid Mechanics, Vol. 283, pages 141–173, 1995.

[313] Yuen M. C. and Chen L. W. *On Drag of Evaporating Liquid Droplets.* Combustion Science and Technology, Vol. 14, pages 147–154, 1976.

[314] Yuen M. C. and Chen L. W. *Heat-Transfer Measurements of Evaporating Liquid Droplets.* International Journal of Heat and Mass Transfer, Vol. 21, pages 537–541, 1978.

[315] Zhang Y. S. and Shi S. X. *Experimental and Numerical Study of the Diesel Fuel Spray from Pintle Nozzles.* In International Symposium COMODIA 90, pages 287–292, 1990.

[316] Zienkiewicz O. C. and Taylor R. L. *The Finite Element Method, Volume 2 – Solid and Fluid Mechanics: Dynamics and Non-Linearity*, 4^{th} ed. McGraw-Hill Book Company, 1991.

[317] Ziman H. J. *A Computer Prediction of Chemically Reacting Flows in Stirred Tanks.* Ph.D. thesis, Imperial College of Science, Technology and Medicine, University of London, 1990.